Claudia Zimmermann

Experimental investigation and computational modelling of thermal boundary layers in turbulent natural convection

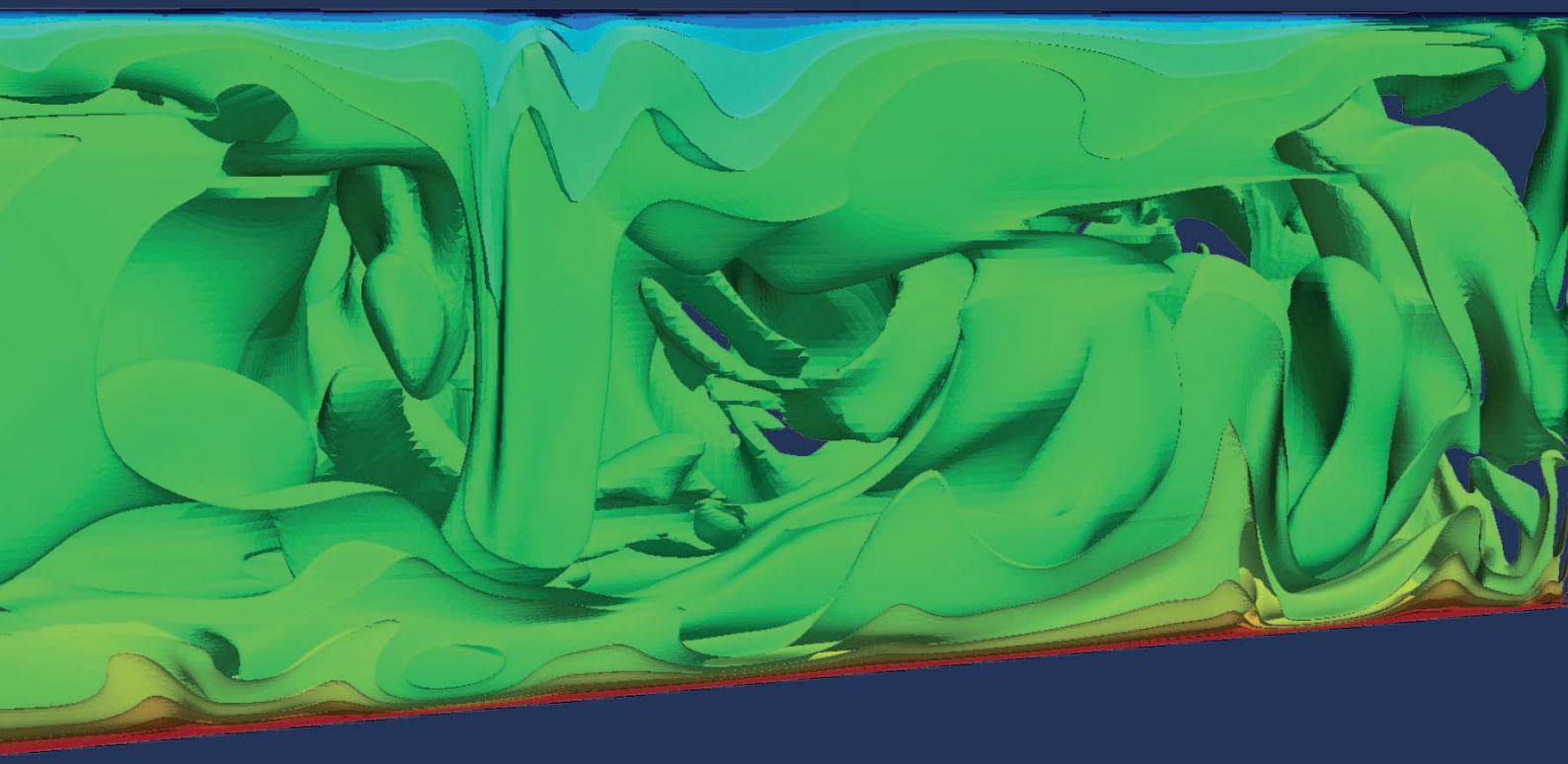

Cuvillier Verlag Göttingen
Internationaler wissenschaftlicher Fachverlag

Experimental investigation and computational
modelling of thermal boundary layers in turbulent natural convection

Experimental investigation and computational modelling of thermal boundary layers in turbulent natural convection

Vom Fachbereich Produktionstechnik
der
UNIVERSITÄT BREMEN

zur Erlangung des Grades
Doktor-Ingenieur
genehmigte

Dissertation

von
Dipl.-Math. Claudia Zimmermann

Gutachter: Prof. Dr. Claus Braxmaier
Prof. Dr.-Ing. Suad Jakirlić, Technische Universität Darmstadt

Tag der mündlichen Prüfung: 07. Mai 2015

Bibliografische Information der Deutschen Nationalbibliothek
Die Deutsche Nationalbibliothek verzeichnet diese Publikation in der Deutschen Nationalbibliographie; detaillierte bibliographische Daten sind im Internet über http://dnb.d-nb.de abrufbar.
1. Aufl. - Göttingen: Cuvillier, 2015
Zugl.: Bremen, Univ., Diss., 2015

Nonnenstieg 8, 37075 Göttingen
Telefon: 0551-54724-0
Telefax: 0551-54724-21
www.cuvillier.de

1. Auflage 2015
Gedruckt auf umweltfreundlichem, säurefreiem Papier aus nachhaltiger Forstwirtschaft.

ISBN 978-3-7369-9061-6
eISBN 978-3-7369-8061-7

To my loving parents.

"Difficulties are just things to overcome, after all."

Ernest Shackleton, 1909

Acknowledgements

First of all, I wish to express my sincere gratitude to my advisers Prof. Dr. Hans J. Rath and PD Dr.-Ing. habil. Rodion Groll for their excellent support and valuable guidance during my PhD thesis at the *Center of Applied Space Technology and Microgravity* (ZARM) at the Bremen University.

Regrettably, Prof. Dr. Hans J. Rath passed away in the year 2012, before he could see the product of both their guidance. It is my pleasure to thank both of them, but especially PD Dr.-Ing. habil. Rodion Groll, for the great opportunity to do a PhD thesis in his group and for the motivating, supportive and inspiring cooperation.

I would like to give special thanks to Prof. Dr. Claus Braxmaier, who fortunately took the place of Prof. Dr. Hans J. Rath, and Prof. Dr.-Ing. Suad Jakirlić from the *Darmstadt University of Technology* for being my supervisors and their always helpful encouragement.

A particular thanks is indebted to my fellow team members Kristofer Leach, Stephan Reichel, Fabian Fastabend and Torben Schadowski, my colleagues Diana Gaulke and Želimir Marojević as well as our students Björn Klose and Jacob Wessels for their instructive comments, inspiring scientific discussions, continuous encouragement and splendid times.

I owe a special thanks to Torben Schadowski and Rico Schultz for the skilful support during the developing and constructing periods of the experimental test cases and following test series. Further, I am grateful to the members of the mechanical workshop at the ZARM institute for the valuable assistance concerning the experimental constructions. In this connection, I would like to express many thanks to Henrik Kassai and Holger Oelze for their full motivation regarding the realisation of the experiment in the centrifuge.

Additionally, I would like to thank my colleagues Ronald Mairose and Peter Prengel for their constant willingness to help with all questions which concerned the technical equipment and other problems. I thank particularly my colleague Holger Faust who has always been a tremendous help no matter the task or circumstances.

My eternal gratitude goes to my parents Erika and Wolf-Dieter Zimmermann and my brother Dr. Stefan Zimmermann for years of patience and everlasting support during my whole education.

I would like to thank deeply Dr. Christian Malchin, Dr.-Ing. Aleksander Grah, Dr.-Ing. Stefan Schenke, Tanja Benitsch and Jana Gottermeyer for their friendly and amazing motivation and their constant and reassuring help.

This thesis was sponsored by the *Zentrale Forschungsförderung of the Bremen University* as well as by the *North-German Supercomputing Alliance* (HLRN) which provided access to their computer facilities during the whole project.

I would also like to acknowledge Dr. C. Resagk from the *Ilmenau University of Technology* for providing experimental data which made it possible to validate some of the numerical simulations.

Last but not least, I would like to thank all my colleagues at ZARM institute, who I have not mentioned by name, for an enjoyable and unforgettable time.

Zusammenfassung

Motivation

Konvektionsströmungen sind eines der fundamentalen Probleme der Strömungsmechanik. Diese Art von Strömungen spielt z. B. in der Meteorologie eine entscheidende Rolle. Ausgelöst durch Sonneneinstrahlung in der Atmosphäre können Konvektionsströmungen bedingt durch wirkende Corioliskräfte, welche durch die Erdrotation hervorgerufen werden, zu Wirbelstürmen oder Tornados heranwachsen. Daher ist das Verständnis dieser Luftströmungen gerade in Zeiten von Klimaveränderungen besonders wichtig. Auch in industriellen Anwendungen sind Konvektionsströmungen von großer Bedeutung, da sie hier als passive Kühler für elektrische Bauteile eingesetzt werden. Hierdurch sollen Fehleranfälligkeiten und mögliche Lärmquellen alternativer Kühlteile reduziert werden.

Konvektionsströmungen entstehen in einem Fluid immer durch einen massebasierten Wärmetransport zwischen zwei unterschiedlich temperierten Regionen. Wird die Bewegung des Fluids alleine durch den auf dem Wärmeunterschied basierenden Dichtegradienten im Fluid angetrieben, ohne dass eine äußere Kraft zusätzlich auf das Fluid einwirkt, so spricht man von einer *natürlichen Konvektionsströmung*. Diese Art von Konvektionsströmung im Fluid *Luft* steht im Fokus dieser Arbeit. Obwohl natürliche Konvektionsströmungen in der Vergangenheit immer wieder Gegenstand vieler theoretischer, sowie experimenteller und numerischer Untersuchungen waren, sind noch viele Fragen offen. Daher ziehen diese Strömungen immer noch ein großes wissenschaftliches Interesse auf sich.

Zielsetzung und Aufbau der Arbeit

Diese Arbeit beschäftigt sich vor allem mit der numerischen Modellierung turbulenter, natürlicher Konvektionsströmungen. Hierbei wird neben der numerischen Analyse der Strömungen in unterschiedlichen Test-Konfigurationen, eine Konfiguration zusätzlich experimentell untersucht. Die realisierten Rayleigh-Zahlen liegen dabei in einem Bereich von $2,33 \cdot 10^6 \leq \mathrm{Ra} \leq 1,58 \cdot 10^9$. Die Prandtl-Zahl liegt in allen Fällen bei $\mathrm{Pr} = 0,71$, was den untersuchten Temperaturintervallen des verwendeten Fluids, *Luft*, entspricht.

Für die numerische Modellierung der Strömungen wird für jede Test-Konfigurationen eine dreidimensionale, kompressible, transiente und turbulente *Large-Eddy Simulation* (kurz: *LES*) mittels des Open-Source Softwareprogramms *OpenFOAM®* durchgeführt. Die Bezeichnung *kompressibel* bezieht sich in diesem Fall auf Änderungen der Dichtegradi-

enten im Fluid, welche durch die vorherrschenden Temperaturunterschiede hervorgerufen werden. Sie bezieht sich nicht auf eine Spezifikation über den Begriff der *Mach-Zahl*. Innerhalb der Simulation wird ein kompressibles Turbulenz-Modell eingesetzt, da die inkompressiblen Turbulenz-Modelle den Einfluss der variierenden Dichtegradienten auf die Turbulenz-Produktion bisher noch nicht zufriedenstellend abbilden können. Als kompressibles Turbulenz-Modell wird das Modell von *Fureby* gewählt, welches auf dem so genannten *Smagorinsky Modell* beruht. Das numerische Modell verwendet keine *Boussinesq-Approximation*. Die Temperaturabhängigkeiten der Fluidgrößen werden durch das *Sutherland Modell* berücksichtigt.

Zu Beginn der Arbeit werden als erstes die theoretischen strömungsmechanischen Zusammenhänge beschrieben, die benötigt werden, um die allgemeinen Navier-Stokes Gleichungen eines kompressiblen, instationären Strömungsproblems aufzustellen. Hieraus wird dann im Folgenden das mathematische Modell herausgearbeitet, welches die betrachteten turbulenten, natürlichen Konvektionsströmungen dieser Arbeit beschreibt. In diesem Zusammenhang werden ebenfalls die wichtigsten Fluideigenschaften betrachtet.

Um eine numerische Untersuchung der Konvektionsströmungen durchführen zu können, müssen geeignete mathematische Verfahren und numerische Methoden zur Lösung des zuvor aufgestellten mathematischen Modells formuliert werden. In diesem Zusammenhang wird sowohl die numerische Methode der LES vorgestellt als auch eine analytische Betrachtung der Strömungen, vor allem im Bereich der Wandnähe, erläutert.

Anschließend folgt der Schwerpunkt der Arbeit. Dieser widmet sich der numerischen Modellierung und Analyse drei verschiedener Strömungskonfigurationen, von denen eine ebenfalls experimentell untersucht wird. In allen drei Test-Konfigurationen werden die turbulenten Konvektionsströmungen in einem abgeschlossenen, rechteckigen Container, welcher mit dem Fluid *Luft* gefüllt ist, modelliert. Das Fluid ist durch die Wände des Containers begrenzt und wird von zwei gegenüberliegenden Wänden des Containers beheizt. Die beiden Wände werden isotherm temperiert. Zwischen den beiden Wänden liegt eine konstante Temperaturdifferenz vor.

Die Wahl der zu beheizenden Wände hat einen entscheidenden Einfluss auf die sich ausbildende Strömung im Inneren des Containers. Die jeweiligen Test-Konfigurationen unterscheiden sich daher vor allem in der Orientierung der beiden beheizten Wände relativ zu dem wirkenden, äußeren Gravitationsfeld von einander. Es wurde die einfache Form eines rechteckigen Containers als Test-Konfiguration für alle drei Test-Fälle gewählt, damit mögliche auftretende Schwierigkeiten und Fehleranfälligkeiten einer komplexen Geometrie von vornherein vermieden werden. Trotzdem sind diese Test-Konfigurationen ausreichend und werden oft eingesetzt um turbulente, natürliche Konvektionsströmungen in Experiment und Simulation zu untersuchen.

Alle drei Test-Konfigurationen bauen aufeinander auf. Die erste Test-Konfiguration, mit *VerCon* im Verlauf der Arbeit gekennzeichnet, stellt die Ausgangskonfiguration einer turbulenten, natürlichen Konvektionsströmung dar. In diesem Fall werden zwei der vertikalen, gegenüberliegenden Wände isotherm beheizt. Im Gegensatz zu den anderen beiden Test-Konfigurationen stellt sich hierdurch nach einiger Zeit eine quasi-stationäre Strömung im Container ein. Bei den beiden anderen Test-Konfigurationen, mit *RayCon* und *CenCon* gekennzeichnet, werden zwei der horizontalen Wände isotherm beheizt. Diese Konfiguration wird auch als *Rayleigh-Bénard Problem* bezeichnet. Die jeweils anderen, nicht beheizten Wände weisen in jeder Test-Konfiguration unterschiedliche Randbedingungen auf, um somit mögliche Einflüsse der Randbedingungen auf das sich einstellende Strömungsprofil im Container zu untersuchen.

Da *VerCon* den Ausgangszustand für die beiden anderen Test-Konfigurationen darstellt, ist es ausschlaggebend und wichtig, zunächst die Dynamik und Eigenschaften der Strömung in dieser Konfiguration zu modellieren und zu verstehen. Mit den zu diesem Zeitpunkt gewonnenen Erkenntnissen und dem ebenfalls validierten numerischen Modell der LES werden beide anderen Konfiguration anschließend analysiert. *RayCon* unterscheidet sich von *VerCon* (abgesehen von den unterschiedlichen Längenverhältnissen) nur in der Wahl der beheizten Wände, die im Vergleich zu *VerCon* um 90° gedreht sind. Diese Drehung hat allerdings einen entscheidenden Einfluss auf das Strömungsprofil im Container.

Der Test-Fall *CenCon* wird als letzter Punkt dieser Arbeit behandelt. Zusätzlich zu der numerischen Analyse wird außerdem eine experimentelle Studie dieses Falles durchgeführt. *CenCon* ist wie *RayCon* als ein Rayleigh-Bénard Problem aufgebaut, unterscheidet sich von diesem aber durch den zusätzlichen Einfluss einer Corioliskraft, welche auf das Fluid innerhalb des Containers wirkt. Im Experiment wird die Corioliskraft durch eine gleichförmige Rotationsbewegung der Test-Konfiguration unter erhöhter Gravitationsbedingung in einer Zentrifuge erzeugt. Um dies in der Simulation zu modellieren, muss das numerische Modell der LES im Vergleich zum dem im Fall von *RayCon* verwendeten Modells modifiziert werden, um die zusätzlichen Relativbeschleunigungen auf das Fluid abbilden zu können.

Die aus dem Einfluss der Corioliskraft resultierenden zusätzlichen Relativbeschleunigungen, welche auf die künstlich erzeugte, vertikale Konvektionsströmung im Fluid wirken, sollen genau die Relativbeschleunigungen simulieren, welche in der Atmosphäre durch die Erdrotation entstehen und dort einen Wirbelsturm erzeugen können. Die experimentellen Bedingungen in der Test-Konfiguration von *CenCon* sollen somit die Strömungsverhältnisse wiedergeben, die in der Atmosphäre zu Beginn eines Hurrikans oder Wirbelsturms vorherrschen. Um solche Effekte stabil und ohne die Hilfe zusätzlicher Gebläse, wie sie in anderen Versuchsständen eingesetzt werden, erzeugen zu können, muss der Radius der

Zentrifuge entsprechend groß sein, was in der genutzten, institutseigenen Großzentrifuge der Fall ist.

In allen zu untersuchenden Konfigurationen sollen die numerischen Simulationen Aufschluss über die Verteilung der Fluideigenschaften, wie Temperatur, Geschwindigkeit oder Wärmetransport (charakterisiert durch die Nußelt-Zahl) vor allem in Nähe der beheizten Wände geben. Die numerische Abbildung dieser Verteilungen ist wichtig, um die Dynamik der Strömung sowie die Turbulenz-Produktion in dieser verstehen zu können.

Außerdem soll die numerische als auch experimentelle Studie der letzten Test-Konfiguration, *CenCon*, Erkenntnisse darüber liefern, wie sich die wirkende Corioliskraft auf die Fluideigenschaften, das Strömungsprofil und die Turbulenz-Produktion auswirkt. Hierbei wird vor allem ein stabilisierender Effekt der Corioliskraft auf die turbulente Strömung untersucht. Alle Ergebnisse der numerischen Studien werden mit gleichartigen numerischen bzw. experimentellen Analysen aus der Literatur verglichen.

Ergebnisse der Arbeit

Test-Konfiguration *VerCon*

Die numerischen Ergebnisse der ersten Test-Konfiguration *VerCon* werden mit Hilfe einer experimentellen Studie desselben Geometrie-Aufbaus aus [Tian00a], [Tian00b] validiert. Die Randbedingungen der nicht beheizten Seitenwände weisen in der experimentellen Studie eine wärmeleitende Eigenschaft auf. Diese Randbedingung lässt sich in der numerischen Simulation nicht exakt abbilden. Es werden daher vier unterschiedliche Temperaturrandbedingungen, von denen eine die wärmeleitende Randbedingung des Experimentes approximiert, getestet und gegen die Ergebnisse von [Tian00a] verglichen.

Zusätzlich zu einer dreidimensionalen Simulation wird ebenfalls eine zweidimensionale Simulation durchgeführt, um einerseits Aussagen zu dem in [Tian00a] erwähnten zweidimensionalen Strömungsprofil in der mittleren Geometrie-Ebene treffen zu können, als andererseits auch mögliche Einflüsse der Gitterauflösung beobachten zu können.

Die im Verlauf der Arbeit erzielten numerischen Ergebnisse approximieren sehr gut die Daten der experimentellen Studie unter Berücksichtigung, dass in der Simulation unterschiedliche Temperaturrandbedingungen gewählt wurden und das numerische Modell keine Boussinesq-Approximation verwendet. Die numerischen Ergebnisse zeigen dieselben Profilverläufe der untersuchten Fluideigenschaften wie im Experiment von [Tian00a]. Zwischen den Ergebnissen der drei- und zweidimensionalen Simulationen treten starke Abweichungen auf, welche sich größtenteils durch numerischen Einflüsse und durch die Wahl der Gitterauflösung erklären lassen. Weitere mögliche Einflüsse müssten in zukünftigen Studien analysiert werden, um hier andere Erklärungen gänzlich auszuschließen. Im

Vergleich zu den experimentellen Ergebnissen aus [Tian00a], [Tian00b] zeigt sich, dass die Konvektionszellen aller Simulationen in ihrer Lage verschoben und teils größer sind.

Für die Analyse des zweidimensionalen Strömungsprofils in der mittleren Geometrie-Ebene wird die vertikale Geschwindigkeitskomponente an unterschiedlichen Positionen in der Tiefe der Test-Konfiguration entlang der horizontalen Achse ausgewertet. Die verschiedenen Profile zeigen kaum Unterschiede zueinander, was auf ein zweidimensionales Strömungsprofil schließen lässt. Um diesen Aspekt genauer zu untersuchen, wird auch die transversalen Geschwindigkeitskomponente auf unterschiedlichen Höhen entlang der horizontalen Achse auf der mittleren Geometrie-Ebene analysiert. Zwar weisen die Profile der transversalen Geschwindigkeitskomponente nur kleine maximale Werte auf, aber gleichzeitig ist eine deutliche Grenzschicht in Nähe der beheizten Wände erkennbar, was als Indiz für ein dreidimensionales Strömungsprofil angesehen werden kann.

Die numerische Studie von *VerCon* zeigt, dass das gewählte Modell der LES geeignet ist, um das Strömungsprofil und dessen Eigenschaften in der gewählten Test-Konfiguration einer turbulenten natürlichen Konvektionsströmung gut abzubilden. Berücksichtigt man die unterschiedlichen Temperaturrandbedingungen an den Seitenwänden in beiden Studien, zeigen die Simulationsergebnisse, dass die dreidimensionale numerische Studie die Ergebnisse der experimentellen Studie in [Tian00a], [Tian00b] in allen untersuchten Fällen gut approximiert. Das mit *VerCon* validierte numerische Modell der LES und die in diesem Fall gewonnen Informationen werden im nächsten Schritt auf die Test-Konfiguration von *RayCon* angewandt. Diese Konfiguration einer turbulenten natürlichen Konvektion baut wie oben erwähnt direkt auf *VerCon* auf.

Test-Konfiguration *RayCon*

Um auch im Falle von *RayCon* mögliche Einflüsse der Gitterauflösung zu untersuchen, werden zwei numerische Studien mit unterschiedlichen Gitterauflösungen durchgeführt, welche sich vor allem im Bereich der beheizten Wände in ihren Auflösungen unterscheiden. Die zeitlich und räumlich gemittelten Strömungsprofile der Fluidgrößen weisen alle ein asymmetrisches Profil auf, was typisch für eine nicht-Boussinesqe, natürliche Konvektionsströmung in der Konfiguration eines Rayleigh-Bénard Problems ist. Asymmetrische Profile werden ebenfalls in anderen Studien turbulenter Rayleigh-Bénard Konvektionen in unterschiedlichen Fluiden beobachtet, wie z. B. in der Studie von [Ahlers06] oder in der Studie von [Wu1991] sowie in [Zhang1997].

Bei der Auswertung des Temperaturprofils an zwei spiegel-symmetrischen Positionen auf der mittleren Geometrie-Ebene der Test-Konfiguration treten deutliche Abweichungen der Temperaturwerte zwischen diesen beiden Positionen auf, obwohl die Symmetrie des Aufbaus ähnliche Ergebnisse erwarten ließe. Ebenfalls werden signifikante Abweichungen im Temperaturprofil zwischen beiden Gitterauflösungen deutlich. Die Untersuchung der Struk-

tur und Lage der Konvektionszellen zeigt, dass durch unterschiedliche quasi-stationäre Zustände die Reproduzierbarkeit des Temperaturprofils zerstört wird.

Die Analyse der thermalen Wandgrenzschicht durch Auswertung des dimensionslosen Temperaturprofils weist eine gute Übereinstimmung mit der analytischen Funktion von *Hölling et al.* in [Hölling05], [Hölling06] auf. Ebenfalls stimmen die Simulationsergebnisse sehr gut mit der Theorie einer Nußelt-Rayleigh-Zahl-Korrelation von [Grossmann00] für die betrachtete Prandtl Zahl überein.

Die numerischen Ergebnisse werden ebenfalls einer vergleichbaren experimentellen Studie aus [Ebert08] gegenübergestellt. Es zeigt sich, dass die numerischen Ergebnisse von den Messergebnissen in [Ebert08] deutlich abweichen. Höhere Temperaturgradienten und somit folglich höhere Nußelt-Zahlen der experimentellen Studie in [Ebert08] führen zu signifikanten Abweichungen, welche auf einen höheren Wärmefluss im Experiment schließen lassen. Diese Vermutung wird dadurch unterstützt, dass die experimentellen Ergebnisse von [Ebert08] ebenfalls stark von den Studien in [Grossmann00] und [Hölling06] abweichen, mit welchen die Ergebnisse dieser Arbeit allerdings gut übereinstimmen.

Weiterhin weisen die Temperaturprofile in [Ebert08] eine anti-symmetrische Form auf, die numerischen Ergebnisse hingegen durchgängig asymmetrische Profile. Diese asymmetrische Form ist durch nicht-Boussinesqe Effekte im Fluid begründet und wird ebenfalls in der numerischen Studie von [Horn11] nachgewiesen. Diese Studie beschäftigt sich mit dem Vergleich von Rayleigh-Bénard Konvektionen, bei denen sowohl eine Boussinesq-Approximation als auch keine Boussinesq-Approximation berücksichtigt wird.

Abschließend lässt sich für die Analyse des Test- Falles *RayCon* sagen, dass das Modell der gewählten LES ebenfalls auch in dieser Konfiguration die Dynamik der Strömung sowie die Verteilung der Fluidgrößen sehr gut abbildet. Die numerischen Ergebnisse approximieren gut die theoretischen Daten vergleichbarer analytischer Studien in [Grossmann00] und in [Hölling06]. Ein Vergleich der Ergebnisse beider Gitterauflösungen zeigt, dass es notwendig ist, vor allem die wandnahen Bereiche numerisch fein aufzulösen, um zufriedenstellende Ergebnisse erzielen zu können. Dies ist um so wichtiger, wenn in diesem Bereich keine Wandfunktion im numerischen Modell verwendet wird.

Test-Konfiguration *CenCon*

Die Erkenntnisse und Ergebnisse der beiden zuvor behandelten Test-Konfigurationen führen im Folgenden der Arbeit zu der Analyse der dritten Test-Konfiguration *CenCon*. Im Experiment als auch in der Simulation werden zwei Zustände der Test-Konfiguration berücksichtigt. Im ersten Zustand führt die Test-Konfiguration eine Rotationsbewegung aus, während sie im zweiten Zustand keine Bewegung ausführt und in diesem Zustand dem Fall *RayCon* ähnelt. Auf verschiedenen vertikalen Ebenen der Test-Konfiguration wird das zweidimensionale Strömungsprofil sowohl numerisch als auch im zugehörigen Experiment untersucht. Die erzielten Ergebnisse der numerischen Studie stimmen gut mit

denen des Experimentes überein und zeigen einhergehende Strukturen und Eigenschaften des Strömungsprofils, sowohl unter Rotation als auch im nicht-rotierenden Zustand. Im nicht-rotierenden Zustand weisen beide Ergebnisse großskalige Strukturen auf, wie sie für ein Rayleigh-Bénard Problem typisch sind.

Unter Rotation erhöht sich die Anzahl turbulenter Strukturen in beiden Studien. Ebenfalls nimmt die Anzahl von Wirbeln mit höheren Rayleigh-Zahlen in beiden Studien zu. Der Einfluss der Corioliskraft auf das Fluid erhöht somit das Auftreten irregulärer Strukturen, welche stark miteinander vermischt sind. Die auftretenden Wirbelstrukturen werden unter Rotation und mit erhöhter Rayleigh Zahl deutlich kleinsskaliger als im Fall von kleineren Rayleigh Zahlen. Eine Ausrichtung der Wirbelstrukturen an der Rotationsachse wie im Falle von kleineren Rayleigh Zahlen kann dann nicht mehr beobachtet werden.

Die zeitlich gemittelten Strömungsprofile der ausgewählten Fluidgrößen der Simulation stimmen ebenfalls mit theoretischen Annahmen gut überein. Die Ergebnisse ohne Rotation ähneln den Ergebnissen von *RayCon* aufgrund des vergleichbaren Aufbaus. Der Einfluss der wirkenden Corioliskraft und die daraus resultierende Ablenkung der Fluidpartikel kann ebenfalls gut in den Strömungsprofilen und in der Visualisierung der Konvektionszellen beobachtet werden.

Allerdings können keine erhöhten Nußelt-Zahlen unter Rotation beobachtet werden, wie es in einer ähnlichen numerischen Studie in [Horn11] der Fall ist. Die Nußelt-Zahlen sind niedriger als im nicht-rotierenden Fall und konvergieren erst mit höheren Rayleigh-Zahlen gegen die Werte des nicht-rotierenden Falles. Die Temperaturgradienten divergieren mit steigenden Rayleigh-Zahlen deutlich von denen des nicht-rotierenden Falls. Aufgrund der rotierenden Bewegung der Test-Konfiguration ist die Turbulenz-Produktion im Fluid höher. Allerdings sind die resultierenden, turbulenten Strukturen kleiner und deutlich irregulärer als im nicht-rotierenden Fall. Dieser Aspekt lässt nicht darauf schließen, dass der Wärmetransport in der Test-Konfiguration unter Rotation unbedingt höher sein muss als im nicht-rotierenden Fall.

Zusammenfassend ist zu sagen, dass die durchgeführte LES die Konvektion in der Test-Konfiguration von *CenCon* sowohl unter Rotation als auch ohne Rotation gut numerisch abbildet. Im Experiment bildet sich eine voll turbulente natürliche Konvektionsströmung aus. Die Corioliskraft wirkt sich entscheidend auf die turbulenten Strukturen in der Test-Konfiguration aus. Neben einer Verschiebung der Strukturen und einer Verzerrung der Konvektionszellen (im Vergleich zum nicht-rotierenden Zustand) erhöht die Rotationsbewegung die Turbulenz-Produktion im Fluid. Eine stabilisierende Wirkung der Corioliskraft kann nicht beobachtet werden. Die Corioliskraft führt hingegen zur Entstehung von irregulären, stark vermischten Strukturen im Fluid sowie zur Entstehung von Wirbeln. Mit zunehmender Rayleigh-Zahl erscheinen die turbulenten Strukturen kleinskaliger. Die Anzahl der sichtbaren Wirbelregionen steigt mit zunehmender Rayleigh-Zahl an.

Abschließende Bemerkungen und Ausblick

Alle durchgeführten LES Studien dieser Arbeit eignen sich sehr gut, um die zu untersuchenden Strömungen in der jeweiligen Test-Konfiguration numerisch abzubilden. Es treten in jeder Test-Konfiguration asymmetrische Profile der analysierten Fluideigenschaften auf, welche durch nicht-Boussinesqe Effekte im Fluid verursacht werden. Alle untersuchten Strömungsprofile approximieren gut die experimentellen, analytischen und numerischen Vergleichsdaten.

Die Corioliskraft und die damit auftretenden zusätzlichen Relativbeschleunigungen im Test-Fall *CenCon* haben einen entscheidenden Einfluss auf das sich entwickelnde Strömungsprofil und die Turbulenzproduktion. Allerdings kann kein stabilisierender Effekt der Corioliskraft auf die turbulenten Strukturen erkannt werden. Die Corioliskraft führt vielmehr zu stark vermischten, irregulären Strukturen und Wirbeln.

Es ist bemerkenswert, dass die Ergebnisse des Temperaturprofils von *RayCon* die Reproduzierbarkeit und damit auch die Vergleichbarkeit der Ergebnisse statistischer Analysen von Fluideigenschaften in Frage stellen. Obwohl die numerischen Ergebnisse über hinreichend große Zeitintervalle gemittelt werden, treten zwischen den Ergebnissen spiegelsymmetrischer Auswertungspositionen deutliche Abweichungen in den Profilwerten auf, welche sich auf unterschiedliche quasi-stationäre Zustände der Konvektionszellen im Container zurückführen lassen. Diese quasi-stationäre Zustände zerstören die Reproduzierbarkeit der numerischen Temperaturprofile.

In zukünftigen Studien wäre sicherlich ein Vergleich zwischen dem in dieser Arbeit gewählten Turbulenz-Modell von Fureby und einem kompressiblen, dynamischen Smagorinsky-Modell von Interesse. Weiterhin wäre der Einfluss der Wahl des Feinstrukturmodells der thermalen Diffusivität von Bedeutung. Im Hinblick auf *CenCon* und den Experimentaufbau in der Zentrifuge wären hydrodynamische Stabilitätsuntersuchungen, wie z. B. der Einfluss von kleineren Störpartikeln, welche ins Fluid eingebracht werden, wichtige Aspekte. Neben der Durchführung einer lokalen Temperaturmessung sowie einer Mikro-LDA, wären eine Modifikation der Längenverhältnisse der Test-Konfiguration und eine Variation der relativen Rotationsbeschleunigungen ebenfalls spannende und entscheidende Aspekte für eine weitergehende Analyse der Konvektionsströmung in dieser Konfiguration.

Abstract

Convective flow is one of the fundamental problems in fluid dynamics. Many theoretical, experimental and numerical investigations have been performed in the past, but still these flows are not quite understood and play a decisive role. The understanding of these flows is of great interest in many areas, as, for example, in meteorology where they appear as wind caused by the solar radiation in the Earth's atmosphere and can result in storms or even hurricanes. Moreover, these flows are of great importance in industrial applications where they are used as passive cooling systems instead of fans to reduce possible noise exposures and technical failures.

Convective flow is always generated as a result of a heat flux between different heated regions in a fluid. If the convection is only driven by local density changes inside the fluid without any other acting influences, the flow is called a *natural convection*.

The main focus of this thesis lies on the numerical investigation of a turbulent natural convection in air analysed in three different test case configurations. The natural convection is realised in each test case between two faced walls which are heated isothermally but with a constant temperature difference between them. The heat transfer inside the fluid is characterised by increasing temperature gradients near the heated walls and a dominating convective mass exchange in the bulk region. Turbulent shear layers arise in the fluid which increase the intensity of turbulence. The dynamic of the flow, the turbulence production and the behaviour of the fundamental fluid properties are the main aspects of the investigations in this thesis.

For each test case a compressible, 3-dimensional, transient, turbulent Large-Eddy Simulation is performed with help of the open-source software package *OpenFOAM®* . As turbulence model a compressible coupled model without a Boussinesq-approximation is chosen considering the mentioned density changes inside the fluid.

Outstanding is the third test case. In this special case the influence of an impressed Coriolis force on the unsteady turbulent structures inside the fluid should be observed in a numerical as well as in an experimental study. In the experimental study, the same conditions as in the atmosphere in the beginning of a twister or hurricane should be realised by a rotational movement of the test case in a large scale centrifuge. The numerical results of this thesis are validated to the data of comparable experimental test case studies as well as theoretical and numerical data from the literature.

Contents

Nomenclature

Roman Symbols

Symbol	Description	Unit
a	speed of sound	m/s
$\boldsymbol{a}$	acceleration vector	m/s^2
$\boldsymbol{a}_c$	Coriolis acceleration vector	m/s^2
a_r, a_φ	components of an acceleration vector	m/s^2
$\boldsymbol{a}_P$	centripetal acceleration vector	m/s^2
$\boldsymbol{a}_Z$	centrifugal acceleration vector	m/s^2
$\boldsymbol{b}$	body force vector	N
c_e	turbulence model coefficient, $c_e = 1.046$	
c_k	turbulence model coefficient, $c_k = 0.02$	
c_p	specific heat at a constant volume	J/(kgK)
c_{p_0}	free stream specific heat constant	J/(kgK)
c_v	specific heat at a constant pressure	J/(kgK)
e	internal energy per unit mass	m^2/s^2
e_0	internal energy per unit mass of a fluid particle at rest	m^2/s^2
$\boldsymbol{e}_i$	unit vector of system S_I	
$\boldsymbol{e}'_i$	unit vector of system S'_R	
$f, \tilde{f}$	arbitrary function	
g	arbitrary function	
$\boldsymbol{g}$	gravitational acceleration vector	m/s^2
h	enthalpy per unit mass	m^2/s^2
h_0	enthalpy per unit mass of a fluid particle at rest	m^2/s^2
k	kinetic energy per unit mass	m^2/s^2

$\boldsymbol{k}$	vector of body forces	N
k	coefficient of heat transmission	$\mathrm{W/(Km^2)}$
k_{sgs}	subgrid scale kinetic energy	$\mathrm{m^2/s^2}$
k_L	wave number	1/m
l_{sgs}	subgrid length scale	m
m	mass	kg
m	fluid particle	
n	revolutions per minute	rev./min
n	amount of substance of gas	mol
$\boldsymbol{n}$	normal vector	
$n_{\mathrm{Pr}}, n_{\rho\beta}, n_{\rho\lambda}, n_c$	model coefficients	
p	pressure	Pa
$\bar{p}$	mechanical pressure	Pa
$\boldsymbol{p}$	direction vector	
p_{rgh}	dynamic pressure	Pa
q_w	wall heat flux density	$\mathrm{W/m^2}$
$\dot{\boldsymbol{q}}$	heat flux density vector	$\mathrm{W/m^2}$
q_{sgs}	subgrid velocity scale	m/s
$\boldsymbol{r}$,$\boldsymbol{R}$	radius vector	m
$\boldsymbol{r}_P$, $\boldsymbol{r}_A$, $\boldsymbol{r}_{AP}$	position vectors	m
r_{ref}	reference value	
s	entropy	J/K
t	time	s
t_{k_L}	Kolmogorov time scale	s
$\boldsymbol{u}$	velocity vector	m/s
u_x, u_y, u_z	components of velocity vector with respect to a system S	m/s
$\boldsymbol{u}_{k_L}$	Kolmogorov velocity scale vector	m/s
$u_{q,\mathrm{ref}}$	reference velocity	m/s
$\boldsymbol{u}_{BL}, \boldsymbol{U}_{BL}$	reference velocity vector	m/s

$\boldsymbol{u}_{\tau_w}$	wall shear stress velocity vector	m/s
$\left.\frac{\partial u}{\partial y}\right\|_{\tilde{w}=0}$	velocity gradient at the heated wall	1/s
v	specific volume	m^3/kg
v	eigenvalue	
$\boldsymbol{v}$	velocity vector	m/s
w_j	weighted coefficient	
$\mathbf{x}$	positions vector	
x, y, z	Cartesian coordinates with respect to a system S_I	
x', y', z'	Cartesian coordinates with respect to a system S'_R	
y_{w1}	first cell midpoint in vertical direction from the heated wall	m
A	matrix	
C	modelling coefficient	
C_{ch}	Churchill constant	
$C^+, C_u^+, C_\theta^+, C_\Theta^\times$	modelling constants	
C_{ij}	Clark tensor	m^2/s^2
C_S	Smagorinsky constant	
C_1	Sutherland coefficient	$kg/(K^{0.5}ms)$
D	height of the experimental or computational setup	m
D	modelling coefficient	
E_{tot}	total energy per unit volume	J/m^3
$\boldsymbol{F}$	force vector	N
F_w	flow resistance force	N
F_C	Coriolis force	N
F	quadratic function	
H	height of the experimental or computational setup	m

G	filter function	
$\boldsymbol{I}$	vector of momentum	kg m/s
$\boldsymbol{I}$	Identity tensor	
I_{eff}	effective electrical current	A
J	Jacobian matrix	
K	total energy	J
L	length of the experimental setup	m
	or computational setup	
L_{ij}	Leonard tensor	m^2/s^2
M	molecular weight	kg/mol
M	set of fluid particles	
M	decomposition matrix	
N	decomposition matrix	
Q	source term	
Q	criterion to identify vortex regions	Hz^2
Q	heat per unit volume	J/m^3
$\dot{Q}$	heat flux	W
R	electrical resistance	Ω
R_{ij}	Reynolds tensor	m^2/s^2
R_0	universal gas constant, $R_0 = 8.3144621$	$\text{J}/(\text{K mol})$
P	pre - conditioning matrix	
P_e	electrical power rating	W
P_t	temperature power rating	W
S	surface of a control volume	
S_{ij}	strain rate tensor tensor	1/s
S^*_{ij}	deviatoric part of the strain rate tensor	1/s
S_I	inertial system	
S'_R	relative to S_I rotated system	
T	temperature	K
T_{centre}	temperature in the center	K

	of the setup	
T_{cold}	temperature at the cold wall	K
T_f	temperature in the fluid	K
T_{hot}	temperature at the hot wall	K
T_{low}	temperature at the lower wall	K
T_{mean}	mean temperature between temperatured walls	K
T_q	reference temperature	K
T_{ref}	reference temperature	K
T_{up}	temperature at the upper wall	K
T_w	temperature at the wall	K
T_S	Sutherland Temperature	K
T_{τ_w}	friction temperature	K
T_0	free stream temperature	K
T_∞	temperature measured in great distance from the wall	K
$\left.\frac{\partial T}{\partial y}\right\|_{\tilde{w}=0}$	temperature gradient at the heated wall	K/m
$\bar{U}$	mean velocity averaged over a time period	m/s
U_{eff}	effective voltage	V
V	volume	m^3
V_A	mole volume	m^3/mol
W	width of the experimental or computational setup	m
W	work per unit volume	J/m^3

Greek Symbols

Symbol	Description	Unit
α, φ	angle	°
α	thermal diffusivity	kg/(ms)
α_{eff}	effective thermal diffusivity	kg/(ms)

α_i	constructing parameter	
α_{sgs}	subgrid scale thermal diffusivity	kg/(ms)
α_{t}^*	time- and area - averaged turbulent thermal diffusivity coefficient	kg/(ms)
$\tilde{\alpha}$	heat transfer coefficient	$\text{W/(Km}^2\text{)}$
β	thermal expansions coefficient	1/K
β_i	constructing parameter	
δ	thickness of a material	m
δ_{ij}	Kronecker Delta	
$\delta_{BL,u}$	velocity boundary layer thickness	m
$\delta_T, \delta_{BL,T}$	temperature boundary layer thickness	m
γ	modelling factor	
ϵ	convergence error	
ϵ_t	turbulence dissipation rate	m^2/s^3
ϵ_τ	truncation error	
η_{k_L}	Kolmogorov scale	m
κ	thermal diffusivity coefficient	m^2/s
κ	Karman constant, $\kappa = 0.41$	
κ_θ	modelling constant	
λ	thermal conductivity	W/(Km)
λ	interpolation factor	
λ	eigenvalue	
μ	dynamic viscosity	kg/(ms)
μ_{eff}	effective dynamic viscosity	kg/(ms)
μ_{ref}	reference dynamic viscosity	kg/(ms)
μ_{sgs}	subgrid scale dynamic viscosity	kg/(ms)
μ_0	free stream dynamic viscosity	kg/(ms)
ν	kinematic viscosity	m^2/s
ν_{eff}	effective kinematic viscosity	m^2/s
ν_{sgs}	subgrid scale kinematic viscosity	m^2/s

ν_0	free stream kinematic viscosity	m^2/s
ξ	material vector of a fluid particle	
π	mathematical number, $\pi = 3.14159\ldots$	
ρ	specific density	kg/m^3
ρ_0	free stream density	kg/m^3
$\boldsymbol{\rho}$	residuum vector	
σ_{rms}	standard deviation	
τ_{ij}	deformation tensor	$kg/(ms^2)$
τ_{ij}^{a}	anisotropic part of the deformation tensor	$kg/(ms^2)$
$\tau_{ij}^{\mathrm{a,mod}}$	modelled anisotropic part of the deformation tensor	$kg/(ms^2)$
τ_w	wall shear stress	$kg/(ms^2)$
$\tau_{w,t}$	turbulent part of the wall shear stress $\boldsymbol{\tau}_w$	$kg/(ms^2)$
φ	arbitrary continuous function	
$\boldsymbol{\omega}$	angular velocity vector	rad/s
$\tilde{\boldsymbol{\omega}}$	vorticity	1/s
Δ	grid filter length	m
$\Delta_{\mathrm{hot/cold}}$	temperature change across the hot/cold boundary layer	K
ΔT	temperature difference between temperatured walls	K
Γ	diffusion coefficient	$kg/(ms)$
Φ_{ref}	reference value	
Ω	control volume	m^3
Ω_{ij}	rotational tensor	1/s
Ω_0	control volume at time t_0	m^3
$\partial\Omega$	boundary of control volume Ω	
Ψ	arbitrary space-time variable	

Dimensionless numbers

Symbol	Description
Co	Courant number
Ec	Eckert number
Gr	Grashof number
Ma	Mach number
Nu	Nusselt number
Pe	Péclet number
Ra	Rayleigh number
$\mathrm{Ra}_{\mathrm{crit}}$	critical Rayleigh number
Re	Reynolds number
$\mathrm{Re}_{\mathrm{crit}}$	critical Reynolds number
Pr	Prandtl number
$\mathrm{Pr}_{\mathrm{sgs}}$	turbulent Prandtl number
St	Stokes number
T^*, T^+	non - dimensional temperature
$u^+, u^\times, \tilde{u}^+$	non-dimensional velocity
x^+	non - dimensional length
$y^+, y^*, y^\times$	non - dimensional length
$\eta^+, \tilde{\eta}^+$	non - dimensional length
θ^+, $\theta^\times$	non-dimensional temperature
$\tau^+_{w,t}$	non - dimensional wall shear stress
Γ	aspect ratio
Θ^*	non-dimensional temperature

Abbreviations

Symbol	Description
BDS	backward differencing scheme
CDS	central differencing scheme
CV	control volume

DNS	Direct Numerical Simulation
FDM	finite difference method
FDS	forward differencing scheme
FEM	finite element method
FVM	finite volume method
LES	Large - Eddy Simulation
NOB	Non - Oberbeck - Boussinesq convection
OB	Oberbeck - Boussinesq convection
RANS	Reynolds-Averaged-Navier - Stokes Simulation
RB	Rayleigh-Bénard
UDS	upwind differencing scheme
tol	tolerance value
2D	two - dimensional
3D	three - dimensional

Subscripts

Symbol	Description
eff	effective quantity
sgs	subgrid scale
t	turbulent
w	lateral wall
$\tilde{w}$	heated wall

Sets

Symbol	Description
$\mathbb{R}$	set of real numbers

1. Introduction

1.1. Motivation

Convective flows play an important role in many different areas, as, for example, in geology where these flows arise in the Earth's mantle causing a movement of the continental plates, the so-called *continental drift*. Convective flows are also used, to mention an example from another area, in form of passive cooling systems in industrial applications to reduce technical failures. Actually in everyday life, one can observe a convective flow, for example, during cooking a soup. Regarding a possible climate change, the understanding of these flows is especially important, because appearing as wind in the atmosphere they can result in a twister or even hurricane due to a Coriolis acceleration of the Earth's rotation.

If the convection is only driven by local density changes resulting from temperature differences inside the fluid, it is called a *natural convection*. In case of an additionally acting mechanical force, e. g. blower or pump, which drives the convection from outside, one would call it a *forced convection*.

1.2. Thesis purpose and outline

The main aspect of this thesis is the numerical investigation of a turbulent natural convection in *air* which is generated in different test case configurations between two opposite, isothermally heated walls. The focus of the investigation lies, beside the numerical modelling, on the understanding of the flow dynamic, the turbulence production and the fundamental fluid properties. Therefore, a compressible, 3-dimensional, transient, turbulent Large-Eddy Simulation (short: *LES*) without a Boussinesq-approximation is performed with help of the open-source software package *OpenFOAM®*. "Compressible" means in this case that density changes which are caused in the fluid by temperature differences are considered by the numerical model. "Compressible" does not include a definition in terms of the Mach number.

A compressible turbulence model is chosen, because, so far, incompressible models are not able to reflect fully the influence of varying density gradients on the turbulence production. Further, a compressible model is especially in one test case relevant due to an

intensified gravitational force field in this case. As turbulence model, the compressible model of *Fureby* is chosen which is a modification of the so called *Smagorinsky model* for compressible flows. Temperature dependent fluid properties are considered in all simulations by the *Sutherland model*.

The turbulent natural convective flows are analysed in three different test case configurations. Two of these test cases are numerically analysed (*VerCon* and *RayCon*) while the third one (*CenCon*) is investigated in an experimental study. The flow is limited in all setups by an enclosed rectangular container whose aspect ratios vary in each test case configuration. The container properties are chosen simplified to reduce especially complexity aspects. Nevertheless, they are still sufficient and commonly used regarding the investigation of fluid properties and flow structures in a turbulent natural convection.

The choice of the heated walls varies in all setups. The orientation of these walls relative to the effective direction of gravity effects significantly the profile of the main flow field inside the test case. The first setup (marked by *VerCon*) is made of a rectangular container where two of the vertical walls are heated isothermally, while both other cases (*RayCon* and *CenCon*) consist of a rectangular container where both horizontal walls are heated isothermally. Lateral walls of each setup are designed with different boundary conditions to analyse possible influences on the flow field inside the container.

The configurations of *RayCon* and *CenCon* are also called a *Rayleigh-Bénard problem* (short: RB problem). In contrast to *RayCon*, the setup of *CenCon* is additionally influenced by a Coriolis acceleration. The effect of the Coriolis acceleration is realised by a rotational movement of the test case under hyper-gravity in a large-scale centrifuge. While *CenCon* is rotating uniformly, possible influences on the flow structures, turbulence production and fluid properties due to the Coriolis acceleration should be investigated. All test cases are based on each other. The gained information and results of both first test cases, *VerCon* and *RayCon*, lead to the analyse of the third test case, *CenCon*.

The first main aspect in this thesis is the numerical investigation and understanding of the test cases *VerCon* and *RayCon*. Therefore, several fluid properties are estimated between the heated walls in each test case. Especially in the thermal boundary layer near these heated walls, the temperature as well as the velocity and Nusselt number profiles are important in order to understand the structure and dynamic of the flow and its turbulence production. The second main aspect is the numerical as well as experimental analysis of the influence of the Coriolis acceleration on the RB problem in the setup of *CenCon*.

Due to the vertical orientation of the heated walls in *VerCon*, the flow reaches a quasi-steady state after a while. This configuration of a turbulent natural convection represents the basis for both other test cases. Hence, it is very important and essential to study and understand first the flow dynamic and the behaviour of the fluid properties in this con-

figuration. The gained information and the at this point also validated numerical model of the chosen LES is required to analyse and understand both other cases.

The setup of *RayCon* is based directly on *VerCon* with its by 90° rotated heated walls. The setup of *CenCon* results from *RayCon* in its layout and in the realised flow dynamic as well as in the behaviour of the fluid properties regarding the state without a rotational movement of the test case. But, in contrast to *RayCon*, a rotation is additionally impressed on the setup which generates the additionally acting Coriolis acceleration. This realised relative acceleration affects the generated vertical convective flow inside the RB cell of *CenCon*. The conditions in the rotating setup of *CenCon* should simulate the atmospheric conditions in the beginning of a twister or hurricane. To generate these effects in the experimental setup without the help of additional air blowers, as they are used in other experimental setups, the radius of the centrifuge has to be sufficiently large, which is fulfilled in our case. The effect of the Coriolis acceleration is realised in the simulation by an implemented modified governing equation system (compared to the one of *RayCon*) which considers the additionally acceleration. *CenCon* is analysed at the end of this thesis on the basis of the beforehand obtained results of *RayCon*.

The numerical results of this thesis are validated to data of comparable experimental test cases as well as theoretical and numerical data from the literature. The realised Rayleigh-numbers lie in the range of $2.33 \times 10^6 \leq \mathrm{Ra} \leq 1.58 \times 10^9$. For *VerCon* it lies at $\mathrm{Ra} = 1.58 \times 10^9$, for *RayCon* between $6.16 \times 10^7 \leq \mathrm{Ra} \leq 4.1 \times 10^8$ and for *CenCon* between $2.33 \times 10^6 \leq \mathrm{Ra} \leq 4.32 \times 10^7$. The Prandtl number stays in each case at $\mathrm{Pr} = 0.71$ which represents the used fluid, air, in the chosen temperature intervals.

In the beginning of this thesis, the Navier-Stokes equations of a general compressible unsteady flow problem are presented. Outgoing from these equations, the governing equation system is derived which describes the observed turbulent natural convection. Subsequently, the computational methods and the mathematical model of the LES, which are used to solve the afore stated equations, are discussed. Before the particular test case configurations are explained in detail and the obtained results are demonstrated as main aspect of this thesis, the required thermodynamic properties of a turbulent natural convection are presented.

1.3. Related and previous studies

In the beginning of the 20th century, the French physicist *Henri Claude Bénard* (1874 - 1939) and the English physicist *Lord Rayleigh* (1842 - 1919) (former *John William Strutt*), performed the first analyses of a natural convection between two, horizontal, heated walls (see [Bénard1900], [Rayleigh1916]). This configuration of a natural convection is also called *Rayleigh-Bénard problem* named after both scientists. Since then, numerous studies in-

vestigating convective flow in different configurations were performed in an experimental, as well as a theoretical and a numerical way.

[Dafa'Alla1996] and [Betts00], for example, perform an experimental investigation of a low-level turbulent natural convection in air in a rectangular container with vertical heated walls and an aspect ratio of $\Gamma = 28.6$. While in the study of [Dafa'Alla1996] a Rayleigh number of $\mathrm{Ra} = 0.86 \times 10^6$ is realised, the study of [Betts00] investigates a Rayleigh number of $\mathrm{Ra} = 1.43 \times 10^6$ and one of $\mathrm{Ra} = 0.86 \times 10^6$. The main aspects of both studies lie on the temperature as well as velocity profiles between the heated walls. Based on the experimental study of [Dafa'Alla1996], [Versteegh1998] implements a *Direct Numerical Simulation* (short: DNS) for the same setup and for Rayleigh numbers between $5.4 \times 10^5 \leq \mathrm{Ra} \leq 5 \times 10^6$ and obtains an adequate approximation of the experimental results.

Furthermore, [Ziai1983], [Mergui1993], [Lankhorst1991] and [Tian00a], [Tian00b] analyse each a natural convection of a low-level turbulence in an experimental setup for different Rayleigh numbers. In [Tian00a], [Tian00b] a Rayleigh number of $\mathrm{Ra} = 1.58 \times 10^9$ is realised and in [Mergui1993] one of $\mathrm{Ra} = 1.7 \times 10^9$, while [Ziai1983] and [Lankhorst1991] investigate smaller values of $\mathrm{Ra} = 5 \times 10^8$ and $\mathrm{Ra} = 3.9 \times 10^8$. All studies examine mainly the profiles of the fluid properties between the heated walls in the vertical midplane, e. g. temperature and Nusselt number profiles. The experimental data in [Tian00a], [Tian00b] is used in the following to validate the numerical data of test case *VerCon* in chapter 5.

The opposite configuration of a natural convection between horizontal, heated walls, a Rayleigh-Bénard problem, was also the subject of many numerical as well as experimental studies in the last decade of years. One of the experimental studies can be found in [Funfschilling04] which investigates experimentally the plume motion and large-scale circulation in a methanol-filled cylindrical RB convection for Rayleigh numbers between $7 \times 10^7 \leq \mathrm{Ra} \leq 3 \times 10^9$ and a Prandtl number of $\mathrm{Pr} = 6$. One of the main goals of his study is the understanding of the periodically plume emission in the system. In [Maystrenko07] the boundary layer thickness in a RB convection in air in dependence on the fluid properties skewness and kurtosis is analysed. The convection cell has an aspect ratio of $\Gamma_x = 5$, $\Gamma_y = 1$ and the investigated Rayleigh numbers are $6 \times 10^7 \leq \mathrm{Ra} \leq 6 \times 10^8$.

Complementary to the previously mentioned study of [Maystrenko07], [Ebert08] measures in the same setup the temperature distribution and local heat flux density in air for Rayleigh numbers between $6.16 \times 10^7 \leq \mathrm{Ra} \leq 6.02 \times 10^8$ to obtain information about the local and global heat flux distribution mainly in the regions near the heated walls. In [Weiss11], a RB problem in a water-filled cylindrical cell with an aspect ratio of $\Gamma = 1/2$ is analysed for Rayleigh numbers between $2 \times 10^8 \leq \mathrm{Ra} \leq 1 \times 10^{11}$ as to the measurement of the Nusselt number and large scale circulation structures.

An example for a numerical study of a RB problem can be found in [Seiter1995], who models with help of a LES as well as a DNS a convective flow in air and in sodium generated between infinite horizontal channels. The Rayleigh numbers in this study lie at $\mathrm{Ra} = 2.5 \times 10^6$ and $\mathrm{Ra} = 10^7$. [Seiter1995] discusses the analysis of flow structures in the channels as well as the statistical evaluation of fluid properties for small Prandtl numbers. [Reeuwijk08a] and [Reeuwijk08b] investigate, with help of a DNS and periodic boundary conditions, the kinematic boundary layer and the heat flux in a RB configuration for an aspect ratio of $\Gamma = 4$, different Rayleigh numbers between $10^5 \leq \mathrm{Ra} \leq 10^8$ and a Prandtl number of $\mathrm{Pr} = 1$.

Shiskina et al. concentrate in [Shishkina06, Shishkina08, Shishkina09] mainly on three-dimensional, time-dependent DNS and well-resolved LES of turbulent RB problems in air and water using a Boussinesq-approximation. The test case consists of a wide cylindrical container. The realised Rayleigh numbers lie between $10^5 \leq \mathrm{Ra} \leq 10^{10}$. The main goals of these studies are the investigation of the thermal dissipation rate and the interaction of thermal plumes.

Similar to the previous studies, the study in [Silano10] performs in his study a DNS, using a Boussinesq-approximation, of a cylindrical cell with an aspect ratio of $\Gamma = 1/2$ for a range of Prandtl numbers between $10^{-1} \leq \mathrm{Pr} \leq 10^4$ as well as Rayleigh numbers between $10^5 \leq \mathrm{Ra} \leq 10^9$. The main goal of this study lies in the understanding of Nusselt-Reynolds-number dependencies in relation to the chosen Rayleigh and Prandtl numbers. Furthermore, *van der Poel et al.* investigate in [Poel13] differences between a 2- and a 3-dimensional RB convection in a cylindrical cell with varying aspect ratios for Prandtl numbers of $\mathrm{Pr} = 4.38$ and $\mathrm{Pr} = 0.7$ up to a Rayleigh number of $\mathrm{Ra} = 10^8$. Therefore, numerical results are compared to experimental data. The main aspect in this study are the Nu(Ra)- and also the Nu(Pr)-dependencies. Similarities between the 2D- and 3D-convection can be found for some parameter ranges. But also large differences are revealed, mainly for the case of $\mathrm{Pr} < 1$ and low aspect ratios, which have a significant effect on the Nusselt and Reynolds number distribution in the 2D-convection.

Complementary to the previously mentioned studies, [Ahlers06] searches experimentally and theoretically for differences between a convection with and without a Boussinesq-approximation. A natural convection for which a Boussinesq-approximation is assumed is called Oberbeck-Boussinesq (short: OB) convection, while a natural convection without a Boussinesq-approximation is called non-Oberbeck-Boussinesq (short: NOB) convection. The realised Rayleigh numbers lie in [Ahlers06] between $10^8 \leq \mathrm{Ra} \leq 10^{11}$. The cylindrical cell has an aspect ratio of $\Gamma \approx 1$. The study investigates the convection in water and in glycerol.

Considering an analytical formulation describing a natural convection, the possibly first approach to a formulated law of the turbulent boundary layer in the near wall region in a

natural convection can be found in [George1979]. For the laminar region of the boundary layer an analytical function can be found in [Pohlhausen1921]. *Pohlhausen* states in his study a solution for a flow over an infinitely long plate.

In the last years, the studies of [Hölling05, Hölling06] discuss analytical functions describing the turbulent thermal and velocity boundary layer in a natural convective flow for different ranges of Rayleigh as well as Prandtl numbers. The theory is valid for a configuration with vertical or for one with horizontal, heated walls. [Grossmann00, Grossmann01] describe in their studies possible Rayleigh-Nusselt-number-dependencies of strong RB problems valid in different regimes in the Rayleigh number versus Prandtl number phase space. The resulting power laws and defined regimes are discussed and updated in the study of [Stevens13].

Regarding studies which deal also, as it is the case in this thesis, with a Coriolis force influence, the studies of [Brown08a] and [Brown08b] can be mentioned. In both studies measurements of large-scale circulations are performed in several water-filled cylindrical convection cells of an aspect ratio of $\Gamma = 1$ and for $\mathrm{Pr} = 4.38$. In [Brown08a] the analysed Rayleigh numbers lie between $3 \times 10^8 \leq \mathrm{Ra} \leq 10^{11}$, while they lie at $\mathrm{Ra} \geq 10^{10}$ in the second study [Brown08b]. The experiments in [Brown08a] investigate the angular orientation of a turbulent large scale circulation as a function of time. In [Brown08b] the influence of a Coriolis force (caused by the Earth's rotation) on the development of large-scale structures is investigated over several days periods. The results show clockwise and counter-clockwise revolutions of the circulation plane orientation.

In the study of [Horn11], on the one hand, a three-dimensional DNS of a NOB convection is compared to one of an OB convection in a cylindrical cell of an aspect ratio of $\Gamma = 1$. The cell is filled with water ($\mathrm{Pr} = 4.38$) and the investigated Rayleigh number lies at $\mathrm{Ra} = 10^8$. The results show an asymmetrical temperature profile in the NOB convection as well as higher mean temperatures in the geometry centre than in case of the OB convection. On the other hand, an additional influence of a rotational movement of the NOB convection is analysed. The rotational movement of the cell leads to higher Nusselt numbers compared to a non-rotating cell.

To model mathematically a turbulent natural convection in a numerical simulation, different approaches can be found in the literature. The American meteorologist *Joseph Smagorinsky* was the first who formulated a turbulence model based on a formulation of the eddy viscosity, see [Smagorinsky1963]. The model uses also the assumption of a Boussinesq-approximation. The Smagorinsky model is widely used in LES methods and it is also the basis for several other turbulence models, as in [Germano1991, Lilly1992]. Both studies modify the Smagorinsky model to a dynamic version. In the study of [Fureby1996] a modified version of the Smagorinsky model is formulated for compressible flows. The study of [Deardorff1973] discusses the choice of the grid filter length in connection with

the Smagorinsky model concerning the use of subgrid transport equations for atmospheric turbulence.

To obtain a successful performance of a LES, the turbulent Prandtl number has to be chosen carefully in the turbulence model. Therefore, several studies on this topic can be found. For example, a suggestion of a turbulent Prandtl number in combination with an unstructured grid can be found in [Okong'O 00] or also in [Kosović02, Sergent03, Erlebacher1992] who develop new subgrid scale models. In [Kosović02, Erlebacher1992] turbulence models are presented which can be applied on compressible flows without using a Boussinesq-approximation. Furthermore, [Kenjereš1999, Sergent03] demonstrate turbulence models which use additional force terms to describe a turbulent natural convection.

In comparison to the mentioned related studies, in this thesis a compressible well-resolved LES is performed to model numerically a turbulent natural convection in air in three different test case setups. In each test case a different Rayleigh number range is analysed. In one test case, the natural convection is generated between two vertical, heated walls. In both other test cases a RB convection is realised (two horizontal, heated walls). The chosen computational grid of each test case is high-resolved, especially in the near wall regions. But all used computational grids consists of a smaller number of cells than it would be the case in a DNS.

The used compressible turbulence model is based on the mentioned model of Fureby in [Fureby1996]. Compared to most of the above related studies, the mathematical model of this thesis deals with the assumption of a non-Boussinesq fluid to investigate possible differences to the studies which consider a Boussinesq-approximation. Outstanding is the third test case, in which the influence of a Coriolis force on the development of turbulent as well as large-scale structures inside the fluid is analysed numerically as well as in an experimental study. The influence of the Coriolis acceleration is realised in the experiment by a rotational movement of the test case in a large scale centrifuge.

Note that some of the presented contents of this thesis are also discussed in extracts in the articles [Zimmermann12], [Zimmermann14a], [Zimmermann14b] and [Zimmermann15].

1.4. Conservation of mass

To describe a flow problem by a mathematical model, the flow properties and its movement have to be formulated by appropriate equations. These equations have to determine the *kinematic* as well as *transport* and *thermodynamic* properties of the flow. The first mentioned group includes properties of the flow field, e. g. velocity and angular velocity, while the two other mentioned groups describe properties of the fluid itself, e. g. frictional tensions or thermal diffusion and pressure, density or temperature. Next to the

description of the continuity motion also the thermodynamic properties like diffusion, momentum and heat transfer have to be formulated. The equations of viscous flows are well known in fluid dynamics. At this point, they are presented in their basic form for a three-dimensional flow problem. The following demonstrations are based on [Spurk07], chapter 1 and 2 and [White1991], chapter 1 and 2. The governing equations which model the flow properties and its movement are derived in the following from an infinitesimal small and finitely large fluid control volume Ω, as is indicated in figure 1.1. The following evaluations are done based on the information in [Spurk07], chapter 1, 1.2.1-1.2.5.

The control volume is separated from the rest of the fluid by a closed surface $\partial\Omega$. The volume consists of a set of infinitely many fluid particles, which are denoted by the set $\tilde{M}$. To model the movement of the flow, it has to be possible to identify the set of fluid particles in time and space. From the movement of the fluid particles in Ω, the movement of the whole flow can be concluded on the macroscopic level. The fluid volume is assumed to be *celestial*. Further, it is assumed as *continuum*. Hence, each fluid particle can be considered as material particle and the density as continuous function of time and position. Note, that the continuity assumption must not be fulfilled in every technical flow problem.

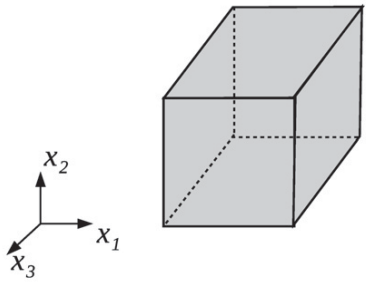

Figure 1.1.: Fluid control volume Ω (as seen in [Oertel06]).

The form of each fluid particle is variable in time and can change continually. Therefore, one particle has to be identified not by its form, but by a specified vector $\boldsymbol{\chi}$, which is characteristic for each particle. The movement of one particle can then be characterised at a time instant t_0 by its position vector $\boldsymbol{x}$ in relation to a chosen origin of a particular three-dimensional coordinate system

$$\boldsymbol{\chi} = \boldsymbol{x}(t_0)\,. \tag{1.4.1}$$

Or for the whole flow

$$\boldsymbol{x} = \boldsymbol{x}(\boldsymbol{\chi}, t)\,, \quad \text{or} \quad x_i = x_i(\chi_j, t) \quad \text{with} \quad i, j = 1, 2, 3\,. \tag{1.4.2}$$

Note, that $\boldsymbol{\chi}$ is a time independent vector. Equation (1.4.2) formulates a mapping between the referenced configuration at a time instant t_0 to the actual one at time t. The

formulation with $\boldsymbol{\chi}$ and time t is called *material description* or *Lagrangian description*, where $\boldsymbol{\chi}$ is the *material coordinate*. The velocity and acceleration of one fluid particle can be formulated in terms of $\boldsymbol{\chi}$ by

$$u_i(\chi_j, t) = \left[\frac{\partial x_i}{\partial t}\right]_{\chi_j}, \quad a_i(\chi_j, t) = \left[\frac{\partial u_i}{\partial t}\right]_{\chi_j}, \quad \text{with} \quad i, j = 1, 2, 3\,. \tag{1.4.3}$$

The index χ_j specifies the deviation for the χ_j-th point in the material. The first equation in (1.4.3) is called the *material* deviation of the velocity.

For the most problems in fluid mechanics, the above material notation is modified, to describe the flow at a specific location $\boldsymbol{x}$ and time t and not any longer in the material coordinate. With (1.4.3) each material coordinate can be transformed to the independent variables of a field coordinate $\boldsymbol{x}$ and time t. This transformation between both vectors is a *bijective* function (one-to-one correspondence). Equation (1.4.2) can then be rewritten as

$$\boldsymbol{\chi} = \boldsymbol{\chi}(\boldsymbol{x}, t)\,, \tag{1.4.4}$$

which describes the material point, which is at the place $\boldsymbol{x}$ at time t. The transformation for the velocity between both vectors is then

$$\boldsymbol{u}(\boldsymbol{\chi}, t) = \boldsymbol{u}\left[(\boldsymbol{\chi}(\boldsymbol{x}, t), t\right] = \boldsymbol{u}(\boldsymbol{x}, t)\,. \tag{1.4.5}$$

The notation in the field coordinate $\boldsymbol{x}$ and time t is called *field* or *Euler's description*. This notation describes the path of one particle at a time instant t and hence its position at t.

Sometimes it is more important to describe the changes of a material particle, and not the change in time at a given location. The change of $\boldsymbol{u}(\boldsymbol{x}, t)$ at $\boldsymbol{x}$ is not in every case the acceleration, which the material point felt in $\boldsymbol{x}$ at time t, e.g. for the case of a steady flow where the change of the velocity is zero at a specified location. If a material point proceed from $\boldsymbol{x}$ to $\boldsymbol{x} + d\boldsymbol{x}$, where $d\boldsymbol{x}$ is an element of the path line, it felt a change in $\boldsymbol{u}(\boldsymbol{x}, t)$, If the velocity is given in material coordinates, then the material derivative is given by (1.4.3), as mentioned before. If the velocity is described in field coordinates $\boldsymbol{u}(\boldsymbol{x}, t)$, the material derivative with respect to t can be formulated for a fixed $\boldsymbol{\chi}$ as

$$\frac{d\boldsymbol{u}}{dt} = \left[\frac{\partial \boldsymbol{u}\left(\boldsymbol{x}(\boldsymbol{\chi}, t), t\right)}{\partial t}\right]_{\boldsymbol{\chi}}. \tag{1.4.6}$$

In equation (1.4.6), the position $\boldsymbol{x}$ in $\boldsymbol{u}(\boldsymbol{x}, t)$ is replaced by the path coordinates of the fluid particle which is located in $\boldsymbol{x}$ at time t. The conservation of mass, momentum and energy have to be fulfilled in the following. The evaluation of the continuity equation is discussed in the following based on [Spurk07], chapter 1, 1.2.5 and chapter 2. The form

of the control volume varies during the motion. The region in space to which the volume is extended at time t, is denoted by $\Omega(t)$. The total mass m in the bounded volume Ω is determined by the sum of the particular material elements dm over the set of all material particles $\tilde{M}$

$$m = \int_{\tilde{M}} dm = \int_{\Omega(t)} \rho(\boldsymbol{x}, t)\, d\Omega \tag{1.4.7}$$

with the continuous function of space of density $\rho(\boldsymbol{x}, t)$. Note, that $\tilde{M}$ should consists the whole time of the same set of material points. Equation (1.4.7) can also be formulated for an arbitrary continuous function φ over a region $\Omega(t)$ in space

$$\int_{\tilde{M}} \varphi(\boldsymbol{\chi}, t)\, dm \; = \int_{\Omega(t)} \varphi(\boldsymbol{x}, t)\rho(\boldsymbol{x}, t)\, d\Omega. \tag{1.4.8}$$

In the following, the dependence on the coordinates is omitted and it infers from the range of each given integral. The mass in the bounded fluid volume has to be constant in time due to the conservation of mass. Hence, this is fulfilled for each mass particle in $\tilde{M}$

$$\frac{D}{Dt} m = 0\,, \qquad \frac{D}{Dt}(dm) = 0\,, \tag{1.4.9}$$

where $\dfrac{D}{Dt}$ denotes the *material derivative* in time. With the connection in (1.4.9), the fact, that φ is continuously differentiable and regarding the *Leibniz rule* (for further information see [Heuser09], chapter 4), the variation rate in time of equation (1.4.8) is subsequently

$$\frac{D}{Dt} \int_{\tilde{M}} \varphi\, dm \; = \frac{D}{Dt} \int_{\Omega(t)} \varphi\rho\, d\,\Omega \; = \int_{\Omega(t)} \frac{D}{Dt}(\varphi\rho)\, d\,\Omega. \tag{1.4.10}$$

Due to the Leibniz rule, the derivation of a continuously differentiable function can be done “under” the integral. An equivalent expression to (1.4.10) is

$$\frac{D}{Dt} \int_{\Omega(t)} \varphi\, d\,\Omega \; = \int_{\Omega} \frac{D}{Dt}\varphi\, d\,\Omega + \int_{\Omega} \varphi \frac{D}{Dt}(\, d\,\Omega). \tag{1.4.11}$$

Without loss of generality, the variable domain $\Omega(t)$ can be replaced by a fixed domain Ω which coincides with $\Omega(t)$ at time t, for the detailed derivation of (1.4.11) see [Spurk07], chapter 1, 1.2.5. Regarding equation (1.4.11), also the following formulation is valid

$$\frac{D}{Dt} \int_{\Omega(t)} \varphi\, d\Omega = \int_{\Omega} \left(\frac{\partial \varphi}{\partial t} + \frac{\partial \varphi u_i}{\partial x_i} \right) d\Omega\,, \tag{1.4.12}$$

where $\dfrac{\partial}{\partial t}$ denotes the partial derivative in time. Due to the fact, that φ is continuously differentiable in Ω, application of the theorem of Gauss (for further details to Gauss's theorem see [Amann08], chapter 3) on (1.4.12) produces the so-called *Reynolds' transport theorem*

$$\frac{D}{Dt}\int_{\Omega(t)} \varphi \, d\Omega = \int_{\Omega} \frac{\partial \varphi}{\partial t} \, d\Omega + \int_{\partial\Omega} \varphi \boldsymbol{u} \cdot \boldsymbol{n} \, dA \,, \tag{1.4.13}$$

where $\partial\Omega$ is the orientated bounded surface of Ω and $\boldsymbol{n}$ its normal vector. The Reynolds' transport theorem expresses the variation rate in time of the material volume integral to the rate of change of an arbitrary quantity φ, which is expressed in terms of the integral over Ω and in terms of its flux trough the bounded surface $\partial\Omega$ of Ω. At a time instant t, both control volumes Ω and $\Omega(t)$ coincide with each other (see [Spurk07], chapter 2, 2.1).

As mentioned above, the mass in the fluid volume should be time independent and constant. Regarding equation (1.4.12) with $\varphi = \rho$ the conservation of mass in (1.4.9) is transformed to

$$\frac{Dm}{Dt} = \frac{D}{Dt}\int_{\Omega(t)} \rho \, d\Omega = \int_{\Omega} \left(\frac{\partial \rho}{\partial t} + \frac{\partial \rho u_i}{\partial x_i} \right) d\Omega \, = 0 \,. \tag{1.4.14}$$

Because the range of the integral Ω is chosen arbitrarily, it can be concluded, that the continuous integrand must vanish and the conservation of mass can be formulated in its *differential* form

$$\frac{\partial \rho}{\partial t} + \frac{\partial \rho u_i}{\partial x_i} \tag{1.4.15}$$

or

$$\frac{\partial \rho}{\partial t} + \nabla \cdot (\rho \boldsymbol{u}) \,. \tag{1.4.16}$$

Equation (1.4.15) is also called *continuity equation*. If the fluid is a steady flow, it is $\dfrac{\partial \rho}{\partial t} = 0$ and equation (1.4.16) becomes

$$\nabla \cdot (\rho \boldsymbol{u}) \, = 0 \,. \tag{1.4.17}$$

If the volume is not variable in time $\dfrac{\partial \rho}{\partial t} = 0$ and space $\dfrac{\partial \rho}{\partial x} = 0$, the fluid is called *incompressible* and it is

$$\nabla \cdot \boldsymbol{u} \, = 0 \,. \tag{1.4.18}$$

1.5. Conservation of momentum

The next step in this section is the derivation of the momentum balance in the fluid volume Ω. Therefore, preliminary considerations are made. A fluid particle is able to perform four different types of motion or deformation as *translation*, *rotation*, *shear strain* and *extensional stresses*. The first two motions change only the location of the fluid particle, while both last motions modify also its form. The following demonstrations are based on [White1991], chapter 1, 1-3 (especially 1-3.3) and chapter 2, 2.4 as well as [Spurk07], chapter 2, 2.2. The motion is always associated to a change in time. The *translation* is

characterised by a displacement from one to another location $u_x\,dt$, $u_y\,dt$, $u_z\,dt$ of the particle (see as well figure 1.1). A *rotation* can be described by a motion of the fluid volume around a specified rotation axis in a particular angle α. Hence, the rate of the rotation is determined as

$$\frac{\partial\tilde{\Omega}_x}{dt} = \frac{1}{2}\left(\frac{\partial u_z}{\partial y} - \frac{\partial u_y}{\partial z}\right), \quad \frac{\partial\tilde{\Omega}_y}{dt} = \frac{1}{2}\left(\frac{\partial u_x}{\partial z} - \frac{\partial u_z}{\partial x}\right), \quad \frac{\partial\tilde{\Omega}_z}{dt} = \frac{1}{2}\left(\frac{\partial u_y}{\partial x} - \frac{\partial u_x}{\partial y}\right). \tag{1.5.1}$$

Expression (1.5.1) can be summarised as follows

$$\tilde{\boldsymbol{\omega}} = 2\frac{d\tilde{\boldsymbol{\Omega}}}{dt}. \tag{1.5.2}$$

$\tilde{\boldsymbol{\omega}}$ is called *vorticity* of the fluid and can be connected to the velocity by

$$\tilde{\boldsymbol{\omega}} = \nabla \times \boldsymbol{u}, \quad [\tilde{\boldsymbol{\omega}}] = \frac{1}{s}. \tag{1.5.3}$$

Then it is

$$\nabla \cdot \tilde{\boldsymbol{\omega}} = \nabla \cdot (\nabla \times \boldsymbol{u}) = 0. \tag{1.5.4}$$

If $\tilde{\boldsymbol{\omega}} = 0$, the flow is called *irrotational*.

The *shear strain* is characterised as the averaged angle between two lines of the fluid volume which were normal orientated to each other in the unstrained state. The shear strain rate is defined by

$$\epsilon_{xy} = \frac{1}{2}\left(\frac{\partial u_y}{\partial x} + \frac{\partial u_x}{\partial y}\right), \quad \epsilon_{yz} = \frac{1}{2}\left(\frac{\partial u_z}{\partial y} + \frac{\partial u_y}{\partial z}\right), \quad \epsilon_{zx} = \frac{1}{2}\left(\frac{\partial u_x}{\partial z} + \frac{\partial u_z}{\partial x}\right). \tag{1.5.5}$$

Consequently, the strain rates are symmetrical $\epsilon_{ij} = \epsilon_{ji}$. The *extensional strain* can be explained as an increase in the fluid particle's length

$$\epsilon_{xx} = \frac{\partial u_x}{\partial x}, \quad \epsilon_{yy} = \frac{\partial u_y}{\partial y}, \quad \epsilon_{zz} = \frac{\partial u_z}{\partial z} \tag{1.5.6}$$

or

$$\epsilon_{ij} = \begin{pmatrix} \epsilon_{xx} & \epsilon_{xy} & \epsilon_{xz} \\ \epsilon_{yx} & \epsilon_{yy} & \epsilon_{yz} \\ \epsilon_{zx} & \epsilon_{zy} & \epsilon_{zz} \end{pmatrix}. \tag{1.5.7}$$

ϵ_{ij} is a symmetric second-order tensor with the following invariants

$$\begin{aligned} I_1 &= \epsilon_{xx} + \epsilon_{yy} + \epsilon_{zz}, \\ I_2 &= \epsilon_{xx}\epsilon_{yy} + \epsilon_{yy}\epsilon_{zz} + \epsilon_{zz}\epsilon_{xx} - \epsilon_{xy}^2 - \epsilon_{yz}^2 - \epsilon_{zx}^2, \\ I_3 &= \begin{vmatrix} \epsilon_{xx} & \epsilon_{xy} & \epsilon_{xz} \\ \epsilon_{yx} & \epsilon_{yy} & \epsilon_{yz} \\ \epsilon_{zx} & \epsilon_{zy} & \epsilon_{zz} \end{vmatrix}. \end{aligned} \tag{1.5.8}$$

In Newton mechanics, a system is denoted as *inertial*, if its axes are fixed and Newtons first law of motion is satisfied. This implies, that the velocity of an object is constant in the system, if the object is not affected by any forces. Either the object is at a rest or it is moving linearly with a constant velocity (see [Nolting13], chapter 2, 2.2.3). In an inertial system, the variation rate in time of the momentum $\boldsymbol{I} = m\boldsymbol{u}$ equals the sum of all forces $\boldsymbol{F}_k$, which are acting on the system. Thus, for the fluid volume it has to be

$$\frac{D\boldsymbol{I}}{Dt} = \frac{Dm\boldsymbol{u}}{Dt} = \boldsymbol{F} = \sum_k \boldsymbol{F}_k\,, \quad \Rightarrow \quad m\boldsymbol{a} = \boldsymbol{F}\,, \tag{1.5.9}$$

which is *Newtons second law*. $\boldsymbol{a}$ is the acceleration of the fluid particle of mass m. Regarding the density instead of the mass, equation (1.5.9) is written as

$$\rho\frac{D\boldsymbol{u}}{Dt} = \boldsymbol{f} = \boldsymbol{f}_{\text{body}} + \boldsymbol{f}_{\text{surface}} \tag{1.5.10}$$

with the velocity $\boldsymbol{u}$ of the fluid particle and the applied force per unit volume $\boldsymbol{f}$, which acts on the fluid particle. The forces which impact on the fluid particle are divided in two classes, *body forces* and *surface forces*. A body force is usually applied to the entire mass and is impressed by an external field, e. g. the gravitational force $\boldsymbol{g}$. The surface forces are applied by external stresses which result from the surrounding fluid. The whole force, which is acting on the observed fluid volume can be described with help of equation (1.5.10) by an integration over the volume and its surface. The following demonstrations are based on [Spurk07], chapter 2, 2.2. It is

$$\mathbf{F} = \int_{\Omega(t)} \boldsymbol{k}\rho\, d\Omega + \int_{\partial\Omega(t)} \boldsymbol{t}\, d\partial\Omega\,. \tag{1.5.11}$$

The vector $\boldsymbol{k}$ stands for the body forces and the vector $\boldsymbol{t}$ is the so-called *deformation tensor* which compromises the surface forces. The deformation tensor is dependent on space, time and from the orientation of the normal vector $\boldsymbol{n}$ of the surface element. The deformation tensor is a linear combination of the components of $\boldsymbol{n}$. With the Einstein notation it is

$$t_j(\boldsymbol{x}, \boldsymbol{n}, t) = \tau_{ij}(\boldsymbol{x}, t)n_i \quad \text{with} \quad i, j = 1, 2, 3\,, \tag{1.5.12}$$

which is illustrated in figure 1.2. τ_{ji} stands for the magnitude of the i-th component of the deformation tensor, which effects the element of the coordinate plane with the normal vector, which points in the j-th direction.

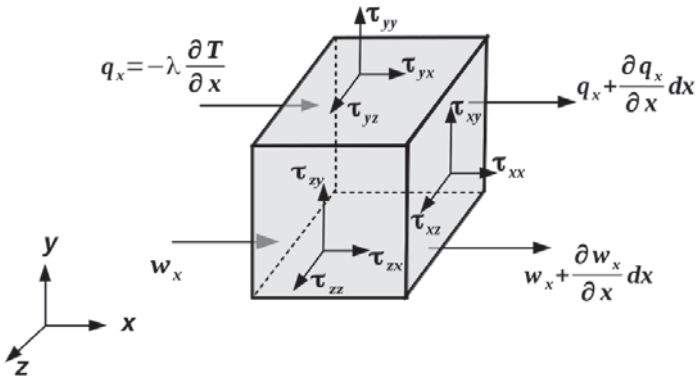

Figure 1.2.: Fluid volume with notation for stresses, heat and work exchange (as seen in [White1991]).

The deformation tensor is a second-order tensor and its matrix notation is

$$\boldsymbol{t} = \boldsymbol{nT} = \boldsymbol{n} \begin{pmatrix} \tau_{11} & \tau_{12} & \tau_{13} \\ \tau_{21} & \tau_{22} & \tau_{23} \\ \tau_{31} & \tau_{32} & \tau_{33} \end{pmatrix} . \tag{1.5.13}$$

The elements at the main diagonal are the normal stresses, the remaining elements are the shear stresses. If the fluid is at rest, the velocity is zero and the shear stresses have to vanish, solely the normal stresses remain. Thus, it is

$$\tau_{ij} = -p\delta_{ij}, \qquad \text{where} \qquad \delta_{ij} = \begin{cases} 1 & i = j, \\ 0 & i \neq j, \end{cases} \tag{1.5.14}$$

where the tensor δ_{ji} is the so-called *Kronecker-Delta*. This case equals the *hydrostatic pressure*

$$t_i = -pn_i, \tag{1.5.15}$$

where the pressure p which is independent of $\boldsymbol{n}$, is its absolute value. In general, the deformation tensor can be separated in

$$\tau_{ij} = -p\delta_{ij} + P_{ij}\,, \tag{1.5.16}$$

where P_{ij} determines the tensor of *frictional tension*. In all common fluids the applied shear is a function of the strain rate

$$\tau_{ij} = f(\epsilon_{ij}) \quad \text{with} \quad i, j = 1, 2, 3. \tag{1.5.17}$$

For the so-called *Newtonian fluids*, which are considered in this thesis, it is

$$\tau_{ij} = 2\mu\epsilon_{ij} = \mu\frac{du_j}{dx_i} \quad \text{with } i,j = 1,2,3 \tag{1.5.18}$$

and the dynamic viscosity μ [kg/ms]. The transport property of the dynamic viscosity μ yields a relation between momentum flux and velocity gradient. As a thermodynamic property it is dependent on temperature and pressure. Its properties are further discussed in section 1.9.

The easiest assumption for the variation of viscous stresses with strain rate is a linear law which was first stated by Sir George Gabriel Stokes in 1845 in form of three assumptions (see [Stokes1845] and [White1991], chapter 2, 2-4). Regarding the first assumption, the stress tensor τ_{ij} of a continuous fluid is a linear function of the strain rates ϵ_{ij}. Second, the fluid is isotropic, hence its properties are independent of direction. And third, if the strain rates are zero, the deformation law equals the hydrostatic pressure, which was already mentioned above. From these three assumptions, Stokes derived the following deformation law which is fulfilled for all gases and mostly fluids (see [White1991], chapter 2, 2-4)

$$\tau_{ij} = -p\delta_{ij} + \mu\left(\frac{\partial u_i}{\partial x_j} + \frac{\partial u_j}{\partial x_i}\right) + \lambda\left(\frac{\partial u_k}{\partial x_k}\right)\delta_{ij} = 0 \tag{1.5.19}$$

with the thermal conductivity λ. Stokes assumed, that the sum of the normal stresses $\tau_{xx}, \tau_{yy}, \tau_{zz}$ are also a tensor invariant, analogously to the invariants of the strain rate in equation (1.5.8). Then, the mechanical pressure p can be supposed to be

$$\bar{p} = -\frac{1}{3}(\tau_{xx}, \tau_{yy}, \tau_{zz})\,. \tag{1.5.20}$$

With the deformation law in (1.5.19), one obtains

$$\bar{p} = -\frac{1}{3}(\tau_{xx}, \tau_{yy}, \tau_{zz}) = p - \left(\lambda + \frac{2}{3}\mu\right)\left(\frac{\partial u_k}{\partial x_k}\right)\delta_{ij}\,. \tag{1.5.21}$$

From this expression follows, that the mean pressure in a deforming viscous fluid does not equal the thermodynamic pressure. Stokes solved this problem by assuming, that

$$\lambda + \frac{2}{3}\mu = 0\,. \tag{1.5.22}$$

Furthermore, the assumption of an incompressible fluid with

$$\left(\frac{\partial u_k}{\partial x_k}\right)\delta_{ij} = 0 \tag{1.5.23}$$

resolves the problem of inequality between both pressure terms. In compressible flows the problem is probably avoided, if the viscous normal stresses are negligible which is the case

in boundary layer flows. For further details see as well [White1991], chapter 2, 2-4.2 and 2-4.3.

The *conservation of momentum* can now be formulated by inserting (1.5.12) in (1.5.11) and regarding Gauss's theorem (see [Spurk07], chapter 2, 2.2)

$$\int_\Omega \left(\rho \frac{Du_i}{Dt} - \rho k_i - \frac{\partial \tau_{ij}}{\partial x_j} \right) d\Omega = 0 \,. \tag{1.5.24}$$

In an analogous manner to the proceeding in section 1.4, the variable domain $\Omega(t)$ is replaced by the fixed domain Ω which coincides with $\Omega(t)$ at time t. The conservation of momentum can be formulated in its differential form by

$$\rho \frac{Du_i}{Dt} = \rho k_i + \frac{\partial \tau_{ij}}{\partial x_j} \tag{1.5.25}$$

and accordingly

$$\rho \frac{D\boldsymbol{u}}{Dt} = \rho \boldsymbol{k} + \nabla \cdot \boldsymbol{T} \,. \tag{1.5.26}$$

Equation (1.5.26) is called *Cauchy momentum equation*. With the Reynolds' transport theorem, equation (1.5.26) can be rewritten as

$$\frac{\partial}{\partial t}(\rho u_i) + \frac{\partial}{\partial x_j}(\rho u_i u_j) = \rho k_i + \frac{\partial}{\partial x_j} \tau_{ij} \,. \tag{1.5.27}$$

Inserting (1.5.19) in (1.5.26), one obtains the so-called *Navier-Stokes equations* which are attributed to Claude Louis Navier ([Navier1823]) and Sir George Gabriel Stokes ([Stokes1845]). In general, also the set of equations which describe the conservation of mass, momentum and energy are called together the *Navier-Stokes equations*. Note, that the exact formulation of the body forces $\boldsymbol{k}$ and surface forces $\boldsymbol{T}$ is always dependent on the particular flow problem.

1.6. Conservation of energy

To describe the movement and properties of the flow completely, besides both already formulated conservation laws, a third one has to be added. Because mechanical energy can be transformed to heat and vice versa, the third conservation law has to involve the balance of energy in the flow. Therefore, the first law of thermodynamics is regarded (for further information see [Spurk07], chapter 2, 2.6, [White1991], chapter 2, 2.5). It states,

that if an amount of work W, which is done to the system, and an amount of heat Q are added to a closed system S, the total energy E_{tot} of the system will increase about

$$dE_{\text{tot}} = dQ + dW\,. \tag{1.6.1}$$

The following demonstrations are based on [White1991], 2, 2.5. For a moving fluid particle, besides the internal energy, the kinetic energy $\frac{1}{2}\boldsymbol{u}^2$ and potential energy $\boldsymbol{gr}$ have to be regarded

$$E_{\text{tot}} = \rho\left(e + \frac{1}{2}\boldsymbol{u}^2 - \boldsymbol{gr}\right) \tag{1.6.2}$$

with the internal energy per unit mass e and the displacement of the particle $\boldsymbol{r}$. Assuming conservation of mass and momentum, the change rate in time of equation (1.6.1) results in

$$\frac{DE_{\text{tot}}}{Dt} = \frac{DQ}{Dt} + \frac{DW}{Dt}\,. \tag{1.6.3}$$

And hence, from equation (1.6.2) it follows

$$\frac{DE_t}{Dt} = \rho\left(\frac{De}{Dt} + \boldsymbol{u}\frac{D\boldsymbol{u}}{Dt} - \boldsymbol{gu}\right)\,. \tag{1.6.4}$$

With help of *Fourier's law*, Q and W can be written in terms of the fluid properties of temperature T and thermal conductivity λ (see in addition figure 1.2)

$$\boldsymbol{q} = -\lambda\nabla T \quad \text{with} \quad [\lambda] = \frac{\mathrm{W}}{\mathrm{m\,K}} = \frac{\mathrm{kg\,m}}{\mathrm{s^3\,K}}\,. \tag{1.6.5}$$

$\boldsymbol{q}$ is the rate of heat flow per unit area. The heat flow varies with temperature fluctuations. With this definition of energy, the particles which flow in the volume are characterised as positive (see in addition figure 1.2). The thermal conductivity λ is, like the dynamic viscosity, a thermodynamical property which varies with temperature and pressure

$$\lambda = \lambda(T, p)\,. \tag{1.6.6}$$

In isotropic materials, the thermal heat conductivity is a scalar, while in non-isotropic materials it is a tensor of second order.

At this point only the heat transfer by heat conduction is regarded in (1.6.5). But in general other heat transfers, e. g. radiation, play possibly a role. Neglecting internal heat production, Q is defined by

$$\frac{DQ}{Dt} = -\nabla\cdot\boldsymbol{q} = \nabla\cdot(\lambda\nabla T)\,. \tag{1.6.7}$$

The work which is done to the fluid volume is expressed by

$$\frac{DW}{Dt} = \nabla \cdot (\boldsymbol{u} \cdot \tau_{ij}) \; = \boldsymbol{u} \cdot (\nabla \cdot \tau_{ij}) + \tau_{ij} \frac{\partial u_i}{\partial x_j} \,. \tag{1.6.8}$$

With help of the momentum equation, one obtains

$$\boldsymbol{u} \cdot (\nabla \cdot \tau_{ij}) = \rho \left(\boldsymbol{u} \frac{D\boldsymbol{u}}{Dt} - \boldsymbol{g} \cdot \boldsymbol{u} \right) \,. \tag{1.6.9}$$

Inserting the expression from (1.6.4), (1.6.7) and (1.6.8) in equation (1.6.3), the most general form of the first law of thermodynamics for moving fluids is formulated as

$$\rho \frac{De}{Dt} = \nabla \cdot (\lambda \nabla T) + \tau_{ij} \frac{\partial u_i}{\partial x_j} \,. \tag{1.6.10}$$

With the continuity equation (1.4.15), (1.5.19) and (1.6.10) it follows

$$\rho \frac{D}{Dt} \left(e + \frac{p}{\rho} \right) = \frac{Dp}{Dt} + \nabla \cdot (\lambda \nabla T) + \tau_{ij} \frac{\partial u_i}{\partial x_j} \tag{1.6.11}$$

with

$$\tau_{ij} \frac{\partial u_i}{\partial x_j} = \tau'_{ij} \frac{\partial u_i}{\partial x_j} - p \nabla \cdot \boldsymbol{u}. \tag{1.6.12}$$

In the following, an analogous expression is formulated in terms of the enthalpy. Considering the specific enthalpy per unit mass, one gets

$$h = e + \frac{p}{\rho} \,. \tag{1.6.13}$$

Equation (1.6.11) can then be modified to

$$\rho \frac{Dh}{Dt} = \frac{Dp}{Dt} + \nabla \cdot (\lambda \nabla T) + \tau'_{ij} \frac{\partial u_i}{\partial x_j} - p \nabla \cdot \boldsymbol{u}. \tag{1.6.14}$$

Analogously to both previous sections, equation (1.6.14) can be rewritten with its partial derivatives as

$$\rho \frac{\partial h}{\partial t} = \frac{\partial p}{\partial t} + \nabla \cdot (\lambda \nabla T) + \phi \,. \tag{1.6.15}$$

1.7. Dimensionless equations of fluid motion

Preceding, the basic flow equations were formulated. To analyse these equations, it can be sometimes easier to non-dimensionalise the equations beforehand. Each system can be described by dimensionless characteristic properties, because a physical solution of a system has to be independent of the chosen system of units. Temperature and veloc-

ity fields, which are the same in dimensionless coordinates, are called *similar fields* (see [Baehr08], chapter 1, 1.1.4). They can be transformed in each other by rescaling. To non-dimensionalise the governing equations, one can use the so-called *Buckingham pi theorem*, which is not presented in detail at this point. For a description it is referred to [White1991], chapter 2, 2-9. The Buckingham pi theorem reveals the required dimensionless parameters which are used to non-dimensionalise the flow equations. Therefore, the variables are divided by constant reference properties, which made them dimensionless. These are for example ([White1991], chapter 2, 2-9)

$$\begin{aligned} x_i^* &= \frac{x_i}{L}\,, & p^* &= \frac{p-p_0}{\rho_0 u_0^2}\,, & u^* &= \frac{u}{u_0}, \\ T^* &= \frac{T-T_0}{T_w-T_0}\,, & t^* &= \frac{t u_0}{L}\,, & \mu^* &= \frac{\mu}{\mu_0}, \\ \rho^* &= \frac{\rho}{\rho_0}\,, & \lambda^* &= \frac{\lambda}{\lambda_0}\,, & \nabla^* &= L\nabla, \\ & & & & c_p^* &= \frac{c_p}{c_{p_0}}, \end{aligned} \tag{1.7.1}$$

where L is a reference length of the flow geometry and u_0 a reference velocity. The notation with the star * stands for the dimensionless parameters. The variables which have an index 0 are *free stream properties*. The free-stream properties describe the flow in a far distant of any solid bodies or walls. These values are mostly known from experimental measurements for particular flow problems. With the new dimensionless parameters, one may reformulated the flow equations. The following explanations are based on the details in [White1991], chapter 2, 2-9. Consequently, the continuity equation from equation (1.4.15) becomes

$$\frac{\partial \rho^*}{\partial t^*} + \nabla^* \cdot \rho^* u^* = 0\,. \tag{1.7.2}$$

It can be seen from (1.7.2), that just the variables have changed. The energy equation in (1.6.15) becomes, this time under consideration of the temperature T,

$$\rho^* c_p^* \frac{DT^*}{Dt^*} = \mathrm{Ec}\frac{Dp^*}{Dt^*} + \frac{1}{\mathrm{Re}\,\mathrm{Pr}}\nabla^* \cdot (\lambda^* \nabla^* T^*) + \frac{\mathrm{Ec}}{\mathrm{Re}}\Phi^*\,. \tag{1.7.3}$$

In (1.7.3) three fundamental dimensionless parameters of heat-transfer problems appear. These are the *Reynolds number* Re, the *Prandtl number* Pr and the *Eckert number* Ec which are defined by

$$\begin{aligned} \mathrm{Re} &= \frac{\rho_0 u_0 L}{\mu_0}\,, \\ \mathrm{Pr} &= \frac{\mu_0 c_{p_0}}{\lambda_0}\,, \\ \mathrm{Ec} &= \frac{u_0^2}{c_{p_0}(T_w - T_0)}\,. \end{aligned} \tag{1.7.4}$$

The notation goes back to the Anglo-Irish physicist *Osborne Reynolds* (1842 - 1912), the German physicist *Ludwig Prandtl* and German scientist *Ernst R. G. Eckert* (1904 - 2004). Note, that the variables ρ, μ, λ, c_p must be determined as thermodynamic functions of the particular fluid by

$$\rho^*, \mu^*, \lambda^*, c_p^* = f(p^*, T^*)\,. \tag{1.7.5}$$

At least, the momentum equation is redefined, at this point only for low speed flows, which are considered in this thesis. In low speed flows, gravitational forces cannot be neglected. Moreover, density differences due to temperature differences have to be accounted under regarding the thermal expansion coefficient β (see also section 1.6, eq. (1.8.20))

$$\rho = \rho_0 + \Delta\rho \approx \rho_0(1 - \beta\Delta T) \quad \text{with} \quad \beta = -\frac{1}{\rho}\left(\frac{\partial\rho}{\partial T}\right)_p\,. \tag{1.7.6}$$

The assumption

$$\rho = \rho_0 + \Delta\rho \approx \rho_0(1 - \beta\Delta T) \tag{1.7.7}$$

is the so-called *Boussinesq-approximation* which is named after the French mathematician and physicist *Valentin Joseph Boussinesq* (1842 - 1929) and German physicist *Anton Oberbeck* (1846 - 1900) ([Boussinesq1903] and [Oberbeck1879]). If the variation rate of temperature and hence of the density is only small, one may consider the density as constant in the governing equations, except in the gravitational term where it depends linear from the temperature. Further, all fluid properties are assumed to be constant over the observed fluid volume. Hence, the momentum equation in (1.5.26) is rewritten as

$$\rho_0\frac{D\boldsymbol{u}}{Dt} \approx -\nabla p - \rho_0\boldsymbol{g}\boldsymbol{k} - \rho_0\beta(T - T_0)\boldsymbol{g} + \nabla\cdot\tau'_{ij}\,. \tag{1.7.8}$$

If one separates the stress tensor in pressure and viscous term with help of (1.5.19) one obtains

$$\tau_{ij}\,\frac{\partial u_i}{\partial x_j} = \tau'_{ij}\frac{\partial u_i}{\partial x_j}\; - p\frac{\partial u_k}{\partial x_k}\delta_{ij}. \tag{1.7.9}$$

With a modified dimensionless pressure P^*

$$P^* = \frac{p + \rho_0\boldsymbol{g} - p_0}{\rho_0 u_0^2} \tag{1.7.10}$$

and $\beta^* = \beta/\beta_0$ the dimensionless momentum equation can be formulated as

$$\frac{D\boldsymbol{u}^*}{Dt^*} = -\nabla^* P^* - \frac{\mathrm{Gr}}{\mathrm{Re}^2}\beta^* T^*\boldsymbol{g}^* + \frac{1}{Re}\nabla^*\cdot\tau^*_{ij}\,. \tag{1.7.11}$$

The term Gr indicates an additional dimensionless parameter, the so-called *Grashof number* which is named after the German engineer *Franz Grashof* (1826 - 1893). It is used concerning natural convective flows and denotes buoyancy effects

$$\mathrm{Gr} = \frac{g\beta_0\rho_0^2 L^3\,(T_w - T_0)}{\mu_0^2}\,, \tag{1.7.12}$$

where T_w and T_0 are two reference temperatures of the flow geometry. In natural convection the motion arises simply due to temperature differences and resulting density differences in the gravitational force field of the Earth. Convective flow problems may be described merely by the Grashof- and Prandtl number, because the Prandtl number becomes the solely resulting parameter. Hence, for these flows the reference velocity has to be modified and the Grashof number is the dominant parameter

$$u_0 = \frac{\mu_0}{\rho_0 L}, \qquad \mathrm{Re} \equiv 1, \qquad \frac{\mathrm{Gr}}{\mathrm{Re}^2} = \mathrm{Gr}\,. \tag{1.7.13}$$

For high speed flows, the gravity is negligible. For the dimensionless formulation of these flows it is pointed to [White1991], chapter 2, 2.9.2.

1.8. Thermodynamic state equations

The previously presented governing equations were derived in their basic form. To investigate a particular flow problem, the equations have to be specified by the particular transport properties and an appropriate thermodynamical state equation. The transport properties are the subject of the following section 1.9. A thermodynamical state is uniquely defined by a number of independent state variables (see [Spurk07], chapter 2, 2.8). The information of this section is based on [White1991], chapter 1, 1-3.12 - 1-3.17, [Spurk07], chapter 2, 2.8 and [Groll10b]. In this thesis only one-phase fluids of ideal gases are investigated. Therefore, for a single component material, a *thermodynamical state* can be described by two independent, arbitrary variables

$$p = \hat{p}(\rho, T)\,, \tag{1.8.1}$$

which specify the value of every other variable of state. The following state equation

$$pV = n\mathrm{R}_0 T \tag{1.8.2}$$

defines an *ideal* gas. R_0 is the so-called *universal gas constant* with

$$R_0 = 8.3144621\frac{\mathrm{J}}{\mathrm{K\,mol}}\,. \tag{1.8.3}$$

n stands for the amount of substance of the gas (in moles). The mass is then defined by

$$m = nM \tag{1.8.4}$$

with the molar mass M. The mole volume V_A is defined by

$$V_A = Mv = \frac{M}{\rho} = \frac{V}{n} \tag{1.8.5}$$

with a specific volume v. With a constant mole mass M, equation (1.8.2) becomes

$$\frac{p}{\rho} = \frac{R_0}{M}T \quad \Rightarrow \quad p \sim \rho T\,. \tag{1.8.6}$$

Afore, the first law of thermodynamics was written as

$$dE_{\text{tot}} = dQ + dW\,, \tag{1.8.7}$$

where Q was the added heat and W the added work to a system S. For a substance which is not moving and which show just infinitesimal changes it is

$$dW = -pdV \quad \text{and} \quad dQ = T\,dS\,. \tag{1.8.8}$$

Therefore, (1.8.7) can be expressed on a unit mass basis by

$$de = T\,dS + \frac{p}{\rho^2}\,d\rho \tag{1.8.9}$$

which is shortly

$$e = \hat{e}(s, \rho) \tag{1.8.10}$$

with the specific entropy s. The expression (1.8.9) combines the first and second law of thermodynamics for infinitesimal processes. The expression in (1.8.10) suffices to determine a fluid thermodynamically. It is called *canonical equation*, because all other properties can be calculated from it. Transformation of equation (1.8.10)

$$de = \frac{\partial e}{\partial s}\,ds + \frac{\partial e}{\partial \rho}\,d\rho \tag{1.8.11}$$

reveals under considering of (1.8.9) the temperature and pressure expression

$$T = \left.\frac{\partial e}{\partial s}\right|_{\rho}\,, \quad p = \rho^2\left.\frac{\partial e}{\partial \rho}\right|_{s}\,. \tag{1.8.12}$$

Another canonical equation is

$$d\,h = T\,ds + \frac{1}{\rho}\,dp \tag{1.8.13}$$

with the enthalpy from (1.6.13). From the canonical relation $h = \hat{h}(s,p)$ the other properties may be estimated

$$T = \left.\frac{\partial h}{\partial s}\right|_p, \quad \frac{1}{\rho} = \left.\frac{\partial h}{\partial p}\right|_s, \quad e = h - \frac{p}{\rho}. \tag{1.8.14}$$

Another state equation is described as follows

$$e = \hat{e}(\rho, T) \tag{1.8.15}$$

and it is called *caloric equation*. Note, that in general, one equation of state, the thermal or the caloric one, does not necessarily define the other one. This is only the case for the canonical one. The change rate of energy in an ideal gas is given by the specific heat capacities at a constant pressure and a constant volume where $|_.$ marks the constant variable

$$\frac{dq}{dT} = \frac{dh}{dT} - v\frac{dp}{dT}, \Rightarrow c_p = \left.\frac{\partial q}{\partial T}\right|_p = \frac{\partial h}{\partial T}, \tag{1.8.16}$$

$$\frac{dq}{dT} = \frac{de}{dT} + p\frac{dv}{dT}, \Rightarrow c_v = \left.\frac{\partial q}{\partial T}\right|_v = \frac{\partial e}{\partial T}. \tag{1.8.17}$$

In a caloric ideal gas it is

$$e = e_0 + c_v T \tag{1.8.18}$$

with $c_v = \text{const.}$ and

$$h = h_0 + c_p T \tag{1.8.19}$$

with $c_p = \text{const}$. The term c_v denotes the specific heat at a constant pressure and c_p the specific heat at a constant volume. The variables with index 0 indicate the energy, respectively, enthalpy at rest. A further important fluid property is the *expansions coefficient* β. It yields a relation for the temperature dependence on the expansion rate of a gas and is formulated by a specific volume v and density ρ

$$\beta = \frac{1}{v}\frac{\partial v}{\partial T} = \rho\frac{\partial}{\partial T}\frac{1}{\rho} = -\frac{\partial \rho/\partial T}{\rho}. \tag{1.8.20}$$

In an ideal gas, the connection between temperature T and expansion coefficient β is given with the help of (1.8.6) by

$$\rho = \frac{pM}{R_0 T} \Rightarrow \frac{\partial \rho}{\partial T} = -\frac{pM}{R_0 T^2} \Rightarrow \beta = \frac{pM}{\rho R_0 T^2} = \frac{1}{T}.$$

As before seen in equation (1.7.6), the buoyant forces in natural convection are proportional to the expansion coefficient β

$$\beta = -\frac{1}{\rho}\left(\frac{\partial \rho}{\partial T}\right)_p . \tag{1.8.21}$$

1.9. Transport properties of a fluid

Fluid properties can be separated in four types, *kinematic properties*, e.g velocity, strain rate, acceleration, *transport properties*, e. g. viscosity, thermal conductivity or mass diffusivity, *thermodynamic properties*, e. g. pressure, density or temperature, and other *miscellaneous properties*, e. g. surface tension, vapour pressure or eddy diffusion coefficients. (see [White1991], chapter 1, 1-3.4). Most of these properties were described in the previous sections. Now, a special focus lies on the dynamic viscosity μ in ideal gases, due to the in this thesis used working fluid, air.

The dynamic viscosity varies with pressure and temperature, because of its connection to molecular interactions. Most typical gas problems are considered at a low reduced pressure. For these problems it is common, to ignore the pressure dependence and model only the temperature dependence. The viscosity increases with temperature in such gases. In the simulations of this thesis, a temperature dependent dynamic viscosity is supposed at an almost atmospheric pressure condition. Besides, the specific heat capacity is assumed to be constant $c_p = \text{const}$. The numerical model is based on the calculation of the specific enthalpy h.

The temperature dependence on μ is described by the model of Sutherland as stated in [Sutherland1893] which uses an idealised intermolecular-force potential. For ideal gases it yields a relation between the dynamic viscosity μ and the absolute temperature T by

$$\mu = \mu_{\text{ref}} \cdot \left(\frac{T}{T_{\text{ref}}}\right)^{3/2} \cdot \left(\frac{T_{\text{ref}} + T_s}{T + T_s}\right) \tag{1.9.1}$$

with a reference dynamic viscosity μ_{ref} at a related reference temperature T_{ref} and the so-called Sutherland temperature T_S which is dependent on the observed gas. Equation (1.9.1) is sometimes used in a simplified form

$$\mu = \frac{C_1 T^{3/2}}{T + T_s} \quad \text{with} \quad C_1 = \frac{\mu_{\text{ref}}}{T_{\text{ref}}^{3/2}}(T_{\text{ref}} + T_s)\,, \tag{1.9.2}$$

where C_1 is the so-called *Sutherland coefficient* which depends also on the gas. For air, the model has an accuracy of 4% $[K]$ ([White1991], chapter 1, 1-3.7). Possible Sutherland coefficients are listed in table 1.1. The values in table 1.1 may be found in [Sutherland1893]

or [Montgomery1947] as well as further information to the model itself. For further information on the model see also [Bircumshaw1929].

$\mu_{\text{ref}}\left[\frac{\text{kg}}{\text{ms}}\right]$	$T_{\text{ref}}\,[\text{K}]$	$T_S\,[\text{K}]$	$C_1\left[\frac{\text{kg}}{\text{ms}\sqrt{\text{K}}}\right]$
$1.716 \cdot 10^{-5}$	273.5	110.4	$1.458 \cdot 10^{-6}$
$1.827 \cdot 10^{-5}$	291.15	120	$1.512 \cdot 10^{-6}$

Table 1.1.: Sutherland coefficients.

The required coefficients are chosen in this thesis with $\mu_{\text{ref}} = 1.827 \cdot 10^{-5}\,\text{kg/ms}$, $T_{\text{ref}} = 291.15\,\text{K}$ and $T_S = 120\,\text{K}$ ([Montgomery1947]). Figure 1.3 shows a plot of the dynamic viscosity values for particular temperatures between $290\,\text{K} - 360\,\text{K}$.

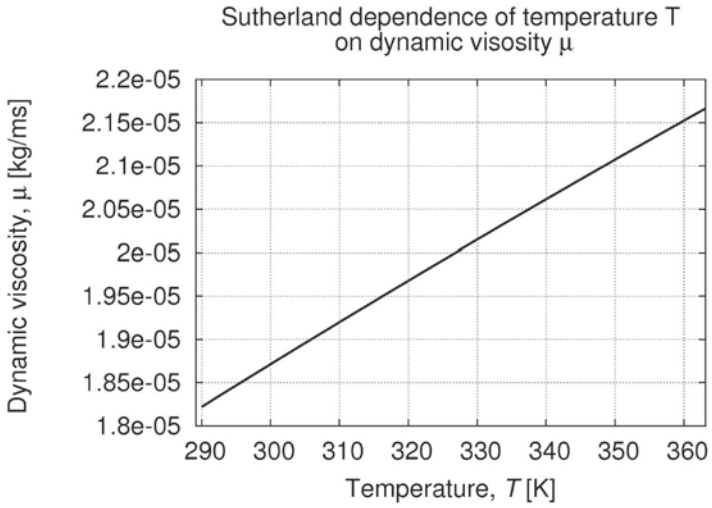

Figure 1.3.: Temperature dependence on the dynamic viscosity μ according to the Sutherland model in [Sutherland1893].

The following formulations are based on the information in [White1991], chapter 1, 1-3. With help of the dynamic viscosity μ and thermal conductivity λ two further important fluid properties are derived, the *kinematic viscosity* ν and the *thermal diffusivity coefficient* κ

$$\nu = \frac{\mu}{\rho}\,, \quad [\nu] = \text{m}^2/\text{s}\,, \quad \kappa = \frac{\lambda}{\rho c_p}\,, \quad [\kappa] = \text{m}^2/\text{s}. \tag{1.9.3}$$

Both properties consist simply of other fluid properties and may be regarded as diffusivity of vorticity and temperature. The relation between both properties gives the before mentioned dimensionless fluid property of the *Prandtl number*, which can also be written as

$$\text{Pr} = \frac{\nu}{\kappa} = \mu\frac{c_p}{\lambda}\,. \tag{1.9.4}$$

The Prandtl number is a measure for relative rates of diffusion. In this thesis, the Prandtl number is in all test cases $\mathrm{Pr} = 0.71$ (air). From the thermal diffusivity coefficient κ an additional thermal diffusivity α is defined by

$$\alpha = \kappa\rho\,, \qquad [\alpha] = \mathrm{kg/ms}. \tag{1.9.5}$$

Hence, α has the same unit as the dynamic viscosity μ. This thermal diffusivity is later required to describe the chosen turbulence model for the observed compressible natural convection.

The Grashof number from section 1.7 is related to a further important dimensionless parameter, which is often used for the description of a convective flow. This parameter is the so-called *Rayleigh number*, which is named after the English physicist *Lord Rayleigh* (1842 - 1919) and which is discussed further in chapter 3, section 3.5. It is defined by

$$\mathrm{Ra} = \mathrm{GrPr} = \frac{g\beta_0 L^3\,(T_w - T_0)}{\nu_0\kappa_0} \tag{1.9.6}$$

or in terms of the dynamic viscosity μ and thermal diffusivity α

$$\mathrm{Ra} = \frac{\rho_0^2 g\beta_0 L^3\,(T_w - T_0)}{\mu_0\alpha_0}\,. \tag{1.9.7}$$

Note, that the Rayleigh number varies significantly with a change of temperature or a change of length L (due to its cube in (1.9.7)). Further, a change of the gravitational force g influences the Rayleigh number, which is discussed later in chapter 7.

1.10. Governing equations of a natural convection

To formulate the particular governing equation system describing a compressible natural convection problem, the basic equations from section 1.4 - 1.6 have to be adapted by help of the fluid properties and thermodynamical state equations.

- Compressible conservation of mass

$$\frac{\partial\rho}{\partial t} + \frac{\partial\rho u_j}{\partial x_j} = 0\,, \tag{1.10.1}$$

- Compressible conservation of momentum

$$\frac{\partial\rho u_i}{\partial t} + \frac{\partial\rho u_i u_j}{\partial x_j} - \frac{\partial}{\partial x_j}\left(\mu\left(\frac{\partial u_i}{\partial x_j} + \frac{\partial u_j}{\partial x_i} - \frac{2}{3}\frac{\partial u_k}{\partial x_k}\delta_{ij}\right)\right) = -\frac{\partial p}{\partial x_i} + \rho g_i, \tag{1.10.2}$$

- Compressible conservation of enthalpy

$$\frac{\partial \rho h}{\partial t} + \frac{\partial \rho h u_j}{\partial x_j} - \frac{\partial}{\partial x_j}\left(\alpha \frac{\partial h}{\partial x_j}\right) = \frac{\partial p}{\partial t} + u_j \frac{\partial p}{\partial x_j}\,. \tag{1.10.3}$$

Equations (1.10.1) - (1.10.3) represent a set of non-linear partial differential equations of second-order with a hyperbolic characterisation. The equations consist of a compressible coupled model. Note, that "compressible" referred in this case to density changes in the fluid due to temperature differences. It indicates no characterisation by the Mach number (for further information it is pointed to [Ferziger02], chapter 1, 1.1). The temperature dependence on the dynamic viscosity μ is defined by the Sutherland model of section 1.9.

The enthalpy h is used instead of the temperature T in equation (1.10.3), due to the definition of the required equations in the used simulation software *OpenFOAM®*. For further information on the simulation software see [OpenFOAMa].

In this thesis, a non-Boussinesq fluid is assumed, hence no Boussinesq-approximation appears in equation (1.10.2), as it was presented in section 1.7 in equation (1.7.7). This aspect and its influence on the simulation results is further discussed in chapter 5 and chapter 7.

2. Computational methods

Most governing equations in fluid mechanics are solved analytically only for a limited number of problems and under certain conditions. The remaining problems have to be estimated by a numerical simulation. Therefore, the particular flow problems are described by an adapted mathematical model of the Navier-Stokes equations (as it was done in chapter 1, section 1.4 - 1.6). To solve the resulting system of non-linear partial differential equations of second order on a particular flow geometry by a computational algorithm, the entire geometrical domain has to be discretised by a numerical *grid* or *mesh*. This grid separates the geometrical domain in a finite number of several sub-domains, e. g. *control volumes* or *nodes*. Before the system of differential equations can be solved at these discrete locations, the equations have to be discretised and approximated in space and time by a set of algebraic equations.

In computational fluid dynamics (short: *CFD*) three discretisation methods are mainly used: *finite difference method* (short: *FD* methods), *finite volume method* (short: *FV* methods) and *finite element method* (short: *FE* methods). These methods are presented in the following. For each flow problem, the geometry is the determining factor for constructing an appropriate grid. In this thesis all flow configurations are presented by a simplified geometry of a rectangular enclosed container. Therefore, a block-structured orthogonal mesh which is constructed like a Cartesian grid would be an obvious choice. The grid consists of diverse levels of sub-domains which consists all of different resolutions. A structured grid is indeed the easiest type of a numerical mesh and has its disadvantages on complex geometrical solution domains. But for the observed geometries of this thesis, a structured grid is the best choice. An advantage of this type of mesh is the regular structure of the resulting system matrix which can be helpful during the computational solving process ([Ferziger02], chapter 2, 2.4.4). The information of this chapter is based on [Ferziger02], [Noll1993], chapter 4, 5, 7, and [Groll10].

2.1. Discretisation methods

2.1.1. Finite difference method (FDM)

All of the above mentioned discretisation methods approximate the system of partial differential equations at the discrete grid locations by an algebraic equation. In the FD

methods this equation describes the unknown variable values at each grid node and also its relation to variables at the neighbouring nodes. The resulting set of algebraic equations for all grid nodes is the approximated solution on the whole computational domain of the partial differential equation system. In the FD methods three approximation schemes are widely used, the *forward differencing scheme* (FDS), *backward differencing scheme* (BDS) and *central differencing scheme* (CDS). All presented schemes are based on the same principle and all of them are explained on the basis of a simplified transport equation

$$\frac{\partial}{\partial x_j} \underbrace{(\rho \varphi u_j)}_{\text{convection}} = \frac{\partial}{\partial x_j} \underbrace{\left(\Gamma \frac{\partial \varphi}{\partial x_j} \right)}_{\text{diffusion}} + \underbrace{q_\varphi}_{\text{source term}} \tag{2.1.1}$$

with density ρ, the j-th component of velocity u_j, the term of diffusivity Γ and the source term q_φ, which are all assumed as known. The arbitrary variable φ is assumed as unknown. The following evaluations are performed analogously to [Ferziger02], chapter 3.

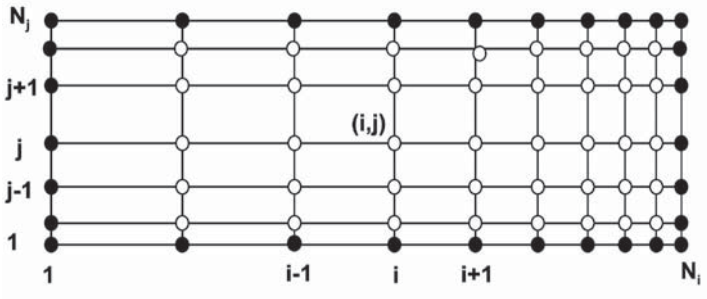

Figure 2.1.: 2D Cartesian structured mesh (as seen in [Ferziger02]).

In FD methods structured grids are usually used which are demonstrated in figure 2.1 on the basis of a 2D example. The filled circles indicate the boundary nodes, the other circles the remaining nodes of the grid. Each node is specified by two coordinates (i, j). The approximations of the first and second order derivatives on the grid are formulated in the following with help of the differential quotient and a Taylor-series expansion of the unknown variable φ around a specified grid node x_i. All presented schemes vary in the choice of this specified grid node.
The Taylor series of a continuously differentiable function $\varphi(x)$ in a point x_i is defined by

$$\begin{aligned} \varphi(x) = \varphi(x_i) + (x - x_i) \left(\frac{\partial \varphi}{\partial x} \right)_i &+ \frac{(x - x_i)^2}{2!} \left(\frac{\partial^2 \varphi}{\partial x^2} \right)_i \\ &+ \ldots + \frac{(x - x_i)^n}{n!} \left(\frac{\partial^n \varphi}{\partial x^n} \right)_i + \mathcal{O}(h^{n+1}) , \end{aligned} \tag{2.1.2}$$

where $\mathcal{O}(h^{n+1})$ stands for terms of the dimension h^{n+1}. h is the step size between two grid points x and x_i with $h = \Delta x = x - x_i$. From here on, the brief formulation $\varphi_{i+1} = \varphi(x_{i+1})$

is used. The *forward differencing scheme* (FDS) formulates the approximation of the first order derivative by a Taylor series of $\varphi(x)$ in the point x_{i+1} which lies in forward direction to x_i

$$\left(\frac{\partial\varphi}{\partial x}\right)_i = \frac{\varphi_{i+1}-\varphi_i}{x_{i+1}-x_i} - \frac{x_{i+1}-x_i}{2}\left(\frac{\partial^2\varphi}{\partial x^2}\right)_i - \ldots - \frac{(x_{i+1}-x_i)^n}{n!}\left(\frac{\partial^n\varphi}{\partial x^n}\right)_i + \mathcal{O}(h^{n+1})\,. \quad (2.1.3)$$

The *backward differencing scheme* (BDS) uses the Taylor series of $\varphi(x)$ in the point x_{i-1} which lies in backward direction to x_i

$$\left(\frac{\partial\varphi}{\partial x}\right)_i = \frac{\varphi_i-\varphi_{i-1}}{x_i-x_{i-1}} + \frac{x_i-x_{i-1}}{2}\left(\frac{\partial^2\varphi}{\partial x^2}\right)_i + \ldots + \frac{(x_i-x_{i-1})^n}{n!}\left(\frac{\partial^n\varphi}{\partial x^n}\right)_i + \mathcal{O}(h^{n+1})\,. \quad (2.1.4)$$

The *central differencing scheme* (CDS) is a combination of both above stated schemes and uses for the approximation both neighboured points of x_i, x_{i+1} and x_{i-1},

$$\left(\frac{\partial\varphi}{\partial x}\right)_i = \frac{\varphi_{i+1}-\varphi_{i-1}}{x_{i+1}-x_{i-1}} - \frac{(x_{i+1}-x_i)^2-(x_i-x_{i-1})^2}{2(x_{i+1}-x_{i-1})}\left(\frac{\partial^2\varphi}{\partial x^2}\right)_i - \ldots - \frac{(x_{i+1}-x_i)^n-(x_i-x_{i-1})^n}{n(x_{i+1}-x_{i-1})}\left(\frac{\partial^n\varphi}{\partial x^n}\right)_i + \mathcal{O}(h^{n+1})\,. \quad (2.1.5)$$

If the distance between two grid nodes is small, the higher order terms in the previous expressions will be also small and can usually be neglected after the first term. The then omitted terms are called the *truncation* or *discretisation error* of each scheme. For the CDS the truncation error is interpreted by

$$\epsilon_r = -\frac{(\Delta x_{i+1})^2-(\Delta x_i)^2}{2(\Delta x_{i+1}+\Delta x_i)}\left(\frac{\partial^2\varphi}{\partial x^2}\right)_i - \frac{(\Delta x_{i+1})^3+(\Delta x_i)^3}{6(\Delta x_{i+1}+\Delta x_i)}\left(\frac{\partial^3\varphi}{\partial x^3}\right)_i + \mathcal{O}(h^4) \quad (2.1.6)$$

with $\Delta x_{i+1} = x_{i+1}-x_i$ and $\Delta x_i = x_i - x_{i-1}$. The truncation error measures the discrepancy between an approximated solution of the scheme and exact analytical solution. Usually it is proportional to a power of the grid space Δx_i. A method is called *consistent*, if the truncation error tends to zero for $\Delta x_i \to 0$ and/or $\Delta t \to 0$.

If the approximation converges with a reduced step size Δx, the error is proportional to $(\Delta x)^k$. k is the exponent of the leading term in the truncation error formulation and it denotes the *order* of the scheme. It specifies how fast the error of a scheme is reduced, when the mesh is refined. All schemes with $k > 0$ are consistent. The error depends along on the grid spacing, always on the discretised derivatives. If the mesh resolution is changed by a constant factor r_e, the distances between the nodes is also changing by this factor, $\Delta x_{i+1} = r_e \Delta x_i$. Hence, the changed resolution has also an influence of the resulting truncation error. For a small step size, the first term becomes the dominating one and the truncation error in (2.1.6) is modified to

$$\begin{aligned}\epsilon_r &\approx \frac{(\Delta x_{i+1})^2 - (\Delta x_i)^2}{2(\Delta x_{i+1} + \Delta x_i)} \left(\frac{\partial^2 \varphi}{\partial x^2}\right)_i \\ &\approx \underbrace{\frac{\Delta x_{i+1}}{2} \left(\frac{\partial^2 \varphi}{\partial x^2}\right)_i}_{\epsilon^{FDS}} - \underbrace{\frac{\Delta x_i}{2} \left(\frac{\partial^2 \varphi}{\partial x^2}\right)_i}_{\epsilon^{BDS}} = \frac{(1 - r_e)\Delta x_i}{2} \left(\frac{\partial^2 \varphi}{\partial x^2}\right)_i\end{aligned} \tag{2.1.7}$$

with the error of the FDS and BDS. The error of these both methods can be approximated by

$$\epsilon_r^{FDS/BDS} \approx \frac{\Delta x_i}{2} \left(\frac{\partial^2 \varphi}{\partial x^2}\right)_i . \tag{2.1.8}$$

For a constant r_e close to 1, the error of the CDS is much smaller as the one of the FDS or BDS, which is the advantage of the CDS.

To solve the Navier-Stokes equations from chapter 1, section 1.10, besides an approximation of the first order derivative, one for the second order derivative has to be found which is done based on the information in [Ferziger02], chapter 3, and [Groll10]. Therefore, the approximation of the first order derivative is executed twice with additional points. For the CDS one obtains

$$\left(\frac{\partial^2 \varphi}{\partial x^2}\right)_i^{CDS} \approx \frac{\left(\frac{\partial \varphi}{\partial x}\right)_{i+\frac{1}{2}} - \left(\frac{\partial \varphi}{\partial x}\right)_{i-\frac{1}{2}}}{(x_{i+\frac{1}{2}} - x_{i-\frac{1}{2}})}, \tag{2.1.9}$$

where

$$x_{i+\frac{1}{2}} - x_{i-\frac{1}{2}} = \frac{1}{2}(x_{i+1} - x_i) + \frac{1}{2}(x_i - x_{i-1}) = \frac{1}{2}(x_{i+1} - x_{i-1}) .$$

Both inner derivatives in (2.1.9) can be written in terms of the FDS and BDS

$$\begin{aligned}\left(\frac{\partial \varphi}{\partial x}\right)_{i+\frac{1}{2}}^{CDS} &= \left(\frac{\partial \varphi}{\partial x}\right)_i^{FDS} \approx \frac{\varphi_{i+1} - \varphi_i}{x_{i+1} - x_i} , \\ \left(\frac{\partial \varphi}{\partial x}\right)_{i-\frac{1}{2}}^{CDS} &= \left(\frac{\partial \varphi}{\partial x}\right)_i^{BDS} \approx \frac{\varphi_i - \varphi_{i-1}}{x_i - x_{i-1}} .\end{aligned} \tag{2.1.10}$$

With the expressions in (2.1.10), equation (2.1.9) is modified to

$$\left(\frac{\partial^2 \varphi}{\partial x^2}\right)_i^{CDS} \approx \frac{\frac{\varphi_{i+1} - \varphi_i}{x_{i+1} - x_i} - \frac{\varphi_i - \varphi_{i-1}}{x_i - x_{i-1}}}{\frac{1}{2}(x_{i+1} - x_i) + \frac{1}{2}(x_i - x_{i-1})} . \tag{2.1.11}$$

The FD methods are a simple and effective way to approximate flows on uncomplex geometries. Higher order schemes can be developed on structured grids without great

difficulties. However, for complex grid structures, the FD methods are not appropriate, which is an important disadvantage. Besides a high accuracy of a discretisation scheme, it should also be *conservative*. Therefore, the balance of each variable in the flow field, e. g. the mass flow, should be fulfilled in the approximated algebraic equations in every volume at steady state and in absence of sources. This is usually not satisfied in FD methods without further precautions ([Ferziger02], chapter 2, 2.6.1).

Note that additionally to the truncation error, the numerical solution is also afflicted with modelling errors of the transport equation model and convergence errors of the selected solving algorithm ([Ferziger02], chapter 2, 2.5.7).

2.1.2. Finite element method (FEM)

These discretisation methods are not supplicated in this thesis and are presented only summarised at this point. In the finite element methods the computational grid is divided in a set of *discrete volumes* or *finite elements*. The grids are usually unstructured and consists in 2D of triangles and in 3D of tetrahedral or hexahedral summits. Before the set of differential equations is integrated over the whole grid, the equations are multiplied by appropriate *weighting functions*. The advantage of these methods is the application on arbitrary grids and an easy grid refinement. For further literature on this topic see, e. g., [Ferziger02], chapter 2.6.3 and [Liu13].

2.1.3. Finite volume method (FVM)

The following explanations are based on [Ferziger02], chapter 4. In the FD methods the first and second order derivatives of the transport equation are approximated in the nodes of the grid by a Taylor series expansion. In contrast to this approach, the FV methods approximate the set of partial differential equations by an integration over each control volume (CV) of the grid. A CV is illustrated in figure 2.2 for a 2D and 3D example.

To obtain, as beforehand, an approximating algebraic equation for each CV, the surface and volume integrals of each CV have to be approximated. Therefore, the grid is no longer determined by the nodes, but rather by the boundary surfaces of the CVs. The cell nodes of each CV should be located in the middle of each volume. The CVs should not overlap each other to obtain a higher accuracy of the method. FV methods can even operate on complex computational domains. But it is difficult to define schemes of higher as second order. The volume integral of the transport equation in (2.1.1) on page 30 can be written as

$$\int_\Omega \frac{\partial}{\partial x_j}(\rho\varphi u_j)\,d\Omega = \int_\Omega \frac{\partial}{\partial x_j}\left(\Gamma\frac{\partial}{\partial x_j}\varphi\right)\,d\Omega + \int_\Omega q_\varphi\,d\Omega\,, \tag{2.1.12}$$

where Ω is one control volume of the grid. In consequence of Gauss's theorem (for further details to Gauss's theorem see [Amann08], chapter 3) the volume integral is transformed in a surface integral for the convective and diffusive term

$$\int_{\partial\Omega} \rho\varphi \boldsymbol{u} \cdot \boldsymbol{n}\, dS = \int_{\partial\Omega} \Gamma\,(\nabla\varphi) \cdot \boldsymbol{n}\, dS + \int_{\Omega} q_\varphi\, d\Omega \tag{2.1.13}$$

with the boundary surface $\partial\Omega$ and its $\boldsymbol{n}$ normal vector.

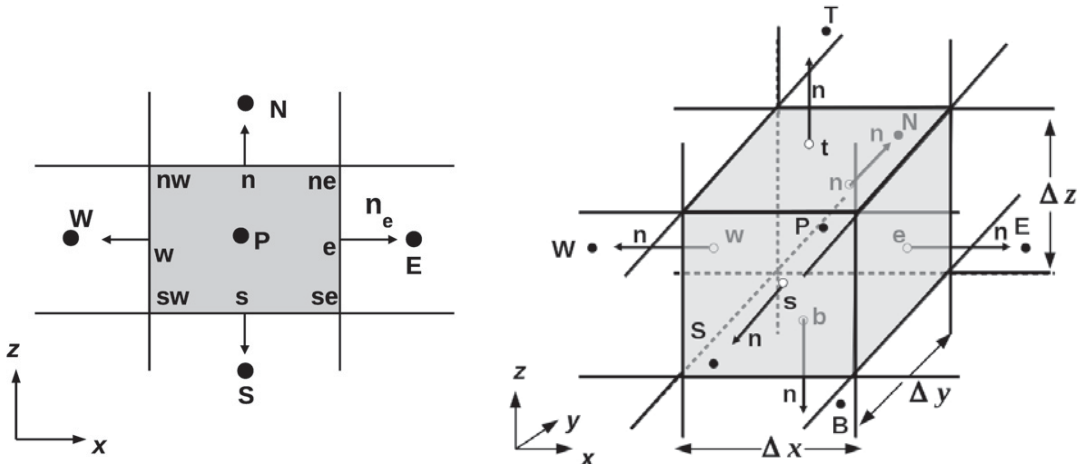

Figure 2.2.: Sketch of a control volume (CV) in 2D (left) and 3D (right) (as seen in [Ferziger02]).

Considering a continuously distribution of the variables over the surfaces, the integral in (2.1.13) can be described by the sum of the particular flows trough each face S_j

$$\sum_j \left((\rho\varphi)_j \cdot (u_j \cdot S_j)\right) = \sum_j \left(\Gamma_j \cdot (\nabla\varphi)_j \cdot S_j\right) + \int_{\Omega} q_\varphi\, d\Omega\,, \tag{2.1.14}$$

where the summand j stands for the number of individual faces S_j of the entire boundary surface $\partial\Omega$. For a characterisation of a CV, the common *compass notation* is used. Therefore, the CV is divided in its six faces (see figure 2.2). The node in the middle of the CV is indicated by P. The points which are located in direction of the y-axis are signified by N and S (north and south). The points which are located in direction of the x-axis are signified by W and E (west and east). The points T and B which are located in direction of the z-axis mark the top and bottom of the CV in a 3-dimensional case. The boundary faces of the CV around P are marked by n, s, e, w. In 2D, these donations would indicate the edges of the particular face. The velocity u_j is always normal to the face S_j.

The surface and volume integral can be approximated by interpolation of variable values either in the midpoint P or one or more extra locations at the cell faces. Three methods are very common for this interpolation, the *Midpoint rule*, the *Trapezoid rule* and *Simpson's rule* (see [Ferziger02], chapter 4.2.). All methods are based on the same principle, but are of different order, due to the utilised numbers of points in which the surface integral

is approximated. At this point only the *Midpoint rule* is presented for a 2-dimensional example. The *Midpoint rule* is defined by

$$F_e = \int_{S_e} f \, dS \approx f_e S_e. \tag{2.1.15}$$

The integral is approximated by the value of f at the cell face's centre and the entire cell face area. This method is an interpolation of second order and needs the value of the integrand f at the position e. Furthermore, an interpolation for the volume integral has to be found. To approximate the volume integral in the easiest way, one takes the product of the mean value and CV volume

$$Q_p = \int_{\Omega} q \, d\Omega = \bar{q} \Delta\Omega \approx q_p \Delta\Omega, \tag{2.1.16}$$

where q_p designates the value at the CV centre. This method is of second order and no interpolation is needed, because in the CV's centre point P all variables are known. For an interpolation of a higher order, the values of q are required at more positions as solely in the centre. Therefore, nodal values have to be interpolated. Some appropriate interpolation methods will be presented in the following section. For examples of 3-dimensional higher-order methods it is referred to [Ferziger02], chapter 4.

Another method for the approximation of the volume integral is the *Gaussian integration*. This method uses besides the estimated values at the grid nodes also so-called *weight coefficients*. For the interval $[-1, 1]$, the integration is formulated in [Liu13] chapter 7, 7.3.4 by

$$F = \int_{-1}^{1} f(\xi) d\,\xi = \sum_{j=1}^{m} w_j f(\xi_j)\,. \tag{2.1.17}$$

The interval $[-1, 1]$ can be transformed to any arbitrary one with help of a linear transformation. The node ξ_j and the weight coefficients w_j should be chosen in a way, that (2.1.17) produces an exact result of a possible high order polynomial. Note that a higher number of nodes does not assure a higher accuracy of the obtained results in any case. But a higher number of nodes will increase the computational effort in any case. The exact number of nodes is dependent on the integrand. An overview of different possible nodes and weight coefficient as well as further information is given in [Liu13] chapter 7, 7.3.4.

2.2. Interpolation schemes

As mentioned in the previously section, the approximation of the surface and volume integrals of the CV requires the variable values at locations other than the cell midpoint

P. Therefore, these values have to be interpolated by the known nodal values. In this section, diverse possibilities for such an interpolation scheme are demonstrated. The listed schemes are explained with help of cell face e for a value φ and its derivatives. This values are needed to estimate the convective $f_c = \rho\varphi\boldsymbol{u}\cdot\boldsymbol{n}$ and diffusive flux $f_d = \Gamma\dfrac{\partial}{\partial x_j}\varphi\cdot\boldsymbol{n}$ through the CV's surface. Note that the used interpolation method is obligated to be of the same order as the chosen integral approximation to receive the same accuracy. The following explanations are based on the information in [Ferziger02], chapter 4 and [Noll1993], chapter 4.

2.2.1. Upwind interpolation scheme (UDS)

This interpolation method is formulated analogously to the information in [Ferziger02], chapter 4.4.1.

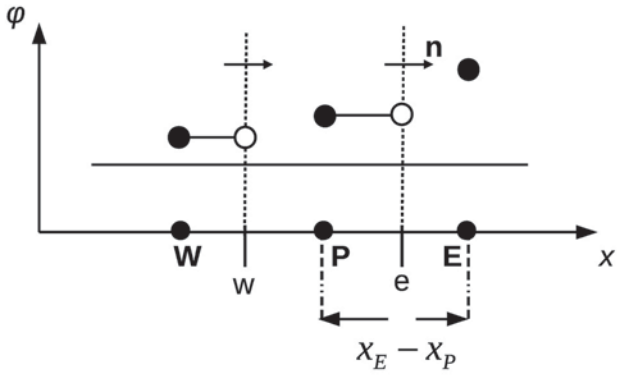

Figure 2.3.: Upwind interpolation scheme (UDS) (as seen in [Noll1993]).

To interpolate the value of φ_e between two nodes P and E at the boarder of face e, it is assumed as the value of the point which is located *upstream* or *upwind* to the boarder e. This interpolation equals the BDS, respectively FDS, in FD methods, as is illustrated in figure 2.3. Hence, the direction of the flux is determining for the definition of φ_e

$$\varphi_e = \begin{cases} \varphi_P & \text{if} \quad (\boldsymbol{u}\cdot\boldsymbol{n})_e > 0, \\ \varphi_E & \text{if} \quad (\boldsymbol{u}\cdot\boldsymbol{n})_e < 0. \end{cases} \tag{2.2.1}$$

The method is of first order, as its Taylor series around P shows

$$\varphi_e = \varphi_P + (x_e - x_P)\left(\frac{\partial\varphi}{\partial x}\right)_P + \frac{(x_e - x_P)^2}{2}\left(\frac{\partial^2\varphi}{\partial x^2}\right)_P + \mathcal{O}(h^3)\,. \tag{2.2.2}$$

The arising truncation error is then

$$f_e^{diff} = \Gamma_e\left(\frac{\partial}{\partial x}\varphi\right)_e\,. \tag{2.2.3}$$

This error term produces a false diffusive flux which is directed normal to the flow. This flux can influence the numerical results in this way that peaks or variations can be smooth out. It can be expressed by

$$\Gamma = \Gamma_e^{\text{real}} + \Gamma_e^{\text{num}}, \tag{2.2.4}$$

where $\Gamma_e^{\text{num}} = (\rho \boldsymbol{u})_e \, \Delta x/2$. This produced numerical diffusion can be even intensified in multidimensional grids. An subsequent disadvantage is the low order of the scheme. Consequently, a fine grid resolution has to be chosen to reach anyway a high accuracy.

2.2.2. Linear interpolation scheme (CDS)

This second order interpolation scheme is described based on [Ferziger02], chapter 4.4.2. The scheme needs for the integral approximation the two nearest nodes relative to the CV face centre e. Hence, it is equivalent to the CDS method for the first order derivative. The interpolation of φ_e is expressed by a weighted average of both nearest nodes E, P as given

$$\varphi_e = \lambda_e \varphi_E + \varphi_P (1 - \lambda_e). \tag{2.2.5}$$

The geometrical interpolation factor λ_e describes the distance between the neighboured points by

$$\lambda_e = \frac{x_e - x_P}{x_E - x_P}\,. \tag{2.2.6}$$

This is demonstrated in figure 2.4 A Taylor-series expansion of φ around P shows, that the scheme is of second order

$$\varphi_e = \varphi_E \lambda_e + \varphi_P (1 - \lambda_e) - \frac{(x_e - x_P)(x_E - x_e)}{2} \left(\frac{\partial^2 \varphi}{\partial x^2} \right)_P + \mathcal{O}(h^3)\,. \tag{2.2.7}$$

Assuming a linear approximation between the nodes P and E, the gradient is approximated by

$$\left(\frac{\partial \varphi}{\partial x} \right)_e \approx \frac{\varphi_E - \varphi_P}{x_E - x_P}\,. \tag{2.2.8}$$

The truncation error is indicated by a Taylor-series around φ_e

$$\epsilon_\tau = \frac{(x_e - x_P)^2 - (x_E - x_e)^2}{2(x_E - x_P)} \left(\frac{\partial^2 \varphi}{\partial x^2} \right)_e - \frac{(x_e - x_P)^3 + (x_E - x_e)^3}{6(x_E - x_P)} \left(\frac{\partial^3 \varphi}{\partial x^3} \right)_e + \mathcal{O}(h^4). \tag{2.2.9}$$

If e is located midway between the nodes P and E, the method is of second order and the leading error term is proportional to $(\Delta x)^2$. If a non-uniform grid is used, the leading term in (2.2.9) is proportional to the term of Δx and a potential grid expansion factor. As all schemes of second order, this one too, may provide an possible additional oscillatory which affects the solution. The important advantage of this FV method is its adaptability

to any kind of geometry. The scheme is conservative, if the values of the surface integrals of two adjoined CV's boundary faces are identical. 3-dimensional higher order schemes are difficult to construct for this type of scheme.

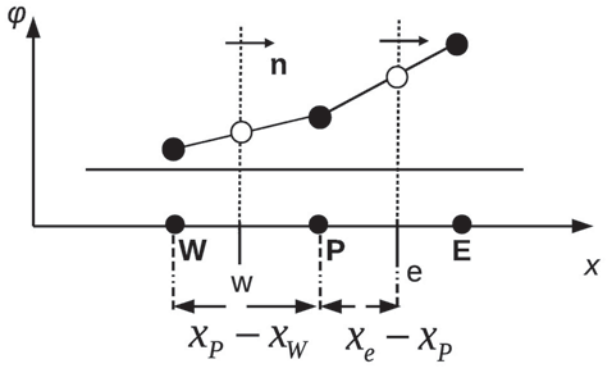

Figure 2.4.: Linear interpolation (CDS) (as seen in [Noll1993]).

2.2.3. Complementary notes

Besides the presented schemes for an approximation of the convective fluxes, there are additionally methods used in CFD, e. g. schemes of higher order or hybrid schemes. In this thesis the afore mentioned methods are sufficient for the examined problems. Hence, a presentation of the other schemes is dispensed at this point and only a short summary is given. For example, there is the *quadratic upwind interpolation* scheme (QUICK) which is of fourth order and similar to the CDS. Instead of a linear function a quadratic one is used to approximate the variables between the nodes P and E.

The *linear upwind* scheme (LUDS) is also of second order, but has a more complex structure than the CDS. Because unbounded solutions can be produced by a LUDS, the CDS should be the better choice. Furthermore, one can create a new scheme by combining two ore more other approximation schemes. This is done in the scheme of *Spalding* which uses a UDS and CDS. For further literature on these topics see, e. g., [Ferziger02], chapter 4.

2.3. Solution methods for linear equation systems

After the discretisation methods for the system of partial differential equations were presented before, solving methods for the resulting system of algebraic equations are illustrated in the following. Even if the resulting system is primarily non-linear, linear equation systems appear during the numerical solving process. Hence, one have to formulate efficient solving methods for such equation systems which is done in the following based on [Ferziger02], chapter 5. A resulting system of linear algebraic equations for the whole computational domain can be written as

$$A_P\varphi_P + \sum_l A_l\varphi_l = q_P \quad \Rightarrow \quad A\varphi = \boldsymbol{q}\,. \tag{2.3.1}$$

The source term q_P on the RHS of equation (2.3.1) contains all terms, that may be calculated in terms of the velocity $\boldsymbol{u}$ and body forces. These terms are presumed as known. P stands for an arbitrary grid node where the partial differential equation is discretised and l for the required neighboured nodes. A_l includes fluid properties, geometrical aspects and in nonlinear equations also the variable values themselves. The vector φ (or column matrix) includes the variable values of the grid nodes. Equation (2.3.1) shows on the RHS a summarised form.

The coefficient matrix A of the system is *square* and *sparse*. *Sparse* indicates, that each equation contains only a few unknowns and hence, only few matrix entries are unequal zero. The exact structure of A depends on the vector entries of φ ([Ferziger02], chapter 3, 3.8). For further explanations of the matrix properties it is pointed to the appendix A, section A.1, A.1.3 on page 275 in this thesis.

Two groups of schemes can be used to find a solution of (2.3.1), the so-called *direct* and the so-called *iterative* solution methods. The direct methods calculate directly a solution by converting the system in (2.3.1), while in the iterative methods a solution is estimated successively in several iteration steps until the final solution satisfies a stop criterion. Usually, the stop criterion is a specified tolerance which should be reached by the solution. Because of a high storage requirement and a possible non linearity of system (2.3.1), iterative methods are used for flow problems in CFD mostly. At this point, only these methods are demonstrated. For an description of the direct methods it is pointed, for example, to [Noll1993], chapter 7.

2.3.1. Iterative methods

The following explanations are based on the information in [Ferziger02], chapter 5, 5.3.1 - 5.3.4, [Noll1993], chapter 7 and [Groll10]. To solve the equation system in (2.3.1) by an iterative method, the matrix A is decomposed in two other matrices

$$A = (M - N)\,, \tag{2.3.2}$$

where M is the so-called *decomposition matrix* and N the so-called *iteration matrix* of the system. The choice of matrix M characterise each iteration method. By inserting (2.3.2) in (2.3.1), it follows

$$M\varphi = N\varphi + \boldsymbol{d} \quad \text{with} \quad \boldsymbol{d} = M^{-1}\boldsymbol{q}\,. \tag{2.3.3}$$

With help of equation (2.3.3), an iteration formulation can be written by

$$\varphi^{n+1} = M^{-1}(N\varphi^n + \boldsymbol{d})\,. \tag{2.3.4}$$

After n iteration steps are preformed, the approximated solution φ^n does not fulfil (2.3.1) exactly and a residuum term $\boldsymbol{\rho}^n$ remains

$$A\varphi^n = \boldsymbol{q} - \boldsymbol{\rho}^n\,. \tag{2.3.5}$$

Subtracting (2.3.5) from (2.3.1) it is

$$A\,(\varphi - \varphi^n) = \boldsymbol{\rho}^n \quad \Rightarrow \quad A\Delta\varphi^{n+1} = \boldsymbol{\rho}^n \tag{2.3.6}$$

with the exact solution φ. Additionally, a formulation of the methods convergence error is determined by

$$\boldsymbol{\epsilon}^n = \varphi - \varphi^n\,. \tag{2.3.7}$$

With the matrix decomposition for φ^{n+1} in (2.3.3) and an exact solution φ, it follows

$$\boldsymbol{\epsilon}^{n+1} = M^{-1}N\boldsymbol{\epsilon}^n\,. \tag{2.3.8}$$

From (2.3.5) a *correction* or *updating* formulation of the solution vector can be expressed by

$$\varphi^{n+1} = \varphi^n + \Delta\varphi^{n+1}\,, \tag{2.3.9}$$

where $\Delta\varphi^{n+1}$ is a correction vector of φ^n. The goal of the whole iteration process is a residuum which converges, in the best case, to zero. The convergence of an iteration method is mainly influenced by the eigenvalues λ_k and eigenvectors v_k of its iteration matrix A, respectively of its decompositions matrices

$$M^{-1}Nv_k = \lambda_k v_k\,. \tag{2.3.10}$$

The maximal eigenvalue of a matrix can be estimated by

$$\lambda_{\max} \approx \frac{\|\boldsymbol{\rho}^n\|}{\|\boldsymbol{\rho}^{n-1}\|} \tag{2.3.11}$$

with a chosen matrix norm $\|\cdot\|$. An iteration method is called *convergent*, if the maximal eigenvalue of its iteration matrix satisfies the following condition

$$\lambda_{\max} = \max_p \|\lambda_p\| < 1\,. \tag{2.3.12}$$

With the expression in (2.3.11), the convergence error can be rewritten as

$$\boldsymbol{\epsilon}^n = \varphi - \varphi^n \approx \frac{\boldsymbol{\rho}^n}{\lambda_{\max} - 1} \tag{2.3.13}$$

and

$$\|\boldsymbol{\epsilon}^n\| \approx \frac{\|\boldsymbol{\rho}^n\|}{\lambda_{\max} - 1}\,. \tag{2.3.14}$$

If the iteration matrix has complex eigenvalues, the error of the iteration method grows no longer exponentially and the above presented method has to be modified. For further details it is referred to [Ferziger02], chapter 5.

A further criterion for convergence of an iteration method can be formulated in terms of the *condition number* of its matrix A. The condition number defines, how intense small changes in the matrix A or source term $\boldsymbol{q}$ effect the solution vector φ. The condition number of a *regular* matrix is defined by

$$k(A) := \|A\|\|A^{-1}\| \quad \text{or} \quad k(A) := \frac{|\lambda_{\max}|}{|\lambda_{\min}|}\,. \tag{2.3.15}$$

The condition number depends on the selected matrix norm, but it is always $k(A) \leq 1$. If the condition number is small, small changes in the matrix A have also only small influence on the solution φ. A small condition number implies a small convergence error of the iteration method. The bigger the condition number of a matrix A is, the slower the iteration scheme converges.

Because the exact solution φ, and consequently the accuracy of the approximated solution φ^n, is not known during the iteration process, another stop criterion for the iteration has to be found. Usually, the reached approximated solution φ^n should fulfil a specified tolerance. This tolerance can be given by

$$\frac{\|\boldsymbol{\rho}^n\|}{r_{\text{ref}}} \leq \text{tol}\,, \tag{2.3.16}$$

where $\|\cdot\|$ is a chosen matrix norm of the residuum vector $\boldsymbol{\rho}$, r_{ref} is a reference value and *tol* a chosen tolerance value. For the correction vector $\Delta\varphi^n$ an equivalent criterion can be found

$$\frac{\|\Delta\varphi^n\|}{\varphi_{\text{ref}}} \leq \text{tol}\,. \tag{2.3.17}$$

Note that both criteria are only working successfully, if the matrix A is well-conditioned. Another approach of solving system (2.3.1) is a so-called *pre-conditioning matrix*. In this case, the system in (2.3.1) is multiplied by a *non-singular* matrix P. "Non-singular" means, that the inverse matrix of P exists. Due to the multiplication

$$P^{-1}A\varphi = P^{-1}\boldsymbol{q}\,, \tag{2.3.18}$$

the resulting problem in (2.3.18) has a smaller condition number than the primarily problem. The iteration formulation of the modified problem is then expressed by

$$P\varphi^{n+1} = q + (P - A)\varphi^n \,. \tag{2.3.19}$$

In terms of the above presented decomposition notation, it is $M = P$ and $N = P - A$.

2.3.1.1. Conjugate gradient methods

The following information of this section is based on the details in [Ferziger02], chapter 5, 5.3.6 and [Noll1993], chapter 7, 7.2.6. In terms of this thesis, the decomposition of matrix A is done by two different methods, the ILU (*incomplete LU decomposition*) and the *incomplete Cholesky factorisation*. Both methods are based on the LU *decomposition*, which is part of the direct methods (for further details see [Ferziger02], chapter 5, 5.2).

In the LU *decomposition*, the matrix A is decomposed as $M = LU = A + N$, where L and U are *triangular matrices*. L is a lower and M an upper triangular matrix. The diagonal elements of matrix L have to be equal unity, $L_{ii} = 1$. The *incomplete Cholesky factorisation* is a modified version of the above LU *decomposition* for symmetric matrices only. The ILU is also based on the LU *decomposition* and can be used for asymmetric, but positive definite matrices A.

The advantage of the ILU method is, that both decomposition matrices L and U can be chosen as sparse matrices, like the system matrix A. For each entry of the matrix A which is zero, the corresponding element in L or U is also set to zero. The matrix product of L and U has to approximate the matrix A as adequate as possible. This factorisation is not exact, but can be used as decomposition matrix M of an iterative method. The factorisation can be done without knowing the vector $\boldsymbol{q}$, which has many advantages as to storage requirements for systems with the same coefficient matrix A.

Both mentioned methods are often used for the matrix decomposition in the so-called *conjugate gradient methods* which belong to the so-called *descents methods*. In their originally form, these methods are only applicable on systems with *symmetrical, positive definite* system matrices. On basis of these methods, the problem in (2.3.1) is equivalent to a minimisation problem of the following form as it is described in [Ferziger02], chapter 5, 5.3.6

$$F = \frac{1}{2}\varphi^T A\varphi - \varphi^T \boldsymbol{q} = \frac{1}{2}\sum_{j=1}^{n}\sum_{i=1}^{n} A_{ij}\varphi_i\varphi_j - \sum_{i=1}^{n}\varphi_i q_i \tag{2.3.20}$$

with respect to all φ_i. The function F may be considered as a surface in hyper-space. F can be minimised with respect to several directions at once by searching only in one direction at a time. This is possible by a careful choice of the search directions. For two directions this could be formulated by

$$\varphi = \varphi_0 + \alpha_1 \boldsymbol{p}_1 + \alpha_2 \boldsymbol{p}_2 \,, \tag{2.3.21}$$

where the values α_1, α_2 should minimise function F in the plane which is spanned by the two direction vectors $\boldsymbol{p}_1, \boldsymbol{p}_2$. If the two search directions are called *A-conjugate* (with respect to the matrix A)

$$\boldsymbol{p}_1 \cdot A\boldsymbol{p}_2 = 0 \,, \tag{2.3.22}$$

the problem in (2.3.21) can be reduced to a minimisation problem for $\boldsymbol{p}_1$ and $\boldsymbol{p}_2$ individually. This approach can be performed for any number of direction vectors, but each direction has to be conjugate to the previous ones. If the matrix A is *non-singular*, the direction vectors are linear independent to each other. The actual search direction has to be chosen as different as possible from the old search directions. The advantage of this method is a decreasing error in each. The amount of the decrease depends on the chosen search direction.

In [Noll1993], chapter 7, 7.2.7, an approach obtaining an iterative solution is formulated as in the following. The exact solution φ^* can be determined by a linear combination of the A-conjugated vectors $\boldsymbol{p}_i$

$$\varphi^* = \varphi_0 + \sum_{j=1}^{n-1} (h_i \cdot \boldsymbol{p}_i) \,, \tag{2.3.23}$$

where n is the number of unknowns of the system. A multiplication of equation (2.3.23) with matrix A and a subsequent following scalar product with $\boldsymbol{p}_i$, leaves to the following expression

$$h_i = \frac{\boldsymbol{p}_i^T (\boldsymbol{q} - A\varphi_0)}{\boldsymbol{p}_i^T A \boldsymbol{p}_i} \,. \tag{2.3.24}$$

With help of expression (2.3.24), a formulation can be found to estimate an improvement of the inertial value φ^0

$$\boldsymbol{\rho}_i = \boldsymbol{q} - A\varphi_i \,, \tag{2.3.25}$$

$$\alpha_i = \frac{\boldsymbol{p}_i^T \boldsymbol{\rho}_i}{\boldsymbol{p}_i^T A \boldsymbol{p}_i} \,, \qquad i \geq 0 \,, \tag{2.3.26}$$

$$\varphi_{i+1} = \varphi_i + \alpha_i \cdot \boldsymbol{p}_i \,, \quad i \geq 0 \,. \tag{2.3.27}$$

The i-th direction vector $\boldsymbol{p}_i$ does not point in the same direction as the i-th residuum vector $\boldsymbol{\rho}_i$. α_i is a constructing parameter which is used to formulate the new solution, the residual vector and also the search direction. The above rules were stated first in [Faddejew1964]. The method reaches after $n-1$ iteration steps the exact solution $\varphi_{n-1} = \varphi^*$ with a negligible rounding error due to (2.3.23). In most problems, the number of iteration steps is smaller than $n-1$. The exact number depends still on the condition number of matrix

A. The condition number can be improved by a pre-conditioning matrix, as presented before. The formulation for the estimation of the vectors $\boldsymbol{p}_i$ is defined differently in each of the conjugate gradient methods.

The coefficient matrices of the discretised equations are usually asymmetrical, due to the convective terms in the governing equations. To avoid a possible asymmetry, the transposed matrix of A, A^T, is chosen as pre-conditioning matrix, because the product of both matrices A, A^T, is a symmetric matrix again. The modified equation system is then

$$A^T A\varphi_{n+1} = A^T \boldsymbol{q}\,. \tag{2.3.28}$$

This approach is called *generalised conjugate gradient method* and is described in the following based on the information in [Noll1993], chapter 7, 7.2.7. Note that the matrix product $A^T A$ is not as well-conditioned as the matrix A itself. The iteration formulation of this generalised conjugate gradient method can be summarised as follows

1) Estimate the residuum by $\boldsymbol{\rho}_0 = \boldsymbol{q} - A\varphi_0$ with the initial vector φ_0.

2) Calculate the i-th solution φ_i from $M\Delta\varphi_i = \boldsymbol{\rho}_i$ with $i \geq 0$.

3) Evaluate the direction vector $\boldsymbol{p}_i$ by

$$\begin{aligned}
\beta_0 &= 0\,, && (2.3.29)\\
\beta_i &= -\frac{\Delta\varphi_i^T A\boldsymbol{p}_{i-1}}{\boldsymbol{p}_{i-1}^T A\boldsymbol{p}_{i-1}}\,, \qquad i \geq 1\,, && (2.3.30)\\
\boldsymbol{p}_i &= \Delta\varphi_i + \beta_i \cdot \boldsymbol{p}_{i-1}\,, \qquad i \geq 0\,. && (2.3.31)
\end{aligned}$$

4) Correct the solution vector by

$$\begin{aligned}
\alpha_i &= \frac{\boldsymbol{p}_i^T \boldsymbol{\rho}_i}{\boldsymbol{p}_i^T A\boldsymbol{p}_i}\,, \qquad i \geq 0\,, && (2.3.32)\\
\varphi_{i+1} &= \varphi_i + \alpha_i \cdot \boldsymbol{p}_i\,, \quad i \geq 0\,. && (2.3.33)
\end{aligned}$$

5) Calculate the new residuum

$$\boldsymbol{\rho}_{i+1} = \boldsymbol{\rho}_i - \alpha_i A\boldsymbol{p}_i, \qquad i \geq 0\,. \tag{2.3.34}$$

6) Repeat steps 2) - 5) until the convergence criterion is reached.

The variable β_i is, as before α_i, a construction parameter. This scheme was published first in [Concus1978]. In its primarily form, the matrix M has to be symmetrical, positive definite and should approximate A. However, according to [Kosmol1993], this condition is not necessary. It is sufficient, that the matrix is diagonal dominant and has a symmetrical

band structure. Hence, the matrix M can be constructed on basis of the above presented ILU or incomplete Cholesky factorisation. According to ([Noll1993], chapter 7, 7.2.7), the resulting method is efficient and stable. Even the poor-conditioned equation system of the pressure-correction can be solved by this method effectively with a relaxation factor of $\alpha = 0.99$. For symmetric matrices A the system in (2.3.1) is solved instead of system (2.3.28) with help of the above described method.

2.3.1.2. Bi-conjugate gradient methods

A further method for the transformation of an asymmetrical matrix problem in a symmetrical one, is the so-called *bi-conjugate gradient method*. This method is described based on the information in [Ferziger02], chapter 5, 5.3.7. The transformation is done as follows

$$\begin{pmatrix} 0 & A \\ A^T & 0 \end{pmatrix} \cdot \begin{pmatrix} \Theta \\ \varphi \end{pmatrix} = \begin{pmatrix} \boldsymbol{q} \\ \boldsymbol{0} \end{pmatrix}. \tag{2.3.35}$$

Equation (2.3.35) can be regarded as a two sub-system, the original problem and the second one which contains the transposed matrix of A. The generalised conjugate gradient method is applied on the transformed system, as it was presented above. Regarding the second system, the above presented iteration steps have to be modified.

Therefore, one has to estimate next to the residuum $\boldsymbol{\rho}_0 = \boldsymbol{q} - A\varphi_0$, also the residuum $\bar{\boldsymbol{\rho}}_0 = \boldsymbol{q} - A^T\varphi_0$ with φ_0. It is also $\boldsymbol{p}_0 = \bar{\boldsymbol{p}}_0$. In step 2) also $M\Delta\varphi_i = \bar{\boldsymbol{\rho}}_i$ has to be solved. In step 3) and 5) calculations of the additional direction vectors $\bar{\boldsymbol{p}}_i$ and the residuum $\bar{\boldsymbol{\rho}}_{i+1}$ (with help of A^T) have to be performed. In step 3) and 4) β_i and α_i are estimated this time with the help of $\bar{\boldsymbol{p}}_i$, $\bar{\boldsymbol{\rho}}_i$ instead of $\boldsymbol{p}_i$, $\boldsymbol{\rho}_i$ The computational effort of this scheme is as twice as much as for a generalised conjugate gradient method, but it needs about the same number of iterations to reach convergence. This method was first published in [Fletcher1976].

2.4. Unsteady problems

So far, the transport equation was treated in a steady state formulation. For unsteady flows, the component of time has to be regarded additionally in the solving algorithm. The following demonstrations in this section are based on [Ferziger02], chapter 6.

Similar to the afore presented discretisation of the equations in space, the time variable has also to be discretised on the computational grid. In contrast to the discretisation in space, the discretisation in time may affect the flow only in a future time direction. Hence, after a calculation has already started, an implemented condition affects the solution only in future time steps and not in the elapsed ones. The discretisation in time has to be

performed always after the discretisation in space is done. As for the discretisation in space, several solution methods can be used for a discretisation in time. In terms of this thesis, just the required schemes of the *explicit* and *implicit Euler method* are presented.

According to [Ferziger02], chapter 6, 6.2.1, the formulation of a time discretisation method equals solving methods for ordinary differential equation problems (short: *ODE*). An initial value problem of first order is expressed for an arbitrary function $\varphi(t)$ by

$$\frac{d\varphi(t)}{dt} = f(t, \varphi(t)), \qquad \varphi(t_0) = \varphi^0 \,. \tag{2.4.1}$$

To find a solution $\varphi(t)$ of the initial value problem in eq. (2.4.1) at a certain time step $t = t_0 + \Delta t$, equation (2.4.1) has to be integrated over an interval $[t_n, t_{n+1}]$

$$\int_{t_n}^{t_{n+1}} \frac{d\varphi}{dt}\, dt = \varphi^{n+1} - \varphi^n = \int_{t_n}^{t_{n+1}} f(t, \varphi(t))\, dt. \tag{2.4.2}$$

The first presented solution method, the so-called *explicit Euler method*, evaluates the function $f(t, \varphi(t))$ with help of the initial point t_n, where the solution is already known

$$\varphi^{n+1} = \varphi^n + f(t_n, \varphi^n)\Delta t \,. \tag{2.4.3}$$

The second solution method, the so-called *implicit Euler method*, uses instead of the initial point t_n the final point t_{n+1}

$$\varphi^{n+1} = \varphi^n + f(t_{n+1}, \varphi^{n+1})\Delta t \,. \tag{2.4.4}$$

The value φ^{n+1} at t_{n+1} is not known a priori, why the method is labelled *implicit*. Both methods require the values of the unknown variable φ merely at two time points, why they are also called *two-levels methods*.

The numerical solution of these methods is called *stable*, if the errors which appear during the solving process are not magnified in the final solution. Many other definitions of a *stable temporal method* can be found in the literature. For example, a scheme is called stable, if the method produces a bounded solution, whenever the exact solution is bounded. One potential definition of stability for the explicit Euler method can be defined by

$$\left| 1 + \Delta t \frac{\partial f(t, \varphi)}{\partial \varphi} \right| < 1 \,. \tag{2.4.5}$$

This state is fulfilled, if $\Delta t \dfrac{\partial f(t, \varphi)}{\partial \varphi}$ is restricted to the unit circle around -1. Then the method is even *conditionally stable*. If the function φ produces only real values, the condition in (2.4.5) becomes

$$\left|\Delta t \frac{\partial f(t,\varphi)}{\partial \varphi}\right| < 2\,. \tag{2.4.6}$$

The implicit Euler method is a so-called *unconditionally stable* method, i.e, it produces a bounded solution in any time step, if it is $\frac{\partial f(t,\varphi)}{\partial \varphi} < 0$. Even if a large step size Δt is used, the resulting solution of the implicit Euler method tends to be smooth. The explicit and the implicit Euler method are schemes of first order. The error of both methods is proportional to the step size Δt.

Discretisation methods of unsteady flows can be formulated analogously to the ones of steady state flows, except for the additional time component which has also to be considered in the methods.

2.4.1. Explicit Euler method

The next step is the application of both methods to the generic transport equation described in (2.1.1) analogously to [Ferziger02], chapter 6, 6.3.1. The *explicit Euler method* method is the simplest method which uses all known variables at the initial time step t_n. This method is demonstrated in the following with help of the transport equation in eq. (2.1.1)

$$\frac{\partial(\rho\varphi)}{\partial t} = -\frac{\partial}{\partial x_j}(\rho\varphi u_j) + \frac{\partial}{\partial x_j}\left(\Gamma\frac{\partial\varphi}{\partial x_j}\right) + q_\varphi = f(t,\varphi(t))\,. \tag{2.4.7}$$

In the following, the exception $\rho = \text{const.}$ is taken, so equation (2.4.7) becomes

$$\frac{\partial\varphi}{\partial t} + \frac{\partial}{\partial x_j}(\varphi u_j) = \frac{\Gamma}{\rho}\frac{\partial^2\varphi}{\partial x_j^2} + q_\varphi. \tag{2.4.8}$$

It is also

$$\varphi_i^n = \varphi(x_i, t_0 + n\Delta t)\,. \tag{2.4.9}$$

Assuming a precedent discretisation in space using a CDS and a uniform grid spacing in x-direction, the algebraic equation for φ_i^{n+1} becomes

$$\varphi_i^{n+1} = \varphi_i^n + \left(-u\frac{\varphi_{i+1}^n - \varphi_{i-1}^n}{2\Delta x} + \frac{\Gamma}{\rho}\frac{\varphi_{i+1}^n + \varphi_{i-1}^n - 2\varphi_i^n}{(\Delta x)^2} + q_i^n\right)\Delta t\,. \tag{2.4.10}$$

Note that in connection with the CDS, the FD as well as FV discretisation method provides in this case the same algebraic equation. To simplify the term in (2.4.10), two dimensionless parameters are introduced. The first parameter d stands for the time which a disturbance needs to be transmitted by diffusion over a distance Δx

$$d = \frac{\Gamma\Delta t}{\rho(\Delta x)^2}\,. \tag{2.4.11}$$

The term d is expressed by the ratio of the time step Δt and a characteristic diffusion time $\frac{\Gamma}{\rho(\Delta x)^2}$. The second parameter is so-called *Courant number*. It is defined as ratio of the time step Δt and the characteristic convection time $u/\Delta x$. Co represents the time which a disturbance needs be transmitted by convection over a distance Δx

$$Co = \frac{u\Delta t}{\Delta x}\,. \tag{2.4.12}$$

With help of the terms in (2.4.11) and (2.4.12), equation (2.4.10) can be rewritten as

$$\varphi_i^{n+1} = (1-2d)\varphi_i^n + \left(d - \frac{Co}{2}\right)\varphi_{i+1}^n + \left(d + \frac{Co}{2}\right)\varphi_{i-1}^n + q_i^n \Delta t. \tag{2.4.13}$$

In the generic transport equation, φ may stand for any transport variable, e.g temperature or a concentration of a substance. Hence, (2.4.13) should reflect a realistic physical relation. As in the situation of a concentration, equation (2.4.13) should not become negative. The request, that the coefficients of all old nodal values should be positive, would imply for the term of diffusivity, that $d - \frac{Co}{2} > 0$ and $d + \frac{Co}{2} > 0$. For the convective term it has to be $1 - 2d > 0$. Thus, stability conditions have to be defined which regard these terms. This theory was invented by the Austrian-Hungarian mathematician *John von Neumann* (born in 1957).

The consideration for the convective term, gives a limit on the time step Δt

$$1 - 2d > 0 \Rightarrow d < \frac{1}{2} \Rightarrow \Delta t < \frac{\rho(\Delta x)^2}{\Gamma}\,. \tag{2.4.14}$$

The considerations for the diffusivity, give the following expressions based on the information in [Groll10]

$$\begin{aligned} d - \frac{Co}{2} > 0 \;\; &\Rightarrow \;\; Co < 2d \Rightarrow \frac{u\Delta t}{\Delta x} < \frac{2\Gamma\Delta t}{\rho(\Delta x)^2} \Rightarrow \frac{\rho u \Delta x}{\Gamma} < 2\,, \\ d + \frac{Co}{2} > 0 \;\; &\Rightarrow \;\; Co > -2d \Rightarrow \frac{u\Delta t}{\Delta x} > -\frac{2\Gamma\Delta t}{\rho(\Delta x)^2} \Rightarrow \underbrace{\frac{\rho u \Delta x}{\Gamma}}_{>0} > -2\,. \end{aligned} \tag{2.4.15}$$

The term $\dfrac{\rho u \Delta x}{\Gamma}$ is the so-called *Péclet number* which is named after the French physicist *Jean Claude Eugène Péclet* (1793 - 1857). From the relations in (2.4.14) and (2.4.15) it follows that

$$\begin{aligned} \frac{\mathrm{Pe}}{\mathrm{Co}} \;\; &> \;\; 2\,, \\ \mathrm{Pe} \;\; &< \;\; 2 \Rightarrow \mathrm{Co} << 1 \Rightarrow \Delta t << \frac{\Delta x}{u}\,. \end{aligned} \tag{2.4.16}$$

Thus, to obtain a stable method the Péclet number has to be smaller than 2. This is a sufficient, but not necessary condition, to obtain a bounded solution. The above presented method is based on the explicit Euler method for ODEs and the CDS for a discretisation in space. Hence, the method has to be of the same order as both used schemes are, i.e first order in time and second order in space.

Note that the coefficient φ_{i+1}^{n-1} in equation (2.4.13) may be possibly negative for flows which are dominated by convective heat transport. One suggestion to avoid this problem is the application of an UDS instead of a CDS in the calculation of the convective term as given in [Ferziger02], chapter 6, 6.3.1. This implies a modified formulation of equation (2.4.10)

$$\varphi_i^{n+1} = \varphi_i^n + \left(-u\frac{\varphi_i^n - \varphi_{i-1}^n}{\Delta x} + \frac{\Gamma}{\rho}\frac{\varphi_{i+1}^n + \varphi_{i-1}^n - 2\varphi_i^n}{(\Delta x)^2} + q_i^n \right) \Delta t\,, \tag{2.4.17}$$

which leads also to a modified version of (2.4.13)

$$\varphi_i^{n+1} = (1 - 2d - Co)\varphi_i^n + d\varphi_{i+1}^n + (d + Co)\,\varphi_{i-1}^n + q_i^n \Delta t. \tag{2.4.18}$$

The stability criterion becomes then

$$\Delta t < \frac{1}{\dfrac{2\Gamma}{\rho(\Delta x)^2} + \dfrac{u}{\Delta x}}\,. \tag{2.4.19}$$

If the convective heat transport is negligible, the criterion has the same formulation as the one in equation (2.4.16). If diffusion is negligible, stability is reached, if

$$Co < 1 \quad \text{or} \qquad \Delta t < \frac{\Delta x}{u}\,, \tag{2.4.20}$$

i.e if the Courant number is less or equal unity. This condition is called *Courant-Friedrich-Lewy condition*. It is named after the American mathematician *Richard Courant* (1888 - 1972), the German mathematician *Kurt Otto Friedrichs* (1901 - 1982) and the German mathematician Hans Lewy (1904 - 1988) ([Courant1928]).

The formulation of a stability criterion becomes very complicated, if convective as well as diffusive heat transports are present, In this case, one can require alternatively, that the conditions in (2.4.19) and (2.4.20) should be fulfilled individually. Note that the restriction on the Courant number implies that a fluid particle is only able to pass maximal one grid length in one time step.

2.4.2. Implicit Euler method

Analogously to section 2.4.1 and to [Ferziger02], chapter 6, 6.3.2, the application of the implicit Euler method, combined by using a CDS approximation for the spatial derivatives, on the generic transport equation leads to

$$\varphi_i^{n+1} = \varphi_i^n + \left(-u \frac{\varphi_{i+1}^{n+1} - \varphi_{i-1}^{n+1}}{2\Delta x} + \frac{\Gamma}{\rho} \frac{\varphi_{i+1}^{n+1} + \varphi_{i-1}^{n+1} - 2\varphi_i^{n+1}}{(\Delta x)^2} + q_i^n \right) \Delta t \,. \tag{2.4.21}$$

With equation (2.4.11) and (2.4.12) one receives

$$\underbrace{(1+2d)\varphi_i^{n+1}}_{A_P \varphi_i^{n+1} \Delta t} + \underbrace{\left(\frac{Co}{2} - d \right) \varphi_{i+1}^{n+1}}_{A_E \varphi_{i+1}^{n+1} \Delta t} + \underbrace{\left(-\frac{Co}{2} - d \right) \varphi_{i-1}^{n+1}}_{A_W \varphi_{i-1}^{n+1} \Delta t} = \underbrace{\varphi_i^n + q_i^n \Delta t}_{Q_i \Delta t} \,. \tag{2.4.22}$$

This method evaluates all fluxes in terms of the unknown variable values at the new time step t_{n+1}. The difference to a system of a steady problem is the extra coefficient A_P and the source term Q_P which arise both from the unsteady term.

The above described method is adequate for using large time steps Δt. Difficulties may appear at coarse grids. Although the scheme produces oscillatory results, it stays stable. This method has a first order truncation order in time. In contrast to the explicit Euler method, the computational effort of is method is high, because it solves a large coupled set of equations and has to store the entire coefficient matrix A as well as an extra source vector in each time step.

2.5. Solution methods for the Navier-Stokes equations

In the previous section, discretisation methods for a generic transport equation were discussed. To solve, as next step, the whole Navier-Stokes equation system, these methods have to be applied in an analogous manner to the momentum and continuity equation which is done in the following based on [Ferziger02], chapter 7 and on [Groll10].

The unsteady and convective terms are of the same type as as before in the generic transport equation and can thus be treated in the same way. The viscous term in the momentum equation has a similar form to the diffusive term of the generic transport equation and can be handled in the most cases in an analogous way. Contributions of viscous effects, e. g. of the bulk viscosity and a contribution due to the spatial variability of the viscosity, have to be treated with extra care. For further information is is pointed out to [Ferziger02], chapter 7, 7.1.1.

Attention should be paid on the diffusive terms in the momentum equation, which require a special treatment. These terms are similar to the preceding examined terms in the generic

transport equation. But this time, the terms consist of vector equations. Moreover, the pressure term has to be handled with extra care. It may be handled either as source term or surface force. The pressure term stands in close connection to the continuity equation and its gradient is coupled with each of the three momentum equations. Hence, there exists no independent equation for its evaluation (see also chapter 1, section 1.10, page 26).

2.5.1. Pressure correction methods

To solve the Navier-Stokes equations based on the variables of *velocity* and *pressure*, their solutions have to simultaneously satisfy the continuity and momentum equation in one time step. This implicates often a great computational effort in solving the resulting algebraic equations of the velocity field. In CFD applications, there are usually two solving methods used.

The first method estimates a local density from the continuity equation. With this density value and by means of a state equation, the pressure is evaluated subsequently. Afterwards, the momentum equation can be solved. Therefore, a dependence between density and pressure must be given. This approach is qualified to solve especially compressible flows. and it is presented in the end of this section. Possible problems arise in flow geometries which have besides a compressible, even an incompressible flow region, e. g. a flow in a Laval nozzle or multiphase flows in which further factors impact the density. For further details on these problems it is referred, for example, to [Ferziger02].

The second mentioned method uses an additional equation from which the pressure is evaluated. The additional equation results from the momentum and continuity equation. This approach is adequate for incompressible as well as compressible flows (see [Noll1993], chapter 5). One method which is based on this approach, is the so-called *pressure correction method* which is used in this thesis. Before the implicit pressure correction methods are explained, an explicit version is presented shortly in the following section.

2.5.1.1. Explicit methods

As first step, an explicit solving method is given for the unsteady Navier-Stokes equations analogously on the information in [Ferziger02], chapter 7, 7.3.2. Therefore, the in space, but not in time, discretised momentum equation is used. For its discretisation an arbitrary method is generally applicable

$$\frac{\partial}{\partial t}(\rho u_i) = \underbrace{-\frac{\partial}{\partial x_j}(\rho u_i u_j) + \frac{\partial \tau_{ij}}{\partial x_j}}_{\zeta_i} - \frac{\partial p}{\partial x_i}\,. \tag{2.5.1}$$

The term ζ_i represents the adjective and viscous terms. Application of the explicit Euler method for unsteady flow problems to equation (2.5.1), leads to

$$(\rho u_i)^{n+1} - (\rho u_i)^n = \Delta t \left(\zeta_i^n - \frac{\partial p^n}{\partial x_i} \right) . \tag{2.5.2}$$

The term ζ_i^n can then be estimated with help of the velocity u_n in time step t_n. After the pressure has been calculated, $\frac{\partial p^n}{\partial x_i}$, the term ρu_i can be determined. In this case, the estimated value of ρu_i in time step $n+1$ does not fulfil the continuity equation. To obtain continuity, one rewrite equation (2.5.2) as

$$\frac{\partial(\rho u_i)^{n+1} - \partial(\rho u_i)^n}{\partial x_i} = \Delta t \left(\frac{\partial}{\partial x_i} \left(\zeta_i^n - \frac{\partial p^n}{\partial x_i} \right) \right) . \tag{2.5.3}$$

The first term stands for the divergence of the new velocity and should be be zero. If continuity was reached in time step n, the second term is zero. Otherwise, it will remain in the equation. This is also the case for the term ζ_i which has to be zero as well, if the density ρ is constant. From equation (2.5.3) follows for the pressure p^n

$$\underbrace{\frac{\partial}{\partial x_i}}_{*} \underbrace{(\frac{\partial p^n}{\partial x_i})}_{\Delta} = \frac{\partial \zeta_i^n}{\partial x_i} . \tag{2.5.4}$$

The term $*$ stem from the continuity equation and the term Δ from the momentum equation. If the equation is solved by p^n, the velocity in time step $n+1$ will be divergence free. The method is then repeated in the subsequent time step $n+2$.

If the pressure gradient had been handled with an implicit scheme, p^n would be replaced by p^{n+1}. The rest of the method would stay the same. If an accuracy in time is obliged in the simulation, modifications of this method commonly operate with time advanced approaches which are more accurate as the explicit Euler method.

2.5.1.2. Implicit methods - SIMPLE

Incompressible flows

The next presented method is used to solve steady flow problems. The following demonstrations are based on [Ferziger02], chapter 7, 7.3.3 - 7.3.4 and on [Groll10].

The method is implicit, due to its low sensitivity of the time step restriction. All presented methods are at explained on the basis of steady incompressible flows, but can also be modified for compressible flows. Note that a pressure or pressure correction is obligated

to enforce the mass conservation in each time step in each method. First, one has to find a solution u_i^n which fulfills the continuity and momentum equation in time step t_n

$$\frac{\partial}{\partial x_j}(\rho u_{i,P}^n) = 0\,, \tag{2.5.5}$$

$$\frac{\partial u_{i,P}^n}{\partial t} + u_{j,P}^n \frac{\partial u_{i,P}^n}{\partial x_j} = -\frac{1}{\rho^n}\frac{\partial p^n}{\partial x_i} + Q_{u_i}^n\,. \tag{2.5.6}$$

When the solution u_i^n is found in t_n, one can advance to the next time step t_{n+1} and derive the solution u_{i+1}^{n+1} with help of one of the previously presented methods for unsteady problems. The new solution u_{i+1}^{n+1} does not satisfy the continuity equation any longer and has to be corrected. This is done with help of the pressure term. The discretised equations for the velocities at the new time step t_{n+1} are written as

$$A_P^{u_i} u_{i,P}^{n+1} + \sum_l A_l^{u_i} u_{i,l}^{n+1} = Q_{u_i}^{n+1} - \left(\frac{\partial p^{n+1}}{\partial x_i}\right)_p\,. \tag{2.5.7}$$

The discretisation in space can be done by each of the previously explained methods. If an implicit method was used for the time discretisation of the momentum equation, the equations in (2.5.7) are a non-linear system. Q includes all terms that may be explicitly formulated in terms of u_i^n as well as body forces or linearised terms that depend on u_i^{n+1} or other variables of the new time step t_{n+1}. The pressure term is not included in the source term Q. P stands for an arbitrary velocity node and l for the neighbouring points. Due to a probable dependence of the coefficients A and the source term Q on the unknown solution u_i^{n+1}, the expression in (2.5.7) has to be estimated by iteration. This is performed in two steps, or rather in two different iteration steps.

First, we have the so-called *outer iteration*. It marks the iterations executed during one time step. During this outer iteration the source matrix and the coefficients are updated. Second, we have the so-called *inner iterations* which are additional iterations executed during one outer iteration. In these inner iterations, the same linear system as in the outer iteration is solved, but this time with fixed matrices. Only the pressure and velocity terms are corrected. In the following, an index m, which marks the outer iteration, replaces the time step index $n+1$. The equations which are solved in an outer iteration are

$$A_P^{u_i} u_{i,P}^{m^*} + \sum_l A_l^{u_i} u_{i,l}^{m^*} = Q_{u_i}^{m-1} - \left(\frac{\partial p^{m-1}}{\partial x_i}\right)_p\,. \tag{2.5.8}$$

The estimated velocities u_i^m of this iteration step does normally not satisfy the discretised continuity equation, because the pressure, which is required in (2.5.8), was estimated in the previous outer iteration or time step. The velocities have to be corrected which implies

a modification of the pressure p. This is done in the following inner iteration and shown next. Equation (2.5.8) is transformed to

$$u_{i,P}^{m^*} = \frac{Q_{u_i}^{m-1} - \sum_l A_l^{u_i} u_{i,l}^{m^*}}{A_P^{u_i}} - \frac{1}{A_P^{u_i}} \left(\frac{\partial p^{m-1}}{\partial x_i} \right)_P . \tag{2.5.9}$$

$u_{i,P}^{m^*}$ is just a predicted value of the iteration m and does not satisfy the continuity equation. Hence, still a velocity $u_{i,P}^{m}$ and a pressure field p^m have to be found which satisfy the continuity and momentum equation. This ideal velocity $u_{i,P}^{m}$ is assumed to be

$$u_{i,P}^{m} = \frac{Q_{u_i}^{m} - \sum_l A_l^{u_i} u_{i,l}^{m}}{A_P^{u_i}} - \frac{1}{A_P^{u_i}} \left(\frac{\partial p^{m}}{\partial x_i} \right)_P . \tag{2.5.10}$$

The corrected velocity can then be formulated as the difference of equation (2.5.10) and (2.5.9)

$$\underbrace{u_{i,P}^{m} - u_{i,P}^{m^*}}_{u'} = \frac{-\sum_l A_l^{u_i} (u_{i,l}^{m} - u_{i,l}^{m^*})}{A_P^{u_i}} - \frac{1}{A_P^{u_i}} \frac{\partial}{\partial x_i} \left(\underbrace{p^m - p^{m-1}}_{p'} \right)_P \tag{2.5.11}$$

with

$$u_i^m = u_i^{m*} + u' , \qquad p^m = p^{m-1} + p' . \tag{2.5.12}$$

Instead of the pressure p a corrected pressure p' is used. The difference of the source terms $Q_{u_i}^{m} - Q_{u_i}^{m-1}$ is neglected entirely in each outer iteration. Moreover, the method neglects also the first term on the RHS in equation (2.5.11), which can cause sometimes a slow convergence of the method. Note that the following term is equal zero

$$\left(\frac{\partial (\rho u_{i,P}^{m})}{\partial x_i} \right)_P = 0, \tag{2.5.13}$$

because it satisfies continuity. By inserting expression (2.5.11) in the continuity equation, a discrete Poisson equation for the pressure correction results

$$\frac{\partial}{\partial x_i} \left[\frac{\rho}{A_P^{u_i}} \left(\frac{\partial p'}{\partial x_i} \right) \right]_P = \left(\frac{\partial (\rho u_{i,l}^{m^*})}{\partial x_i} \right)_P . \tag{2.5.14}$$

With the implicitly solved equation (2.5.14) and a now known pressure p', u_i^m is corrected in a new inner iteration.

$$u_{i,P}^{m} = u_{i,P}^{m^*} - \frac{1}{A_P^{u_i}} \left(\frac{\partial p'}{\partial x_i} \right)_P . \tag{2.5.15}$$

This velocity satisfy the continuity equation, but still not the momentum equation. The outer iteration is finished at this point. The above described process is repeated during another outer iteration until a velocity is reached which satisfy the continuity equation

and the momentum equation. As starting terms for the new outer iteration the terms $u_{i,P}^m$ and p^m are used. The loop of outer iterations is repeated until the terms u' and p' reach a negligible small value. Afterwards, the next time step is started.

The above presented method is called *SIMPLE algorithm*. The abbreviation SIMPLE stands for *Semi-Implicit Method for Pressure-Linked Equations* ([Pantakar1980]). The denotation *semi-implicit* refers to the aspect that the corrections and non-linearity are neglected in the above steps. To ensure the convergence of the method, an under-relaxation is possibly required during the solving process of the momentum equation. Therefore, the following under-relaxation which should be performed after the estimation of the pressure correction is proposed in [Ferziger02], chapter 7, 7.3.4

$$p^m = p^{m-1} + \alpha_p p' \qquad \text{with} \qquad 0 \leq \alpha_p \leq 1\,. \tag{2.5.16}$$

The choice of α_p is flow problem dependent and has to be estimated by trial and error ([Noll1993], chapter 5, 5.2.1). The velocity has then be corrected as given in [Ferziger02], chapter 7, 7.3.4

$$u_{i,P}^{'m} = -\frac{1}{A_P^{u_i}} \left(\frac{\partial p'}{\partial x_i} \right)_P . \tag{2.5.17}$$

If the pressure p is known at the boundary nodes p_{BC}, the pressure p^{m-1} can be assumed as $p^{m-1} = p_{BC}$ at these nodes. Hence, no further correction of the pressure has to be done at the boundary nodes. It is $p'_{BC} = 0$.

The SIMPLE algorithm can be summarised as follows

1) Start the calculation at time-step t_{n+1}. The values u_i^n, p^n are used as initial start values for the estimation of u_i^{n+1}, p^{n+1}.

2) Evaluate $u_i^{m^*}$ from the linear algebraic equation system of the discretised momentum equation.

3) Obtain p' by solving the pressure-correction equation.

4) Estimate u_i^m from the corrected velocities and pressure values. u_i^m satisfy continuity. The conservative fluxes can now be calculated. All other equations in the system can be solved.

5) Go back to step 2. Repeat it onwards until the tolerance criterion is reached and all correction terms are insignificantly small.

6) Move to step 1). Start the loop again for the subsequent time step $t_{n+1} + \Delta t$ until the final step is reached.

Regarding turbulent flows, one additional step has to be considered in the above stated step 4). The effective viscosity has to also be calculated from the turbulent quantities (see chapter 3).

Compressible flows

The above discussed SIMPLE algorithm can be applied on incompressible flows as well as compressible flows. Because the density ρ, viscosity μ and other fluid properties were kept in the equations, the SIMPLE algorithm (as well as the beforehand demonstrated discretisation and solving methods) can be applied also on problems with varying fluid properties.

But however, temperature changes and implied changes of fluid properties have to be considered with extra care. These changes increase the non-linearity of the equation system. One has to consider two possible cases. In the first case, the pressure varies only insignificantly with varying temperature (**case 1**). In the second case, the pressure varies significantly with varying temperature and causes a change in density (**case 2**). For both cases, the SIMPLE algorithm has to be modified, which is explained in the following based on the information in [Ferziger02], chapter 10 and 12.

In **case 1**, two sub-cases have to be regarded. In the *first sub-case*, the fluid is temperature dependent, but the density is assumed to be constant. Hence, the conservation of energy and momentum are coupled and both equations have to be solved simultaneously. Usually, the equations can be solved in a sequential anyway for most problems. Within one outer iteration, the momentum equation, and thus, velocities and pressure are solved with the "old" known values of temperature and fluid properties. Afterwards, the new temperature value is estimated and fluid properties are updated (see [Ferziger02], chapter 12).

In the *second sub-case*, the temperature changes implicate a density change which drives the flow, like it is the case in a natural convection. If these density changes are merely small, a Boussinesq-assumption can be supposed (see chapter 1, section 1.7 on page 18). These problems can then be solved like an incompressible flow problem with the above presented SIMPLE method. Note that the considered Boussinesq-assumption implicates an extra modulation error which increases with rising temperatures and density variations. Non-Boussinesq flows can be treated with help of two different outer iterations for solving the momentum equation, as mentioned before. Within one outer iteration, the momentum equation is solved with help of the "old" known values of temperature and fluid properties. After this outer iteration is done, the new temperature is estimated and the fluid properties are updated in the following outer iteration. This approach is performed in the simulation studies of this thesis. Note that the coupling between the velocity as well as temperature and density may be very strong. The intensity of the coupling depends on

the Prandtl number. Therefore, the equation system can converge slower than in case of isothermal flows. The solving process of these systems increases the computational cost due to a higher complexity and higher storage requirements (see [Ferziger02], chapter 10).

Regarding **case 2**, it exists a modified version of the SIMPLE algorithm which considers the variation of pressure and changes in density. The compressible scheme is based on the above presented SIMPLE algorithm. As mentioned before, these modified method uses the continuity equation to estimate a local density. From this density the pressure can be evaluated with help of a state equation. One commonly used method is based on the approach of [Demirdžić1993]. Because this approach is not used in this thesis, it is pointed to [Ferziger02], chapter 10 for further information.

2.5.1.3. Implicit methods - PISO

Incompressible flows

Another important algorithm for solving steady problems is the so-called *PISO* algorithm ([Issa1986]) which is presented in this section. Its abbreviation stands for *Pressure Implicit with Splitting of Operators*. In the previously presented SIMPLE algorithm, the first term on the RHS of equation (2.5.11) was entirely neglected which can cause a slow convergence or even a possible instability of the method. Therefore, the PISO algorithm approximates this term instead of neglecting it. Hereby, the PISO algorithm has indeed a more complex structure as the SIMPLE algorithm, but it converges faster and provides a greater stability. The following explanations are based on the commentaries in [Ferziger02], chapter 7, 7.3.3 - 7.3.4 and [Groll10].

In the first step of the PISO algorithm, a SIMPLE iteration is done

$$u_{i,P}^{m^*} = \frac{Q_{u_i}^{m-1} - \sum_l A_l^{u_i} u_{i,L}^{m^*}}{A_P^{u_i}} - \frac{1}{A_P^{u_i}} \left(\frac{\partial p^{m-1}}{\partial x_i} \right)_P . \tag{2.5.18}$$

This equation is not yet divergence free. Again an ideal velocity $u_{i,P}^{m^{**}}$ is formulated which satisfies the continuity equation, but is not the final velocity solution.

$$u_{i,P}^{m^{**}} = \frac{Q_{u_i}^{m-\frac{1}{2}} - \sum_l A_l^{u_i} u_{i,l}^{m^{**}}}{A_P^{u_i}} - \frac{1}{A_P^{u_i}} \left(\frac{\partial p^{m-\frac{1}{2}}}{\partial x_i} \right)_P . \tag{2.5.19}$$

Note that only an intermediate step of the outer iteration has been performed up to this point which is indicated by $m - \frac{1}{2}$. To complete the outer iteration m, as before, the difference of equation (2.5.18) and (2.5.19) is used

$$\underbrace{u_{i,P}^{m^{**}} - u_{i,P}^{m^*}}_{u'_{i,P}} = -\frac{\sum_l A_l^{u_i}(u_{i,l}^{m^{**}} - u_{i,l}^{m^*})}{A_P^{u_i}} - \frac{1}{A_P^{u_i}}\frac{\partial}{\partial x_i}\left(\underbrace{p^{m-\frac{1}{2}} - p^{m-1}}_{p'}\right)_P \tag{2.5.20}$$

with

$$u'_{i,P} = u_{i,P}^{m^{**}} - u_{i,P}^{m^*}\,, \quad p' = p^{m-\frac{1}{2}} - p^{m-1}\,. \tag{2.5.21}$$

As in the SIMPLE algorithm, the term of the corrected velocities

$$\frac{\sum_l A_L^{u_i}(u_{i,l}^{m^{**}} - u_{i,l}^{m^*})}{A_P^{u_i}} \tag{2.5.22}$$

is neglected once again. The pressure correction can be estimated from equation (2.5.20) (analogously as before by equation (2.5.14)),

$$\frac{\partial}{\partial x_i}\left[\frac{\rho}{A_P^{u_i}}\left(\frac{\partial p'}{\partial x_i}\right)\right]_P = \left(\frac{\partial(\rho u_{i,l}^{m^*})}{\partial x_i}\right)_P\,. \tag{2.5.23}$$

The first step of the PISO algorithm ends at his point obtaining a divergence free velocity

$$u_{i,P}^{m^{**}} = u_{i,P}^{m^*} - \frac{1}{A_P^{u_i}}\frac{\partial}{\partial x_i}\left(p^{m-\frac{1}{2}} - p^{m-1}\right)_P\,. \tag{2.5.24}$$

Up to this point, the PISO algorithm uses the same scheme as the SIMPLE algorithm. The following second step, which starts at this point and compensates the neglected term $\sum_l A_L^{u_i}(u_{i,l}^{m^{**}} - u_{i,l}^{m^*})/(A_P^{u_i})$, differs completely from the SIMPLE algorithm. Once again, one subtracts the "starting" velocity

$$u_{i,P}^{m^{**}} = \frac{Q_{u_i}^{m-\frac{1}{2}} - \sum_l A_l^{u_i} u_{i,l}^{m^*}}{A_P^{u_i}} - \frac{1}{A_P^{u_i}}\left(\frac{\partial p^{m-\frac{1}{2}}}{\partial x_i}\right)_P \tag{2.5.25}$$

from an ideal velocity, which satisfies continuity,

$$u_{i,P}^{m} = \frac{Q_{u_i}^{m} - \sum_l A_l^{u_i} u_{i,l}^{m^{**}}}{A_P^{u_i}} - \frac{1}{A_P^{u_i}}\left(\frac{\partial p^{m}}{\partial x_i}\right)_P \tag{2.5.26}$$

and gains

$$\underbrace{u_{i,P}^{m} - u_{i,P}^{m^{**}}}_{u''_{i,P}} = -\frac{\sum_l A_l^{u_i}(u_{i,l}^{m^{**}} - u_{i,l}^{m^*})}{A_P^{u_i}} - \frac{1}{A_P^{u_i}}\frac{\partial}{\partial x_i}\left(\underbrace{p^{m} - p^{m-\frac{1}{2}}}_{p''}\right)_P\,, \tag{2.5.27}$$

where

$$u_{i,P}^{''} = u_{i,P}^{m} - u_{i,P}^{m^{**}}\,, \quad \text{and} \quad p^{''} = p^{m} - p^{m-\frac{1}{2}}\,. \tag{2.5.28}$$

Considering that

$$\left(\frac{\partial(\rho u_{i,P}^{m})}{\partial x_i}\right)_P = 0, \tag{2.5.29}$$

an implicit pressure correction follows from equation (2.5.27) by

$$\frac{\partial}{\partial x_i}\left[\frac{\rho}{A_P^{u_i}}\left(\frac{\partial p^{''}}{\partial x_i}\right)\right]_P = \left(\frac{\partial(\rho u_i^{m^{**}})}{\partial x_i}\right)_P - \frac{\partial}{\partial x_i}\left(\rho\frac{\sum_l A_l^{u_i}(u_{i,l}^{m^{**}} - u_{i,l}^{m^{*}})}{A_P^{u_i}}\right)_P . \tag{2.5.30}$$

This time, the term $\sum_l A_L^{u_i}(u_{i,l}^{m**} - u_{i,l}^{m^*})/(A_P^{u_i})$ is not neglected. It can be estimated with help of term $u_{i,P}^{'}$ in equation (2.5.21) and in (2.5.27). Thus, one obtains the corrected velocity

$$u_{i,P}^{m} = u_{i,P}^{m^{**}} - \frac{1}{A_P^{u_i}}\left(\frac{\partial p^{''}}{\partial x_i} + \sum_l A_l^{u_i} u_{i,l}^{'}\right)_P \tag{2.5.31}$$

with the corrected pressure

$$p^{m} = p^{m-\frac{1}{2}} + p'' = p^{m-1} + p' + p''\,. \tag{2.5.32}$$

The proceeding of the PISO algorithm can also be summarised by the overview of the SIMPLE algorithm from page 55. The only exception is the fact, that the additional pressure correction equation and the consequent modification of velocity and pressure have to be additionally regarded in step 4).

An under-relaxation of the pressure correction is not necessarily required in the PISO algorithm, but can be formulated as stated in [Ferziger02], chapter 5, 5.4.3. Within the n-th outer iteration, the resulting algebraic equation for an arbitrary variable φ can be written as

$$A_P\varphi_P^n + \sum_l A_l\varphi_l^n = Q_P\,. \tag{2.5.33}$$

The coefficients A_l and the source term Q can all include terms of φ^{n-1}, which itself does not depend explicitly on φ^n. This time, the system is linear. To ensure stability, it is required that φ^n changes within the outer iteration only by an amount of

$$\varphi^n = \varphi^{n-1} + \alpha_\varphi\left(\varphi^{\text{new}} - \varphi^{n-1}\right)\,. \tag{2.5.34}$$

φ^{new} is the solution of (2.5.33) and it is $0 < \alpha_\varphi < 1$. When the old source vector and coefficients are updated, the old iteration can be replaced by the new one

$$\varphi_P^{\text{new}} = \frac{Q_P - A_l\varphi_l^n}{A_P}\,. \tag{2.5.35}$$

Inserting (2.5.35) in (2.5.34), one obtains a modified equation for the node P by

$$\frac{A_P}{\alpha_\varphi}\varphi_P^n + \sum_l A_l \varphi_l^n = Q_P + \frac{1-\alpha_\varphi}{\alpha_\varphi} A_P \varphi_P^{n-1} \,. \tag{2.5.36}$$

The term $\frac{A_P}{\alpha_\varphi}$ and $Q_P + \frac{1-\alpha_\varphi}{\alpha_\varphi} A_P \varphi_P^{n-1}$ are the adjusted main diagonal matrix elements of A and the modified source vector. Equation (2.5.36) is then solved within the inner iteration. If convergence is reached in the outer iteration, the term of α_φ vanishes and the primarily problem is solved ([Ferziger02], chapter 5, 5.4.3). The best choice of the under-relaxation factors is problem dependent and has to be found, as in the case of the SIMPLE algorithm, by trial and error ([Noll1993], chapter 5, 5.2.1). This version of the presented under-relaxation was stated by [Pantakar1980]. It is an efficient method, because it increases the diagonal dominance of matrix A.

Compressible flows

For the PISO method also a compressible version can be formulated. Because of the similarity between the PISO and the SIMPLE algorithm and the fact, that the compressible version of the SIMPLE algorithm was already discussed in section 2.5.1.2, it is referred at this point to [Issa1986] and [Bressloff01] for further information on the compressible version of the PISO algorithm.

2.5.1.4. Implicit methods - PIMPLE

Besides the SIMPLE and the PISO algorithm, there exists a third widely used algorithm which consists of a combination of both mentioned schemes. This algorithm is called *PIMPLE* and its name is a combination of the name PISO and the name SIMPLE in one word. In one time step, this method performs a loop of several PISO iterations in which the pressure-velocity coupling is solved. At the end of one iteration, the turbulent quantities are estimated by solving the transport equations. The final values obtained at the end of one iteration, which are possibly corrected in advance by an under-relaxation, are the initial values of the next PISO iteration. Either the process of iterations is repeated until a sufficient tolerance of the corrected terms is reached (which implicates a high computational effort) or a predetermined number of iterations is executed. Subsequent, the algorithm goes to the next time step.

If the given number of PISO iterations is equal unity, the PIMPLE algorithm is of the same scheme as the PISO algorithm. The predetermined number of PISO iterations and pressure correction loops within a PISO iteration depend on the complexity of the equation system and on the flow geometry. This predetermined number can influence the stability of the method and should be chosen with care. The PIMPLE algorithm allows the choice

of a higher Courant number $Co > 1$ and bigger time steps during the solving process, whereby the stability is not affected adversely.

2.5.2. Boundary conditions

To solve the set of partial differential equations in the Navier-Stokes equations with a unique solution, besides an initial condition, also a boundary condition has to be defined (see [Ferziger02], chapter 7, 7.7). The definition of a boundary condition has to be chosen very carefully. Boundary and initial conditions play a decisive role by finding a solution and determining its accuracy. In the worst case, inconsiderate chosen conditions may generate an unphysical solution. The boundary nodes in the computational grid have only to one sight neighbour nodes. Hence, the values at these nodes have to be known a priori or have to be extrapolated by data from nodes which are positioned near to the boundary.

In most cases, *Dirichlet*, *Neumann* or *periodic* conditions are implemented as boundary conditions. In terms of a Dirichlet condition a constant value of a variable is given at the boundary nodes and no approximation equation is needed. While in a Neumann condition the variable is given by its derivative and has to be discretised. Examples of both conditions are demonstrated in the chapters 5 - 7, where the investigated setups of this thesis are presented in detail. In a periodic condition the variable value recurs periodically at specified nodes. Convective fluxes are commonly defined at the inlet of the boundary. They are zero at walls and symmetry planes. Diffusive fluxes are sometimes defined at a wall or by boundary variable values.

2.5.3. Grid arrangements

In many complex flow configurations the choice of the discretisation locations is decisive to obtain a solution of the Navier-Stokes equations. Two possible basic arrangements of the computational nodes are shortly illustrated. For a detailed description it is referred to [Ferziger02], chapter 7 and 8. The first method, which is also applied in this thesis, is called *collocated*. It uses the same grid points and control volumes for all variables.

The second presented method is called *staggered*. In this method not all variables are stored at identical grid locations. Consequently, values which have to be estimated by interpolation can now be estimated without any interpolation. Sometimes, this type of distribution can avoid convergence problems and oscillatory solutions of pressure and velocity.

3. Turbulent natural convection in a Large-Eddy Simulation (LES)

The presented Navier-Stokes equations in chapter 1, sections 1.4 - 1.6, can be used to describe *laminar* or *turbulent* flows. Both types of a flow state are defined by different properties. The state between both types is called *transient flow*. A laminar flow can be destabilised either by an interruption, which acts from outside the flow, or it can be become unstable by itself without any interruption. If this happens, the flow becomes turbulent. The *Large-Eddy Simulation* (short: *LES*), which is performed in this thesis, is a numerical method to describe turbulent flows with adapted Navier-Stokes equations.

Whereby, the LES gains more and more attention in the CFD, there exist two further mainly used methods to solve turbulent flows numerically, the *Reynolds-averaged Navier-Stokes Simulation* (short: *RANS*) and the *Direct Numerical Simulation* (short: *DNS*). The RANS uses statistical averaged Navier-Stokes equations, in which all variations in time of the flow variables are eliminated with help of an average determination in terms of time and density. The fluctuations remain in the equations only in terms of their mean values. To solve these adapted equations by the numerical method, these terms have to be formulated by an appropriate turbulence model. A disadvantage of the RANS is the assumption of a complete isotropic flow (see [Oertel06], chapter 3, 3.2.4). If the flow reveals many high fluctuations, due to a complex geometry, for example, the choice of the right turbulence model becomes difficult, because, at best, the model should not erase to many of these fluctuations.

The DNS solves the Navier-Stokes equations directly at the discretisation grid, as the name implies. It estimates the whole turbulent spectrum without any turbulence model or averaged equations and can be used for anisotropic flows. But this method needs a high computational effort due to a required fine grid resolution. With an increasing Reynolds number, the grid resolution has to become sufficiently fine. Thus, the DNS is only adequate for flow problems of small Reynolds numbers (see [Fröhlich06], chapter 5, 5.9.2). For a funded analysis of both mentioned methods it is referred to [Fröhlich06] and [Oertel06]. The following information of this chapter is based mainly on [Fröhlich06], chapter 2, 5, 6 and 8, and [Groll10a].

3.1. Turbulent flow

The change from a laminar in a turbulent flow state can be defined by the Reynolds number Re from chapter 1, section 1.7, equation (1.7.4). In flows of a small Reynolds number, the flow is laminar and follows particular stream profiles which depend on the flow geometry. With an increasing Reynolds number, perturbations of the velocity are not damped any longer by friction forces. After a *critical Reynolds number* $\mathrm{Re}_{\mathrm{crit}}$ is reached, the appearing perturbations change significantly the structure of the flow. The fluctuations increase and the flow becomes turbulent. The critical Reynolds number varies for each flow problem (for further details see [Baehr08], chapter 3, 3.3).

Turbulence is always generated by interactions between flow geometry, fluid properties and boundary conditions. It can be characteristic by the following properties which are described, for example, in [Fröhlich06], chapter 2 and 5. Turbulent flow is usually a 3-dimensional unsteady and rotational problem. The flow is always chaotic and unstructured, dissipative and diffusive. Flow eddies of different sizes appear in the flow and interact with each other on several scales in time and space. The kinetic energy is distributed over multiple scales in time and space. While the great scales are regular, non-homogeneous, individual, diffusive and of high-energy, the small scales feature a universal chaotic form. In contrast to the great scales, the small scales are homogeneous, dissipative and of low-energy They receive most of their energy from the collapse of the great scales.

All turbulent flows are usually inhomogeneous, anisotropic and of a high Reynolds number. They show, in a local meaning, an isotropic structure (see [Schlichting06], chapter 16, 16.5.2). Therefore, the turbulent fluctuations can be considered as isotropic in a local, small vicinity. In this case, the mean velocity is zero and all gradients of the statistic variables converge to zero. According to [Fröhlich06], chapter 2, 2.4, no preferred flow direction exists in this case. Hence, the main diagonals of the deformation and friction tensor in the Navier-Stokes equations are equal (see chapter 3, section 3.5, 1.5, from page 74 on). To model the turbulence in a general way, a space-time variable is separated in its mean value $\overline{\phi}$ and its fluctuation values ϕ' in respect to time

$$\phi = \overline{\phi} + \phi' \,. \tag{3.1.1}$$

This method is also called *Reynolds filtering*. In case of an isotropic flow, it is for the velocity components $\mathbf{u} = (u, v, w)$

$$\overline{u'^2} = \overline{v'^2} = \overline{w'^2} \,, \quad \overline{u'v'} = \overline{u'w'} = \overline{v'w'} = 0 \tag{3.1.2}$$

with the characteristic mean values in time of the fluctuation velocities $\bar{u}', \bar{v}', \bar{w}'$. For the numerical discretisation of a LES the flow is spatial separated in large and small scales,

which are called *subgrid scales* (short: *sgs*). The large scales are solved directly on the discretisation grid, while the subgrid scales are modelled with an adequate turbulence model. The assumption of a local *isotropic turbulence* is fulfilled for the small scales. The size of the biggest flow scales is correlated to the characteristic length L of a given geometry.

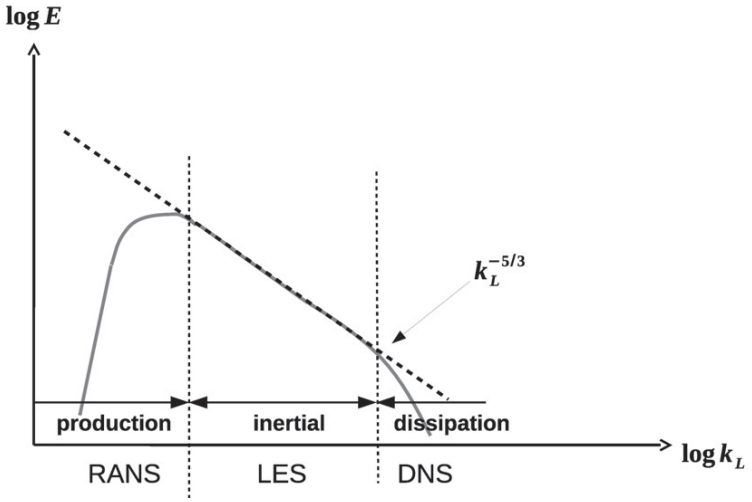

Figure 3.1.: Energy spectrum of isotropic turbulence after Kolmogorov (as seen in [Groll10a]).

Figure 3.1 shows the energy spectrum E of an isotropic turbulence in dependence on the wave number k_L. The wave number can be determined by

$$k_L = \frac{1}{L} \sim \frac{\epsilon_t}{\sqrt[3]{\bar{u}'^2}}. \tag{3.1.3}$$

Here ϵ_t is the turbulent kinetic energy dissipation rate and $\bar{u}'$ is the mean value in time of the characteristic fluctuation velocity of the great scales. Figure 3.1 gives also an overview of the operation range of the before mentioned numerical simulation methods which can be characterised analogously to [Fröhlich06], chapter 2, 2.4.4. In the *area of production* in figure 3.1, the energy spectrum $E(k_L)$ is only dependent on the wave number and on the amount of added and dissipative energy ϵ_t. The flow field and the geometry interact with each other. Consequentially, the kinetic energy of the large scales is produced in this region. A scale analysis leads to

$$E(k_L) = C_k \epsilon_t^{2/3} k_L^{-5/3} \tag{3.1.4}$$

with the *Kolmogorov constant* $C_k \approx 1.5$. Expression (3.1.4) is also called *Kolmogorov 5/3-law* or *Kolmogorov spectrum*. In connection with the previous expression (3.1.4), a characteristic scale for the velocity can be given by

$$u_{k_L} \sim \epsilon_t^{1/3} k_L^{-1/3}. \tag{3.1.5}$$

Further, an expression for the temporal development of eddies of the size $l = 2\pi/k_L$ can be formulated by

$$t_{k_L} \sim \epsilon_t^{-1/3} k_L^{-2/3} \,. \tag{3.1.6}$$

In the *area of production*, the RANS method is used. In the *inertia area*, the large scales interact with each other. The biggest scales collapse and give their energy to smaller scales. In this region a LES is used. The size of the inertia area changes with the variation of the Reynolds number, because the Kolmogorov length is dependent on the Reynolds number as it is formulated in the following equation

$$\frac{L}{\eta_{k_L}} = \mathrm{Re}_L^{3/4} \tag{3.1.7}$$

with $\mathrm{Re}_L = \dfrac{\sqrt{K}L}{\nu}$. Here, K is the total energy with

$$K = c\epsilon_t^{2/3} k_f^{-2/3} \,, \tag{3.1.8}$$

where both coefficients can be chosen as $c = 1$ and $k_f = 6 \cdot (2\pi/0.43\,L)$. If the large eddies collapse and their size becomes about the size of the *Kolmogorov length*,

$$\eta_{k_L} = \left(\frac{\nu^3}{\epsilon_t}\right)^{1/4} \,, \tag{3.1.9}$$

the energy dissipates in heat. This is the *area of dissipation*, where a DNS is usually used. The smallest scales are solved directly by a DNS, as mentioned above, and their size is described by the *Kolmogorov length*.

If the mean free path length between the fluid molecules λ is even significantly smaller than the size of the smallest eddies (and thus smaller than η_{k_L}), the Navier-Stokes equations are still valid in the turbulent case. Because the smallest eddies consists still of enough molecules to fulfil the governing equations. No significant fluid motion of the smaller scales exists beyond a size of η_{k_L}.

3.2. Turbulence modelling

The basic principle in a LES is to divide the flow in its large and small spatial scales. This process is described in the following based on the information in [Fröhlich06], chapter 5. The large scales of the flow are resolved directly at the discretisation grid by the chosen numerical method, while the small scales are too fine to be solved. Therefore, these scales have to be modelled by an adequate turbulence model. These small scales are also called *subgrid scales* and they are marked in the following by the index *sgs*. The subgrid scales

have to model especially the dissipation of the kinetic energy and its influence on the solved large parts. Regarding the filtering process in equation (3.1.1), a space-time variable is separated by a homogeneous filtering function as

$$\psi = \overline{\psi} + \psi' \,, \tag{3.2.1}$$

where $\overline{\psi}$ represents the great scale component, while ψ' represent the modelled component. The filtering process is performed by

$$\overline{\psi}(\mathbf{x}, t) = \int_{-\infty}^{\infty} \int_{-\infty}^{\infty} \psi(\mathbf{r}, t') G(\mathbf{x} - \mathbf{r}, t - t') dt' d\mathbf{r}. \tag{3.2.2}$$

The filter operation with function G in equation (3.2.2) is linear, commutative, differentiable, Galileo invariant, and invertible (see [Fröhlich06], chapter 5, 5.2). Typical filter operations are

$$\text{Top hat filter} \qquad G(x) = \begin{cases} 1/\Delta & |x| \leq \Delta/2 \\ 0 & \text{others} \end{cases} \,, \tag{3.2.3}$$

$$\text{Cut off filter} \qquad G(x) = \frac{1}{\Delta} \left(\frac{\sin(\frac{\pi x}{\Delta})}{\frac{\pi x}{\Delta}} \right) , \tag{3.2.4}$$

$$\text{Gauss filter} \qquad G(x) = \frac{1}{\Delta} \sqrt{\frac{\gamma}{\pi}} \exp\left(-\frac{\gamma x^2}{\Delta^2} \right) , \tag{3.2.5}$$

where γ is an arbitrary model factor. Δ is a space dependent filter length. In the simulation software *OpenFOAM*® the standard used filter is the top hat filter, as it is defined in (3.2.3). If the filter function is applied at both sides of the compressible governing equations in chapter 1, section 1.10, one obtains the following filtered equation system

- Compressible conservation of mass

$$\frac{\partial \overline{\rho}}{\partial t} + \frac{\partial \overline{\rho}\, \overline{u}_j}{\partial x_j} = 0 \,, \tag{3.2.6}$$

- Compressible conservation of momentum

$$\frac{\partial \overline{\rho}\, \overline{u}_i}{\partial t} + \frac{\partial \overline{\rho}\, \overline{u}_i \overline{u}_j}{\partial x_j} - 2\mu \frac{\partial \overline{S}_{ij}}{\partial x_j} = -\frac{\partial \overline{p}}{\partial x_i} - \frac{\partial}{\partial x_j} \tau_{ij} \,, \tag{3.2.7}$$

- Compressible conservation of enthalpy

$$\frac{\partial \overline{\rho} \overline{h}}{\partial t} + \frac{\partial \overline{\rho} \overline{h} \overline{u}_j}{\partial x_j} - \frac{\partial}{\partial x_j} \left(\alpha \frac{\partial \overline{h}}{\partial x_j} \right) + \frac{\partial}{\partial x_j} \underbrace{\rho \left(\overline{u_i h} - \overline{u}_i \overline{h} \right)}_{\tau_{h_i}} = \frac{\partial \overline{p}}{\partial t} + \overline{u}_j \frac{\partial \overline{p}}{\partial x_j} \,, \tag{3.2.8}$$

where

$$\overline{S}_{ij} = \frac{1}{2}\left(\frac{\partial \overline{u}_i}{\partial x_j} + \frac{\partial \overline{u}_j}{\partial x_i}\right) \tag{3.2.9}$$

is the filtered deformation tensor. The term τ_{h_i} stands for the subgrid scale enthalpy flux. The subgrid scales in the term

$$\tau_{ij} = \overline{u_i u_j} - \overline{u}_i \overline{u}_j \tag{3.2.10}$$

cannot be expressed directly by the filtered velocities $\overline{u}_i$. Hence, a turbulence model is required to formulate these terms $\tau_{ij} \approx \tau_{ij}^{\text{model}}(\bar{u})$ with help of the filter length Δ. Most models use as a possible filter length the grid width of the mesh resolution. With help of the chosen turbulence model also the subgrid scale enthalpy flux

$$\tau_{h_i} = \rho\left(\overline{u_i h} - \overline{u}_i \overline{h}\right) \tag{3.2.11}$$

has to be formulated, especially if a coarser grid is used or a flow with a higher Prandtl number should be estimated by the numerical method. A possible formulation can be found in [Fröhlich06], chapter 6, 6.9

$$\tau_{h_i} = -\alpha_{\text{t}} \frac{\partial \overline{h}}{\partial x_i} \tag{3.2.12}$$

with a turbulent thermal diffusivity α_{t} which has to be determined by the turbulence model as well. There exist numerous subgrid scale models which are based on different approaches. In the next section, the chosen turbulence model of this thesis is presented. For an overview of other models and further information on these schemes it is referred to [Fröhlich06].

Due to the Galileo invariance of the Navier-Stokes equations and the Galileo invariance of the filter operation, the filtered equations are also Galileo invariant. All terms that have to be described by a subgrid scale model and can not be resolved directly are presented by the subgrid tensor τ_{ij} in equation (3.2.10) which is discussed in the following based on the information in [Fröhlich06], chapter 5, 5.2.6. Inserting the modelled subgrid scale velocities

$$u_i' = u_i - \bar{u}_i \tag{3.2.13}$$

in (3.2.10), one obtains

$$\tau_{ij} = \underbrace{\overline{\bar{u}_i \bar{u}_j} - \overline{u}_i \overline{u}_j}_{:= L_{ij}} + \underbrace{\overline{u_i' \bar{u}_j} + \overline{\bar{u}_i u_j'}}_{:= C_{ij}} + \underbrace{\overline{u_i' u_j'}}_{:= R_{ij}} \quad . \tag{3.2.14}$$

The so-called *Leonard term* L_{ij} described the product of the not modelled, resolved scales. The *Clark tensor* C_{ij} includes the tensions of the interaction between the modelled, sub-

grid scales and the resolved, large scales. The *Reynolds tensor* R_{ij} describes the influence of the subgrid scales on the not modelled, resolved scales. The term L_{ij} can be evaluated directly from $\bar{u}_i$ and has not to be modelled. Only the term R_{ij} and the sum of $L_{ij} + C_{ij}$ are Galileo invariant. In a modified *model of Germano* [Germano1986] each term of τ_{ij} is Galileo invariant

$$\tau_{ij} = \underbrace{\overline{\bar{u}_i\bar{u}_j} - \bar{\bar{u}}_i\bar{\bar{u}}_j}_{:= L_{ij}^m} + \underbrace{\overline{u_i'\bar{u}_j} + \overline{\bar{u}_i u_j'} - \overline{u_i'}\bar{\bar{u}}_j - \bar{\bar{u}}_i\overline{u_j'}}_{:= C_{ij}^m} + \underbrace{\overline{u_i'u_j'} - \overline{u_i'}\,\overline{u_j'}}_{:= R_{ij}^m} . \tag{3.2.15}$$

The modelling of the term τ_{ij} is the subject of the next section. The subgrid scale model used in this thesis is based on the above Germano separation of τ_{ij} in (3.2.15).

3.3. Subgrid scale models

3.3.1. Smagorinsky model

Before the turbulence model *of Fureby*, which is used in this thesis, is presented, its basis model, the standard incompressible *Smagorinsky model*, is demonstrated. The *Smagorinsky model* is based on a formulation of the subgrid scale eddy viscosity ν_{sgs} and uses a Boussinesq-approximation. The model shows analogies to a statistic turbulence modelling of the unknown Reynolds strains in a RANS (see [Oertel06], chapter 3, 3.2.4). In comparison to a RANS, the modelling effort of a LES is smaller, because the subgrid scales include only a small part of the kinetic energy spectrum.

The *Smagorinsky model* was formulated by the American meteorologist *Joseph Smagorinsky* in [Smagorinsky1963]. To model the viscosity in a LES, an effective viscosity is formulated by the sum of a molecular part ν and a turbulent part ν_{sgs}

$$\nu_{\text{eff}} = \nu + \nu_{\text{sgs}} . \tag{3.3.1}$$

Now, the turbulent subgrid scale viscosity ν_{sgs} has to be described which is done in the following analogously to the description in [Fröhlich06], chapter 6, 6.2.2. First, a modulation of the term $\tau_{ij}^{\text{aniso,model}}$ is given by

$$\tau_{ij}^{\text{aniso, model}} = -\nu_{\text{sgs}} 2\overline{S}_{ij}, \tag{3.3.2}$$

where the anisotropic term

$$\tau_{ij}^{\text{aniso}} = \tau_{ij} - \delta_{ij}\tau_{kk}/3 \tag{3.3.3}$$

is expressed in terms of the deformation tensor $\bar{S}_{ij}$. The not modelled term in

$$\tau_{ij} = \tau_{ij}^{\text{aniso}} + \frac{1}{3}\delta_{ij}\tau_{kk} \tag{3.3.4}$$

can be expressed in the momentum equation (3.2.7) by help of a pseudo pressure term $\bar{P} = \bar{p} + \tau_{kk}/3$ (for details see [Fröhlich06], chapter 6, 6.2.2). Because of the no-slip condition on surfaces, $\tau_{ij} = 0$, the correct estimation of the pressure is guaranteed in the simulation.

The subgrid scale viscosity can be described by

$$\nu_{\text{sgs}} = l_{\text{sgs}} q_{\text{sgs}} \,, \tag{3.3.5}$$

where l_{sgs} is an adequate subgrid scale length and q_{sgs} an adequate subgrid scale velocity. To define l_{sgs}, one can choose a formulation of the filter length alone $l_{\text{sgs}} = \Delta$ or a formulation of the filter length and an additional model coefficient C_s, $l_{\text{sgs}} = C_s\Delta$. q_{sgs} can be determined by $q_{\text{sgs}} = l_{\text{sgs}}\|\overline{S}\|$. Then, one obtains for the eddy viscosity

$$\nu_{\text{sgs}} = (C_S\Delta)^2\|\overline{\mathbf{S}}\| \tag{3.3.6}$$

and hence

$$\tau_{ij}^{\text{Smag}} = -2(C_S\Delta)^2\|\overline{\mathbf{S}}\|\overline{S}_{ij} \,, \tag{3.3.7}$$

where $\|\overline{\mathbf{S}}\| = \sqrt{2\overline{S}_{ij}\overline{S}_{ij}}$. The model coefficient C_S can be estimated with help of the theory of isotropic turbulence and can be found in the literature, e. g. [Fröhlich06]. It varies for different flow problems and geometries. Note that the choice of C_S should not be dependent on the grid filter length Δ, because the grid filter length is problem dependent. Several suggestions can be found in [Fröhlich06]. The Smagorinsky model is an easy and robust method which is adequate for complex flow geometries. Note that the tensors τ_{ij} and $\overline{S}_{ij}$ correlate only weak with each other. Possible disadvantages of this method are the isotropic choice of ν_{sgs} by the norm of $\bar{S}$ and the probable instability of the model due to an improperly choice of C_S.

At this point also the so called *dynamic Smagorinsky models* should be shortly mentioned. In these models the parameter C_S is not chosen as a constant and can vary in space and time. It is estimated by an extra sub-model within the main model. This method should adapt easier physical or numerical conditions. For further details on this subject see [Germano1991, Lilly1992]. Because the computational grids of this thesis consist of homogeneous directions, the standard Smagorinsky model is an adequate choice.

3.3.2. Model of Fureby

The *model of Fureby* in [Fureby1996] is an modification of the standard Smagorinsky model for compressible flows. The model considers additionally the density ρ in the formulation of the subgrid scale dynamic viscosity and in the formulation of the subgrid scale kinetic energy. In the filtering process, a special density-weighted *Favre*-filtering [Favre1983] is used. Therefore, a space-time variable is this time separated as follows by a homogeneous filtering function

$$\psi = \widetilde{\psi} + \psi'' \,. \tag{3.3.8}$$

The component ψ'' stands again for the fluctuations of variable ψ (as in equation (3.2.1)), but marks this time the different filtering method of [Favre1983]. In equation (3.3.8), it is

$$\widetilde{\psi} = \frac{\overline{\rho\psi}}{\overline{\rho}}, \tag{3.3.9}$$

where the filtered variable $\overline{\rho\psi}$ is defined as in equation (3.2.2). With help of equations (3.3.8), (3.3.9) and the equations (3.2.6) - (3.2.8), one obtains the following filtered equation system of a LES where the model of Fureby was considered

- Compressible conservation of mass

$$\frac{\partial\overline{\rho}}{\partial t} + \frac{\partial\overline{\rho}\widetilde{u}_j}{\partial x_j} = 0 \,, \tag{3.3.10}$$

- Compressible conservation of momentum

$$\frac{\partial\overline{\rho}\widetilde{u}_i}{\partial t} + \frac{\partial\overline{\rho}\widetilde{u}_i\widetilde{u}_j}{\partial x_j} - 2\left(\mu + \mu_{\text{sgs}}\right)\frac{\partial\widetilde{S}^*_{ij}}{\partial x_j} = -\frac{\partial\overline{p}}{\partial x_i} + \overline{\rho}g_i \,, \tag{3.3.11}$$

- Compressible conservation of enthalpy

$$\frac{\partial\overline{\rho}\widetilde{h}}{\partial t} + \frac{\partial\overline{\rho}\widetilde{h}\widetilde{u}_j}{\partial x_j} - \frac{\partial}{\partial x_j}\left(\left(\alpha + \alpha_{\text{sgs}}\right)\frac{\partial\widetilde{h}}{\partial x_j}\right) = \frac{\partial\overline{p}}{\partial t} + \widetilde{u}_j\frac{\partial\overline{p}}{\partial x_j} \tag{3.3.12}$$

with the filtered strain rate tensor

$$\widetilde{S}_{ij} = \frac{1}{2}\left(\frac{\partial\widetilde{u}_i}{\partial x_j} + \frac{\partial\widetilde{u}_j}{\partial x_i}\right) \tag{3.3.13}$$

and its deviatoric part

$$\widetilde{S}^*_{ij} = \widetilde{S}_{ij} - \frac{1}{3}\widetilde{S}_{kk}\delta_{ij} \,. \tag{3.3.14}$$

In the model of Fureby, the term of the turbulent subgrid scale diffusivity α_{sgs} is modelled with help of the subgrid scale dynamic viscosity μ_{sgs} and a turbulent Prandtl number Pr_{sgs}. It is

$$\mu_{\text{sgs}} = c_k \bar{\rho} \Delta \sqrt{k_{\text{sgs}}} \qquad \text{and} \qquad \alpha_{\text{sgs}} = \frac{\mu_{\text{sgs}}}{Pr_{\text{sgs}}}. \tag{3.3.15}$$

Here, k_{sgs} is the turbulent subgrid scale kinetic energy with

$$k_{\text{sgs}} = \left(\frac{-\frac{2}{3}\frac{\partial \widetilde{u}_i}{\partial x_i} + \sqrt{\left(\frac{2}{3}\frac{\partial \widetilde{u}_i}{\partial x_i}\right)^2 + 8 c_e c_k (\widetilde{S}_{ij} \widetilde{S}^*_{ij})}}{-2 \cdot \frac{c_e}{\Delta}} \right)^2, \tag{3.3.16}$$

where the model coefficients are $c_k = 0.02$ and $c_e = 1.046$ ([Fureby1996]). The grid filter length Δ depends on the cell edge length of the used Cartesian grid and is chosen as

$$\Delta = (\Delta x \cdot \Delta y \cdot \Delta z)^{1/3} \tag{3.3.17}$$

according to [Deardorff1973]. The temperature-dependence on the fluid properties is described by the model of Sutherland [Sutherland1893] as mentioned in chapter 1, section 1.10. The model uses the assumption of an ideal gas from eq. (1.8.19) and eq. (1.8.21) in chapter 1, section 1.8 on page 23. Further, a Boussinesq-approximation is not included in equation (3.3.11), as it was the case in the unfiltered equations in chapter 1, section 1.10.

Additional force terms which model additionally the natural convection effect in the turbulent flow, as in [Kenjereš1999, Sergent03], are not included in the turbulent viscosity μ_{sgs} in eq. (3.3.15). A consideration of the gravitational force as well as a dependence on the temperature gradient is not considered in the turbulent terms of μ_{sgs} and α_{sgs}. The subgrid scale Prandtl number is chosen as $\text{Pr}_{\text{sgs}} = 0.4$ according to [Kosović02, Sergent03, Erlebacher1992]. The performed numerical tests of this thesis confirmed this choice.

This model was also used and presented in similar form in the studies [Zimmermann12], [Zimmermann14a], [Zimmermann14b] and [Zimmermann15].

3.4. Solving the governing equations in OpenFOAM®

Computational methods and numerical conditions

The mathematical model of a turbulent, three-dimensional natural convection as described in equations (3.3.10) - (3.3.17) is solved using *OpenFOAM®-1.7.1*, a open-source simulation tool (for further information see [OpenFOAMa]). As solution algorithm the solver *buoyantPimpleFOAM* is chosen. The *buoyantPimpleFOAM* is a transient solver for turbulent compressible flows with buoyant effects and heat-transfer. The solver evaluated the previously stated filtered governing equations. Like the name indicates, the solver is based on the PIMPLE algorithm as it is described in chapter 2, section 2.5.1.4. In the

simulation, only one outer iteration is done, hence the solver becomes a PISO algorithm which performs two inner PISO loops. The algorithm estimates in the momentum equation (3.3.11) as pressure the dynamic pressure $\bar{p}_{\mathrm{rgh}} = \frac{1}{2}\bar{\rho}\widetilde{\mathbf{u}}^2$. After a corrected solution of $\bar{p}_{\mathrm{rgh}}$ is found, the total pressure $\bar{p}$ is calculated by

$$\bar{p} = \bar{p}_{\mathrm{rgh}} + \underbrace{\bar{\rho}\mathbf{g}h}_{\text{static pressure}} , \tag{3.4.1}$$

where h is the height of the fluid column over the particular cell node.

All methods and schemes which are used by the solving algorithm are explained in chapter 2. The *time derivatives* are discretised by the implicit Euler method which is of first-order and produces bounded solutions (chap. 2, 2.4.1). The *gradients* are discretised spatially with a Gaussian integration (chap. 2, 2.1.3) and a linear interpolation scheme (CDS) which is a second-order method. (chap. 2, 2.2.2).

A Gauss integration and an additional upwind interpolation is performed for the spatial discretisation of the *divergence* terms. This method is a first-order bounded method (chap. 2, 2.2.1, 2.4.1). The spatial discretisation of the *diffusion term* in the momentum equation is performed with help of a Gauss integration and a linear interpolation scheme (CDS) which is a second-order unbounded method. For the *Laplace terms* as discretisation method the Gaussian integration is chosen together with a linear interpolation scheme (CDS) and an explicit non-orthogonal correction for the surface normal gradients. This combination is of second-order, conservative and an unbounded method.

The maximum Courant number is chosen as maxCo = 0.5. Further, an adjusted time step option is used with an maximum value of maxDelta T $= 1 \cdot 10^{-2}$ s.

The chosen spatial interpolation scheme of the upwind interpolation and the temporal discretisation scheme of the implicit Euler method are both only of first order and may hold disadvantages compared to schemes of higher order. Therefore, also other combinations of numerical schemes were tested during this thesis concerning the same solver. But only with help of the above presented combination of schemes satisfactory results could be obtained. In future studies, further investigations of this aspect could be an important topic.

Also a Gauss integration and an additional linear interpolation scheme (CDS) were used instead of the upwind interpolation scheme for the discretisation of all stated *divergence* terms. For the time discretisation an implicit second-order method, like the *backward* or *Crank Nicholson* scheme, was tested, but produced, despite the higher order, an oscillatory or even no solution. Blending methods were not used in this thesis. A detailed description of these schemes can be found in [Ferziger02].

The resulting algebraic equation system for ρ and the dynamic pressure term p_{rgh} are solved by a preconditioned conjugate gradient solver for symmetric matrices which includes a diagonal incomplete-Cholesky scheme (DIC). The given tolerance for this method lies at $1 \cdot 10^{-8}$. The resulting algebraic equation system for the remaining properties are estimated by a preconditioned bi-conjugate gradient solver for asymmetric matrices which includes a diagonal incomplete LU scheme (DILU) (s. chapter 2, section 2.3). The given tolerance here is $1 \cdot 10^{-6}$. No under-relaxation is used in the pressure correction.

Near to the walls, the turbulent flow is anisotropic and inhomogeneous and it interacts with the walls. Similar to the subgrid scale model, also a wall-law model could be used to describe the turbulence at the wall ([Fröhlich06], chapter 8). Such a model is not used in this thesis. The grid resolution is chosen in a way, that all relevant turbulent scales in the boundary layer are resolved. But the size of the smallest grid cell is still larger than it would be in case of a DNS (see also chapters 5 - 7).

Accuracy of a LES

According to [Fröhlich06], chapter 5, 5.8, the accuracy of a LES is always dependent on the chosen turbulence model, on the accuracy of the numerical discretisation and on the chosen grid resolution. Besides a modulation and discretisation error, the LES shows an uncertainty of the initial condition. The subgrid scales are modelled at the beginning of the simulation by a chosen filter length Δ and a depending wave number k_Δ. This uncertainty grows during the simulated process and increases the numerical error. The error of the turbulence model is about the amount of the wave number k_Δ.

3.5. Natural convection

The following presented information of this chapter are based mainly on the details given in [Schlichting06], chapter 10, 17, 19, [Spurk07], chapter 12, [Pope00], chapter 7, and [Baehr08], chapter 1.

3.5.1. An overview

In a *free* or *natural* convection, the motion of the flow is only enforced by temperature dependent density differences in the gravitational force field of the Earth. Natural convective flows are mostly investigated in an enclosed experimental setup. Hence, the fluid is limited by the side walls. Some of the walls are also temperatured and heat the fluid captured between these walls. Near the heated walls, the temperature of the fluid increases and thus, its density decreases. Therefore, a buoyancy force arises in the fluid which is directed against gravity. A buoyancy effect in an enclosed container is illustrated in figure 3.2. The effects inside the fluid can now be described based on the information

in [Velarde1980]. These buoyancy effects are damped by viscosity effects in the fluid and a heat diffusion between the fluid particles. If the resistance forces are smaller than the buoyancy force, the fluid starts moving. The ratio between buoyancy force on the one side and and viscosity as well as heat diffusion effects on the other side is summarised in the Rayleigh or Grashof number from chapter 1, section 1.7, on page 18.

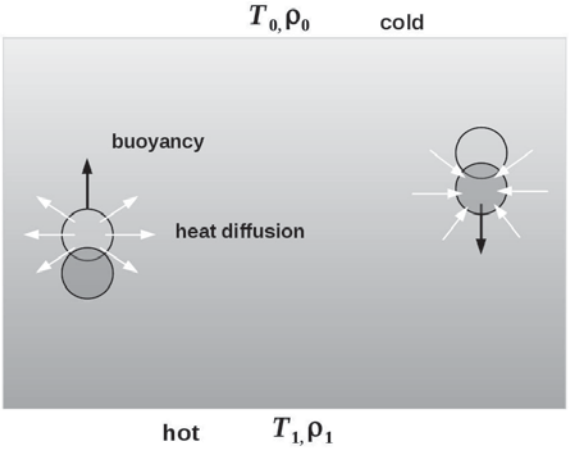

Figure 3.2.: Heat distribution in an enclosed cavity with horizontal, heated walls (as seen in [Velarde1980]).

The sketch shows a fluid layer between two horizontal walls which are heated isothermally, but with a different temperature. Hence, between the upper and lower wall we have a constant temperature difference. At the lower wall the temperature is higher than at the upper wall, but its density is greater, thus $T_0 < T_1$ and $\rho_0 > \rho_1$. Only if the temperature difference between the upper cold and lower hot wall reaches a critical value, the fluid is moving and we can observe a convective heat transport which is based on a mass transport. This critical temperature difference defines the *critical Rayleigh number* which is discussed in the following. Beneath this critical value we can observe only a heat transmission by diffusion.

If a warm fluid particle reaches a higher and thus cooler fluid layer caused by a disturbance of the fluid, the fluid particles around the warm particle have a smaller temperature and hence a bigger density. Thus, the warm fluid particle is affected by a buoyancy force as described above. The buoyancy forces which drive the flow in the fluid can be expressed by

$$\rho = \rho_0 + \Delta\rho \quad \Rightarrow \quad \rho\mathbf{g} = \rho_0\mathbf{g} + \mathbf{g}\Delta\rho\,. \tag{3.5.1}$$

In a natural convection, the momentum and heat transport are coupled and have to be solved together by the numerical method (s. also chapter 1, section 1.10, page 26, and chapter 2, section 2.5.1.2, page 52). To investigate these flows in an experiment or numerical simulation, mostly an enclosed setup is chosen. The setup consists, as mentioned above, of two temperatured side walls, which are either vertical or horizontal orientated

to each other and which hold a fluid layer between them. The lateral walls of the setup can have different boundary conditions, e. g. adiabatic or conducting walls. Normally, the setup has to be of infinite length to erase totally the influence of the side walls, which is not realisable in an experiment. Therefore, it is important, that the length of the test case is at least a multiple of the height (or the depth a multiple of the length in a vertical wall configuration), to generate a small fluid layer between the walls and to reduce as much as possible the influence of the sidewalls on the main flow field.

The orientation of the temperatured walls is decisive for the resulting flow field in the setup, which will be discussed in the following section 3.5.3.2. The change between a laminar natural convection and a turbulent one depends on the instability of the fluid itself or on perturbations from outside the fluid (see also this chapter, section 3.1 on page 64). The Rayleigh number at which a resulting flow inside the fluid changes from a laminar to a turbulent state is called *critical Rayleigh number* $\mathrm{Ra}_{\mathrm{crit}}$. This number varies for each flow problem.

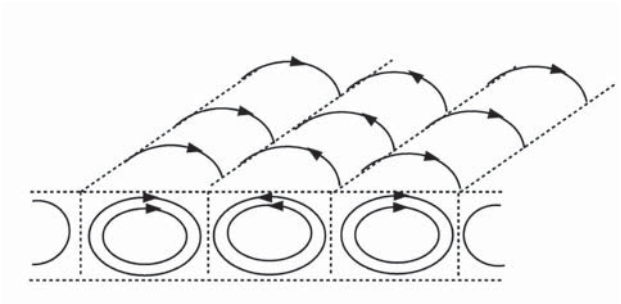

Figure 3.3.: Sketch of *convection cells* or *rolls* in a setup with horizontal, heated walls (as seen in [Getling1998]).

In [Marek12] (chapter 6) the critical Rayleigh number of a horizontal natural convection is given by $\mathrm{Ra}_{\mathrm{crit}} = 1708$. Beneath this Rayleigh number the heat transport is realised only by heat conduction and no flow movement can be detected inside the fluid, because the buoyancy forces are smaller than the viscosity effects. The heat conduction is directed upwards due to the unstable thermal layering. According to [Marek12], a flow movement can be detected for almost each Rayleigh number, in the case of a setup where two of the vertical walls are heated. In this case, the appearing velocities are very small and they are directed parallel relative to the vertical heated walls. They transport only a little amount of heat. This regime of heat transmission exists for $\mathrm{Ra} \leq 10^3$.

If only small temperature differences appear in the flow, the flow can adjust the perturbations. If the temperature differences exceed a critical value, the fluid starts moving and the typical convection cells arise in the flow. These are illustrated in figure 3.3 for a case of horizontal heated walls. These cells result from the ascending hot and descending cold fluid layers driven by local density differences in the gravitational force field. The differ-

entially temperatured fluid layers displace themselves in the flow geometry. The number of convection cells and their composition is up to the dimensions of the geometry and the orientation of the heated walls, as the simulation results will show in chapter 5, section 5.4 from page 122 on and chapter 6, section 6.3 from page 152 on.

3.5.2. Heat transport

Heat transport near walls

In the following, several aspects of heat transport in a fluid are discussed analogously to the information in [Baehr08], chapter 1. Heat transport in a fluid is always directed in direction of the decreasing temperature gradient according to the second law of thermodynamics. There exist three different ways of heat transport in a fluid *heat conduction*, *heat convection* and *heat radiation*. Mainly heat conduction and convection play a major role in fluid dynamics.

A laminar flow is dominated by convection, which is directed stream wise, and a conduction, which is directed normal to the flow. In a turbulent flow, the role of the conduction is taken by the turbulence production ([Ferziger02]). Steady heat conduction is described by the Laplace equation and unsteady conduction by the energy equation in chapter 1, section 1.6 from page 16 on. The energy transmission in a heat conducting material can be described by the heat flux density

$$\dot{\mathbf{q}} = \dot{\mathbf{q}}(\mathbf{x}, t)\,. \tag{3.5.2}$$

Thus, it is for the heat flux

$$d\dot{Q} = \dot{\mathbf{q}}(\mathbf{x}, t)\mathbf{n}\,dA = |\dot{\mathbf{q}}|\cos\beta\,dA\,, \tag{3.5.3}$$

where $\mathbf{n}$ is the unit vector of the surface element dA, which stands to $\dot{\mathbf{q}}$ in an angle β. Different temperature gradients influence the heat conduction inside a material. The temperature field inside the material system can be expressed by

$$T = T(\mathbf{x}, t)\,. \tag{3.5.4}$$

The temperature gradient is then defined by

$$\nabla T = \frac{\partial T}{\partial x}\mathbf{e}_x + \frac{\partial T}{\partial y}\mathbf{e}_y + \frac{\partial T}{\partial z}\mathbf{e}_z\,, \tag{3.5.5}$$

where are $\mathbf{e}_x, \mathbf{e}_y, \mathbf{e}_z$ are the unit vectors of the chosen coordinate system. The temperature gradient is always directed normal to surfaces, which show the same temperature at a particular time instant. The gradient points always in direction of the highest temperature

increase. As mentioned before in chapter 1, section 1.6, equation (1.6.5) on page 17, the heat flux density can be expressed also by the thermal conductivity λ according to *Fourier's law*

$$\dot{\mathbf{q}} = -\lambda \nabla T \,. \tag{3.5.6}$$

The thermal conductivity λ is also temperature dependent

$$\lambda(T) = \frac{\lambda_0}{1 - \beta_0 T} \tag{3.5.7}$$

with a thermal conductivity λ_0 measured at a reference temperature T_0 and the dependent thermal expansion coefficient β_0 (s. also chapter 1, section 1.6, equation (1.8.20), on page 23). To estimate a mean thermal conductivity inside a material between two boundaries, which have different temperatures T_{w1} and T_{w2}, one estimates the mean conductivity λ_m

$$\begin{aligned} \lambda_m &= \frac{1}{T_{w2} - T_{w1}} \int_{T_{w1}}^{T_{w2}} \lambda(T) dT = \frac{\lambda_0}{\beta_0 (T_{w1} - T_{w2})} \ln \frac{1 - \beta_0 T_{w2}}{1 - \beta_0 T_{w1}} \\ &= \frac{\ln(\lambda(T_{w1})/\lambda(T_{w2}))}{\lambda(T_{w1}) - \lambda(T_{w2})} \lambda(T_{w1}) \lambda(T_{w2}) \,. \end{aligned} \tag{3.5.8}$$

With help of equation (3.5.8), the heat flux between both boundaries of the material can be evaluated by

$$\dot{q} = \frac{\lambda_m}{\delta} (T_{w1} - T_{w2}), \tag{3.5.9}$$

where δ is the thickness of the material. The *heat convection* is the composition of heat conduction and energy transmission in the macroscopic movement of the fluid. The fluid layer directly at the wall is called the *boundary layer* of the fluid and will be discussed in detail in the following section 3.5.3.2. Mainly this region is important for the heat and mass transport in the fluid. The temperature change from the wall to the fluid is dependent on the temperature at the wall and the one in the fluid. Either, the wall temperature is higher than the one of the fluid and the wall heats the fluid, or, in the other case, the wall cools the fluid. Figure 3.4 shows the typical profiles of velocity (left) and temperature (right) near a wall.

Directly at the wall, the fluid adheres to the wall and its velocity is zero, assuming a non-frictionless fluid. The velocity increases in distance to the wall, before it reaches its maximum at the end of the boundary layer, which is indicated by δ_t in figure 3.4. Directly at the wall, the energy is only transported by conduction, hence equation (3.5.2) becomes

$$\dot{\mathbf{q}} = -\lambda \left. \frac{\partial T}{\partial y} \right|_w , \tag{3.5.10}$$

where λ depends on the wall temperature. The heat flux density results from the temperature gradient near the wall, as figure 3.4 shows (right plot). With this definition, the local *heat transfer coefficient* can be defined with a known temperature field of the fluid T_f in a great distance from the wall

$$\tilde{\alpha} = \frac{\dot{\mathbf{q}}}{T_\mathrm{w} - T_\mathrm{f}}. \tag{3.5.11}$$

The distance δ_t in figure 3.4 is of the same size as $\lambda/\tilde{\alpha}$ and can be used to describe the thickness of the boundary layer. With the local heat transfer coefficient, a mean value can be obtained by an integration over the particular area A. Afterwards, the whole heat flux $\dot{Q}$ through this area can be calculated by

$$\dot{Q} = \tilde{\alpha}_\mathrm{m} A \Delta T\,. \tag{3.5.12}$$

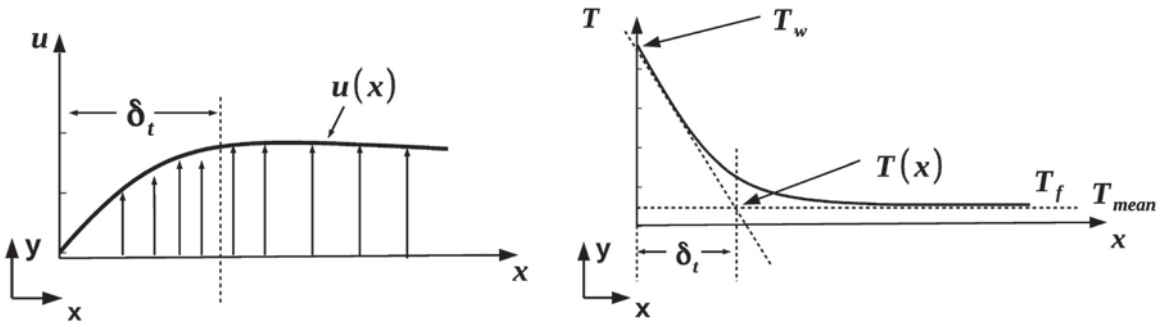

Figure 3.4.: Velocity (left) and temperature (right) profile in vicinity of the heated wall (as seen in [Baehr08]).

In an analogous manner to chapter 1, section 1.7 on page 18, the heat transfer coefficient can be non-dimensionalised

$$\tilde{\alpha} = -\frac{\lambda}{L} \frac{\left.\dfrac{\partial T^*}{\partial y^*}\right|_w}{T^*_\mathrm{w} - T^*_\mathrm{f}} \tag{3.5.13}$$

with a characteristic length L of the flow geometry. The expression in (3.5.13) can be rewritten to

$$\frac{\tilde{\alpha}\, L}{\lambda} = -\frac{\left.\dfrac{\partial T^*}{\partial y^*}\right|_w}{T^*_\mathrm{w} - T^*_\mathrm{f}}\,. \tag{3.5.14}$$

The non-dimensional product of the left hand side in (3.5.14) is the so-called *Nusselt number*, which is named after the German engineer *Ernst Kraft Wilhelm Nußelt* (1882 - 1957). This number is normally used to describe the heat flux in a natural convection. Note that besides the flow geometry and its boundary conditions also the thermal boundary conditions influence the Nusselt number and the other dimensionless parameters. According

to [Baehr08], chapter 1, 1.1.4, in a free convection, the heat flux density do not increase proportional to the term of $T_\mathrm{w} - T_\mathrm{f}$, because $\tilde{\alpha}$ is not independent of $T_\mathrm{w} - T_\mathrm{f}$. Also, the temperature difference $T_\mathrm{w} - T_\mathrm{f}$ drives not only the heat flux, but also the buoyancy force in the flow and consequently the velocity field.

Heat transport between two fluids which are separated by a wall

In case of two fluids which are separated by a wall, a heat transport arises from the fluid with the higher temperature through the wall to the fluid with the lower temperature until a steady state is reached. This process is called *heat transmission*. In the following this aspect is discussed analogously to the information in [Baehr08], chapter 1, 1.2. The heat flux from the fluid with the higher temperature T_1 to the first surface of the wall is defined by

$$\dot{Q} = \tilde{\alpha}_1 A_1 (T_1 - T_{w1}) \,, \tag{3.5.15}$$

where T_{w1} is the temperature of the first surface and A_1 the surface's area, which touches the first fluid. The heat flux inside the wall can be expressed by

$$\dot{Q} = \frac{\lambda_m}{\delta} A_m (T_{w1} - T_{w2}) \tag{3.5.16}$$

with help of equation (3.5.9). λ_m is again the mean heat conductivity inside the wall, δ its thickness and A_m the mean area of both wall surfaces. For the heat flux from the wall to the second fluid, it is analogous to equation (3.5.15)

$$\dot{Q} = \tilde{\alpha}_2 A_2 (T_{w2} - T_2) \,, \tag{3.5.17}$$

where T_{w2} is the temperature at the second wall surface and A_1 the surface's area. The surface temperatures can be neglected. The heat flux through the wall can be written only in terms of the fluid temperatures

$$\dot{Q} = kA(T_1 - T_2) \tag{3.5.18}$$

with

$$\frac{1}{kA} = \frac{1}{\tilde{\alpha}_1 A_1} + \frac{\delta}{\lambda_m A_m} + \frac{1}{\tilde{\alpha}_2 A_2} \,, \quad \left[\frac{1}{kA}\right] = \frac{\mathrm{K}}{\mathrm{W}} \,. \tag{3.5.19}$$

k is the *heat transmission coefficient*, which depends on the area A. Inside the wall, the temperature decreases and the temperatures directly at the wall can be estimated by

$$T_{w1} = T_1 - \frac{kA}{\tilde{\alpha}_1 A_1}(T_1 - T_2) = T_1 - \frac{\dot{Q}}{\tilde{\alpha}_1 A_1} \tag{3.5.20}$$

and by

$$T_{w2} = T_2 + \frac{kA}{\tilde{\alpha}_2 A_2}(T_1 - T_2) = T_2 + \frac{\dot{Q}}{\tilde{\alpha}_2 A_2}\,. \tag{3.5.21}$$

The above presented equations are required for the description of the experimental test case in chapter 7, on page 201. The last type of a possible heat transport in a fluid is the so-called *heat radiation* which appears in form of electro-magnetic waves. This form of energy transport is detected only rarely in fluids and is mainly a phenomenal of solid bodies. The radiation of the temperatured walls in the investigated experimental setup can be neglected. Thus, this form of energy transport is not discussed at this point. For further information it is referred to [Baehr08], chapter 1.

3.5.3. Boundary layers - Velocity and temperature profiles

3.5.3.1. An overview

In this thesis, two configurations of a turbulent natural convection are investigated. Both configurations differ in the choice of the walls which are heated isothermally. This choice and the position of the heated walls relative to the gravitational field, influences the temperature and velocity profiles of the flow. This is demonstrated in figure 3.5. The configuration, where both horizontal walls are heated, is also called a *Rayleigh-Bénard convection* or a *Rayleigh-Bénard problem*, as it was mentioned before. This problem is named after the English physicist *Lord John William Rayleigh* (1842 - 1919) and the French physicist *Henri Claude Bénard* (1874 - 1939) (see [Bénard1900], [Rayleigh1916]).

In the most cases, convective flows are investigated as an incompressible fluid which satisfies a Boussinesq-approximation as in [Shishkina08] and [Shishkina09] (s. also chapter 1, section 1.10, on page 26). Due to an increased gravitational force field in the experimental setup of *CenCon*, the density changes should not be neglected in the numerical method of this case. Therefore, density changes due to temperature differences in the fluid are considered in the numerical model for each test case. Thus, a non-Boussinesq fluid is assumed. In this way, possible differences to studies which consider a Boussinesq-approximation can also be investigated.

A natural convection for which a non-Boussinesq fluid is assumed is also called a *Non-Oberbeck - Boussinesq convection* (NOB) ([Ahlers06]). On the contrary, a convective flow which satisfies a Boussinesq-approximation is called a Oberbeck - Boussinesq convection (OB) ([Ahlers06]). According to [Schlichting06], chapter 10, 10.5, the wall temperature in a natural convection between two heated walls, heats only a small region of the fluid which is located directly near the heated walls. The wall heat flux does not reach the inner layers of the fluid. The inner energy which the fluid receives from the wall is removed by convective heat transport in flow direction along the heated wall. This implies, that the

temperature and also velocity boundary layer thickness have to increase in flow direction along the heated walls. Figure 3.5 on page 82 demonstrates the typical resulting mean temperature and velocity distribution in a natural convection generated between two heated walls (as seen in [Hölling05], [Hölling06]). The left picture shows a configuration where the vertical walls are heated isothermally. The right picture displays a configuration where the horizontal walls are heated. Both configurations are similar to each other, but the heated walls are rotated to each other about 90°. Therefore, also the profiles of the fluid properties must be rotated to each other about 90°.

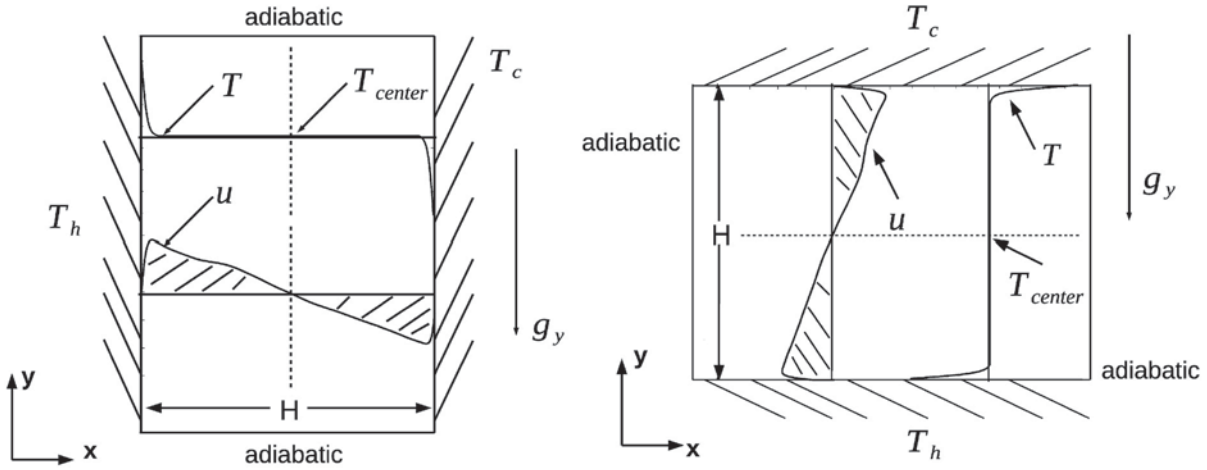

Figure 3.5.: Mean velocity and temperature distribution in an enclosed container with adiabatic lateral walls (as seen in [Hölling05], [Hölling06]). **Left:** Vertical walls are heated. **Right:** Horizontal walls are heated.

In case of a Boussinesq fluid, all fluid properties reveal an anti-symmetrical profile form. The shaded areas under the functions in figure 3.5 are in this case equal to each other. Their size is decreasing with an increasing temperature difference. In case of a NOB convection and temperature dependent fluid properties, the profiles reveal an asymmetry, which is further discussed in chapter 5 and chapter 6 from page 95 on (see also [Ahlers06]). The vertical orientation of the heated walls effects a quasi-steady state flow, after a transient state of the system is passed. In the centre region of the container a temperature T_{center} is reached, which is almost about the mean temperature between both heated walls, $T_{\text{mean}} = (T_{\text{hot}} - T_{\text{cold}})/2 + T_{\text{cold}}$. The velocity at this point is almost equal zero.

In the horizontal configuration, hot lift-streams and cold sink-streams change the temperature field inside the fluid due to the relative direction of gravity. These streams increase the intensity of turbulence and produce an unsteady flow behaviour, which dominates the vertical heat flux in the configuration. Local density differences drive the fluid between the heated walls. The resulting temperature distribution is therefore characterised by increasing temperature gradients in the near wall region and a dominating convective mass exchange the centre region of the container.

3.5.3.2. Turbulent flow

Two layer structure

Most turbulent flows of a high Reynolds number (Re $\rightarrow \infty$) can be characterised by a two layer structure as indicated in figure 3.6 . Note that figure 3.6 is valid for a horizontal or vertical wall configuration. According to ([Hölling05], [Hölling06]), near the wall, the *boundary layer* or *inner layer* can be seen. In this boundary layer, a *viscous sublayer* exists directly at the wall.

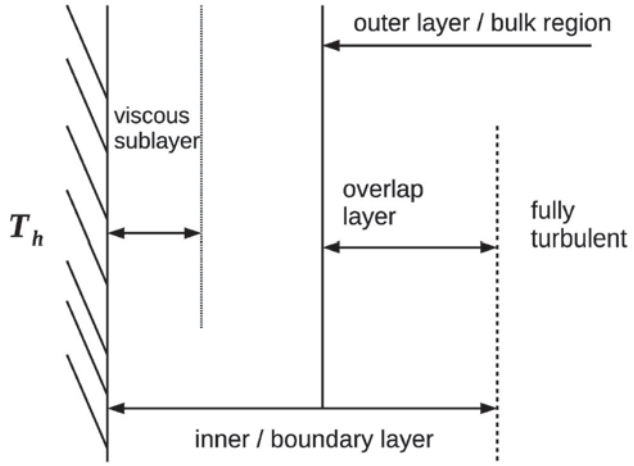

Figure 3.6.: Two layer structure of a turbulent flow in distance to the hot wall (as seen in [Hölling05]).

Most of the distance between both heated walls is covered by the so-called *bulk region* or *outer layer*, which is significantly bigger than the boundary layer. The bulk region has a thickness of about $H/2$, where H is a characteristic length of the flow geometry. In this case is H the distance between both heated walls. In the boundary layer, molecular and turbulent momentum transfer can be detected. The molecular momentum transport is insignificant compared to the turbulent transport in the bulk region where the flow is fully turbulent (see [Schlichting06], chapter 17, 17.1).

According to [Pope00], chapter 7, 7.1, the particular regions in the boundary layer can be characterise as follows by the normal direction to the wall y and the non dimensional wall distance y^+. The inner layer is defined as $y/\delta < 0.1$ and $\delta = H/2$ is defined as the half height between the walls. It is for the viscous sublayer $y^+ < 5$. In this region, viscous stresses are dominant.

Before the *overlap layer* is reached the *viscous wall region* begins ($y^+ < 50$). Here, the contribution of viscous effects to the shear stress is distinctive. The *log-law region* begins at $y^+ > 30$, $y/\delta < 0.3$. The overlap layer is reached at $y^+ > 50$, $y/\delta < 0.1$. The *bulk region* or *outer layer* begins at $y^+ > 50$. Here, diffusive effects are negligible. In the following, analytical functions of the velocity and temperature distribution in the boundary layer

are formulated. The following part deals with turbulent flows in general on the basis of a *Couette flow*, while section 3.5.3.3 deals especially with a natural convection.

Analytical description of the velocity and temperature profiles in the boundary layer

The boundary layer laws are derived from the dimensionless Navier-Stokes equations combined with a subsequent dimension analysis under an assumption of an asymptotic solution for $\mathrm{Re} \to \infty$. Because the main focus of this thesis does not lie on the mathematical derivation of these functions, they are only presented in a summarised form which is formulated in the whole next section analogously to the information in [Schlichting06], chapter 17. For a detailed description of their derivation, it is pointed to [Spurk07] and also to [Schlichting06].

It is assumed, that all variables are understand as turbulent as it was demonstrated for a LES in this chapter from page 63 on. The variables separation in turbulent and viscous parts is not used in the following to obtain a clearer presentation. The boundary layer thickness can be derived on basis of the two-dimensional *Couette flow* for high Reynolds numbers

$$\delta_{BL,u} = \frac{\nu}{u_{\tau_w}} = \frac{H}{\mathrm{Re}_{\tau_w}} \tag{3.5.22}$$

with $\mathrm{Re}_{\tau_w} = \dfrac{u_{\tau_w} H}{\nu}$, where ν is the kinematic viscosity. The Couette flow is observed between two walls where y describes the vertical distance between both walls and x the horizontal distance along the walls. For $\mathrm{Re}_{\tau_w} \to \infty$, the boundary layer δ_{BL} converges to zero. u_{τ_w} in equation (3.5.22) is the wall shear stress velocity

$$u_{\tau_w} = \sqrt{\frac{\tau_w}{\rho}} \tag{3.5.23}$$

with the wall shear stress τ_w

$$\tau_w = \mu \left| \frac{\partial u}{\partial y} \right|_{\mathrm{w}}, \tag{3.5.24}$$

the dynamic viscosity μ, the velocity component u in vertical direction y and the velocity gradient at the wall $\partial u / \partial y$. Note that the velocity u is a function of the following properties

$$u = \tilde{f}(y, H, \nu, \tau_w/\rho). \tag{3.5.25}$$

The characteristic variable of the boundary layer is the non-dimensional distance y^+, which is given by

$$y^+ = \frac{u_{\tau_w}}{\nu} y = \eta^+ \mathrm{Re}_{\tau_w} \tag{3.5.26}$$

with a dimensionless distance $\eta^+ = \dfrac{y}{H}$.

The velocity distribution in the boundary layer is then a function of the non-dimensional distance y^+

$$u^+ = g(y^+)\,. \tag{3.5.27}$$

The expression in (3.5.27) is valid for all turbulent boundary layers with a finite wall shear stress velocity u_{τ_w}. The velocity distribution in the bulk region can be described by a function of the following form

$$u^+ = f(\eta^+, \mathrm{Re}_{\tau_w})\,. \tag{3.5.28}$$

For a region of $0 < \eta^+ < 1$, equation (3.5.28) fulfils the following boundary conditions

$$\begin{aligned} \eta^+ = 0: &\qquad u^+ = 0,\ \tau^+_{w,t} = 0\,, \\ \eta^+ = 1: &\qquad d^2u^+/d\eta^{+2} = 0 \end{aligned} \tag{3.5.29}$$

with

$$u^+ = \frac{u}{u_{\tau_w}}\,, \quad \text{and} \quad \tau^+_{w,t} = \frac{\tau_{w,t}}{\rho u^2_{\tau_w}}\,, \tag{3.5.30}$$

where $\tau_{w,t}$ is the turbulent part of the wall shear stress τ_w and ρ the density. To estimate the solution for the boundary layer and the bulk region, both expressions in (3.5.27) and (3.5.28) have to be equal in the region between both layers. A dimension analysis reveals the following boundary condition for the bulk layer

$$\lim_{\eta^+ \to 0} \frac{du^+}{d\eta^+} = \frac{1}{\kappa \eta^+} \tag{3.5.31}$$

and a condition for the boundary layer

$$\lim_{y^+ \to \infty} \frac{du^+}{dy^+} = \frac{1}{\kappa y^+} \tag{3.5.32}$$

with the so-called *Karman constant* $\kappa = 0.41$. Integration of the equation in (3.5.32) leads to

$$\lim_{y^+ \to \infty} u^+(y^+) = \frac{1}{\kappa} \ln y^+ + C^+_u. \tag{3.5.33}$$

The integration constant C^+_u is assumed with $C^+_u = 0.5$ for smooth walls, according to experimental measurements ([Schlichting06], chapter 17, 17.1).

Equation (3.5.33) is also called the *logarithmic overlapping law* or *logarithmic wall law*. It describes, how the universal law $u^+(y^+)$ acts for $y^+ \to \infty$. In [Schlichting06] (chapter 17, 17.1) the following analytical expression of the universal wall law is given which was formulated by [Gersten1992]

$$\begin{aligned}
\frac{du^+}{dy^+} &= \frac{1}{1+\underbrace{(A+B)y^{+3}}_{\Lambda}} + \frac{By^{+3}}{1+\kappa By^{+4}}\,, \\
u^+ &= \frac{1}{\Lambda}\left[\frac{1}{3}\ln\frac{\Lambda y^+ + 1}{\sqrt{(\Lambda y^+)^2 - \Lambda y^+ + 1}} + \frac{1}{\sqrt{3}}\left(\arctan\frac{2\Lambda y^+ - 1}{\sqrt{3}} + \frac{\pi}{6}\right)\right] \\
&\quad + \frac{1}{4\kappa}\ln(1+\kappa By^{+4})
\end{aligned} \tag{3.5.34}$$

with the following values

$$\begin{aligned}
&\kappa = 0.41\,, \quad A = 6.1\cdot 10^{-4}, \quad B = 1.43\cdot 10^{-3}\,, \\
&\Lambda = 0.127\,, \quad C_u^+ = \frac{2\pi}{3\sqrt{3}\Lambda} + \frac{1}{4\kappa}\ln(\kappa B) = 5.0\,,
\end{aligned} \tag{3.5.35}$$

which result from experimental measurements. Both equations in (3.5.34) fulfil the condition in (3.5.33). The boundary layer can be described by the following regions as in [Schlichting06], chapter 17, 17.1

$$\begin{aligned}
&\text{viscous sublayer :} && 0 \le y^+ < 5\,, \quad u^+ = y^+\,, \\
&\text{transient layer :} && 5 < y^+ < 70\,, \quad \text{eq. (3.5.34)}\,, \\
&\text{overlapping layer :} && 70 < y^+\,, \quad u^+ = \frac{1}{\kappa}\ln y^+ + C_u^+\,.
\end{aligned} \tag{3.5.36}$$

A universal boundary layer law can be formulated also for the temperature profile. This is described in the following analogously to [Schlichting06], 17, 17.1.2.7.

In the velocity boundary layer theory, the kinematic viscosity ν is a decisive property. This part is taken by the thermal diffusivity coefficient $\kappa = \lambda/(\rho\, c_p)$ in the temperature boundary layer theory. If κ is almost of the same dimension as ν, the velocity and temperature boundary layer are also almost of the same size.

The temperature boundary layer has only a universal character, if its size lies within the size of the velocity boundary layer. This is satisfied in flows where $\mathrm{Pr} = \nu/\kappa > 0.5$ is fulfilled. The thickness of the thermal boundary layer can be given by ([Spurk07], chapter 12)

$$\delta_{BL,T} \sim L\mathrm{Re}_{\tau_w}^{-1/2}\,. \tag{3.5.37}$$

It is assumed that the heat flux density q_w is constant directly at the wall in the boundary layer. The fluid properties are also assumed as constant. Analogously to u_{τ_w} a friction temperature can be defined by

$$T_{\tau_w} = -\frac{q_w}{\rho c_p u_{\tau_w}}\,. \tag{3.5.38}$$

The dimensionless temperature is defined by

$$\theta^+ = \frac{T - T_w}{T_{\tau_w}}. \tag{3.5.39}$$

Analogously to the proceeding of the velocity boundary layer, an adjustment of boundary layer and bulk region leads to a temperature distribution in the overlapping region

$$\lim_{y^+ \to \infty} \theta^+(y^+, \mathrm{Pr}) = \frac{1}{\kappa_\theta} \ln y^+ + C_\theta^+(\mathrm{Pr})\,. \tag{3.5.40}$$

According to [Schlichting06] (chapter 17, 17.1.2.7), a definition for both constants C_θ^+, κ_θ can be given. The constant κ_θ is $\kappa_\theta = 0.47$. For smooth walls, the constant C_θ^+ is now given as a function of the Prandtl number Pr as

$$C_\theta^+(\mathrm{Pr}) = 13.7\,\mathrm{Pr}^{2/3} - 7.5\,, \quad (\mathrm{Pr} > 0.5)\,. \tag{3.5.41}$$

3.5.3.3. Natural convection

The above stated analytical solutions of the velocity and temperature in the boundary layer are now discussed for a turbulent natural convection between two vertical walls which are heated, as it was presented in figure 3.5, right picture, on page 82. The following information are based on the details in [Schlichting06], chapter 10, 19 and [Spurk07], chapter 12.

y is now the horizontal direction and describes the distance between the heated walls. The governing equations in (1.10.2) - (1.10.3) in chapter 1, section 1.10, on page 26 are considered now for a natural convection along an endless vertical plate. These equations are solved under certain conditions. In a natural convection in air the influence of dissipation can be neglected. Also a turbulent natural convection between two vertical, heated walls can be characterised by a two layer structure as indicated in figure 3.6.

Analytical description of velocity and temperature profiles in the boundary layer

At first, a laminar natural convection with a Boussinesq-approximation is considered analogously to [Schlichting06], chapter 10, 10.5. For the thickness of the thermal boundary layer it is

$$\delta_T \sim L\mathrm{Gr}^{-1/4} \sim \sqrt{\nu} \tag{3.5.42}$$

with the Grashof number $\mathrm{Gr} = \mathrm{Ra}/\mathrm{Pr}$ and the kinematic viscosity ν ([Spurk07], chapter 12, 12.3). As mentioned before in chapter 1, section 1.7, no given reference velocity appears in a convective flow. Therefore, the Grashof number Gr is used instead of the Reynolds number in the above formulation. For $\mathrm{Gr} \gg 1$, we have $\delta_T/L \ll 1$ and the flow has a boundary layer character. Note that this time y stands for the horizontal axis which points

away from the in this case vertical, heated wall. x stand for the vertical direction along the heated wall. The characteristic velocity in the boundary layer can then be given by

$$u_{BL} = \sqrt{\beta_\infty \Delta T g_x L}\,. \tag{3.5.43}$$

T_∞ denotes the temperature in great distance from the wall and β_∞ the depending thermal expansion coefficient. Further it is $\Delta T = |T_w - T_\infty|$. One can define a dimensionless temperature and velocity as

$$\Theta^* = \frac{T - T_\infty}{T_w - T_\infty}\,, \quad \tilde{u}^+ = \frac{u}{u_{BL}} \tag{3.5.44}$$

and the dimensionless variables as

$$x^+ = \frac{x}{L}\,, \quad \tilde{\eta}^+ = \frac{y}{L}\mathrm{Gr}^{1/4}\,, \tag{3.5.45}$$

where x is the component in vertical direction and y in horizontal direction. With help of equation (3.5.44) and (3.5.45) one obtains the following function for the temperature profile in the boundary layer

$$\Theta^*(x, y) = \Theta^*(\tilde{\eta}^+)\,. \tag{3.5.46}$$

For a formulation of the Nusselt number distribution in the boundary layer different expressions can be found. [Schlichting06] (chapter 10, 10.5), for example, states the following connection between Nusselt number and Grashof number

$$\mathrm{Nu} = -\mathrm{Gr}^{1/4}\left(\left|\frac{\partial\Theta^*}{\partial\tilde{\eta}^+}\right|_{\tilde{\mathrm{w}}}\right) \tag{3.5.47}$$

with the gradient at the heated wall (marked by index $\tilde{\mathrm{w}}$), while [Spurk07] (chapter 12, 12.3) gives a connection between Nusselt number, Grashof number and Prandtl number by

$$\mathrm{Nu} = \left(\frac{\mathrm{GrPr}}{2.43478 + 4.884\mathrm{Pr}^{1/2} + 4.95283\mathrm{Pr}}\right)^{1/4}. \tag{3.5.48}$$

To consider the temperature dependent fluid properties and hence nonlinear density effects, which arise in a non-Boussinesq fluid, corrections of the above stated expression (3.5.48) have to be made. The stated corrections were proposed from [Herwig1985], [Herwig1984] and can be found in a summarised form in [Schlichting06], chapter 10, 10.5.6.

The above equations are valid for a laminar flow. Assuming $T_w = \text{const.}$, it is

$$\frac{\mathrm{Nu}}{\mathrm{Nu}_{f_B}} = \left(\frac{\mathrm{Pr}_w}{\mathrm{Pr}_\infty}\right)^{n_{\mathrm{Pr}}} \left(\frac{\rho_w\beta_\infty}{\rho_\infty\beta_w}\right)^{n_{\rho\beta}} \left(\frac{\rho_w\lambda_w}{\rho_\infty\lambda_\infty}\right)^{n_{\rho\lambda}} \left(\frac{c_{pw}}{c_{p\infty}}\right)^{n_c} \tag{3.5.49}$$

with $c_p = \dfrac{2(p-p_\infty)}{\rho V^2}$. The index f_B represents the results with the Boussinesq assumption. The index ∞ denotes the values in great distance from the wall. For the appearing coefficients in (3.5.49) the following values are assumed

$$n_{\mathrm{Pr}} = -0.206\left(1+1.415\mathrm{Pr}_\infty^{-0.7}\right)^{-0.605}\,, \quad n_{\rho\beta} = -0.070\,, \quad n_{\rho\lambda} = 0.308\,, \quad n_c = 0.202. \tag{3.5.50}$$

The expression in (3.5.49) is a good local approximation of the Nusselt number. For a turbulent flow, the turbulent transport properties have to be considered in the above expressions as it is formulated in [Schlichting06] (chapter 19, 19.3). For great Grashof numbers, the flow can be also described by a two layer structure with a viscous sublayer and a fully turbulent outer layer. The characteristic reference velocity is in then

$$U_{BL} = (\Delta T g_x \beta_\infty \kappa_\infty)^{1/3} \tag{3.5.51}$$

with the thermal diffusivity coefficient κ_∞ at T_∞. Universal boundary layer laws of the velocity $u^\times$ and temperature $\theta^\times$ can be formulated in the viscous sublayer with an assumption of $\mathrm{Pr}_\infty = \mathrm{Pr}$ by

$$\begin{aligned} u^\times &= \frac{u}{u_{q,\mathrm{ref}}} = f_1(y^\times, \mathrm{Pr}) \quad \text{and} \quad \lim_{y^\times\to\infty} u^\times = \kappa_1\cdot(y^\times)^{1/3} - C^\times(\mathrm{Pr})\,, \\ \theta^\times &= \frac{T-T_w}{T_q} = f_2(y^\times, \mathrm{Pr}) \quad \text{and} \quad \lim_{\theta^\times\to\infty} \theta^\times = \kappa_2\cdot(y^\times)^{-1/3} - C_\theta^\times(\mathrm{Pr})\,. \end{aligned} \tag{3.5.52}$$

This approach was formulated by [Gersten1992] and given in [Schlichting06], chapter 19, 19.3. u is the turbulent velocity component in vertical direction. Further, it is

$$u_{q,\mathrm{ref}} = \left(\frac{\Delta T \beta g_x \nu \kappa}{L}\right)^{1/4}\,, \quad y^\times = \frac{y u_{q,\mathrm{ref}}}{\nu}\,, \quad T_q = \frac{\Delta T \kappa}{L u_{q,\mathrm{ref}}} \tag{3.5.53}$$

with the thermal diffusivity coefficient κ and two constants κ_1, κ_2. Both constants can be found in [Schlichting06], chapter 19, 19.3 with $\kappa_1 = 27$, $\kappa_2 = 5.6$ which was proposed by [Gersten1992]. The universal functions $C^\times(\mathrm{Pr})$, $C_\theta^\times(\mathrm{Pr})$ in equation (3.5.52) are dependent of the Prandtl number. It is

$$C_\theta^\times(\mathrm{Pr}) = \frac{\mathrm{Pr}^{1/2}}{0.24\,(\Psi(\mathrm{Pr}))^{1/4}}\,, \quad \Psi(\mathrm{Pr}) = \left(1+\left(\frac{C_{ch}}{\mathrm{Pr}}\right)^{9/16}\right)^{-16/9}\,, \tag{3.5.54}$$

which was proposed by [Churchill1983] and stated in [Schlichting06] (chapter 19, 19.3). The *Churchill constant* is stated as $C_{ch} = 0.46$. It is also

$$\Psi(\mathrm{Pr}\to\infty) = 1 \quad \text{and} \quad \Psi(\mathrm{Pr}\to 0) = 2.2\,\mathrm{Pr}. \tag{3.5.55}$$

In the overlapping layer an adjustment of the temperature leads to

$$\frac{T_w - T_\infty}{T_q} = C_\theta^\times(\mathrm{Pr}). \tag{3.5.56}$$

An expression of a Nusselt number relation can be formulated by

$$\mathrm{Nu} = 0.15(\Psi(\mathrm{Pr}))^{1/3}\mathrm{Gr}^{1/3} = 0.15(\Psi(\mathrm{Pr})\mathrm{Ra})^{1/3}\,, \tag{3.5.57}$$

where the Nusselt number is estimated in vertical direction along the vertical heated wall.

Complementary notes

The above considerations are formulated for a natural convection between vertical heated walls which fulfils a Boussinesq-approximation. In the following of this thesis, analytical functions of the temperature in the boundary layer are described also for a configuration with horizontal heated walls. These functions are based on the above theory and are similar to the equations (3.5.40) and (3.5.46). The modified functions are proposed by *Hölling et al.* in [Hölling06], [Hölling05] and they are presented in chapter 6, section 6.3.3, on page 164. There, they are compared to the simulation results. Further, a Nusselt-Rayleigh-number dependence for a Prandtl number of Pr = 0.71 can be formulated for the observed horizontal turbulent natural convection. Therefore, modified expressions of *Grossmann et al.* in [Grossmann00] are used which are similar to the one given in equation (3.5.57).

4. Computational and experimental test case studies - An overview

The purpose of the three following chapters 5 - 7 is the numerical and in one case also experimental investigation of three configurations of a turbulent natural convective flow in air. The analysis is based on the previously discussed theory from chapters 1 - 3. This short chapter should give a summarised introduction of the three used test case configurations.

4.1. Test case configurations

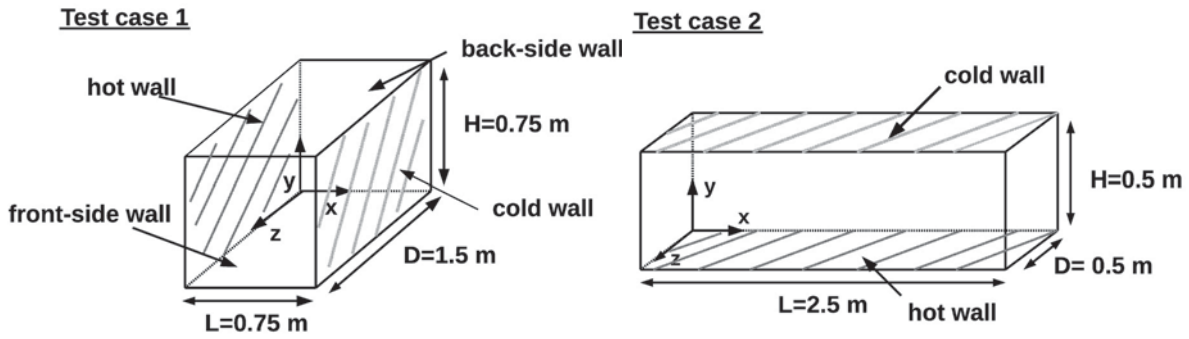

Figure 4.1.: Left: Scheme of test case *VerCon* (see also [Zimmermann14a]). **Right:** Scheme of test case *RayCon* (see also [Zimmermann12], [Zimmermann15]).

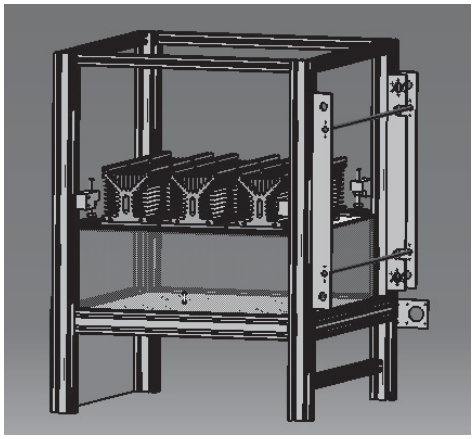

Figure 4.2.: Scheme of test case *CenCon*.

The main focus lies in all studies on the numerical modelling and understanding of the flow dynamic, its turbulence production, the fundamental fluid properties and the flow structure inside the fluid. All three configurations consist of a rectangular enclosed container with smooth walls which is filled with air. The container properties are chosen simplified in each case to reduce especially complexity aspects. Nevertheless, the setups are still sufficient and commonly used regarding the investigation of convective flows. The walls of the container limit the expansion of the fluid. Two opposite walls of the setup are isothermally heated with a constant temperature difference between them. All setups vary in their aspect ratios and especially in the choice of the two heated walls. The orientation of these heated walls relative to the direction of gravity, effects significantly the main flow field. Lateral walls of all setups are designed with different boundary conditions, e.g. adiabatic walls or a fixed temperature condition. A sketch of all three test case configurations is given in figures 4.1 and 4.2.

The first setup of **VerCon** (left picture in figure 4.1) is built of a container where two of the vertical walls are heated, while both other cases, **RayCon** and **CenCon**, consist of a container where the horizontal walls are heated (right picture in figure 4.1 and figure 4.2). Both later mentioned configurations are so-called *Rayleigh-Bénard convection* problems. The first test case is denoted by **VerCon**, because the convection (*Con*) is generated between the vertical heated walls (*Ver*). The second test case **RayCon** is named after the Rayleigh-Bénard (*Ray*) convection (*Con*). The third test case **CenCon** is also a Rayleigh-Bénard convection (*Con*) problem which is additionally rotating in a large-scale centrifuge (*Cen*) with a constant angular velocity.

All three test cases are based on each other. Due to the parallel orientation of the vertical, heated walls relative to the direction of gravity in *VerCon*, a quasi-steady state is reached after a while in the setup. This configuration of a natural convection represents the basis for both other test cases. This case has to be understood first to use the gained information on the investigation of *RayCon* and finally of *CenCon*. Regarding the layout, test case *CenCon* and *RayCon* have a similar construction to each other. But in contrast to *RayCon*, a Coriolis force should affect the test case of *CenCon* which is generated by a rotational movement of the test cell. To analyse the influences of the Coriolis force on the test case, two different modes are analysed in case of *CenCon*.

First, the RB cell is studied in a non-rotation mode, similar to the investigation of *RayCon*. Second, the RB cell is analysed while it is rotating under hyper-gravity in the centrifuge. While *CenCon* is rotating, possible influences on the flow structures, the turbulence production and the fluid properties due to the Coriolis acceleration should be investigated in the simulation as well as in the experiment. The additional accelerations are realised in the simulation by a set of modified governing equations compared to the equations of *RayCon*.

4.2. Boundary conditions

All test cases can be characterised by the non-dimensional parameters of Rayleigh number **Ra**, Prandtl number **Pr** and the aspect ratio $\mathbf{\Gamma} = \frac{L}{H}$, where L and H are characteristic lengths of the geometrical setup (see also chapter 1, section 1.4 and chapter 3, section 3.5). All parameters correspond to the mean temperature value T_{mean} taken between both isothermally heated walls with $T_{\text{mean}} = T_{\text{cold}} + \frac{T_{\text{hot}} - T_{\text{cold}}}{2}$. The Prandtl number stays in each case at $\text{Pr} = 0.71$ which represents the used fluid, air, in the chosen temperature intervals. The analysed range of Rayleigh-numbers varies in each study. The main conditions of each test case can be given summarised by

1) **VerCon**: rectangular container filled with air, two of the vertical walls are heated, different boundary conditions on lateral walls, numerical investigation, characteristic numbers: $\text{Ra} = 1.58 \times 10^9$, $\text{Pr} = 0.71$, $\Gamma_x = \frac{L}{H} = 1$, $\Gamma_z = \frac{D}{L} = 2$.

2) **RayCon**: rectangular container filled with air, both horizontal walls are heated, adiabatic lateral walls (a Rayleigh-Bénard problem), numerical investigation, characteristic numbers: $6.16 \times 10^7 \leq \text{Ra} \leq 4.1 \times 10^8$, $\text{Pr} = 0.71$, $\Gamma_x = \frac{L}{H} = 5$, $\Gamma_y = \frac{H}{D} = 1$.

3) **CenCon**: rectangular container filled with air, both horizontal walls are heated, conducting and adiabatic lateral walls (a Rayleigh-Bénard problem), investigation in an experimental as well as numerical study, consideration of an additional Coriolis force influencing the fluid inside the test case, characteristic numbers:
$2.33 \times 10^6 \leq \text{Ra} \leq 4.32 \times 10^7$, $\text{Pr} = 0.71$, $\Gamma_x = \frac{D}{H} = 2.9$ and $\Gamma_y = \frac{L}{D} = 1$.

4.3. Numerical simulation and computational mesh

For each test case a compressible LES of a non-Boussinesq fluid is performed which is based on the before presented model of Fureby (s. chapter 3, section 3.3.2). The assumption of a non-Boussinesq fluid is especially relevant in the numerical investigation of *CenCon*, due to an intensified gravitational force field, which effects the test case while it is rotating under hyper-gravity. Furthermore, the influence of density changes in the fluid due to temperature differences should be investigated in all cases to compare the results to other studies which consider a Boussinesq fluid for similar test cases.

For the numerical investigations all computational geometries have to be discretised spatially by an appropriate mesh. Due to the rectangular setup of the test cases, a Cartesian block-structured mesh is chosen which is divided in 27 sub-blocks with different mesh resolutions. The chosen block partition enables an exterior zone in vicinity to all walls where a finer mesh resolution can be chosen easily and independently of the other sub-blocks to resolve the boundary layers. A fine resolution or wall function is essential in the boundary

layers, because the turbulent structures are generated mainly in this region. In the middle of the geometry, large flow scales are dominant and the mesh can consist in this region of a coarser resolution than close to the walls. The basic idea of the mesh structure of each case is illustrated on the basis of the *RayCon* geometry in figure 4.3. The first layer of cells is cubical formed. Regarding figure 4.3, it is $\Delta x_1 = \Delta y_1 = \Delta z_1$ in the first layer of cells.

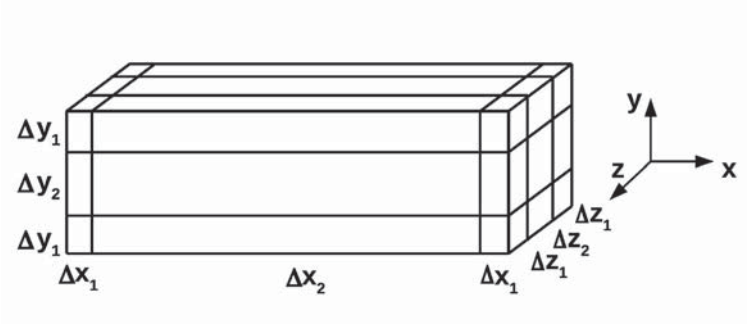

Figure 4.3.: Scheme of the computational geometry and block-partition of the mesh resolution on the basis of *RayCon*.

Because test case *VerCon* builds the basis for both other test cases, it is investigated as first step in the following chapter 5. Afterwards, the gained information and the performed numerical model of the LES are used to analyse both other test cases. Because *CenCon* is based on *RayCon* in its layout and its flow dynamics in the non-rotating mode, it is is analysed in chapter 7 on the basis of the gained information of *RayCon* from chapter 6. The results of all three test cases are compared to data of comparable experimental test cases as well as theoretical and numerical data from the literature.

5. Case studies - Test case *VerCon*, vertical, heated walls

5.1. Configuration of *VerCon* and its boundary conditions

The first test case *VerCon* is built of a rectangular enclosed container, as it is illustrated in figure 5.1. Note that some of the following presented contents of this section and the following section are also discussed in [Zimmermann14a]. The container consists of two isothermally heated walls which are heated differentially with a constant temperature difference. The container is filled with air. The heated walls are orientated in vertical direction, so that the temperature gradient is normal relative to the direction of gravity. This orientations implies a quasi-steady state flow in the container. To validate the results of the non-Boussinesq 3-dimensional LES of this setup an comparable experimental setup from *Tian et al.* in [Tian00a], [Tian00b] is chosen.

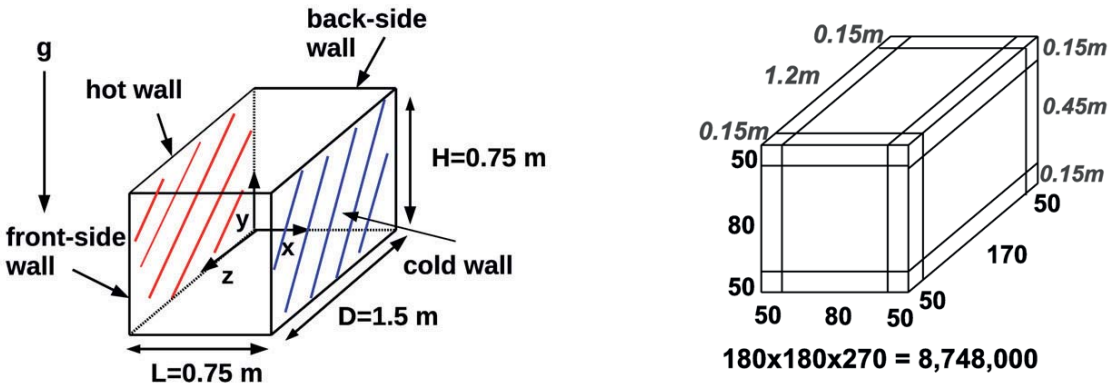

Figure 5.1.: Left: Configuration of *VerCon*. **Right:** Scheme of the computational geometry and mesh resolution with $(180 \times 180 \times 270)$ cells, 3D simulation (as in [Zimmermann14a]).

Tian et al. investigate a low level turbulent natural convection in an air-filled vertical square container for a Rayleigh number of $\mathrm{Ra} = 1.58 \times 10^9$ and a Prandtl number of $\mathrm{Pr} = 0.71$. The experiment, and hence the computational setup, is built of a length (L) of 0.75 m, a height (H) of 0.75 m and a depth (D) of 1.5 m. Therefore, the aspect ratios are $\Gamma_x = \frac{L}{H} = 1$ and $\Gamma_z = \frac{D}{L} = 2$. According to [Tian00a], the chosen experimental setup should offer a 2-dimensional main flow field at the xy-midplane. Between the heated walls

a constant temperature difference of $\Delta T = 323.15\,\mathrm{K} - 283.15\,\mathrm{K} = 40\mathrm{K}$ exists. In [Tian00a], the horizontal walls are highly conducting. Due to a non-slip condition, the velocity field at all walls is zero ($\mathbf{u} \equiv \mathbf{0}$) (*Dirichlet condition*). For the total pressure p, the boundary conditions are taken as a zero normal gradient at all walls of the computational geometry (*Neumann condition*), due to the non-slip condition of the velocity (mass conservation). The index w stands for variables estimated directly at the *lateral wall*. The index $\tilde{w}$ stands for variables estimated directly at one of the *heated walls*. It is

$$\left.\frac{\partial p}{\partial x}\right|_{\tilde{\mathrm{w}}} = 0, \quad \text{for } x = 0\,\mathrm{m} \text{ and } x = 0.75\,\mathrm{m}, \quad \text{with } 0 \le y \le 0.75\,\mathrm{m},\ 0 \le z \le 1.5\,\mathrm{m},$$
$$\left.\frac{\partial p}{\partial y}\right|_{\mathrm{w}} = 0, \quad \text{for } y = 0\,\mathrm{m} \text{ and } y = 0.75\,\mathrm{m}, \quad \text{with } 0 \le x \le 0.75\,\mathrm{m},\ 0 \le z \le 1.5\,\mathrm{m},$$
$$\left.\frac{\partial p}{\partial z}\right|_{\mathrm{w}} = 0, \quad \text{for } z = 0\,\mathrm{m} \text{ and } z = 1.5\,\mathrm{m}, \quad \text{with } 0 \le y \le 0.75\,\mathrm{m},\ 0 \le x \le 0.75\,\mathrm{m}.$$

The initial field of the total pressure p is assumed to be constant at $1 \cdot 10^5\,\mathrm{Pa}$ inside the computational geometry. Because the chosen solver *buoyantPimpleFoam* in OpenFOAM® estimates first the field of the dynamic pressure p_{rgh} and subsequent the field of the total pressure p, also an boundary condition for the dynamic pressure p_{rgh} has to be specified (see also chapter 3, section 3.4 and equation (3.4.1)). The boundary condition of the dynamic pressure p_{rgh} is defined by the option *buoyantPressure*. This option is a specified boundary condition in OpenFOAM®. It calculates the normal gradient of the dynamic pressure p_{rgh} from the local normal density gradient and the gravitational force field vector $\mathbf{g}$ by

$$\left.\frac{\partial p_{\mathrm{rgh}}}{\partial x}\right|_{\tilde{\mathrm{w}}} = \left.\frac{\partial \rho}{\partial x}\right|_{\tilde{\mathrm{w}}} g_x, \quad \text{for } x = 0\,\mathrm{m} \text{ and } x = 0.75\,\mathrm{m}, \quad \text{with } 0 \le y \le 0.75\,\mathrm{m},\ 0 \le z \le 1.5\,\mathrm{m},$$
$$\left.\frac{\partial p_{\mathrm{rgh}}}{\partial y}\right|_{\mathrm{w}} = \left.\frac{\partial \rho}{\partial y}\right|_{\mathrm{w}} g_y, \quad \text{for } y = 0\,\mathrm{m} \text{ and } y = 0.75\,\mathrm{m}, \quad \text{with } 0 \le x \le 0.75\,\mathrm{m},\ 0 \le z \le 1.5\,\mathrm{m},$$
$$\left.\frac{\partial p_{\mathrm{rgh}}}{\partial z}\right|_{\mathrm{w}} = \left.\frac{\partial \rho}{\partial z}\right|_{\mathrm{w}} g_z, \quad \text{for } z = 0\,\mathrm{m} \text{ and } z = 1.5\,\mathrm{m}, \quad \text{with } 0 \le y \le 0.75\,\mathrm{m},\ 0 \le x \le 0.75\,\mathrm{m}.$$

This option is assumed to be a uniform value, hence the normal gradient of the dynamic pressure p_{rgh} is taken as $1 \cdot 10^5\,\mathrm{Pa}$ at all walls, which is also the value of the internal field of p_{rgh} inside the geometry. Hence, inside the box an almost atmospheric pressure condition is generated.

In the experimental study of [Tian00a], the sidewalls are highly conducting. This boundary condition cannot be realised in the numerical simulation. Only an ideal linear boundary configuration can be modelled. The values of the boundary condition match only in the corner regions with the values of the experimental boundary condition, as it imaged in figure 5.2 by a plot of the non-dimensional temperature. The non-dimensional temperature is defined by

$$T^* = \frac{T_{\text{mean}} - T_{\text{cold}}}{T_{\text{hot}} - T_{\text{cold}}}, \tag{5.1.1}$$

where $T_{\text{mean}} = T_{\text{cold}} + (T_{\text{hot}} - T_{\text{cold}})/2$ is the mean temperature between the isothermally heated walls. Additionally to this boundary condition, three further conditions are investigated at the lateral walls in the numerical study.

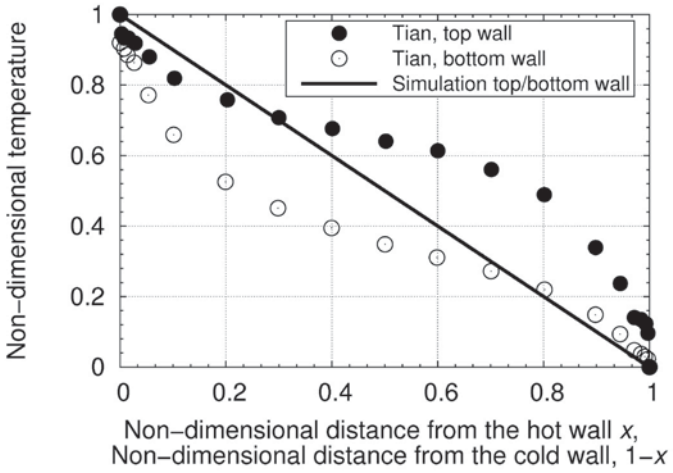

Figure 5.2.: Temperature boundary condition at the lateral walls. Data of [Tian00a] compared to the data of the linear bc simulation. - solid line: Top/bottom wall in the simulation (2D/3D). Study [Tian00a]: •: top wall, ○: bottom wall.

All conditions are compared to the perfectly conducting condition of the experiment. The additional realised conditions are

1) *adiabatic walls*,

2) *fixed temperature of* $T_{low} = 296\,K$ *at the lower wall and of* $T_{up} = 310\,K$ *at the upper wall*,

3) *fixed temperature condition of* $T_{low/up} = 303\,K$ *at the lower and upper wall*,

4) *linear temperature distribution at the lower and upper wall (s. figure 5.2).*

For the *adiabatic* boundary condition the normal gradient of the temperature has to be zero at the non-heated, horizontal walls

$$\left.\frac{\partial T}{\partial y}\right|_{\text{w}} = 0, \quad \text{for } y = 0\,\text{m} \text{ and } y = 0.75\,\text{m}, \quad \text{with } 0 \le x \le 0.75\,\text{m},\ 0 \le z \le 1.5\,\text{m},$$
$$\left.\frac{\partial T}{\partial z}\right|_{\text{w}} = 0, \quad \text{for } z = 0\,\text{m} \text{ and } z = 1.5\,\text{m}, \quad \text{with } 0 \le x \le 0.75\,\text{m},\ 0 \le y \le 0.75\,\text{m}.$$

The initial internal temperature field T_{IF} is chosen equally to the mean average temperature in the experimental setup with $T_{\text{IF}} = T_{\text{mean}} = 303.15\,\text{K}$. The Rayleigh number and

the Prandtl number stay in all numerical studies at $\mathrm{Ra} = 1.58 \times 10^9$ and $\mathrm{Pr} = 0.71$. To describe and understand the structure of the flow, diverse characteristic fluid properties have to be analysed. To assure a validation of the numerical model with the experiment, the same variables as in the study of [Tian00a] are estimated. In [Tian00a], the measurement period was about 4 minutes at every measuring point. Considering a steady-state of the system, a estimation time interval of $\Delta t = 200\,\mathrm{s} - 400\,\mathrm{s}$ is considered in the simulation. The numerical data are averaged over an interval of $\Delta t = 200\,\mathrm{s} - 400\,\mathrm{s}$ in the simulated process with an intermediate steps size of $\Delta t = 3\,\mathrm{s}$ for the 3D simulation cases and $\Delta t = 1\,\mathrm{s}$ for the 2D simulations. A time-averaged value of an arbitrary variable f in a time interval $[t_1, t_2]$ is formulated by

$$\bar{f} = \frac{1}{t_2 - t_1} \int_{t_1}^{t_2} f \, dt. \tag{5.1.2}$$

The simulation assumes a non-Boussinesq fluid (s. chapter 1, section 1.7, from page 18). Consequently, fluid properties, as density ρ, the thermal expansions coefficient β, the thermal diffusion coefficient α and dynamic viscosity μ are assumed to be temperature dependent. The two recent parameters are calculated by the Sutherland model from chapter 1, section 1.9 from page 24 on. The turbulent Prandtl number $\mathrm{Pr}_{\mathrm{sgs}}$ is taken as $\mathrm{Pr}_{\mathrm{sgs}} = 0.4$ (s. chapter 3, section 3.3.2). The word *boundary condition* is abbreviated by the term *bc* in the following.

5.2. Computational mesh of *VerCon*

To perform the numerical simulation, the geometry has to be discretised spatially by an appropriate mesh. Due to the rectangular test case configuration, a Cartesian block-structured mesh is chosen which is divided in twenty-seven sub-blocks.

A sketch of the mesh resolution is demonstrated in figure 5.1 (right picture). A snapshot of the mesh resolution of the particular walls is exhibit in figures 5.3 - 5.4 on page 99. Because of symmetry aspects, only a quarter is presented of the front/back walls and a quarter of the horizontal/heated walls.

The partition of the mesh enables an exterior zone in vicinity to all walls where a finer resolution can be easily chosen independently of the other sub-blocks. Mainly in this region, the turbulent structures are generated. Thus, a fine resolution or wall function is essential in this region. According to [Pope00], chapter 7, 7.1, the viscous wall region near the walls is important concerning the grid resolution of a LES. In a region of $y^+ < 20$, the turbulence production, dissipation and kinetic energy reach their peak values. Thus, the filter and grid width have to be sufficiently small to resolve 80% of the energy everywhere, also in the viscous wall region. Hence, y^+ should be $y^+ < 1$ in the first cell midpoint from

the wall. Further, in a LES, the size of one cell should be nowhere bigger than ten-times of the size of the Kolmogorov length which is fulfilled by the chosen mesh. The first layer of cells in the corner regions is cubical formed. Near to the walls, the mesh is clustered and the cell ratios decrease in direction to the walls to resolve the boundary layers which lie in the first sub-block near the walls. In this way, all relevant turbulent scales can be resolved and no wall functions have to be used in the numerical model. In the middle of the geometry, large flow scales are dominant and the mesh has a coarser resolution than close to the walls.

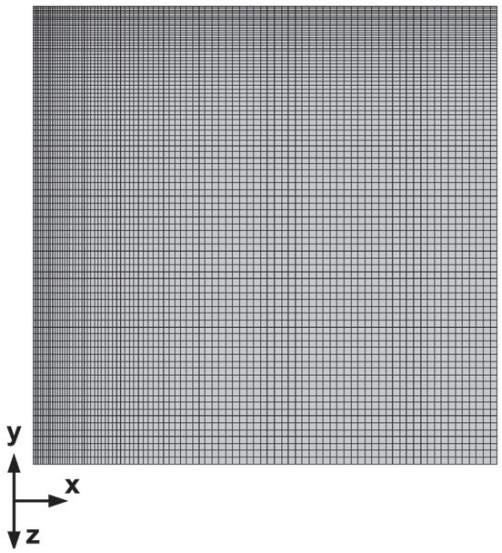

Figure 5.3.: Mesh resolution of the computational geometry of *VerCon*, see figure 5.1, 3D simulation, quarter of the front/back wall.

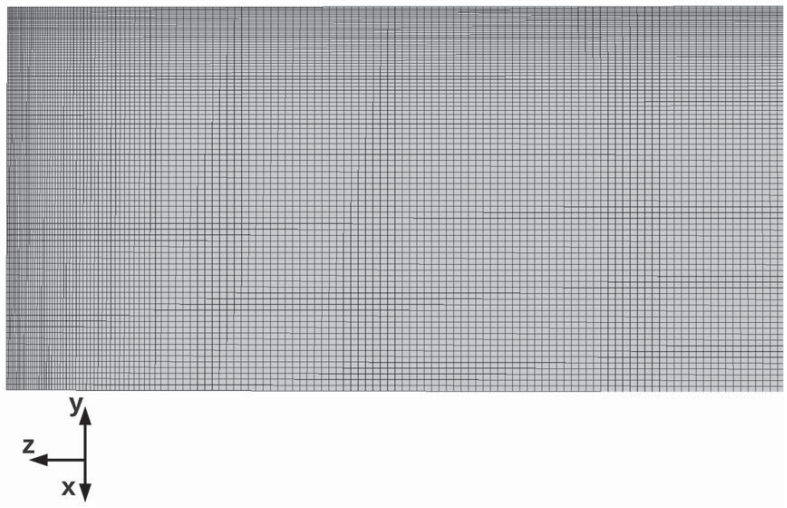

Figure 5.4.: Mesh resolution of the computational geometry of *VerCon*, see figure 5.1, 3D simulation, quarter of the heated/side walls.

In [Tian00a], the first experimental measurement point is located at $3.4 \cdot 10^{-4}$ m in vertical distance from the hot wall. In the simulation, the first grid point should be located as

near as possible at this same position, but simultaneously, the total cell number of the mesh should be limited to 10 million cells. As consequence, the final mesh consists of $(180 \times 180 \times 270) = 8,748,000$ cells in (x, y, z)-direction. The first grid point is located at $y_{w1} = 6.9 \cdot 10^{-4}\,\mathrm{m}$ in vertical distance from the hot/cold wall. To analyse possible mesh dependencies, additionally to the 3D simulation a 2D simulation is performed. The 2D simulation consists of a mesh with $(750 \times 750) = 562,500$ cells. The cells are equally spaced over the plane. The first grid point is located at $y_{w1} = 5.0 \cdot 10^{-4}\,\mathrm{m}$ in vertical direction from the hot/cold wall.

In a DNS, the Kolmogorov length is a scale for the size of the smallest turbulent eddies. These smallest eddies have to be resolved by the computational grid (s. also chapter 3). According to equation (3.1.7) in chapter 3, section 3.1 on page 66, the Kolmogorov length can be estimated by

$$\frac{L}{\eta} = \mathrm{Re}_L^{3/4}\,. \tag{5.2.1}$$

With a higher Reynolds number, the Kolmogorov length becomes larger and the mesh resolution must be adapted. In a LES, the grid resolution has not to be as fine as in a DNS. In natural convection the characteristic flow variable is the Rayleigh or Grashof number. According to equation (1.9.6) in chapter 1, section 1.9 it is

$$\mathrm{Ra} = \mathrm{GrPr} = \frac{g\beta_0 L^3\,(T_w - T_0)}{\nu_0 \kappa_0}\,. \tag{5.2.2}$$

According to [Schlünder1970], the Grashof number can be related to the Reynolds number by the following formulation for a natural convection

$$\mathrm{Gr} = 2.5\mathrm{Re}^2. \tag{5.2.3}$$

With help of eq. (5.2.1) and equations (5.2.2), (5.2.3), the Kolmogorov length can then be written in terms of the Rayleigh number

$$\eta_{k_L} \approx \frac{L}{\mathrm{Re}^{3/4}} = \frac{L}{\left(\dfrac{1}{0.71 \cdot 2.5}\mathrm{Ra}\right)^{3/8}}. \tag{5.2.4}$$

For a Rayleigh number of $\mathrm{Ra} = 1.58 \times 10^9$, the Kolmogorov length is then

$$\eta_{k_L} \approx 3.4 \cdot 10^{-4}\,\mathrm{m}. \tag{5.2.5}$$

The size of the smallest cell in the 3D resolution is $\Delta_x/\Delta_y/\Delta_z = 1.38 \cdot 10^{-3}\,\mathrm{m}$. For the 2D resolution it is $\Delta_x/\Delta_y = 1 \cdot 10^{-3}\,\mathrm{m}$. Hence, the size of the smallest cell is in both grids

larger than the Kolmogorov length. Thus, the chosen resolution is not as small as it have to be in a DNS. Table 5.1 contains an overview of reached values of the non-dimensional wall distance y^+ for the first cell midpoint y_{w1} and various boundary conditions in the fully turbulent flow at $t = 200\,\mathrm{s}$ and averaged values over an interval of $\Delta t = 200\,\mathrm{s} - 400\,\mathrm{s}$ (s. chapter 3, section 3.5, 3.5.3.2, eq. (3.5.26) on page 84). The values are estimated in the first grid point y_{w1} at position $x = 0.375\,\mathrm{m}$, $z = 0.75\,\mathrm{m}$. At this position the observed fluid properties profiles are analysed in the following. It is for all values $y^+ < 1$ in y_{w1}. Further, in a LES, the size of one cell should be nowhere bigger than ten-times of the size of the Kolmogorov length which is fulfilled by both chosen resolutions.

BC	**3D**		**2D**	
	$t = 200\mathrm{s}$	$\Delta t = 200 - 400\mathrm{s}$	$t = 200\mathrm{s}$	$\Delta t = 200 - 400\mathrm{s}$
adiabatic	$y^+ = 0.112$	$\bar{y}^+ = 0.056$	$y^+ = 0.048$	$\bar{y}^+ = 0.532$
linear temperature	$y^+ = 0.332$	$\bar{y}^+ = 0.811$	$y^+ = 0.190$	$\bar{y}^+ = 0.232$
$T_{\mathrm{low}} = 296\,\mathrm{K}$,$T_{\mathrm{up}} = 310\,\mathrm{K}$	$y^+ = 0.490$	$\bar{y}^+ = 0.176$	$y^+ = 0.165$	$\bar{y}^+ = 0.172$
$T_{\mathrm{low/up}} = 303\,\mathrm{K}$	$y^+ = 0.319$	$\bar{y}^+ = 0.706$	$y^+ = 0.311$	$\bar{y}^+ = 0.222$

Table 5.1.: Non-dimensional distance y^+ estimated in the first cell midpoint y_{w1} in the fully turbulent flow at $t = 200\,\mathrm{s}$ and as averaged value over $\Delta t = 200\,\mathrm{s} - 400\,\mathrm{s}$. $\mathrm{Ra} = 1.58 \times 10^9$, different boundary conditions.

5.3. Temperature profile

5.3.1. Temperature distribution between the heated walls estimated along the horizontal axis

The flow movement in the container is initialised by the temperature difference between the vertical, heated walls.

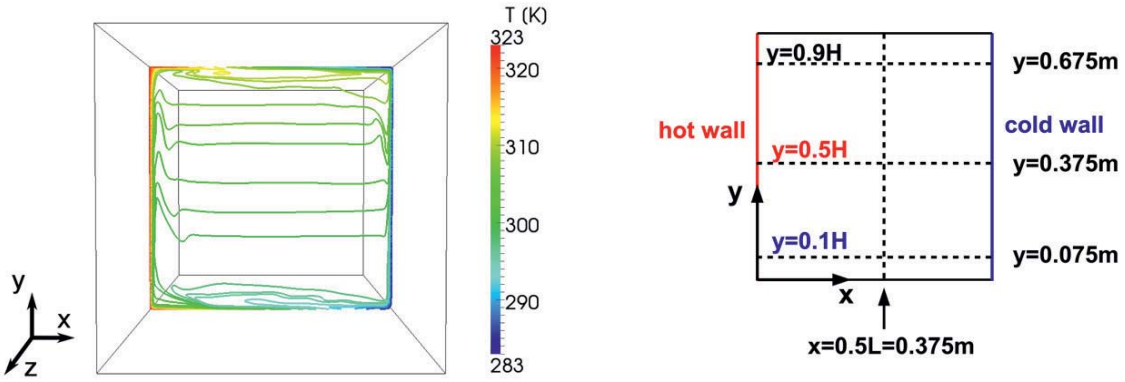

Figure 5.5.: Temperature profile between the heated walls. **Left:** Instantaneous temperature profile of a natural convection with vertical, heated walls and a linear bc at the lateral walls, $t = 400\,\mathrm{s}$ (as in [Zimmermann14a]). **Right:** Evaluation points of the horizontal temperature profile at the vertical xy-midplane at $z = 0.75\,\mathrm{m}$.

Hence, one main aspect of the numerical study lies on the temperature distribution between the heated walls. Note that some of the following presented contents are also discussed in extracts in [Zimmermann14a]. Figure 5.5 demonstrates a typical quasi steady-state temperature profile for a natural convection in a setup with vertical isothermally heated walls. The picture shows the numerical results after $t = 400\,\mathrm{s}$ in the simulated process for a linear temperature boundary condition.

Near to the vertical walls, the temperature can be described by a linear law. This is demonstrated in figure 5.6 on page 103 for the simulation data and the data of [Tian00a] at the xy-midplane at midheight at $y = 0.375\,\mathrm{m}$ ($y = 0.5\,\mathrm{H}$) and $z = 0.75\,\mathrm{m}$. It is clearly visible, that the simulation can be approximated by a linear function (black solid line), but that the gradients underrun the ones of the experiment. In [Tian00a], a 2-dimensional flow field at the xy-midplane is considered. Therefore, the temperature profile is measured only at the xy-midplane, at $x = 0.375\,\mathrm{m}$, $z = 0.75\,\mathrm{m}$ and different heights, $y_1 = 0.1\mathrm{H}$, $y_2 = 0.5\mathrm{H}$ and $y_3 = 0.9\mathrm{H}$ (s. figure 5.5, right picture). The temperature profile of the 3D and 2D simulations are plotted for all cases against the data of [Tian00a] in figures 5.7 and 5.8 on pages 104 - 105. The thermal boundary layer near the vertical, heated walls can clearly be seen in all results.

Steep temperature gradients appear close to the heated walls, before they reach their minimum at ca. 0.03 m afar from the hot wall, respectively at ca. 0.73 m for cold wall. At these points the bulk region of the flow begins. Before the bulk region is reached, the profiles make a low ascent at height $y_2 = 0.5\,\mathrm{H}$ and height $y_3 = 0.9\,\mathrm{H}$. The temperature in the bulk region is almost stationary and equals the averaged mean temperature between the hot and the cold wall. For the mean temperature it is $T_{\mathrm{mean}} = (T_{\mathrm{hot}} - T_{\mathrm{cold}})/2 + T_{\mathrm{cold}}$.

The variation of the thermal boundary layer thickness reported in [Tian00a] can clearly be seen in the numerical data. Additionally, a dependence of the boundary layer thickness on the boundary condition can be detected. The boundary layer increases in flow direction which is in the simulations, as well as in the experiment of [Tian00a], a clockwise direction. The clockwise direction was expected according to chapter 3, section 3.5, 3.5.3.2, page 83. The simulation profiles are not formed anti-symmetrically as in the experiment, but asymmetrical. According to [Gifford1991], the anti-symmetrical profile vanishes for a non-Boussinesq- approximation as it is considered in the numerical model.

At midheight, all simulations approximate the bulk temperature of the measured data. In vicinity of both horizontal walls the *adiabatic* results deviate significantly from the experimental data, especially at height $y_1 = 0.1\,\mathrm{H}$ and height $y_3 = 0.9\,\mathrm{H}$. These deviations are caused by the different boundary conditions of the simulation and experiment. Adiabatic horizontal walls entail no heat flux, thus lower temperatures exist near these walls. According to [Tian00a], the vertical thermal boundary layer of an experiment with conducting walls has to be thicker as the boundary layer of one with adiabatic walls.

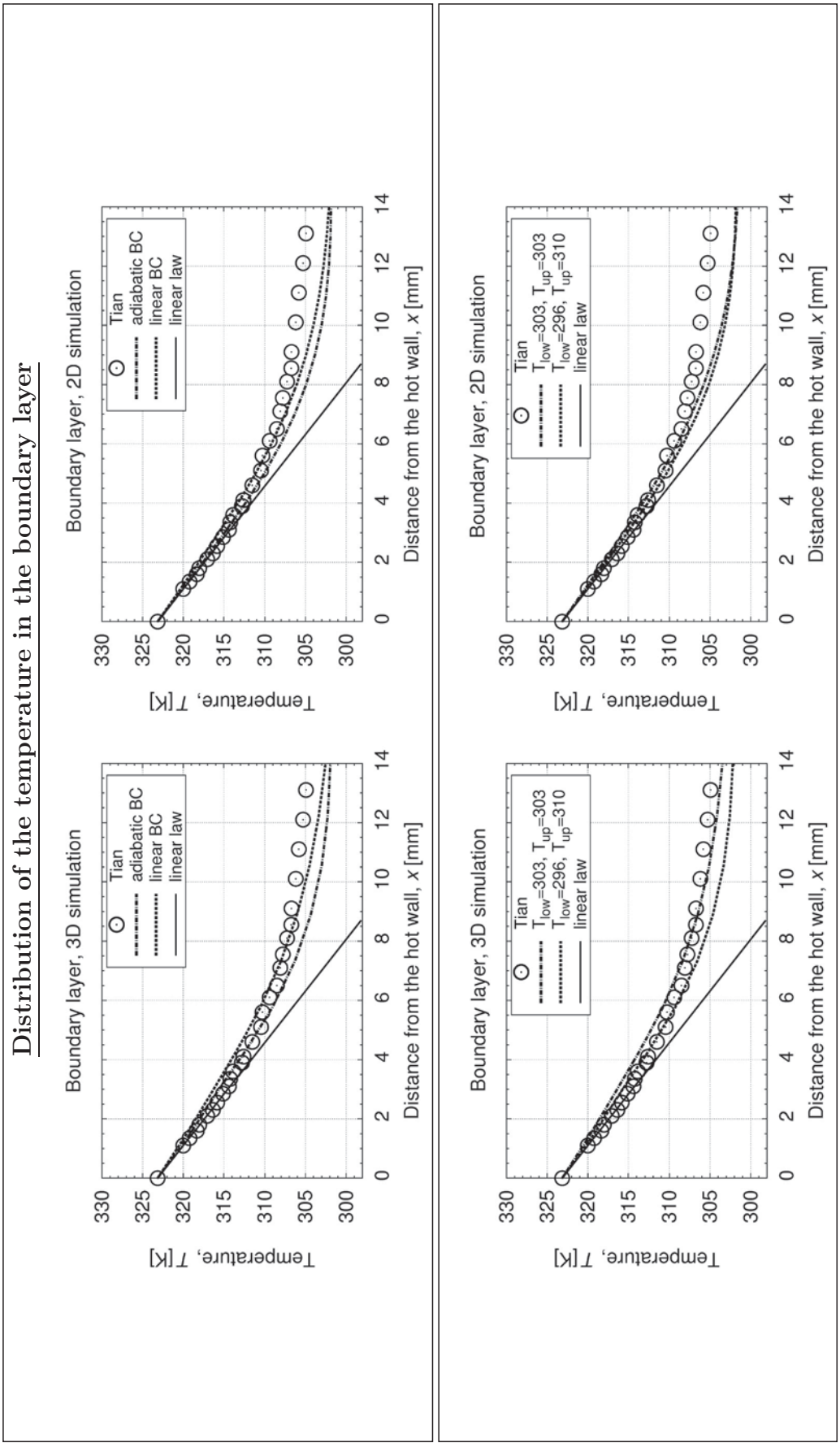

Figure 5.6.: Time-averaged temperature profile in the boundary layer near the hot wall estimated along the horizontal x-axis at midheight $y = 0.375\,\mathrm{m}$ ($y = 0.5\,\mathrm{H}$) (vertical xy-midplane). **Top box**: Adiabatic bc (black broken line $\cdot - \cdot$) and linear bc (black dashed line $- - -$). **Bottom box**: $T_{\mathrm{low}} = 296\,\mathrm{K}$, $T_{\mathrm{up}} = 310\,\mathrm{K}$ (black broken line $\cdot - \cdot$), $T_{\mathrm{low/up}} = 303\,\mathrm{K}$ (black dashed line $- - -$). **In each box**: 3D simulation (left) and 2D simulation (right). **In each picture:** ○: [Tian00a], $\mathrm{Ra} = 1.58 \times 10^9$. **-** solid black line: linear law.

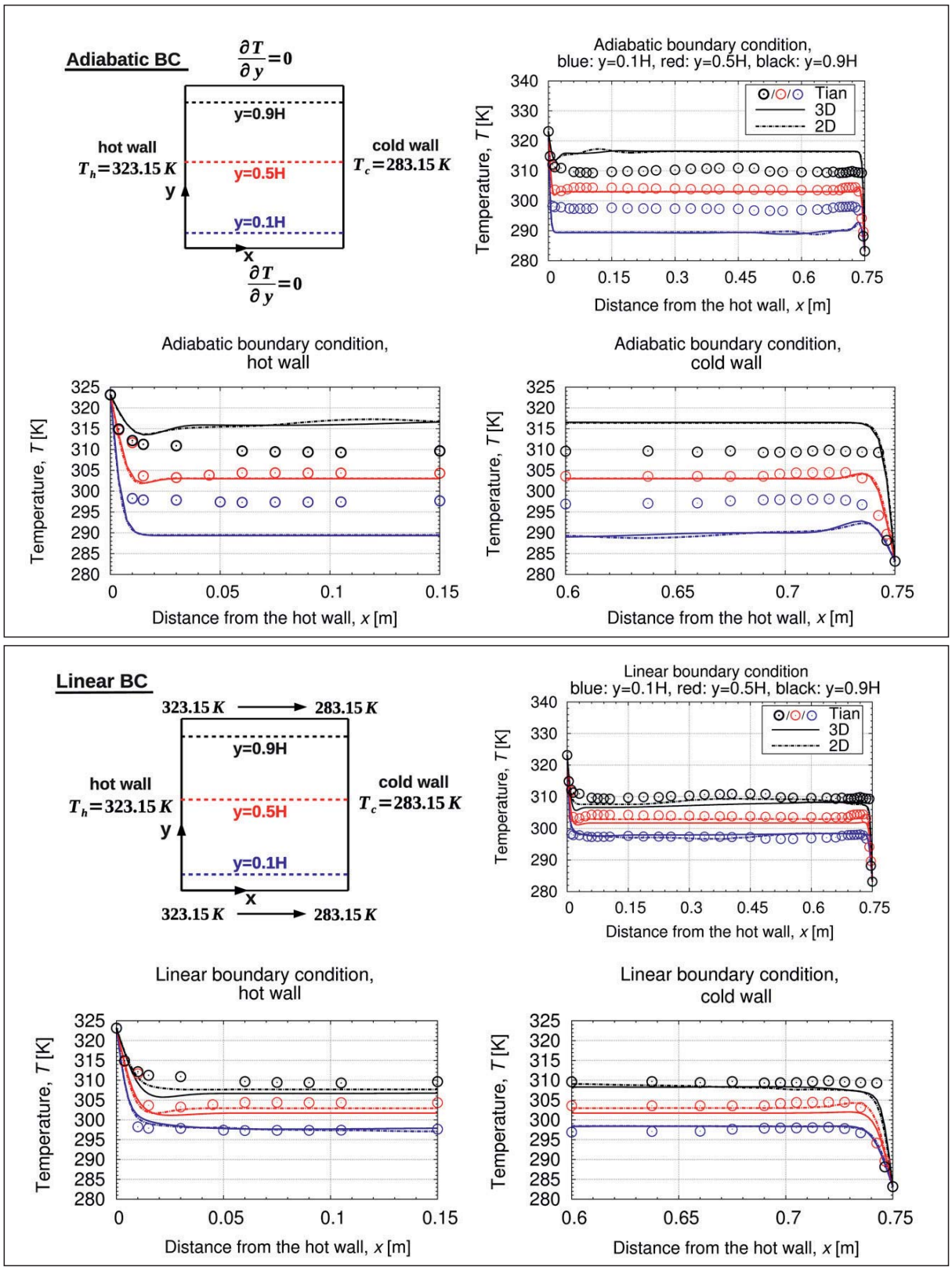

Figure 5.7.: Time-averaged temperature profile between the hot and cold wall, at the vertical xy-midplane, at $z = 0.75\,\mathrm{m}$, estimated along the horizontal x-axis and different heights. **Top box:** Adiabatic bc. **Bottom box:** Linear bc. **Top row in each box:** Overview. **Bottom row in each box:** Detailed plot of the hot/cold wall. **In all pictures:** $y_1 = 0.1\mathrm{H}$ (blue), $y_2 = 0.5\mathrm{H}$ (red) and $y_3 = 0.9\mathrm{H}$ (black), **-** solid line: 3D, **--** dashed line: 2D. **o**: study [Tian00a], $\mathrm{Ra} = 1.58 \times 10^9$ (as in [Zimmermann14a]).

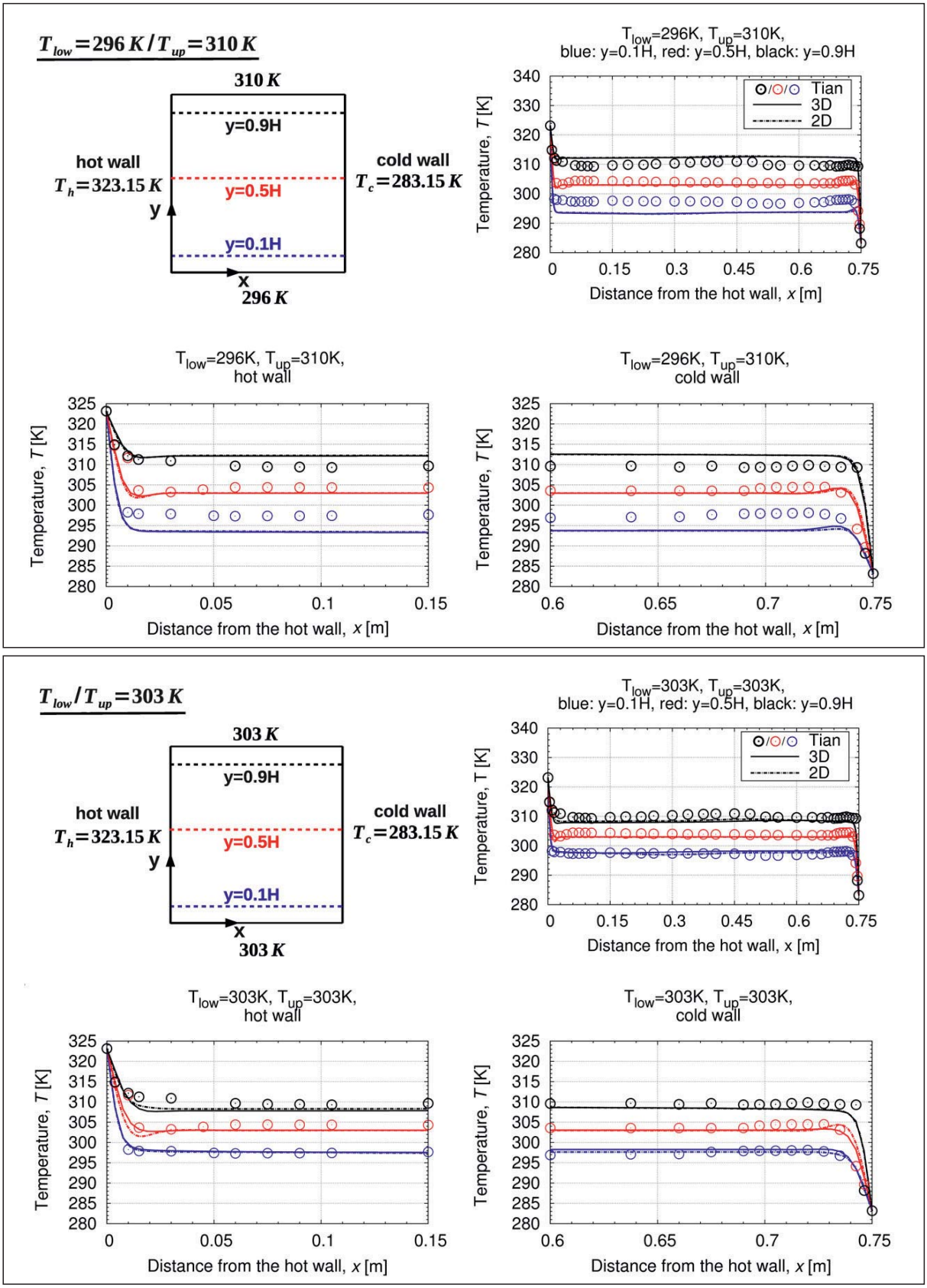

Figure 5.8.: Time-averaged temperature profile between the hot and cold wall, at the vertical xy-midplane, at $z = 0.75\,\mathrm{m}$, estimated along the horizontal x-axis and different heights. **Top box:** $T_{\mathrm{low}} = 296\,\mathrm{K}$, $T_{\mathrm{up}} = 310\,\mathrm{K}$. **Bottom box:** $T_{\mathrm{low/up}} = 303\,\mathrm{K}$. **Top row in each box:** Overview. **Bottom row in each box:** Detailed plot of the hot/cold wall. **In all pictures:** $y_1 = 0.1\mathrm{H}$ (blue), $y_2 = 0.5\mathrm{H}$ (red) and $y_3 = 0.9\mathrm{H}$ (black), **-** solid line: 3D, **- -** dashed line: 2D. ○: study [Tian00a], $\mathrm{Ra} = 1.58 \times 10^9$.

This conclusion could be seen in the *adiabatic* simulation results at both vertical walls. The only exception are the results at the hot wall at height $y_3 = 0.9\,\mathrm{H}$. This aspect could be a possible hint at shifted circulation zones and is further discussed in section 5.4.1. The 2D plot shows only slight deviations to the 3D one at the top hot and bottom cold corner. The results of $T_{\mathrm{low}} = 296\,\mathrm{K}$, $T_{\mathrm{up}} = 310\,\mathrm{K}$ are similar to the results of case $T_{\mathrm{low/up}} = 303\,\mathrm{K}$. Both simulations show higher values than in the experiment in vicinity to the upper wall, but lower ones in vicinity to the bottom wall. The results of the 2D simulations match almost exactly with the 3D simulations. Both simulation cases approximate well the experimental data, considering the different boundary conditions.

The case of $T_{\mathrm{low/up}} = 303\,\mathrm{K}$ reveals the best approximation to the experimental results. rmal boundary layer of this case is slightly bigger than in the experiment at the hot wall at height $y_1 = 0.1\,\mathrm{H}$. At the cold wall the boundary layer is slightly smaller. This behaviour is vice versa at height $y_3 = 0.9\,\mathrm{H}$ and both walls.

It is noteworthy, that the *linear boundary condition* case approximates the experiment only at height $y_1 = 0.1\,\mathrm{H}$ well. Even though the temperature of the bc at the top left corner is higher than in the experiment, the temperature profile at height $y_3 = 0.9\,\mathrm{H}$ lies beneath the experimental one. The thermal boundary layer is slightly thicker than in the experiment, especially at the cold wall at height $y_3 = 0.9\,\mathrm{H}$, respectively at the hot wall at height $y_1 = 0.1\,\mathrm{H}$. The results of the 2D simulation differ significantly from the 3D results, especially at both upper heights.

5.3.2. Temperature fluctuations between the heated walls estimated along the horizontal axis

The previous section 5.3.1 dealt with the time-averaged temperature values at the xy-midplane estimated along the horizontal x-axis. These profiles characterise the flow field in the container. An additional important focus lies now on the fluctuations of these temperature profiles which are essential for an accurate turbulence modelling (s. chapter 3 and [Fröhlich06]).

The fluctuations are given by the standard deviation σ_{rms}. Fluctuations related to a particular fluid property, e. g. temperature T, are denoted with the index *rms*, hence T_{rms}. For finitely many values x_i, the standard deviation is calculated by

$$\sigma_{\mathrm{rms}} = \left(\frac{1}{n} \sum_{i=1}^{n} (x_i - \bar{x})^2 \right)^{\frac{1}{2}}, \quad \text{where} \quad \bar{x} = \frac{1}{n} \sum_{i=1}^{n} x_i \,. \tag{5.3.1}$$

n stands for the size of the observed sample and $\bar{x}$ is the averaged mean value of the sum of the values x_i. Figures 5.9 - 5.10 on pages 108 - 109 present the fluctuation values of the

simulations plotted against the ones of the experimental data in [Tian00b]. The profiles are estimated at the xy-midplane, at $z = 0.75\,\mathrm{m}$, along the horizontal x-axis and three different heights, $y_1 = 0.1\mathrm{H}$, $y_2 = 0.5\mathrm{H}$, $y_3 = 0.9\mathrm{H}$. For a better demonstration of all results together in one plot, a constant is added to the particular results of each height. These constants are $y_1 : +0$, $y_2 : +4$ and $y_3 : +8$. Oscillations appear in all profiles mainly in the boundary layer near the heated walls.

The peak values are located in vicinity to the heated walls. The profiles indicate a clockwise flow direction, as it was seen before in the temperature profiles in section 5.3.1. The maximal peak values are located at the bottom hot and top cold corner. The temperature values, and consequently its standard deviation values, are almost stationary in the bulk region. There, the fluctuations of the simulations equal almost the fluctuations of the experiment in [Tian00b]. The experimental data shows a symmetrical profile only at midheight. At both other heights asymmetrical profiles can be seen. [Tian00b] explains these asymmetries by possible changes of fluid properties.

The fluctuations in case of the *adiabatic* simulation are lower than the experimental results at every height. Besides, significant asymmetries are visible at height $y_1 = 0.1\,\mathrm{H}$ and at height $y_3 = 0.9\,\mathrm{H}$ which are mirror-imaged to the ones of the experiment. The 2D and 3D simulations show the same deviations to each other as before in the temperature profiles (s. figure 5.7 on page 104). The results of the *linear* bc case and both fixed temperature bc cases are again very similar to each other.

Although these profiles differ clearly from the experiment in [Tian00b], they reveal a similar profile tendency, but with smaller peak values. The highest peak values are located at the top cold and bottom hot corner. Noteworthy are the high fluctuations of the 2D cases in the bulk region which imply flow movements in horizontal direction (s. section 5.4.1). These high deviations could possibly be caused by numerical effects of the chosen numerical methods or the chosen grid resolution. This aspect has to be further investigated in future studies to obtain a clearer reason.

The maximum fluctuation value is about 3 K in the experiment of [Tian00b]. For the *adiabatic* bc case the maximum value is about 2 K, for the *linear* bc case it is about 2 K, for the $T_{\mathrm{low}} = 296\,\mathrm{K}$, $T_{\mathrm{up}} = 310\,\mathrm{K}$ case about 1 K and for the $T_{\mathrm{low/up}} = 303\,\mathrm{K}$ case about 1 K. Concluding, all profiles of the temperature fluctuations reflect the temperature profiles from section 5.3.1.

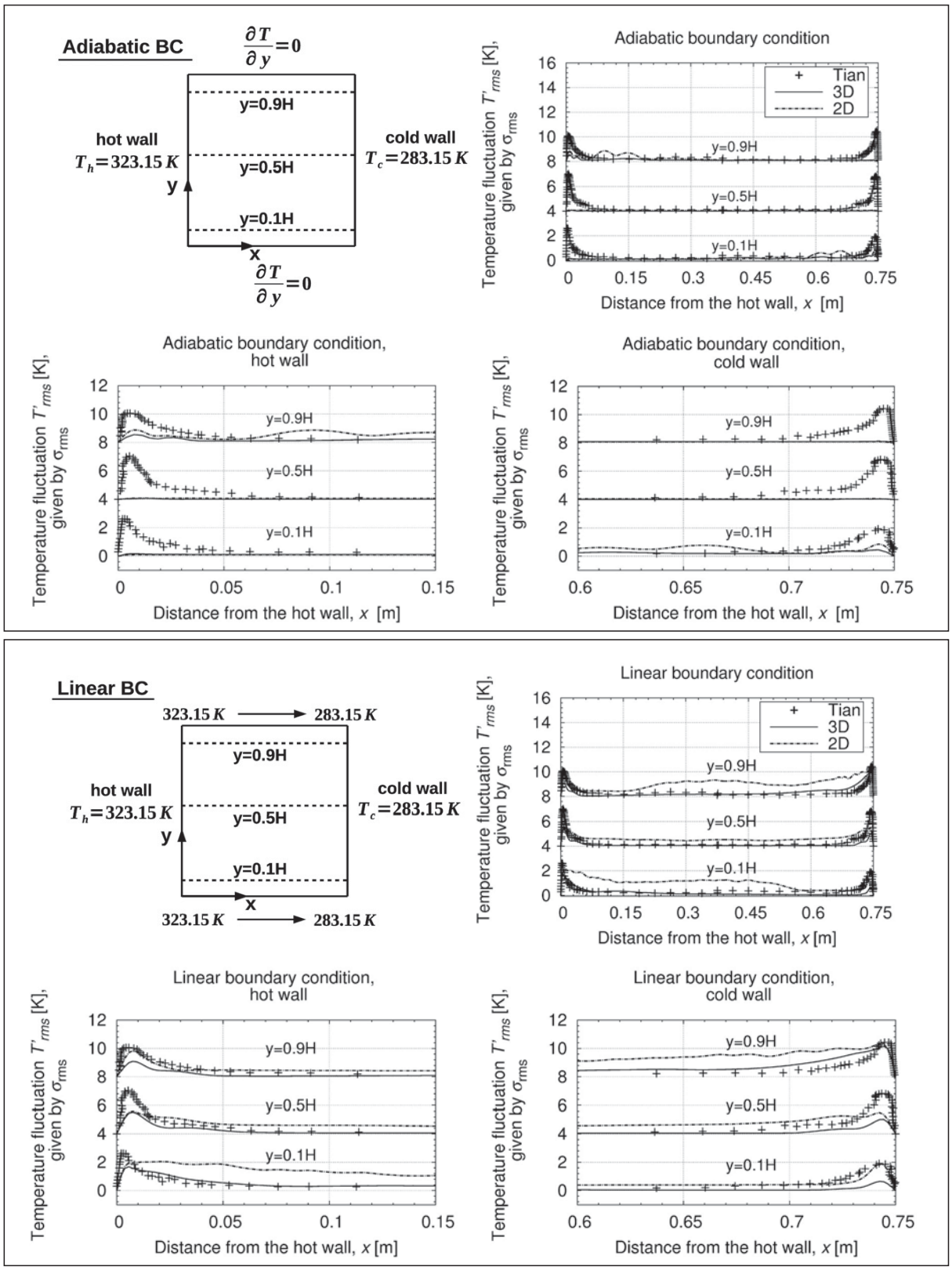

Figure 5.9.: Time-averaged profile of the temperature fluctuations between the hot and cold wall, at the vertical xy-midplane, at $z = 0.75\,\mathrm{m}$, estimated along the horizontal x-axis and different heights, given by the standard deviation σ_{rms}. **Top box:** Adiabatic bc. **Bottom box:** Linear bc. **Top row in each box:** Overview. **Bottom row in each box:** Detailed plot of the hot/cold wall. **In all pictures: -** solid line: 3D, **--** dashed line: 2D. **+**: study [Tian00a], $\mathrm{Ra} = 1.58 \times 10^9$.

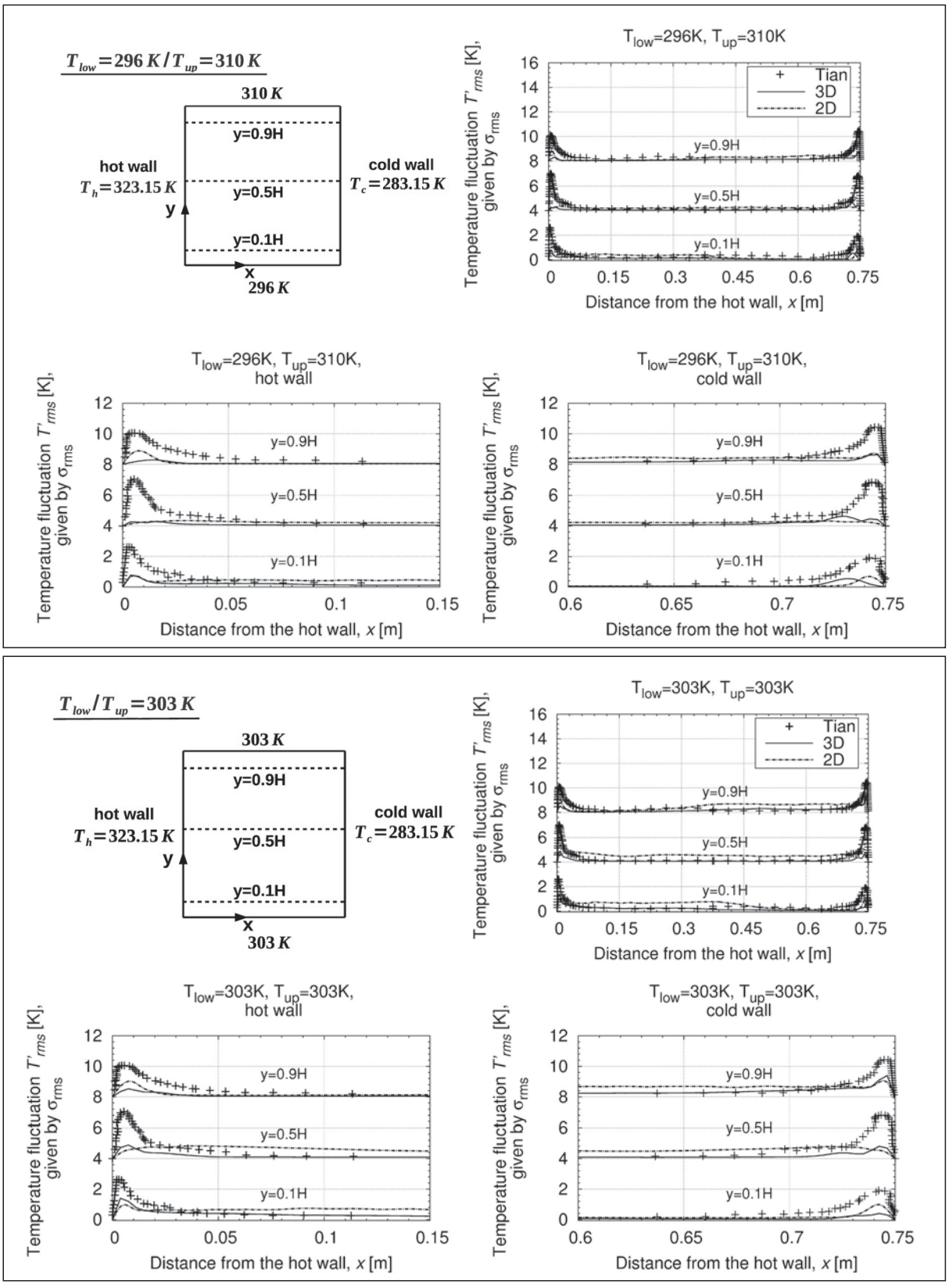

Figure 5.10.: Time-averaged profile of the temperature fluctuations between the hot and cold wall, at the vertical xy-midplane, at $z = 0.75\,\mathrm{m}$, estimated along the horizontal x-axis and different heights, given by the standard deviation σ_{rms}. **Top box:** $T_{\mathrm{low}} = 296\,\mathrm{K}$, $T_{\mathrm{up}} = 310\,\mathrm{K}$. **Bottom box:** $T_{\mathrm{low/up}} = 303\,\mathrm{K}$. **Top row in each box:** Overview. **Bottom row in each box:** Detailed plot of the hot/cold wall. **In all pictures: -** solid line: 3D, **- -** dashed line: 2D. **+**: study [Tian00a], $\mathrm{Ra} = 1.58 \times 10^9$.

5.3.3. Profile of the non-dimensional temperature profile between the top and bottom wall estimated along the vertical axis

Afore, the temperature profile was estimated between the isothermally heated walls at the xy-midplane in horizontal direction. A further important indicator for the flow dynamic is the temperature profile between the bottom and top wall at the xy-midplane along the vertical y-axis (s. figure 5.5 on page 101). This profile is analysed in this section on the basis of the non-dimensional temperature T^* which is defined in [Tian00a] by

$$T^* = \frac{T - T_{\text{cold}}}{T_{\text{hot}} - T_{\text{cold}}}. \tag{5.3.2}$$

The profile is plotted at the xy-midplane at $x = 0.375\,\text{m}$ ($x = 0.5\,\text{L}$) along the vertical y-axis. The results are shown in figure 5.11 on page 111 for the 2D and 3D simulations. Besides the study of [Tian00a], further studies are additionally compared to the simulation results.

In [Mergui1993] a geometry with aspect ratios of $\Gamma_x = 0.923, \Gamma_z = 0.3$ and a Rayleigh number of $\text{Ra} = 1.7 \times 10^9$ is investigated experimentally. In [Ziai1983] a convection cell with aspect ratios of $\text{Ar}_x = 5, \text{Ar}_z = 2$ and a Rayleigh number of $\text{Ra} = 5 \times 10^8$ is analysed experimentally. [Ziai1983] and [Mergui1993] use both adiabatic boundary conditions at the horizontal walls. [Lankhorst1991] performs an experimental study of a cell with conducting walls and aspect ratios of $\text{Ar}_x = 1, \text{Ar}_z = 0.2$. The investigated Rayleigh numbers is $\text{Ra} = 3.9 \times 10^8$.

The Prandtl number stays in all studies at $\text{Pr} = 0.71$. [Tian00a] concludes an agreement to the experimental results in [Mergui1993]. According to [Tian00a], the differences between [Tian00a] and [Ziai1983] result from a possible heat loss through the passive vertical walls in [Ziai1983]. As it can be seen in the plot, the results of [Lankhorst1991] lie close to the results of [Tian00a] and [Mergui1993], despite the adiabatic boundary condition.

The *adiabatic* 3D simulation deviates from the results of the other studies, as it was expected due to the different boundary condition. In the container middle, the results of [Tian00a] and [Mergui1993] are approximated by the simulation data. The *adiabatic* 2D and 3D simulation correspond at the bottom wall to the experimental study of [Ziai1983] due to the same boundary condition, but the simulations show deviations at the top wall. The deviations to [Ziai1983] in the container middle could possibly be caused by the different realised Rayleigh numbers and different aspect ratios. Near the bottom and top wall, the *linear* bc case and $T_{\text{low}} = 296\,\text{K}, T_{\text{up}} = 310\,\text{K}$ approximate well the results of [Tian00a] and and the adiabatic ones of [Mergui1993], which is remarkable. The $T_{\text{low/up}} = 303\,\text{K}$ case approximates near the bottom wall the results of [Tian00a] and [Mergui1993] as well as of [Lankhorst1991], but at the top wall also the adiabatic results of [Ziai1983].

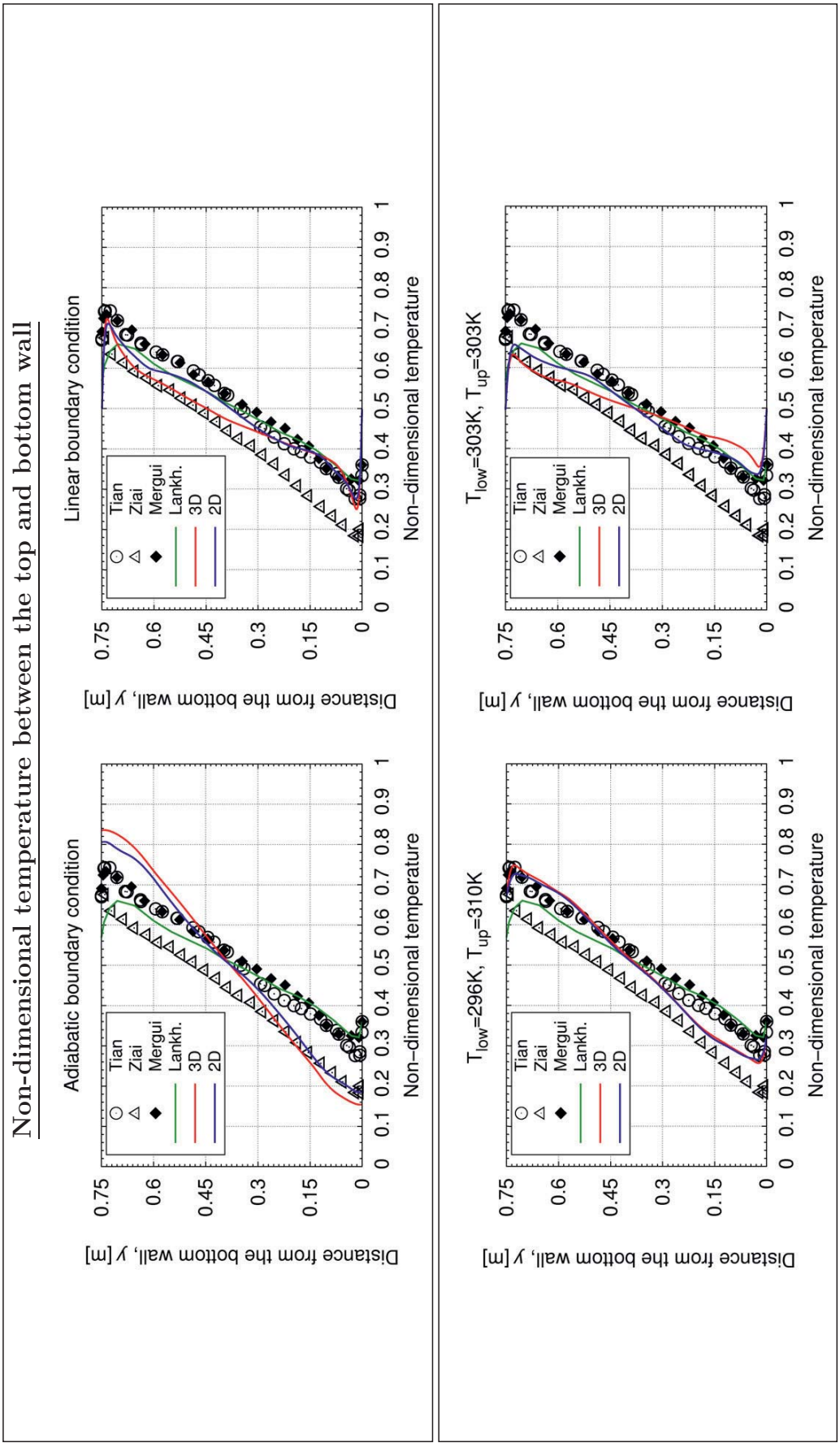

Figure 5.11.: Non-dimensional temperature profile between the top and bottom wall, estimated along the vertical y-axis, at the xy-midplane, at $x = 0.375\,\mathrm{m}$, $z = 0.75\,\mathrm{m}$. **Top box:** Adiabatic bc (left), linear bc (right) **Bottom box:** $T_{\mathrm{low}} = 296\,\mathrm{K}$, $T_{\mathrm{up}} = 310\,\mathrm{K}$ (left), $T_{\mathrm{low/up}} = 303\,\mathrm{K}$ (right). **In all pictures:** – red solid line: 3D, - blue solid line: 2D. **o**: study [Tian00a], $\mathrm{Ra} = 1.58 \times 10^9$, △: study [Ziai1983], $\mathrm{Ra} = 5 \times 10^8$, $Ar_x = 5$, $Ar_z = 2$, ◆: study [Merguí1993], $\mathrm{Ra} = 1.7 \times 10^9$, $Ar_x = 0.923$, $Ar_z = 0.3$, - green solid line: study [Lankhorst1991], $\mathrm{Ra} = 3.9 \times 10^8$, $Ar_x = 1$, $Ar_y = 0.2$.

Deviations between the 2D and 3D simulations with a fixed temperature bc arise especially in the upper half of the container, as it was seen before in the temperature profile in figure 5.7 on page 104.

5.3.4. Nusselt number profile

Besides temperature and velocity distribution, a further aspect of great interest is the heat flux distribution in the container, which is determined by the Nusselt number. Note that some of the following presented contents are also discussed in extracts in [Zimmermann14a]. According to [Tian00a], the local Nusselt number is described by

$$\mathrm{Nu} = -\frac{L}{T_{\mathrm{hot}} - T_{\mathrm{cold}}} \left.\frac{\partial T}{\partial x}\right|_{\tilde{\mathrm{w}}} , \tag{5.3.3}$$

where L is the container length between the heated walls, T_{cold} the temperature of the cold wall, T_{hot} the temperature of the hot wall and $\frac{\partial T}{\partial x}\big|_{\tilde{\mathrm{w}}}$ the temperature gradient directly at the heated walls $\tilde{\mathrm{w}}$. With the definition in equation (5.3.3), the heat flux is positive defined in direction from the hot wall into the container and from there to the cold wall. The heat flux from the bottom wall in direction to the container middle and along the top wall is also defined positive.

5.3.4.1. Nusselt number profile estimated along the heated walls, vertical axis

The Nusselt number is evaluated along the isothermally heated walls and plotted in figures 5.12 - 5.15 on pages 114 - 115 and 116 - 117. Additionally results of similar experimental and numerical studies are also presented in the plots. Complementary to figures 5.12 - 5.15, table 5.2 on page 113 gives an overview of the time-averaged local Nusselt number values estimated at the hot/cold wall at midheight $y = 0.375\,\mathrm{m}$.

The presented percentage is related to the difference between the results of [Tian00a] and the results of the simulations in this thesis. Additionally to the local estimated values, also area-averaged Nusselt number values are presented which are estimated over the complete hot/cold wall for all studies. Besides the data of [Tian00a], the experimental study of [Mergui1993] for a Rayleigh number of $\mathrm{Ra} = 1.7 \times 10^9$ and aspect ratios of $\mathrm{Ar}_x = 0.923$, $\mathrm{Az}_x = 0.3$ is plotted in figures 5.12 - 5.13.

Moreover, a numerical analysis of a similar case by [Beghein93a] is discussed in the figures 5.14 - 5.15. [Beghein93a], [Beghein93b] test in their studies a perfectly conducting boundary condition at the lateral walls as well as an adiabatic condition, as in the study of [Mergui1993], for an aspect ratio of $\mathrm{Ar}_x = 1$ and Rayleigh numbers of $\mathrm{Ra} = 1.34 \times 10^9$ and $\mathrm{Ra} = 1 \times 10^{10}$. The case of [Beghein93a] with $\mathrm{Ra} = 1.34 \times 10^9$ is now discussed concerning the Nusselt number distribution. According to [Tian00a], in the conducting

case of [Beghein93a], a zero Nusselt number value becomes visible in the hot bottom and top cold corner which could not be approved by the data in [Tian00a] or in any of the performed simulations. The adiabatic values of [Beghein93a] exceed in the beginning of the heated walls also the values of the adiabatic investigation in [Mergui1993]. The Nusselt number profiles in the performed simulations are mirror-imaged to the above stated main circulation cell in the container. In the hot bottom corner, the Nusselt number reveals a quite low value caused by the influence of the cooler horizontal boundary layer at the bottom wall. It reaches its peak value near the bottom wall, before it descends along the hot wall until it arrives at its minimum in the top hot corner where it is almost zero. For the cold wall this process is inverted. The form of the Nusselt number profile resembles the one of the temperature gradients where the maximum values decrease also in flow direction. The results of the *adiabatic* bc case and the *linear* bc case are plotted in figure 5.12 each for the 3D (left picture) and 2D (right picture) simulation type.

Case	**local Nu** (at midheight)		**averaged Nu**	
	hot wall	cold wall	hot wall	cold wall
[Tian00a]	57.1	59.5	64.0	65.3
[Mergui1993]	49.6	43.8	N/A	N/A
[Beghein93a]	53.28	54.05	N/A	N/A
adiabatic bc, 3D	57.1	57.7	67.05	67.18
	-	(-3.03 %)	(4.76 %)	(2.88 %)
adiabatic bc, 2D	52.71	57.80	62.49	62.61
	(-7.69 %)	(-2.86%)	(-2.36%)	(-4.12%)
linear bc, 3D	46.8	47.7	51.47	54.15
	(-18.04%)	(-19.83%)	(-19.58%)	(-17.08%)
linear bc, 2D	48.50	50.84	51.28	50.13
	(-15.06%)	(-14.55%)	(-19.88%)	(-23.23%)
$T_{\text{low}} = 296\,\text{K}$, $T_{\text{up}} = 310\,\text{K}$, 3D	54.30	58.62	62.79	63.38
	(-4.09%)	(-1.48%)	(-1.89%)	(-2.94%)
$T_{\text{low}} = 296\,\text{K}$, $T_{\text{up}} = 310\,\text{K}$, 2D	51.71	56.39	59.28	59.77
	(-9.44%)	(-5.23%)	(-7.38%)	(-8.47 %)
$T_{\text{low/up}} = 303\,\text{K}$, 3D	47.90	50.27	56.15	57.64
	(-15.51%)	(-16.11%)	(-12.26%)	(-11.73%)
$T_{\text{low/up}} = 303\,\text{K}$, 2D	52.71	57.80	54.82	54.10
	(-7.69%)	(-2.86%)	(-14.34%)	(-17.15%)

Table 5.2.: Time-averaged local Nusselt number values estimated at the hot/cold wall at $y = 0.375\,\text{m}$ (midheight) and area-averaged Nusselt number values estimated over the complete hot/cold wall. Simulation data compared to data of [Tian00a], [Mergui1993] and [Beghein93a].

It is noteworthy that the *adiabatic* 3D simulation matches at midheight of the hot wall exactly with the values of [Tian00a] (s. in addition table 5.2). The cold wall value at this position is slightly lower than in the experiment.

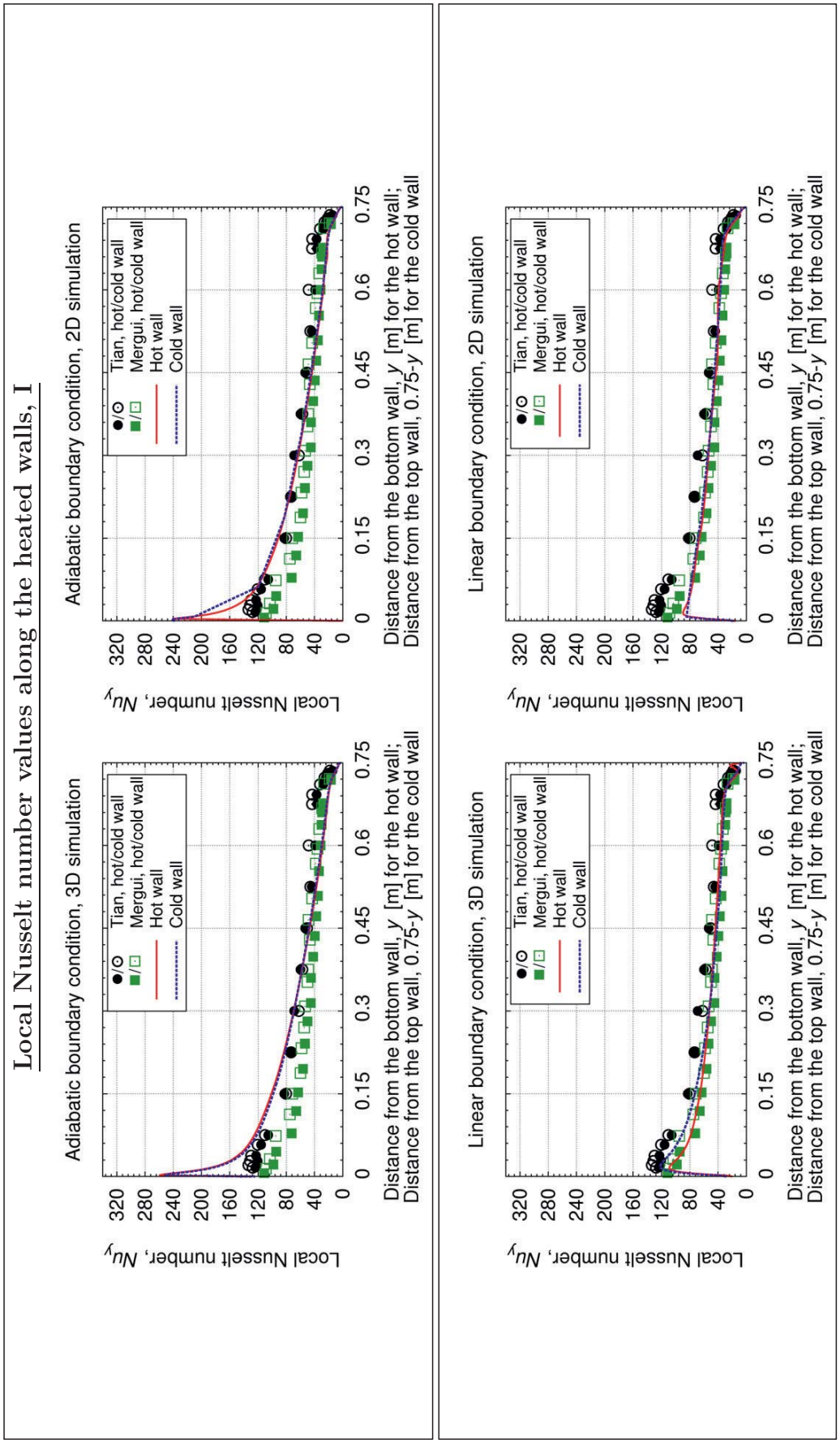

Figure 5.12.: Time-averaged profile of the local Nusselt number estimated along the heated walls, vertical y-axis. **Top box:** Adiabatic bc. **Bottom box:** Linear bc. **In each box: Left:** 3D simulation, **Right:** 2D simulation. **In each picture:** - red solid line: hot wall, - - - blue dashed line: cold wall. Study [Tian00a]: •: hot wall, ○: cold wall, $\mathrm{Ra} = 1.58 \times 10^9$. Study [Mergui1993]: ■: hot wall, □: cold wall, $\mathrm{Ra} = 1.7 \times 10^9$ (as in [Zimmermann14a]).

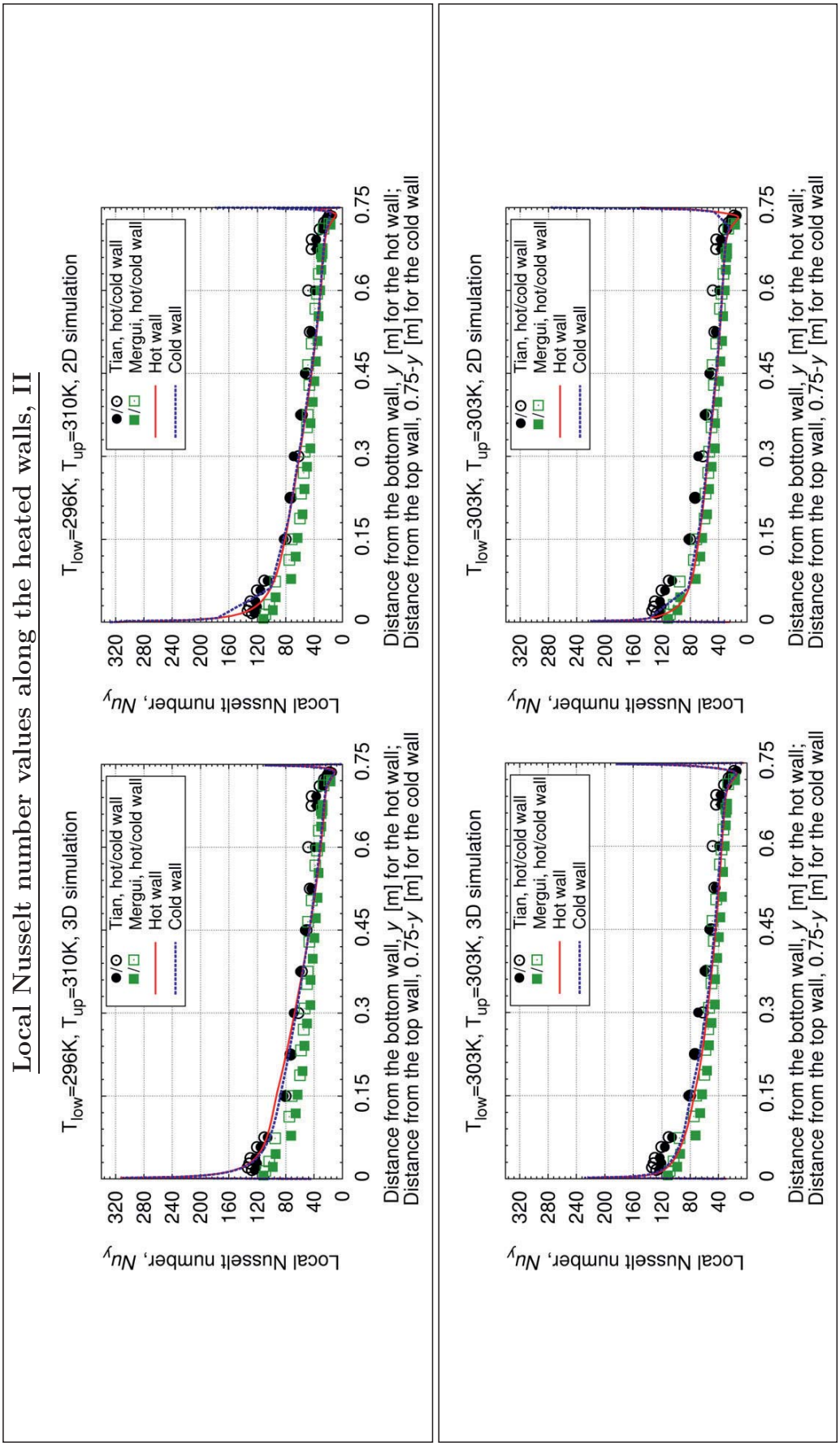

Figure 5.13.: Time-averaged profile of the local Nusselt number estimated along the heated walls, vertical y-axis. **Top box:** $T_{\mathrm{low}} = 296\,\mathrm{K}$, $T_{\mathrm{up}} = 310\,\mathrm{K}$. **Bottom box:** $T_{\mathrm{low/up}} = 303\,\mathrm{K}$. **In each box: Left:** 3D simulation, **Right:** 2D simulation. **In each picture:** - red solid line: hot wall, - - - blue dashed line: cold wall. Study [Tian00a]: •: hot wall, ○: cold wall, $\mathrm{Ra} = 1.58 \times 10^9$. Study [Mergui1993]: ■: hot wall, □ cold wall, $\mathrm{Ra} = 1.7 \times 10^9$.

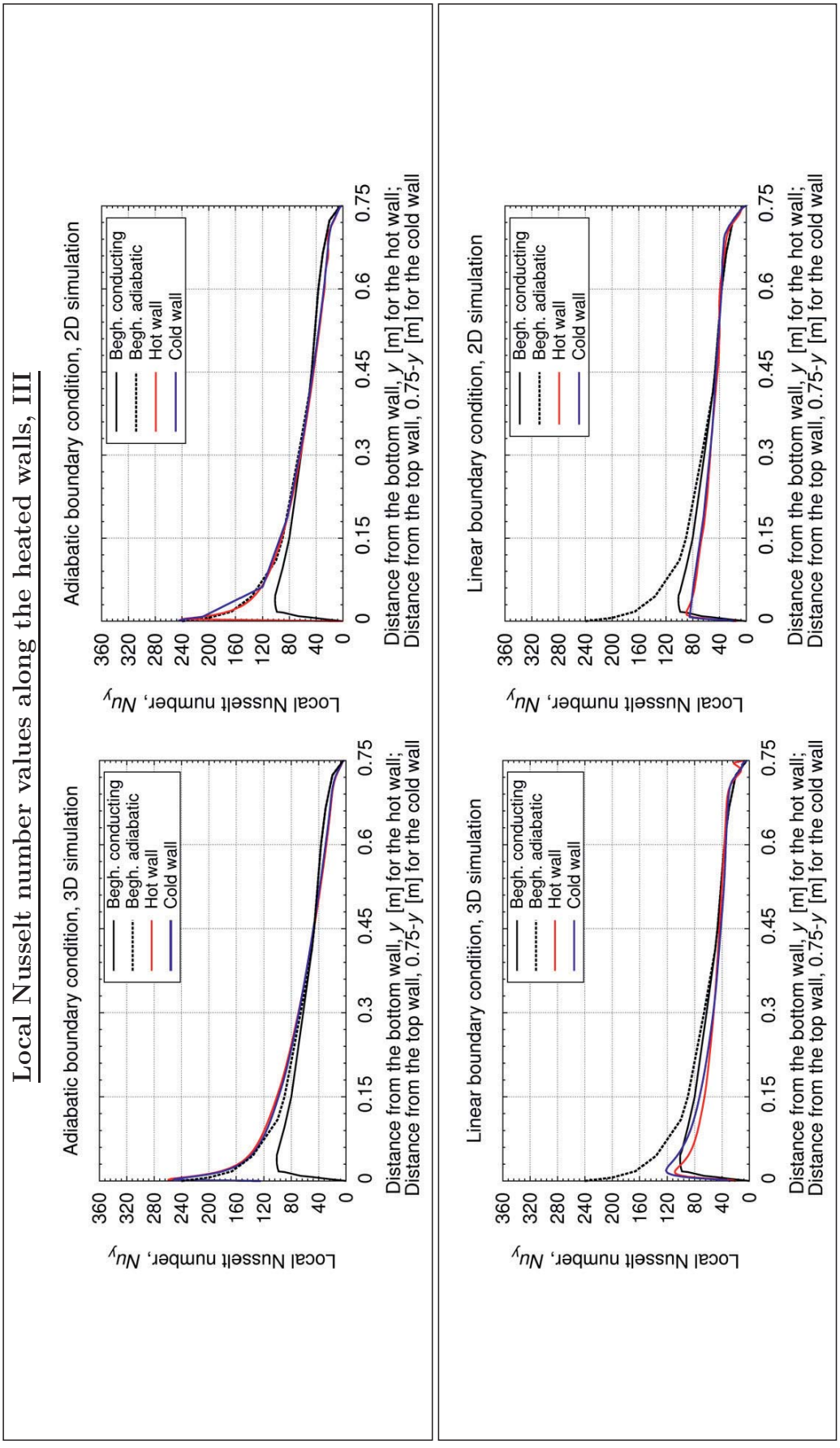

Figure 5.14.: Time-averaged profile of the local Nusselt number estimated along the heated walls, vertical y-axis. **Top box:** Adiabatic bc. **Bottom box:** Linear bc. **In each box: Left:** 3D simulation, **Right:** 2D simulation. **In each picture:** - red solid line: hot wall, - blue solid line: cold wall. Study [Beghein93a]: - black solid line: conducting bc, $\mathrm{Ra} = 1.34 \times 10^9$, - - black dashed line: adiabatic bc, $\mathrm{Ra} = 1.34 \times 10^9$.

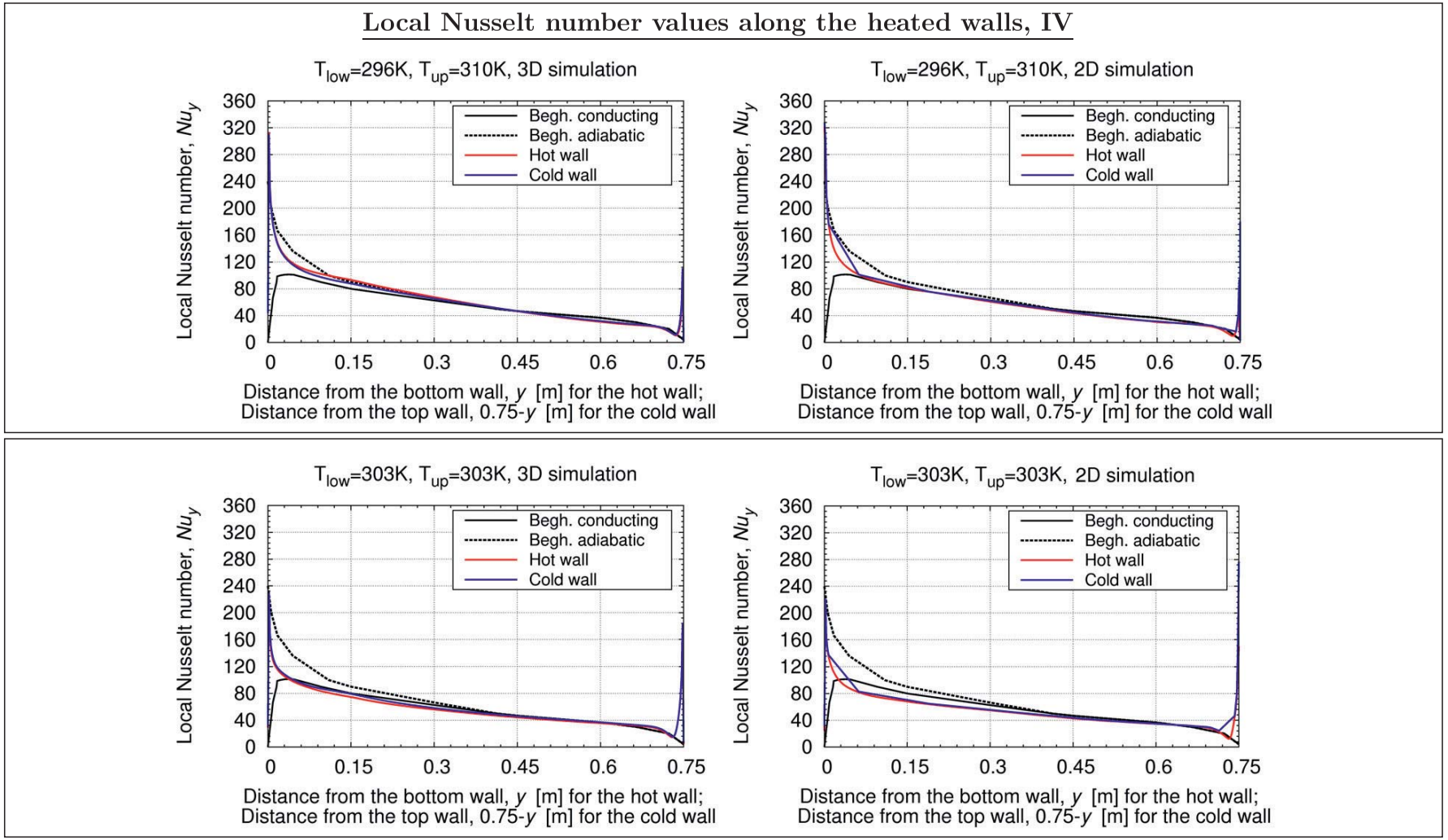

Figure 5.15.: Time-averaged profile of the local Nusselt number estimated along the heated walls, vertical y-axis. **Top box:** $T_{\text{low}} = 296\,\text{K}$, $T_{\text{up}} = 310\,\text{K}$. **Bottom box:** $T_{\text{low/up}} = 303\,\text{K}$. **In each box**: **Left:** 3D simulation, **Right:** 2D simulation. **In each picture:** - red solid line: hot wall, - blue solid line: cold wall. Study [Beghein93a]: - black solid line: conducting bc, $\text{Ra} = 1.34 \times 10^9$, - - black dashed line: adiabatic bc, $\text{Ra} = 1.34 \times 10^9$.

The time-averaged local Nusselt number values and also the area-averaged values of the *adiabatic* bc case deviate at most about 5% from the experiment, which can be neglected. From midheight on, the values underrun the experimental results due to lower temperature gradients (s. figure 5.7 on page 104). The *adiabatic* bc case does not approximate the conducting simulation of [Beghein93a], as it was expected. But the 2D and 3D simulation approximate the adiabatic data of [Beghein93a]. The visible differences are effected by higher realised Rayleigh numbers in [Beghein93a]. The 2D *adiabatic* simulation displays an equal tendency as the 3D case and shows only differences to the 3D simulation in vicinity to the heated walls.

The results of both simulation types of the *linear* bc case reveal an analogue profile to the one in [Tian00a], as it was expected due to the similar boundary condition. The 3D case presents higher results than the 2D case, which is caused by steeper temperature gradients. The time-averaged local Nusselt number values deviate at midheight significantly of about at most 20% from the results of the experimental study in [Tian00a], the area-averaged values even about 24%. This might possibly be caused by lower temperature gradients in the simulation. The numerical data approximate well the experimental study of [Mergui1993]. In case of both other fixed temperature boundary conditions, high values can be seen in the top and bottom cold corner (see figures 5.14 - 5.15). On the contrary to both other cases, the Nusselt number values increase this time significantly in the corner regions due to the fixed boundary condition at the horizontal walls. The heat flux from these walls interacts in this region with the heat flux from the vertical, heated walls.

The 3D and 2D simulation case of $T_{\mathrm{low}} = 310\,\mathrm{K}$ and of $T_{\mathrm{up}} = 296\,\mathrm{K}$ approximate the data of [Tian00a] along the heated walls, but reveal lower values. At the bottom hot corner, respectively top cold corner, the peak values of the $T_{\mathrm{low}} = 303\,\mathrm{K}$, $T_{\mathrm{up}} = 303\,\mathrm{K}$ case are lower than the ones of the $T_{\mathrm{low}} = 296\,\mathrm{K}$, $T_{\mathrm{up}} = 310\,\mathrm{K}$ case, due to lower temperature gradients. The simulations of $T_{\mathrm{low}} = 296\,\mathrm{K}$, $T_{\mathrm{up}} = 310\,\mathrm{K}$ differ about at most 10% from the experiment in [Tian00a]. The simulations of $T_{\mathrm{low/up}} = 303\,\mathrm{K}$ differ about at most 17% from the experiment. In comparison to the results of [Beghein93a] all results of the fixed temperature bc cases show significantly differences at the top and bottom wall due to the different boundary conditions. In the bulk region, the simulations approximate the results of [Beghein93a] for the conducting as well as for the *adiabatic* bc case.

5.3.4.2. Nusselt number profile estimated along the top and bottom wall, horizontal axis

Besides the Nusselt number profile estimated along the heated walls in figure 5.12 - 5.15 on pages 114 - 117 the profile along the top and bottom wall is discussed in this section on the basis of figures 5.16 and 5.17 on pages 119 - 120. The results are compared only to the study of [Tian00a].

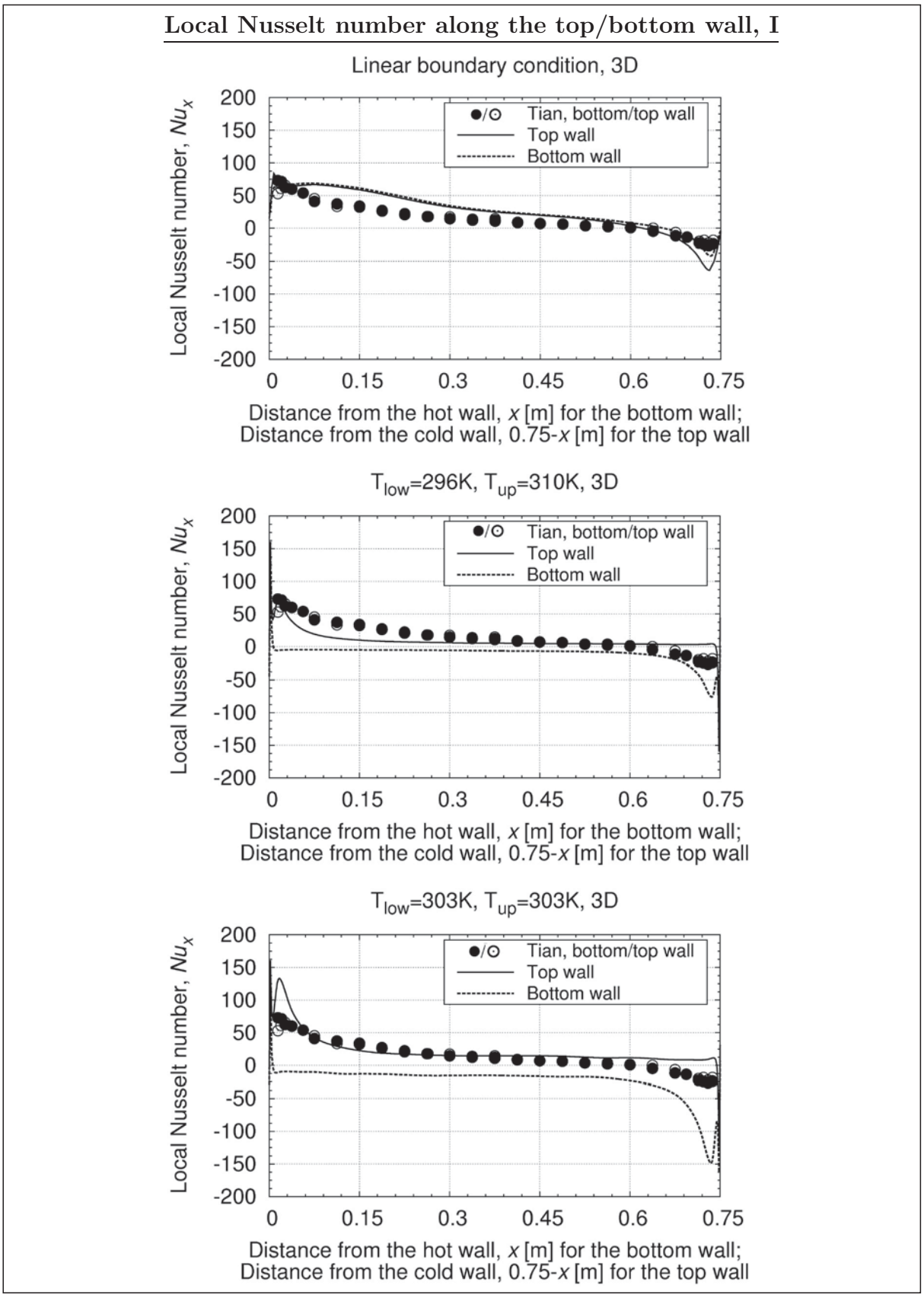

Figure 5.16.: Time-averaged profile of the local Nusselt number estimated along the top and bottom wall, horizontal x-axis, 3D simulation. **Top:** Linear bc. **Middle:** $T_{\text{low}} = 296\,\text{K}$, $T_{\text{up}} = 310\,\text{K}$. **Bottom:** $T_{\text{low/up}} = 303\,\text{K}$. **In all pictures: -** black solid line: top wall. **--** black dashed line: bottom wall. Study [Tian00a]: •: bottom wall, ○: top wall, $\text{Ra} = 1.58 \times 10^9$.

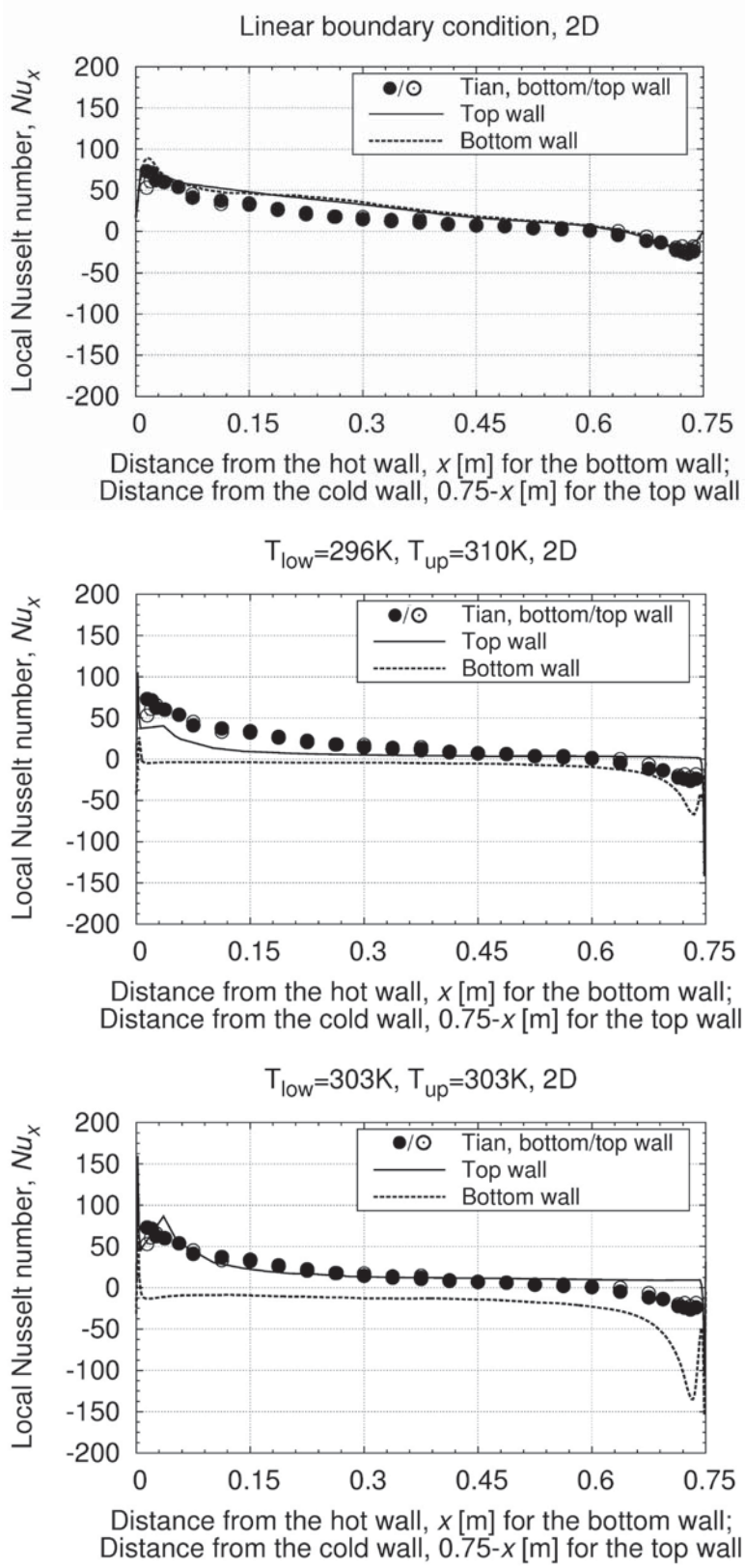

Figure 5.17.: Time-averaged profile of the local Nusselt number estimated along the top and bottom wall, horizontal x-axis, 2D simulation. **Top:** Linear bc. **Middle:** $T_{\mathrm{low}} = 296\,\mathrm{K}$, $T_{\mathrm{up}} = 310\,\mathrm{K}$. **Bottom:** $T_{\mathrm{low/up}} = 303\,\mathrm{K}$. **In all pictures: -** black solid line: top wall. **- -** black dashed line: bottom wall. Study [Tian00a]: •: bottom wall, ○: top wall, $\mathrm{Ra} = 1.58 \times 10^9$.

Because adiabatic walls entail no wall heat flux, no results are presented this time for the *adiabatic* bc case. Both *linear* bc simulations converge to the profile structure of the experiment. In the corner regions, higher values than in [Tian00a] are obtained in consequence of a higher temperature condition at these locations. The values along the horizontal walls are still higher than in the experiment, but they descend due to the also decreasing temperature condition at the top and bottom wall. In the near of the faced vertical hot, respectively vertical cold, wall, the values converge again to the experimental data. Significant variances between the 2D and 3D case arise only in the corner regions.

According to [Tian00a], two further recirculation zones are indicated by the change of the heat flux direction in the corner regions of the cold wall. These zones are characterised by the observed negative Nusselt number values (s. in addition figure 5.20). In the experiment, one recirculation region begins at about $x = 0.6\,\mathrm{m}$ in distance from the hot wall, and one at about $x = 0.15\,\mathrm{m}$ in distance from the cold wall. In the simulations, these regions are slightly shifted closer to the cold wall, as it was seen before in section 5.4.1.

In case of the *linear* bc, the first region begins in the 2D and 3D simulation at about $x = 0.65\,\mathrm{m}$ in distance from the hot wall, the second at about $x = 0.1\,\mathrm{m}$ in distance from the cold wall. Both other fixed temperature bc cases reveal similar results to each other. The values are similar to the data of the *linear* bc case, but the 3D and 2D simulations show in both cases high peak values close to the hot, respectively cold wall. At this positions, the heat fluxes of the vertical wall interacts with the heat flux of the horizontal wall.

The Nusselt number values are almost negative along the whole bottom wall. Thus, the heat flux direction points this time from the container to the bottom wall. Therefore, the air layer, which is located near the bottom wall, has to be warmer than the wall itself. Along the top wall, the same effect can be seen. But this time, the Nusselt number is positive almost along the whole top wall. This aspect is more distinctive in case of the $T_{\mathrm{low/up}} = 303\,\mathrm{K}$ condition than in case of the $T_{\mathrm{low}} = 310\,\mathrm{K}, T_{\mathrm{up}} = 296\,\mathrm{K}$ condition. The recirculation zones are this time significantly shifted to the ones in the experimental results. Both cases show one recirculation zone in the top cold corner and one near the bottom hot corner. The recirculation zones lie close to the heated walls. In both cases the first region begins at about $x = 0.003\,\mathrm{m}$ in distance from the hot wall, the second one at about $x = 0.74\,\mathrm{m}$ in distance from the cold wall.

Concluding, the *linear* bc case shows indeed the highest local differences to the data of [Tian00a] in table 5.2. But it features also the most similar profile form to the one of the experiment. The other simulation cases show a good approximation to [Tian00a] along the cold and hot wall. But the values in the bottom hot and top cold corner exceed significantly the experimental ones. This is also the case for the profiles along the top and bottom wall.

5.4. Velocity profile

In this section, the velocity distribution between the heated walls is discussed to understand further the flow dynamic inside the test case. Note that some of the following presented contents are also discussed in extracts in [Zimmermann14a]. The velocity interacts with the temperature profile. Only if the velocity field is known, the temperature field can be estimated in the numerical simulation. Before the *vertical* and *horizontal* velocity components are analysed in detail, the velocity distribution in the whole setup is presented. The arising *circulation zones* or rather *convection cells* can be sketched on the basis of velocity stream tracers. The convection cells were introduced before in chapter 3, section 3.5 on page 82.

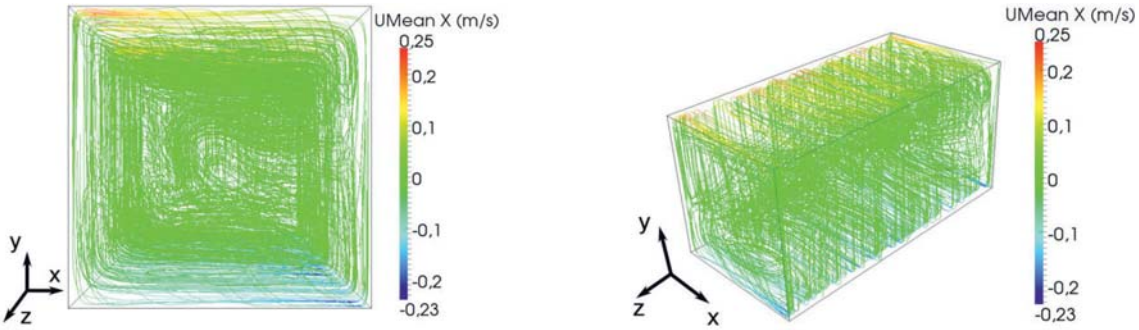

Figure 5.18.: Snapshots of the instantaneous mean horizontal velocity distribution in the simulation at $t = 400\,\mathrm{s}$, linear boundary condition. **Left:** Front view. **Right:** Top side view.

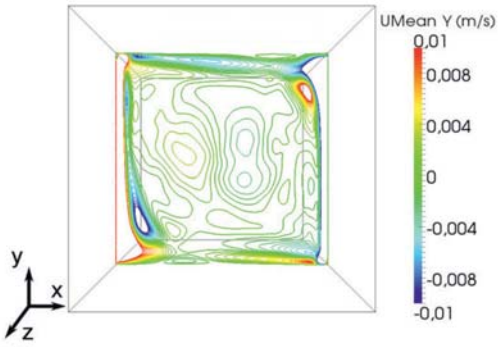

Figure 5.19.: Snapshot of the instantaneous mean vertical velocity distribution (contour lines) at the vertical xy-midplane, at $z = 0.75\,\mathrm{m}$, $t = 400\,\mathrm{s}$. Linear boundary condition (as in [Zimmermann14a]).

Figure 5.18 shows a snapshot of the instantaneous mean horizontal velocity distribution in the container at $t = 400\,\mathrm{s}$ in the simulated process for the *linear* bc case. The snapshot gives an impression of the velocity distribution of a natural convection problem in a container with two vertical, heated walls. In figure 5.18 only one big convection cell is visible which is 3-dimensional, as it was expected due to the container layout. Local

fluctuations arise in the cell during the simulated process, which are shown in the following. As a further example, a snapshot of the instantaneous mean velocity field at the xy-midplane is presented in figure 5.19 on page 122. The snapshot displays the results of the mean velocity in the *linear* bc case at $t = 400\,\mathrm{s}$ in the simulated process. The shown velocity values are time-averaged to the point of the presented time-step based on a average process in the simulation software itself. For a clearer presentation of the circulation zones, the snapshot shows the velocity distribution only for a limited range of values between $[-0.01\,\mathrm{m/s}, 0.01\,\mathrm{m/s}]$. An exterior, clockwise circulation region becomes visible in figure 5.19. Also two inner circulations are revealed, which are clearly visible in the left bottom and top right corner. Both circulations have also a clockwise direction.

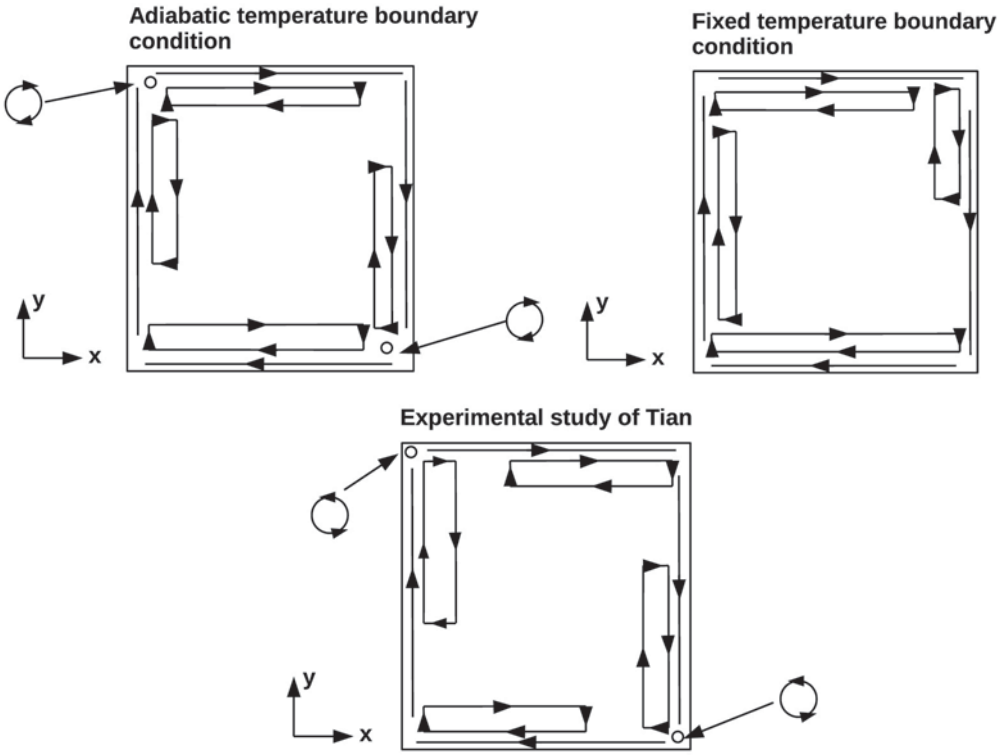

Figure 5.20.: Sketch of the time-averaged convection cell structures in the container. **Top left:** Sketch for the adiabatic boundary condition. **Top right:** Sketch for all fixed temperature boundary conditions. **Bottom right:** Sketch of the cells in the experiment, as seen in [Tian00a].

Figure 5.20 on page 123 illustrate the time-averaged mean velocity distribution in the container cell for all simulations and the experimental test case as illustrated in [Tian00a]. The numerical simulation data are averaged over an interval of $\Delta t = 200\,\mathrm{s} - 400\,\mathrm{s}$ in the simulated process. For the 3D simulation the intermediate steps size lies at $\Delta t = 3\,\mathrm{s}$, while it lies for the 2D simulations at $\Delta t = 1\,\mathrm{s}$. The distribution of the *adiabatic* bc case is pictured in the top left plot. All other simulation cases show a similar distribution and can be presented by the sketch in the top right figure. As one can see, the cell arrangement in the simulations deviates from the one in the experiment. According to [Tian00a],

small recirculation zones can be seen in the left top and right bottom corner in the experiment. These both zones are not visible in the numerical studies of the *fixed* bc case. However, in the *adiabatic* case, two additionally circulation zones appear in the bottom cold and top hot corner, but with another circulation direction as in [Tian00a]. The inner circulation zones of the *adiabatic* bc case are shifted compared to the other bc cases and the experiment. The inner circulation zones in the *fixed* bc case differ from the *adiabatic* bc case and also from [Tian00a]. In the following part, the mean vertical and horizontal velocity components are investigated between the heated walls at the xy-midplane along the horizontal x-axis.

5.4.1. Velocity distribution between the heated walls estimated along the horizontal axis

5.4.1.1. Vertical velocity component

Figure 5.21 gives a plot of the time-averaged vertical velocity profile in the boundary layer near the hot wall at the xy-midplane ($z = 0.75\,\mathrm{m}$) at $y = 0.375\,\mathrm{m}$ (midheight, $y = 0.5\,\mathrm{H}$)) estimated along the horizontal x-axis. Some of the following presented contents are also discussed in extracts in [Zimmermann14a]. It can be seen, that the boundary layer consists of a two layer structure. The boundary layer is divided at the point where the velocity reaches its maximum. According to [Tian00a], the inner layer of the boundary layer can be described in close distance to the wall by a linear law, due to a constant heat flux in this region. This was expected according to the information in chapter 3, section 3.5, 3.5.3.2. The linear law is plotted by the solid black line in figure 5.21. The boundary layer of the simulations can be approximated by a linear law. But the simulations exceed in all cases the peak values of the experiment and show steeper gradients. These higher velocity values agree with the steeper temperature gradients compared to the experimental results as it was seen in figure 5.6 on page 103.

Due to a higher velocity close to the hot wall, the heat flux of this wall is transmitted faster into the fluid than in the experiment. The vertical velocity component is estimated between the heated walls at the xy-midplane, at $x = 0.375\,\mathrm{m}$, $z = 0.75\,\mathrm{m}$ and three different heights, $y_1 = 0.1\mathrm{H}$, $y_2 = 0.5\mathrm{H}$ and $y_3 = 0.9\mathrm{H}$. The results are plotted in figures 5.22 - 5.23 on pages 126 - 127. For a better demonstration of all results together in one plot, a constant was added to the results of each height, which are $y_1 : +0$, $y_2 : +1$ and $y_3 : +2$. Note, that the scale of the plotted region in the detailed view is changed compared to other estimated profiles, to obtain a clearer presentation near the heated walls. As in the temperature profiles in section 5.3.1, a clockwise flow direction can be seen and also an increase of the boundary layer in flow direction. The flow structure along the hot wall is inverted to the one along the cold wall.

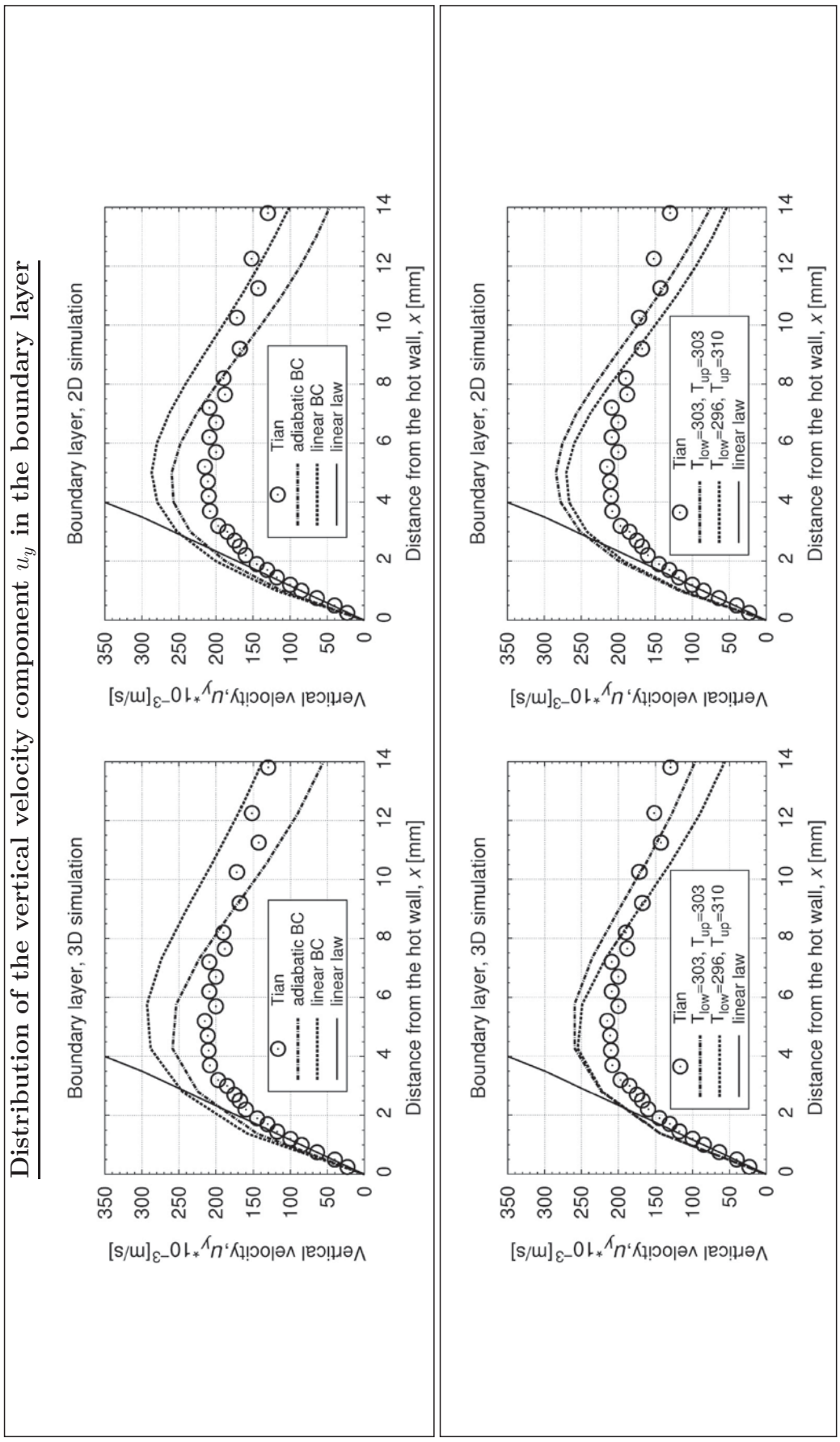

Figure 5.21.: Time-averaged profile of the vertical velocity component u_y in the boundary layer near the hot wall, at midheight $y = 0.375\,\mathrm{m}$ ($y = 0.5\,\mathrm{H}$) (vertical xy-midplane). **Top box**: Adiabatic bc (black broken line $\cdot - \cdot$) and linear bc (black dashed line $- - -$). **Bottom box**: $T_{\mathrm{low}} = 296\,\mathrm{K}$, $T_{\mathrm{up}} = 310\,\mathrm{K}$ (black broken line $\cdot - \cdot$), $T_{\mathrm{low/up}} = 303\,\mathrm{K}$ (black dashed line $- - -$). **In each box**: 3D simulation (left) and 2D simulation (right). **In each picture:** ○: [Tian00a], $\mathrm{Ra} = 1.58 \times 10^9$. **-** solid black line: linear law.

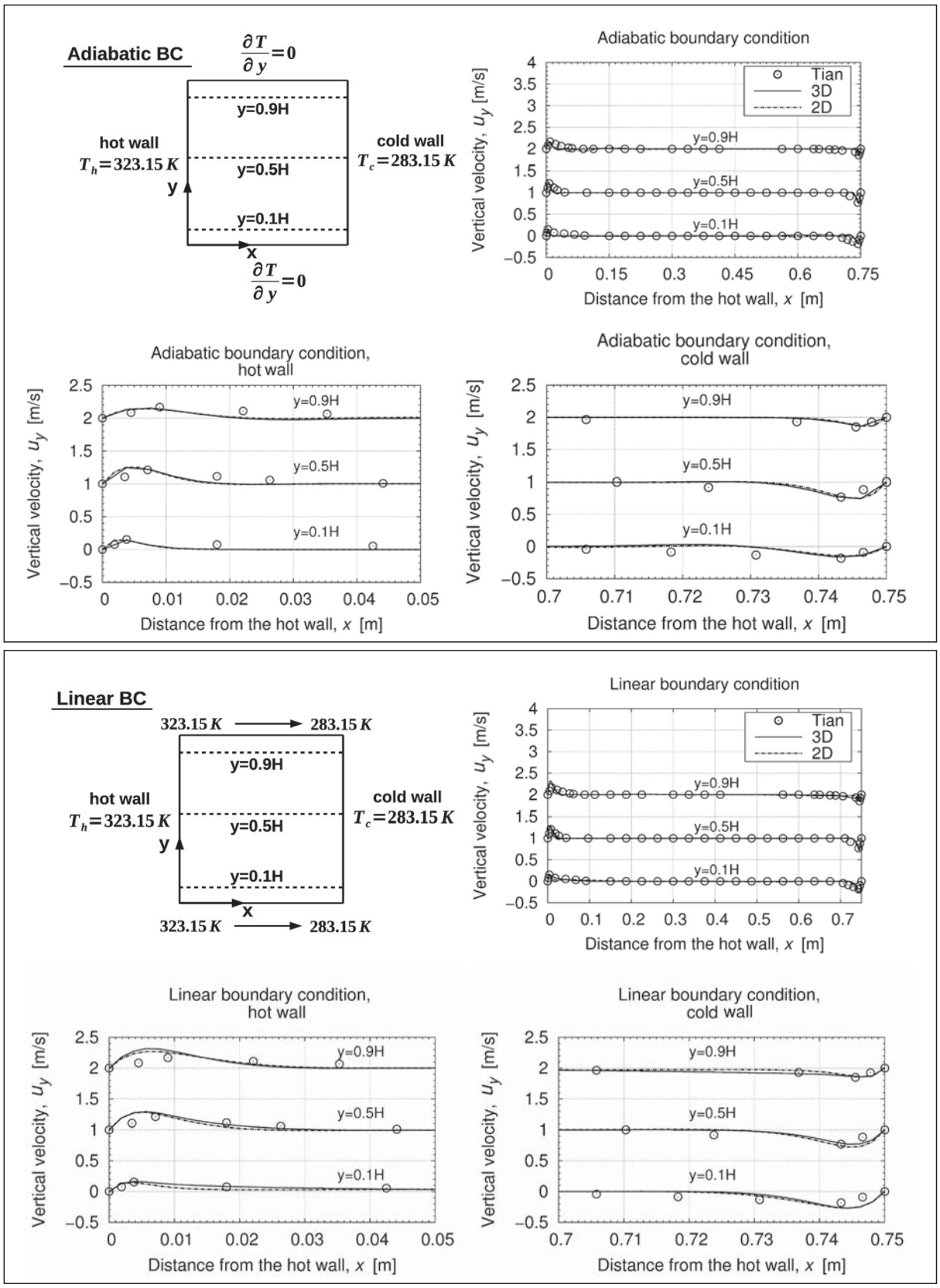

Figure 5.22.: Time-averaged vertical velocity profile (u_y) between the hot and cold wall, estimated at the vertical xy-midplane, at $z = 0.75\,\mathrm{m}$, and different heights, along the horizontal x-axis. **Top box:** Adiabatic bc. **Bottom box:** Linear bc. **Top row in each box:** Overview. **Bottom row in each box:** Detailed plot of the hot/cold wall. **In all pictures: -** solid line: 3D, **- -** dashed line: 2D. ∘: study [Tian00a], $\mathrm{Ra} = 1.58 \times 10^9$ (as in [Zimmermann14a]).

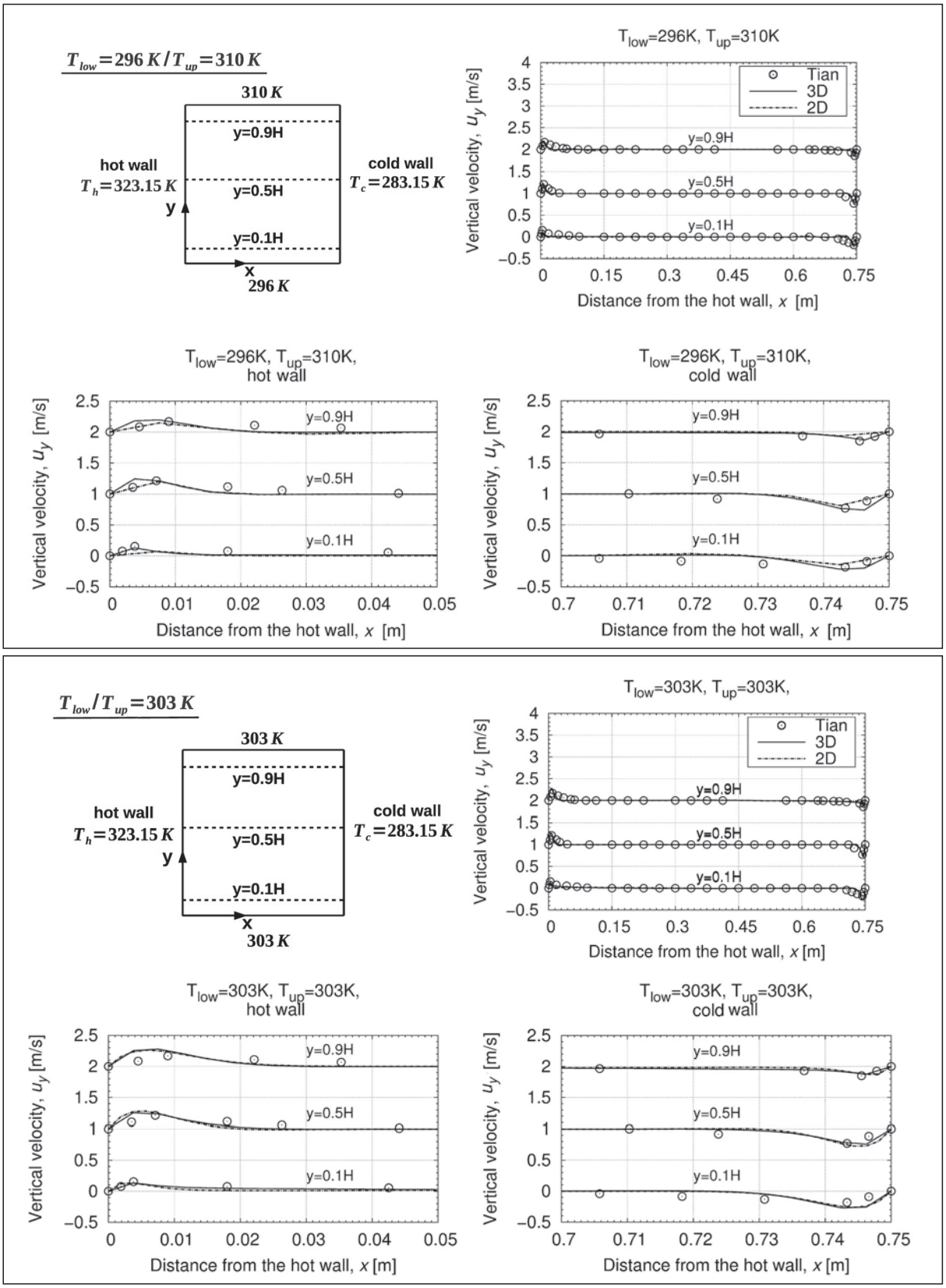

Figure 5.23.: Time-averaged vertical velocity profile (u_y) between the hot and cold wall, estimated at the vertical xy-midplane, at $z = 0.75\,\mathrm{m}$, and different heights, along the horizontal x-axis. **Top box:** $T_{\mathrm{low}} = 296\,\mathrm{K}$, $T_{\mathrm{up}} = 310\,\mathrm{K}$. **Bottom box:** $T_{\mathrm{low/up}} = 303\,\mathrm{K}$. **Top row in each box:** Overview. **Bottom row in each box:** Detailed plot of the hot/cold wall. **In all pictures: -** solid line: 3D, **- -** dashed line: 2D. **o**: study [Tian00a], $\mathrm{Ra} = 1.58 \times 10^9$.

The boundary layer reaches its maximum width at the hot wall at height $y_3 = 0.9\,\mathrm{H}$, respectively at the cold wall at height $y_1 = 0.1\,\mathrm{H}$. The boundary layer reaches in all cases a width of about 0.035 m at height $y_3 = 0.9\,\mathrm{H}$. At $y_1 = 0.1\,\mathrm{H}$ it has only a width of about 0.015 m. Thus, the thermal boundary layer lies within the velocity boundary layer in all cases, as it was expected according to chapter 3, section 3.5, 3.5.3.2, (see also figures 5.7 - 5.8, on pages 104 - 105).

Negative values appear between the inner and outer layer in the results of [Tian00a] which indicate a reverse flow region. These negative values appear also in each simulation case. The vertical velocity component reveals in the simulations high peak values at every height close to the vertical walls. These peak values are mirror-imaged to the ones in the temperature profile in figures 5.7 - 5.8 on pages 104 and 105. After the velocity has reached its peak value close to the hot wall, the velocity profile descends and a minor decrease with negative values can be noticed outside the boundary layer at the hot wall (vice versa at the cold wall). Beyond this point, the profile ascends again and the bulk region is reached where the velocity becomes almost stationary. According to [Tian00a], this decrease/increase outside the boundary layer might possibly indicate two further clockwise circulation zones.

The *adiabatic* profile shows a slightly smaller boundary layer than the experiment, as it was the case in the temperature profile. Hence, the peak values are located in this case closer to the heated walls and lie beneath the experimental ones. No significant differences arise between the 2D and 3D simulation results. The peak values differ only slightly from each other. The profiles of the fixed temperature bc cases approximate well the results of [Tian00a], as it was the case in the temperature profiles. Due to the different temperature conditions at the horizontal walls, the peak values of the simulations are in all cases higher than in the experiment.

Moreover, the peak values are located closer to the vertical walls. The only exception are the values in the left bottom and right top corner. The peak values descend after midheight, except for the *linear* bc case. In this case, the maximum value is reached at height $y_3 = 0.9\,\mathrm{H}$ for the hot, respectively $y_1 = 0.1\,\mathrm{H}$ for the cold, wall. The profile of the $T_{\mathrm{low}} = 303\,\mathrm{K}$, $T_{\mathrm{up}} = 303\,\mathrm{K}$ case reveals a smoother profile near to the vertical walls than in both other cases. Comparing the 2D and 3D simulation results of these cases to each other, no great differences are visible. Only the $T_{\mathrm{low}} = 296\,\mathrm{K}$, $T_{\mathrm{up}} = 310\,\mathrm{K}$ case show deviations between both simulation types near the heated walls at all three heights.

5.4.1.2. Horizontal velocity component

Analogously to the previous part, figure 5.24 and 5.25 on pages 130 - 131 present the time-averaged *horizontal* velocity component estimated at the xy-midplane at the same positions as before. For a better demonstration of all results together in one plot, a con-

stant was added to the results of each height, which are $y_1 : +0$, $y_2 : +1$ and $y_3 : +2$. The horizontal velocity component has a great influence on the development of the horizontal boundary layer. Significant fluctuations become visible in the experiment as well in the simulations along the container middle near the horizontal walls, especially at height $y_1 = 0.1\,\mathrm{m}$ and $y_2 = 0.9\,\mathrm{m}$. No significant amplitudes can be detected at midheight in the simulation results.

According to [Tian00a], the observed fluctuations near the horizontal walls indicate another interior clockwise circulation zone which is located next to the main external circulation, as it was seen in figure 5.20. The peak values of the horizontal component lie beneath the ones of the vertical component, as it was expected due to the main circulation zone in figure 5.18 on page 122. The simulation results of the *adiabatic* bc case approximate the experiment well directly at the heated walls. At height $y_3 = 0.9\,\mathrm{m}$, the 3D values are smaller than in the experiment, but the 2D simulation approximates the experiment closely. The results at height $y_1 = 0.1\,\mathrm{m}$ and height $y_3 = 0.9\,\mathrm{m}$ are mirror-imaged to each other in both simulation types. This deviation to the experiment might possibly be caused by the shifted circulation zones as seen in figure 5.20 on page 123. In the simulation, the inner horizontal circulation zone near the top wall, respectively bottom wall, lies closer to the left wall, respectively right wall, than in the experiment. The inner vertical circulation zones close to the heated walls show even an inverted flow direction compared to [Tian00a].

The *linear* bc case approximates well the experiment. The peak values of the 3D simulation, located at height $y_1 = 0.1\,\mathrm{m}$ and height $y_3 = 0.9\,\mathrm{m}$, are inverted to the 2D case which indicate shifted circulation zones in both simulations. Positive velocity values become visible in the experiment in the centre region at height $y_3 = 0.9\,\mathrm{m}$, while negative values arise in the 3D simulation at this position. This aspect is possibly caused by the displaced circulation zones in the 3D simulation. At height $y_1 = 0.1\,\mathrm{m}$, the 3D simulation presents positive velocity values between $x = 0.15\,\mathrm{m} - 0.75\,\mathrm{m}$, while the 2D case reveals negative ones in this region. Hence, the circulation zone in the 2D simulation has to be displaced to the convection cell in the 3D case. Both other cases with a *fixed temperature boundary condition* are similar to the *linear* bc case. The 2D and 3D results are shifted to each other, but the results reveal smaller deviations to each other than both simulations in the *linear* bc case.

Concluding, the vertical velocity component of the *adiabatic* bc case and of the simulation with the $T_{\mathrm{low}} = 296\,\mathrm{K}$, $T_{\mathrm{up}} = 310\,\mathrm{K}$ condition approximate the experimental data of [Tian00a] closer than both other bc cases. For the horizontal component, this is also the case for the *adiabatic* condition. The other cases show higher and also shifted results compared to the experiment. The vertical velocity component is mirror-imaged to the temperature profile in all cases.

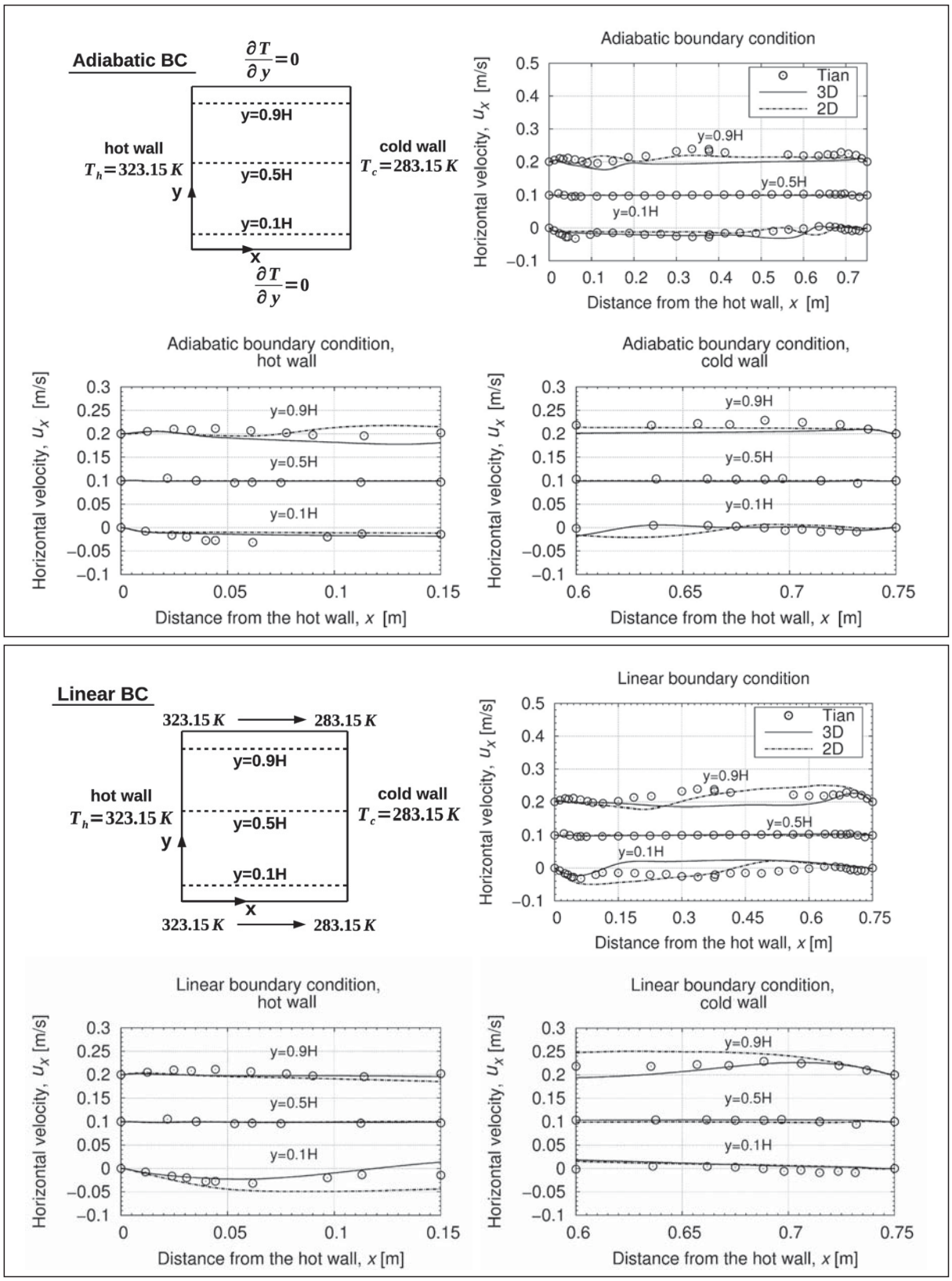

Figure 5.24.: Time-averaged horizontal velocity profile (u_x) between the hot and cold wall, estimated at the vertical xy-midplane, at $z = 0.75\,\mathrm{m}$, and different heights, along the horizontal x-axis. **Top box:** Adiabatic bc. **Bottom box:** Linear bc. **Top row in each box:** Overview. **Bottom row in each box:** Detailed plot of the hot/cold wall. **In all pictures: -** solid line: 3D, **- -** dashed line: 2D. **o**: study [Tian00a], $\mathrm{Ra} = 1.58 \times 10^9$.

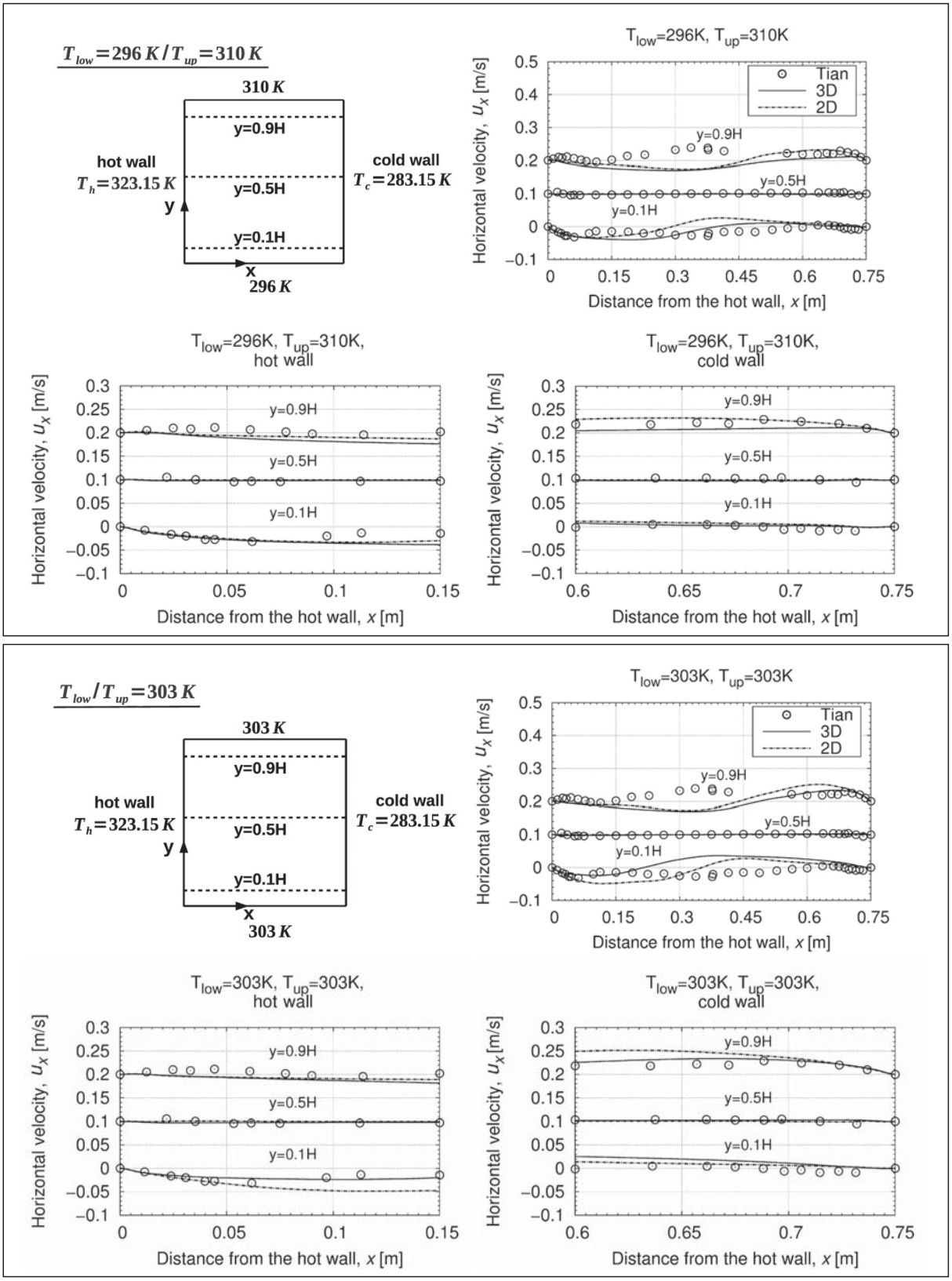

Figure 5.25.: Time-averaged horizontal velocity profile (u_x) estimated between the hot and cold wall, estimated at the vertical xy-midplane, at $z = 0.75\,\mathrm{m}$, and different heights, along the horizontal x-axis. **Top box:** $T_{\mathrm{low}} = 296\,\mathrm{K}$, $T_{\mathrm{up}} = 310\,\mathrm{K}$. **Bottom box:** $T_{\mathrm{low/up}} = 303\,\mathrm{K}$. **Top row in each box:** Overview. **Bottom row in each box:** Detailed plot of the hot/cold wall. **In all pictures: -** solid line: 3D, **- -** dashed line: 2D. **o**: study [Tian00a], $\mathrm{Ra} = 1.58 \times 10^9$.

The high fluctuations of the horizontal component, which appear mainly in the right upper (about $x = 0.45\,\mathrm{m} - 0.72\,\mathrm{m}$) and left lower bulk region (about $x = 0.15\,\mathrm{m} - 0.45\,\mathrm{m}$), can be also found in the temperature profile. Significant deviations can be seen especially between the 2D and 3D cases, which have to be further investigated in future studies. The highest values of both components are reached in the *linear* bc case. The highest absolute value of the vertical velocity component u_y is reached at the hot bottom wall in the 3D-simulation and it is about $0.4\,\mathrm{m/s}$. The highest absolute value of the horizontal velocity component u_x is reached at the hot bottom and top cold wall in the 2D-simulation and it is about $0.5\,\mathrm{m/s}$.

5.4.2. Investigation of a 2-dimensional flow field at the vertical xy-midplane

Tian et al. consider in the experimental setup a 2-dimensional flow at the xy-midplane. To generate a 2-dimensional flow field in a 3-dimensional geometry like the observed one, the depth of the experimental setup has to be long enough to neglect the influences of the front and back side walls on the flow field. In the observed test case the determining aspect ratio is $\Gamma_z = \frac{D}{L} = 2$. To investigate whether the setup offers actually a 2-dimensional flow field, the vertical velocity component u_y is analysed at three different depth positions in the setup. If there arise no significant differences between the particular velocity values, a 2-dimensional flow at the xy-midplane can be assumed.

Analogously to the approach in [Tian00a], the vertical velocity component u_y is evaluated along the horizontal x-axis at midheight ($y = 0.375\,\mathrm{m}$) at three different depth positions of $z = 0.15\,\mathrm{m}$, $z = 0.80\,\mathrm{m}$ and $z = 1.2\,\mathrm{m}$. The results are illustrated in figure 5.26 on page 133. All results lie very close to each other. For the *adiabatic* bc case, the peak values differ only about a maximum of 3% from each other. Thus, one can assume a 2-dimensional flow field at the xy-midplane of the container in this case. For the *linear* bc case and $T_{\mathrm{low}} = 303\,\mathrm{K}$, $T_{\mathrm{up}} = 303\,\mathrm{K}$-condition the peak values deviate about a maximum of 6% from each other and for the case of $T_{\mathrm{low}} = 303\,\mathrm{K}$, $T_{\mathrm{up}} = 303\,\mathrm{K}$ even about a maximum of 10%. Furthermore, all estimated results reveal an asymmetrical profile. But however, the deviations of the peak values have no visible effect on the remaining main flow profile. Hence, a 2-dimensional flow can also be assumed.

To investigate this aspect further, the transversal velocity component u_z is estimated along the horizontal x-axis between the heated walls at the xy-midplane, at $z = 0.75\,\mathrm{m}$, and different heights. The values are estimated at three different heights in the container, $y_1 = 0.1\mathrm{H}$, $y_2 = 0.5\mathrm{H}$, $y_3 = 0.9\mathrm{H}$. The results are plotted in figure 5.27 on page 134. For a better demonstration of the results together in one plot, a constant is added to the results of each height which are $y_1 : +0$, $y_2 : +3$, $y_3 : +6$.

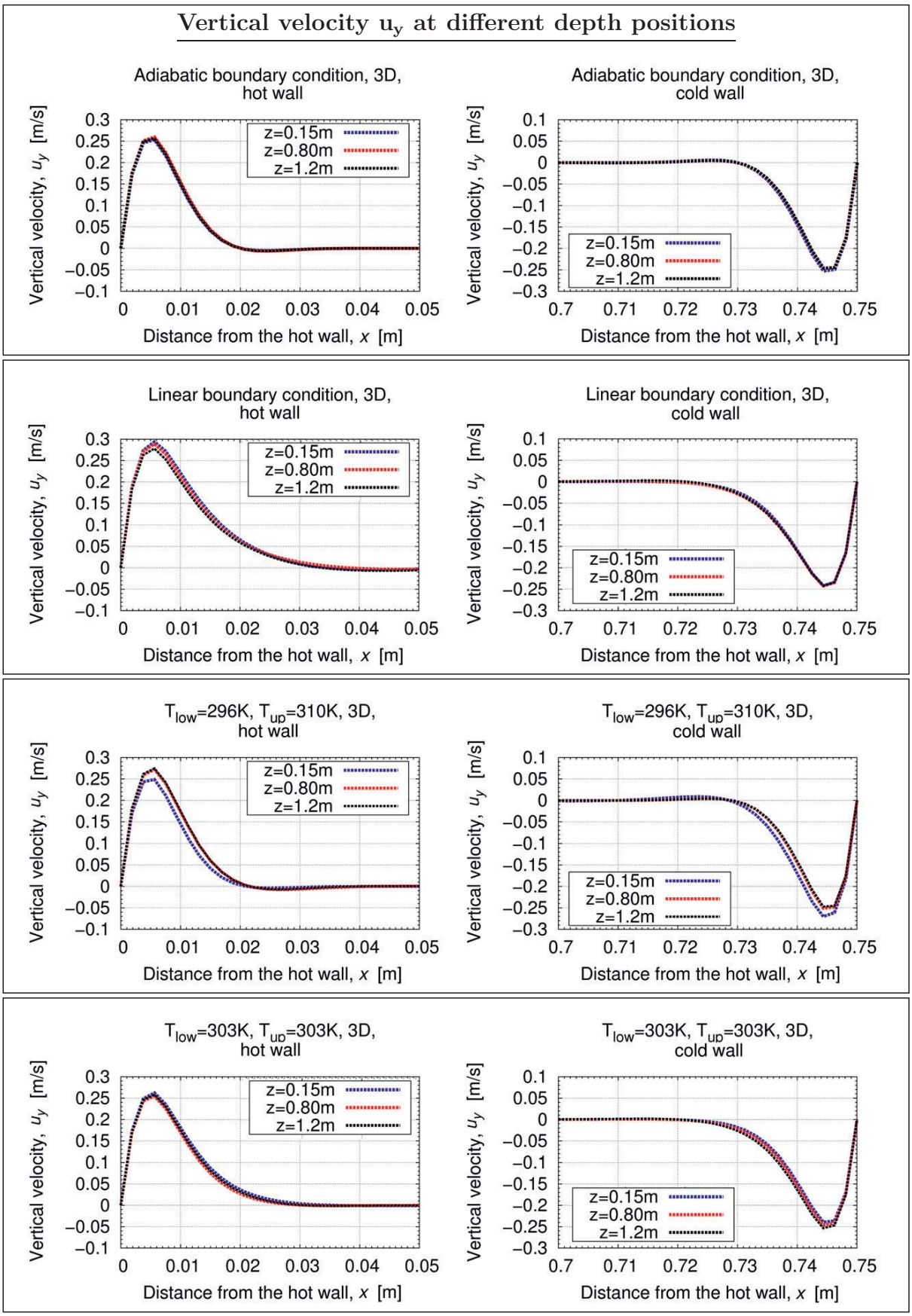

Figure 5.26.: Time-averaged profile of the vertical velocity (u_y) between the heated walls, estimated at $y = 0.375\,\mathrm{m}$, and different depth positions (z-axis) along the horizontal x-axis. 3D simulations. **Top to bottom:** Adiabatic bc, linear bc, $T_{\mathrm{low}} = 296\,\mathrm{K}$, $T_{\mathrm{up}} = 310\,\mathrm{K}$, $T_{\mathrm{low/up}} = 303\,\mathrm{K}$. -- blue dashed line: $z = 0.15\,\mathrm{m}$, -- red dashed line: $z = 0.80\,\mathrm{m}$, -- black dashed line: $z = 1.2\,\mathrm{m}$.

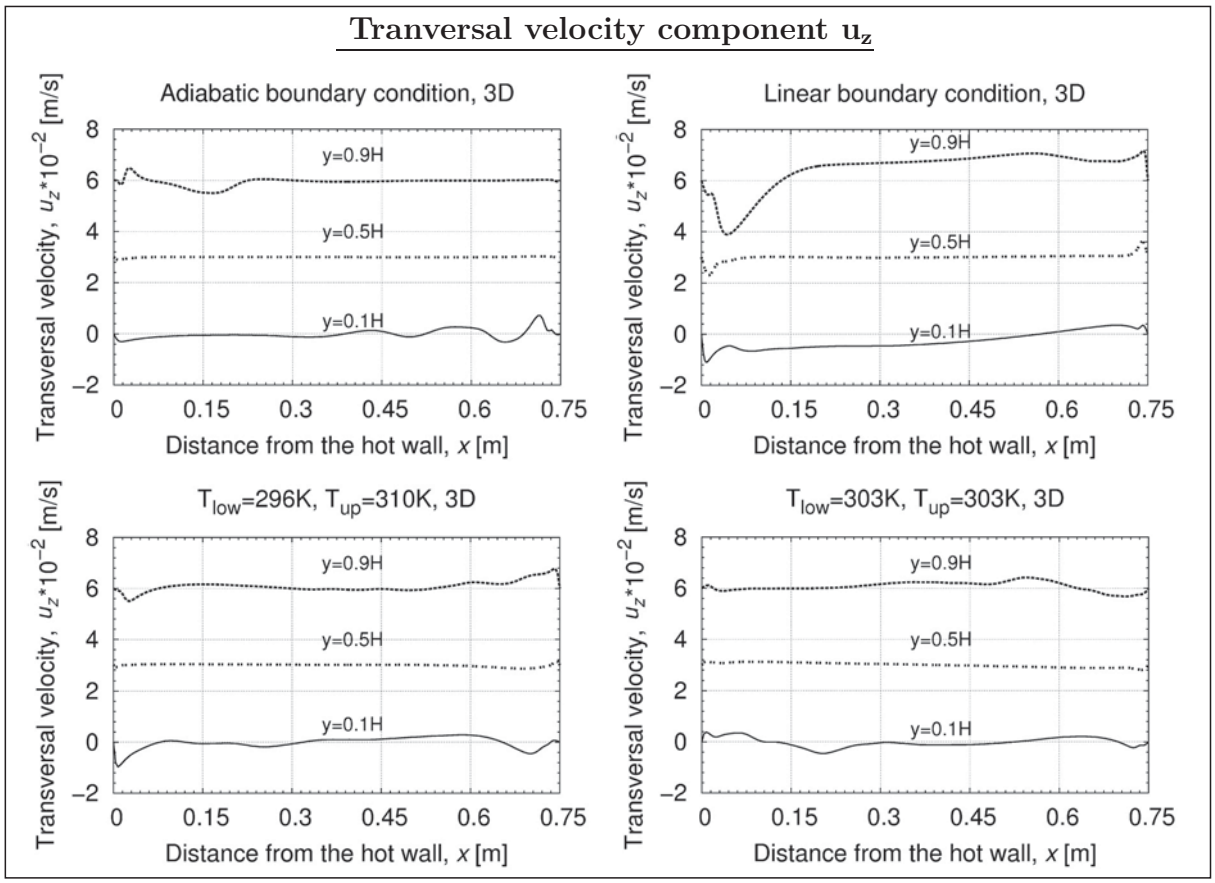

Figure 5.27.: Time-averaged profile of the transversal velocity component (u_z) between the hot and cold wall, estimated at the vertical xy-midplane, $z = 0.75\,\mathrm{m}$, and different heights along the horizontal x-axis. 3D simulations. **Clockwise direction, starting top left:** Adiabatic bc, linear bc, $T_{\mathrm{low}} = 296\,\mathrm{K}$, $T_{\mathrm{up}} = 310\,\mathrm{K}$, $T_{\mathrm{low/up}} = 303\,\mathrm{K}$. - black solid line: $y = 0.1\,\mathrm{H}$, $\cdots$ black dotted line: $y = 0.5\,\mathrm{H}$, $- - -$ black dashed line: $y = 0.9\,\mathrm{H}$,

The transversal velocity component u_z was not measured in [Tian00a]. Thus, no comparable experimental data exist in this case. But if a 2-dimensional flow field is generated at the xy-midplane in the container, the time-averaged values of the transversal velocity component u_z have to be zero.

As it can be seen in figure 5.27, all simulation results do not satisfy this condition. A boundary layer can clearly be seen in all results, which is especially distinctive in the *linear* bc case. The peak values of the u_z profiles are reached in the corner regions which agrees with the profiles of both other components, u_x and u_y. In the *adiabatic* bc case, the peak values are shifted compared to the locations of the other peak values in all cases.

The highest values are reached in the *linear* bc case with an absolute value of about $0.02\,\mathrm{m/s}$ at the top hot corner. In comparison to the vertical and horizontal component u_y, u_x, the values of u_z are about a factor of 10^{-1} smaller. Therefore, one can assume a 2-dimensional flow field at the xy-midplane anyway.

5.4.3. Velocity fluctuations between the heated walls estimated along the horizontal axis

5.4.3.1. Vertical component

The fluctuations of the *vertical* velocity component u_y are illustrated in figures 5.28 - 5.29 on pages 137 - 138, complementary to the profiles of the temperature fluctuations in section 5.3.2. Due to a better presentation of all results in one plot, a constant is added to the results of each height which are this time y_1 : +0, y_2 : +0.1 and y_3 : +0.2. The values are given by the standard deviation from equation (5.3.1) on page 106. The profiles in [Tian00b] are characterised by high peak values in the boundary layer close to the hot and cold wall. At height $y_3 = 0.9\,\mathrm{m}$ the maximum value is reached. At every height, a steady-state flow is clear visible in the bulk region. All profiles reveal an anti-symmetrical form. Directly at the heated walls the fluctuation is, as the velocity itself, zero.

The simulation profiles reveal a similar form to one of the experiment, but show an asymmetrical form. It is noteworthy, that the peak values of the 3D simulations are about a factor of 10^{-3} smaller than in the experiment. The 2D simulation data do not comply with the 3D cases, because the fluctuations are mainly located along the bulk region. This behaviour was seen before in the results of the temperature fluctuations in section 5.3.2, figures 5.9 and 5.10 on page 108 and 109. For the *adiabatic boundary condition* minor fluctuations can be seen at the top hot and bottom cold corner. In the 2D simulations the fluctuations arise also mainly in this region. The results for the 3D cases of the fixed temperature boundary conditions show a similar tendency as the experiment. The steady state flow arises in this cases at an equal position as in the experiment. In all 2D simulations high fluctuations along the container middle become visible at every height.

The *linear* bc case exceeds the values of the experiment at the top hot corner. The 2D and the 3D simulation of the $T_{\mathrm{low}} = 303\,\mathrm{K}$, $T_{\mathrm{up}} = 303\,\mathrm{K}$-condition case show higher peak values than all other simulations and higher values than the experimental data.

5.4.3.2. Horizontal component

The results of the fluctuations of the velocity component u_x are presented in figures 5.30 - 5.31 on pages 139 - 140. The experimental profiles reveal a form which is similar to the ones of the fluctuations of the vertical component u_y. High peak values are located in the boundary layer close to the heated walls. But these peak values are smaller than the ones of the fluctuations of the vertical component u_y. In the container middle, the fluctuations become almost zero. According to [Tian00b], at height $y_1 = 0.1\,\mathrm{m}$ and height $y_3 = 0.9\,\mathrm{m}$ a non steady state flow is expected and can also clearly be seen in the experiment due to the conducting bc at the horizontal walls.

Modest peak values appear in both simulation types of the *adiabatic* bc case at height $y_1 = 0.1\,\mathrm{m}$ and $y_3 = 0.9\,\mathrm{m}$, as it was observed before in the results of the fluctuations of the vertical component u_y. The values are smaller than the experimental ones. The 2D simulation differs especially at the top hot and bottom cold corner from the 3D simulation, as it was the case for the horizontal velocity results u_x in section 5.4.1, figure 5.24 on page 130. All simulations with a fixed temperature boundary condition reveal similarities to each other, as it was the case before in the results of the fluctuations of the vertical component u_y.

For the 3D *linear boundary condition* simulation, high values arise only at the hot bottom and top cold corner which match with the values of the experiment. Remarkably are the high fluctuations of the 2D simulation for this boundary condition. Both other 3D simulations of a fixed boundary condition show smaller values than in [Tian00b] at most of the positions. The estimated values approximate the experimental data only at the hot bottom and cold top corner. The peak values are shifted to the ones of the experiment and appear mainly in the bulk region near the upper cold and lower hot corner. Noteworthy are the significant fluctuations in the 2D simulation cases, especially in case of the *linear* bc and the vertical component.

In [Tian00a] the maximum values are about $0.08\,\mathrm{m/s}$ for the vertical component u_y and about $0.04\,\mathrm{m/s}$ for the horizontal component u_x. In case of the *adiabatic* bc these values lie at about $0.04\,\mathrm{m/s}$ for the vertical component u_y and at about $0.02\,\mathrm{m/s}$ for the horizontal component u_x. For the *linear* bc case these values are about $0.07\,\mathrm{m/s}$ for the vertical component u_y and about $0.04\,\mathrm{m/s}$ for the horizontal component u_x.

For the case of the $T_{\mathrm{low}} = 296\,\mathrm{K}$, $T_{\mathrm{up}} = 310\,\mathrm{K}$-condition these values are about $0.03\,\mathrm{m/s}$ for the vertical component u_y and about $0.03\,\mathrm{m/s}$ for the horizontal component u_x. For the case of the $T_{\mathrm{low/up}} = 303\,\mathrm{K}$-condition these values are about $0.05\,\mathrm{m/s}$ for the vertical component u_y and about $0.04\,\mathrm{m/s}$ for the horizontal component u_x. Concluding, the 3D simulation results of the fixed temperature boundary condition cases approximate the tendency of the experimental results in both components with high peak values close to the heated walls.

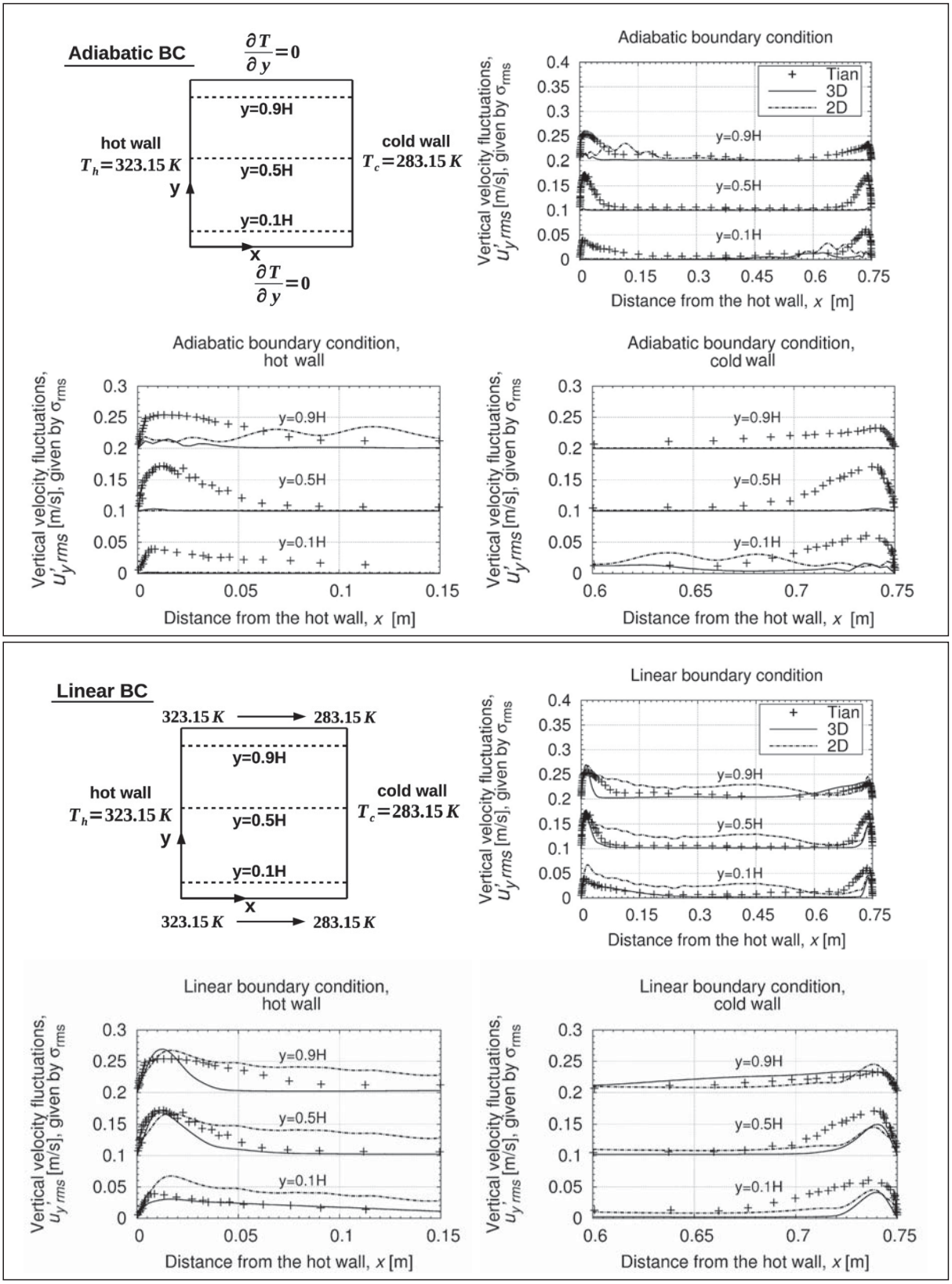

Figure 5.28.: Time-averaged profile of the vertical velocity fluctuations between the hot and cold wall, estimated at the vertical xy-midplane, at $z = 0.75\,\mathrm{m}$, and different heights, along the horizontal x-axis, given by the standard deviation σ_{rms}. **Top box:** Adiabatic bc. **Bottom box:** Linear bc. **Top row in each box:** Overview. **Bottom row in each box:** Detailed plot of the hot/cold wall. **In all pictures: -** solid line: 3D, **--** dashed line: 2D. **+**: study [Tian00a], $\mathrm{Ra} = 1.58 \times 10^9$.

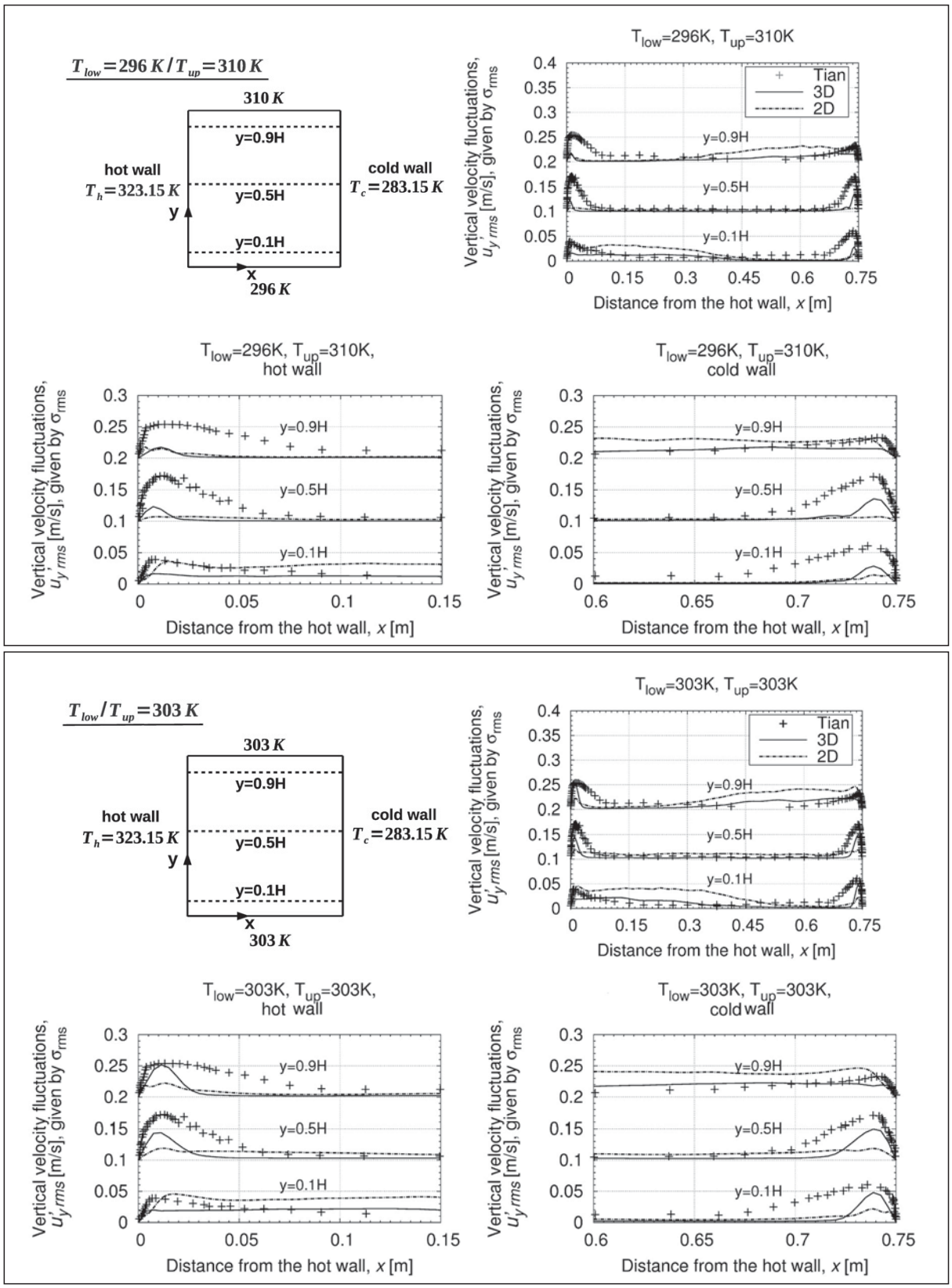

Figure 5.29.: Time-averaged profile of vertical velocity fluctuations between the hot and cold wall, estimated at the vertical xy-midplane, at $z = 0.75\,\mathrm{m}$, and different heights, along the horizontal x-axis, given by the standard deviation σ_{rms}. **Top box:** $T_{\mathrm{low}} = 296\,\mathrm{K}$, $T_{\mathrm{up}} = 310\,\mathrm{K}$. **Bottom box:** $T_{\mathrm{low/up}} = 303\,\mathrm{K}$. **Top row in each box:** Overview. **Bottom row in each box:** Detailed plot of the hot/cold wall. **In all pictures: -** solid line: 3D, **- -** dashed line: 2D. **+**: study [Tian00a], $\mathrm{Ra} = 1.58 \times 10^9$.

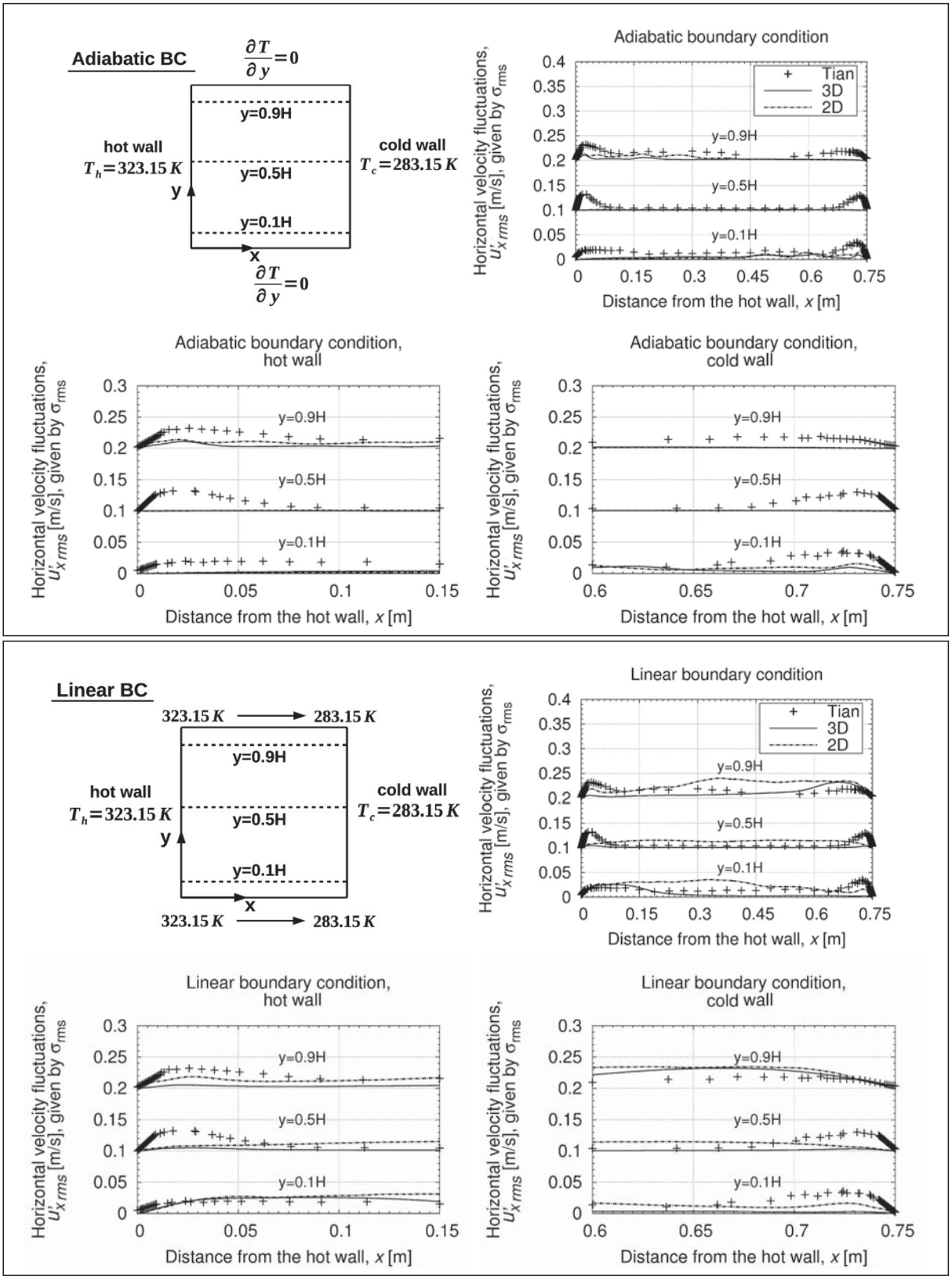

Figure 5.30.: Time-averaged profile of the horizontal velocity fluctuations between the hot and cold wall, estimated at the vertical xy-midplane, at $z = 0.75\,\mathrm{m}$, and different heights, along the horizontal x-axis, given by the standard deviation σ_{rms}. **Top box:** Adiabatic bc. **Bottom box:** Linear bc. **Top row in each box:** Overview. **Bottom row in each box:** Detailed plot of the hot/cold wall. **In all pictures: -** solid line: 3D, **- -** dashed line: 2D. **+**: study [Tian00a], $\mathrm{Ra} = 1.58 \times 10^9$.

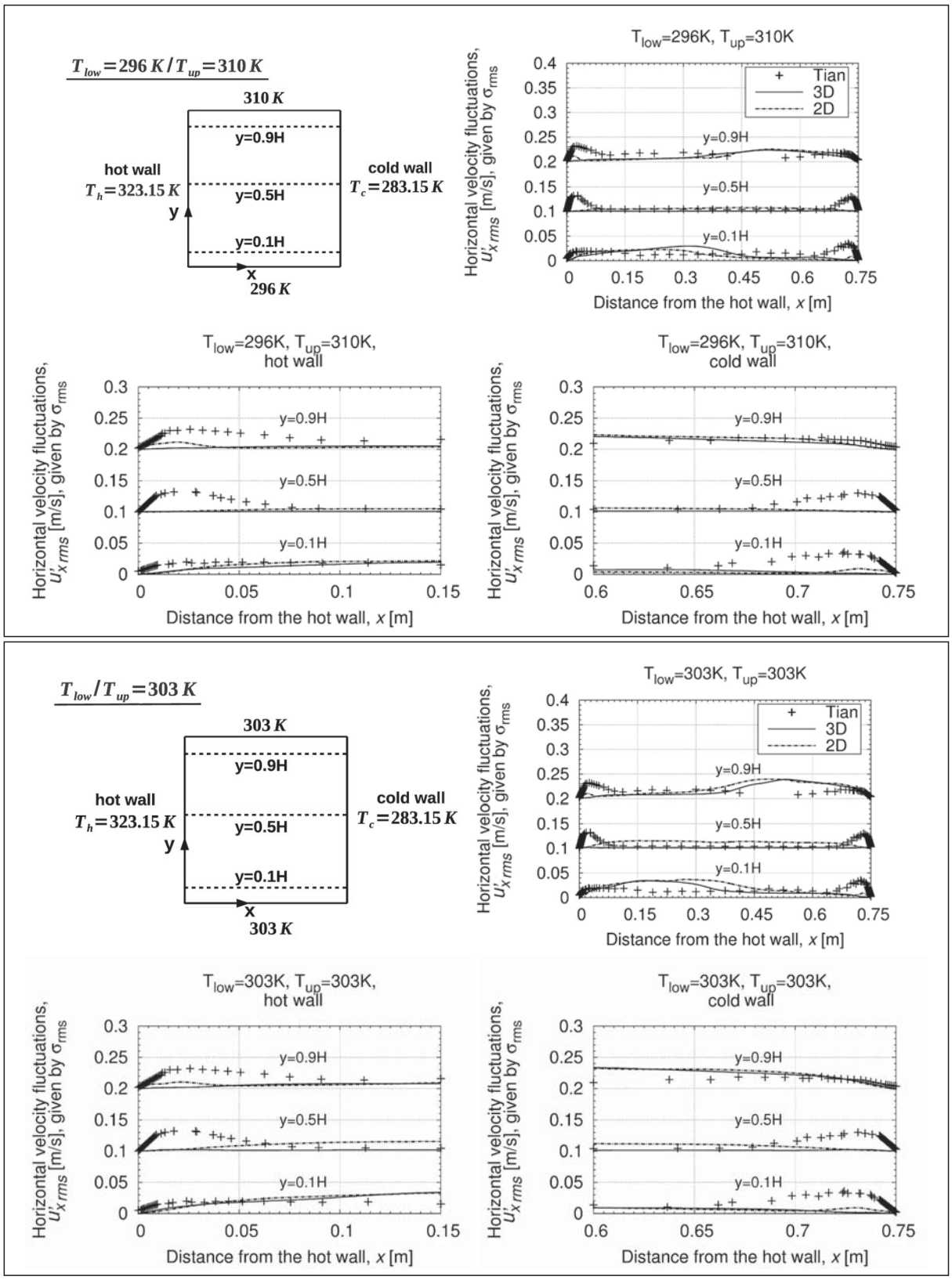

Figure 5.31.: Time-averaged profile of the horizontal velocity fluctuations between the hot and cold wall, estimated at the vertical xy-midplane, at $z = 0.75\,\mathrm{m}$, and different heights, along the horizontal x-axis, given by the standard deviation σ_{rms}. **Top box:** $T_{\mathrm{low}} = 296\,\mathrm{K}$, $T_{\mathrm{up}} = 310\,\mathrm{K}$. **Bottom box:** $T_{\mathrm{low/up}} = 303\,\mathrm{K}$. **Top row in each box:** Overview. **Bottom row in each box:** Detailed plot of the hot/cold wall. **In all pictures: -** solid line: 3D, **- -** dashed line: 2D. **+**: study [Tian00a], $\mathrm{Ra} = 1.58 \times 10^9$.

5.4.4. Profile of the non-dimensional horizontal velocity component between the top and bottom wall estimated along the vertical axis

In addition to the velocity profiles estimated at the xy-midplane along the horizontal x-axis, the velocity distribution at the xy-midplane along the vertical y-axis is analysed in this section. Therefore, the non-dimensional horizontal velocity component u_x/u_0 is estimated analogously as in [Tian00a]. It is assumed that $u_0 = \sqrt{g_y \beta \mathrm{H} \Delta T} = 1\,\mathrm{m/s}$, according to [Tian00a]. Besides the data of [Tian00a], a further numerical study of [Beghein93b] is compared to the simulation data. The values of all studies are plotted in figure 5.32 on page 142. [Beghein93b] investigates a convection cell with aspect ratios of $\mathrm{Ar}_x = 1$, and $\mathrm{Ra} = 1 \times 10^{10}$.

Tian et al. report in [Tian00a] a stationary flow region in vertical direction between the positions $y = 0.2\,\mathrm{m}$ and $y = 0.56\,\mathrm{m}$. Furthermore, *Tian et al.* observe a reverse flow at the end of the boundary layer. On the contrary, the study of [Beghein93b] shows a stationary flow region (where the velocity values are close to zero) in the centre of the container only. The values of the *adiabatic* simulation are shifted to the experimental results of [Tian00a], as it was seen before in the horizontal velocity profile in figure 5.24 on page 130.

The 2D simulation shows higher peak values as in case of the 3D simulation. At the top wall, the estimated values of the 3D simulation are significantly small to the values of the 2D simulation. In the 3D case the stationary flow can be detected at the position of about $y = 0.53\,\mathrm{m}$ only. For the 2D simulation a stationary flow region is visible near the positions of about $y = 0.37\,\mathrm{m}$ and of about $y = 0.3\,\mathrm{m}$. No reverse flow can be detected in both simulation types.

The *adiabatic* simulations approximate rather the study of [Beghein93b]. Both simulation types of the *linear* bc case reveal a stationary as well as a reverse flow region. In comparison to [Tian00a], the stationary flow regions are smaller and the reverse flow regions of both simulations are dislocated. Therefore, the boundary layers near the horizontal walls are smaller than the one of the experiment, especially in case of the 3D simulation.

In the 2D simulation, the stationary flow region can be detected between the positions of about $y = 0.54\,\mathrm{m}$ and of about $y = 0.3\,\mathrm{m}$. In the 3D simulation, the stationary flow region can be detected between the positions of about $y = 0.45\,\mathrm{m}$ and of about $y = 0.3\,\mathrm{m}$. This was also visible in the profile of the horizontal velocity at both outer positions in figure 5.24 on page 130. The peak values in case of the *linear* bc are higher than in the experiment of [Tian00a] due to the different boundary condition. The profiles of the 2D and 3D simulation are slightly dislocated to each other. The peak values of the 3D simulation exceed the values of the 2D simulation and also the peak values of the other simulation cases.

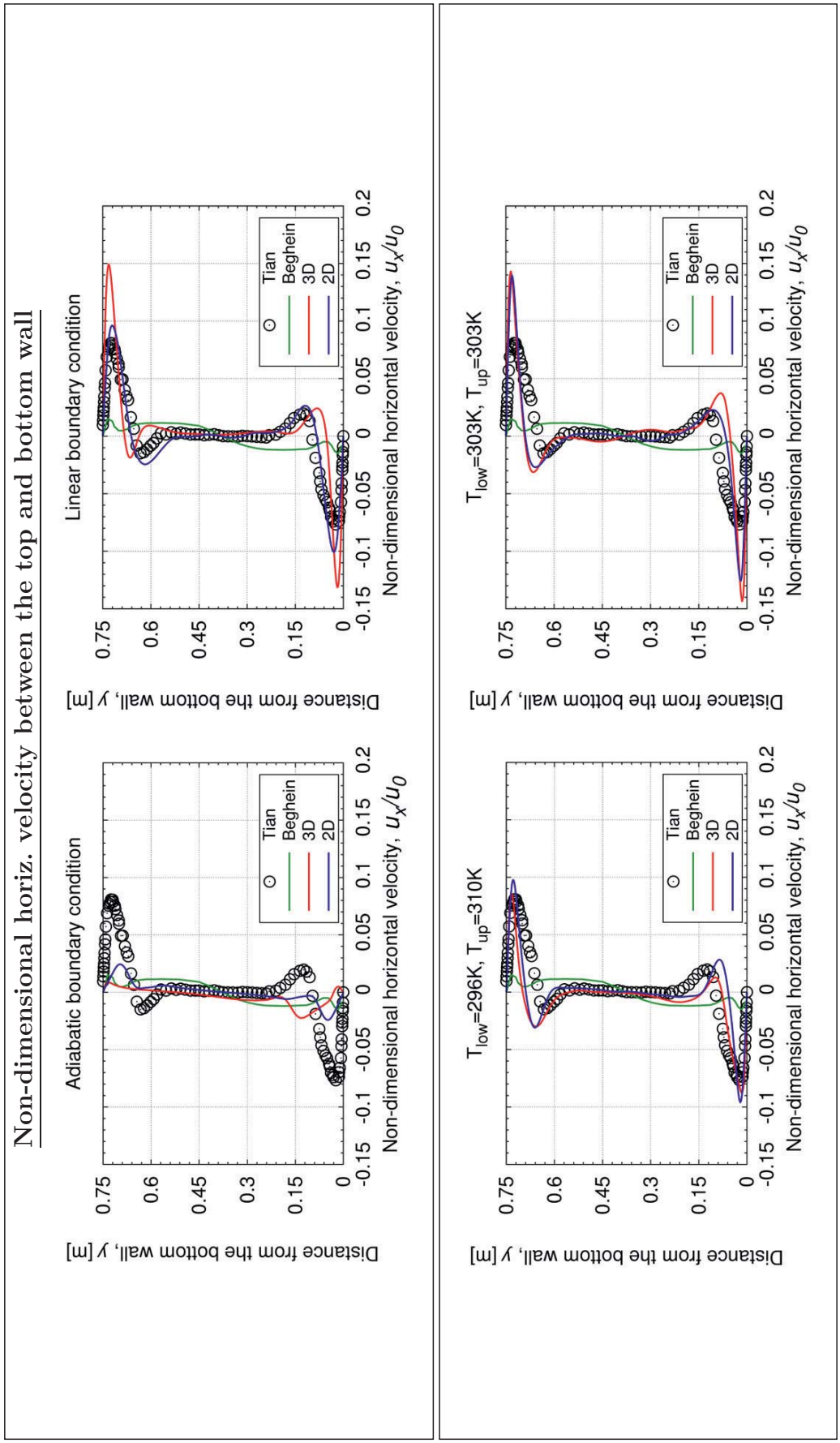

Figure 5.32.: Time-averaged non-dimensional horizontal velocity profile between the top and bottom wall, estimated along the vertical y-axis, at the vertical xy-midplane, at $x = 0.375\,\mathrm{m}$, $z = 0.75\,\mathrm{m}$. **Top box:** Adiabatic bc (left), linear bc (right). **Bottom box:** $T_{\mathrm{low}} = 296\,\mathrm{K}$, $T_{\mathrm{up}} = 310\,\mathrm{K}$ (left), $T_{\mathrm{low/up}} = 303\,\mathrm{K}$ (right). **In all pictures:** - red solid line: 3D simulation, - blue solid line: 2D simulation. ○: study [Tian00a], $\mathrm{Ra} = 1.58 \times 10^9$, - green solid line: study [Beghein93b], $\mathrm{Ra} = 1 \times 10^{10}$.

The results of the 2D and 3D simulation of $T_{\text{low}} = 303\,\text{K}$, $T_{\text{up}} = 303\,\text{K}$ lie close to each other. Near the bottom wall, the profiles of the 2D and 3D simulation are slightly dislocated to each other. Both cases reveal a stationary and a reverse flow region. The last mentioned region is dislocated compared to the experiment of [Tian00a]. In both cases, the stationary flow regions are smaller than in the experiment. In the 2D simulation, the stationary flow region can be detected between the positions of about $y = 0.43\,\text{m}$ and of about $y = 0.33\,\text{m}$. In the 3D simulation, the stationary flow region can be detected between the positions of about $y = 0.55\,\text{m}$ and of about $y = 0.36\,\text{m}$.

The closest approximation to the results of [Tian00a] gives the $T_{\text{low}} = 296\,\text{K}$, $T_{\text{up}} = 310\,\text{K}$ case. The observed reverse flow regions, as well as the peak values, are located in this case closest to the ones of the experiment. But, the peak values exceed the experimental peak values due to the different boundary condition. In both simulation cases, the stationary flow regions are significantly smaller than in the experiment. In the 2D simulation, the stationary flow region can be detected between the positions of about $y = 0.4\,\text{m}$ and of about $y = 0.34\,\text{m}$. In the 3D simulation, the stationary flow region can be detected between the positions of about $y = 0.39\,\text{m}$ and of about $y = 0.37\,\text{m}$.

As before, only small differences appear between the 2D and 3D simulation in this case. In case of the *adiabatic* bc, *linear* bc and $T_{\text{low}} = 296\,\text{K}$, $T_{\text{up}} = 310\,\text{K}$ bc, the stationary flow regions of the 3D simulations are smaller than in case of the 2D simulation. The boundary layers close to the horizontal walls of the 3D simulation lie in case of the $T_{\text{low}} = 296\,\text{K}$ and $T_{\text{up}} = 310\,\text{K}$ bc and $T_{\text{low/up}} = 303\,\text{K}$ bc (at the top wall) within the boundary layers of the 2D simulation. These aspects could possibly be caused by mesh dependencies.

5.4.5. Wall shear stress profile along the heated walls estimated along the vertical axis

Afore in section 5.3.4 from page 112 on, the Nusselt number was discussed which was based on the temperature wall gradients. This section deals now with a variable which is based on the velocity wall gradients, the *wall shear stress*. Note that some of the following presented contents are also discussed in extracts in [Zimmermann14a]. According to [Tian00a], a cubic law can be assumed to formulate the velocity profile in the outer region of the inner boundary layer. Therefore, the shear stress τ along the heated walls $x = 0\,\text{m}$, respectively $x = 0.75\,\text{m}$, is described in [Tian00a] by the following expression for Newtonian fluids

$$\tau_w = \mu \left.\frac{\partial u_y}{\partial x}\right|_{\tilde{\text{w}}}, \quad [\tau_w] = \text{kg/ms}^2, \tag{5.4.1}$$

with the gradient of the vertical velocity component $\left.\frac{\partial u_y}{\partial x}\right|_{\tilde{\text{w}}}$ directly at the heated walls (index $\tilde{\text{w}}$) and a depending dynamic viscosity μ.

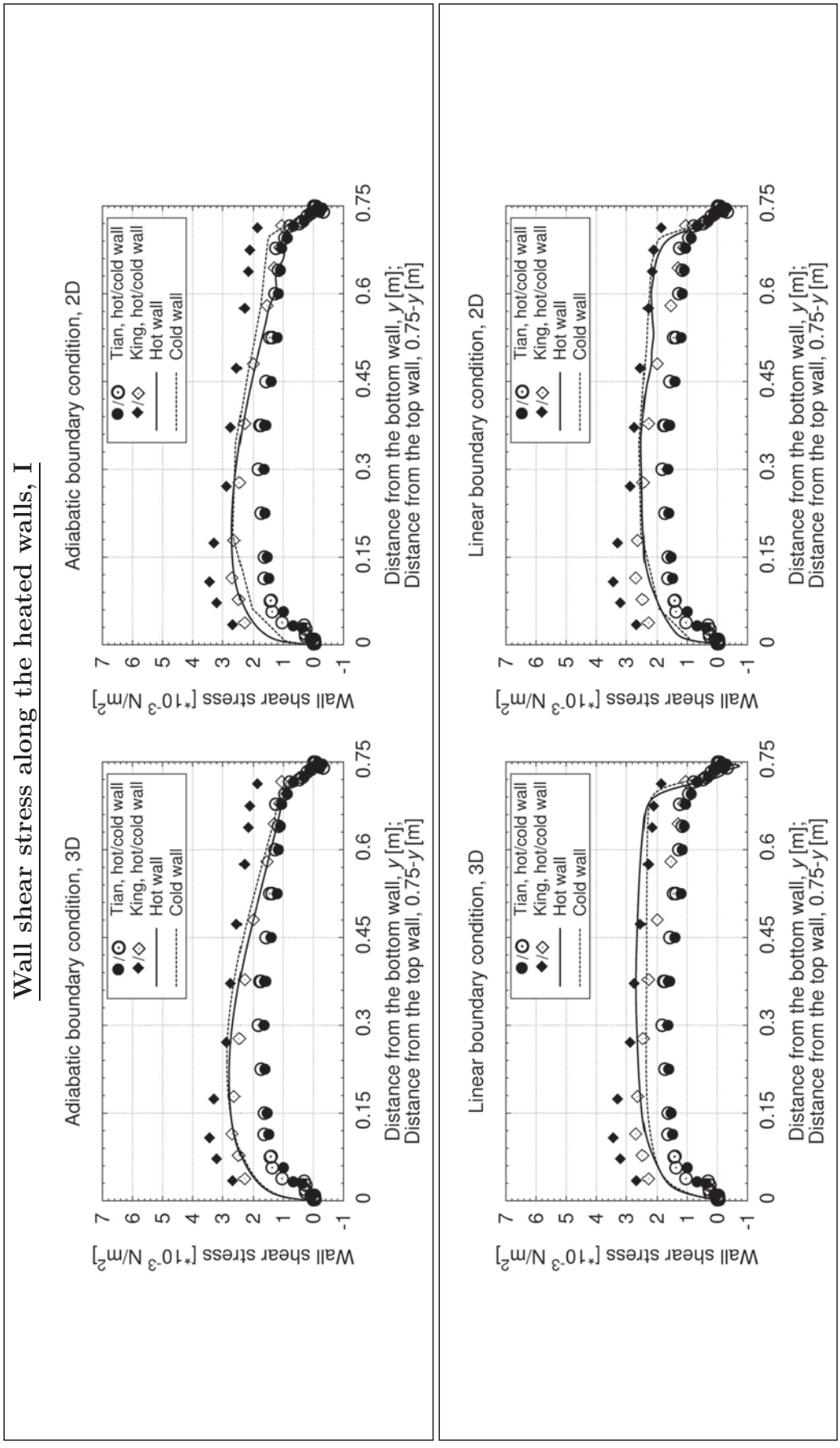

Figure 5.33.: Time-averaged wall shear stress profile estimated along the hot and cold wall, vertical y-axis. **Top box:** Adiabatic bc. **Bottom box:** Linear bc. **In each box:** 3D simulation (left), 2D simulation (right). **In all pictures: -** black solid line: hot wall. **- -** black dashed line: cold wall. Study [Tian00a]: ●: hot wall, ○: cold wall, $\mathrm{Ra} = 1.58 \times 10^9$. Study [King1989]: ◆: hot wall, ◇: cold wall, $\mathrm{Ra} = 4.5 \times 10^{10}$ (as in [Zimmermann14a]).

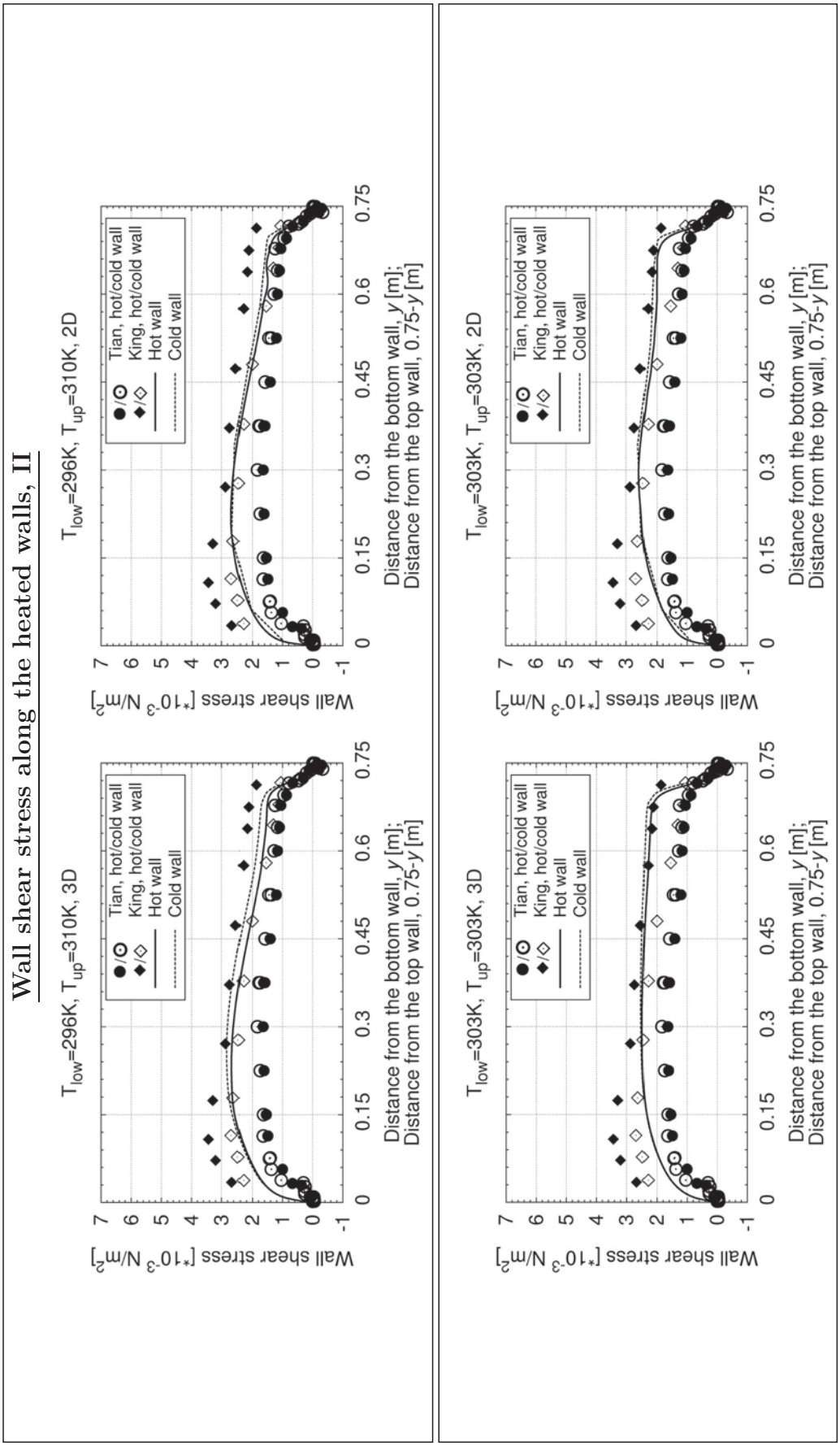

Figure 5.34.: Time-averaged wall shear stress profile estimated along the hot and cold wall, vertical y-axis. **Top box:** $T_{\mathrm{low}} = 296\,\mathrm{K}$, $T_{\mathrm{up}} = 310\,\mathrm{K}$. **Bottom box:** $T_{\mathrm{low/up}} = 303\,\mathrm{K}$. **In each box:** 3D simulation (left), 2D simulation (right). **-** black solid line: hot wall. **- -** black dashed line: cold wall. Study [Tian00a]: ●: hot wall, ○: cold wall, $\mathrm{Ra} = 1.58 \times 10^9$. Study [King1989]: ◆: hot wall, ◇: cold wall, $\mathrm{Ra} = 4.5 \times 10^{10}$.

As the figures 5.33 - 5.34 on pages 144 and 145 illustrate, the shear stress rises, in an analogue manner to the velocity, along the vertical walls to its peak value and then back to zero in the corner regions. The 3D simulation results (black solid lines) are presented together with the ones of the 2D case (black dashed lines) and with the data of two experimental studies. In addition to [Tian00a], another experimental setup of [King1989] is considered. [King1989] examines also a natural convection in a container with aspect ratio of $\mathrm{Ar}_x = 5$ and $\mathrm{Ra} = 3.53 \times 10^8$.

The experimental results in [Tian00a] reveal an asymmetry in the corner regions. Due to the negative values at the top hot and bottom cold corner, *Tian et al.* suppose an anti-clockwise vortex in this region. According to [Tian00a] and as visible in the figures 5.33 - 5.34, the data of [King1989] show higher values than the data in [Tian00a], which are possibly caused by a different investigated Rayleigh number. The differences between the values of [Tian00a] and of [King1989] at the heated walls can be explained by a possible heat loss in the cavity of [King1989] as it is supposed in [Tian00a].

All simulation results of this thesis reveal negative values in the top hot and bottom cold corner which indicate also an anti-clockwise vortex as mentioned in [Tian00a]. The values along the heated walls are higher than the values of [Tian00a], due to higher velocity gradients and higher (temperature dependent) dynamic viscosity values. The simulation values lie closer to the data of [King1989] than to the data of [Tian00a].

The estimated profiles of all simulation cases show an asymmetrical form. For the fixed temperature boundary conditions, the differences between the hot/cold (and also between the 2D/3D cases) appear mainly after midheight ($y = 0.375\,\mathrm{m}$) at both heated walls. In the *adiabatic* bc case, the 2D and 3D simulations deviate significantly from each other at the hot and cold wall. No case approximates best the experimental results. All simulations display deviations along the heated walls. But the fixed boundary cases lie closer to the experimental results than the *adiabatic* simulation, as it was expected due to the similar boundary conditions.

5.5. Concluding comments

In this section, the results of a compressible, non-Boussinesq LES were presented for a turbulent natural convection in an air-filled rectangular container where the vertical walls were heated.

To analyse possible mesh resolution dependencies, additionally to a 3-dimensional simulation also a 2-dimensional simulation was performed. The realised Rayleigh number lied at $\mathrm{Ra} = 1.58 \times 10^9$ with a Prandtl number of $\mathrm{Pr} = 0.71$. The main investigated aspects of this chapter were

1) temperature profile and its fluctuations estimated between the heated walls at the vertical xy-midplane,

2) non-dimensional temperature profile estimated between the top and bottom wall at the vertical xy-midplane,

3) Nusselt number profile estimated along the heated walls as well as top and bottom wall,

4) location of the convection cells,

5) velocity profile and its fluctuations estimated between the heated walls (vertical and horizontal component),

6) investigation of a 2-dimensional flow profile at the vertical xy-midplane,

7) non-dimensional temperature profile estimated between the top and bottom wall at the vertical xy-midplane,

8) wall shear stress profile estimated along the heated walls.

All presented results were time-averaged over an interval of $\Delta t = 200\,\mathrm{s} - 400\,\mathrm{s}$ in the simulated process. For the 3D simulation the intermediate steps size was $\Delta t = 3\,\mathrm{s}$, while it was $\Delta t = 1\,\mathrm{s}$ for the 2D simulations. The results were compared to an comparable experimental setup from [Tian00a], [Tian00b]. In the experiment, the observed setup consisted of a container with conducting later walls. In the simulation, four different related boundary conditions were tested at the later walls. Additionally to the 3-dimensional simulation, a 2-dimensional simulation was executed, to investigate the in [Tian00a] mentioned two-dimensional flow field at the vertical xy-midplane.

In contrast to the results of [Tian00a], the convection cells were dislocated in all cases. This aspect could be caused by the different boundary conditions between experiment and simulation. Regarding the different boundary conditions between the simulations and the experiment in [Tian00a], the results of the analysed fluid properties in all 3D simulations approximated well the experimental results. No simulation case conformed best in all estimated fluid properties with the measured data in [Tian00a].

Summarising, the case of the fixed temperature boundary condition of $T_{\mathrm{low}} = 303\,\mathrm{K}$, $T_{\mathrm{up}} = 303\,\mathrm{K}$ revealed a good approximation in most of the evaluated profiles. The results of the 2-dimensional and 3-dimensional simulations showed in most cases similar results. But the profiles of the velocity as well as temperature fluctuations revealed significant deviations between the 2-dimensional and 3-dimensional simulations.

To analyse the by [Tian00a] assumed 2-dimensional flow field, the vertical velocity component was evaluated at different depth positions in the container. The profile at each

position revealed just small differences to the profiles at the other positions. These deviations appeared mainly close to the horizontal walls. The negligible deviations were a possible indication of a 2-dimensional flow field.

The additionally investigated profiles of the transversal velocity component showed low peak values at different height-positions in the container, but also a distinctive flow boundary layer. In comparison to the vertical and horizontal component, the peak values of the transversal velocity component were about a factor of 10^{-1} smaller. Therefore, a 2-dimensional flow field at the xy-midplane can be assumed.

Concluding, the performed compressible, non-Boussinesq 3-dimensional LES is an adequate choice to model this configuration of a turbulent natural convection in a test case with two vertical, heated walls. The significant deviations between the 3-dimensional and 2-dimensional simulations have to be further investigated to find additional explanations as the certain one of grid dependencies.

6. Case studies - Test case *RayCon*, a Rayleigh - Bénard problem

In an analogues manner to the previous chapter, the numerical non-Boussinesq model of a compressible LES is used in this chapter to analyse the test case of *RayCon*. *RayCon* consists of an an air-filled rectangular container. In contrast to *VerCon*, the heated walls are this time the two horizontal ones. Hence, the temperature gradient points parallel relative to the direction of gravity. This configuration is called a *Rayleigh-Bénard problem* (short: *RB*) problem or a *RB convection*, as it was mentioned before and already discussed in chapter 3, section 3.5.

Because the isothermally heated walls are the horizontal ones in a RB problem, the convective flow is generated against gravity. As mentioned in chapter 3, section 3.5, the fluid inside the test cell is driven by local density differences based on existing temperature differences. Increasing temperature gradients in the near wall region and a convective mass exchange in the bulk outline the heat transmission. Due to this heat transfer turbulent shear layers parallel to the direction of gravity are generated inside the fluid, which increase the intensity of turbulence and dominate the vertical heat flux. In contrast to *VerCon*, the flow does not result in a quasi-steady state flow. Note that some of the following presented results of this chapter are also discussed in extracts in [Zimmermann12] and [Zimmermann15].

6.1. Configuration of *RayCon* and its boundary conditions

A sketch of the computational geometry is displayed in figure 6.1, left picture. The RB cell is realised by an enclosed rectangular container with a length (L) of 2.5 m, a depth (D) of 0.5 m and a height (H) of 0.5 m. Hence, the aspect ratios are $\Gamma_x = \frac{L}{H} = 5$ and $\Gamma_y = \frac{H}{D} = 1$. The working fluid in the container is air. All walls are smooth. The velocity field at all walls is zero due to a non-slip-condition ($\mathbf{u} \equiv 0$). The boundary condition of the total pressure p is taken with a zero gradient-option at all walls, as it was the case before for *VerCon* in chapter 5. The initial field of p inside the computational geometry is assumed to be constant at $1 \cdot 10^5$ Pa. The boundary condition of the dynamic pressure p_{rgh}

is realised by the option *buoyantPressure* (for the description see also chapter 5). Inside the container an almost atmospheric pressure condition is generated. The horizontal walls are heated homogeneously with a constant temperature difference $\Delta T = T_{\text{hot}} - T_{\text{cold}}$, between the lower hot and upper cold wall. Lateral walls are adiabatic.

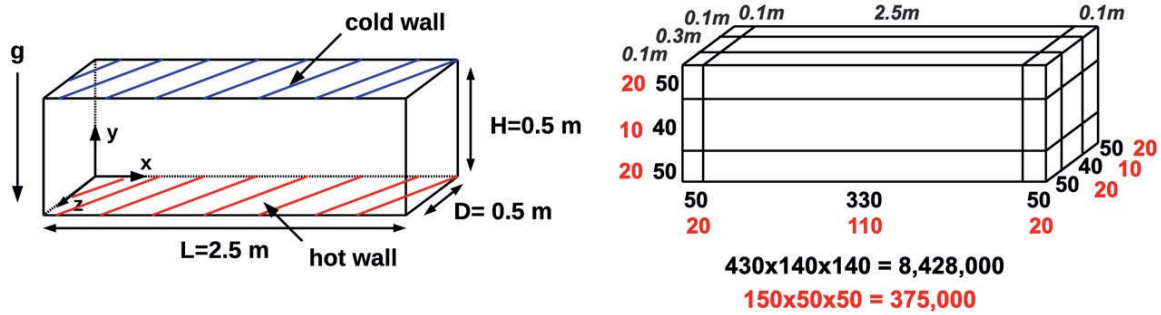

Figure 6.1.: Left: Configuration of *RayCon*. **Right:** Scheme of the computational geometry and mesh resolution with (430 × 140 × 140) cells (black numbers), (150 × 50 × 50) cells (red numbers) (similar to [Zimmermann12], [Zimmermann15]).

Thus, the normal temperature gradient at the side walls is zero. The index w stands for the *lateral wall* in the following. For both side walls and the front/back wall the boundary conditions are

$$\left.\frac{\partial T}{\partial x}\right|_w = 0, \quad \text{for } x = 0\,\text{m} \text{ and } x = 2.5\,\text{m}, \quad \text{with } 0 \leq y \leq 0.5\,\text{m},\ 0 \leq z \leq 0.5\,\text{m},$$
$$\left.\frac{\partial T}{\partial z}\right|_w = 0, \quad \text{for } z = 0\,\text{m} \text{ and } z = 0.5\,\text{m}, \quad \text{with } 0 \leq x \leq 2.5\,\text{m},\ 0 \leq y \leq 0.5\,\text{m}.$$

The investigated Rayleigh numbers are in this study $\text{Ra} = 6.16 \times 10^7$, $\text{Ra} = 1.92 \times 10^8$ and $\text{Ra} = 4.1 \times 10^8$. These numbers were chosen to compare the numerical results to an analogous experiment of [Ebert08] in the end of this chapter. The Prandtl number stays in all cases $\text{Pr} = 0.71$. The turbulent Prandtl number Pr_{sgs} is taken as $\text{Pr}_{\text{sgs}} = 0.4$ (s. chapter 3, section 3.3.2).

6.2. Computational mesh of *RayCon*

The simulation geometry consists of a structured Cartesian mesh which is built of twenty-seven sub-blocks, similar to the previous setup of *VerCon* in chapter 5. The mesh resolution of the computational geometry is indicated in figure 6.1.

The first grid point in vertical direction from the wall should be located as close as possible in vicinity to the wall. But at the same time, a total cell number should be limited to 10 million cells. To observe the influence of the mesh resolution on the numerical results, mainly in close distance to the heated walls, two different grid resolutions are chosen.

Both grids are constructed as indicated in figure 6.1. The fine grid has a resolution of $(430 \times 140 \times 140) = 8,428,000$ cells and the coarser grid one of $(150 \times 50 \times 50) = 375,000$ cells. The first grid point in vertical direction from the wall is located at $y_{w1} = 4.6 \cdot 10^{-4}\,\mathrm{m}$ in case of the fine grid, in case of the coarse grid it lies at $y_{w1} = 1.25 \cdot 10^{-3}\,\mathrm{m}$.

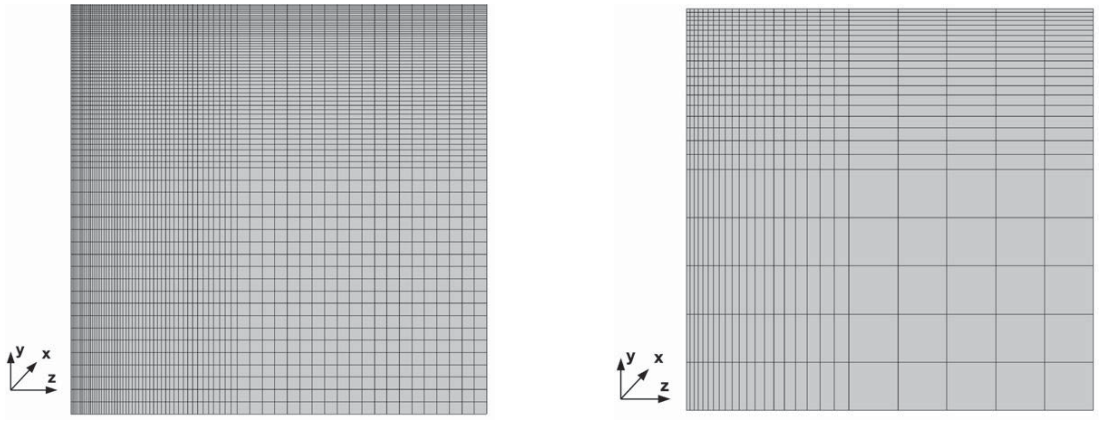

Figure 6.2.: Mesh resolution of the computational geometry of *RayCon*, see figure 6.1, quarter of the left/right side wall. **Left:** $(430 \times 140 \times 140)$ cells. **Right:** $(150 \times 50 \times 50)$ cells.

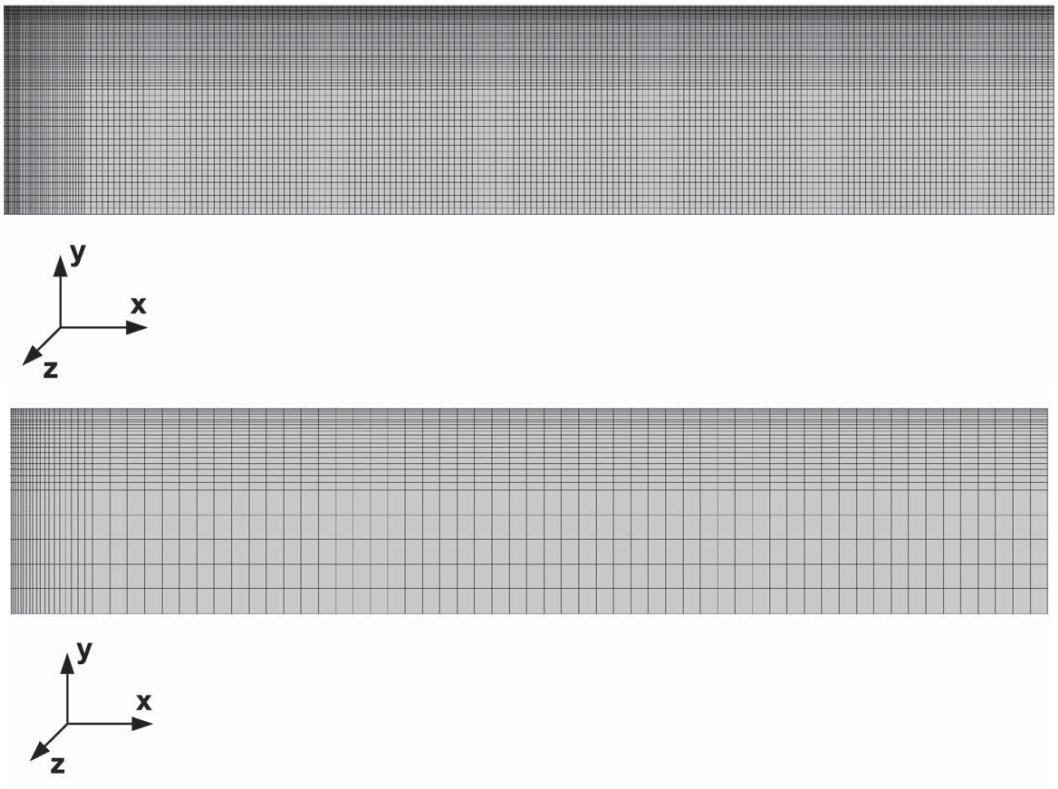

Figure 6.3.: Mesh resolution of the computational geometry of *RayCon*, see figure 6.1, quarter of the lateral (and heated) walls. **Top**: $(430 \times 140 \times 140)$ cells. **Bottom**: $(150 \times 50 \times 50)$ cells.

Because of symmetry aspects, only a quarter of the particular walls with its mesh resolution is displayed in figure 6.2 and figure 6.3. As before in chapter 5, the partition of

the mesh enables an exterior zone in vicinity to all walls where a finer resolution can easily be chosen independently of the other sub-blocks. Mainly near the heated walls, steep temperature gradients and turbulent structures are generated in the thermal boundary layer. Thus, a fine resolution or wall function is essential here. The first layer of cells is cubical formed. Directly at the walls, the mesh is clustered and the cell ratios decrease to the walls to resolve the boundary layers which lie in the first sub-block near the walls. In this way, all relevant turbulent scales can be resolved and no wall functions have to be considered in the computational model. Especially in the corner regions and closely to the walls both grid resolutions reveal their main differences.

Ra	$(\mathbf{430 \times 140 \times 140})$		$(\mathbf{150 \times 50 \times 50})$	
	$t = 200\,\mathrm{s}$	$\Delta t = 200\,\mathrm{s} - 380\,\mathrm{s}$	$t = 200\,\mathrm{s}$	$\Delta t = 200\,\mathrm{s} - 380\,\mathrm{s}$
6.16×10^7	$y^+ = 0.139$	$\bar{y}^+ = 0.122$	$y^+ = 0.382$	$\bar{y}^+ = 0.436$
1.92×10^8	$y^+ = 0.252$	$\bar{y}^+ = 0.245$	$y^+ = 0.679$	$\bar{y}^+ = 0.619$
4.1×10^8	$y^+ = 0.317$	$\bar{y}^+ = 0.339$	$y^+ = 0.689$	$\bar{y}^+ = 0.941$

Table 6.1.: Non-dimensional distance y^+ estimated in y_{w1} for different Rayleigh numbers (Ra) in the fully turbulent flow at $t = 200\,\mathrm{s}$ and as averaged value over $\Delta t = 200\,\mathrm{s} - 380\,\mathrm{s}$.

Table 6.1 contains an overview of the non-dimensional wall distance y^+ estimated in the first cell midpoint y_{w1} for all investigated Rayleigh numbers in the fully turbulent flow in the simulated process (s. chapter 3, section 3.5, 3.5.3.2, eq. (3.5.26) on page 84). The values are calculated in the first cell midpoint y_{w1} at $x = 1.185\,\mathrm{m}$, $z = 0.25\,\mathrm{m}$. At this position the observed fluid properties are also estimated in the following. It is for all values $y^+ < 1$ in y_{w1} (see also chapter 5, section 5.1, 5.2). The size of one cell is nowhere bigger than ten-times of the size of the Kolmogorov length. The simulation considers, as mentioned before, a non-Boussinesq-approximation (s. chapter 1, section 1.7, from page 18 on). Consequently, fluid properties, as density ρ, thermal expansions coefficient β, thermal diffusion coefficient α and dynamic viscosity μ are assumed to be temperature dependent. The temperature dependence is considered by the Sutherland model from chapter 1, section 1.9 from page 24 on.

6.3. Temperature profile

6.3.1. Temperature distribution between the heated walls estimated at different positions, vertical axis

As before, the main attention of the computational investigation lies on the temperature distribution between the two horizontal, isothermally heated walls in the container. Figure 6.4 presents the unsteady dominant turbulent flow in the computational setup of *RayCon*.

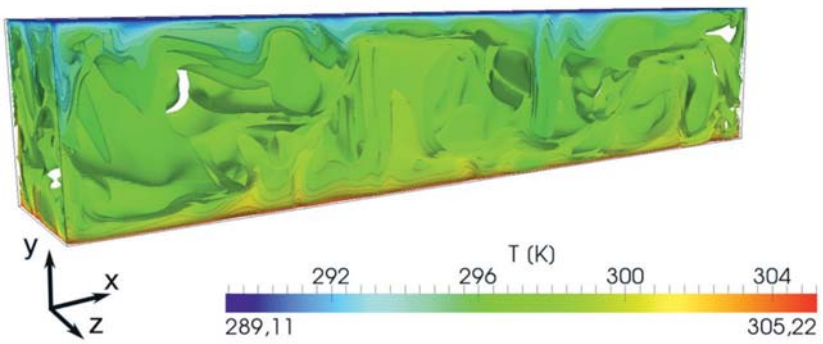

Figure 6.4.: Instantaneous temperature profile visualised by iso-surfaces, simulation data of $\mathrm{Ra} = 1.92 \times 10^8$ at $t = 380\,\mathrm{s}$, $(430 \times 140 \times 140)$ cells (see also [Zimmermann15]).

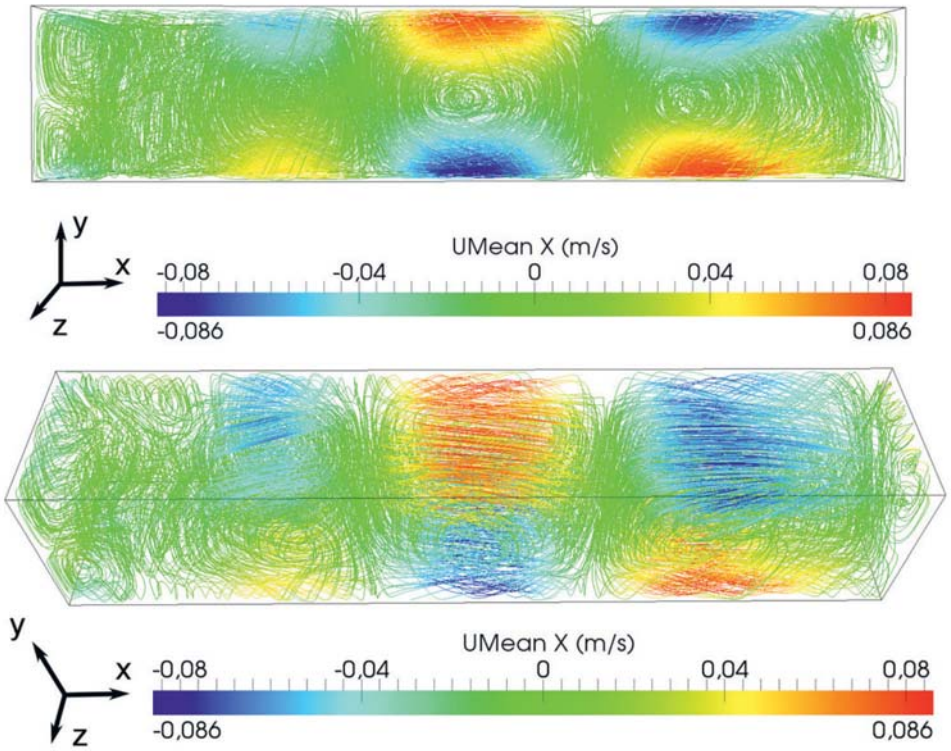

Figure 6.5.: Snapshots of the instantaneous mean horizontal velocity distribution, simulation data of $\mathrm{Ra} = 1.92 \times 10^8$ at $t = 380\,\mathrm{s}$, $(430 \times 140 \times 140)$ cells. **Top row:** Front view. **Bottom row:** Top view (see also [Zimmermann15]).

It displays a snapshot of the instantaneous temperature field between the heated walls at $t = 380\,\mathrm{s}$ in the simulated process indicated by the temperature iso-surfaces for the case of $\mathrm{Ra} = 1.92 \times 10^8$ and $(430 \times 140 \times 140)$ cells. An iso-surfaces connects locations of the grid with each other which have in one time instant the same temperature value. Note that some of the following contents in this section are also presented in extracts in [Zimmermann12] and [Zimmermann15]. Table 6.2 lists the temperature boundary conditions at the hot and cold wall for the investigated Rayleigh numbers. Figure 6.5 shows a snapshot of the mean horizontal velocity distribution in the container at $t = 380\,\mathrm{s}$ in the

simulated process exemplary for case Ra $= 1.92 \times 10^8$. The velocity values shown are time-averaged until the exposed time-step. Three convection cells are visible. They are 3-dimensional and have a thickness of the amount of the computational geometry depth of $D = 0.5\,\mathrm{m}$. They are located next to each other along the length-side of the geometry. With help of the velocity distribution in the container, the next section discusses the temperature profile estimated at different positions at the vertical cross-section.

Rayleigh number Ra	**ΔT** [K]	**T cold wall** [K]	**T hot wall** [K]
6.16×10^7	4.83	290.44	295.27
1.92×10^8	16.11	305.22	289.11
4.1×10^8	41.15	288.10	329.25

Table 6.2.: Temperature boundary conditions at the hot and cold wall.

Temperature profile estimated at position $\mathbf{x = 1.185\,m}$, $\mathbf{z = 0.25\,m}$

Figure 6.6 establishes the time-averaged temperature profile between the heated walls estimated along the vertical y-axis at the xy-midplane at $x = 1.185\,\mathrm{m}$, $z = 0.25\,\mathrm{m}$ for both grids. The values are averaged over a time interval of $\Delta t = 200\,\mathrm{s} - 380\,\mathrm{s}$ in the simulated process respecting the settlement of the system. The results of the fine grid resolution are marked by solid lines. The coarse grid results are marked by the dashed lines. All temperature gradients show no anti-symmetrical form, like it was expected for a non-Boussinesq RB convection according to [Ahlers06]. This behaviour is further discussed in the following section 6.3.2.

Noteworthy are the major grid dependencies in close distance to the heated walls. The importance of a sufficiently fine grid can clearly be seen at the cold wall. The coarse grid results reveal in all cases smaller temperature gradients at the cold wall and steeper temperature gradients at the hot wall than the fine grid results. With increasing Rayleigh numbers, the temperature gradients of both resolutions deviate more from each other. In the bulk region, the profiles reach an almost constant temperature and almost no deviations can be detected.

To investigate these deviations between both grid resolutions further, the distribution of the mean velocity inside the container is examined next. On the basis of the mean velocity distribution the *circulation zones* or rather *convection cells* can be sketched by stream tracers at the vertical cross-section in the container. These convection cells are typical for a natural convection and were introduced before in chapter 3, section 3.5, on page 82.

Based on the presentation of the mean velocity distribution in figure 6.5, the next section discusses the distribution of convection cells in the container for each case and both grid resolutions. Besides the discussion of the time-averaged velocity distribution, the temperature profile is estimated additionally to position $x = 1.185\,\mathrm{m}$ at the mirror-imaged

position, $x = 1.315\,\mathrm{m}$. Because the setup of *RayCon* is symmetrical, similar temperature profiles at both mirror-imaged positions are expected. The results are displayed in the next section in figures 6.9 - 6.15 on pages 157 - 161.

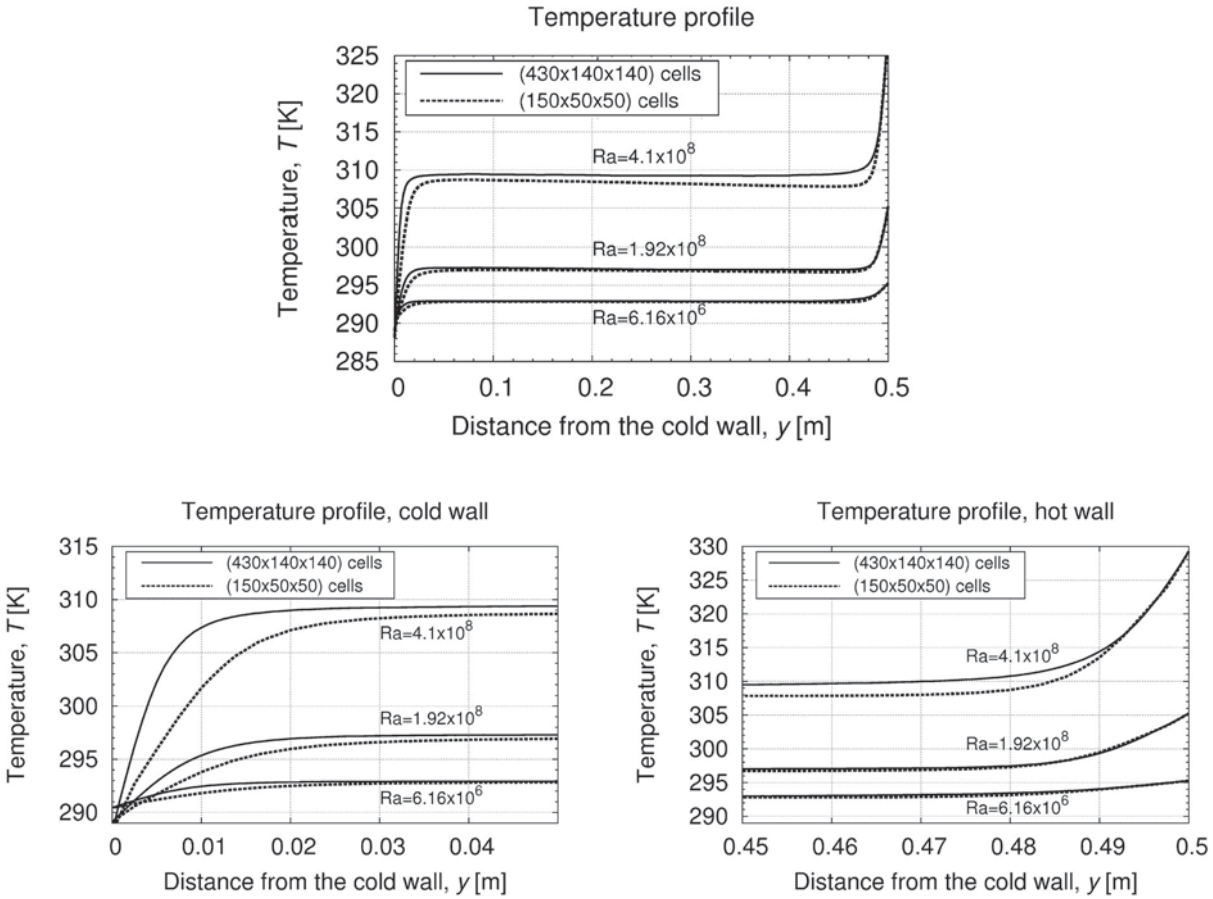

Figure 6.6.: Time-averaged temperature profile between the heated walls at the vertical xy-midplane at $x = 1.185\,\mathrm{m}$, $z = 0.25\,\mathrm{m}$. **Top:** Overview. **Bottom:** Detailed plot of the temperature profile at the cold (left) and hot wall (right). **In all pictures: -** solid lines: $(430 \times 140 \times 140)$ cells, **- -** dashed lines: $(150 \times 50 \times 50)$ cells (similar to [Zimmermann12], [Zimmermann15]).

Coherent structures in the test case and temperature profiles at position $\mathrm{x} = 1.185\,\mathrm{m}$ versus position $\mathrm{x} = 1.315\,\mathrm{m}$

The number of visible circulation zones, or convection cells, varies during the evolution time. The height/width ratio of these zones is changing from a factor slightly lower than 1 to a factor near 1.5. Because the ratio of container length and cell width is not an integer, a small gap δ can be generated at one side of the container. In this area no structured flow can be detected. The convection cell distribution will show, that the detected major grid dependencies between the estimated temperature distributions are caused in both resolution types by different quasi stable-states in the setup. These quasi stable-states are analysed in the following on the basis of the velocity distribution.

Rayleigh number Ra= 6.16×10^7

Figure 6.7 displays the circulation zones for the case of Ra $= 6.16 \times 10^7$ and a mesh resolution of $(430 \times 140 \times 140)$ cells.

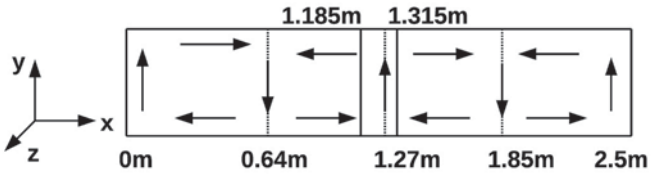

Figure 6.7.: Convection cells in the container for Ra $= 6.16 \times 10^7$ and $(430 \times 140 \times 140)$ cells (see also [Zimmermann15]).

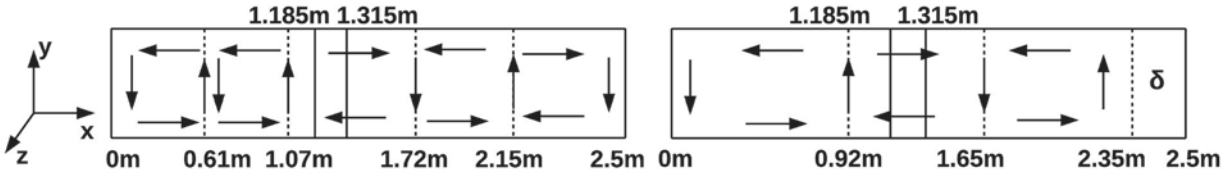

Figure 6.8.: Convection cells in the container for Ra $= 6.16 \times 10^7$, $(150 \times 50 \times 50)$ cells (see also [Zimmermann15]). In the beginning of the simulated process, at $t = 200\,\mathrm{s}$, (left) and in the end of the simulation, at $t = 380\,\mathrm{s}$, (right).

The convection cells are displayed on the basis of the estimation of the mean velocity distribution at the vertical cross section. The velocity values of all results were each time-averaged until the investigated shown time-step. In all figures, both mirror-imaged positions, $x = 1.185\,\mathrm{m}$ and $x = 1.315\,\mathrm{m}$, are marked.

In the beginning of the simulation, four convection cells arise in the container and exist until the end of the simulated process at $t = 380\,\mathrm{s}$. No δ-area is detectable. The cells are almost of the same size. The arrows in figure 6.7 (and in the following figures) stand for the negative or positive circulation direction of the cells related to the coordinate system in the container, as it is indicated in figure 6.1. In the beginning of the coarse grid simulation, four convection cells exist in the setup and no δ-area is visible. All cells are almost of the same size. At $t = 380\,\mathrm{s}$ in the simulated process, the cell number has been changed from four to three. On the right side of the container a δ-area with a width of $0.15\,\mathrm{m}$ can be seen. Next, the differences between the temperature profiles ob both simulation types at position $x = 1.185\,\mathrm{m}$ are discussed on the basis of the presented circulation zones.

It will be seen, that the differences between the temperature profiles of both mesh resolutions result from different cell structures existing at the investigated location. Regarding figure 6.8 and the fine grid at the end of the simulation, position $x = 1.185\,\mathrm{m}$ lies near the edge of one circulation zone. At the coarse grid, this position is located closer to the centre

of a circulation zone. At both isothermal walls, the values of the coarse grid resolution show steeper temperature gradients and thus smaller values than in case of the fine grid (see section 6.3.1, figure 6.6 on page 155). Regarding the opposite circulation direction of the cells at position $x = 1.185\,\mathrm{m}$ and both grid resolutions, the air layers at the cold wall have a longer exposition time and at the hot wall a shorter exposition time than in case of the fine grid.

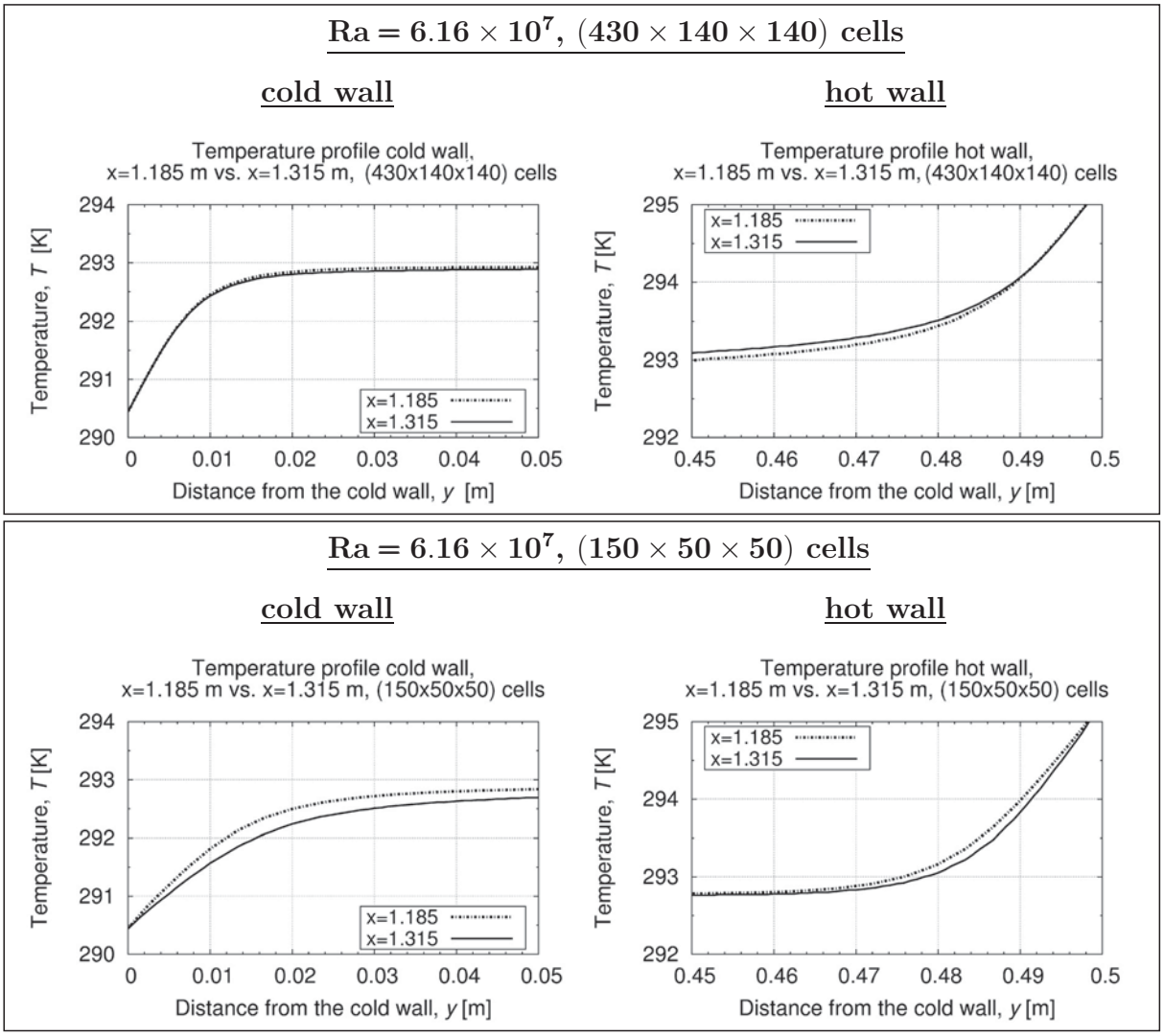

Figure 6.9.: Time-averaged temperature profile at the vertical xy-midplane, at the positions $x = 1.185\,\mathrm{m}$, $x = 1.315\,\mathrm{m}$ ($z = 0.25\,\mathrm{m}$) for the cold (left) and hot (right) wall. $\mathbf{Ra = 6.16 \times 10^7}$ (as in [Zimmermann15]). **Top box:** $(430 \times 140 \times 140)$ cells. **Bottom box:** $(150 \times 50 \times 50)$ cells.

As next step, the temperature profiles estimated at both mirror-imaged positions at the xy-midplane, $x = 1.185\,\mathrm{m}$ and $x = 1.315\,\mathrm{m}$, are plotted against each other in figure 6.9. Because the setup has a symmetrical layout, similar temperature profiles would be expected at both mirror-imaged positions. The results obtained at position $x = 1.185\,\mathrm{m}$ are marked by the dashed black line. The results at position $x = 1.315\,\mathrm{m}$ are marked

by the solid black line in figure 6.9. In case of the cold wall and fine grid resolution, the values estimated at $x = 1.185\,\mathrm{m}$ lie above the values estimated at $x = 1.315\,\mathrm{m}$, while they lie beneath them in case of the hot wall. In figure 6.7, both mirror-imaged positions are located near the end of one convection cell. Therefore, the temperature profiles of both positions show at the cold wall only small differences. At the hot wall, the values at position $x = 1.185\,\mathrm{m}$ are lower than the values at $x = 1.315\,\mathrm{m}$. Possibly, the air layers at $x = 1.185\,\mathrm{m}$ are influenced already by ascending air layers of the neighbour cell.

In case of the coarse grid resolution, a deviation between both locations can clearly be seen. At position $x = 1.185\,\mathrm{m}$, the values lie over the values at position $x = 1.315\,\mathrm{m}$ at both heated walls. This aspect could possibly be caused by a longer exposition time of the air layers at the hot wall and a shorter exposition time of the air layers at the cold wall for position $x = 1.185\,\mathrm{m}$. Regarding the convection cell distribution, the differences between the temperature profiles at both estimated positions result from different cell structures existing at these locations.

Rayleigh number Ra$= 1.92 \times 10^8$

In figure 6.10, the cell distribution in the container is presented for $\mathrm{Ra} = 1.92 \times 10^8$ and the fine grid.

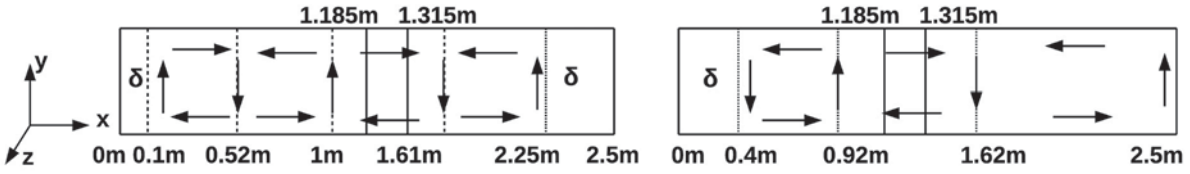

Figure 6.10.: Convection cells in the container for $\mathrm{Ra} = 1.92 \times 10^8$, $(430 \times 140 \times 140)$ cells (see also [Zimmermann15]). In the beginning of the simulated process, at $t = 200\,\mathrm{s}$, (left) and in the end of the simulation, at $t = 380\,\mathrm{s}$, (right).

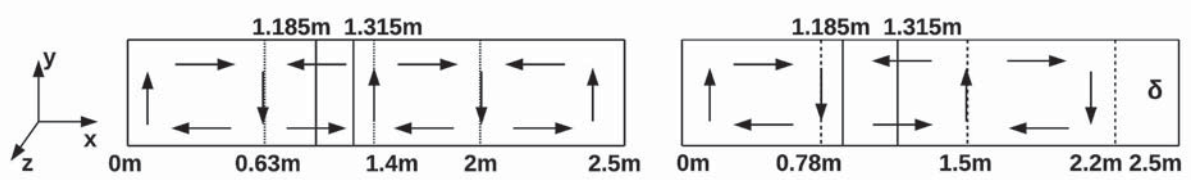

Figure 6.11.: Convection cells in the container for $\mathrm{Ra} = 1.92 \times 10^8$, $(150 \times 50 \times 50)$ cells (see also [Zimmermann15]). In the beginning of the simulated process, at $t = 200\,\mathrm{s}$, (left) and in the end of the simulation, at $t = 380\,\mathrm{s}$, (right).

In the beginning of the simulated process, four convection cells arise whose ratios increase from left to right. A δ-area of about 0.25 m arise at the right side of the container as well as one of about 0.1 m at the left side. At $t = 380\,\mathrm{s}$ in the simulated process, both cells on

the right side has been merged together and the size of the middle cell has grown. A δ-area unfolds at the left side of the container. It has a width of 0.4 m. The coarse grid shows four convection cells in the beginning of the simulated process (s. figure 6.11), no δ-area is visible. At $t = 380\,\mathrm{s}$ a δ-area of about 0.3 m exists at the right side of the box. The number of cells is reduced to three which are all of almost the same size. In figure 6.6 on page 155, the temperature profiles of both resolution types reveal no significant deviations at the hot wall. The results of the coarse grid lie slightly beneath the ones of the fine grid.

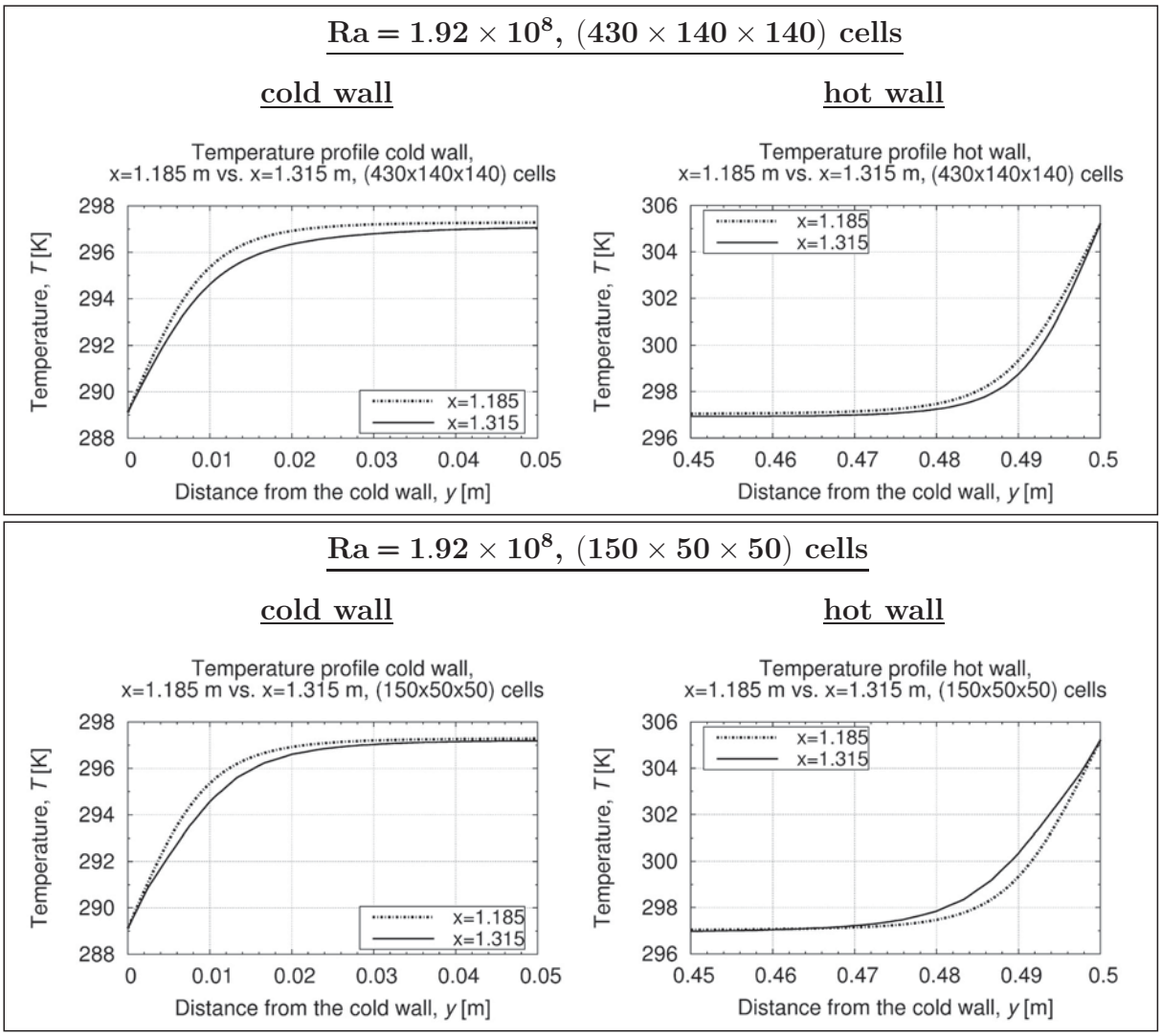

Figure 6.12.: Time-averaged temperature profile at the vertical xy-midplane, at the positions $x = 1.185\,\mathrm{m}$, $x = 1.315\,\mathrm{m}$ ($z = 0.25\,\mathrm{m}$) for the cold (left) and hot (right) wall. $\mathbf{Ra = 1.92 \times 10^8}$ (as in [Zimmermann15]). **Top box:** $(430 \times 140 \times 140)$ cells. **Bottom box:** $(150 \times 50 \times 50)$ cells.

At the cold wall significant deviations can be seen between both resolutions with higher values at the fine grid. In case of the fine grid, position $x = 1.185\,\mathrm{m}$ lies slightly closer to the middle of one convection cell than it is the case at the coarse grid (see in figure 6.11). In case of the coarse grid and $x = 1.185\,\mathrm{m}$, the air layers have a possibly shorter exposition

time at the hot wall (and hence reveal smaller temperatures) and a longer exposition time at the cold wall than in case of the fine grid resolution (and hence reveal smaller temperatures). The at both mirror-imaged positions, $x = 1.185\,\mathrm{m}$ and $x = 1.315\,\mathrm{m}$, estimated temperature profiles are illustrated in figure 6.12. Deviations are visible at both heated walls in case of both resolutions. The results of the fine grid and position $x = 1.185\,\mathrm{m}$ are higher than the values at $x = 1.315\,\mathrm{m}$ at both walls. In case of the coarse grid, the values at $x = 1.185\,\mathrm{m}$ are higher than at position $x = 1.315\,\mathrm{m}$ at the cold wall, which is vice versa at at the hot wall.

The distribution of the mirror-imaged positions at the fine grid is similar to the one in case $\mathrm{Ra} = 6.16 \times 10^7$ and the coarse grid. Hence, analogous conclusions about the influences on the temperature profiles can be made at this point. The air layers at $x = 1.185\,\mathrm{m}$ have a longer exposition time at the hot wall and a shorter exposition at the cold wall. At the coarse grid and the hot wall, the temperature values at position $x = 1.185\,\mathrm{m}$ lie beneath the ones at position $x = 1.315\,\mathrm{m}$ due to a shorter exposition time. At the cold wall, the temperature values at position $x = 1.185\,\mathrm{m}$ lie over the ones at position $x = 1.315\,\mathrm{m}$. This aspect could be possibly caused by influencing descending air layers of the neighbour cell at $x = 1.315\,\mathrm{m}$ Position $x = 1.185\,\mathrm{m}$ lies closer to the edge of one cell than position $x = 1.315\,\mathrm{m}$.

Rayleigh number Ra$= 4.1 \times 10^8$

Figure 6.13 displays the circulation zones for $\mathrm{Ra} = 4.1 \times 10^8$ and the fine grid resolution.

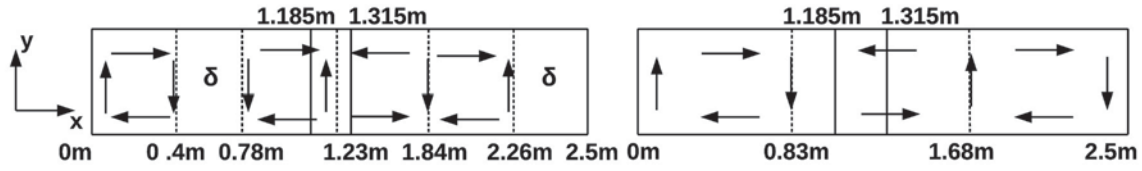

Figure 6.13.: Convection cells in the container for $\mathrm{Ra} = 4.1 \times 10^8$, $(430 \times 140 \times 140)$ cells (see also [Zimmermann15]). In the beginning of the simulated process, at $t = 200\,\mathrm{s}$, (left) and in the end of the simulation, at $t = 380\,\mathrm{s}$, (right).

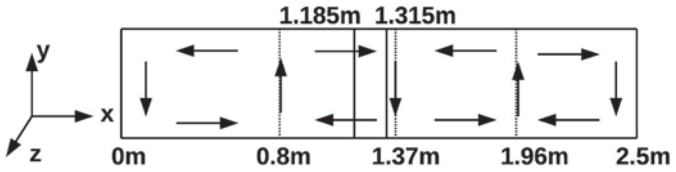

Figure 6.14.: Convection cells in the container for $\mathrm{Ra} = 4.1 \times 10^8$, $(150 \times 50 \times 50)$ cells (see also [Zimmermann15]).

In the beginning of the simulation, four cells are visible and two δ-area exist of about 0.38 m and 0.24 m. At $t = 380$ s in the simulated process, the number of cells has been changed to three which are all almost of the same size. A δ-area cannot be seen. The cell distribution of the coarse grid is sketched in figure 6.14. Four convection cells exist from the beginning of the simulated process until its end. The left cell has the biggest ratio while the other three cells are almost of the same size. No δ-area can be detected.

Comparing the location of position 1.185 m in the end of the simulated process for both resolutions related to the convection cell distribution, it can be seen that this position lies almost at the same location for both grids. Hence, one would expect similar temperature values at this position in both resolution types. But the values of the coarse grid are smaller than the values of the fine grid at both heated walls.

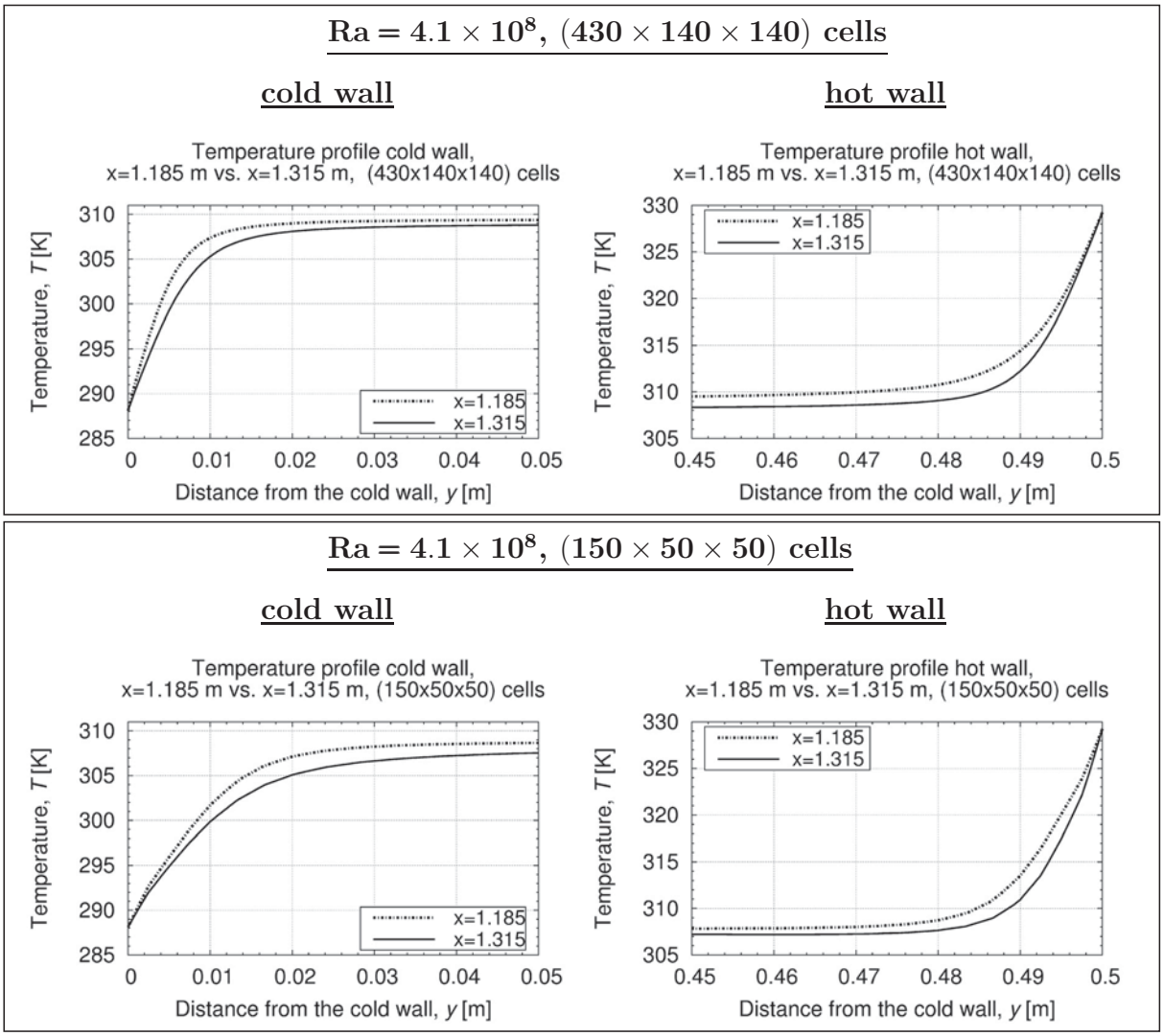

Figure 6.15.: Time-averaged temperature profile at the vertical xy-midplane, at the positions $x = 1.185$ m, $x = 1.315$ m ($z = 0.25$ m) for the cold (left) and hot (right) wall. $\mathbf{Ra = 4.1 \times 10^8}$ (as in [Zimmermann15]). **Top box:** $(430 \times 140 \times 140)$ cells. **Bottom box:** $(150 \times 50 \times 50)$ cells.

The higher values at the cold and hot wall in case of the fine grid might be a possible consequence of a higher heat transmission than in case of the coarse grid. The temperature profiles of both grid resolutions estimated at the mirror-imaged positions, $x = 1.185\,\mathrm{m}$ and $x = 1.315\,\mathrm{m}$, are plotted in figure 6.15. Major grid dependencies appear also in this case which are distinctive this time. This dependencies are produced by the observed different quasi stable-states. The results at position $x = 1.185\,\mathrm{m}$ exceed the ones at position $x = 1.315\,\mathrm{m}$ in case of both grid resolutions and both heated walls. Regarding the fine grid, higher values can be seen at $x = 1.185\,\mathrm{m}$ than at position $x = 1.315\,\mathrm{m}$ at both heated walls (s. figure 6.15). At the beginning of the simulation, both positions are located near the end of two circulation zones. In the end of the simulation both positions lie in the middle of one cell. This transmission cause possibly the higher values at position $x = 1.185\,\mathrm{m}$ in case of the fine grid.

In case of the coarse grid, higher values arise at position $x = 1.185\,\mathrm{m}$ than at position $x = 1.315\,\mathrm{m}$ at both heated walls. Position $x = 1.185\,\mathrm{m}$ lies closer to the middle of one cell than position $x = 1.315\,\mathrm{m}$. At the hot wall, the higher values are caused by a longer exposition time of air layers at this wall and a higher heat transmission than at position $x = 1.315\,\mathrm{m}$. At the cold wall, the higher values at position $x = 1.185\,\mathrm{m}$ are caused by a shorter exposition time of the air layers at the cold wall than at position $x = 1.315\,\mathrm{m}$.

Concluding, the analysed distribution of convection cells shows that the deviations between the temperature profiles at both mirrored-imaged positions are caused by different quasi-stable states which are generated during the simulation process in the container. These altered quasi-stable states produce further the deviations between both mesh resolutions. The schemes of the convection cells in figures 6.7 - 6.14 show for each Rayleigh number an opposite circulation direction at the hot, respectively cold, wall between the fine and coarse grid resolution at $x = 1.185\,\mathrm{m}$. This aspect could also be observed for position $x = 1.315\,\mathrm{m}$, except in case of $\mathrm{Ra} = 6.16 \times 10^7$. These opposite directions have also an influence of the deviations between both grid resolutions. Because different coherent structures exist in the container at the analysed positions and reveal additionally in some cases an opposite circulation orientation, the reproducibility of the temperature profiles is destroyed between both mesh resolutions and also between both mirrored-imaged positions.

6.3.2. Investigation of non-Boussinesq-effects in the fluid on the basis of the temperature profile

This section deals with the further investigation of the before in section 6.3.1 mentioned asymmetrical temperature profiles. [Ahlers06] reports in his study also a not anti-symmetrical, but rather asymmetrical temperature profile for a strongly turbulent non-Boussinesq RB convection (short: *NOB*) in water and glycerol for investigated Rayleigh

numbers between $10^8 \leq \mathrm{Ra} \leq 10^{11}$. *Ahlers et al.* state in [Ahlers06] that the thermal boundary layer thickness varies, because the values of the heat conductivity λ vary also against the height of the container. Another reason can be found in the temperature values which decrease across the thermal boundary layer. This aspect is caused by NOB effects in the fluid according to [Ahlers06].

To determine these effects, the following variables are analysed. In a NOB convection, the mean temperature $T_{\mathrm{mean}} = \dfrac{T_{\mathrm{hot}} - T_{\mathrm{cold}}}{2} + T_{\mathrm{cold}}$ between the hot and cold wall does not equal usually the temperature in the centre of the container (denoted by T_{centre}), as it is the case in an OB convection (see also chapter 3, section 3.5, 3.5.3.1). The temperature T_{centre} is defined in [Ahlers06] as

$$T_{\mathrm{centre}} = T_{\mathrm{hot}} - \Delta_{\mathrm{hot}} \; = \; T_{\mathrm{cold}} + \Delta_{\mathrm{cold}} \, ,$$

where Δ_{hot} is the temperature change across the bottom hot boundary layer and Δ_{cold} is the temperature change across the top cold boundary layer. In general, T_{centre} can be smaller or larger than T_{mean}, due to different properties of each working fluid according to [Ahlers06]. For example, [Wu1991] reports that it is $\Delta_{\mathrm{hot}} < \Delta_{\mathrm{cold}}$ for a NOB in cryogenic helium. [Zhang1997], on the contrary, observes the inverted relation $\Delta_{\mathrm{hot}} > \Delta_{\mathrm{cold}}$ in a NOB convection in glycerol. The total temperature change inside the container is defined, according to *Ahlers et al.* [Ahlers06], as

$$\chi = \chi_{\Delta} = \Delta_{\mathrm{hot}} / \Delta_{\mathrm{cold}} \, . \tag{6.3.1}$$

Ahlers et al. assume, that the total temperature difference between both heated walls can be formulated as the sum of the temperature changes across the thermal boundary layers. In the bulk region, the temperature is almost constant. Thus, the total temperature difference has to be as mentioned in [Ahlers06]

$$\Delta = \Delta_{\mathrm{cold}} + \Delta_{\mathrm{hot}} \, . \tag{6.3.2}$$

With equations (6.3.1) and (6.3.2) *Ahlers et al.* formulate in [Ahlers06] and expression of the temperature change in the top cold and bottom hot boundary layers

$$\Delta_{\mathrm{hot}} = \frac{\chi}{1+\chi}\Delta \, , \quad \Delta_{\mathrm{cold}} = \frac{1}{1+\chi}\Delta \, . \tag{6.3.3}$$

The table 6.3 on page 164 presents the noticed temperature drops in the simulation in case of the fine grid (estimated according to equation (6.3.1) and (6.3.3)). It stands out, that the temperature change of the hot boundary layer is smaller than the one of the cold boundary layer $\Delta_{\mathrm{hot}} < \Delta_{\mathrm{cold}}$ in case of $\mathrm{Ra} = 6.16 \times 10^7$ and $\mathrm{Ra} = 4.1 \times 10^8$. But in case of $\mathrm{Ra} = 1.92 \times 10^8$, this relation is inverted $\Delta_{\mathrm{hot}} > \Delta_{\mathrm{cold}}$. Hence, no uniform statement can

be made for the NOB convection concerning the fine grid resolution. On the contrary, all cases of the coarse grid resolution satisfy the relation $\Delta_{\mathrm{hot}} > \Delta_{\mathrm{cold}}$. The particular values of these cases can be found in table 6.4.

(430 × 140 × 140) cells Ra	$T_{\mathrm{mean}}[K]$	$T_{\mathrm{centre}}[K]$	$\Delta_{\mathrm{hot}}[K]$	$\Delta_{\mathrm{cold}}[K]$	χ
6.16×10^7	292.86	292.91	2.36	2.47	0.96
1.92×10^8	297.17	297.08	8.14	7.97	1.02
4.1×10^8	308.63	309.24	19.92	21.14	0.95

Table 6.3.: Temperature change across the boundary layers according to [Ahlers06] for diverse Rayleigh numbers, (430 × 140 × 140) cells.

(150 × 50 × 50) cells Ra	$T_{\mathrm{mean}}[K]$	$T_{\mathrm{centre}}[K]$	$\Delta_{\mathrm{hot}}[K]$	$\Delta_{\mathrm{cold}}[K]$	χ
6.16×10^7	292.86	292.84	2.43	2.4	1.01
1.92×10^8	297.17	296.93	8.29	7.82	1.06
4.1×10^8	308.63	308.31	20.85	20.21	1.03

Table 6.4.: Temperature change across the boundary layers according to [Ahlers06] for diverse Rayleigh numbers, (150 × 50 × 50) cells.

6.3.3. Analytical model of the non-dimensional temperature profile

To validate the computational results of the estimated temperature profiles, they are compared to an analytical function. Note that some of the following results are also discussed in extracts in [Zimmermann12] and [Zimmermann15].

In [Hölling06] and [Hölling05] analytical functions are given for the temperature distribution in the thermal boundary layer near the heated walls for a RB problem with constant fluid properties. In the simulations of this thesis temperature dependent fluid properties are used. To compare the analytical function of [Hölling06] and [Hölling05] with the simulation results, the fluid properties of the simulation are time-averaged over an interval of $\Delta t = 200\,\mathrm{s} - 380\,\mathrm{s}$ and subsequently averaged over the distance between the heated walls. The following proceeding is based on the boundary layer theory presented in chapter 3, section 3.5, 3.5.3.2 from page 83 on. But at this point, a RB convection with horizontal heated walls is regarded. *Hölling et al.* define in [Hölling06] a characteristic temperature T_{ref} based on the wall heat flux and the following characteristic fluid properties

$$T_{\mathrm{ref}} = \left(\frac{\nu\kappa}{g\beta}\right)^{(1/4)} \left(\left.\frac{\partial T}{\partial y}\right|_{\tilde{\mathrm{w}}}\right)^{(3/4)} = \left(\mathrm{L}\left.\frac{\partial T}{\partial y}\right|_{\tilde{\mathrm{w}}}\right)^{(3/4)} \sqrt[4]{\frac{T_{\mathrm{hot}} - T_{\mathrm{cold}}}{\mathrm{Ra}}}\,. \tag{6.3.4}$$

With help of T_{ref}, a non-dimensional temperature T^+ is then formulated in [Hölling06] by

$$T_h^+ = \frac{T_{\mathrm{hot}} - T(y^*)}{T_{\mathrm{ref}}}\,, \qquad T_c^+ = \frac{T(y^*) - T_{\mathrm{cold}}}{T_{\mathrm{ref}}}\,, \tag{6.3.5}$$

where the indices represent the hot (h) or cold (c) wall and y^* is a non-dimensional wall distance. This last mentioned variable is defined by [Hölling06] as

$$y^* = \frac{y}{T_{\mathrm{ref}}} \left.\frac{\partial T}{\partial y}\right|_{\tilde{\mathrm{w}}} = \frac{y}{\mathrm{L}} \sqrt[4]{\left(\mathrm{L} \left.\frac{\partial T}{\partial y}\right|_{\tilde{\mathrm{w}}}\right) / \left(\frac{T_{\mathrm{hot}} - T_{\mathrm{cold}}}{\mathrm{Ra}}\right)} \tag{6.3.6}$$

with the temperature gradient $\partial T/\partial y$ directly at the hot/cold wall and a characteristic length L of the geometry. In this thesis, L stands for the distance between the heated walls, thus $L = H$. In [Hölling06], the boundary layer near the heated walls is, as mentioned before, divided into a two layer-structure. The boundary layer consists of a *conductive boundary layer* directly at the heated walls and a *turbulent boundary layer* close to these walls. The conductive boundary layer can be expressed generally by a linear non-dimensional formulation

$$T^+ = y^*\,. \tag{6.3.7}$$

For the turbulent boundary layer a logarithmic law is proposed in [Hölling06] with two coefficients C and D which have to be determined for each particular flow problem

$$T^+ = C \cdot \ln(y^*) + D\,. \tag{6.3.8}$$

According to [Hölling06], the coefficient D may vary with the Rayleigh number. The coefficient C is determined with help of several experimental and numerical studies as $C = 0.1$ ([Hölling06]). The expression in equation (6.3.7) is of the same form as it was stated before concerning the boundary layer in chapter 3, section 3.5, 3.5.3.3, eq. (3.5.46) on page 88. The expression in equation (6.3.8) is of the same form as it was stated before concerning the overlapping layer in chapter 3, section 3.5, 3.5.3.2, eq. (3.5.40) on page 87. But the coefficients, which were suggested by [Schlichting06], are adjusted this time.

The simulation results approximate well the analytical functions for both regions. The results are displayed in case of the fine grid in figure 6.16 for the cold (left) and hot (right) wall and all realised Rayleigh numbers. The results are estimated along the vertical y-axis at the vertical cross-section, at $x = 1.185\,\mathrm{m}$, $z = 0.25\,\mathrm{m}$. The black solid line in figure 6.16 displays the analytical function $T^+ = y^*$ of the conductive boundary layer from eq. (6.3.7). The black dashed line marks the logarithmic wall function of the turbulent boundary layer with $C = 0.1$ and $D = 5.5$ from eq. (6.3.8). It can be seen that the conductive boundary layer at the hot and cold wall ($y^* < 3$) is well approximated by the results of all cases. The turbulent boundary layer at the hot wall ($y^* \geq 30$) can be

approximated by the logarithmic wall function with small deviations. Hence, the chosen mesh resolution is sufficiently fine in this case. In the turbulent boundary layer at the cold wall, the temperature is influenced by plumes from the hot wall and the coefficient D has to be modified to obtain a better approximation of the logarithmic wall function. Note that the visible plateau in the results of the turbulent layer is not exactly horizontal, otherwise there would be no heat flux in this region and the coefficient C have to be equal zero.

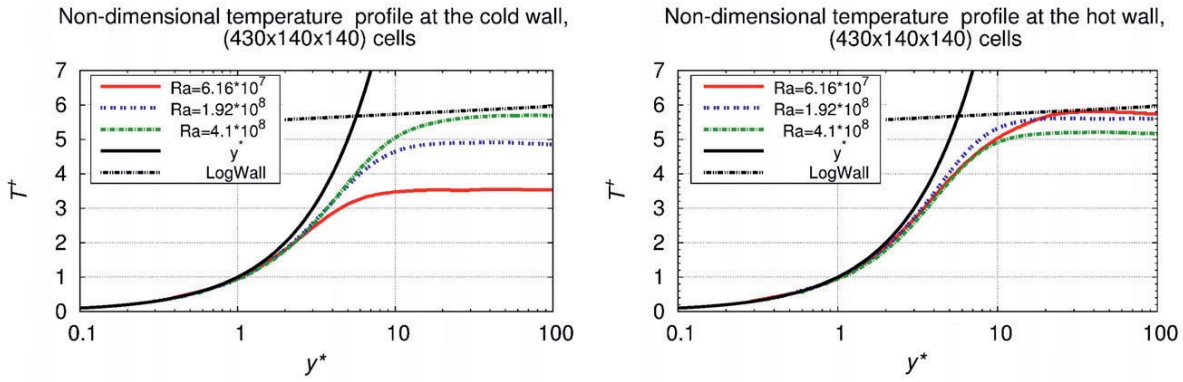

Figure 6.16.: Non-dimensional temperature profile T^+ in the boundary layer estimated at the vertical xy-midplane, at $x = 1.185$m, $z = 0.25$m. Ra $= 6.16 \times 10^7$ (red line $-$), Ra $= 1.92 \times 10^8$ (blue dashed line $- -$), Ra $= 4.1 \times 10^8$ (green dashed line $- \cdot -$), $(\mathbf{430 \times 140 \times 140})$ **cells** (as in [Zimmermann12]). **Left:** T^+ at the cold wall. **Right:** T^+ at the hot wall.

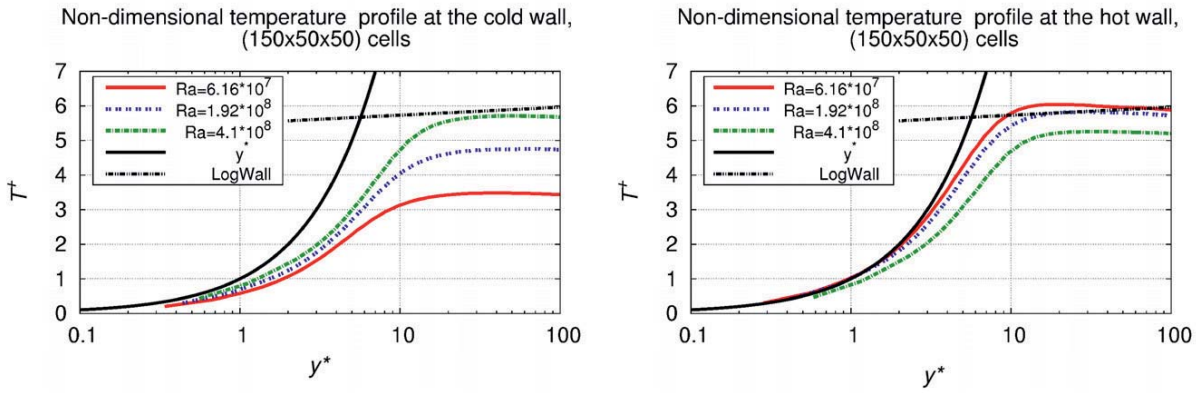

Figure 6.17.: Non-dimensional temperature profile T^+ in the boundary layer estimated at the vertical xy-midplane, at $x = 1.185$m, $z = 0.25$m. Ra $= 6.16 \times 10^7$ (red line $-$), Ra $= 1.92 \times 10^8$ (blue dashed line $- -$), Ra $= 4.1 \times 10^8$ (green dashed line $- \cdot -$), $(\mathbf{150 \times 50 \times 50})$ **cells** (as in [Zimmermann12]). **Left:** T^+ at the cold wall. **Right:** T^+ at the hot wall.

Figure 6.17 illustrates analogously to the previous results the estimated non-dimensional temperature profile in case of the coarse grid. The values in the conductive layer at the cold wall fall below the analytical $T^+ = y^*$ function from eq. (6.3.7). This behaviour

is caused by smaller temperature gradients compared to the fine mesh (s. figure 6.6 on page 155). In the turbulent boundary layer at the cold wall, the profiles are influenced by plumes from the hot wall. The values are smaller than the logarithmic wall function caused by smaller temperature gradients (s. figure 6.6 on page 155). At the hot wall, the results approximate in all cases the analytical $T^+ = y^*$ function of the conductive layer. The values in the turbulent layer at the hot wall are higher than at the cold wall. But they approximate not in all cases the logarithmic wall function. Therefore, the coefficient D has to be adjusted in both cases. At about ($y^* > 50$), a transition from the turbulent layer to the bulk region begins (outer layer). At this point, the influence from the other wall is reinforcing.

Modification of the analytical formulations

As mentioned before, the coefficient D in equation (6.3.8) may vary with the Rayleigh number and have to be modified from case to case according to [Hölling06]. This aspect can also be seen in the profiles of the non-dimensional temperature in the turbulent layer for both grid resolutions in in figures 6.16 - 6.17. Especially for the results at the cold wall of both mesh types a adaption of coefficient D can possibly improve the approximation. To obtain an possible improvement of the approximation in the turbulent boundary layer, the coefficient D is modified in the following

$$
\begin{aligned}
\mathbf{Ra = 6.16 \times 10^7}: \; & T^+_{\text{hot-fine}} = 0.1 \cdot \ln(y^*) + 5.45, \quad T^+_{\text{hot-coarse}} = 0.1 \cdot \ln(y^*) + 5.75 \\
& T^+_{\text{cold-fine}} = 0.1 \cdot \ln(y^*) + 3.25, \quad T^+_{\text{cold-coarse}} = 0.1 \cdot \ln(y^*) + 3.14, \\
\mathbf{Ra = 1.92 \times 10^8}: \; & T^+_{\text{hot-fine}} = 0.1 \cdot \ln(y^*) + 5.3 \quad T^+_{\text{hot-coarse}} = 0.1 \cdot \ln(y^*) + 5.5, \\
& T^+_{\text{cold-fine}} = 0.1 \cdot \ln(y^*) + 4.58, \quad T^+_{\text{cold-coarse}} = 0.1 \cdot \ln(y^*) + 4.38, \\
\mathbf{Ra = 4.1 \times 10^8}: \; & T^+_{\text{hot-fine}} = 0.1 \cdot \ln(y^*) + 4.78, \quad T^+_{\text{hot-coarse}} = 0.1 \cdot \ln(y^*) + 4.92, \\
& T^+_{\text{cold-fine}} = 0.1 \cdot \ln(y^*) + 5.3, \quad T^+_{\text{cold-coarse}} = 0.1 \cdot \ln(y^*) + 5.34.
\end{aligned}
\tag{6.3.9}
$$

The formulations of the modified functions with an adapted coefficient D are formulated in equation (6.3.9) for all Rayleigh numbers and both grid resolutions. The obtained non-dimensional temperature profiles of the simulations (as seen in figures 6.16 - 6.17) are then compared graphically to the modified functions in figure 6.18 on page 168. The modified functions of equation (6.3.9) are displayed by the red coloured line. The blue coloured line represents the analytical function of the conductive layer with $T^+ = y^*$ from equation (6.3.7). With the modified coefficients D, the simulation results of the non-dimensional temperature profile approximate well both regions in the thermal boundary layer and conform with the theoretical assumptions of [Hölling06].

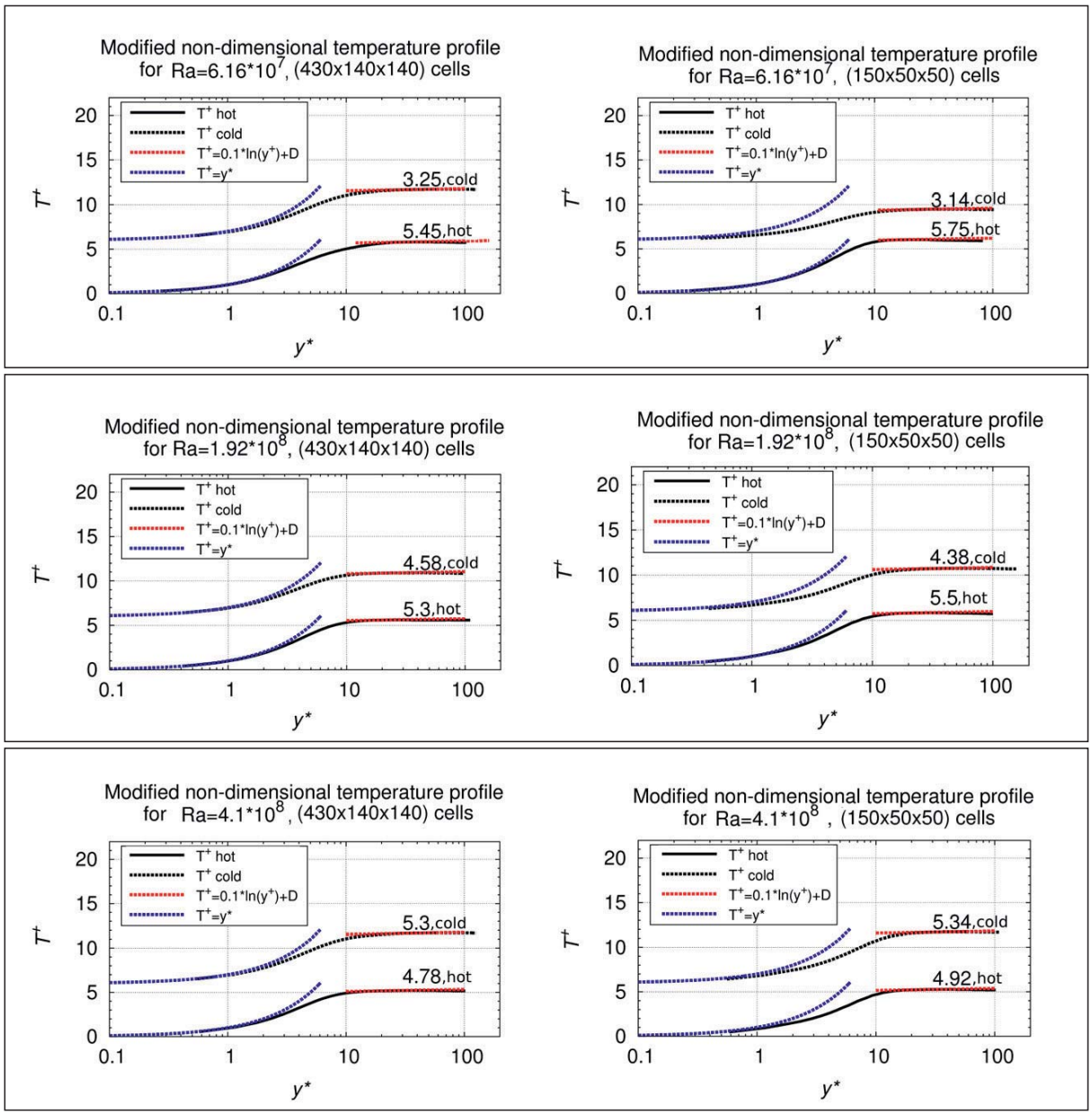

Figure 6.18.: Modified non-dimensional temperature profile T^+, estimated at the vertical xy-midplane, at $x = 1.185$m, $z = 0.25$m. **Left:** $(430 \times 140 \times 140)$, **right:** $(150 \times 50 \times 50)$ cells. **In each picture:** Top plotted function: cold wall. Bottom plotted function: hot wall. **Top box:** $\mathrm{Ra} = 6.16 \times 10^7$. **Middle box:** $\mathrm{Ra} = 1.92 \times 10^8$. **Bottom box:** $\mathrm{Ra} = 4.1 \times 10^8$.

6.3.4. Nusselt number profile estimated at the heated walls

In this section, the heat flux in the container is investigated on the basis of the Nusselt number. Note that some of the following results are also presented in extracts in [Zimmermann12] and [Zimmermann15]. The Nusselt number is defined as

$$\mathrm{Nu} = \left.\frac{\partial T}{\partial y}\right|_{\tilde{w}} \frac{H}{\Delta T}, \tag{6.3.10}$$

where $\frac{\partial T}{\partial y}\Big|_{\tilde{w}}$ is the temperature gradient directly at the cold, respectively hot, wall. H stands for the distance between both heated walls. In [Grossmann00] and in [Hölling06] theoretical considerations about possible Rayleigh-Nusselt number dependence of a strong RB problem are discussed which is based on the presented theory in chapter 3, section 3.5, 3.5.3.2 from page 83 on.

Grossmann et al. on the one hand, define in [Grossmann00] for their theory different regimes in the Rayleigh number versus Prandtl number phase space. The theory is based on the thermal and kinematic dissipation rate in the thermal boundary layer and in the bulk region only. The distance between the heated walls is neglected. The different regimes are defined whether the contribution of the thermal or of the kinetic boundary layer has a bigger influence in the particular region. For each such a regime a power law of the Nusselt number is given with different determining pre-factors in [Grossmann00]. For the investigated Rayleigh numbers of this thesis, $6.16 \times 10^7 \leq \mathrm{Ra} \leq 4.1 \times 10^8$, and $\mathrm{Pr} = 0.71$, the regime I_l comes into consideration. The depending power law is described in [Grossmann00] by

$$\mathrm{Nu} = 0.27 \cdot \mathrm{Ra}^{1/4}\mathrm{Pr}^{1/8}. \tag{6.3.11}$$

Hölling et al. on the other hand formulate in [Hölling06] an asymptotic Nu-Ra correlation for arbitrary Rayleigh numbers $\mathrm{Ra} < \infty$ which is given as

$$\mathrm{Nu} = \frac{\mathrm{Ra}^{1/3}}{[\frac{\mathrm{C}}{2}\ln(\frac{0.078}{16}\mathrm{Ra}^{1.323}) + 2\mathrm{D}]^{4/3}}, \quad \mathrm{C} = 0.1 \text{ and } \mathrm{D} = -\frac{14.94}{\mathrm{Ra}^{0.25}} + 3.43. \tag{6.3.12}$$

The reached Nusselt number values of the simulations are compared in the next part to the values estimated with help of both of these mentioned theories.

Nusselt number profile estimated at the hot and cold wall

The Nusselt number values which were reached in the simulations at the hot and cold wall are listed in the following table 6.5 for all investigated Rayleigh numbers and both mesh resolutions. The results were estimated by equation (6.3.10) and time-averaged over an interval of $\Delta t = 200\,\mathrm{s} - 380\,\mathrm{s}$ in the simulated process. Subsequently, the values were area-averaged over the whole cold, respectively hot, wall. The results in table 6.5 show clearly a significant difference between the Nusselt number at the hot wall and the one at the cold wall, especially for $\mathrm{Ra} = 4.1 \times 10^8$.

These deviations are caused by deviations between the effective thermal diffusivity at the heated walls and deviations between the temperature gradients at both heated walls. The fluid properties influence directly the Nusselt number as the following equation shows

$$\mathrm{Nu} = \frac{q}{\alpha_{\mathrm{eff}} C_p} \cdot \frac{h}{\Delta T} = \frac{\partial T}{\partial y}\Big|_{\tilde{w}} \frac{H}{\Delta T}. \tag{6.3.13}$$

The values of the effective thermal diffusivity conform for both grid resolutions with the temperature boundary conditions in table 6.1 on page 152. It is noteworthy, that the values of the effective thermal diffusivity show for the case of $\mathrm{Ra} = 6.16 \times 10^7$ and for the case of $\mathrm{Ra} = 1.92 \times 10^8$ the same results between both grid resolutions.

	$\mathbf{Nu_c}$	$\mathbf{Nu_h}$	$\alpha_{\mathbf{eff\text{-}c}}$ [kg/ms]	$\alpha_{\mathbf{eff\text{-}h}}$ [kg/ms]	$\left.\frac{\partial T}{\partial y}\right\|_{\mathbf{c}}$ [K/m]	$\left.\frac{\partial T}{\partial y}\right\|_{\mathbf{h}}$ [K/m]
$(\mathbf{430 \times 140 \times 140})$						
$\mathrm{Ra} = 6.16 \times 10^7$	22.35	24.33	$2.64 \cdot 10^{-5}$	$2.68 \cdot 10^{-5}$	215.90	234.980
$\mathrm{Ra} = 1.92 \times 10^8$	30.54	29.37	$2.63 \cdot 10^{-5}$	$2.75 \cdot 10^{-5}$	955.52	946.34
$\mathrm{Ra} = 4.1 \times 10^8$	39.37	35.97	$2.61 \cdot 10^{-5}$	$3.14 \cdot 10^{-5}$	3240.20	2960.60
$(\mathbf{150 \times 50 \times 50})$						
$\mathrm{Ra} = 6.16 \times 10^7$	22.04	22.01	$2.64 \cdot 10^{-5}$	$2.68 \cdot 10^{-5}$	212.90	212.57
$\mathrm{Ra} = 1.92 \times 10^8$	29.96	29.82	$2.63 \cdot 10^{-5}$	$2.75 \cdot 10^{-5}$	959.94	955.52
$\mathrm{Ra} = 4.1 \times 10^8$	39.54	35.68	$2.62 \cdot 10^{-5}$	$2.94 \cdot 10^{-5}$	3236.50	2919.90

Table 6.5.: Comparison of time- and area-averaged values of the Nusselt number, the thermal diffusivity and the temperature gradients estimated at the cold and hot wall (marked by index **c**, respectively index **h**). $\mathrm{Ra} = 6.16 \times 10^7$, $\mathrm{Ra} = 1.92 \times 10^8$, $\mathrm{Ra} = 4.1 \times 10^8$ and both mesh resolutions.

In figure 6.19, the simulation results of the Nusselt number from table 6.5 are plotted versus the data which is based on the theoretical assumptions of [Grossmann00] (solid black line) and the assumptions of [Hölling06] (dashed black line) (see also eq. (6.3.11) and eq. (6.3.12) on page 169). The results at the hot wall are displayed by + and the ones at the cold wall by ∘.

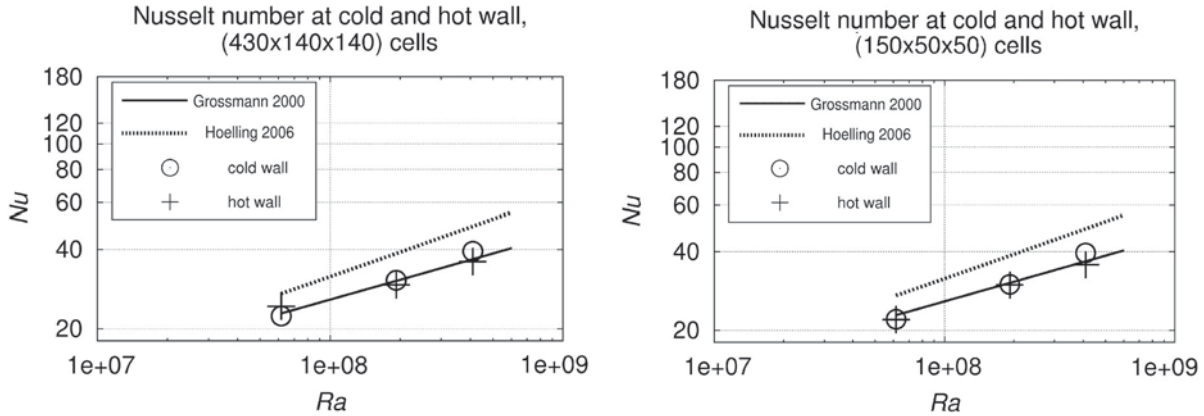

Figure 6.19.: Nu-Ra dependence at the cold and hot wall compared to data of [Grossmann00] (see eq. (6.3.11)) and [Hölling06] (see eq. (6.3.12)), Pr = 0.71. **Left:** (430 × 140 × 140) cells. **Right:** (150 × 50 × 50) cells. +: Hot wall. ∘: Cold wall. **- -** black dashed line: [Hölling06]. **-** black solid line: [Grossmann00].

The simulation results approximate in all cases the consideration of [Grossmann00]. The exact values which are estimated according to [Grossmann00] by equation (6.3.11) and according to [Hölling06] by equation (6.3.12) are given in table 6.10 on page 190, where the values are compared to an analogous experimental setup of [Ebert08].

Nusselt number values, shared factor for the hot and cold wall together

The Nusselt number values estimated in [Grossmann00] (see eq. (6.3.11)) are valid for the complete observed flow. No division is made between values at different locations, as for example the hot or cold wall. Therefore, in this section, a Nusselt number value valid for the whole setup of the container should be formulated for each resolution case and all Rayleigh numbers. To obtain such a common Nusselt number, an averaged shared factor between the values estimated at the hot and at the cold wall is required, as it is the case in the law of [Grossmann00] in eq. (6.3.11). Thus, a uniform factor has to be estimated valid for both walls.

This is done by a linear approximation between the estimated factor for the hot and the estimated factor for the cold wall. First, for the Nusselt number values given in table 6.5 an averaged factor is estimated with help of equation (6.3.11) for all Rayleigh numbers regarding each heated wall and both mesh types. Second, an averaged shared factor valid for both heated walls together is calculated. In case of the $(150 \times 50 \times 50)$ cells resolution, the mean factors for each heated wall are listed in table 6.6.

$(150 \times 50 \times 50)$ cells	Factor cold wall	Factor hot wall
$\mathrm{Ra} = 6.16 \times 10^7$	0.260	0.260
$\mathrm{Ra} = 1.92 \times 10^8$	0.266	0.264
$\mathrm{Ra} = 4.1 \times 10^8$	0.290	0.262
Mean factors	0.272	0.262

Table 6.6.: Estimation of a mean factor for all Rayleigh numbers regarding the hot and cold wall, estimated with help of eq. (6.3.11), $(150 \times 50 \times 50)$ cells.

Subsequently, as averaged shared factor a value of $\mathbf{0.267}$ is estimated valid for both heated walls together. With this shared factor the following modified values of the Nusselt number are calculated

$$\begin{aligned} \mathrm{Nu} &= 0.267 \cdot (6.16 \times 10^7)^{1/4} \cdot (0.71)^{1/8} = 22.66, \\ \mathrm{Nu} &= 0.267 \cdot (1.92 \times 10^8)^{1/4} \cdot (0.71)^{1/8} = 30.11, \\ \mathrm{Nu} &= 0.267 \cdot (4.1 \times 10^8)^{1/4} \cdot (0.71)^{1/8} = 36.40. \end{aligned} \tag{6.3.14}$$

Analogously, one estimate an averaged shared factor in case of $(430 \times 140 \times 140)$ cells (see table 6.7). With an averaged shared factor of $\mathbf{0.272}$ for both heated walls together, the modified Nusselt numbers are then

$$\begin{aligned} \mathrm{Nu} &= 0.272 \cdot (6.16 \times 10^7)^{1/4} \cdot (0.71)^{1/8} = 23.09, \\ \mathrm{Nu} &= 0.272 \cdot (1.92 \times 10^8)^{1/4} \cdot (0.71)^{1/8} = 30.68, \\ \mathrm{Nu} &= 0.272 \cdot (4.1 \times 10^8)^{1/4} \cdot (0.71)^{1/8} = 37.08. \end{aligned} \tag{6.3.15}$$

(430 × 140 × 140) cells	Factor cold wall	Factor hot wall
$\mathrm{Ra} = 6.16 \times 10^7$	0.263	0.287
$\mathrm{Ra} = 1.92 \times 10^8$	0.271	0.260
$\mathrm{Ra} = 4.1 \times 10^8$	0.289	0.264
Mean factors	0.274	0.270

Table 6.7.: Estimation of a mean factor for all Rayleigh numbers regarding the hot and cold wall, estimated with help of eq. (6.3.11), (430 × 140 × 140) cells.

In figure 6.20 the above estimated adapted Nusselt number values from eq. (6.3.14) and eq. (6.3.15) are plotted against the theoretical data of [Grossmann00] (solid black line) and [Hölling06] (dashed black line).

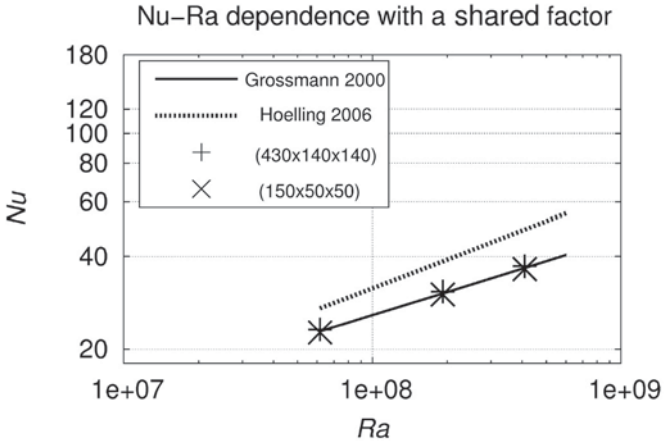

Figure 6.20.: Nu-Ra dependence with an adapted shared factor for the hot and cold wall together, compared to data of [Hölling06]: − − − (black dashed line) (see eq. (6.3.12)) and [Grossmann00]: − (black solid line) (see eq. (6.3.11)). Simulation data: **+:** (430 × 140 × 140) cells, **×:** (150 × 50 × 50) cells.

The results of the (430×140×140) cells mesh are displayed by **+** and the ones of the (150× 50 × 50) cells mesh by **×**. The averaged simulation results with a shared factor for both heated walls match well with the data of [Grossmann00]. The results of [Hölling06] exceed the theoretical ones of [Grossmann00] and still the ones of the simulation evaluations. But it has to be regarded that the assumption of [Hölling06] with $\mathrm{Ra} \to \infty$ is not realisable in

an enclosed test case setup as it is used in this study. *Stevens et. al* update in [Stevens13] the in [Grossmann00] and [Grossmann01] given regimes in the Rayleigh number versus Prandtl number phase space and the pre-factors of the belonging power laws. In the updated version, the regime $\mathrm{II_u}$ comes this time into consideration for the simulation data of $\mathrm{Ra} = 6.16 \times 10^7$. Further, for the cases $\mathrm{Ra} = 1.92 \times 10^8$ and $\mathrm{Ra} = 4.1 \times 10^8$, the regime $\mathrm{IV_u}$ comes now into consideration concerning all times $\mathrm{Pr} = 0.71$. The power law of the Nusselt number belonging to regime $\mathrm{II_u}$ is valid for $1 \times 10^6 \leq \mathrm{Ra} \leq 6.5 \times 10^7$ and $0.71 \leq \mathrm{Pr} \leq 100$. It is

$$\mathrm{Nu} = 0.51 \cdot \mathrm{Ra}^{1/5}. \tag{6.3.16}$$

The power law of the Nusselt number belonging to regime $\mathrm{IV_u}$ is valid for a range of $6.5 \times 10^6 < \mathrm{Ra} \leq 1 \times 10^{14}$ and $0.71 \leq \mathrm{Pr} \leq 100$. It is given by

$$\mathrm{Nu} = 0.050 \cdot \mathrm{Ra}^{1/3}. \tag{6.3.17}$$

These new power laws are plotted together with the "old" power law from equation (6.3.11) of [Grossmann00] (black solid line) in figure 6.21 next to the simulation data for the time-averaged values with a shared factor from eq. (6.3.14) and eq. (6.3.15).

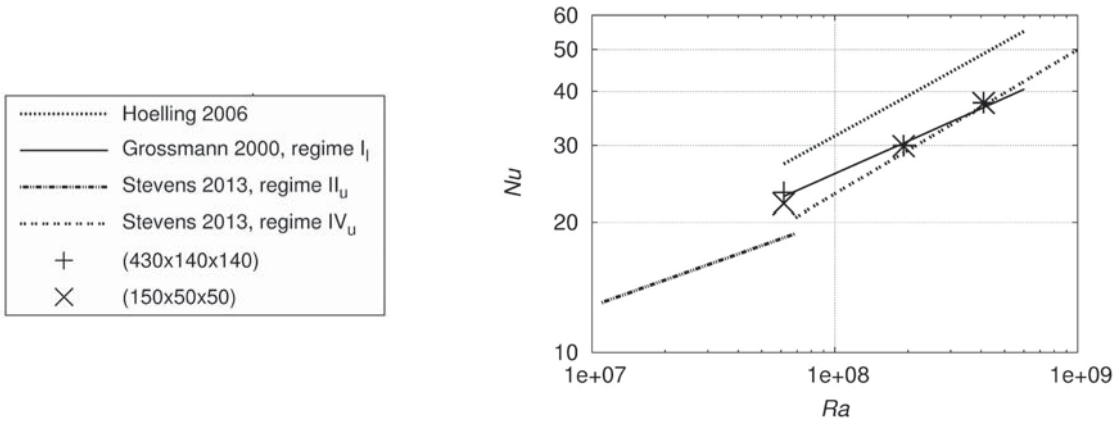

Figure 6.21.: Nu-Ra dependence with an adapted shared factor for the hot and cold wall together, compared to theoretical data. [Hölling06]: − − − (black dashed line) (see eq. (6.3.12)). [Grossmann00]: − (black solid line): Regime $\mathrm{I_l}$ (see eq. (6.3.11)). [Grossmann01]/[Stevens13]: − · · − (black dashed/dotted line): Regime $\mathrm{II_u}$ (see eq. (6.3.16)). [Grossmann01]/[Stevens13]: · · · (black dotted line): Regime $\mathrm{IV_u}$. (see eq. (6.3.17)). Simulation data: +: $(430 \times 140 \times 140)$ cells, ×: $(150 \times 50 \times 50)$ cells (see also [Zimmermann15]).

The power law for $\mathrm{II_u}$ from equation (6.3.16) is illustrated by a black dashed/dotted line and the power law for $\mathrm{IV_u}$ from equation (6.3.17) by a black dotted line. Additionally, the data of [Hölling06] are displayed by a black dashed line (see eq. (6.3.12)). As one can see in figure 6.21, the simulation data for $\mathrm{Ra} = 6.16 \times 10^7$ lie closer to the "old" power law from eq. (6.3.11) of [Grossmann00] than to the updated power law of regime $\mathrm{II_u}$. But it has to be regarded, that the given power law in [Stevens13] is valid for a big range of

Prandtl number values and that the observed case lies near to the boarder between two regimes. The values for $\mathrm{Ra} = 1.92 \times 10^8$ lie close to the new updated power law of regime $\mathrm{IV_u}$. In case of $\mathrm{Ra} = 4.1 \times 10^8$ the values match exactly the new updated power law of regime $\mathrm{IV_u}$.

Averaged Nusselt number values at the hot and cold wall, mean values

Now we consider a simple mean average value between the Nusselt number values of both heated walls given in table 6.5 for each Rayleigh number. Considering these mean Nusselt number values between the hot and cold wall, a good approximation of the data of [Grossmann00] (solid black line) can also be reached. This is displayed in figure 6.22.

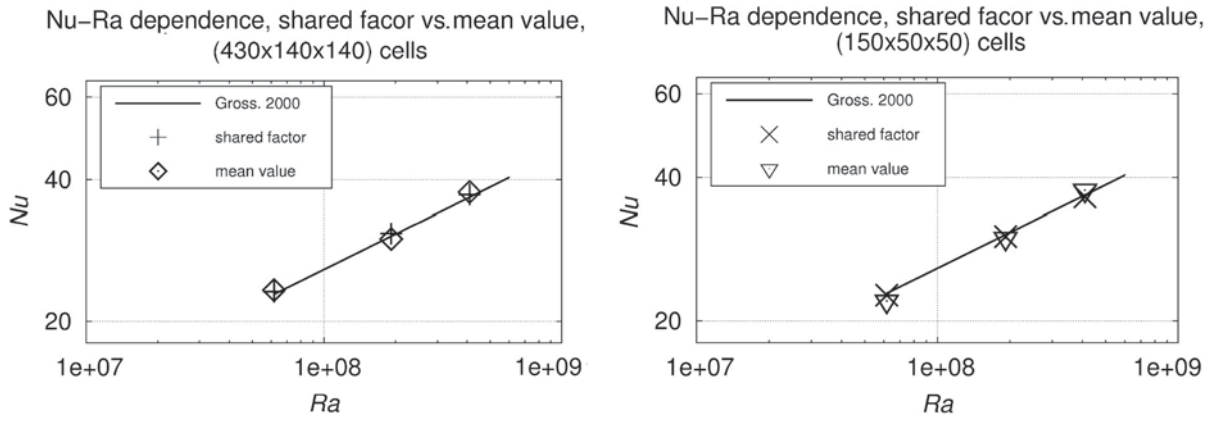

Figure 6.22.: Nu-Ra dependence. Values estimated acc. to eq. (6.3.15) and eq. (6.3.14) (shared factors) compared to the mean values between the heated walls from table 6.5 and to [Grossmann00] (see eq. (6.3.11)). [Grossmann00]:— (black solid line). **Left:** $(430 \times 140 \times 140)$ cells, +**:** shared factor values, ◇**:** mean values between hot and cold wall. **Right:** $(150 \times 50 \times 50)$ cells, ×**:** shared factor values, ▽: mean values between hot and cold wall.

Additionally the values estimated with the shared factors from eq. (6.3.15) and eq.(6.3.14) are displayed also in figure 6.22. The values with the shared factors are displayed by pluses + for $(430 \times 140 \times 140)$ cells and by crosses × for $(150 \times 50 \times 50)$ cells, as before in figure 6.20. The mean averaged values are plotted by diamonds ◇ for $(430 \times 140 \times 140)$ cells and by triangles ▽ for $(150 \times 50 \times 50)$ cells. As the results in figure 6.22 show, the values of the shared averaged factors lie closer to the data of [Grossmann00] than the mean values between the hot and cold wall, but these values also approximate well the data of [Grossmann00].

6.3.5. Profile of the effective dynamic viscosity μ_{eff} and the effective thermal diffusivity α_{eff} between the heated walls, vertical axis

In this section, the dynamic viscosity μ and the connected thermal diffusivity α are analysed for both grid resolutions.

Effective dynamic viscosity μ_{eff} and subgrid-scale dynamic viscosity μ_{sgs} between the heated walls

We know from chapter 1, section 1.9 that the effective dynamic viscosity μ_{eff} consists of two parts, the *molecular part* or *resolved part* μ which stands for the great scales and the turbulent *subgrid-scale part* μ_{sgs} which stands for the small scales and has to be modelled with help of a turbulence model. It is

$$\mu_{\text{eff}} = \mu + \mu_{\text{sgs}} \,. \tag{6.3.18}$$

The top three plots in figure 6.23 display the time-averaged profile of the effective dynamic viscosity μ_{eff} between the heated walls estimated at the xy-midplane, at $x = 1.185\,\text{m}$ and $z = 0.25\,\text{m}$, along the vertical y-axis. Complementary to the profiles of μ_{eff}, the bottom three plots in figure 6.23 display analogously the time-averaged profile of the subgrid-scale dynamic viscosity μ_{sgs} at the same position. The plots show the results of both mesh resolutions and all Rayleigh numbers. The fine grid resolution is presented by the solid black line and the coarse resolution by the dashed black line.

An asymmetry appears in all profiles, at it was expected due to the non-Boussinesq effects in the fluid. The subgrid-scale part μ_{sgs} shows the same behaviour as the effective part μ_{eff}, as it was expected due to the flow profile. The form of all plots in figure 6.23 reveal the structure of the computational mesh. At 0.1 m, respectively 0.4 m, the change from the fine resolution in the boundary layer to the coarse resolution in the bulk region can clearly be seen. Due to the relation $\alpha = \mu/\text{Pr}$, the profiles of the thermal diffusivity α should show an similar form as the profiles in 6.23, as we will see in the following.

Effective thermal diffusivity α_{eff} and subgrid-scale thermal diffusivity α_{sgs} between the heated walls

Analogously to the dynamic viscosity μ_{eff} we now discuss the thermal diffusivity α_{eff} profiles. We know from chapter 1, section 1.9 that the effective thermal diffusivity α_{eff} consists also of two parts, the *molecular part* or *resolved part* α and the turbulent *subgrid-scale part* α_{sgs}. It is

$$\alpha_{\text{eff}} = \alpha + \alpha_{\text{sgs}} \,. \tag{6.3.19}$$

The time-averaged profiles of both variables are plotted in figure 6.24. The values are estimated at the xy-midplane, at $x = 1.185\,\text{m}$ and $z = 0.25\,\text{m}$, along the vertical y-axis. The plots illustrate the profiles for both mesh resolutions and all Rayleigh numbers. The fine grid resolution is presented by the solid black line and the coarse resolution by the dashed black line. An asymmetry appears in all profiles, at it was expected due to the non-Boussinesq effects. The values of α_{eff}, (respectively μ_{eff}) of the coarse grid exceed the values of the fine grid, which is remarkable.

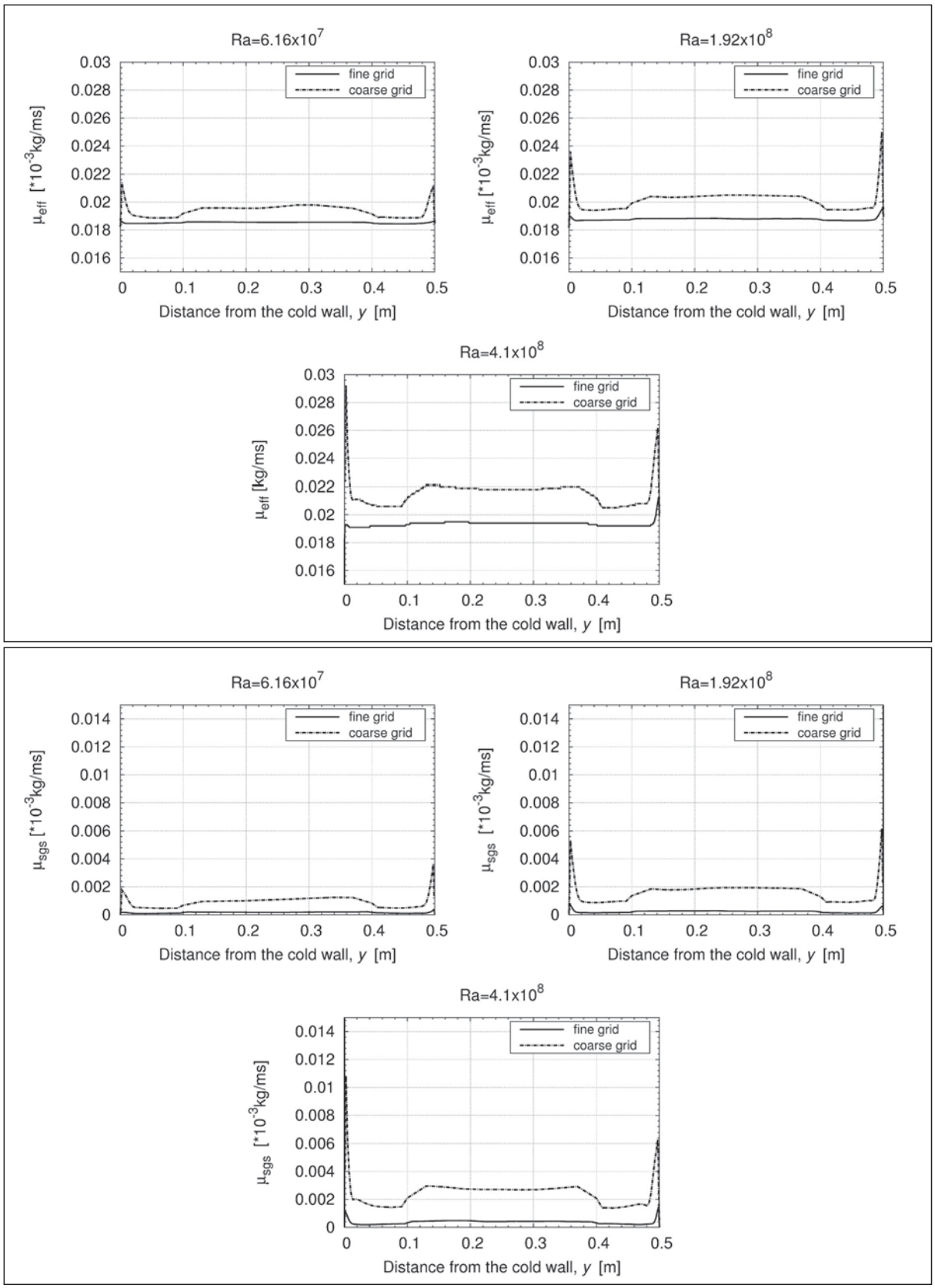

Figure 6.23.: Top box: Time-averaged profile of the effective dynamic viscosity μ_{eff} between the heated walls. **Bottom box:** Time-averaged profile of the subgrid-scale dynamic viscosity μ_{sgs} between the heated walls. Estimated at $x = 1.185\,\text{m}$, $z = 0.25\,\text{m}$. **Clockwise direction, starting left top:** $\text{Ra} = 6.16 \times 10^7$, $\text{Ra} = 1.92 \times 10^8$, $\text{Ra} = 4.1 \times 10^8$. **-** black solid line $(430 \times 140 \times 140)$ cells, **- -** black dashed line $(150 \times 50 \times 50)$ cells.

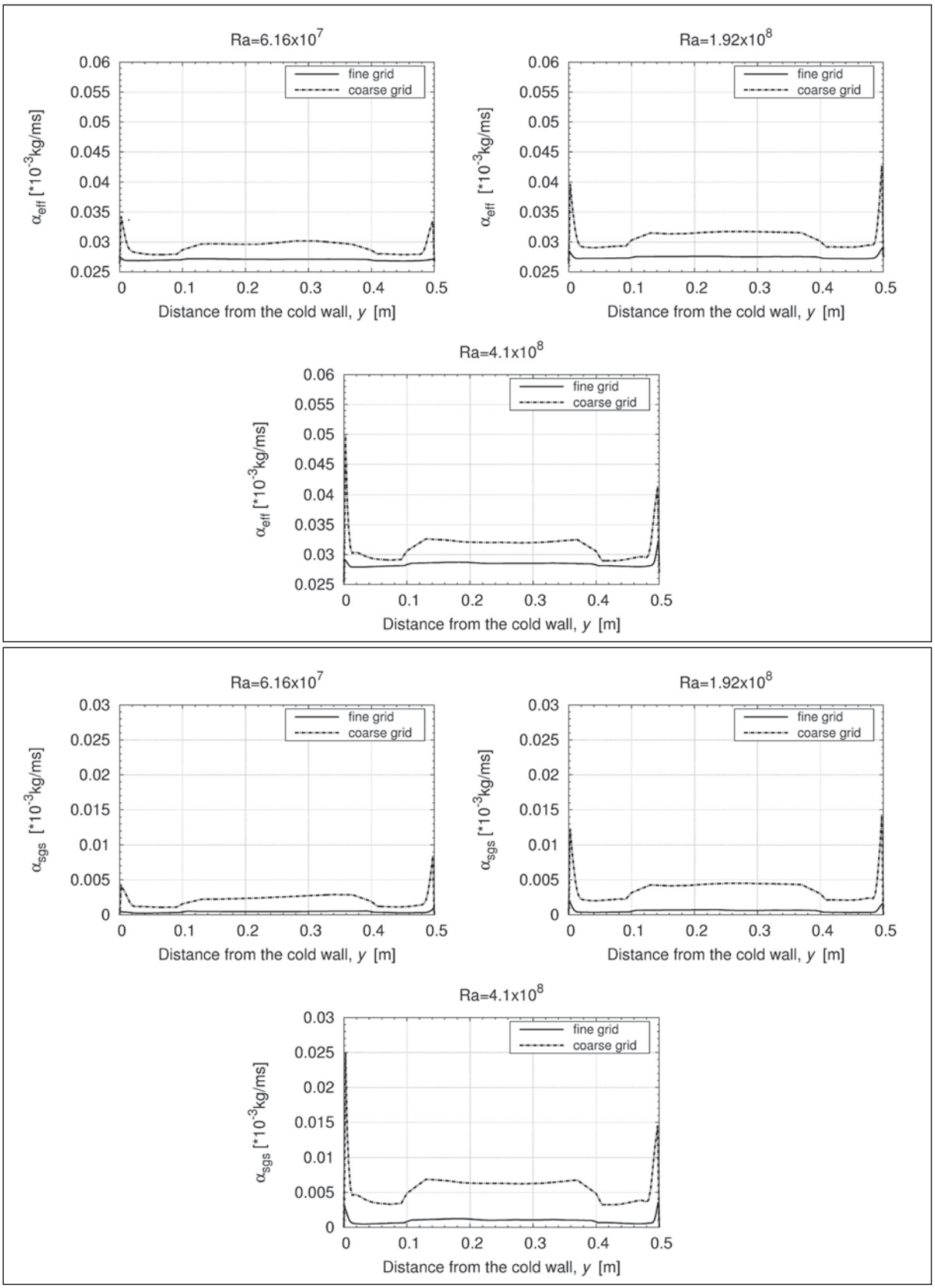

Figure 6.24.: Top box: Time-averaged profile of the effective thermal diffusivity α_{eff} between the heated walls. **Bottom box:** Time-averaged profile of the subgrid-scale thermal diffusivity α_{sgs} between the heated walls. Estimated at $x = 1.185\,\text{m}$, $z = 0.25\,\text{m}$. **Clockwise direction, starting left top:** $\text{Ra} = 6.16 \times 10^7$, $\text{Ra} = 1.92 \times 10^8$, $\text{Ra} = 4.1 \times 10^8$. **-** black solid line: $(430 \times 140 \times 140)$ cells, **- -** black dashed line: $(150 \times 50 \times 50)$ cells.

This can be seen clearly directly at the heated walls. Due to this higher thermal diffusivity values, in the results of the coarse grid also higher temperature gradients should be expected at the hot wall and lower temperature gradients at the cold wall. This is not the case for the hot wall, as figure 6.6 in section 6.3.1, on page 155 shows. All temperature gradients of the coarse grid at the hot wall are smaller than the ones of the fine grid, especially for a higher Rayleigh number. This aspect has to be caused by numerical deviations of the coarse grid resolution.

Ratio of μ_{sgs}/μ

To compare directly the resolved components and the *sgs*-contributions of the simulation with each other, we discuss the behaviour of the following relation

$$\frac{\mu_{\text{sgs}}}{\mu}\,. \tag{6.3.20}$$

The above formulated term describes a ratio between the modelled subgrid-scale part μ_{sgs} and the resolved part μ of the effective dynamic viscosity $\mu_{\text{eff}}=\mu+\mu_{\text{sgs}}$.

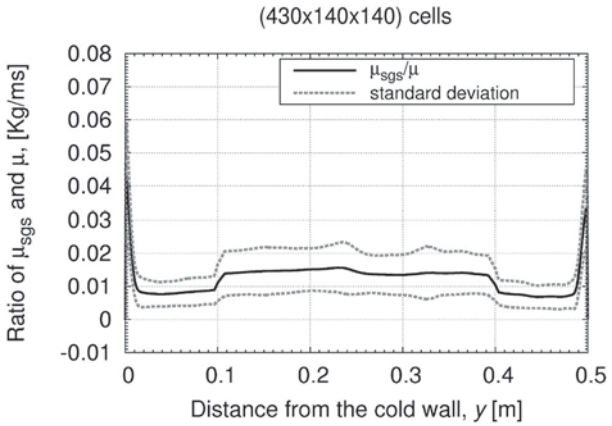

Figure 6.25.: Time-averaged profile of the ratio μ_{sgs}/μ (s. eq. (6.3.20)). Estimated between the heated walls at the vertical xy-midplane ($x = 1.185\,\text{m}$, $z = 0.25\,\text{m}$). $\text{Ra} = 1.92 \times 10^8$.
- black solid line: $(430 \times 140 \times 140)$ cells. - - - grey dashed line: standard deviation (s. [Zimmermann15]).

Figure 6.25 displays the time-averaged profile of the relation in equation (6.3.20) exemplary for $\text{Ra} = 1.92 \times 10^8$, $(140 \times 140 \times 430)$ cells. Additionally, the standard deviation of the profile is plotted. The values are estimated, analogously to the temperature profile, at the xy-midplane, at $x = 1.185\,\text{m}$, $z = 0.25\,\text{m}$, along the vertical y-axis.

The form of the profile is equal to the above analysed profiles of the effective dynamic viscosity μ_{eff}. The transition between regions of different mesh resolutions can clearly be seen in the profile. All reached values in figure 6.25 are smaller than unity. Hence, the chosen grid resolution is not as small as in a DNS. This can also be shown by the Kol-

mogorov length. In a DNS the Kolmogorov length is a scale for the size of the smallest turbulent eddies which have to be resolved by the computational grid (s. also chapter 3). According to equation (5.2.4) on page 100 in chapter 5, it is

$$\eta_{k_L} \approx \frac{L}{\left(\frac{1}{0.71 \cdot 2.5}\mathrm{Ra}\right)^{3/8}}. \tag{6.3.21}$$

Table 6.8 lists the values of the Kolmogorov length which are estimated according to equation (5.2.4) for all Rayleigh numbers in this study. The smallest cell in the mesh of both resolutions is cubical formed. Its size in the fine grid is $\Delta_x/\Delta_y/\Delta_z = 9.2 \cdot 10^{-4}\,\mathrm{m}$. For the coarse grid the size is $\Delta_x/\Delta_y/\Delta_z = 2.5 \cdot 10^{-3}\,\mathrm{m}$. As table 6.8 shows, the size of the smallest cell of both resolutions is bigger than the Kolmogorov length of all cases. Hence, the chosen resolution is not as small as in a DNS.

Rayleigh number Ra	**Kolmogorov length** η_{k_L}
6.16×10^7	$7.44 \cdot 10^{-4}\,\mathrm{m}$
1.92×10^8	$4.85 \cdot 10^{-4}\,\mathrm{m}$
4.1×10^8	$3.65 \cdot 10^{-4}\,\mathrm{m}$

Table 6.8.: Kolmogorov length η_{k_L} accord. to eq. (6.3.21) for several Rayleigh numbers.

6.4. Global heat flux structure

To obtain further information on the development of the asymmetrical temperature profile, the heat flux in the container is investigated in another approach. Therefore, a description of the global heat flux structure in the container is formulated. To begin with, the generation of an asymmetrical fluid property profile is illustrated in a demonstrative way.

Imagine two different air volumes in the container, a hot and a cold one, which have a different size. Figure 6.26 demonstrates this aspect by a simplified scheme of the two different volumes. The bigger volume of hot air should ascend and the smaller volume of cold air should descend. Then, the raising hot air displaces the cold air in vicinity of the cold wall. As a consequence, the heat flux at the cold wall has to be smaller than the one at the hot wall. Also, the temperature gradient at the cold wall has to be smaller than the gradient at the hot wall. Because the container is an enclosed system, both mass flows of the volumes have to be equal,

$$A_+ \rho_+ u_+ = A_- \rho_- u_- \,. \tag{6.4.1}$$

Since the density of the cold volume has to be higher than the density of the hot volume $\rho_- > \rho_+$, it follows

$$\frac{A_+ u_+}{A_- u_-} = \frac{\rho_-}{\rho_+} > 1 \tag{6.4.2}$$

and thus

$$A_+ u_+ > A_- u_- \quad \text{and} \quad A_+ u_+ - A_- u_- > 0\,. \tag{6.4.3}$$

Consequently, the profiles of the fluid properties in a NOB convection have to be asymmetrical. This aspect shall be demonstrated in the next part by different fluid properties profiles which influence the heat flux in the container.

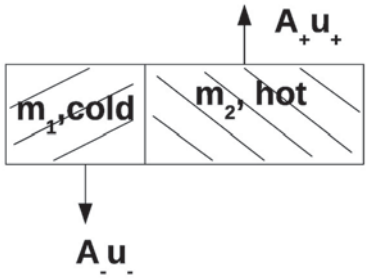

Figure 6.26.: Scheme of two different fluid volumes with different temperatures and different sizes.

Estimation of a global heat flux variable and its profile at constant planes parallel to the heated walls

The turbulent enthalpy equation from chapter 3, section 3.3.2 on page 71, is modified into a time-averaged problem over an appropriate interval $[t_0, T]$

$$\frac{1}{T-t_0}\int_{t_0}^{T} \frac{\partial \bar{\rho}\widetilde{h}}{\partial t} + \frac{\partial \bar{\rho}\widetilde{u}_j\widetilde{h}}{\partial x_j} - \frac{\partial}{\partial x_j}\left((\alpha + \alpha_{sgs})\,\frac{\partial \widetilde{h}}{\partial x_j}\right) dt = \frac{1}{T-t_0}\int_{t_0}^{T} \frac{\partial \bar{p}}{\partial t} + \widetilde{u}_j \frac{\partial \bar{p}}{\partial x_j}\,. \tag{6.4.4}$$

Therefore, the following equation holds

$$\nabla \cdot (\overline{\bar{\rho}\tilde{\mathbf{u}}\tilde{h}}) - \nabla \cdot ((\alpha^* + \alpha^*{}_{sgs})\nabla\overline{\tilde{h}}) = \overline{\tilde{\mathbf{u}}\nabla\bar{p}} \approx 0\,. \tag{6.4.5}$$

Here, α^* presents a time-averaged, constant molecular thermal diffusivity and α^*_{sgs} presents a time-averaged subgrid-scale thermal diffusivity. Experimental data have shown, that the pressure fluctuations $\overline{\tilde{\mathbf{u}}\nabla\bar{p}}$ in the thermal boundary layer are insignificant in comparison to the fluctuations of the temperature and specific enthalpy [Spurk07]. Thus according to [Cebeci1968] and [Spurk07] (chapter 19, 19.1), the term on the RHS in equation (6.4.5)

is negligible. Subsequently, equation (6.4.5) is area-averaged over planes A which are located parallel to the cold/hot wall. The term $<>_A$ denotes the area-averaged values

$$\begin{aligned}&\frac{1}{A}\int_A \left(\nabla\cdot(\overline{\bar{\rho}\tilde{\mathbf{u}}\tilde{\bar{h}}})\right) - \nabla\cdot((\alpha^* + \alpha^*{}_{sgs})\nabla\tilde{\bar{h}})\,dA \\ &= \nabla\cdot\left\langle(\overline{\bar{\rho}\tilde{\mathbf{u}}\tilde{\bar{h}}})\right\rangle_A - \nabla\cdot\left\langle(\alpha^* + \alpha^*{}_{sgs})\nabla\tilde{\bar{h}}\right\rangle_A .\end{aligned} \tag{6.4.6}$$

Equation (6.4.6) can be modified into

$$\nabla\cdot\left(\langle\bar{\bar{\rho}}\rangle_A\,\langle\tilde{\bar{\mathbf{u}}}\rangle_A\left\langle\tilde{\bar{h}}\right\rangle_A + \tilde{\Delta}\right) = \nabla\cdot\left((\alpha^* + \alpha^*_{\text{sgs}})\nabla\left\langle\tilde{\bar{h}}\right\rangle_A\right) \tag{6.4.7}$$

with

$$\tilde{\Delta} := -\alpha^*_t\nabla\left\langle\tilde{\bar{h}}\right\rangle_A . \tag{6.4.8}$$

The new term $\tilde{\Delta}$ in (6.4.8) includes an additionally time- and area-averaged turbulent thermal diffusivity α^*_t. This thermal diffusivity α^*_t should characterise the global plumes structures in the container. Equation (6.4.7) can now be transformed into

$$\nabla\cdot\left(\langle\bar{\bar{\rho}}\rangle_A\,\langle\tilde{\bar{\mathbf{u}}}\rangle_A\left\langle\tilde{\bar{h}}\right\rangle_A\right) = \nabla\cdot\left(\underbrace{(\alpha^* + \alpha^*_{\text{sgs}} + \alpha^*_t)}_{=:\,\alpha_{\text{global}}}\nabla\left\langle\tilde{\bar{h}}\right\rangle_A\right) . \tag{6.4.9}$$

Integration of equation (6.4.9) provides

$$\langle\bar{\bar{\rho}}\rangle_A\,\langle\tilde{\bar{\mathbf{u}}}\rangle_A\left\langle\tilde{\bar{h}}\right\rangle_A + C = \alpha_{\text{global}}\nabla\left\langle\tilde{\bar{h}}\right\rangle_A . \tag{6.4.10}$$

The integration constant C is determined by the boundary conditions at the heated walls. From the non-slip condition, $\mathbf{u} = 0$, and a zero turbulent and subgrid scale thermal diffusivity, $\alpha_t = \alpha_{\text{sgs}} = 0$, it follows, that $\alpha_{\text{global}} = \alpha^*$. Hence, it is

$$C = \alpha^*\nabla\left\langle\tilde{\bar{h}}\right\rangle_A|_{\tilde{\text{w}}} = -\langle\bar{q}\rangle_A|_{\tilde{\text{w}}} . \tag{6.4.11}$$

Here, $\langle\bar{q}\rangle_A$ is the time- and area-averaged heat flux at the heated walls. Substitution of equation (6.4.11) in (6.4.10) leads to

$$\langle\bar{\bar{\rho}}\rangle_A\,\langle\tilde{\bar{\mathbf{u}}}\rangle_A\left\langle\tilde{\bar{h}}\right\rangle_A - \langle\bar{q}\rangle_A|_{\tilde{\text{w}}} = \alpha_{\text{global}}\nabla\left\langle\tilde{\bar{h}}\right\rangle_A \tag{6.4.12}$$

and

$$\alpha_{\text{global}} = \frac{\left|\langle\bar{\bar{\rho}}\rangle_A\,\langle\tilde{\bar{\mathbf{u}}}\rangle_A\left\langle\tilde{\bar{h}}\right\rangle_A - \langle\bar{q}\rangle_A|_{\tilde{\text{w}}}\right|}{\left|\nabla\left\langle\tilde{\bar{h}}\right\rangle_A\right|} . \tag{6.4.13}$$

Equation (6.4.13) gives an expression for the global thermal diffusivity structure in the container.

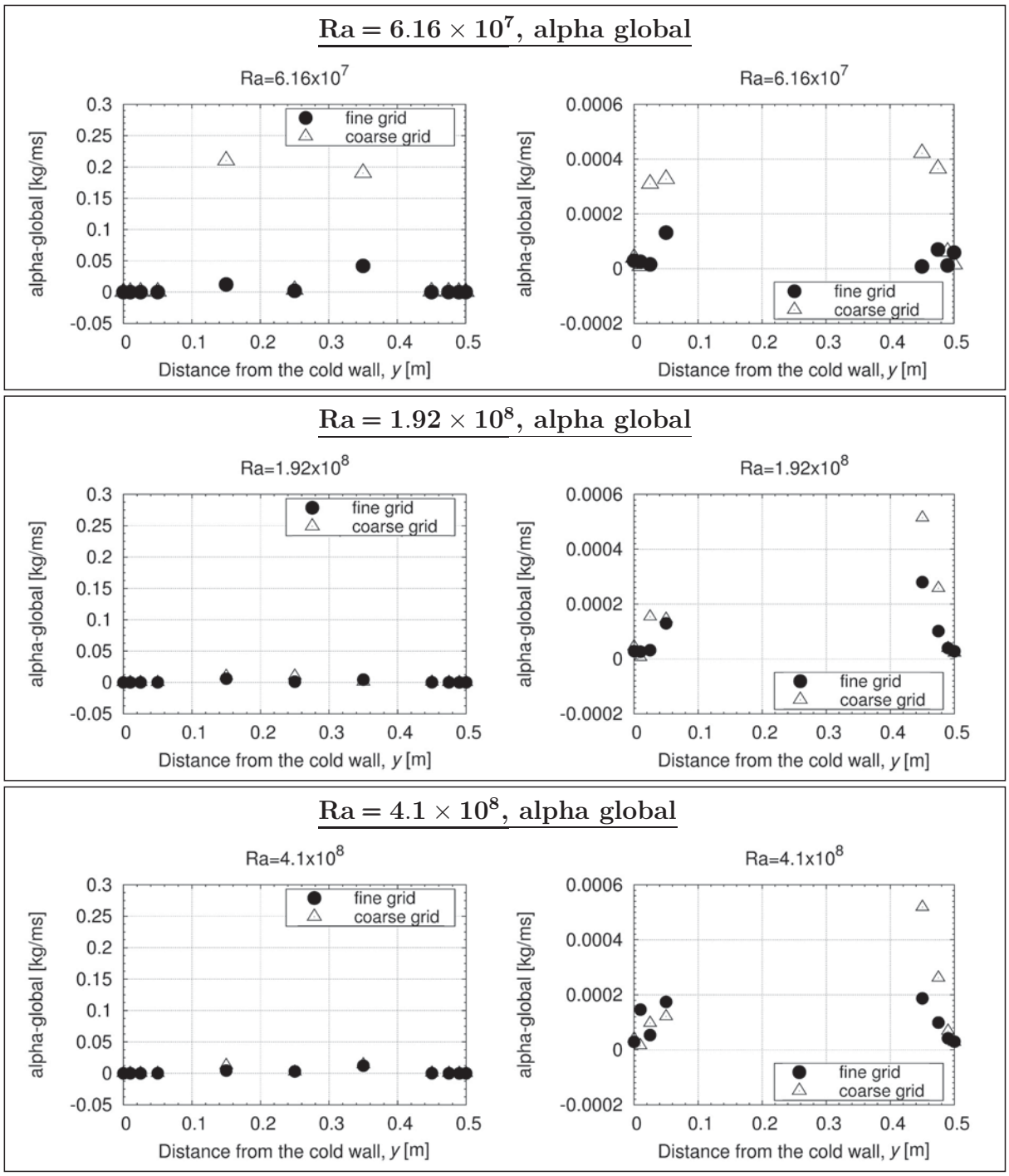

Figure 6.27.: Time- and area-averaged α_{global}-profile estimated at constant planes parallel to the cold/hot wall. **Top box:** Ra $= 6.16 \times 10^7$. **Middle box:** Ra $= 1.92 \times 10^8$. **Bottom box:** Ra $= 4.1 \times 10^8$. **Left picture in each box:** Overview. **Right picture in each box:** Detailed plot. **In all pictures:** •: $(430 \times 140 \times 140)$ cells, △: $(150 \times 50 \times 50)$ cells.

To avoid an influence of the gradient direction in equation (6.4.13), the absolute value of α_{global} is taken into account in the following. Because the main aspect of the investigation of α_{global} lies on the values at the xy-midplane, only the vertical velocity component u_y is considered in the following. Figure 6.27 on page 182 pictures the distribution of α_{global} at

planes parallel to the cold wall. The results show the area-averaged values for all Rayleigh numbers and both grids. The investigated planes are located at $y_1 = 0\,\mathrm{m}$, $y_2 = 0.01\,\mathrm{m}$, $y_3 = 0.025\,\mathrm{m}$, $y_4 = 0.05\,\mathrm{m}$, $y_5 = 0.15\,\mathrm{m}$, $y_6 = 0.25\,\mathrm{m}$, $y_7 = 0.35\,\mathrm{m}$, $y_8 = 0.45\,\mathrm{m}$, $y_9 = 0.475\,\mathrm{m}$, $y_{10} = 0.49\,\mathrm{m}$ and $y_{11} = 0.5\,\mathrm{m}$.

All estimations reveal an asymmetrical profile which is especially distinctive in vicinity of the heated walls, as it was the case in the temperature profiles in section 6.3.1, figure 6.6 on page 155. The asymmetry can be clearly seen in the detailed plots at the right side in each case in 6.27.

The values at the planes near the cold wall are smaller than the values at the planes near the hot wall. The values of α_{global} near the heated walls rise until they reach their maximum near the bulk region, at plane $y = 0.15\,\mathrm{m}$, respectively plane $y = 0.35\,\mathrm{m}$. At this point, the values of α_{global} drop down, but they are still higher than at the planes close to the heated walls. This behaviour matches with the temperature profiles where steep gradients were located near the walls and an almost constant temperature could be detected in the bulk region.

The values of the coarse grid resolution near the heated walls are mostly higher than the values of the fine grid. α_{global} reaches its absolute maximum value for $\mathrm{Ra} = 6.16 \times 10^7$ and the fine grid at plane $y = 0.35\,\mathrm{m}$ with a value of $0.042\,\mathrm{kg/ms}$. In case of the coarse grid resolution, α_{global} reaches its absolute maximum value for $\mathrm{Ra} = 6.16 \times 10^7$ at plane $y = 0.35\,\mathrm{m}$ with a value of $0.210\,\mathrm{kg/ms}$.

Profile of α_{global} influencing fluid properties at constant planes parallel to the heated walls - enthalpy, velocity, density and pressure

To investigate the asymmetrical form of α_{global}, the influencing fluid properties, enthalpy, velocity, density and pressure are analysed at the same planes parallel to the heated walls. The above distribution of α_{global} in figure 6.27, is caused by each variable in equation (6.4.13).

The distributions of the time- and area-averaged variables $< \overline{\tilde{h}} >_A$, $< \overline{\tilde{u}_y} >_A$, $< \overline{\overline{\rho}} >_A$, $< \overline{\overline{p}} >_A$ are plotted in figures 6.28 - 6.29 on pages 184 - 185.

Also these properties should reveal a asymmetrical profile. Higher values of these properties and a higher wall heat flux influence directly α_{global}. The heat flux at the heated walls is constant due to the constant temperature conditions.

The enthalpy gradient reaches its peak values at the heated walls, analogously to the temperature profile in section 6.3.1, figure 6.6 on page 155. The values become smaller towards the bulk of the container. The enthalpy itself reaches its maximum at the hot wall and its minimum at the cold wall, as it was expected. The density values show a tendency which is vice versa to the one of the enthalpy, due to its temperature dependence.

The vertical velocity component reaches its minimum at the planes which lie close to the heated walls. The pressure values have a almost linear distribution over the container. Its minimum is reached at the cold wall and its maximum at the hot wall. All profiles show an asymmetrical form which causes also the asymmetrical form of α_{global}.

Mainly in close distance to the heated walls this asymmetry is distinctive, as it is also the case in the profile of α_{global}. In case of the pressure, the visible significant differences between both grid resolutions are compensated by the visible significant differences of the density values $< \overline{\rho} >_A$. Deviations between both grid resolutions can be observed. The higher values in the α_{global} profile for $(150 \times 50 \times 50)$ cells are caused especially by higher values of the enthalpy $< \widetilde{\overline{h}} >_A$, the vertical velocity and the enthalpy gradient as well as the wall heat flux. The both last mentioned variables are discussed in the following.

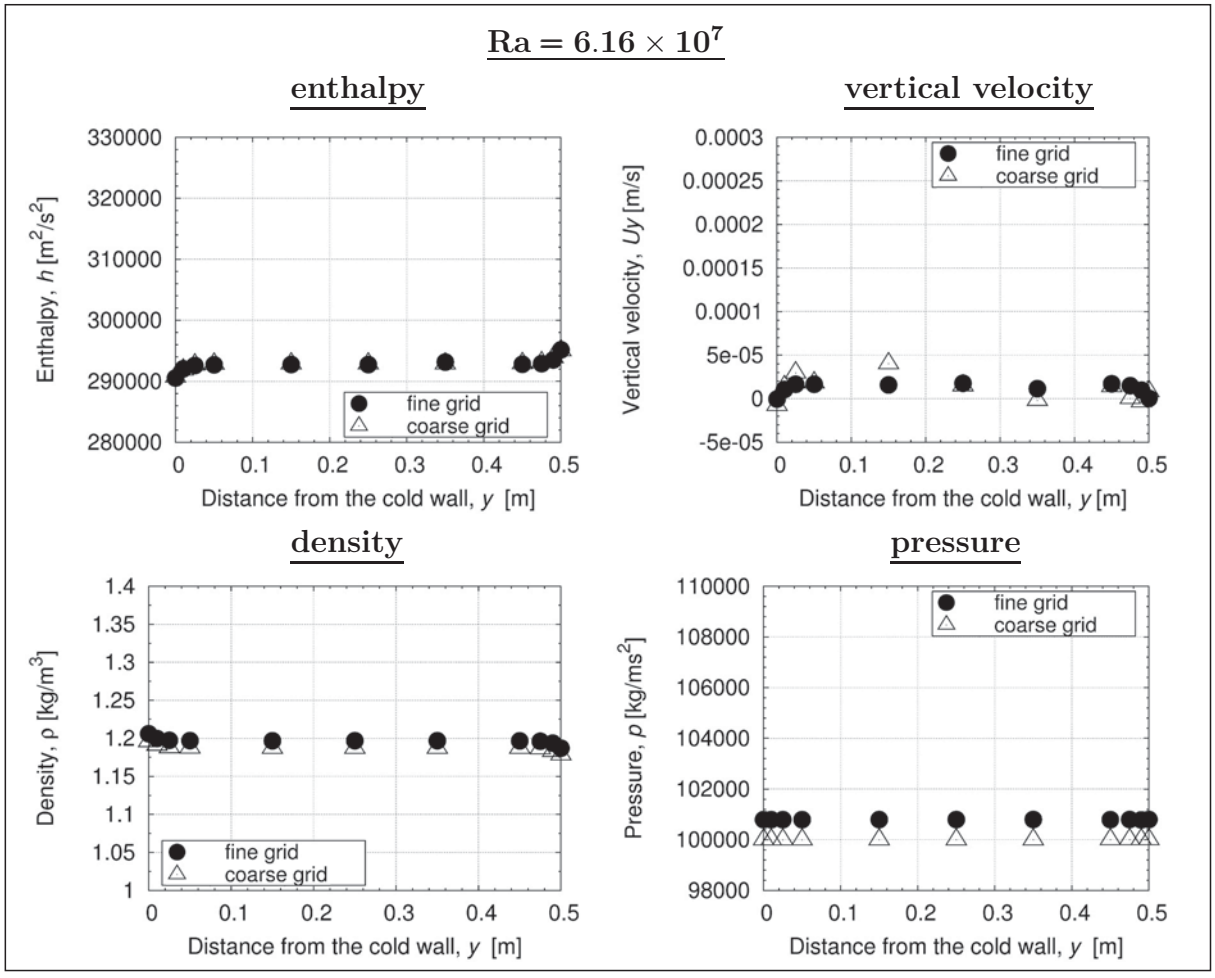

Figure 6.28.: Clockwise direction, starting left top: Time- and area-averaged profiles of enthalpy, vertical velocity, density, pressure estimated at constant planes parallel to the cold/hot wall. Ra $= 6.16 \times 10^7$. **In all pictures:** •: $(430 \times 140 \times 140)$ cells, △: $(150 \times 50 \times 50)$ cells.

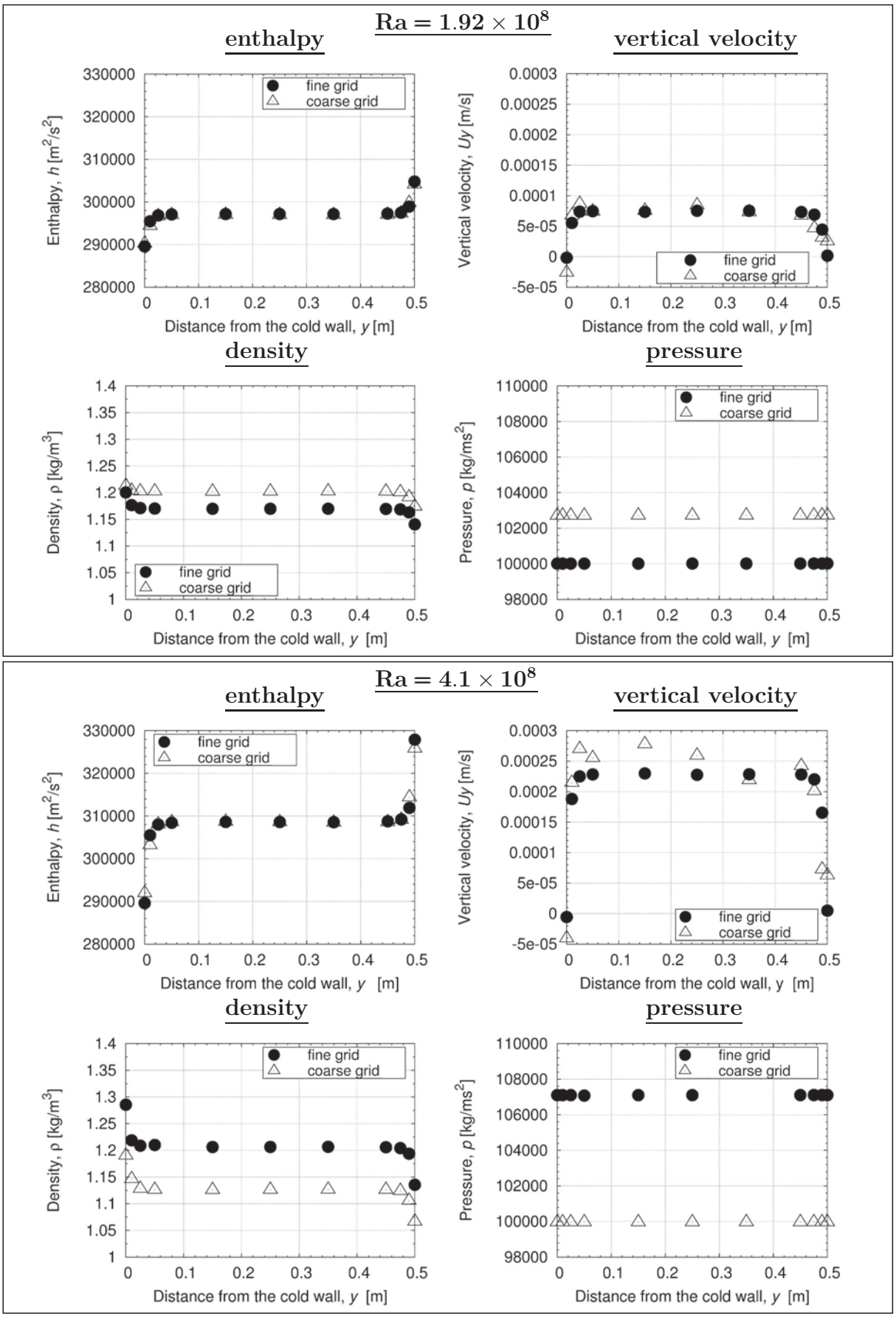

Figure 6.29.: Time- and area-averaged profiles of enthalpy, vertical velocity, density, pressure estimated at const. planes parallel to the cold/hot wall. **Top box**: Ra $= 1.92 \times 10^8$. **Bottom box**: Ra $= 4.1 \times 10^8$. **In all pictures:** •: $(430 \times 140 \times 140)$ cells, △: $(150 \times 50 \times 50)$ cells.

Profile of the enthalpy gradient and wall heat flux at constant planes parallel to the heated walls

The gradient of the enthalpy $< \overline{\tilde{h}} >_A$ is plotted in figure 6.30 for all Rayleigh numbers and both grid resolutions.

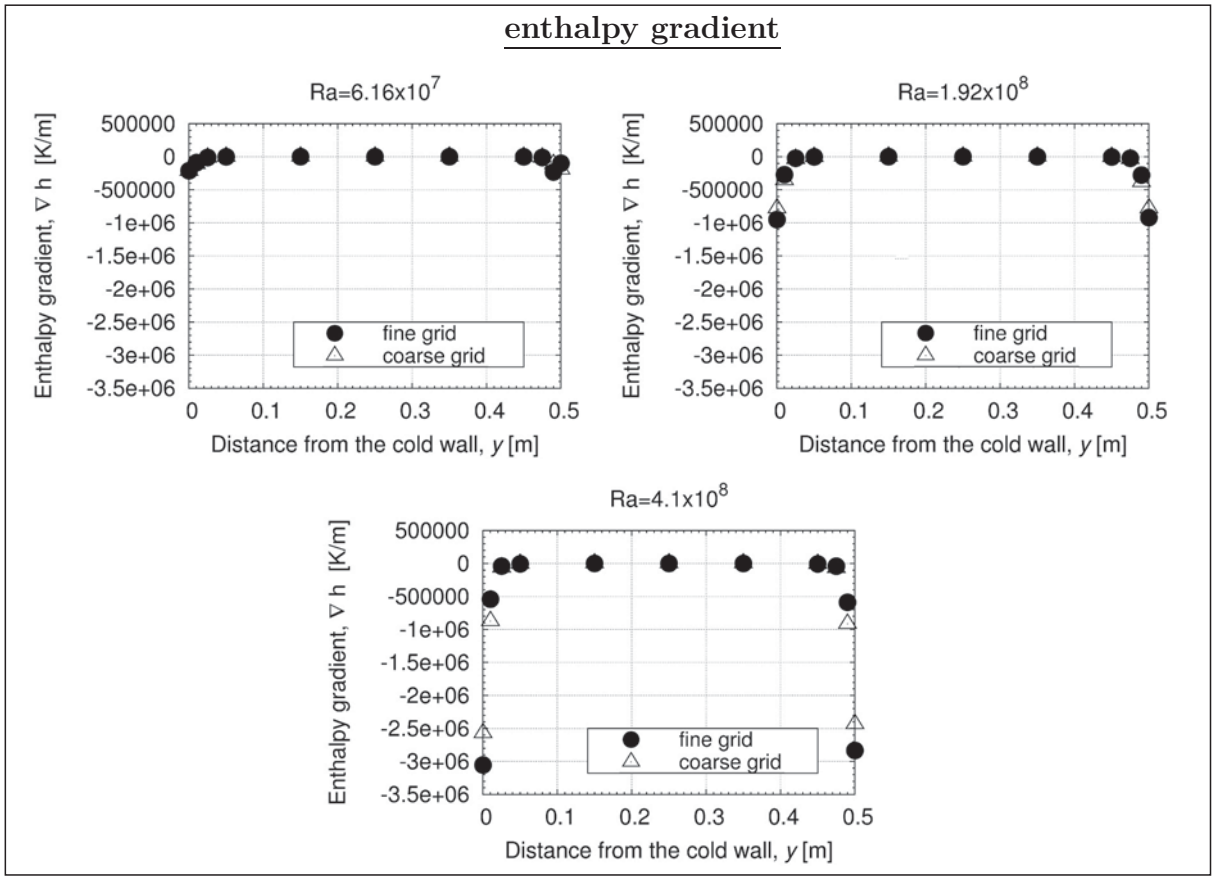

Figure 6.30.: Time- and area-averaged profiles of the enthalpy gradient estimated at constant planes parallel to the cold/hot wall. **Clockwise direction, starting left top:** $\mathrm{Ra} = 6.16 \times 10^7$, $\mathrm{Ra} = 1.92 \times 10^8$, $\mathrm{Ra} = 4.1 \times 10^8$. **In all pictures:** •: $(430 \times 140 \times 140)$ cells, △: $(150 \times 50 \times 50)$ cells.

wall heat flux [W/m^2]	**Ra** $= 6.16 \times 10^7$		**Ra** $= 1.92 \times 10^8$		**Ra** $= 4.1 \times 10^8$	
	cold	hot	cold	hot	cold	hot
$(430 \times 140 \times 140)$	5.71	6.29	25.75	25.89	86.29	85.09
$(150 \times 50 \times 50)$	5.71	5.63	25.42	26.41	87.10	86.48

Table 6.9.: Time- and area-averaged values of the wall heat flux estimated at the cold/hot wall for different Rayleigh numbers and both mesh resolutions.

The profiles of the enthalpy gradient show also an asymmetrical form, especially direct at the heated walls, as it was expected due to the asymmetrical profile of the enthalpy

$< \overline{\tilde{h}} >_A$ (s. figures 6.28 - 6.29). Close to the heated walls significant deviations appear between both grid resolutions, as it was also the case in the enthalpy profiles $< \overline{\tilde{h}} >_A$.

Complementary to the profiles of the enthalpy gradient, the values of the wall heat flux are listed in table 6.9 for all Rayleigh-numbers and both grid resolutions. The wall heat flux is described by the term $\langle \overline{q} \rangle_A$ in equation (6.4.13). The listed values are time- and also area-averaged over the whole cold, respectively hot, wall. Also in these values an asymmetry between the hot and cold wall is visible.

Summarising, the asymmetrical profile of α_{global} as well as the deviations between both grid resolutions in α_{global} result from the interactions of the observed variables which were estimated above. All variables show asymmetrical profiles and influence directly the profile of α_{global}.

Profile of the correlations of term $\left\langle \overline{\bar{\rho}\tilde{\mathbf{u}}\tilde{h}} \right\rangle_A$ at constant planes parallel to the heated walls

Figures 6.31 - 6.32 on page 188 and page 189 present the profiles of the correlations of the product in term $\left\langle \overline{\bar{\rho}\tilde{\mathbf{u}}\tilde{\bar{h}}} \right\rangle_A$ for all Rayleigh numbers and both grid resolutions.

Because the asymmetry of α_{global} is caused by the interactions of the observed particular variables, also the correlations of term $\left\langle \overline{\bar{\rho}\tilde{\mathbf{u}}\tilde{\bar{h}}} \right\rangle_A$ have to be analysed.

The influences of these correlations may not be directly visible in the profile of α_{global} or in the profiles of the other observed variables in equation (6.4.13). The distributions show similar forms to the individual profiles of each variable in term $\left\langle \overline{\bar{\rho}\tilde{\mathbf{u}}\tilde{\bar{h}}} \right\rangle_A$.

Again, asymmetries are revealed which are resulting from the asymmetrical behaviour of the particular variables. Concluding, the asymmetry of the global heat flux profile α_{global}, which causes also the asymmetrical form of the temperature profiles, is generated by the asymmetrical behaviour of the above plotted fluid properties. These properties influence directly the global heat flux structure in the test cell. Also [Ahlers06] reports asymmetrical profiles of fluid properties in a NOB convection in water and glycerol, which emphasises the obtained results.

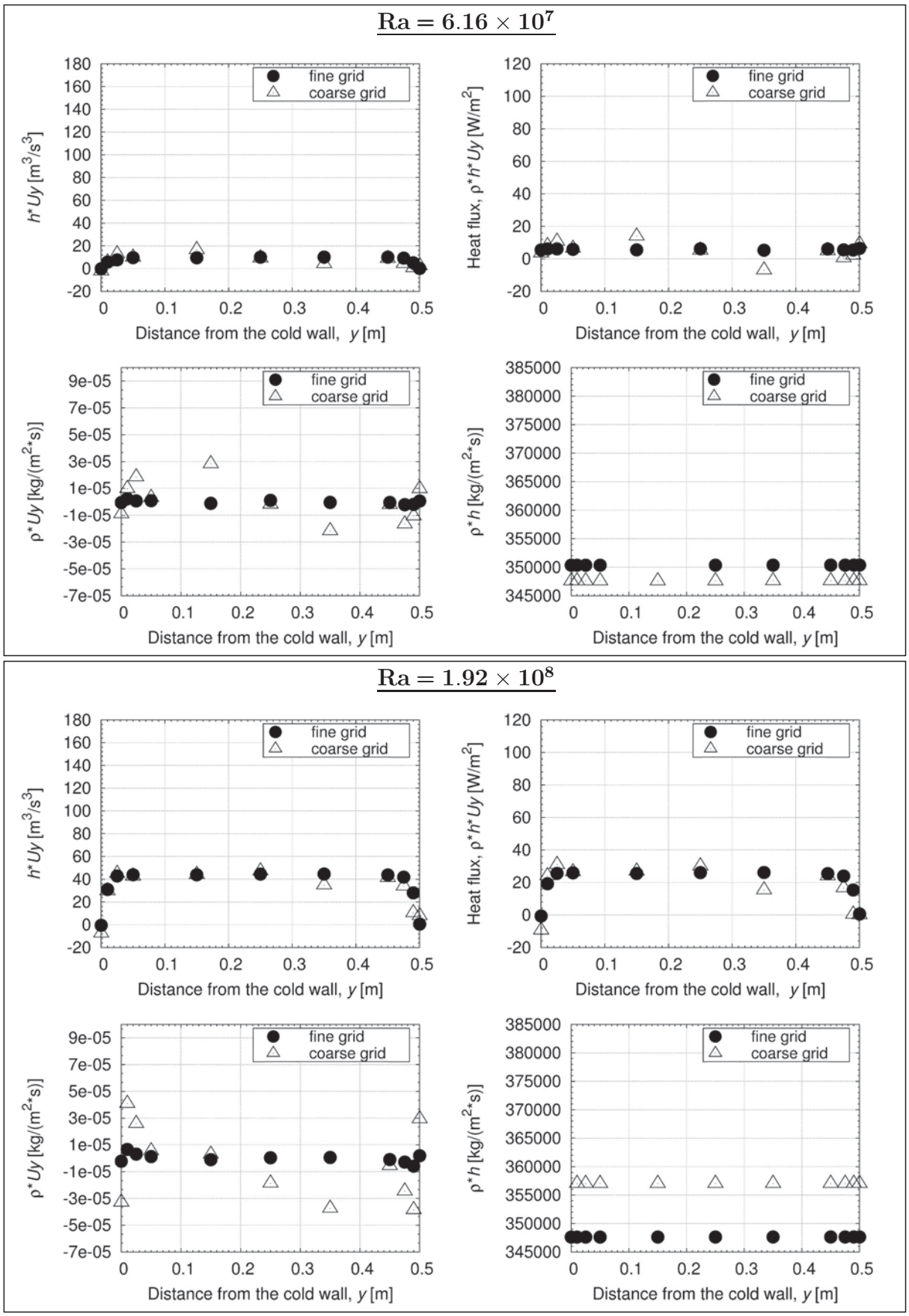

Figure 6.31.: Time- and area-averaged profiles of $\left\langle \overline{\tilde{h}\tilde{u}_y} \right\rangle_A$, $\left\langle \overline{\bar{\rho}\tilde{h}\tilde{u}_y} \right\rangle_A$, $\left\langle \overline{\bar{\rho}\tilde{u}_y} \right\rangle_A$, $\left\langle \overline{\bar{\rho}\tilde{h}} \right\rangle_A$ estimated at constant planes parallel to the cold/hot wall. **Top box**: Ra $= 6.16 \times 10^7$. **Bottom box**: Ra $= 1.92 \times 10^8$. **In all pictures:**•: $(430 \times 140 \times 140)$ cells, △: $(150 \times 50 \times 50)$ cells.

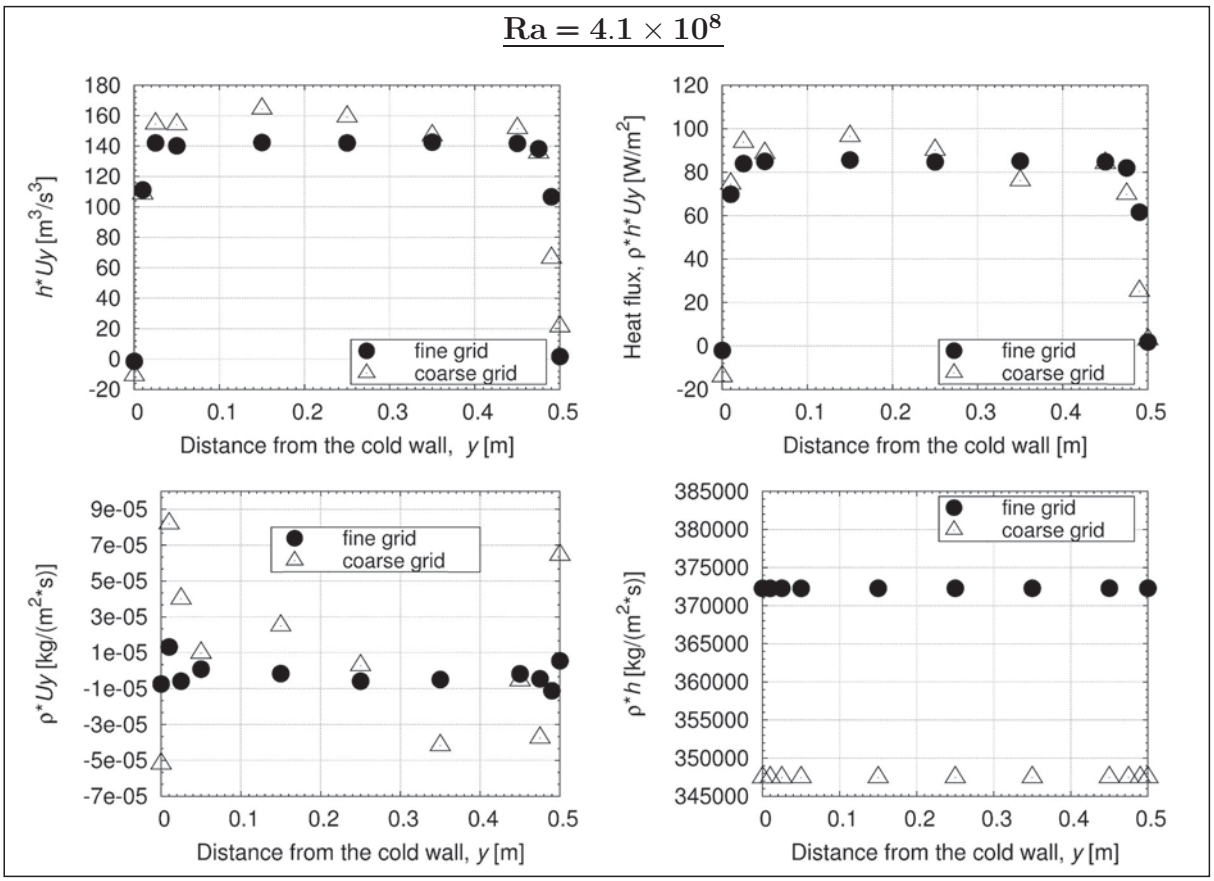

Figure 6.32.: Time- and area-averaged profiles of $\left\langle \overline{\tilde{h}\tilde{u}_y} \right\rangle_A$, $\left\langle \overline{\bar{\rho}\tilde{h}\tilde{u}_y} \right\rangle_A$, $\left\langle \overline{\bar{\rho}\tilde{u}_y} \right\rangle_A$, $\left\langle \overline{\bar{\rho}\tilde{h}} \right\rangle_A$ estimated at constant planes parallel to the cold/hot wall. $\mathrm{Ra} = 4.1 \times 10^8$. **In all pictures:** •: $(430 \times 140 \times 140)$ cells, △: $(150 \times 50 \times 50)$ cells.

6.5. Simulation results versus experimental data

Nusselt number profile estimated at the heated walls - averaged values of the simulation

In this section, the simulation results are compared as last step to an analogous experimental setup of *Ebert et al.* in [Ebert08]. The experiment has the same dimensional configuration, and temperature conditions as the computational geometry. First, the experimental Nusselt number values and the results of the simulation should be discussed. Note that some of the following contents are also presented in extracts in [Zimmermann12] and [Zimmermann15].

In [Ebert08], the local heat flux is evaluated at two positions, at $x_c = 1.185\,\mathrm{m}$ and at $x_p = 1.835\,\mathrm{m}$ at the hot and cold wall. From these values, the local Nusselt number is estimated at these positions. Subsequently, the temperature wall gradients are estimated from these local values. The measured values of the experiment are listed together with the simulation results in table 6.10.

Additionally, the data of the theoretical studies in [Grossmann00] and [Hölling06] are given.

Nu	1	2	3	$(430 \times 140 \times 140)$	$(150 \times 50 \times 50)$
$\mathbf{Ra = 6.16 \times 10^7}$					
cold	22.92	27.18	x_c 77.04 x_p 70.84	22.35 (1: -2.49%) (2: -17.78%)	22.04 (1: -3.84%) (2: -18.91%)
hot	22.92	27.18	x_c 74.57 x_p 80.82	24.33 (1: +6.15%) (2: -10.49%)	22.01 (1: -3.97%) (2: -19.02%)
$\mathbf{Ra = 1.92 \times 10^8}$					
cold	30.45	38.60	x_c 89.19 x_p 83.80	30.54 (1: +0.30%) (2: -20.88%)	29.96 (1: -1.61%) (2: -23.38%)
hot	30.45	38.60	x_c 83.80 x_p 95.53	29.37 (1: -3.55%) (2: -23.91%)	29.82 (1: -2.10%) (2: -22.75%)
$\mathbf{Ra = 4.1 \times 10^8}$					
cold	36.81	48.89	x_c 89.38 x_p 99.06	39.37 (1: +6.95%) (2: -19.47%)	39.54 (1: +7.42%) (2: -19.12%)
hot	36.81	48.89	x_c 110.39 x_p 97.72	35.97 (1: -2.28%) (2: -26.43%)	35.68 (1: -3.07%) (2: -27.02%)

Table 6.10.: Time- and area-averaged Nusselt number values estimated at the cold/hot wall of the simulation compared to theoretical values of [Grossmann00] (indicated by **1**, see also eq. (6.3.11)) of [Hölling06] (indicated by **2**, see also eq. (6.3.12)) as well as to local data of [Ebert08] (indicated by **3**, values estimated at position $x_c = 1.185\,\mathrm{m}$ and $x_p = 1.835\,\mathrm{m}$).

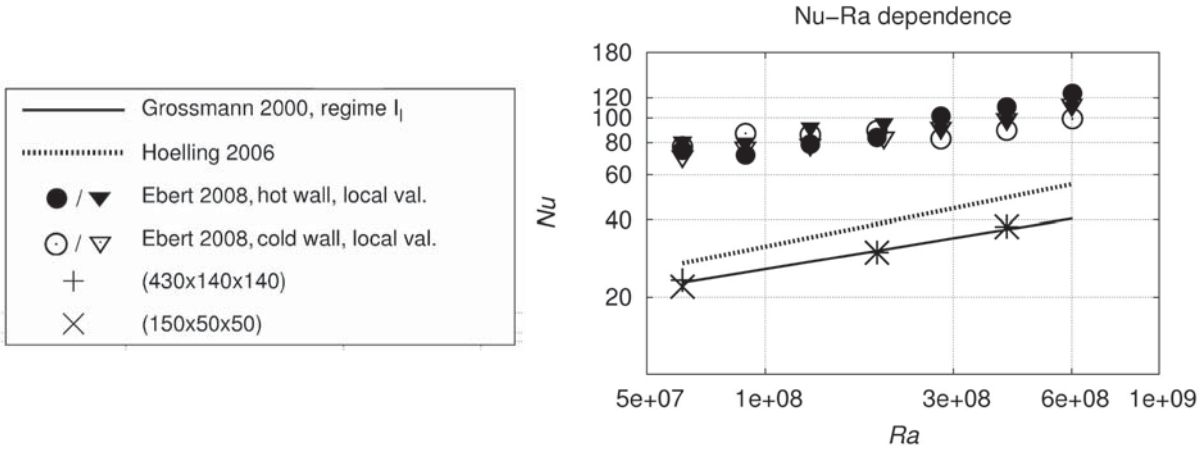

Figure 6.33.: Nu-Ra dependence at the heated walls of the simulation compared to data of [Grossmann00], [Hölling06] and [Ebert08]. Pr = 0.71. [Grossmann00]: **-** black solid line, [Hölling06]: **- -** black dashed line. study [Ebert08]: **cold wall**: ∘ at $x_c = 1.185\,\mathrm{m}$, ▽ at $x_p = 1.835\,\mathrm{m}$ (similar to [Zimmermann12] and [Zimmermann15]). **hot wall**: • at $x_c = 1.185\,\mathrm{m}$, ▼ at $x_p = 1.835\,\mathrm{m}$. Simulation data: +: $(430 \times 140 \times 140)$ cells. ×: $(150 \times 50 \times 50)$ cells.

The percentage notation in table 6.10 gives the deviation between the simulation results and the theoretical values of [Grossmann00]. The simulation results deviate only in a range of 8% from the values of [Grossmann00] (indicated by number "1"). The simulation results deviate about a maximum of 27% from the values of [Hölling06] (indicated by number "2"). But it has to be regarded, as mentioned before, that the assumption of [Hölling06] with $\mathrm{Ra} \to \infty$ is not realisable in an enclosed test case setup as it is used in this study.

As table 6.10 shows, the experimental results of [Ebert08] are very high and exceed not only the values of the simulation data but also the values of both theoretical estimations. Afore, we have seen in figure 6.21 on page 173 that the simulation results of the averaged Nusselt number values with a shared factor approximated well the theoretical assumptions of [Grossmann00], respectively the modified theories of [Grossmann01] and of [Stevens13] (see also eq. (6.3.15) and eq.(6.3.14) on pages 171 - 172). A graphical comparison between these averaged simulation values to the study of [Ebert08] is shown in figure 6.33. Additionally, the values which are based on the theory of [Grossmann00] and [Hölling06] are also plotted in figure 6.33.

Figure 6.33 shows clearly that the local values of the experiment of [Ebert08] exceed significantly not only the simulation data, but also the values which are based on the theoretical assumptions of [Grossmann00] and [Hölling06] (as well as the updated values of [Grossmann01] and of [Stevens13] (see figure 6.21)).

To analyse these high deviations between the experiment of [Ebert08] and the simulations of this thesis further, the local Nusselt number values are estimated in the simulation at the same both positions, $x_c = 1.185\,\mathrm{m}$ and $x_p = 1.835\,\mathrm{m}$, as in the experiment.

Nusselt number profile at the heated walls - local values of the simulation at the positions $\mathbf{x_c = 1.185\,m}$ and $\mathbf{x_p = 1.835\,m}$, hot and cold wall

Table 6.12 lists the local Nusselt number values estimated in the simulation and in the experimental study of [Ebert08]. In [Ebert08], the local Nusselt number values were estimated at position $x_c = 1.185\,\mathrm{m}$ and $x_p = 1.835\,\mathrm{m}$ at the hot and cold wall. At these positions the simulation data was also estimated for all Rayleigh number cases and both grid resolutions.

The values in table 6.12 show, that also the local values of the simulation differ significantly from the ones of the experiment, as it was the case before for the averaged values in table 6.10. In the worst case, the values of the simulation lie about 80% under the values of the experiment.

Regarding a tendency of the Nusselt number distribution in the experimental values, one can give the following overview in table 6.11. H marks the values at the hot wall and C

the values at the cold wall at the positions $x_c = 1.185\,\mathrm{m}$ and $x_p = 1.835\,\mathrm{m}$. The given tendency can also be observed in the simulations for all cases, except for case $\mathrm{Ra} = 1.92 \times 10^8$ and the coarse grid resolution.

	$\mathrm{Ra} \leq 1.92 \times 10^8$	$\mathrm{Ra} > 1.92 \times 10^8$
x_c	H < C	H > C
x_p	H > C	H < C

Table 6.11.: Tendency of the Nusselt number distribution in the experiment of [Ebert08]. Position $x_c = 1.185\,\mathrm{m}$ and $x_p = 1.835\,\mathrm{m}$.

local Nu		[Ebert08]	$(430 \times 140 \times 140)$	$(150 \times 50 \times 50)$
$\mathbf{Ra = 6.16 \times 10^7}$				
hot	x_c	74.57	14.49	16.38
	x_p	80.82	25.61	23.63
cold	x_c	77.04	29.37	19.30
	x_p	70.84	13.88	14.26
$\mathbf{Ra = 1.92 \times 10^8}$				
hot	x_c	83.8	22.8	28.85
	x_p	95.53	33.0	21.36
cold	x_c	89.19	27.18	22.41
	x_p	83.3	22.62	33.30
$\mathbf{Ra = 4.1 \times 10^8}$				
hot	x_c	110.39	34.84	35.34
	x_p	97.72	26.16	29.81
cold	x_c	89.38	29.96	29.37
	x_p	99.06	46.21	31.15

Table 6.12.: Time-averaged local Nusselt number values estimated at the cold and hot wall at $x_c = 1.185\,\mathrm{m}$ and $x_p = 1.835\,\mathrm{m}$. Simulation data compared to the study of [Ebert08].

Temperature distribution between the heated walls, estimated at position $\mathbf{x = 1.185\,m}$, vertical axis

Complementary to the before presented results, the temperature profiles of the simulations are compared at this point to the experimental data. In figure 6.34 on page 193, the temperature profiles of the experiment are plotted versus the simulation data for all Rayleigh numbers and both grid resolutions. Note that some of the following presented are also discussed in extracts in [Zimmermann12]. As before, the values are estimated between the heated walls at the xy-midplane, at $x = 1.185\,\mathrm{m}, z = 0.25\,\mathrm{m}$, along the vertical y-axis. A detailed plot of the cold and hot wall is shown additionally in figure 6.35. The

anti-symmetrical form of the experimental data stands out. But we have seen that the asymmetrical profiles of the simulations were typical for a NOB convection, according, for example, to [Ahlers06]. In the bulk region, the simulations approximate the experimental data. Even the results of case Ra $= 4.1 \times 10^8$ and $(430 \times 140 \times 140)$ cells approximate the experimental data at the cold wall. The visible deviations between experiment and simulation are intensified in case of the coarse grid results.

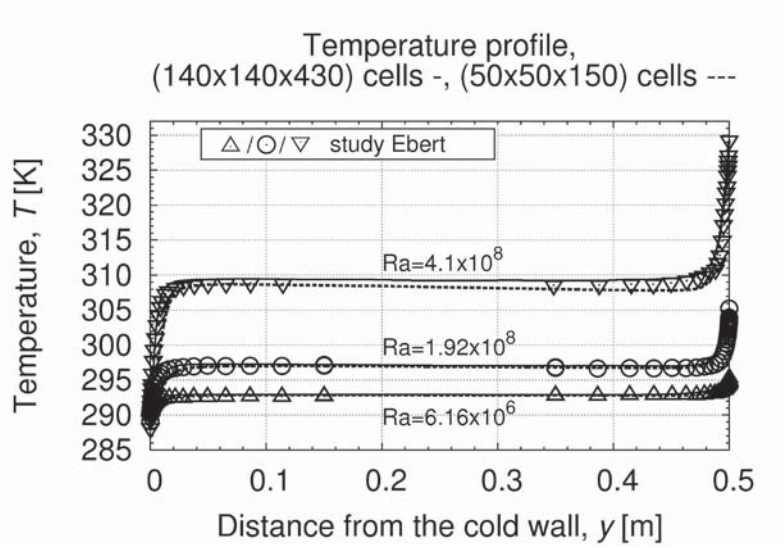

Figure 6.34.: Time-averaged temperature profile between the heated walls. Estimated at the xy-midplane, at $x = 1.185\,\mathrm{m}$ and $z = 0.25\,\mathrm{m}$, vertical y-axis. Simulation data compared to experimental data of [Ebert08]. Study [Ebert08]: △: Ra $= 6.16 \times 10^7$. ○: Ra $= 1.92 \times 10^8$. ▽: Ra $= 4.1 \times 10^8$. **-** solid lines: $(430 \times 140 \times 140)$ cells, **- -** dashed lines: $(150 \times 50 \times 50)$ cells.

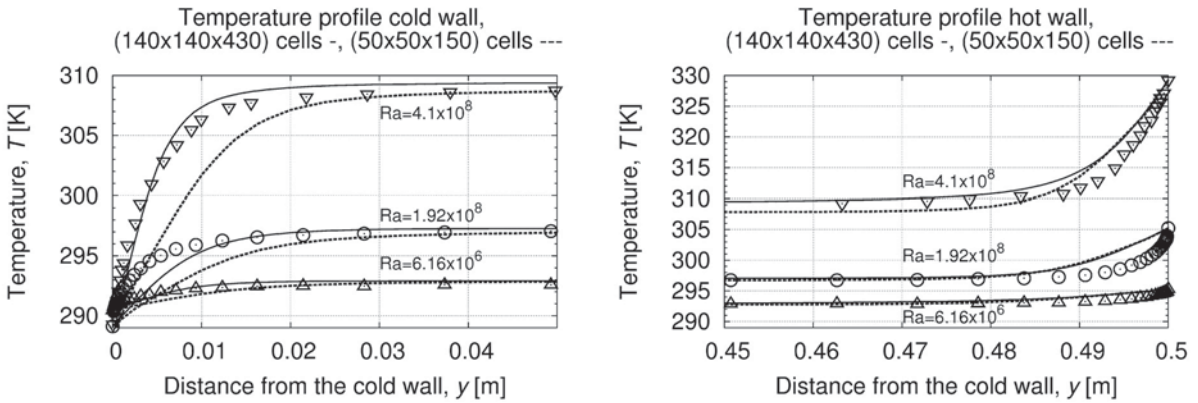

Figure 6.35.: Time-averaged temperature profile between the heated walls. Estimated at the xy-midplane, at $x = 1.185\,\mathrm{m}$ and $z = 0.25\,\mathrm{m}$, vertical y-axis. Simulation data compared to experimental data of [Ebert08] (similar to [Zimmermann12]). **Left:** Cold wall. **Right:** Hot wall. **In each picture:** study [Ebert08]: △: Ra $= 6.16 \times 10^7$. ○: Ra $= 1.92 \times 10^8$. ▽: Ra $= 4.1 \times 10^8$. **-** solid lines: $(430 \times 140 \times 140)$ cells, **- -** dashed lines: $(150 \times 50 \times 50)$ cells.

Table 6.13 presents local values of the temperature gradient, estimated at the hot and cold wall in the study of [Ebert08] ($x_c = 1.185\,\mathrm{m}$), together with global values of the experiment as well as the simulation data. The global values were estimated by [Ebert08] from global Nusselt number values which were estimated according to the theoretical estimations of [Hölling06] and equation (6.3.12) on page 169.

$\left.\frac{\partial T}{\partial y}\right\|_{\tilde{w}}$ [K/m]	[Ebert08] local ($x_c = 1.185\,\mathrm{m}$)	[Ebert08] global	($430 \times 140 \times 140$)	($150 \times 50 \times 50$)
$\mathbf{Ra = 6.16 \times 10^7}$				
cold	743	263	214.72 (-18.36%)	212.90 (-19.05%)
hot	719	263	234.98 (-10.65%)	212.57 (-19.17%)
$\mathbf{Ra = 1.92 \times 10^8}$				
cold	2876	1243	955.52 (-20.84%)	959.94 (-22.77%)
hot	2702	1243	946.34 (-23.87%)	955.52 (-23.13%)
$\mathbf{Ra = 4.1 \times 10^8}$				
cold	7345	4024	3240.20 (-27.44%)	3236.50 (-19.57%)
hot	9072	4024	2960.60 (-26.43%)	2919.90 (-27.44%)

Table 6.13.: Time- and area-averaged temperature gradients estimated at the cold and hot wall. Simulation data compared to local and global values of [Ebert08] (estimated at the cold/hot wall at position $x_c = 1.185\,\mathrm{m}$).

The percentage notation describes the difference between the simulation data and the global estimations of [Ebert08]. The high local Nusselt number values in the experiment are reflected in high temperature gradients as table 6.13 shows. Also the global values of [Ebert08] differ maximal of about 28% from the simulations, as it was expected, because the simulation data lie beneath the Nusselt number values of [Hölling06] which were the basis for the estimation of the global values in [Ebert08].

Complementary to the before presented temperature profiles, the temperature values are illustrated again this time with a standard deviation in figures 6.36 - 6.37 on pages 195 - 196. The standard deviations are estimated according to equation (5.3.1) in chapter 5, section 5.3.2. Unfortunately, information on the standard deviation of the data in [Ebert08] were only disposable for case Ra = 1 92 $\times 10^8$

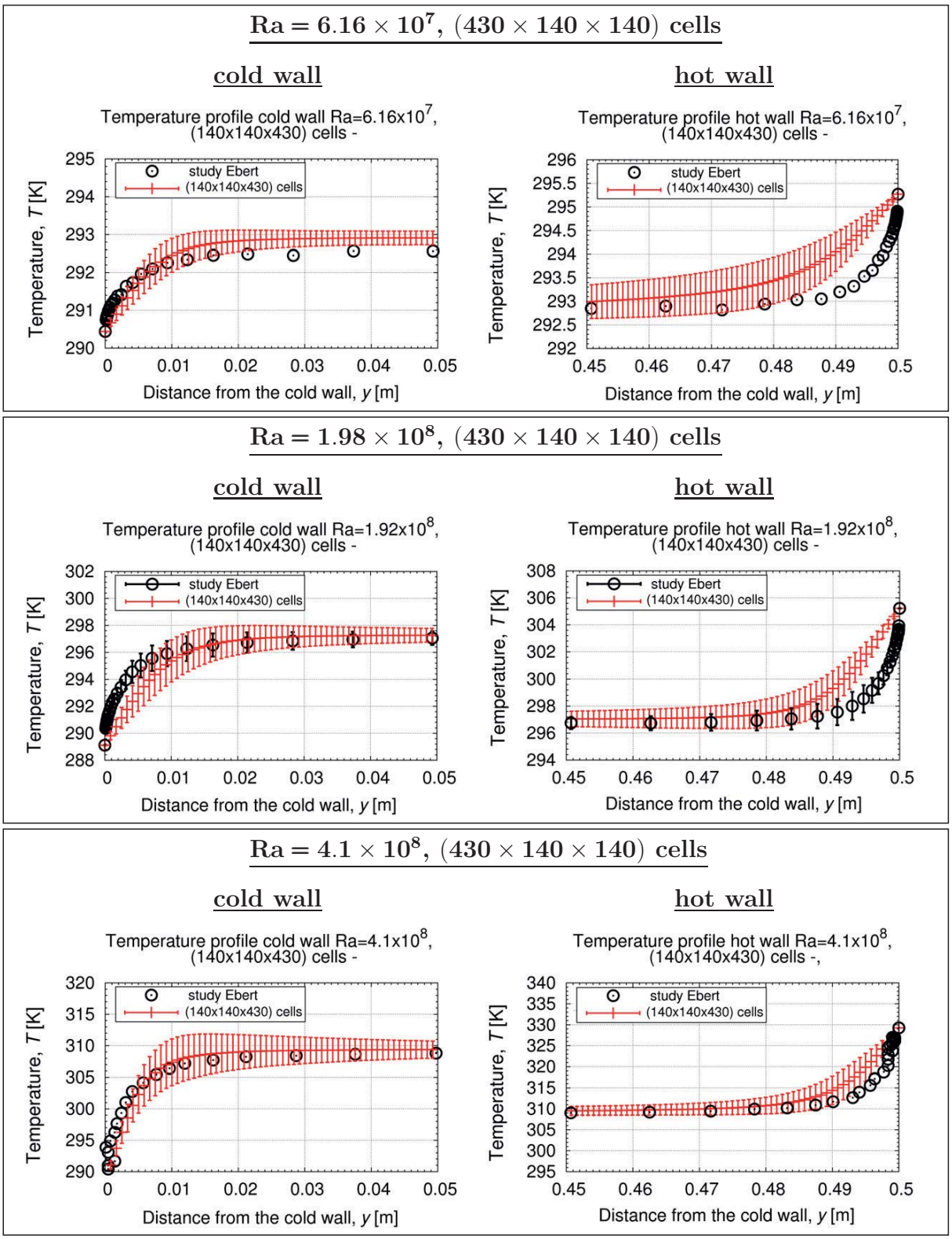

Figure 6.36.: Time-averaged temperature profile between the heated walls with standard deviation. Estimated at the xy-midplane, at $x = 1.185\,\mathrm{m}$ and $z = 0.25\,\mathrm{m}$, vertical y-axis. Simulation data compared experimental data of [Ebert08]. **Left:** Cold wall. **Right:** Hot wall. **Top box:** $\mathrm{Ra} = 6.16 \times 10^7$. **Middle box:** $\mathrm{Ra} = 1.92 \times 10^8$. **Bottom box:** $\mathrm{Ra} = 4.1 \times 10^8$. **In each picture:** - red line: $(430 \times 140 \times 140)$ cells, ∘ study [Ebert08].

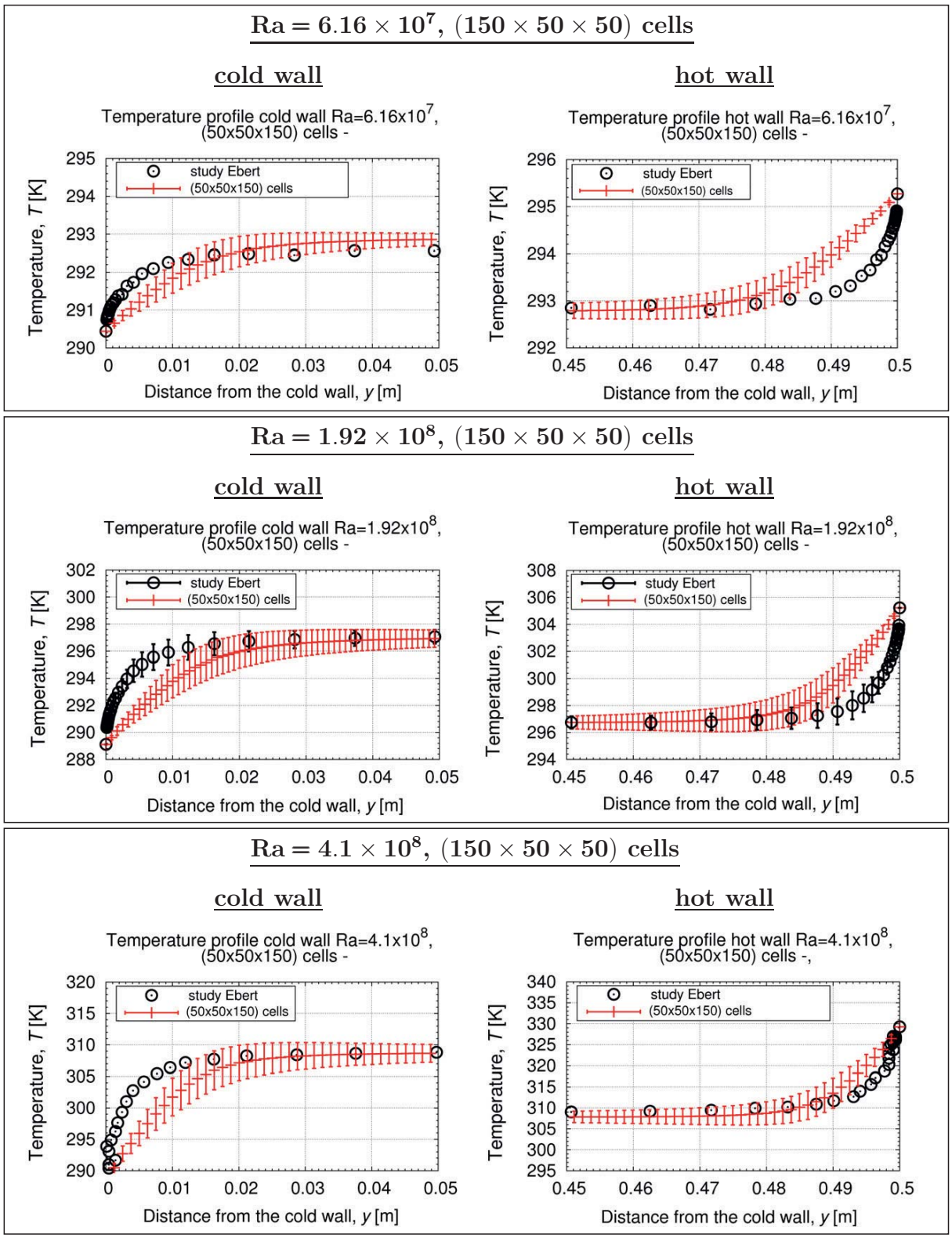

Figure 6.37.: Time-averaged temperature profile between the heated walls with standard deviation. Estimated at the xy-midplane, at $x = 1.185\,\mathrm{m}$ and $z = 0.25\,\mathrm{m}$, vertical y-axis. Simulation data compared experimental data of [Ebert08]. **Left:** Cold wall. **Right:** Hot wall. **Top box:** $\mathrm{Ra} = 6.16 \times 10^7$. **Middle box:** $\mathrm{Ra} = 1.92 \times 10^8$. **Bottom box:** $\mathrm{Ra} = 4.1 \times 10^8$. **In each picture:** – red solid line: $(150 \times 50 \times 50)$ cells, ∘ study [Ebert08].

Hence, only for this case the standard deviation of the experimental values is presented in figures 6.36 - 6.37 on pages 195 - 196. In vicinity to the heated walls, only a slight increase of the standard deviation is visible. In direction to the bulk region, the values of the standard deviation rise.

Close before the bulk region is reached, the values become smaller and are almost constant. The values at the hot wall are at the most positions smaller than at the cold wall, except for the case of $\mathrm{Ra} = 6.16 \times 10^7$ and the fine grid resolution. The highest fluctuations are located between the turbulent boundary layer and the conductive layer, as it was expected. This is also the case in the data of [Ebert08] in figure 6.36 for case $\mathrm{Ra} = 1.92 \times 10^8$.

Non-dimensional temperature profile in the thermal boundary layer at the cold/hot wall, vertical axis

As last step, the non-dimensional temperature profile of the simulation is compared to one for the experimental test case in [Ebert08] (see figure 6.38). Note that some of the following results are also discussed in extracts in [Zimmermann15]. The simulation values are again time-averaged. To illustrate the non-dimensional temperature profile for the experimental test case, the in [Ebert08] given temperature values were normalised with help of equation (6.3.5).

To obtain a reference temperature for the experimental case, the in the simulation estimated fluid properties values were used, because the fluid properties required in eq. (6.3.4) were not given in [Ebert08] for the experimental case. In this way both non-dimensional profiles were normalised on the basis of the same properties. For a better demonstration of all results together in one plot, a constant is added to the results of each Rayleigh number. The constants are $\mathrm{Ra} = 6.16 \times 10^7 : +0$, $\mathrm{Ra} = 1.92 \times 10^8 : +9$ and $\mathrm{Ra} = 4.1 \times 10^8 : +18$.

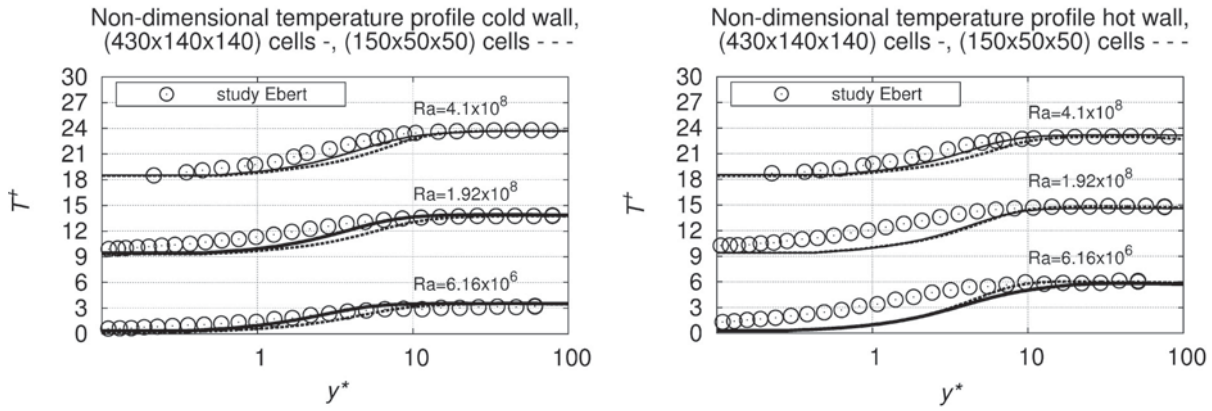

Figure 6.38.: Time-averaged non-dimensional temperature profile in the boundary layer, simulation data compared to [Ebert08] (see also [Zimmermann15]). Estimated at the xy-midplane, at $x = 1.185$m, $z = 0.25$m, vertical y-axis. **Left:** Cold wall. **Right:** Hot wall. **In each picture:** **-** solid lines: $(430 \times 140 \times 140)$ cells, **- -** dashed lines: $(150 \times 50 \times 50)$ cells, ○: study [Ebert08].

The deviations of the temperature values between simulation and experiment from figure 6.35 and table 6.13 are recovered in the non-dimensional profile, as it was expected. The significant differences between both studies concerning the temperature profiles as well as Nusselt number values might be due to a possible higher heat flux in the experiment, and consequently, a more intensive mixing of hot and cold streams between the walls.

6.6. Concluding comments

In this chapter, a compressible, non-Boussinesq LES was performed for a RB convection in an air-filled enclosed container where the two horizontal walls were heated. The realised Rayleigh numbers were $\mathrm{Ra} = 6.16 \times 10^7$, $\mathrm{Ra} = 1.92 \times 10^8$ and $\mathrm{Ra} = 4.1 \times 10^8$ with a Prandtl number of $\mathrm{Pr} = 0.71$. To observe the influence of the mesh resolution on the numerical results, especially in close distance to the heated walls, two different grid resolutions were performed. The simulation results were compared to theoretical data of [Ahlers06], [Hölling06] as well of [Grossmann00, Grossmann01], respectively [Stevens13] and subsequent to an analogous experiment in [Ebert08]. The investigated main aspects of this chapter were

1) temperature profile between the heated walls estimated at different positions, along the vertical axis, at the vertical cross-section,

2) location of the convection cells visualised by the mean velocity distribution,

3) investigation of non-Boussinesq-effects in the fluid on the basis of the temperature profile, compared to data of [Ahlers06],

4) analytical model of the non-dimensional temperature profile, especially in the thermal boundary layer near the heated walls, at the vertical cross-section,

5) profile of the effective dynamic viscosity μ_{eff} and thermal diffusivity α_{eff} between the heated walls, estimated along the vertical axis, at the vertical cross-section,

6) estimation of a global heat flux variable and its profile as well as the influencing fluid properties, estimated at constant planes parallel to the heated walls,

7) local and area-averaged Nusselt number profiles at the heated walls, compared to data of [Grossmann00, Grossmann01], [Stevens13] and [Hölling06],

8) comparison of simulation results to experimental data of [Ebert08], on the basis of the Nusselt number and temperature profile as well as the non-dimensional temperature profile.

All presented results were time-averaged over an interval of $t = 200\,\mathrm{s} - 380\,\mathrm{s}$ in the simulated process with an intermediate steps size of $\Delta t = 1\,\mathrm{s}$. The profiles of the temperature as well as of the global heat flux structure and its dependent fluid properties revealed an asymmetrical profile in the results of both grid resolutions. This asymmetry was also reported by [Ahlers06] for a non-Boussinesq convection in water as well as in glycerol and also by [Horn11] for a DNS of a non-Boussinesq convection in water. The asymmetry was founded in the non-Boussinesq effects of density changes which were caused by temperature differences in the fluid.

Major grid dependencies were caused by different quasi-stable states, which could be seen on the basis of the temperature profile estimated at two mirror-imaged positions at the vertical cross-section and also on the basis of the convection cell arrangement in the container. Because different coherent structures existed at the mirror-imaged positions with, in some cases, also an opposite circulation orientation, the reproducibility of the temperature profiles was destroyed.

The non-dimensional temperature profile of the thermal boundary layer approximated the analytical function of [Hölling06]. The Nusselt- and Rayleigh number-dependence of the simulation approximated well the theoretical data of [Grossmann00, Grossmann01], respectively of [Stevens13] for the investigated Rayleigh numbers and a Prandtl number of $\mathrm{Pr} = 0.71$. The deviations between the dynamic viscosity profiles (and also thermal diffusivity) for both resolutions could be possibly caused by numerical effects and by grid dependencies and should be further investigated to state a distinct explanation.

In comparison to a comparable experimental setup in [Ebert08], the simulation showed significantly deviations in the temperature profiles which were caused by higher Nusselt number values in the study of [Ebert08]. These higher values might be caused by a possible higher heat flux in the experimental setup. The fact, that the experimental local Nusselt number values in [Ebert08] exceeded also significantly the analytical theory of [Grossmann00] and of [Hölling06] points also to a higher heat flux in the experiment and explains the deviations to the simulation results. The anti-symmetrical form of the temperature profiles in the experiment in comparison to the asymmetrical form in the simulation was due to non-Boussinesq effects in the simulation.

[Horn11] investigated with help of a DNS a non-Boussinesq convection as well as a Boussinesq convection in water in a setup with an unit aspect ratio and a Rayleigh number of $\mathrm{Ra} = 10^8$. Besides [Ahlers06], also *Horn et al.* report an asymmetrical temperature profile in the non-Boussinesq convection compared to an anti-symmetrical profile in the Boussinesq convection. Further, *Horn et al.* observed an increased bulk temperature as well as a different boundary layer thickness in the non-Boussinesq convection, which could also be revealed in the simulation compared to the experimental study of [Ebert08].

The performed compressible, non-Boussinesq Large-Eddy simulation is an adequate choice to model a Rayleigh-Bénard convection in the presented test case configuration. The obtained results approximated very well the expected theoretical assumptions. The results showed that it is essential to choose a well-resolved mesh especially in the near wall region when no wall-function is used in the numerical model.

7. Case studies - Test case *CenCon*, a Rayleigh-Bénard problem affected by the Coriolis force

7.1. Configuration of *CenCon* in the experiment

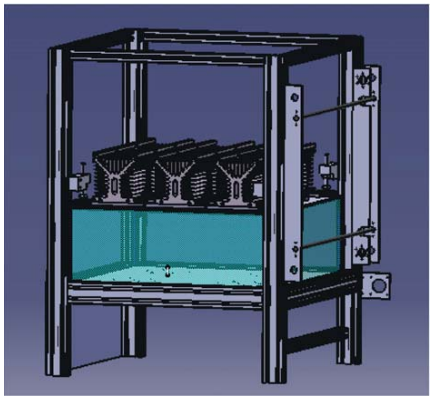

Figure 7.1.: CAD drawing of the experimental test case of *CenCon*.

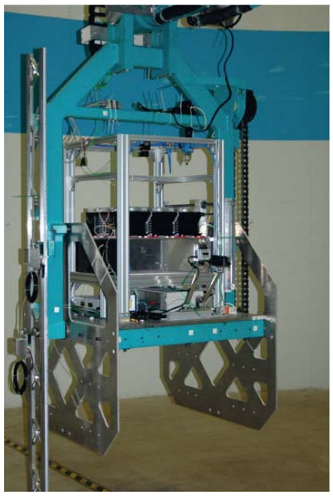

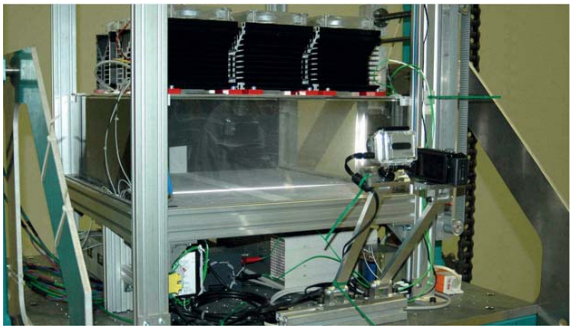

Figure 7.2.: Photographs of the experimental setup of *CenCon* installed in the institute's centrifuge.

The previously presented chapters 5 and 6 examine a turbulent natural convection in two different setup configurations. As mentioned before, the choice of the two heated walls is the determining factor for the development of the main flow field. Note that some of the presented results and discussions in the following are also illustrated in extracts in [Zimmermann14b].

In this section, the influence of a Coriolis force field impressed on the configuration of a RB problem is investigated in an experimental as well as a numerical study. The main purpose lies on the analysis of a possible stabilising effect of the Coriolis force on the turbulent unsteady flow structures. Temperature and velocity distributions are influenced by an interacting of thermal convection and conduction in the setup. In the experiment the same conditions as in the atmosphere in the beginning of a twister or hurricane should be realised but in smaller dimensions.

The relative accelerations which are caused in the atmosphere by the Earth's rotation are realised in the experiment by a uniform-rotational movement of the setup in a large-scale centrifuge belonging to the institute. To analyse the influence of the Coriolis acceleration on the turbulent flow structures, two different modes are investigated in the experiment as well as in the simulation. First, the test case is investigated in a non-rotation mode. Second, the test case is analysed while it is uniformly rotating in the large-scale centrifuge. Differences between both modes will be observed.

The setup of *CenCon* consists of a rectangular air-filled container which has a similar layout to the RB cell of *RayCon* in chapter 6. Regarding *CenCon*, both horizontal walls are heated isothermally. A technical drawing of the experimental setup is presented in figure 7.1 on page 201. Additionally, figure 7.2 shows two photographs of the test case installation in the centrifuge.

Regarding the dimensions of the experimental test case, the layout was restricted to the conditions in the centrifuge. Further, the influence from the sidewalls on the main flow field should be reduced by choosing a bigger length than height of the setup (s. chapter 3, section 3.5). The experimental test case consists of a container with a length (L) of 0.6 m, a height (H) of 0.2 m and a depth (D) of 0.6 m. Hence, the aspect ratios are $\Gamma_x = \frac{D}{H} = 2.9$ and $\Gamma_y = \frac{L}{D} = 1$.

The sidewalls are made of polymethyl methacrylate (PMMA) assuring a visualisation of the turbulent flow structures in the container. Each sidewall have a thickness of 0.01 m. An almost atmospheric pressure condition is generated inside the container. A rectangular layout was chosen due to visualisation aspects. The corner regions may imply disadvantages concerning later used tracer particles, but a cylindrical cell would have implied possible disadvantages concerning optical effects, e .g. optical refractions or reflections. At the right side of the experimental test case a displaceable light-slit-section is installed

consisting of a a light-source of type *Schölly®*, *1000.xenon 4*, *article number 04087* with 230 V, 50/60 Hz and 1.25/2.5 A. The optic is made of a line light with a diameter of 0.015 m (*Schölly®*, *QWF.8050*). The light-slit-section can be moved along an elevating screw at the right side of the container driven by a small motor. It can be stopped in frequent intervals of 0.01 m or 0.05 m along the container side. The whole experimental setup is attached to an aluminium frame serving as an attachment possibility for other equipment, e. g. light-section, power supplies and video cameras. Further, the frame should serve as stabilisation for the whole setup.

Layout of heating and cooling circuits in the setup of *CenCon*

The container is heated isothermally from below and cooled from above with a constant temperature difference between both heated walls. Both walls are made of aluminium plates. The side walls do not satisfy an adiabatic condition. The walls are conducting and a possible heat loss trough the side walls has to be considered (s. appendix A.2.1, from page 278 on). An isolation layer of foam is attached between all walls to reduce a possible heat loss.

A technical drawing of the heating/cooling plate can be found in figure 7.3. The heating plate of the setup is build of four tubular heating components of type *Hewid®* RHK/q. They are fixed two in a row under the aluminium plate. The elements have each a diameter of 0.14 m (s. figure 7.3, left picture). The centre of one component is adjusted in a distant of 0.150 m to the side edge of the plate. The distance from one elements centre to the centre of its neighbour is 0.3 m. The maximum voltage of one heating segment is $230\,V$ and its maximum power rate $300\,W$. The cooling plate is realised of nine Peltier elements of type *multicomp* $TE1-12715\,L$ which are placed uniformly in parallel rows above the top plat (s. figure 7.3, right picture).

The Peltier elements have each a diameter of 0.05 m. The centre of each element is adjusted in a distance of 0.125 m to the side edge. The distance from one elements centre to the centre of its neighbour is 0.35 m. The Peltier elements have a maximum voltage of 15.4 V and a maximum electric current of 15 A. Generally, Peltier elements have a relative low efficiency factor which is in this case of about $\eta = 30\%$. Therefore, three rectangular extruded heat sinks of type *Fischer Elektronik*, SK 109 1000 SA are fixed additionally above the Peltier elements to enforce the heat transmission. One heat sink has a length of 0.5 m, a height of 0.135 m and a width of 0.125 m.

Moreover, three customary computer cooling fans are placed on top of each heat sink to intensify the heat transmission further. Two controller systems (*RS components*, *KS 45-112*) regulate the temperature calibration of both heated plates. Each controller operates within an error range of ± 2 K. A schematic diagram of the temperature controlling circuits is given in figure 7.4. The heating segments are connected in a parallel diagram, as the left

picture in figure 7.4 on page 204 shows. Theoretically, the effective electric current ranges between $I_{\text{eff}} = [0\,A,\, 5.1\,A]$. With a voltage interval of $U_{\text{eff}} = [0\,V,\, 230\,V]$, the maximum external resistance of the circuit is then

$$R_{i_{\text{total}}} = \frac{U_{\text{eff}}}{I_{\text{eff}}} = \frac{230\,V}{5.1\,A} = 45.11\,\Omega, \tag{7.1.1}$$

according to *Ohm's law* and *Kirchhoff's laws* (see [Kuchling1999], chapter 28).

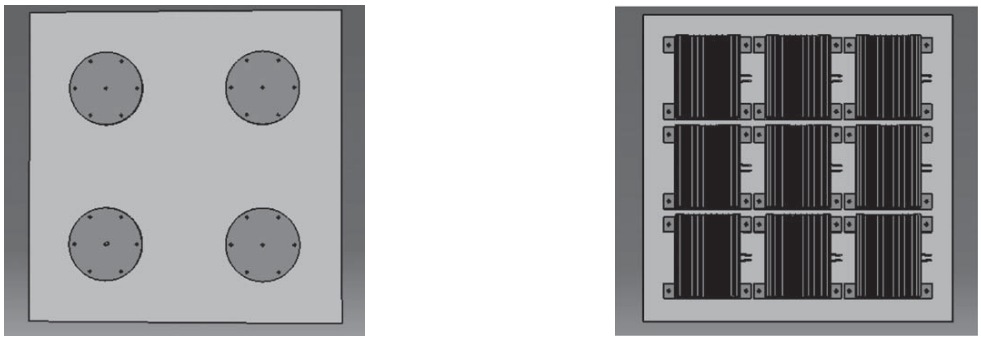

Figure 7.3.: CAD drawing of the heating (left) and cooling plate (right) in the experimental setup of *CenCon*.

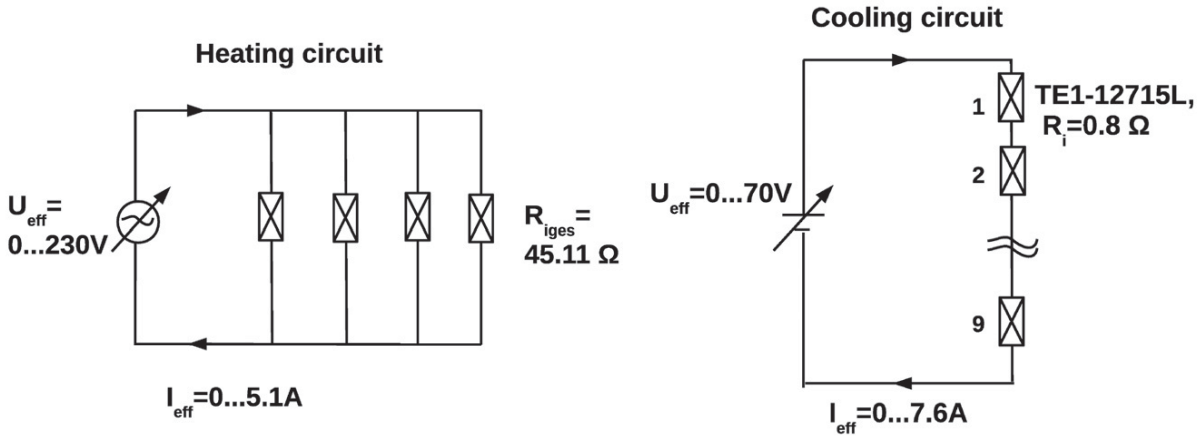

Figure 7.4.: Temperature controlling circuits in the experimental setup of *CenCon*. **Left:** Heating. **Right:** Cooling.

The outcome of the complete electrical power rating is an approximated value of about

$$P_{e_{\text{total}}} = U_{\text{eff}} I_{\text{eff}} \sim [0\,\text{kW},\, 1.17\,\text{kW}]\,. \tag{7.1.2}$$

The nine Peltier elements are connected in series. According to their data sheet, all elements have a theoretical internal resistance of $R_i = 0.8\,\Omega$. In the operating mode an internal resistance of $1.02\,\Omega$ was measured. With a voltage range of $U_{\text{eff}} = [0\,V,\, 70\,V]$ and $I_{\text{eff}} = [0\,\text{A},\, 7.6\,\text{A}]$, the complete electrical power rating of the cooling plate becomes about

$$P_{e_{\text{total}}} = U_{\text{eff}} I_{\text{eff}} = [0\,W,\ 532\,W]\ . \tag{7.1.3}$$

Due to the low efficiency factor of the Peltier elements with $\eta = 30\,\%$, the temperature power rating is minimised in the operating mode to an approximate value of

$$P_{\text{temp}} = Pe_{\text{total}}\,.\eta \sim 160\,W\,. \tag{7.1.4}$$

The maximal convective heat flux of the heating plate is estimated approximatively to $\dot{Q}_{\text{hot}} = 101.93\,\text{W}$. The high power rating of the heating plate should minimise waiting periods of temperature adjustments. Also, it has to compensate a possible heat loss through the side walls (for the estimation see A, section A.2.1, on page 278). In comparison to the maximum heating power, the maximum value of the cooling power is very low, but sufficient to hold the wall temperature constant at 293.15 K as counter reference to the heating plate.

Infrared snapshots of the heating and cooling process in the experimental setup of *CenCon*

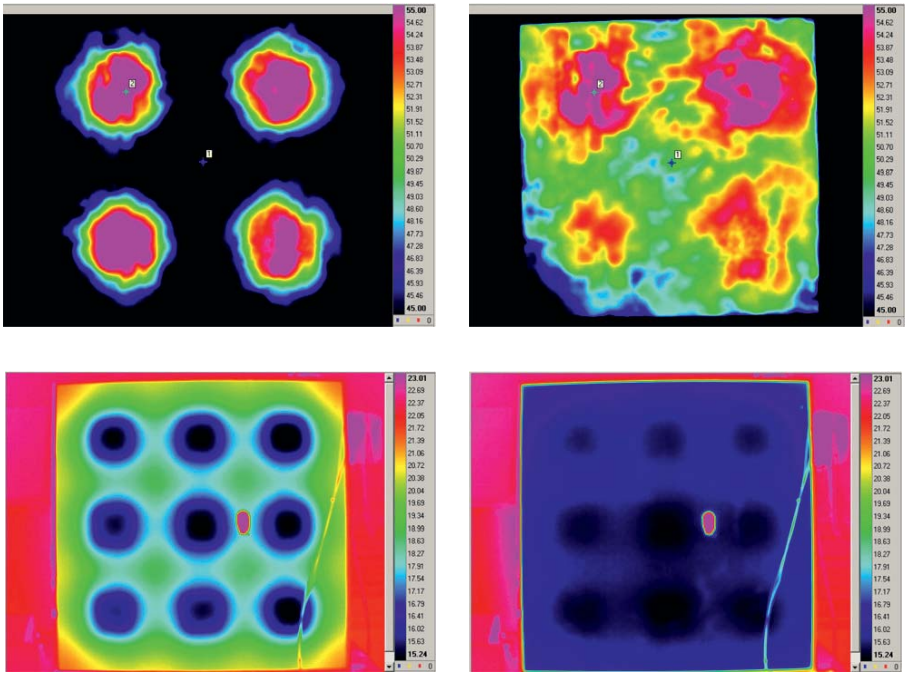

Figure 7.5.: Infrared pictures of the heating/cooling process in the experimental setup of *CenCon*. **Top row:** Heating process. **Bottom row:** Cooling process. **Left:** In the beginning. **Right:** In a stable mode.

Figure 7.5 illustrates a top view of the heating and cooling plate seen by an infrared camera of model *Flir® SC7600 BB InSb*. The camera spots a broadband of [1.5 μm, 5.1 μm]

and has a 640×512 pixel detector. It is calibrated at a constant temperature of 313.15 K. The measuring equipment of the camera works accurate within ± 0.05 K. Hence, the temperature indications in the pictures are also accurate in an interval of ± 0.05 K.

Both pictures in the top row of figure 7.5 show the heating process in the beginning (right) and in a stable mode (left). Both bottom pictures display the cooling process in the beginning (right) and in a stable mode (left). The small white patches in the pictures of the heating plate (top row) and the pink coloured patches visible in the images of the cooling plate indicate the temperature sensors which were used to evaluate the homogeneity of the temperature distribution. The heating plate features a temperature homogeneity within an error range of ± 5 K. For the cooling plate it is even ± 0.1 K.

7.2. Installation of *CenCon* in the centrifuge system

Figure 7.6 gives an overview of the centrifuge-configuration. The blue coloured parts in figure 7.6 form the base frame of the centrifuge system. The green coloured parts mark the rotator shaft and its both rotating arms.

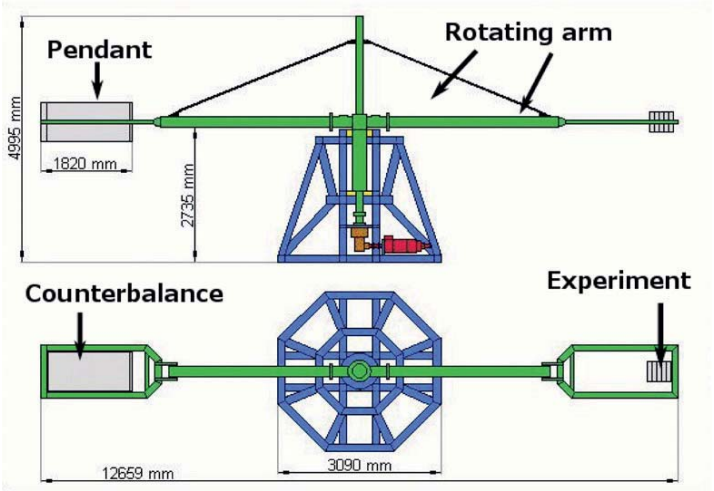

Figure 7.6.: Scheme of the institute centrifuge ([ZARM], s. also [Zimmermann14b]). **Top:** Side view. **Bottom:** Top view.

At each side of one arm a free running pendant is installed. The experiment is fixed at the right pendant. At the opposite pendant a counterbalance is installed. The rotational radius of the system is 5.42 m. The acceleration of the centrifuge can be controlled up to 5.42 g. Figure 7.7 gives in the left figure a sketch of the test case installed in the centrifuge together with an overview over its relevant geometrical properties. The right picture shows a photograph of the same setup. Note that some of the presented results and discussions in the following are also illustrated in extracts in [Zimmermann14b].

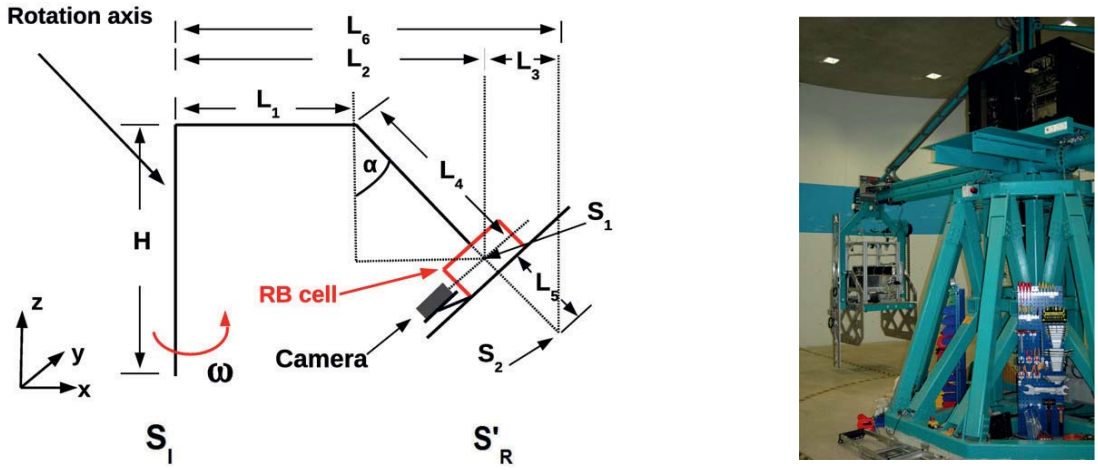

$H = 2.735\,\mathrm{m}$	$L_1 = 3.724\,\mathrm{m}$	$L_2 = 4.742\,\mathrm{m}$	$L_3 = 0.361\,\mathrm{m}$
$L_4 = 1.411\,\mathrm{m}$	$L_5 = 0.4\,\mathrm{m}$	$L_6 = 5.103\,\mathrm{m}$	$\alpha = 46.167°$
$n = 13.704$ rpm	S_1: $1.41\,g$	S_2: $1.44\,g$	tot. weight: $107.5\,\mathrm{kg}$

Figure 7.7.: Left: Scheme of *CenCon* installed in the centrifuge with characteristic properties. **Right:** Photograph of the container installed in the centrifuge (as in [Zimmermann14b]).

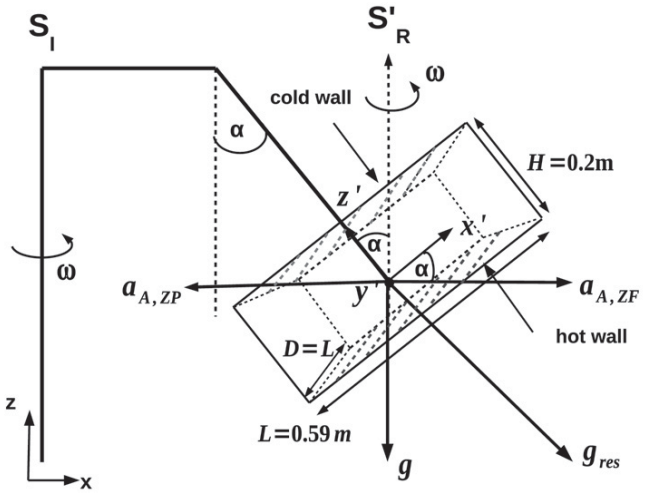

Figure 7.8.: Detailed sketch of the test cell of setup *CenCon* in the centrifuge.

Figure 7.8 displays additionally a close-up sketch of the RB cell installed in one of the rotating arms in the centrifuge. Due to the rotational movement in the rotation mode of the centrifuge, besides a Coriolis acceleration also a centrifugal acceleration $\boldsymbol{a}_{A,\mathrm{ZF}}$ as well as a higher gravitational acceleration $\mathbf{g}_{\mathrm{eff}}$ affects the setup (see figure 7.8). The gravitational acceleration $\mathbf{g}_{\mathrm{eff}}$ is measured by two sensors installed in the experimental setup. The sensors are marked in figure 7.7 by S_1 and S_2. The first sensor S_1 is located in the centre of the container and the second sensor half a meter below the first one. The gravitational

acceleration has a linear distribution between both sensors. The mass centre of the whole setup is located 0.89 m below the location of S_1. While rotating, a rotation angle arises between the rotation axis of the centrifuge and its pendants, due to the design of the centrifuge. This angle is denoted by α in figure 7.7 and figure 7.8. The resulting angle depends on the chosen angular velocity of the rotation axis. While rotating, its minimal deflection is about $\alpha = 46.167°$.

To record the flow structures in the experimental test case, a camera of type *Sony HDR-PJ260VE* is fixed in front of the container at point K in a distance of 0.1 m from the side wall parallel to the centre line of the container (see figure 7.7). A detailed scheme of the camera installation is additionally illustrated in figure 7.9. Due to symmetry aspects of the setup, only one half of the container is recorded by the camera.

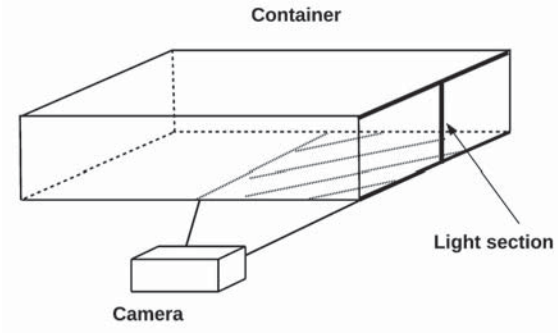

Figure 7.9.: Scheme of the container-camera installation with mounted light-section in the experimental setup of *CenCon* (as in [Zimmermann14b]).

Flow visualisation by tracer particles

To record the flow movement by the camera, it has to be visualised by tracer particles moving inside the flow, this aspect is also discussed in [Zimmermann14b]. The particles visualise the flow profile dependent on time and place without influencing the flow itself. Thus, dimension and weight of the tracer particles play a decisive role. The flow resistance and inertia of a moving tracer particle should not exceed a critical value and should have the same density as air. Moreover, the particle should be detectable by the camera. Particles of magnesium carbonate (MgCO3) are used as tracer particles. It is assumed that in an ideal case, a tracer particle can be modelled by a spherical object. The flow resistance F_w of a spherical object can be circumscribed by the force which the suspending air encounter its movement. This can be formulated for a laminar flow by the inner friction of air which is expressed for a 2-dimensional case by the law of Stokes ([Oertel06], chapter 2, 2.4.6)

$$F_w = 6\pi\mu r u\,. \tag{7.2.1}$$

Here, μ is the dynamic viscosity of air, r the radius of the spherical particle and u its approaching velocity. It follows

$$6\pi\mu r u = mg = V\rho g = \frac{4}{3}\pi r^3 \rho g. \tag{7.2.2}$$

The highest realisable temperature difference between the isothermally heated walls in the experimental setup lies at $\Delta T = 60\,\mathrm{K}$, the minimal one lies at $\Delta T = 3\,\mathrm{K}$. Hence, one can assume two dependent mean values of the inner temperature field in the container with $T_{\mathrm{hot},\,1} = 353.15\,\mathrm{K}$, $T_{\mathrm{hot},\,2} = 296.15\,\mathrm{K}$, $T_{\mathrm{cold}} = 293.15\,\mathrm{K}$

$$T_{\mathrm{mean1}} = \frac{T_{\mathrm{hot}} - T_{\mathrm{cold}}}{2} + T_{\mathrm{cold}} = 323.15\,\mathrm{K}\,, \tag{7.2.3}$$

$$T_{\mathrm{mean2}} = \frac{T_{\mathrm{hot}} - T_{\mathrm{cold}}}{2} + T_{\mathrm{cold}} = 294.65\,\mathrm{K}\,. \tag{7.2.4}$$

For both values the following fluid properties can be considered approximately as ([VDI06], Dbb2 - Dbb16)

$$T_{\mathrm{mean1}}: \quad g = 9.81\,\mathrm{m/s^2}, \quad \bar{u}_1 = 0.3\,\mathrm{m/s}, \quad \rho_1 = 1.112\,\mathrm{kg/m^3}, \quad \mu_1 = 1.917\cdot 10^{-5}\,\mathrm{kg/ms},$$
$$T_{\mathrm{mean2}}: \quad g = 9.81\,\mathrm{m/s^2}, \quad \bar{u}_2 = 0.01\,\mathrm{m/s}, \quad \rho_2 = 1.189\,\mathrm{kg/m^3}, \quad \mu_2 = 1.821\cdot 10^{-5}\,\mathrm{kg/ms}$$

with an assumed mean approaching velocity $\bar{u}$. With equation (7.2.2) it is

$$r_1 = 1.54\cdot 10^{-3}\,\mathrm{m} \qquad \text{and} \qquad r_2 = 2.65\cdot 10^{-4}\,\mathrm{m}. \tag{7.2.5}$$

Hence, the used tracer particles should have at most a radius of $2.65\cdot 10^{-4}\,\mathrm{m}$, which is fulfilled by the used magnesium particles in this study. A possible influence from the tracers on the flow structures can be formulated by the non-dimensional *number of Stokes* and with help of equation (7.2.1) ([Laurien09], chapter 3, 3.4.2).

$$\mathrm{St} = \frac{F_w}{\mu u \mathrm{L}} = \frac{6\pi r}{\mathrm{L}} \approx 0.056, \tag{7.2.6}$$

where L is the characteristic length of the setup. In the case of *CenCon*, L is the distance between the heated walls with $\mathrm{L} = \mathrm{H} = 0.2\,\mathrm{m}$. If $\mathrm{St} \ll 1$, the momentum of the tracer particles is negligible and they move inside the flow without disturbing it. According to equation (7.2.6), the chosen tracer particles can be used. A possible electrostatic charge of the PMMA side walls influencing the movement of the tracer particles is inhibit by use of an ioniser of the model *Simco Aerostat XC*.

7.3. Two arbitrary, relative to each other moving systems

7.3.1. General statements

A motion is always described relatively to a related reference frame which depends on a connected observer. In a system which is relative accelerated to an inertial system the momentum conservation law is no longer valid, due to non-negligible inertia forces. The conservation of mass and energy rest unchanged in this system (see [Spurk07], chapter 2, 2.4 and also chapter 1, section 1.5, from page 11 on).

The system of *CenCon* is relative rotating to the inertial system of the centrifuge axis. To model the flow in the rotating container of *CenCon*, the Navier-Stokes equations from chapter 1, section 1.10 on page 26 have to be modified. For an observer in the rotating system it is more important to describe the motion in his own system than in inertial system. Because the observer can only perform measurements in his own system. Therefore, one has to determine what a possible observer, which is connected to the system of *CenCon*, sees in it.

Thus, the conservation of momentum has to be reformulated in terms of variables and accelerations which appear only in the rotating system of *CenCon*. To begin with, we make some assumptions for two general to each other moving systems. The following information is referred to [Spurk07], chapter 2, 2.4.

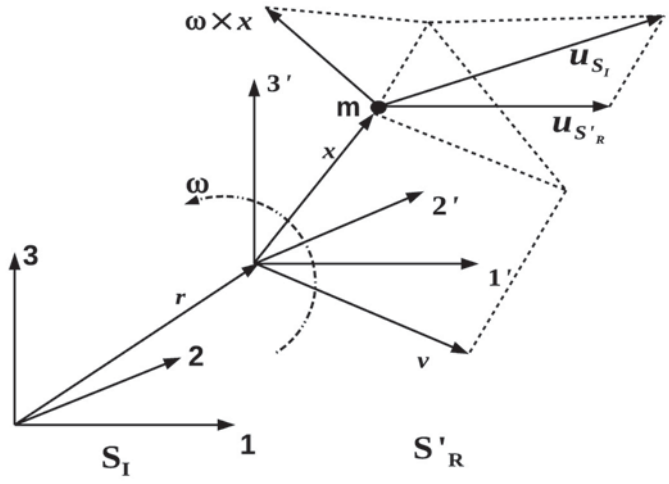

Figure 7.10.: Two relative to each other moving systems S_I, S'_R (as seen in [Spurk07]).

The inertial system is denoted in the following by S_I. The relative to S_I moving system is denoted by S'_R. The system S'_R fulfils relative to S_I a translation with a velocity $\boldsymbol{u}$ and a rotation with an angular velocity $\boldsymbol{\omega}$ (s. figure 7.10). For a detailed derivation of the angular velocity $\boldsymbol{\omega}$ it is pointed to the appendix of this thesis, appendix A, section A.1.4, on page 277.

In the relative to S_I rotating system S'_R a uniformly moving fluid particle m perceives an acceleration, which causes a change in its velocity direction. Hence, S'_R is a non inertial system. The additional forces, which affect the fluid particle, are called *fictitious forces*. Due to these forces, an observer in the inertial system S_I notices a uniform, linear movement of the fluid particle m in the non-inertial system S'_R.

It is assumed that forces and momenta are the same in both systems. The time measurements should be independent in each system, hence, it is $t = t'$ in both systems. But the variation in time of each vector, e. g. velocity vector, depends on the particular reference frame. The system S_I consists of the coordinate axes $(1, 2, 3)$ and the system S'_R of the coordinate axes $(1', 2', 3')$. The following evaluation of the modified conservation of momentum is done analogously to the statements in [Spurk07], chapter 2, 2.4.

The time derivative of a position vector of an arbitrary fluid particle can be expressed in S'_R by

$$\left.\frac{D}{Dt}\boldsymbol{x}\right|_{S'_R} = \boldsymbol{u}_{S'_R}\,. \tag{7.3.1}$$

$\boldsymbol{u}_{S'_R}$ is the relative velocity of the fluid particle in S'_R. In the system S_I, the position vector of the particle is described by $\boldsymbol{x} + \boldsymbol{r}$. Its time derivative is then

$$\left.\frac{D}{Dt}(\boldsymbol{x} + \boldsymbol{r})\right|_{S_I} = \boldsymbol{u}_{S_I}\,. \tag{7.3.2}$$

$\boldsymbol{u}_{S_I}$ is the absolute velocity in S_I. It can be formulated in terms of the relative velocity $\boldsymbol{u}_{S'_R}$, the velocity $\boldsymbol{v}$ of the origin of S'_R

$$\boldsymbol{v} = \left.\frac{D}{Dt}\boldsymbol{r}\right|_{S_I} \tag{7.3.3}$$

and the circumferential velocity $\boldsymbol{\omega} \times \boldsymbol{x}$ which arises from the rotation of the coordinate system S'_R at position $\boldsymbol{x}$. Altogether, the absolute velocity in S_I is then determined by

$$\boldsymbol{u}_{S_I} = \boldsymbol{u}_{S'_R} + \boldsymbol{\omega} \times \boldsymbol{x} + \boldsymbol{v}\,. \tag{7.3.4}$$

With the expressions in equations (7.3.1) - (7.3.4) the time derivative of the vector $\boldsymbol{x}$ can be expressed in both systems by

$$\left.\frac{D}{Dt}\boldsymbol{x}\right|_{S_I} = \left.\frac{D}{Dt}\boldsymbol{x}\right|_{S'_R} + \boldsymbol{\omega} \times \boldsymbol{x}\,. \tag{7.3.5}$$

The expression in (7.3.5) is valid for each arbitrary vector, for further details see [Spurk07], chapter 2, 2.4. Therefore the following is also valid. If $\boldsymbol{x} = \boldsymbol{\omega}$, the variations in S_I equal the variations in S'_R,

$$\left.\frac{D}{Dt}\boldsymbol{\omega}\right|_{S_I} = \left.\frac{D}{Dt}\boldsymbol{\omega}\right|_{S'_R} = \frac{d}{dt}\boldsymbol{\omega}\,. \tag{7.3.6}$$

Note that equation (7.3.6) is only fulfilled for the vector of the angular velocity or vectors which point parallel to it. To modify the conservation of momentum as it was formulated in chapter 1, section 1.5, the variation in time of the absolute velocity $\boldsymbol{u}_I$ in system S_I is required. With help of equation (7.3.6), it follows from equation (7.3.4)

$$\begin{aligned}\left.\frac{D}{Dt}\boldsymbol{u}_{S_I}\right|_{S_I} &= \left.\frac{D}{Dt}\boldsymbol{u}_{S'_R}\right|_{S_I} + \left.\frac{D}{Dt}(\boldsymbol{\omega}\times\boldsymbol{x})\right|_{S_I} + \left.\frac{D}{Dt}\boldsymbol{v}\right|_{S_I} \qquad (7.3.7)\\ &= \left.\frac{D}{Dt}\boldsymbol{u}_{S'_R}\right|_{S'_R} + \boldsymbol{\omega}\times\boldsymbol{u}_{S'_R} + \boldsymbol{\omega}\times(\underbrace{\left.\frac{D}{Dt}\boldsymbol{x}\right|_{S'_R}}_{\boldsymbol{u}_{S'_R}} + \boldsymbol{\omega}\times\boldsymbol{x}) + \left.\frac{D}{Dt}\boldsymbol{\omega}\right|_{S'_R}\times\boldsymbol{x} + \underbrace{\left.\frac{D}{Dt}\boldsymbol{v}\right|_{S_I}}_{\boldsymbol{a}},\end{aligned}$$

which can be summarised by

$$\left.\frac{D}{Dt}\boldsymbol{u}_{S_I}\right|_{S_I} = \left.\frac{D}{Dt}\boldsymbol{u}_{S'_R}\right|_{S'_R} + 2\boldsymbol{\omega}\times\boldsymbol{u}_{S'_R} + \boldsymbol{\omega}\times(\boldsymbol{\omega}\times\boldsymbol{x}) + \frac{d\boldsymbol{\omega}}{dt}\times\boldsymbol{x} + \boldsymbol{a}\,. \tag{7.3.8}$$

This formulation of the compressible conservation of momentum is only valid in the inertial system S_I. But under consideration of (7.3.8), the absolute velocity $\boldsymbol{u}_{S_I}$ can be formulated in terms of the relative rotating system S'_R. As result one obtains

$$\rho\left.\frac{D}{Dt}\boldsymbol{u}_{S'_R}\right|_{S'_R} = \rho\boldsymbol{k} + \nabla\cdot\boldsymbol{T} - \left(\rho\boldsymbol{a} + 2\rho\boldsymbol{\omega}\times\boldsymbol{u}_{S'_R} + \rho\boldsymbol{\omega}\times(\boldsymbol{\omega}\times\boldsymbol{x}) + \rho\frac{d\boldsymbol{\omega}}{dt}\times\boldsymbol{x}\right)\,. \tag{7.3.9}$$

Equation (7.3.9) gives an expression of the compressible conservation of momentum which is valid in system S'_R. Note that the meaning of body force vector $\boldsymbol{k}$ and deformation tensor $\boldsymbol{T}$ in (7.3.9) are independent of the observed reference frame. But their components have to be adapted to the particular accelerated system, in this case to S'_R.

The term $\rho\boldsymbol{a}$ becomes zero, if the origin of S'_R is not moving or only with constant velocity. This will be the case in the test case *CenCon*. The term $2\rho\boldsymbol{\omega}\times\boldsymbol{u}_{S'_R}$ stands for the *Coriolis acceleration* which becomes zero, if the observed particle is not moving in S'_R. The term $\rho\boldsymbol{\omega}\times(\boldsymbol{\omega}\times\boldsymbol{x})$ describes the *centrifugal acceleration*. Even if the particle is at rest in system S'_R, this term remains in equation (7.3.9). Thus, the terms in brackets in (7.3.9) describe additional inertial forces which result from the relative motion of S'_R to S_I.

7.3.2. Formulations in the simulation software OpenFOAM®

The previous conclusions can be used to modify the Navier-Stokes equation from chapter 1, section 1.10 as they are implemented in the OpenFOAM® software (for further details

see [OpenFOAMa]) concerning this thesis. Note that the filter formulation of the LES is omitted at first to obtain a clear presentation. For the inertial system S_I, the compressible momentum equations are formulated as (s. chapter 1, section 1.10, equation (1.10.2))

$$\frac{\partial \rho \boldsymbol{u}_{S_I}}{\partial t} + \nabla \cdot (\rho \boldsymbol{u}_{S_I} \boldsymbol{u}_{S_I}) - \nabla \cdot \mu (\nabla \boldsymbol{u}_{S_I} + (\nabla \boldsymbol{u}_{S_I})^T - \frac{2}{3} \nabla \cdot \boldsymbol{u}_{S_I}) \mathbf{I} \; = \; -\nabla \overline{p} \; + \; \rho \boldsymbol{g} \, . \quad (7.3.10)$$

Next, equation (7.3.10) will be modified to a compressible momentum equation which is valid in the rotating reference frame S'_R. This is done analogously to the statements in [OpenFOAMb]

$$\begin{aligned} \nabla \cdot \boldsymbol{u}_{S_I} &= \nabla \cdot \left(\boldsymbol{u}_{S'_R} + \boldsymbol{\omega} \times \boldsymbol{x} \right) = \nabla \cdot \boldsymbol{u}_{S'_R} = 0, \quad \text{since} \quad \nabla \cdot (\boldsymbol{\omega} \times \boldsymbol{x}) = 0, \quad (7.3.11) \\ \nabla \cdot \nabla (\boldsymbol{u}_{S_I}) &= \nabla \cdot \nabla \left(\boldsymbol{u}_{S'_R} + \boldsymbol{\omega} \times \boldsymbol{x} \right) = \nabla \cdot \nabla \boldsymbol{u}_{S'_R} = 0, \quad \text{since} \quad \nabla \cdot \nabla \left(\boldsymbol{\omega} \times \boldsymbol{x} \right) = 0. \end{aligned}$$

Taking (7.3.8) as well as (7.3.11) into account and considering the Reynold's transport theorem, one obtains

$$\begin{aligned} \left. \frac{D}{Dt} \boldsymbol{u}_{S_I} \right|_{S_I} &= \left. \frac{D}{Dt} \boldsymbol{u}_{S'_R} \right|_{S'_R} + 2\boldsymbol{\omega} \times \boldsymbol{u}_{S'_R} + \boldsymbol{\omega} \times (\boldsymbol{\omega} \times \boldsymbol{x}) + \frac{d\boldsymbol{\omega}}{dt} \times \boldsymbol{x} + \boldsymbol{a} \quad (7.3.12) \\ &= \frac{\partial \boldsymbol{u}_{S'_R}}{\partial t} + \boldsymbol{u}_{S'_R} \cdot \nabla \boldsymbol{u}_{S'_R} + 2\boldsymbol{\omega} \times \boldsymbol{u}_{S'_R} + \boldsymbol{\omega} \times (\boldsymbol{\omega} \times \boldsymbol{x}) + \frac{d\boldsymbol{\omega}}{dt} \times \boldsymbol{x} + \boldsymbol{a} \\ &= \frac{\partial \boldsymbol{u}_{S'_R}}{\partial t} + \nabla \cdot (\boldsymbol{u}_{S'_R} \boldsymbol{u}_{S'_R}) + 2\boldsymbol{\omega} \times \boldsymbol{u}_{S'_R} + \boldsymbol{\omega} \times (\boldsymbol{\omega} \times \boldsymbol{x}) + \frac{d\boldsymbol{\omega}}{dt} \times \boldsymbol{x} + \boldsymbol{a}. \end{aligned}$$

The term $\rho \boldsymbol{a}$ in (7.3.9) vanishes, if the origin of system S'_R is not moving or only with constant velocity relative to S_I which is the case in this study. Hence, also $\boldsymbol{a}$ in (7.3.12) vanishes. With help of eq. (7.3.12), one can express a compressible momentum equation in terms of the relative velocity $\boldsymbol{u}_{S'_R}$ which is valid in the rotating system S'_R

$$\begin{aligned} &\frac{\partial \rho \boldsymbol{u}_{S'_R}}{\partial t} + \nabla \cdot (\rho \boldsymbol{u}_{S'_R} \boldsymbol{u}_{S'_R}) - \nabla \cdot \mu (\nabla \boldsymbol{u}_{S'_R} + (\nabla \boldsymbol{u}_{S'_R})^T - \frac{2}{3} \nabla \cdot \boldsymbol{u}_{S'_R}) \mathbf{I} + 2\rho \boldsymbol{\omega} \times \boldsymbol{u}_{S'_R} \\ &\qquad + \rho \frac{d\boldsymbol{\omega}}{dt} \times \boldsymbol{x} + \rho \boldsymbol{\omega} \times (\boldsymbol{\omega} \times \boldsymbol{x}) + \underbrace{\rho \boldsymbol{a}}_{=0} = -\nabla \overline{p} + \rho \boldsymbol{g}. \quad (7.3.13) \end{aligned}$$

In the software package OpenFOAM® the solution algorithm *buoyantPimpleFOAM* is chosen, which was presented before in chapter 3, section 3.4. This time the solver uses the modified governing equations considering the rotational movement (this time with the filtering operation done in the process of the LES). The complete set of modified filtered governing equations in the rotating system S'_R can then be written as follows

- Compressible conservation of mass

$$\frac{\partial \overline{\rho}}{\partial t} + \nabla \cdot (\overline{\rho}\widetilde{\boldsymbol{u}}_{S'_R}) = 0\,, \tag{7.3.14}$$

- Compressible conservation of momentum

$$\begin{aligned}\frac{\partial \overline{\rho}\widetilde{\boldsymbol{u}}_{S'_R}}{\partial t} \;+\; & \nabla \cdot (\overline{\rho}\widetilde{\boldsymbol{u}}_{S'_R}\widetilde{\boldsymbol{u}}_{S'_R}) - \nabla \cdot (\mu + \mu_{\text{sgs}})\left(\nabla \widetilde{\boldsymbol{u}}_{S'_R} + (\nabla \widetilde{\boldsymbol{u}}_{S'_R})^T - \frac{2}{3}\nabla \cdot \widetilde{\boldsymbol{u}}_{S'_R})\mathbf{I}\right. \\ + \; & \underbrace{2\overline{\rho}\boldsymbol{\omega} \times \widetilde{\boldsymbol{u}}_{S'_R}}_{\text{Coriolis acceleration}} + \underbrace{\overline{\rho}\boldsymbol{\omega} \times (\boldsymbol{\omega} \times \boldsymbol{x})}_{\text{centrifugal acceleration}} + \underbrace{\overline{\rho}\frac{d\boldsymbol{\omega}}{dt} \times \boldsymbol{x}}_{=0} = -\nabla \overline{p} + \overline{\rho}\boldsymbol{g}_{S'_R},\end{aligned} \tag{7.3.15}$$

- Compressible conservation of enthalpy

$$\frac{\partial \overline{\rho}\widetilde{h}}{\partial t} + \nabla \cdot (\overline{\rho}\widetilde{\boldsymbol{u}}_{S'_R}\widetilde{h}) - \nabla \cdot ((\alpha + \alpha_{\text{sgs}})\nabla \widetilde{h}) = \frac{\partial \overline{p}}{\partial t} + \widetilde{\boldsymbol{u}}_{S'_R} \cdot \nabla \bar{p}, \tag{7.3.16}$$

where $\boldsymbol{x}$ is the position vector between the origin of the rotating system S'_R and the observed fluid particle in the container.

Note that if Cartesian coordinates are used, the values of all scalars in the governing equations, especially in the momentum equations, are not dependent on the chosen coordinate system (see [Spurk07], appendix, A.2). Hence, the scalar field of density ρ, dynamic viscosity μ and subgrid scale viscosity μ_{sgs} have the same values in system S_I as in system S'_R. This is also the case for the scalar fields of enthalpy h as well as thermal diffusivity α and its subgrid scale part α_{sgs}. The tensor fields keep their physical meanings in both systems, but their components have to be adapted to the relative moving reference system S'_R, as mentioned before. This is demonstrated on the basis of the gravitational force vector $\boldsymbol{g}$ for system S'_R in the following section.

7.4. The system of *CenCon* in the centrifuge

To formulate the modified governing equations for the specified problem of *CenCon* and the centrifuge, the conservation of momentum in (7.3.15) has to be adapted to the dimensions of the whole setup. The required terms of $\boldsymbol{u}_{S'_R}$, $\frac{d\boldsymbol{\omega}}{dt} \times \boldsymbol{x}$, $2\boldsymbol{\omega} \times \widetilde{\boldsymbol{u}}_{S'_R}$, $\boldsymbol{\omega} \times (\boldsymbol{\omega} \times \boldsymbol{x})$ and $\boldsymbol{a}$ have to be expressed in terms of the experimental setup *CenCon*. The continuity and energy equation stay the same as they were formulated before in (7.3.14), (7.3.16).

In the configuration of the centrifuge and experimental test case, the whole system can be divided in two sub-systems. The rotational movement of the container relative to the rotating axis of the centrifuge is a uniform motion. Therefore, one can chose the centrifuge

axis as the *inertial system* S_I and the container as the relative to S_I *rotating system* S'_R, as it is indicated in figure 7.11 and also in figure 7.8.

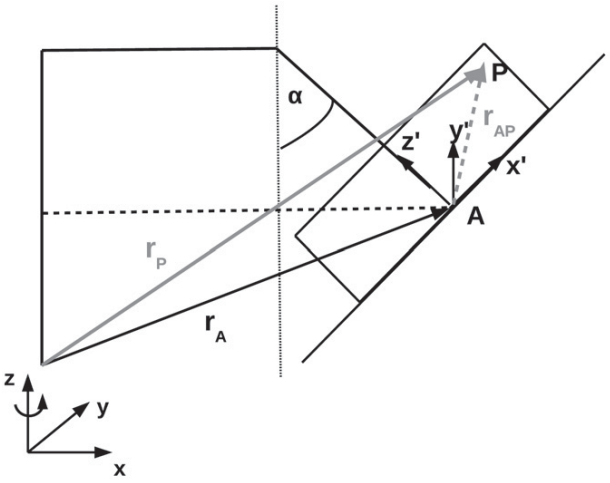

Figure 7.11.: Both coordinate systems, S_I (centrifuge axis) and S'_R (container) regarding the setup of *CenCon*.

The origin of the inertial system S_I should be at the end of the rotor shaft in the centrifuge, hence at the end of the rotation axis. The system is denoted by the components (x, y, z). The origin of the rotating reference frame S'_R should be located in the container centre. The system is denoted by the components (x', y', z').

7.4.1. General statements

For the formulation of the absolute velocity $\boldsymbol{u}_{S'_R}$ and its time derivative in the governing equations one requires the vector $\boldsymbol{r}_{AP}$ (which equals vector $\boldsymbol{x}$ in eq. (7.3.15)).

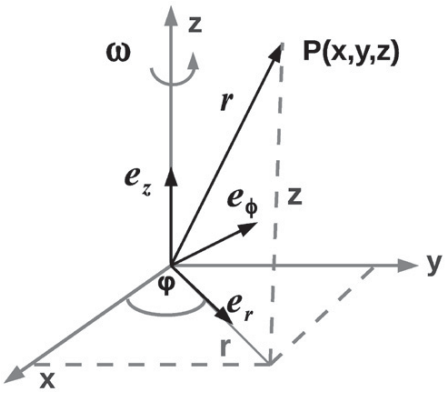

Figure 7.12.: Cylindrical coordinates of an arbitrary point P (as seen in [Richard11]).

For the formulation of the absolute velocity $\boldsymbol{u}_{S_I}$ and its time derivative the term $\boldsymbol{r}_A$ is required (s. figure 7.11). To specify these terms and also the fictitious forces, which act

on a fluid volume in the container, we express the coordinates in the rotating reference frame S'_R in relation to the inertial frame of the centrifuge S_I. It is convenient to perform such a transformation between both systems in cylindrical polar coordinates with (z, r, φ). The following formulations are based on the information in [Nolting13], chapter 1, 2 and [Spurk07], appendix, A.2. One can specify the position vector $\boldsymbol{r}$ of an arbitrary point P in cylindrical coordinates by its components r, z and its basis vectors $\boldsymbol{e}_r, \boldsymbol{e}_z$ (s. figure 7.12 and [Richard11], chapter 3, 3.5.2)

$$\boldsymbol{r}_P = \boldsymbol{e}_r r + \boldsymbol{e}_z z\,, \tag{7.4.1}$$

where $\boldsymbol{e}_z$ is time-independent. In cylindrical polar coordinates it is for the unit vectors

$$\begin{aligned} d\boldsymbol{e}_z &= 0\,, \\ d\boldsymbol{e}_r &= \boldsymbol{e}_\varphi d\varphi \Rightarrow \dot{\boldsymbol{e}}_r = \frac{d\varphi}{dt}\boldsymbol{e}_\varphi = \boldsymbol{\omega} \times \boldsymbol{e}_r, \\ d\boldsymbol{e}_\varphi &= -\boldsymbol{e}_r d\varphi \Rightarrow \dot{\boldsymbol{e}}_\varphi = -\frac{d\varphi}{dt}\boldsymbol{e}_r = -\boldsymbol{\omega} \times \boldsymbol{e}_\varphi, \\ \boldsymbol{e}_r &= \boldsymbol{e}_\varphi \times \boldsymbol{e}_z. \end{aligned} \tag{7.4.2}$$

The term $\dot{\boldsymbol{e}}_\cdot = \frac{d}{dt}\boldsymbol{e}_\cdot$ defines the derivation in time of one unit vector. The velocity $\boldsymbol{v}_P$ in P is the time derivation of the position vector $\boldsymbol{r}_P$ in equation (7.4.1)

$$\boldsymbol{v}_P = \dot{\boldsymbol{r}}_P = \boldsymbol{e}_r\dot{r} + \dot{\boldsymbol{e}}_r r + \boldsymbol{e}_z\dot{z} + \dot{\boldsymbol{e}}_z z = \boldsymbol{e}_r \underbrace{\dot{r}}_{v_r} + \boldsymbol{e}_\varphi \underbrace{r\dot{\varphi}}_{v_\varphi} + \boldsymbol{e}_z \underbrace{\dot{z}}_{v_z}. \tag{7.4.3}$$

The time derivation of second order of vector $\boldsymbol{r}_P$ gives the acceleration $\boldsymbol{a}_P$ in point P

$$\boldsymbol{a}_P = \dot{\boldsymbol{v}}_P = \ddot{\boldsymbol{r}}_P = \boldsymbol{e}_r \underbrace{(\ddot{r} - r\dot{\varphi}^2)}_{a_r} + \boldsymbol{e}_\varphi \underbrace{(r\ddot{\varphi} + 2\dot{r}\dot{\varphi})}_{a_\varphi} + \boldsymbol{e}_z \underbrace{\ddot{z}}_{a_z}. \tag{7.4.4}$$

In the experiment, the container is turned by an angle α and translated in $x-$ and subsequently in $z-$ direction relative to the centrifuge axis. This transformation is described by the vector $\boldsymbol{r}_A$, as is indicated in figure 7.13. The following evaluations are done analogously to [Nolting13], chapter 1. An arbitrary position vector in system S'_R can be formulated in its general expression by

$$\boldsymbol{r}' = \sum_{i=1}^{3} x'_i \boldsymbol{e}'_i\,. \tag{7.4.5}$$

The vector $\boldsymbol{x'}$ in the system S'_R is then defined by

$$x'_j = \sum_{i=1}^{3} x_i(\boldsymbol{e}_i \boldsymbol{e}'_j) = \sum_{i=1}^{3} \cos\varphi_{ji} x_i, \quad \text{with} \quad j = 1, 2, 3\,, \tag{7.4.6}$$

where x_i is a vector in system S_I and (e_1, e_2, e_3) are again the unit vectors in S_I. The vectors (e'_1, e'_2, e'_3) are the unit vectors in system S'_R.

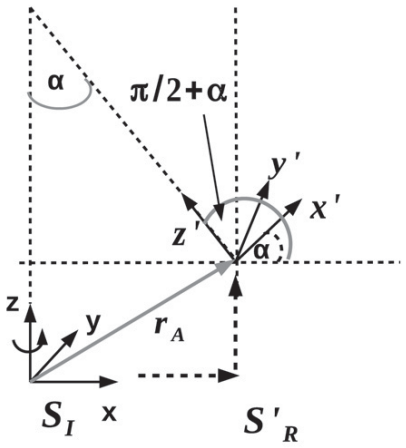

Figure 7.13.: Location of the container S'_R relative to system S_I.

The inner product of $\boldsymbol{e}_i\boldsymbol{e}'_j$, respectively $\cos\varphi_{ji}$, defines the rotational matrix between both systems, where j stands for the j-th coordinate axis in S'_R and i for the i-th coordinate axis in S_I. The term φ_{ji} defines the angle between the axis j in S'_R and the axis i in S_I. The rotational matrix is not allocated to any basis of both systems. Because the rotational matrix is an *orthogonal* matrix, its transposed matrix equals its inverse matrix. The inverse transformation between both systems is given by

$$x_j = \sum_{i=1}^{3} x'_i(\boldsymbol{e}'_i\boldsymbol{e}_j) = \sum_{i=1}^{3} \cos\varphi_{ij} x'_i \quad \text{with} \quad j = 1, 2, 3\,. \tag{7.4.7}$$

In Cartesian coordinates, the unit vectors and the components of a tensor can be described by the same above transformation expression. Hence it is

$$\boldsymbol{e}'_i = \sum_{k=1}^{3} d_{ik}\boldsymbol{e}_k \quad \text{with} \quad d_{im} = \boldsymbol{e}'_i \cdot \boldsymbol{e}_m = \cos\varphi_{im} \quad \text{and} \quad i,\, m = 1, 2, 3\,. \tag{7.4.8}$$

The inverse transformation is formulated as

$$\boldsymbol{e}_i = \sum_{i=1}^{3} d_{ki}\boldsymbol{e'}_i \quad \text{with} \quad k = 1, 2, 3\,. \tag{7.4.9}$$

For an arbitrary second order tensor $\boldsymbol{T}$, the transformation can be formulated with help of (7.4.9) analogously to the statements in [Spurk07], appendix, A.2.,

$$\boldsymbol{T} = t_{ij}\boldsymbol{e}_i\boldsymbol{e}_j = \sum_{i=1}^{3}\sum_{j=1}^{3} t_{ij}\boldsymbol{e}_i\boldsymbol{e}_j = \sum_{i=1}^{3}\sum_{j=1}^{3} t_{ij}\cos\varphi_{ik}\cos\varphi_{jl}\boldsymbol{e}'_k\boldsymbol{e}'_l \qquad k, l = 1, 2, 3\,. \tag{7.4.10}$$

Because of the orthogonality of tensor $\boldsymbol{T} = \boldsymbol{T}'$, the transformed components in S'_R are

$$t'_{kl} = \cos\varphi_{ik}\cos\varphi_{jl}t_{ij}. \tag{7.4.11}$$

The inverse transformation for the components in S_I is then described by

$$t_{kl} = \cos\varphi_{ki}\cos\varphi_{lj}t'_{ij}. \tag{7.4.12}$$

The above described transformation laws are adapted in the following on the transformation between system S_I and system S'_R in the centrifuge. As mentioned before, the components of vector fields have to be modified in the rotating system S'_R. For the gravitational force vector $\boldsymbol{g}$ in S_I it is

$$\boldsymbol{g}_{S_I} = (g_x, g_y, g_z) = (0, 0, -9.81\,\mathrm{m/s}). \tag{7.4.13}$$

In system S'_R, the components of $\boldsymbol{g}$ are transformed to $\boldsymbol{g}'_{S'_R} = (g'_x, g'_y, g'_z)$. According to equation (7.4.6), it is then in S'_R

$$\begin{aligned} g'_x &= g_x\cos\alpha + g_y\cos 90^\circ + g_z\cos(90^\circ - \alpha), \\ g'_y &= g_x\cos 90^\circ + g_y\cos 0^\circ + g_z\cos(90^\circ), \\ g'_z &= g_x\cos(90^\circ + \alpha) + g_y\cos 90^\circ + g_z\cos(\alpha)\,. \end{aligned} \tag{7.4.14}$$

Hence it is

$$\boldsymbol{g}'_{S'_R} = (g_z\cos(90^\circ - \alpha), 0, g_z\cos(\alpha))\,. \tag{7.4.15}$$

7.4.2. Two relative to each other moving systems, the centrifuge axis and the test container

7.4.2.1. The non-rotating system S_I of the centrifuge axis

With help of figures 7.11 - 7.12 and equations (7.4.1) - (7.4.4) the position vector $\boldsymbol{r}_A$, the velocity vector $\boldsymbol{v}_A$ and the acceleration vector $\boldsymbol{a}_A$ can be defined in point A seen from S_I by

$$\begin{aligned} \boldsymbol{r}_A &= (H - L_4\cos\alpha)\boldsymbol{e}_z + (L_1 + L_4\sin\alpha)\boldsymbol{e}_r, \\ \boldsymbol{u}_A &= (L_1 + L_4\sin\alpha)\dot{\boldsymbol{e}}_r, \\ \boldsymbol{a}_A &= (L_1 + L_4\sin\alpha)\ddot{\boldsymbol{e}}_r. \end{aligned} \tag{7.4.16}$$

$\boldsymbol{u}_A$ equals the afore presented absolute velocity $\boldsymbol{u}_{S_I}$ in equation (7.3.2). With the assumptions in equation (7.4.2), the acceleration vector $\boldsymbol{a}_A$ in point A in equation (7.4.16) is formulated in S_I as

$$\boldsymbol{a}_A = (L_1 + L_4 \sin\alpha)\left[\dot{\boldsymbol{\omega}} \times \boldsymbol{e}_r + \boldsymbol{\omega} \times (\boldsymbol{\omega} \times \boldsymbol{e}_r)\right]. \tag{7.4.17}$$

In the inertial system of the centrifuge S_I, the angular velocity $\boldsymbol{\omega}$ has to be constant, i. e. $\boldsymbol{\omega} = \text{const.}$, thus it is

$$\left.\begin{array}{ll} \dot{\boldsymbol{\omega}} = 0, & \boldsymbol{\omega} \perp \boldsymbol{e}_r\,, \\ \boldsymbol{\omega} \| \boldsymbol{e}_z \Rightarrow \boldsymbol{e}_\varphi = \boldsymbol{\omega} \times \boldsymbol{e}_z = 0 & \end{array}\right\} \begin{array}{l} \boldsymbol{\omega} \times \boldsymbol{e}_r = \omega \boldsymbol{e}_\varphi \\ \boldsymbol{\omega} \times \boldsymbol{e}_\varphi = -\omega \boldsymbol{e}_r. \end{array} \tag{7.4.18}$$

As result of equation (7.4.18), the vector $\boldsymbol{a}_A$ in equation (7.4.17) becomes

$$\begin{aligned} \Rightarrow \boldsymbol{a}_A &= (L_1 + L_4 \sin\alpha)\,(\boldsymbol{\omega} \times (\boldsymbol{\omega} \times \boldsymbol{e}_r)) = (L_1 + L_4 \sin\alpha)\,(\boldsymbol{\omega} \times (\omega \boldsymbol{e}_\varphi)) \\ &= -\underbrace{(L_1 + L_4 \sin\alpha)}_{|\boldsymbol{r}_A|}\,\omega^2 \boldsymbol{e}_r. \end{aligned} \tag{7.4.19}$$

Estimation of the acceleration vector a_A and deflecting angle α

The acceleration vector $\boldsymbol{a}_A$ in equation (7.4.19) describes the centripetal acceleration $\boldsymbol{a}_{A,\mathrm{ZP}}$, which acts on the container centre seen from S_I. The centripetal acceleration has a negative value, because it points in the inward direction to the centrifuge axis. The centripetal acceleration $\boldsymbol{a}_A$ depends on the radius $\mathbf{r}_A$ and the angular velocity $\boldsymbol{\omega}$. Its absolute value is the same as the one of the centrifugal acceleration $\boldsymbol{a}_{A,\mathrm{ZF}}$.

The centrifugal acceleration $\boldsymbol{a}_{A,\mathrm{ZF}}$ acts in the opposite direction of the centripetal acceleration $\boldsymbol{a}_{A,\mathrm{ZP}}$. $\boldsymbol{a}_{A,\mathrm{ZF}}$ points away from the centrifuge axis and it is counted positive. This is illustrated in figure 7.8 on page 207. The deflection angle α can be circumscribed by

$$\tan\alpha = \left| -\frac{\boldsymbol{\omega}^2}{\boldsymbol{g}} (L_1 + L_4 \sin\alpha) \right|. \tag{7.4.20}$$

Due to the rotational movement of the centrifuge, a higher effective gravitational component $\boldsymbol{g}_{\mathrm{eff}}$ affects the experimental cell. It can be determined with help of figure 7.8 on page 207

$$g_{\mathrm{eff}} = \sqrt{\boldsymbol{g}^2 + \boldsymbol{a}_{A,\mathrm{ZF}}}. \tag{7.4.21}$$

g_{eff} increases with an increasing angular velocity $\boldsymbol{\omega}$ (see equation (7.4.19)). In the beginning of the rotation mode, a pre-determined angular velocity $\boldsymbol{\omega}$ of the centrifuge axis has to be chosen. The resulting deflection angle α depends on this absolute value, as is demonstrated in figure 7.8 on page 207. The higher $\boldsymbol{\omega}$, the bigger becomes the deflection angle α. The essential angular velocity component ω_z which is pointing along the rotation axis is defined by

$$\omega_z = 2\pi \mathrm{n}, \tag{7.4.22}$$

where n is the number of revolutions per minute (rpm). With a given angular velocity $\boldsymbol{\omega}$, α can be determined approximately with help of $\boldsymbol{a}_{A,ZF}$ and $\boldsymbol{g}$ by

$$\alpha = \arctan\left(\frac{|\boldsymbol{a}_{A,ZF}|}{|\boldsymbol{g}|}\right). \tag{7.4.23}$$

With help of equation (7.4.20) ω_z can then also be formulated as

$$\omega_z = \sqrt{\frac{g_z \tan(\alpha)}{L_1 + L_4 \sin(\alpha)}}. \tag{7.4.24}$$

The main goal of the experiments is to gain information of the influence of the Coriolis acceleration on the turbulent flow structures. Hence, a high Coriolis acceleration is preferable. The Coriolis force is defined by

$$\boldsymbol{F}_{\mathrm{C}} = -2m\,(\boldsymbol{\omega} \times \boldsymbol{u})\,. \tag{7.4.25}$$

It is named after the French physicist and mathematician *Gaspard Gustave de Coriolis* [Coriolis1835]. If a fluid particle moves in a known angle β relative to the rotation axis of the system, respectively relative to the direction of the angular velocity vector $\boldsymbol{\omega}$, the resulting Coriolis force can be written as

$$F_{\mathrm{C}} = 2\,m\omega\,u \sin\beta. \tag{7.4.26}$$

Consequently, the deflection angle α between centrifuge axis and its rotating arm has next to the angular velocity an implication of the intensity of the resulting Coriolis acceleration due to an increasing distance between centrifuge axis and the container (s. figure 7.8 on page 207 and equation (7.4.19) on page 219). Because the exact fluid movement and velocity values are not known a priori, one has to make the following assumptions.

Due to the design of the centrifuge, the minimal deflection angle α in the rotation mode is $\alpha = 46.167°$. To obtain a as possible high Coriolis acceleration, a high angular velocity $\boldsymbol{\omega}$ should be chosen. Thus, the resulting angle α will lie between $46.167° \leq \alpha \leq 90°$. In this range the sine function in equation (7.4.26) grows continuously.

Regarding the resulting angle α, the influence of the gravitational force vector $\boldsymbol{g}_{\mathrm{eff}}$ has also to be considered. To obtain a typical RB problem, the direction of the heated walls should be pointing normal relative to the effective gravity acceleration. With an increasing angular velocity $\boldsymbol{\omega}$ this aspect is still fulfilled, but the resulting effective gravitational acceleration $\boldsymbol{g}_{\mathrm{eff}}$ is also increasing and gains bigger influence on the RB convection inside the container. Due to its increasing value, the typical RB problem is destroyed and the fluid is not only influenced by a high Coriolis acceleration, which is the intention of this

study, but also simultaneously by a hyper gravity effect. Because an increasing angle α and thus an increasing vector $\boldsymbol{g}_{\text{eff}}$ debilitate more and more the typical RB problem, a possible high Coriolis acceleration with a possible small influence of the vector $\boldsymbol{g}_{\text{eff}}$ should be realised. Therefore, a theoretical value of $\alpha = 45°$ is the best choice. But, due to the design of the centrifuge, the minimal value has to be at $\alpha = 46.167°$. With a predetermined value of $\alpha = 46.167°$, the centrifuge rotates with 13.704 revolutions per minute (rpm) due to its layout. The resulting angular velocity ω_z is then

$$\omega_z = 2\pi \mathrm{n} = 2\pi \cdot 13.704 \text{ rev./min} = 2\pi \cdot 0.2284 \text{ rev./s} = 1.435 \,\text{rad/s}, \tag{7.4.27}$$

according to equation (7.4.22). The centrifugal acceleration $\boldsymbol{a}_{A,\text{ZF},S_1}$ in point of the first sensor S_1 can be theoretically estimated as $|\boldsymbol{a}_{A,\text{ZF},S_1}| \approx 1g$, according to equation (7.4.19), respectively

$$\begin{aligned} |\boldsymbol{a}_{A,\text{ZF},S_1}| &= \left|-(L_1 + L_4 \sin\alpha)\,\omega^2 \boldsymbol{e}_r\right| \\ &= (3.724\,\text{m} + 1.411\,\text{m} \cdot \sin(46.167°)) \cdot (1.435\,\text{rad/s})^2 = 0.995g\,. \end{aligned} \tag{7.4.28}$$

With help of equation (7.4.21) and $|\boldsymbol{a}_{A,\text{ZF},S_1}| = 0.995g$ a resulting gravitational force vector $\boldsymbol{g}_{\text{eff}}$ can be theoretically estimated as by its absolute value

$$|\boldsymbol{g}_{\text{eff}}| = \left|\sqrt{\boldsymbol{g}^2 + \boldsymbol{a}^2_{A,\text{ZF},S_1}}\right| = 1.41\,g\,. \tag{7.4.29}$$

This values was also measured by sensor S_1 in the middle of the container (s. figure 7.7). The centrifugal acceleration $|\boldsymbol{a}_{A,\text{ZF},S_2}|$ in S_2 has to be theoretically, according to equation (7.4.19),

$$|\boldsymbol{a}_{A,\text{ZF},S_2}| = \left|-(L_1 + (L_4 + \Delta_m)\sin\alpha)\,\omega^2 \boldsymbol{e}_r\right| = 1.07g \tag{7.4.30}$$

with $\Delta_m = 0.5\,\text{m}$. With help of equation (7.4.29) and the value of $|\boldsymbol{a}_{A,\text{ZF},S_2}| = 1.07g$ a resulting gravitational force value is theoretically estimated for position S_2 by

$$|\boldsymbol{g}_{\text{eff}}| = \left|\sqrt{\boldsymbol{g}^2 + \boldsymbol{a}^2_{\text{A, ZF},S_2}}\right| = 1.465\,g. \tag{7.4.31}$$

The centrifuge measured in S_2 a gravitational force value of $1.44\,g$, which is about 1.73% smaller than the value of $1.465\,g$. With help of equation (7.4.20) and the values of a_{A,ZF,S_1} and a_{A,ZF,S_2} one obtains the following theoretical values of α

$$\alpha_1 = 45.143° \quad \text{and} \quad \alpha_2 = 43.063°\,. \tag{7.4.32}$$

The first estimated value α_1 lies about 2.22% under the measured value of $\alpha = 46.167°$. The second estimated value α_2 lies about 6.72% under the angle α.

7.4.2.2. The rotating system S'_R of the test container

Concerning two arbitrary, relative to each other moving systems, as it is displayed in figure 7.14, one can describe the time-dependent position vector $\boldsymbol{r}(t)$ of a particle m (which is located in system S'_R) seen from system S_I by

$$S_I : \qquad \boldsymbol{r}(t) = \boldsymbol{r}_0(t) + \boldsymbol{r}'(t). \tag{7.4.33}$$

Note that in the following the time dependence of the described vectors are assumed without describing it explicitly. The following assumptions are formulated analogously to [Nolting13], chapter 2. The derivative in time of vector $\boldsymbol{r}'$ can then be described in system

$$S'_R : \qquad \dot{\boldsymbol{r}}' = \sum_{j=1}^{3} \dot{x}'_j \boldsymbol{e}'_j. \tag{7.4.34}$$

The axes are not changing for the observer in system S'_R who rotates with it, but they do for an observer in system S_I. Thus, it is

$$S_I : \qquad \dot{\boldsymbol{r}} = \dot{\boldsymbol{r}}_0 + \sum_{j=1}^{3} (\underbrace{\dot{x}'_j \boldsymbol{e}'_j}_{A} + \underbrace{x'_j \dot{\boldsymbol{e}}'_j}_{B}). \tag{7.4.35}$$

$\dot{\boldsymbol{r}}_0$ stands for the relative velocity of both origins of the coordinate systems. Term A stands for the velocity of particle m in system S'_R. Term B stands for the velocity of an fixed with system S'_R rotating particle seen from system S_I. For this particle only the direction of the axes are changing but not the components x'.

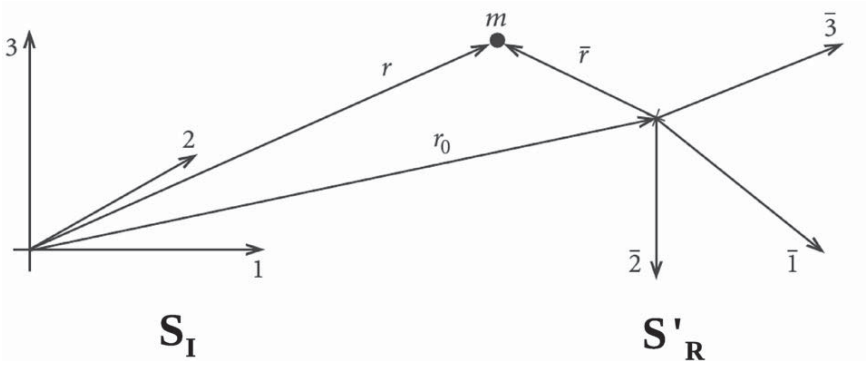

Figure 7.14.: Two arbitrary, relative to each other moving systems: position vector $\boldsymbol{r}(t)$ of a particle m (as seen in [Nolting13]).

Term B can be modified with help of the angular velocity $\boldsymbol{\omega}$ which describes the rotational movement of system S'_R around the origin of S'_R. With help of equation (7.4.34), equation (7.4.35) becomes

$$S_I: \quad \boldsymbol{r} = \dot{\boldsymbol{r}}_0 + \dot{\boldsymbol{r}}' + \boldsymbol{\omega} \times \boldsymbol{r}' \;\Rightarrow\; \frac{d}{dt}(\boldsymbol{r} - \boldsymbol{r}_0) = \underbrace{\frac{d}{dt}\boldsymbol{r}'}_{a} = \underbrace{\dot{\boldsymbol{r}}' + \boldsymbol{\omega} \times \boldsymbol{r}'}_{b}, \tag{7.4.36}$$

where term a describes the derivation in time seen by system S_I and term b the derivation in time in system S'_R of vector $\boldsymbol{r}'$. The above considerations are used in the following for both observed systems of the container and the centrifuge axis. The complete description of a fluid particle in point P in figure 7.11 on page 215 seen by an observer in system S_I can be formulated with help of the equations in (7.4.16) as

$$S_I: \quad \boldsymbol{r}_P = \boldsymbol{r}_A + \boldsymbol{r}'_{AP}\,, \qquad \boldsymbol{u}_P = \boldsymbol{u}_A + \boldsymbol{u}'_{AP}\,, \qquad \boldsymbol{a}_P = \boldsymbol{a}_A + \boldsymbol{a}'_{AP}\,. \tag{7.4.37}$$

The vectors $\boldsymbol{r}_A\,, \boldsymbol{u}_A\,, \boldsymbol{a}_A$ were described already in section 7.4.2.1 from page 218 on. To describe the position vector $\boldsymbol{r}'_{AP}$ of an arbitrary fluid particle at point P seen by an observer in system S_I, an extra angle φ is needed. The transformation between both systems can be understand as a rotation of the origin of S'_R relative to the origin of S_I by angle α. Subsequent, S'_R is translated in horizontal direction (in the xy-plane) about $L_1 + L_4 \sin\alpha$ and in vertical direction (z-axis) about $H - L_4 \cos\alpha$ (s. figure 7.15).

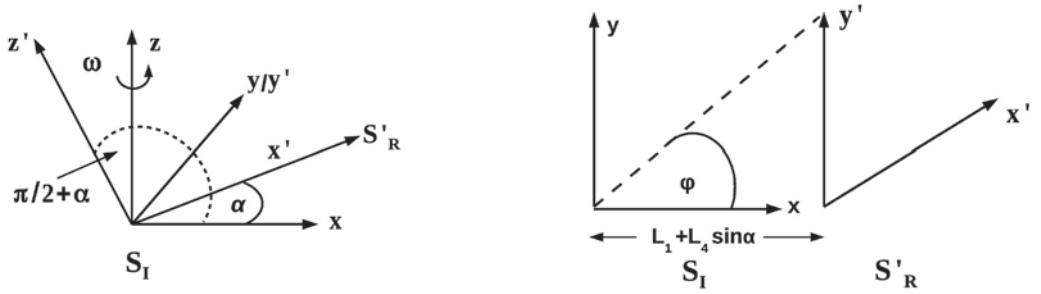

Figure 7.15.: Left: Sketch of the by an angle α rotated system S'_R relative to system S_I. **Right:** Horizontal translation of S'_R from S_I about an amount of $(L_1 + L_4 \sin\alpha)$ (xy-plane, top view).

Thus, it is possible to describe $\boldsymbol{r}'_{AP}$ and its first and second order derivative in time directly on the basis of the unit vectors $\boldsymbol{e}_r$, $\boldsymbol{e}_\varphi$ of system S_I. Therewith, an observer in S_I obtains

$$\begin{aligned} \boldsymbol{r}'_{AP}\,|_{S_I} &= x(\boldsymbol{e}_z \sin\alpha + \boldsymbol{e}_r \cos\alpha) + z(\boldsymbol{e}_z \cos\alpha - \boldsymbol{e}_r \sin\alpha) \\ &+ \boldsymbol{e}_\varphi \left[(L_1 + L_4 \sin\alpha) \sin\left(\arctan\left(\frac{y}{L_1 + L_4 \sin\alpha} \right) \right) \right] \\ &+ \boldsymbol{e}_r \left[\sqrt{(L_1 + L_4 \sin\alpha)^2 + y^2 + (H - L_4 \cos\alpha)^2} - (L_1 + L_4 \sin\alpha) \right]. \end{aligned} \tag{7.4.38}$$

Considering system S'_R, the angular velocity $\boldsymbol{\omega}$ is not constant, $\dot{\boldsymbol{\omega}} \neq$ const.. The first and second derivation in time of equation (7.4.38) leads to the velocity $\boldsymbol{u}'_{AP}$ and the acceleration $\boldsymbol{a}'_{AP}$ in equation (7.4.39) valid for the fluid particle in point P (seen from S_I)

$$
\begin{aligned}
\boldsymbol{u}'_{AP}\,|_{S_I} &= \dot{x}(\boldsymbol{e}_z\sin\alpha+\boldsymbol{e}_r\cos\alpha)+x(\boldsymbol{\omega}\times\boldsymbol{e}_r)\cos\alpha\\
&+ \dot{z}(\boldsymbol{e}_z\cos\alpha-\boldsymbol{e}_r\sin\alpha)-z(\boldsymbol{\omega}\times\boldsymbol{e}_r)\sin\alpha\\
&+ \dot{\boldsymbol{e}}_\varphi\left[(L_1+L_4\sin\alpha)\sin\left(\arctan\left(\frac{y}{L_1+L_4\sin\alpha}\right)\right)\right]\\
&+ \boldsymbol{e}_\varphi\left[(L_1+L_4\sin\alpha)\cos\left(\arctan\left(\frac{y}{L_1+L_4\sin\alpha}\right)\right)\left(\frac{(L_1+L_4\sin\alpha)}{(L_1+L_4\sin\alpha)^2+y^2}\right)2y\dot{y}\right]\\
&+ \dot{\boldsymbol{e}}_r\left[\sqrt{(L_1+L_4\sin\alpha)^2+y^2+(H-L_4\cos\alpha)^2}-(L_1+L_4\sin\alpha)\right]\\
&+ \boldsymbol{e}_r\left[\frac{1}{2}\left[(L_1+L_4\sin\alpha)^2+y^2+(H-L_4\cos\alpha)^2\right]^{-1/2}2y\dot{y}\right], \qquad (7.4.39)
\end{aligned}
$$

$$
\left.\begin{aligned}
\boldsymbol{u}'_{AP}\,|_{S_I} &= \boldsymbol{e}_z(\dot{x}\sin\alpha+\dot{z}\cos\alpha)+\boldsymbol{e}_r(\dot{x}\cos\alpha-\dot{z}\sin\alpha)\\
&+ \boldsymbol{e}_\varphi\left[(L_1+L_4\sin\alpha)\cos\left(\arctan\left(\tfrac{y}{L_1+L_4\sin\alpha}\right)\right)\left(\tfrac{(L_1+L_4\sin\alpha)}{(L_1+L_4\sin\alpha)^2+y^2}\right)2y\dot{y}\right]\\
&+ \boldsymbol{e}_r\left[\tfrac{1}{2}\left[(L_1+L_4\sin\alpha)^2+y^2+(H-L_4\cos\alpha)^2\right]^{-1/2}2y\dot{y}\right]
\end{aligned}\right\}\dot{\boldsymbol{r}}'_{AP,S'_R}
$$

$$
\left.\begin{aligned}
&+(-\boldsymbol{\omega}\times\boldsymbol{e}_\varphi)\left[(L_1+L_4\sin\alpha)\sin\left(\arctan\left(\tfrac{y}{L_1+L_4\sin\alpha}\right)\right)\right]\\
&+(\boldsymbol{\omega}\times\boldsymbol{e}_r)\Big[(x\cos\alpha-z\sin\alpha)\\
&+\sqrt{(L_1+L_4\sin\alpha)^2+y^2+(H-L_4\cos\alpha)^2}-(L_1+L_4\sin\alpha)\Big]
\end{aligned}\right\}\boldsymbol{\omega}\times\boldsymbol{r}'_{AP},
$$

$$
\begin{aligned}
\boldsymbol{a}'_{AP}\,|_{S_I} &= \boldsymbol{e}_z(\ddot{x}\sin\alpha+\ddot{z}\cos\alpha)+\boldsymbol{e}_r(\ddot{x}\cos\alpha-\ddot{z}\sin\alpha)\\
&+ \boldsymbol{e}_\varphi\Big[-(L_1+L_4\sin\alpha)\sin\left(\arctan\left(\tfrac{y}{L_1+L_4\sin\alpha}\right)\right)\left(\left(\tfrac{(L_1+L_4\sin\alpha)}{(L_1+L_4\sin\alpha)^2+y^2}\right)2y\dot{y}\right)^2\\
&\quad+(L_1+L_4\sin\alpha)\cos\left(\arctan\left(\tfrac{y}{L_1+L_4\sin\alpha}\right)\right)\\
&\quad\cdot\left[\left(-\tfrac{(L_1+L_4\sin\alpha)}{((L_1+L_4\sin\alpha)^2+y^2)^2}\left(2y\dot{y}\right)^2\right)+\left(\tfrac{(L_1+L_4\sin\alpha)}{(L_1+L_4\sin\alpha)^2+y^2}\right)\left(2\dot{y}^2+2y\ddot{y}\right)\right]\Big]\\
&+ \boldsymbol{e}_r\Big[-\tfrac{1}{4}\left[(L_1+L_4\sin\alpha)^2+y^2+(H-L_4\cos\alpha)^2\right]^{-3/2}4y^2\dot{y}^2\\
&\quad+\tfrac{1}{2}\left((L_1+L_4\sin\alpha)^2+y^2+(H-L_4\cos\alpha)^2\right)^{-1/2}\left(2\dot{y}^2+2y\ddot{y}\right)\Big]
\end{aligned}\Bigg\}\ddot{\boldsymbol{r}}'_{AP,S'_R}
$$

$$
\left.\begin{aligned}
&+(-\boldsymbol{\omega}\times(-\boldsymbol{\omega}\times\boldsymbol{e}_\varphi))\left[(L_1+L_4\sin\alpha)\sin\left(\arctan\left(\tfrac{y}{L_1+L_4\sin\alpha}\right)\right)\right]\\
&+(\boldsymbol{\omega}\times(\boldsymbol{\omega}\times\boldsymbol{e}_r))\Big[(x\cos\alpha+z\sin\alpha)\\
&\quad+\left[\sqrt{(L_1+L_4\sin\alpha)^2+y^2+(H-L_4\cos\alpha)^2}-(L_1+L_4\sin\alpha)\right]\Big]
\end{aligned}\right\}\boldsymbol{\omega}\times(\boldsymbol{\omega}\times\boldsymbol{r}'_{AP})
$$

$$
\left.\begin{aligned}
&+(-\dot{\boldsymbol{\omega}}\times\boldsymbol{e}_\varphi)(L_1+L_4\sin\alpha)\sin\left(\arctan\left(\tfrac{y}{L_1+L_4\sin\alpha}\right)\right)\\
&+(\dot{\boldsymbol{\omega}}\times\boldsymbol{e}_r)\Big[(x\cos\alpha+z\sin\alpha)\\
&\quad+\left[\sqrt{(L_1+L_4\sin\alpha)^2+y^2+(H-L_4\cos\alpha)^2}-(L_1+L_4\sin\alpha)\right]\Big]
\end{aligned}\right\}\dot{\boldsymbol{\omega}}\times\boldsymbol{r}'_{AP}
$$

$$
\left.\begin{aligned}
&+2(-\boldsymbol{\omega}\times\boldsymbol{e}_\varphi)\Big[(L_1+L_4\sin\alpha)\\
&\qquad\cdot\cos\left(\arctan\left(\tfrac{y}{L_1+L_4\sin\alpha}\right)\right)\left(\tfrac{(L_1+L_4\sin\alpha)}{(L_1+L_4\sin\alpha)^2+y^2}\right)2y\dot{y}\Big]\\
&+2(\boldsymbol{\omega}\times\boldsymbol{e}_r)\Big[(\dot{x}\cos\alpha-\dot{z}\sin\alpha)\\
&\quad+\left[\tfrac{1}{2}\left[(L_1+L_4\sin\alpha)^2+y^2+(H-L_4\cos\alpha)^2\right]^{-1/2}2y\dot{y}\right]\Big]
\end{aligned}\right\}2(\boldsymbol{\omega}\times\dot{\boldsymbol{r}}'_{AP,S'_R}).
$$

where term $\ddot{\boldsymbol{r}}'_{AP,S'_R}$ describes the second derivation in time of $\boldsymbol{r}'_{AP}$ in system S'_R. The second expression of the velocity vector $\boldsymbol{u}'_{AP}$ stated in (7.4.39) was reformulated with help of the angular velocity vector $\boldsymbol{\omega}$ and equation (7.4.2) as well as equation (7.4.18). The above term $\dot{\boldsymbol{r}}'_{AP,S'_R}$ describes the derivation in time of $\boldsymbol{r}'_{AP}$ in system S'_R seen from S_I (see also eq. (7.4.36)) and it is

$$\boldsymbol{u}'_{AP}\,|_{S_I} = \dot{\boldsymbol{r}}'_{AP,S'_R} + \boldsymbol{\omega} \times \boldsymbol{r}'_{AP}\,. \tag{7.4.40}$$

The second order derivation in time of vector $\boldsymbol{r}'_{AP}$ (in equation (7.4.38)) is the acceleration vector $\boldsymbol{a}'_{AP}$ valid for point P formulated in equation (7.4.39) (seen from S_I). This expression can be summarised as

$$\boldsymbol{a}'_{AP}\,|_{S_I} = \ddot{\boldsymbol{r}}'_{AP,S'_R} + \boldsymbol{\omega} \times (\boldsymbol{\omega} \times \boldsymbol{r}'_{AP}) + \dot{\boldsymbol{\omega}} \times \boldsymbol{r}'_{AP} + 2(\boldsymbol{\omega} \times \dot{\boldsymbol{r}}'_{AP,S'_R})\,. \tag{7.4.41}$$

All terms which are subsumed in term $2\,(\boldsymbol{\omega} \times \dot{\boldsymbol{r}}'_{AP})$ in (7.4.41) describe the Coriolis acceleration which acts in system S'_R at the fluid particle in point P. All terms which are subsumed in the expression $\boldsymbol{\omega} \times (\boldsymbol{\omega} \times \boldsymbol{r}'_{AP})$ stand for the centrifugal acceleration acting in system S'_R at point P. The formulation in eq. (7.4.41) can now be used to describe the vector $\boldsymbol{a}_P$ in (7.4.37).

The above formulations were presented as an illustrative example how the additional accelerations, which have to be considered in the conservation of momentum in equation (7.3.13), can be described in the observed system of test case *CenCon* for an arbitrary fluid particle in point P.

7.5. The system of *CenCon* in the simulation

7.5.1. Configuration of *CenCon* and its boundary conditions

Figure 7.16 shows the computational setup of *CenCon* (left picture) and a scheme of its computational mesh partition (right picture). Note that the test case is also presented shortly in [Zimmermann14b]. To analyse the influence of the Coriolis acceleration on the turbulent flow structures inside the container, two different modes are investigated in the simulation as well as in the experimental study, as it was mentioned before. First, the test case is investigated in a non-rotation mode like it was the case before for test case *RayCon*. Second, the test case is analysed while it is uniformly rotating in the large-scale centrifuge.

Differences between both modes will be observed. The additional accelerations of the rotational movement are considered in the numerical simulation with help of the modified governing equations in section 7.3.1, eq. (7.3.13). The computational geometry of the container has the same dimensions and properties as the experimental cell. Note that the

origin of the coordinate system is in the centre position of the container and that the z-axis is this time the vertical axis.

As mentioned before, the experimental setup is filled with air. The walls are smooth. The two horizontal walls are heated homogeneously with a constant temperature difference between the lower hot and upper cold wall, $\Delta T = T_{\mathrm{hot}} - T_{\mathrm{cold}}$. In the simulation, the lateral walls are modelled with an idealistic boundary condition of adiabatic walls.

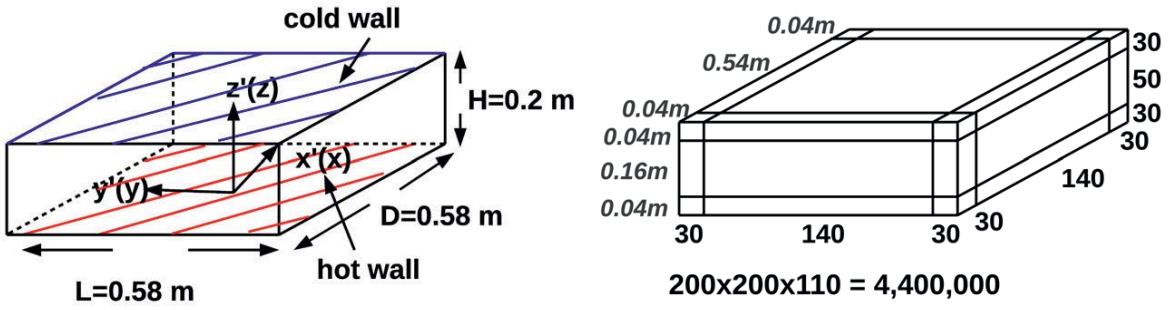

Figure 7.16.: Left: Computational configuration of *CenCon*. **Right:** Scheme of the computational geometry with its mesh resolution of $(200 \times 200 \times 110)$ cells (see also [Zimmermann14b]).

Hence, the normal temperature gradient at the side walls is zero. The index w stands for *lateral wall* in the following. For the side walls and the front/back wall it is

$$\left.\frac{\partial T}{\partial y}\right|_{\mathrm{w}} = 0, \quad \text{for } y = -0.29\,\mathrm{m} \text{ and } y = 0.29\,\mathrm{m}, \quad \text{with } -0.29 \leq x \leq 0.29\,\mathrm{m},\ -0.1 \leq z \leq 0.1\,\mathrm{m},$$
$$\left.\frac{\partial T}{\partial x}\right|_{\mathrm{w}} = 0, \quad \text{for } x = -0.29\,\mathrm{m} \text{ and } x = 0.29\,\mathrm{m}, \quad \text{with } -0.29 \leq y \leq 0.29\,\mathrm{m},\ -0.1 \leq z \leq 0.1\,\mathrm{m}.$$

The velocity field at all walls is zero due to a non-slip-condition ($\mathbf{u} \equiv 0$). The boundary condition of the total pressure p is taken with a zero gradient-option at all walls, as it was the case before for *VerCon* in chapter 5. The initial field of p is assumed to be constant at $1 \cdot 10^5$ Pa inside the computational geometry. The boundary condition of the dynamic pressure p_{rgh} is realised by the option *buoyantPressure* (for the description see also chapter 5). Inside the box an almost atmospheric pressure condition is generated. The hot wall has a maximum heating power amount of 1.17 kW.

A possible heat loss through the side walls has to be considered in the experimental setup which is neglected in the numerical study (s. A, section A.2.1, on page 278). The initial inner temperature field can be assumed as constant in the experiment as well as in the simulation. This temperature field is chosen equally to the temperature at the cold wall, because it approximates the ambient temperature in the centrifuge, hence it is $T_{\mathrm{IF}} = T_{\mathrm{cold}} = 293.15\,\mathrm{K}$.

The simulation does not use a Boussinesq-approximation (s. chapter 1, section 1.7, on page 18). Consequently, temperature dependent fluid properties are calculated by the

Sutherland model from chapter 1, section 1.9 from page 24 on. The turbulent Prandtl number $\mathrm{Pr}_{\mathrm{sgs}}$ is taken with $\mathrm{Pr}_{\mathrm{sgs}} = 0.4$ (s. chapter 3, section 3.3.2).

The realised Rayleigh-numbers in the simulation and experiment

The Rayleigh number is determined by the mean temperature

$$T_{\mathrm{mean}} = (T_{\mathrm{hot}} - T_{\mathrm{cold}})/2 + T_{\mathrm{cold}} \tag{7.5.1}$$

between the hot and cold wall and its depending fluid properties (s. chapter 1, section 1.9 on page 24, equation (1.9.7)). The cold wall temperature is always regulated constant at 293.15 K, due to the layout of the temperature controlling in the experiment.

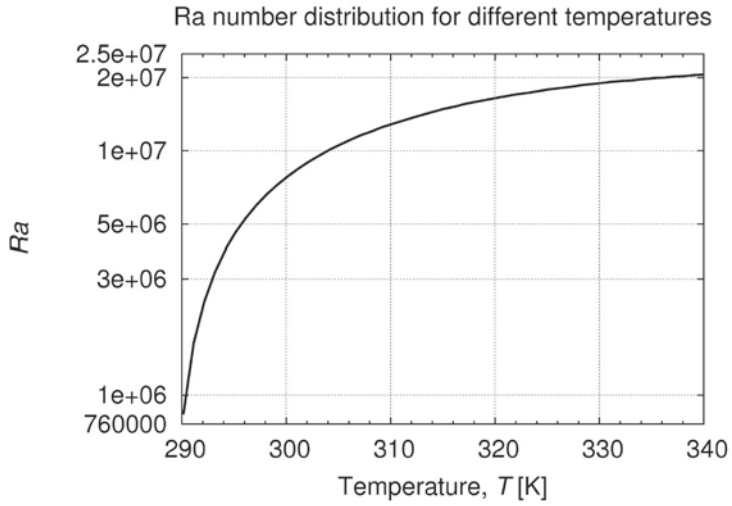

Figure 7.17.: Rayleigh number distribution for different temperatures.

With help of the regulation at the hot wall T_{hot}, different mean temperatures T_{mean} and hence several Rayleigh numbers can be realised in the experiment as well as in the simulation. This is illustrated in figure 7.17 for a temperature range of 290 K − 340 K. If the Rayleigh number Ra exceeds a critical value, turbulent structures are generated in the convective flow which increase with an increasing Rayleigh number (s. chapter 3, section 3.5 on page 76). Thus, a as high as possible Rayleigh number should be realised in the experiment. As figure 7.17 shows, the Rayleigh number does not rise any more significantly between a temperature range of 320 K − 338.15 K.

To obtain a mean temperature of $T_{\mathrm{mean}} = 338.15\,\mathrm{K}$ in the setup, the temperature at the hot wall has to be at 383.15 K which cannot be realised in the experiment. The peak temperature at the hot wall is limited to $T_{\mathrm{hot}} = 353.15\,\mathrm{K}$ due to the layout of the temperature controlling. This implies a maximum mean temperature of $T_{\mathrm{mean}} = 323.15\,\mathrm{K}$ and a maximal Rayleigh number of $\mathrm{Ra}_{\mathrm{max}} = 3.06 \times 10^7$. Thus, Rayleigh numbers in the

range of $2.33 \times 10^6 \leq \mathrm{Ra} \leq 3.06 \times 10^7$ can be realised in the experiment and thus in the simulation. Table 7.1 lists the temperature boundary conditions at the hot and cold wall for the mentioned Rayleigh numbers in the non-rotation mode $\mathrm{rot}_{\mathrm{off}}$. Note that the effective gravitational force g_{eff} is about 1.4 times higher in the rotation mode than in the non-rotation mode (s. equation 7.4.21 on page 219). As a result, the Rayleigh number rises with a higher effective gravitational force g_{eff} (s. chapter 1, section 1.9 on page 24, equation (1.9.7)). The modified Rayleigh numbers for $g_{\mathrm{eff}} = 1.4\,g$ in the rotation-mode $\mathrm{rot}_{\mathrm{on}}$ are listed in table 7.2. The values lie this time between $3.29 \times 10^6 \leq \mathrm{Ra} \leq 4.32 \times 10^7$. The deviations between the effective Rayleigh numbers of both modes could have been compensated by adapted temperature conditions. But the intention of the experiment was to realise the same temperature conditions in both modes.

Rayleigh number Ra	$\boldsymbol{\Delta T}$ [K]	$\mathbf{T_{mean}}$ [K]	**T** [K] cold wall	**T** [K] hot wall
2.33×10^6	3	294.65	293.15	296.15
3.83×10^6	5	295.65	293.15	298.15
6.33×10^6	8.5	297.4	293.15	301.65
1.06×10^7	15	300.65	293.15	308.15
1.80×10^7	28	307.15	293.15	321.15
3.06×10^7	60	323.15	293.15	353.15

Table 7.1.: Rayleigh numbers and temperature conditions at the hot and cold wall of *CenCon*, non-rotation mode $\mathrm{rot}_{\mathrm{off}}$, $g_{\mathrm{eff}} = 1g$.

Rayleigh number Ra	$\boldsymbol{\Delta T}$ [K]	$\mathbf{T_{mean}}$ [K]	**T** [K] cold wall	**T** [K] hot wall
3.29×10^6	3	294.65	293.15	296.15
5.39×10^6	5	295.65	293.15	298.15
8.93×10^6	8.5	297.4	293.15	301.65
1.50×10^7	15	300.65	293.15	308.15
2.54×10^7	28	307.15	293.15	321.15
4.32×10^7	60	323.15	293.15	353.15

Table 7.2.: Rayleigh numbers and temperature conditions at the hot and cold wall of *CenCon*, rotation mode $\mathrm{rot}_{\mathrm{on}}$, $g_{\mathrm{eff}} = 1.4g$.

7.5.2. Computational mesh of *CenCon*

Because the design of the computational geometry of *CenCon* is similar to the computational geometry of *RayCon* from chapter 6, the computational mesh is constructed as

before as a Cartesian-structured mesh with twenty-seven sub-blocks. The number of grid cells is chosen based on the number of cells of *RayCon*, but it is adjusted to the new dimensions. The mesh resolution contains of $(200 \times 200 \times 110)$ cells, as it is indicated in figure 7.16 in the right scheme. Figure 7.18 on page 229 displays a snapshot of the mesh resolution for the side and top/bottom walls of the computational geometry. Because of symmetry aspects, it is sufficient to present only a quarter of the mesh resolution of the particular walls.

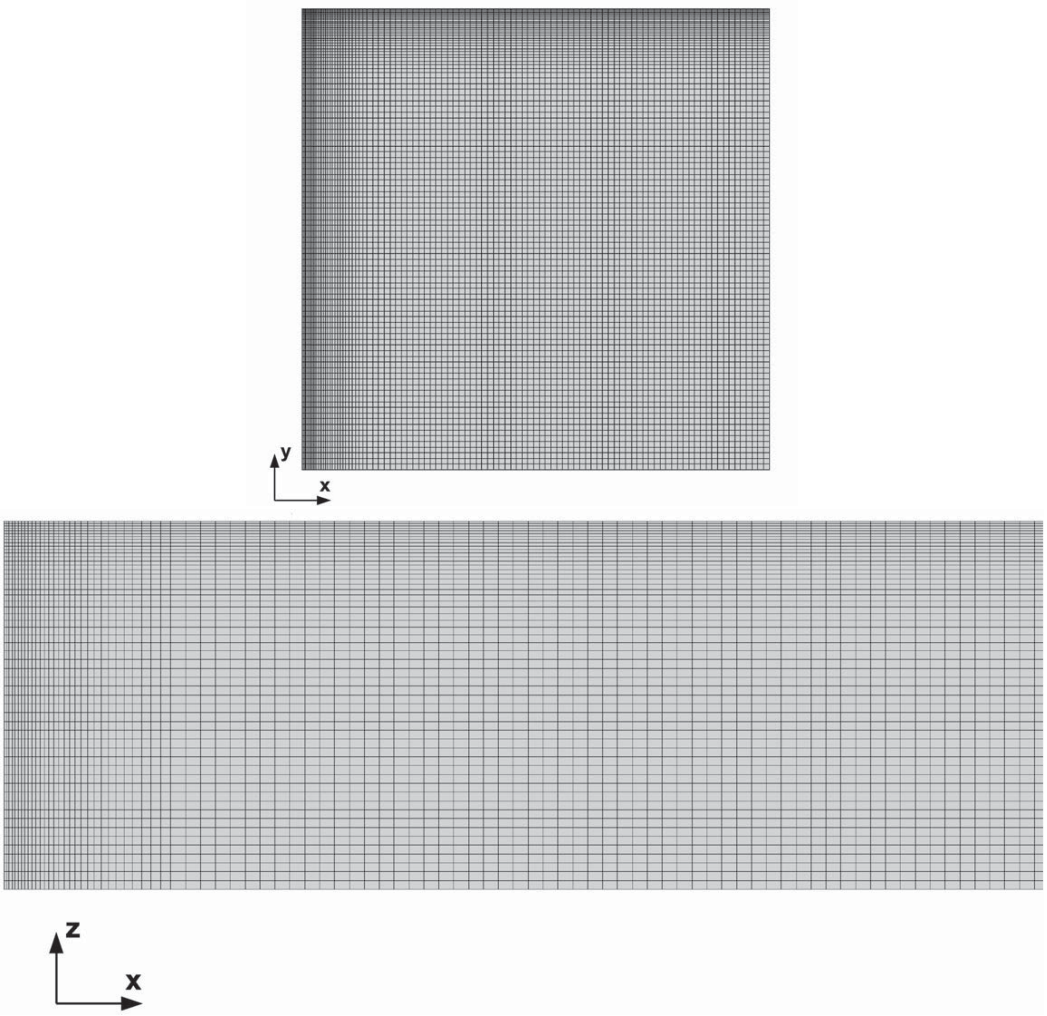

Figure 7.18.: Mesh resolution of the computational geometry of *CenCon* in figure 7.16, $(200 \times 200 \times 110)$ cells. **Top:** Quarter of the top/bottom (heated) wall. **Bottom:** Quarter of the side walls.

As before, the mesh composition allows an exterior zone in vicinity to all walls, where the resolution is clustered and the cell ratios decrease in direction to the walls to resolve the boundary layers which lie in the first sub-block near the walls. This partition of the mesh enables in the exterior zone a finer resolution which can easily be chosen independently off the other blocks. The first layer of cells is cubical formed. In this way, all relevant turbulent scales can be resolved and no wall functions have to be considered in the numerical model.

The first grid point is located at $y_{w1} = 3.06 \cdot 10^{-4}\,\mathrm{m}$ in vertical distance from the heated walls. The size of one cell is nowhere bigger than ten-times of the size of the Kolmogorov length which is important for a successful LES. As mentioned before, the Kolmogorov is length a scale for the smallest turbulent eddies which have to be resolved in a DNS by the computational grid (s. chapter 3, section 3.1, on page 66, equation (3.1.9)). According to equation (5.2.4) on page 100 in chapter 5, it is

$$\eta_{k_L} \approx \frac{L}{\left(\frac{1}{0.71 \cdot 2.5}\mathrm{Ra}\right)^{3/8}}. \tag{7.5.2}$$

Table 7.3 lists the Kolmogorov length for the realised Rayleigh numbers in the non-rotation mode, according to eq. (7.5.2). The Rayleigh numbers in the rotation-mode $\mathrm{rot}_{\mathrm{on}}$ are higher than in the non-rotation mode $\mathrm{rot}_{\mathrm{off}}$. Hence, the resulting Kolmogorov lengths are smaller. Therefore, only the non-rotation mode is discussed at this point. The smallest cell in the mesh is cubical formed, it is $\Delta_x/\Delta_y/\Delta_z = 6.1 \cdot 10^{-4}\,\mathrm{m}$.

Rayleigh number Ra ($g_{\mathrm{eff}} = 1g$)	**Kolmogorov length** η_{k_L}
2.33×10^6	$1.02 \cdot 10^{-3}$
3.83×10^6	$8.43 \cdot 10^{-4}$
6.33×10^6	$6.98 \cdot 10^{-4}$
1.06×10^7	$5.75 \cdot 10^{-4}$
1.80×10^7	$4.72 \cdot 10^{-4}$
3.06×10^7	$3.87 \cdot 10^{-4}$

Table 7.3.: Kolmogorov length η_{k_L} for several Rayleigh numbers according to eq. (7.5.2), non-rotation mode $\mathrm{rot}_{\mathrm{off}}$, $g_{\mathrm{eff}} = 1g$.

As table 7.3 shows, the Kolmogorov length is in case of the three first Rayleigh-numbers bigger than the size of the smallest cell. In the last three cases, the smallest cell size is bigger than the Kolmogorov length which was the intention of the chosen mesh resolution. Because the Kolmogorov length decreases with higher Rayleigh numbers the mesh was designed concerning the highest Rayleigh number. Table 7.4 lists the non-dimensional wall distance y^+ in the first cell midpoint y_{w1} for all realised Rayleigh numbers in the fully turbulent flow in the non-rotation mode $\mathrm{rot}_{\mathrm{off}}$ (s. chapter 3, section 3.5, 3.5.3.2, eq. (3.5.26) on page 84). Table 7.5 gives analogously an overview of the non-dimensional wall distance y^+ in the first cell midpoint y_{w1} in the rotation mode $\mathrm{rot}_{\mathrm{on}}$. The values of the rotation mode are higher than the values in the non-rotation mode $\mathrm{rot}_{\mathrm{off}}$ due to the higher velocities reached close to the heated walls. For all values it is $y^+ < 1$ in y_{w1}(see also chapter 5, section 5.1, 5.2).

Rayleigh number ($g_{\text{eff}} = 1g$)	**(200 × 200 × 110)** y^+	
	$t = 200\text{s}$	$\Delta t = 200\,\text{s} - 400\,\text{s}$
2.33×10^6	$y^+ = 0.071$	$\bar{y}^+ = 0.073$
3.83×10^6	$y^+ = 0.129$	$\bar{y}^+ = 0.153$
6.33×10^6	$y^+ = 0.112$	$\bar{y}^+ = 0.113$
1.06×10^7	$y^+ = 0.164$	$\bar{y}^+ = 0.154$
1.80×10^7	$y^+ = 0.115$	$\bar{y}^+ = 0.158$
3.06×10^7	$y^+ = 0.106$	$\bar{y}^+ = 0.182$

Table 7.4.: Non-dimensional distance y^+ estimated in the first cell midpoint y_{w1} in the fully turbulent flow at $t = 200\,\text{s}$ and as averaged value over $\Delta t = 200\,\text{s} - 400\,\text{s}$, non-rotation mode rot_{off}, $g_{\text{eff}} = 1g$.

Rayleigh number ($g_{\text{eff}} = 1.4g$)	**(200 × 200 × 110)** y^+	
	$t = 200\text{s}$	$\Delta t = 200\,\text{s} - 400\,\text{s}$
3.29×10^6	$y^+ = 0.239$	$\bar{y}^+ = 0.201$
5.39×10^6	$y^+ = 0.239$	$\bar{y}^+ = 0.239$
8.93×10^6	$y^+ = 0.232$	$\bar{y}^+ = 0.237$
1.5×10^7	$y^+ = 0.227$	$\bar{y}^+ = 0.231$
2.54×10^7	$y^+ = 0.223$	$\bar{y}^+ = 0.227$
4.32×10^7	$y^+ = 0.229$	$\bar{y}^+ = 0.220$

Table 7.5.: Non-dimensional distance y^+ estimated in the first cell midpoint y_{w1} in the fully turbulent flow at $t = 200\,\text{s}$ and as averaged value over $\Delta t = 200\,\text{s} - 400\,\text{s}$, rotation mode rot_{on}, $g_{\text{eff}} = 1.4g$.

7.6. Simulation results of *CenCon*

7.6.1. Convection cell structures in the test case visualised by the mean velocity distribution

7.6.1.1. Non-rotation mode

Scheme of the convection cells

In the following, the arrangement of the convection cells inside the container in the simulation is discussed for the non-rotation mode rot_{off} as well as for the rotation mode rot_{on} (see also [Zimmermann14b]). Figure 7.19 and figure 7.20 show schemes of the convection cell arrangement in the non-rotation mode rot_{off} for a front as well as for a top view of

the setup of *CenCon*. The arrows should only clarify the opposite circulation movements. For $\Delta T = 3\,\mathrm{K}, 5\,\mathrm{K}$ and $\Delta T = 8.5\,\mathrm{K}, 28\,\mathrm{K}$ one convection cell can be detected (figure 7.19, top row, left sketch). In the case of $\Delta T = 60\,\mathrm{K}$, the location of the cells is similar to the previously cases. But the circulation direction is inverted, as it is indicated in figure 7.19, right picture, top row. For $\Delta T = 15\,\mathrm{K}$ two convection cells appear in the front view, as the picture in the bottom row in figure 7.19 shows. Both cells are extended to the depth of the container and reach until its end.

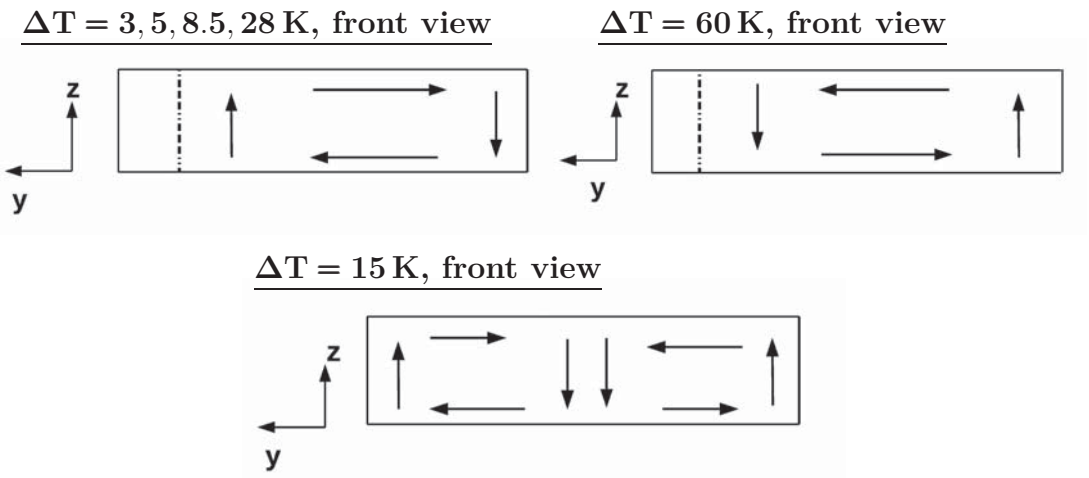

Figure 7.19.: Schemes of the convection cell arrangement in the container, **non-rotation mode $\mathbf{rot_{off}}$**, front view. **Top:** $\Delta T = 3\,\mathrm{K}, 5\,\mathrm{K}$, $8.5\,\mathrm{K}$, $28\,\mathrm{K}$ (left), $\Delta T = 60\,\mathrm{K}$ (right). **Bottom:** $\Delta T = 15\,\mathrm{K}$.

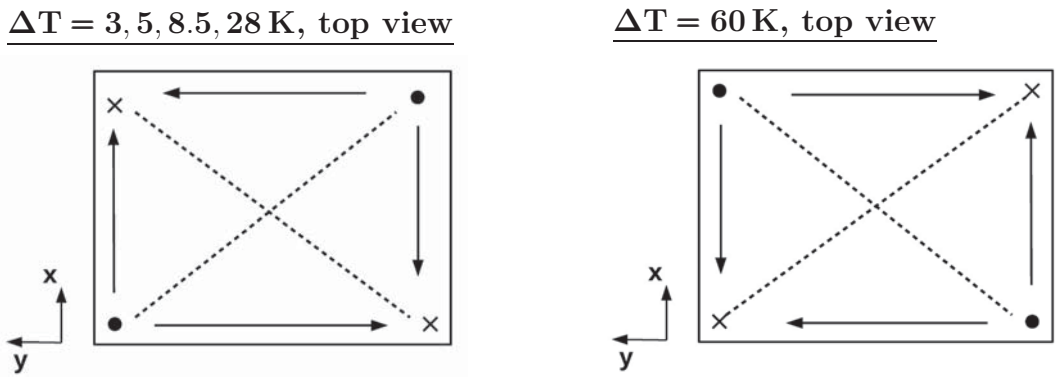

Figure 7.20.: Schemes of the convection cells in the container, **non-rotation mode $\mathbf{rot_{off}}$**, top view, **Left:** $\Delta T = 3\,\mathrm{K}$, $\Delta T = 5\,\mathrm{K}$, $8.5\,\mathrm{K}$, $28\,\mathrm{K}$. **Right:** $\Delta T = 60\,\mathrm{K}$.

Figure 7.20 demonstrates schemes of the convection cells in a top view of the container. The left sketch illustrates the cell composition for for $\Delta T = 3\,\mathrm{K}, 5\,\mathrm{K}, 8.5\,\mathrm{K}, 28\,\mathrm{K}$. The right sketch shows the one for $\Delta T = 60\,\mathrm{K}$. The points stand for a vertical circulation direction which goes from the bottom to the top wall of the container. The crosses denote an inverse vertical circulation from the top to the bottom wall. For $\Delta T = 3\,\mathrm{K}, 5\,\mathrm{K}, 8.5\,\mathrm{K}, 28\,\mathrm{K}$ and $\Delta T = 60\,\mathrm{K}$ four convection cells arise in the container.

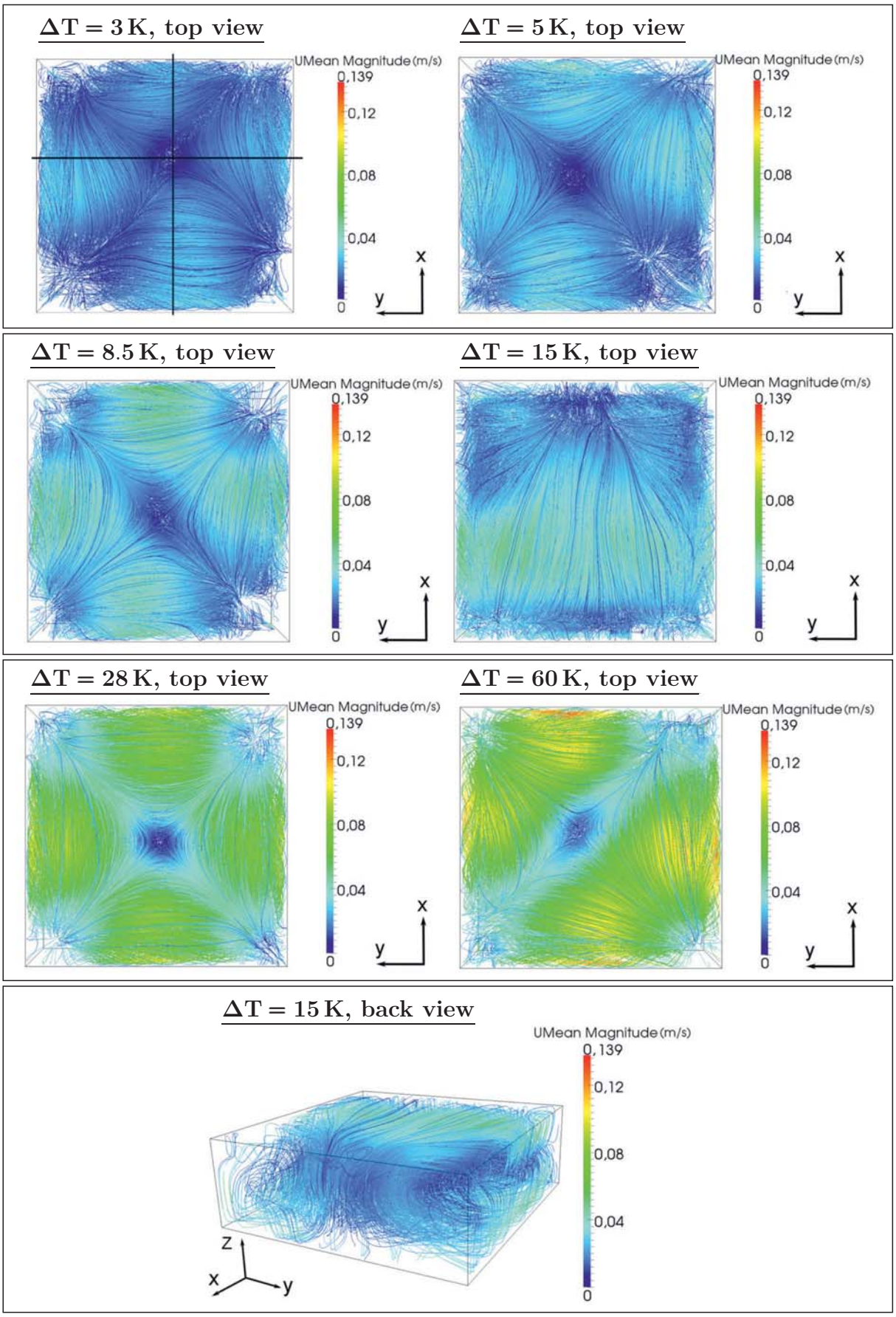

Figure 7.21.: Instantaneous snapshots of the convection cell structures in *CenCon*, **non-rotation mode rot$_{\text{off}}$**, top view. **Top to bottom:** $\Delta T = 3$K ([Zimmermann14b]), $\Delta T = 5$K, $\Delta T = 8.5$K, $\Delta T = 15$K, $\Delta T = 28$K, $\Delta T = 60$K, $\Delta T = 15$K, $t = 400$ s, simulation results.

For $\Delta T = 60\,\mathrm{K}$, the orientation of the circulation has changed as it was seen before in the front view pictures (right picture in figure 7.19). For $\Delta T = 15\,\mathrm{K}$ only two convection cells can be seen next to each other which are extended over the whole container depth, see also figure 7.21 bottom picture.

Snapshots of the convection cells in the simulated process

The following cell arrangements are illustrated on the basis of the instantaneous magnitude of the mean velocity distribution. Each of the following plots show the velocity values which were time-averaged to the point of the presented time-step. The snapshots in each figure were made with help of the visualisation software *ParaView*, version 3.11.

The snapshot of $\Delta T = 15\,\mathrm{K}$ in figure 7.21 shows the arising cells at $t = 400\,\mathrm{s}$ in the simulated process and the non-rotation mode $\mathrm{rot}_{\mathrm{off}}$. A large circulation movement can be detected in horizontal x-direction. Figure 7.21 presents also the convection cell arrangement of the other cases in a top view. The typical convection cell structures of a RB problem, as it was seen before in the results of *RayCon* in chapter 6, appear. In consequence to the square base layout of *CenCon*, four convection cells arise in the setup, except in case of $\Delta T = 15\,\mathrm{K}$. Two cells are located each parallel to the one side wall of the test case, respectively front/back wall. All four cells contact each other near the container middle. This point of contact is marked exemplary for case $\Delta T = 3\,\mathrm{K}$ by two black lines in figure 7.21 (left picture, top row). Table 7.6 lists the different positions of this point for each case. The cell size and the location of the contact-point vary in each ΔT-case.

Case	Location	
$\Delta T = 3\mathrm{K}$	$x = 0.07\,\mathrm{m},$	$y = -0.1\,\mathrm{m}$
$\Delta T = 5\mathrm{K}$	$x = 0.02\,\mathrm{m},$	$y = 0.03\,\mathrm{m}$
$\Delta T = 8.5\mathrm{K}$	$x = -0.01\,\mathrm{m},$	$y = 0.03\,\mathrm{m}$
$\Delta T = 28\mathrm{K}$	$x = -0.02\,\mathrm{m},$	$y = -0.01\,\mathrm{m}$
$\Delta T = 60\mathrm{K}$	$x = 0.02\,\mathrm{m},$	$y = 0.04\,\mathrm{m}$

Table 7.6.: Point of contact between the convection cells near the container middle, concerning the coordinate origin $(x, y, z) = (0, 0, 0)$, $t = 400\,\mathrm{s}$, **non-rotation mode $\mathrm{rot}_{\mathrm{off}}$.**

7.6.1.2. Rotation mode

In the rotation mode $\mathrm{rot}_{\mathrm{on}}$ of the test case, a changed convection cell arrangement is expected due to the effect of the Coriolis accelerations. [Alonso1967] (chapter 6, 6.4) describes theoretically a displacement of a falling body in the Earth's atmosphere affected by the Coriolis force caused by the Earth's rotation. The resulting conclusions can be adapted to the rotating system of the container in the centrifuge of this study. This aspect is also discussed similarly in [Zimmermann14b].

Scheme of the convection cells

Figure 7.22 on page 236 illustrates a possible displacement of a moving fluid particle in the container. If the movement of the particle is parallel relative to the rotation axis z of the centrifuge system S_I, no Coriolis effect can be detected in the container. In all other cases a Coriolis acceleration affects the particles movement. If the rotation axis in S_I is turned by a known angle relative to the direction of the particles motion in the rotating system S'_R, the resulting Coriolis force can be estimated by equation (7.4.26) in section 7.4.2 on page 220.

The left sketch in figure 7.22 on page 236 pictures a displacement of a particle which is moving along the z'-axis in S'_R. Due to the given layout, the vector $\boldsymbol{\omega} \times \boldsymbol{u}'_{S'_R}$ points in direction of the positive y'-axis. The vector of the Coriolis acceleration $-2\left(\boldsymbol{\omega} \times \boldsymbol{u}'_{S'_R}\right)$ points then in the negative direction of the y'-axis. The moving particle will also be displaced in this direction. Combining this effect with the centrifugal effect, the particle will also be displaced additionally in direction of the negative x'-axis (see [Alonso1967], chapter 6, 6.4).

The right sketch in figure 7.22 shows a displacement of a particle which moves in the $x'y'$-plane. The vector $\boldsymbol{u}'_{S'_R}$ points perpendicular relative to the angular velocity vector $\boldsymbol{\omega}$. Therefore, the Coriolis acceleration $-2\boldsymbol{\omega} \times \boldsymbol{u}'_{S'_R}$ is perpendicular relative to the vectors of $\boldsymbol{\omega}$ and $\boldsymbol{u}'_{S'_R}$. It makes an angle α with the horizontal $x'y'$-plane. The resulting Coriolis acceleration consists of a vertical component (marked by $a_{\mathrm{c,V}}$ in figure 7.22) and a horizontal component (marked by $a_{\mathrm{c,H}}$ in figure 7.22). The horizontal component displaces the particle from a straight line to the right in direction of the negative x'-axis. Due to this component, hurricanes or whirlwinds are generated in the atmosphere. The vertical component is small compared to the acceleration of the effective gravity (see [Alonso1967], chapter 6, 6.4). This theoretically described displacement of fluid particles in the container, is now illustrated on the basis of the velocity distributions in the simulation results.

Snapshots of the convection cells in the simulated process

The snapshots in figures 7.23 - 7.25 on pages 236 - 237 show the instantaneous vertical and horizontal velocity structures in the container at $t = 400\,\mathrm{s}$ in the simulated process for different views and the cases of $\Delta T = 3\,\mathrm{K}$ as well as $\Delta T = 60\,\mathrm{K}$. For a better presentation, the pictures of case $\Delta T = 5\,\mathrm{K}, 8.5\,\mathrm{K}, 15\,\mathrm{K}$ and $\Delta T = 28\,\mathrm{K}$ are placed in the appendix A, section A.2.2, figures A.3 - A.4 from page 282 on. Due to the Coriolis acceleration, the coherent structures in the container have to change in comparison to the ones in the non-rotation mode. The label U_{rel} in figures 7.23 - 7.26 denotes the relative velocity values in the rotating system S'_R which consider the additional accelerations in the container. The velocity U_{rel} correspond to the before mentioned velocity $\boldsymbol{u}_{S'_R}$ in equation (7.3.14) - (7.3.16) on page 214.

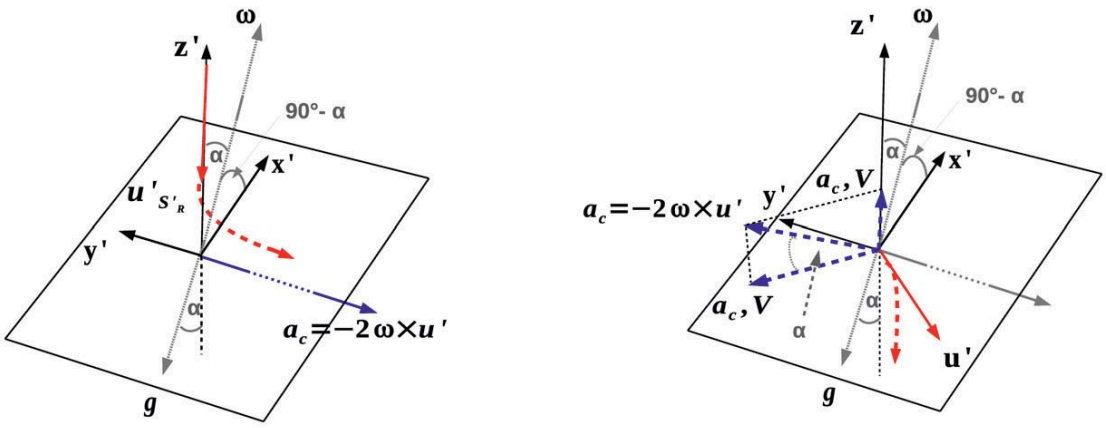

Figure 7.22.: Coriolis acceleration $\boldsymbol{a_c}$ and a possible resulting displacement of a moving fluid particle, rotation mode $\mathrm{rot_{on}}$ (as seen in [Alonso1967]). **Left:** Movement along the z'-axis. **Right:** Movement in the $x'y'$-plane (see also [Zimmermann14b]).

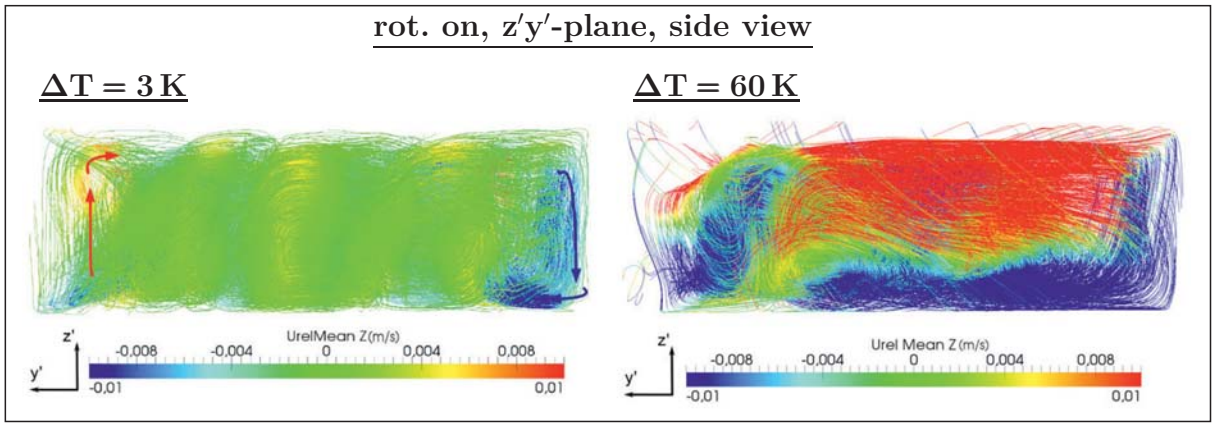

Figure 7.23.: Instantaneous snapshots of the mean vertical velocity structures in the $z'y'$-plane, **rotation mode** $\mathbf{rot_{on}}$, side view, $t = 400\,\mathrm{s}$. **Left:** $\Delta T = 3\mathrm{K}$. **Right:** $\Delta T = 60\mathrm{K}$.

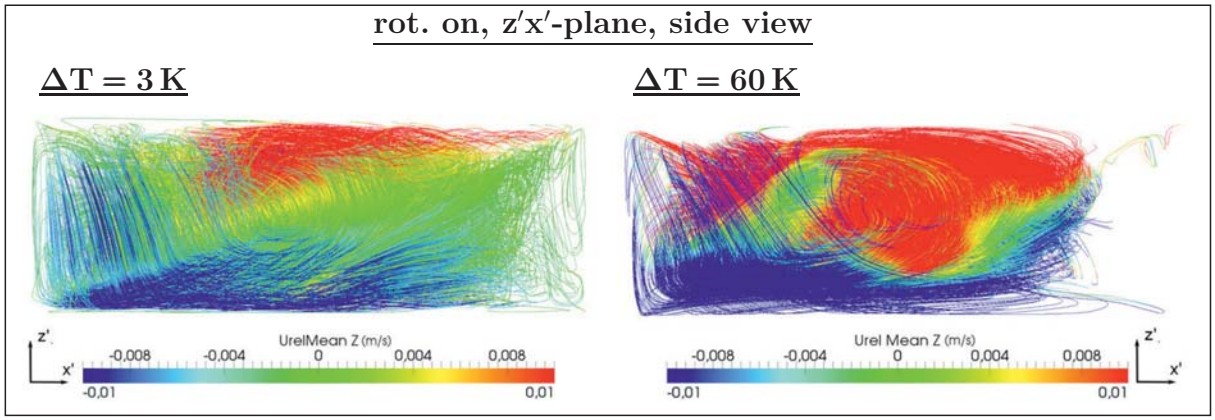

Figure 7.24.: Instantaneous snapshots of the mean vertical velocity structures in the $z'x'$-plane, **rotation mode** $\mathbf{rot_{on}}$, side view, $t = 400\,\mathrm{s}$. **Left:** $\Delta T = 3\mathrm{K}$. **Right:** $\Delta T = 60\mathrm{K}$.

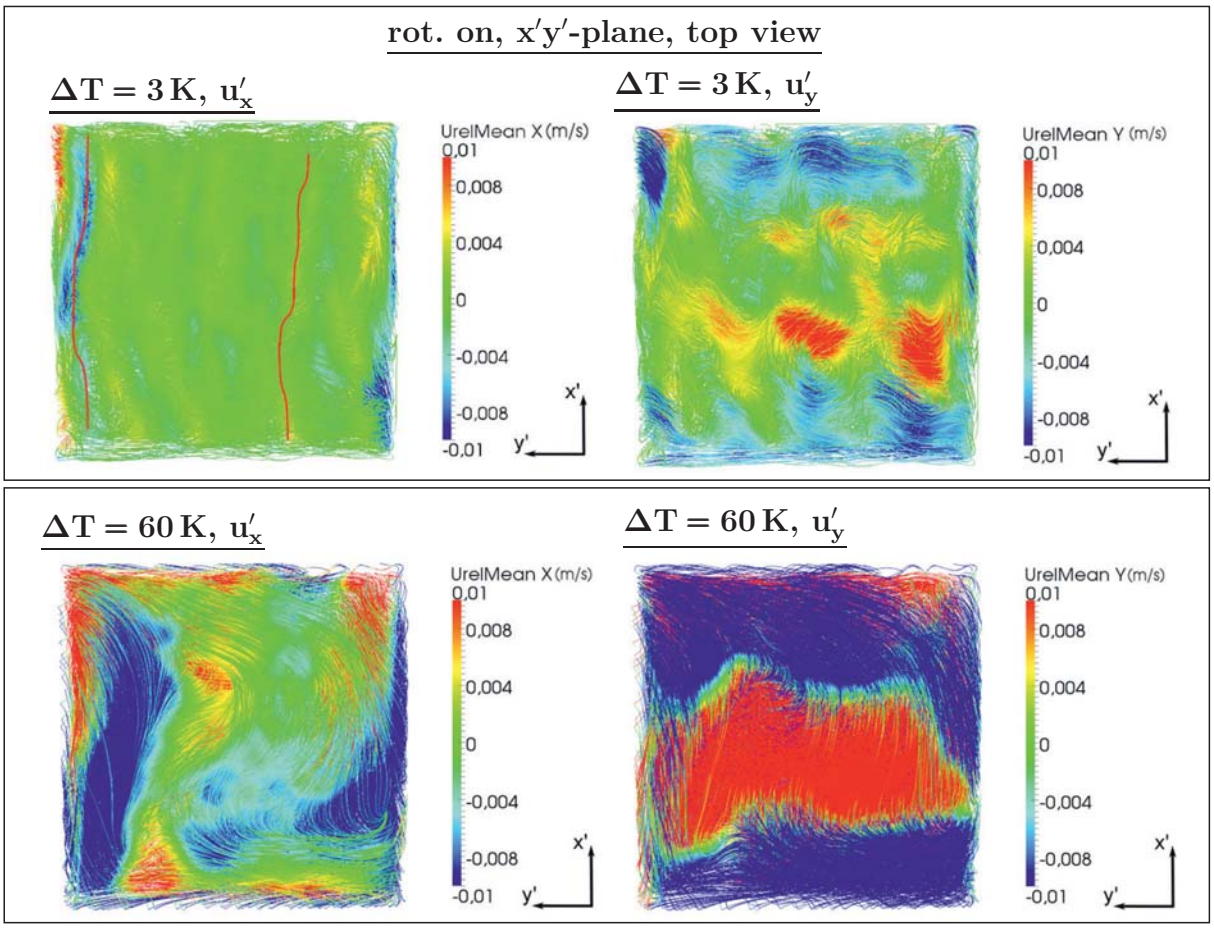

Figure 7.25.: Instantaneous snapshots of the mean horizontal velocity structures in the $x'y'$-plane, rotation mode $\mathrm{rot}_{\mathrm{on}}$, top view, $t = 400\,\mathrm{s}$. **Left:** $u_{x'}$-component. **Right:** $u_{y'}$-component. **Top row:** $\Delta T = 3\mathrm{K}$ (as in [Zimmermann14b]). **Bottom row:** $\Delta T = 60\mathrm{K}$.

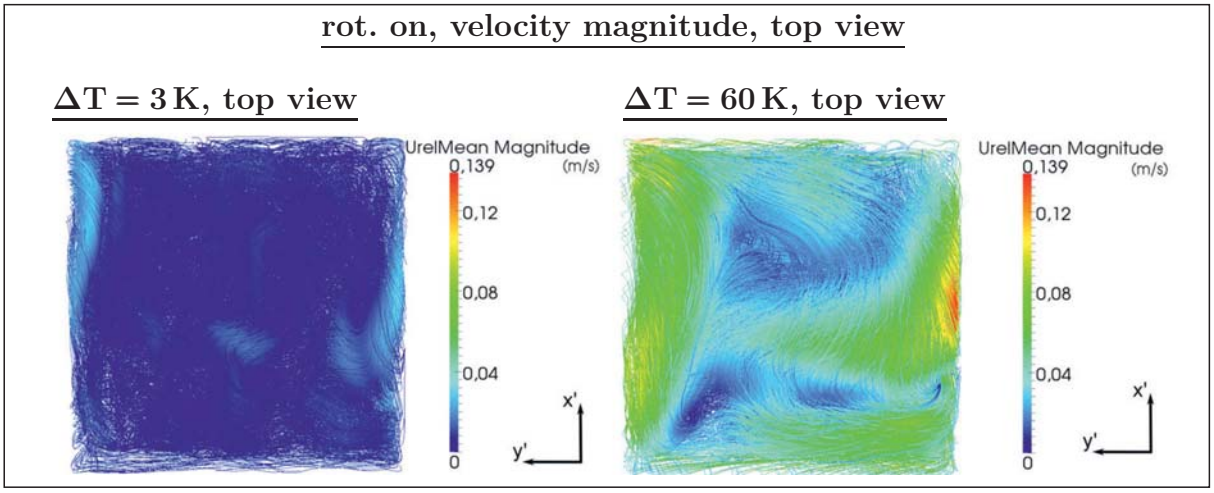

Figure 7.26.: Instantaneous snapshots of the mean velocity magnitude, **rotation mode $\mathrm{rot}_{\mathrm{on}}$**, top view, $t = 400\,\mathrm{s}$. **Left:** $\Delta T = 3\mathrm{K}$. **Right:** $\Delta T = 60\mathrm{K}$.

The cell structure of case $\Delta T = 3\,\mathrm{K}$ has been changed in the container in comparison to the non-rotation mode. The before mentioned displacement caused by the Coriolis force, produces this time several convection cells which are mixed which each other. The convection cells are located next to each other along the container's depth. In figure 7.24 on page 236 an additional side view of the $z'x'$-plane for $\Delta T = 3\,\mathrm{K}$ is shown. The snapshot reveals large scale structures. This is also the case for $\Delta T = 5\,\mathrm{K}, 8.5\,\mathrm{K}, 15\,\mathrm{K}, 28\,\mathrm{K}$. In all cases these structures have the same circulation orientation.

The visible structures for $\Delta T = 3\,\mathrm{K}$ are distorted compared to the non-rotation mode due to the Coriolis acceleration. An up and down movement and wave-like structures of the flow can be seen. Figure 7.23 reveals also large circulation structures for $\Delta T = 60\,\mathrm{K}$. Figure 7.24 on page 236 (right picture) illustrates a side view of the $z'x'$-plane for the case $\Delta T = 60\,\mathrm{K}$. The cell structures seemed to be more mixed than in case of $\Delta T = 3\,\mathrm{K}$.

The cell arrangement has been changed in comparison to the non-rotation mode due to the Coriolis acceleration. The above described arrangement of convection cells for $\Delta T = 3\,\mathrm{K}$ and $\Delta T = 60\,\mathrm{K}$ can also be seen in a visualised top view of the horizontal velocity components at $t = 400\,\mathrm{s}$ in the simulated process in figure 7.25 on page 237. The snapshots in figure 7.26 on page 237 show additionally the instantaneous structures of the velocity magnitude seen in a top view for $\Delta T = 3\,\mathrm{K}$, $\Delta T = 60\,\mathrm{K}$ at $t = 400\,\mathrm{s}$.

Especially for the small temperature difference of $\Delta T = 3\,\mathrm{K}$ and a small effective Rayleigh number, the displacement of the convection cells is clearly visible. In the container exist turbulent and mixed up structures. The flow structures seemed to be larger for higher Rayleigh numbers. Vortex structures can clearly be seen in case of $\Delta T = 3\,\mathrm{K}$. It is also visible that the cells are distorted and drifted to one side of the container in comparison to the non-rotation mode due to the Coriolis acceleration and the deflection angle relative to the rotation axis of the centrifuge.

In comparison to smaller ΔT, the flow structures reveal in case of $\Delta T = 15\,\mathrm{K}$, $\Delta T = 28\,\mathrm{K}$ larger spatial scales. For $\Delta T = 15\,\mathrm{K}$ and $\Delta T = 28\,\mathrm{K}$, vortexes can also clearly be seen in the left bottom corner in the top view pictures in figure A.5 in the appendix A.2.2 (marked by the red coloured circle). For $\Delta T = 60\,\mathrm{K}$, the flow structures seem to become bigger than in case of $\Delta T = 15\,\mathrm{K}$ and of $\Delta T = 28\,\mathrm{K}$.

The large scale structures in case of $\Delta T = 60\,\mathrm{K}$ reach almost over the whole container length. Possible vortex structures cannot be detected in this case. It is assumed that the vortexes would exceed the dimensions of the container. Hence, no vortex structures are developed in this case due to the restriction of the side walls of the setup. This aspect should be investigated in future studies by a modification of the aspect ratios.

All simulation results show significantly a displacement of the flow structures caused by the Coriolis acceleration. Furthermore, vortex structures arise in the test case. In the atmosphere, these observed vortexes would possibly become whirlwinds or cyclones due to

the significantly higher velocities as well as bigger spatial scales. It has also to be regarded that no cyclones could be generated in both studies because the aspect of evaporation was not realised which drives cyclones or whirlwinds in the atmosphere.

Even if it is not possible to reach as high Reynolds and Grashof numbers as in a fully developed twister in the atmosphere, it could be seen in this study that the Coriolis acceleration implies turbulent rotational flows with visible arising vortex structures. The flow structures differ significantly from the structures in the non-rotation mode.

7.6.2. Fluid properties profiles estimated in the simulation

7.6.2.1. Time- and area-averaged fluid properties estimated at the heated walls - Nusselt number, temperature wall gradient and wall heat flux density

ΔT [K]	eff. Ra	heat flux dens. [W/m^2]		∇T [K/m]		Nusselt number	
		hot	cold	hot	cold	hot	cold
$\mathrm{rot_{on}}$, 1 K	1.11×10^6	0.37	0.35	13.84	13.24	2.77	2.65
$\mathrm{rot_{off}}$, 1 K	7.89×10^5	0.97	0.96	36.46	36.10	7.29	7.72
$\mathrm{rot_{on}}$, 3 K	3.29×10^6	2.78	2.79	103.63	104.67	6.91	6.98
$\mathrm{rot_{off}}$, 3 K	2.33×10^6	3.79	3.81	141.20	143.23	9.41	9.55
$\mathrm{rot_{on}}$, 5 K	5.39×10^6	6.13	6.11	227.11	229.60	9.084	9.18
$\mathrm{rot_{off}}$, 5 K	3.83×10^6	7.30	7.21	270.39	270.97	10.82	10.84
$\mathrm{rot_{on}}$, 8.5 K	8.93×10^6	13.14	13.14	482.66	493.47	11.36	11.61
$\mathrm{rot_{off}}$, 8.5 K	6.33×10^6	14.06	14.16	515.26	531.92	12.15	12.52
$\mathrm{rot_{on}}$, 15 K	1.50×10^7	28.41	28.38	1026.21	1065.94	13.68	14.21
$\mathrm{rot_{off}}$, 15 K	1.06×10^7	28.54	28.65	1030.78	1076.21	13.74	14.35
$\mathrm{rot_{on}}$, 28 K	2.54×10^7	65.29	65.28	2283.64	2451.79	16.31	17.51
$\mathrm{rot_{off}}$, 28 K	1.80×10^7	62.45	62.55	2184.30	2349.25	15.60	16.78
$\mathrm{rot_{on}}$, 60 K	4.32×10^7	177.10	177.69	5761.36	6673.98	19.20	22.25
$\mathrm{rot_{off}}$, 60 K	3.06×10^7	162.90	162.98	5299.48	6121.27	17.66	20.40

Table 7.7.: Time- and area-averaged values of fluid properties estimated at the hot and cold wall for different effective Rayleigh numbers, non-rotation mode $\mathrm{rot_{off}}$ ($g_{\mathrm{eff}} = 1g$) and rotation mode $\mathrm{rot_{on}}$ ($g_{\mathrm{eff}} = 1.4g$). Results of the simulation.

In the experiment, no measured data of any fluid property could be gained inside the container due to restricted financial circumstances of the project. Thus, the main intention of the first test series concerning the analysed experiment was to gain visualised data of flow structures. Measured values of fluid properties inside the container may be a possible

step in future works. Note that the Nusselt number behaviour is also discussed similarly in [Zimmermann14b]. Table 7.7 lists therefore only the simulation results of the fluid properties wall heat flux density, wall temperature gradients and Nusselt number values estimated at the hot and cold wall for all temperature boundary conditions in both modes. The values are time-averaged as well as area-averaged over the whole cold/hot wall. The time-averaging interval was chosen as $\Delta t = 200\,\mathrm{s} - 400\,\mathrm{s}$ in the simulated process (with respect to a settlement of the system) with an intermediate steps size of $\Delta t = 1\,\mathrm{s}$.

In the DNS study of [Horn11] slightly increasing Nusselt number values are observed in a rotating RB convection cell compared to a non-rotating RB cell regarding a non-Boussinesq fluid in both cases. As table 7.7 shows, the values estimated in the non-rotation mode $\mathrm{rot_{off}}$ exceed the ones estimated in the rotation mode $\mathrm{rot_{on}}$ until a temperature difference of $\Delta T = 8.5\,\mathrm{K}$. With higher ΔT this relation becomes vice versa. Further, the deviations between both modes decrease with higher ΔT.

Complementary to the results of $\Delta T = 3\,\mathrm{K}$ and $\Delta T = 60\,\mathrm{K}$, additional simulations were performed for $\Delta T = 1\,\mathrm{K}$ in both modes. The realised effective Rayleigh numbers are in these cases $\mathrm{Ra_{eff/rot\text{-}off}} = 7.89 \times 10^5$ and $\mathrm{Ra_{eff/rot\text{-}on}} = 1.11 \times 10^6$. Both temperature conditions were not investigated in the experiment. The additional simulations should only clarify the following results of the estimated fluid properties.

Due to the different realised effective Rayleigh numbers in both modes, one has to compare rather the results of $\Delta T = 3\,\mathrm{K}$ in the rotation mode $\mathrm{rot_{on}}$ with the results of $\Delta T = 5\,\mathrm{K}$ in the non-rotation mode $\mathrm{rot_{off}}$ to obtain statements of the fluid properties behaviour depending on the Rayleigh number. Therefore, the results of the fluid properties are discussed in the following on the basis of the effective Rayleigh numbers $\mathrm{Ra_{eff}}$ and not on the basis of the temperature difference.

Figure 7.27 displays the dependence of the reached Nusselt number values on the effective Rayleigh numbers (top row) for the analysed Prandtl-number of $\mathrm{Pr} = 0.71$. Further, the dependence of the wall temperature gradient (middle row) and wall heat flux density (bottom row) on the effective Rayleigh numbers are displayed. The right plot illustrates the values estimated at the cold wall, while the left plot displays the results estimated at the hot wall. The results of the non-rotation mode $\mathrm{rot_{off}}$ are marked by the solid black line with crosses. The results of the rotation mode $\mathrm{rot_{on}}$ are plotted by the dashed black line with pluses.

In case of the Nusselt numer, higher values of the non-rotation mode $\mathrm{rot_{off}}$ are reached than in case of the rotation mode $\mathrm{rot_{on}}$ at both heated walls. At the hot wall, the results of both modes converge to each other for a effective Rayleigh number of $\mathrm{Ra_{eff}} = 3.06 \times 10^7$. Slightly higher Nusselt number values in the rotation mode $\mathrm{rot_{on}}$ cannot be observed, as it is the case in the study of [Horn11]. The Nusselt number values are than in the rotation

mode and and converge to the result of the non-rotation mode only for higher effective Rayleigh numbers.

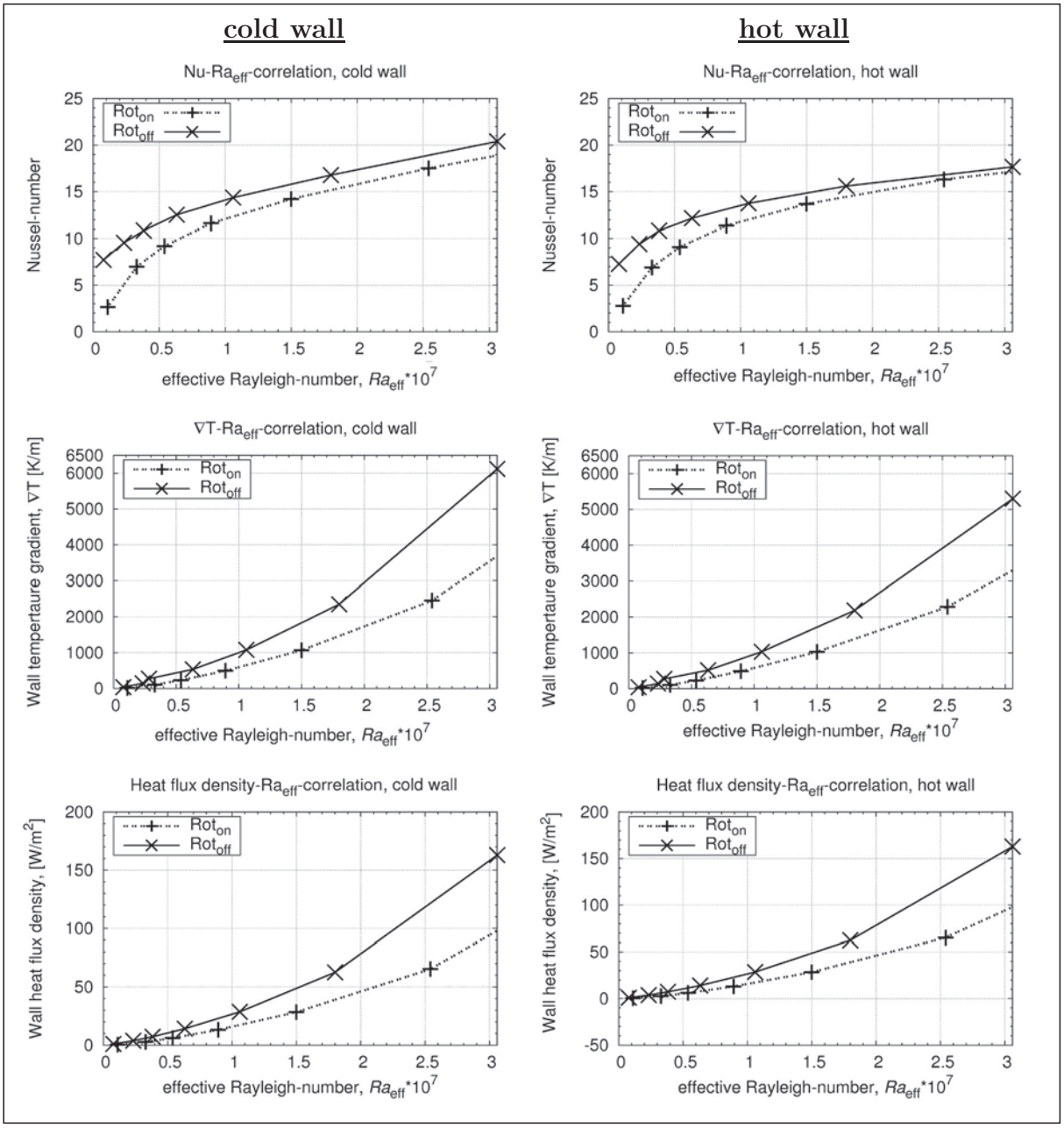

Figure 7.27.: Top: Nu-Ra_{eff} correlation. **Middle:** Correlation of time- and area-averaged wall temperature gradient and effective Rayleigh number Ra_{eff}. **Bottom:** Correlation of time- and area-averaged wall heat flux density and effective Rayleigh number Ra_{eff}. **Left:** Cold wall. **Right:** Hot wall. **In all pictures:** $\times - \times$ (black solid line with crosses): non-rotation mode rot_{off}, $- - + - - +$ (black dashed line with pluses): rotation mode rot_{on}. Results of the simulation. $Pr = 0.71$ (s. also [Zimmermann14b]).

The results of the time- and area-averaged wall temperature gradient as well as of the wall heat flux density are plotted complementary in figure 7.27. Both results show an inverted relation as in case of the Nusselt number values, as it was expected. With smaller effective

Rayleigh numbers both modes lie close to each other. With increasing effective Rayleigh numbers, the results of both modes diverge more from each other. Higher Nusselt number values were not necessarily expected in the rotation mode $\mathrm{rot_{on}}$. Due to the rotational movement, the turbulence production is indeed higher, but the turbulent structures and vortexes are also smaller and more irregular than in the non-rotation mode $\mathrm{rot_{off}}$, as we will discuss in the following. Hence, the heat flux inside the container has not to be necessarily more intensive than in the non-rotation mode $\mathrm{rot_{off}}$.

7.6.2.2. Time-averaged fluid properties estimated at constant planes normal to the heated walls - maximum velocities values

Complementary to the plots in figure 7.27 on page 241, the absolute time-averaged maximum values of the velocity are plotted in relation to the effective Rayleigh numbers in figure 7.28 on page 243.

The plots show the maximum values estimated at constant planes normal to the heated walls at two depth positions, $x_2(x_2') = -0.1\,\mathrm{m}$, $x_3(x_3') = -0.2\,\mathrm{m}$. The results are estimated in both modes. The values of the non-rotation mode $\mathrm{rot_{off}}$ are marked by the black solid line with pluses. The values of the rotation mode $\mathrm{rot_{on}}$ are displayed by the black dashed line with crosses.

The u_z-component in the non-rotation mode $\mathrm{rot_{off}}$ reaches its maximum value at position $x_2(x_2') = -0.1\,\mathrm{m}$ for $\Delta T = 5\,\mathrm{K}$, $\mathrm{Ra_{eff}} = 3.83 \times 10^6$. At position $x_3(x_3') = -0.2\,\mathrm{m}$ the maximum value is reached for $\Delta T = 28\,\mathrm{K}$, $\mathrm{Ra_{eff}} = 1.06 \times 10^7$. The maximum value of u_x at position $x_2(x_2') = -0.1\,\mathrm{m}$ is reached for the non-rotation mode $\mathrm{rot_{off}}$ at $\Delta T = 60\,\mathrm{K}$, $\mathrm{Ra_{eff}} = 3.06 \times 10^7$. In case of position $x_3(x_3') = -0.2\,\mathrm{m}$, the maximum value is reached for $\Delta T = 15\,\mathrm{K}$, $\mathrm{Ra_{eff}} = 1.06 \times 10^7$.

The highest value of the u_y-component in the non-rotation mode $\mathrm{rot_{off}}$ is reached at both positions for $\Delta T = 60\,\mathrm{K}$ and $\mathrm{Ra_{eff}} = 3.06 \times 10^7$, as it was expected due to the convection cell distribution. The significant decreasing values at both positions in case of the non-rotation mode $\mathrm{rot_{off}}$ and $\Delta T = 15\,\mathrm{K}$, $\mathrm{Ra_{eff}} = 1.06 \times 10^7$ are caused by the different convection cell distribution.

The values of the u_y-component reveal an increasing tendency, except of the visible low value for $\Delta T = 15\,\mathrm{K}$ and $\mathrm{Ra_{eff}} = 1.06 \times 10^7$. In the rotation mode $\mathrm{rot_{on}}$, the maximum velocity values lie beneath the ones of the non-rotation mode $\mathrm{rot_{off}}$. The highest values are reached for both positions in case of the component $u_{y'}$ and the highest effective Rayleigh number. The profile of $u_{y'}$ shows an increasing tendency. Both other components $u_{x'}$ and $u_{z'}$ are similar to each other. The highest values are reached for both components at both estimated x'-positions for $\Delta T = 28\,\mathrm{K}$, $\mathrm{Ra_{eff}} = 2.54 \times 10^7$.

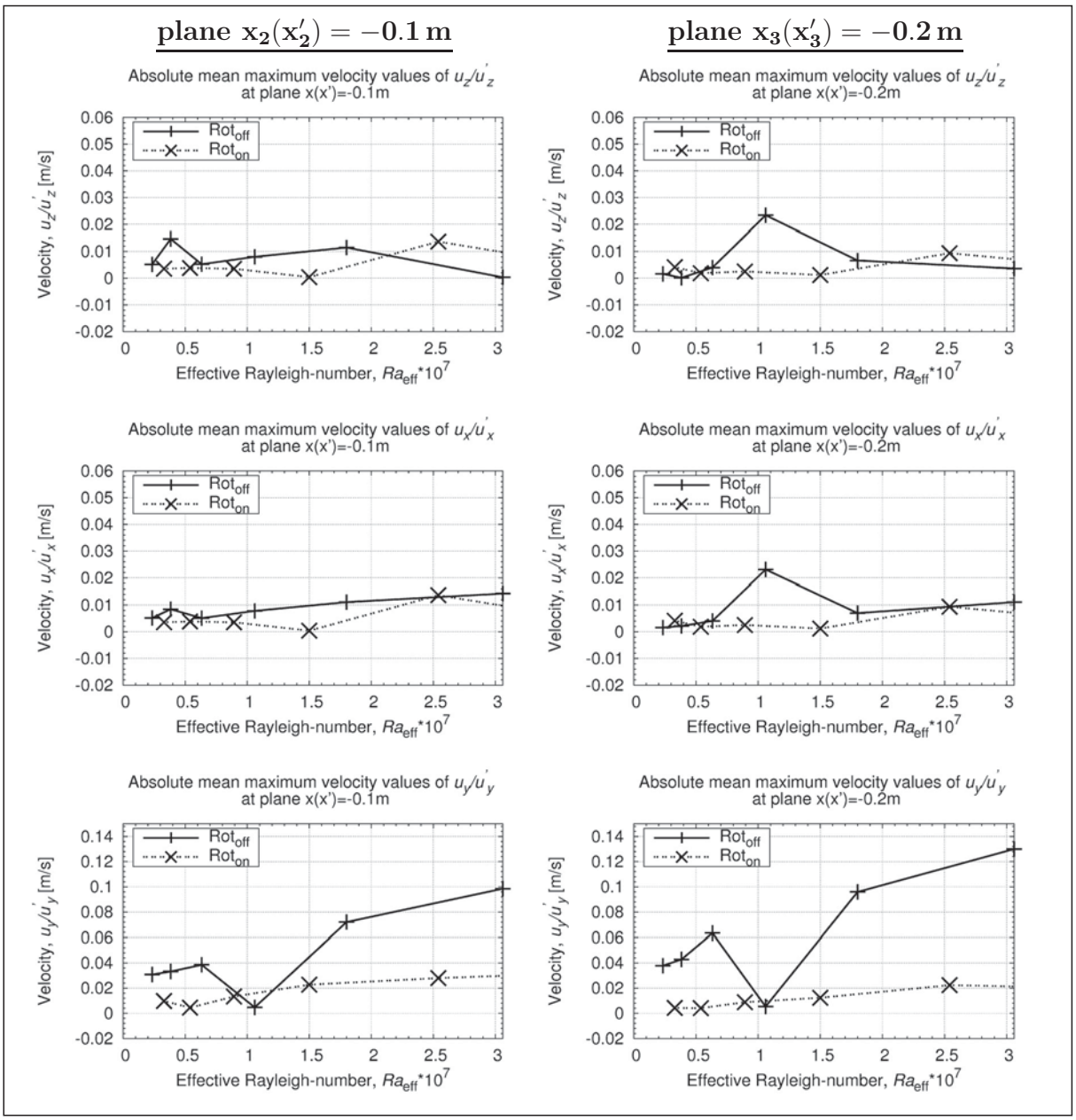

Figure 7.28.: Time-averaged absolute maximum velocities in relation to the effective Rayleigh number estimated at plane $x_2(x_2') = -0.1\,\mathrm{m}$ (left) and $x_3(x_3') = -0.2\,\mathrm{m}$ (right). $\mathrm{Pr} = 0.71$.**Top**: $u_{z(z')}$-component. **Middle**: $u_{x(x')}$-component. **Bottom**: $u_{y(y')}$-component. **In all pictures**: $+-+$ (black solid line with pluses): non-rotation mode $\mathrm{rot}_{\mathrm{off}}$, $\cdots+\cdots+$ (black dashed line with crosses): rotation mode $\mathrm{rot}_{\mathrm{on}}$.

7.6.2.3. Time-averaged profiles between the heated walls - temperature, density, velocity and Coriolis acceleration, estimated along the vertical $z(z')$-axis and different depth positions

Before the results of different fluid properties profiles between the heated walls are discussed, the distribution of the horizontal centrifugal acceleration component $a_{x'}$ is plotted in figure 7.29. It is estimated between the side walls of the test case along the horizontal x'-axis at $y' = 0\,\mathrm{m}$ and three different heights $z'_1 = -0.1\,\mathrm{m}$ (black dashed line), $z'_2 = 0\,\mathrm{m}$ (black solid line) and $z'_3 = 0.1\,\mathrm{m}$ (black dotted line).

The centrifugal acceleration is dependent on the radius $\boldsymbol{r}$ between the rotation axis and the position of the fluid particle as well as the angular velocity $\boldsymbol{\omega}$ (see also equation (7.4.19) in section 7.4.2 on page 219). Because the angular velocity $\boldsymbol{\omega}$ is constant in this case, a linear distribution is expected which varies only with the radius $\boldsymbol{r}$.

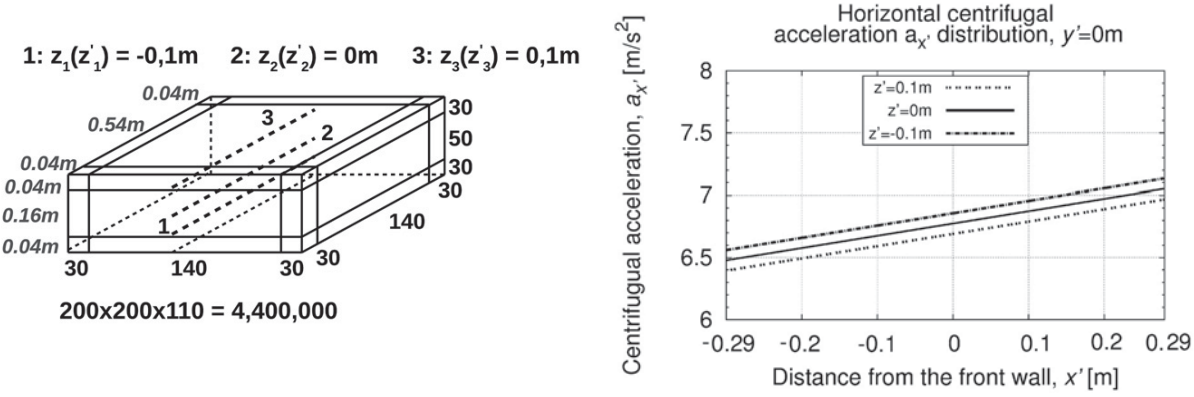

Figure 7.29.: Distribution of the time-averaged horizontal centrifugal acceleration component $a_{x'}$ between the side walls of the container, estimated along the x'-axis at different heights of the vertical z'-axis. **Left**: Estimation positions. **Right**: Results of the simulation.

Figures 7.32 - 7.37 on pages 246 - 252 present the time-averaged profiles of temperature T, velocity $\boldsymbol{u}$, density ρ and Coriolis acceleration components between the heated walls estimated along the $z(z')$-axis at $y(y') = 0\,\mathrm{m}$ at different depth $x(x')$-positions. The results are estimated in both modes in the simulation. They are time-averaged over an interval of $\Delta t = 200\,\mathrm{s} - 400\,\mathrm{s}$ in the simulated process. Note that the origin of both coordinate systems lies in the container centre.

The estimated positions are $x(x') = -0.2\,\mathrm{m}$ **-** (black solid line), $x(x') = -0.1\,\mathrm{m}$ (red solid line), $x(x') = 0\,\mathrm{m}$ (blue solid line), $x(x') = 0.1\,\mathrm{m}$ (black dashed line), $x(x') = 0.2\,\mathrm{m}$ (red dashed line), and $x(x') = 0.25\,\mathrm{m}$ (blue dashed line). Figure 7.30 gives a sketch of the locations of the evaluation positions in the container *CenCon*. Only the results of $\Delta T = 3\,\mathrm{K}$ and $\Delta T = 60\,\mathrm{K}$ are presented at this point for a better presentation. The results of the other cases can be found in the appendix A, section A.2.2.2, figures A.6 -

A.13 on pages 285 - 293. Due to a better presentation, the legend of the plots is presented separately in the below figure 7.31.

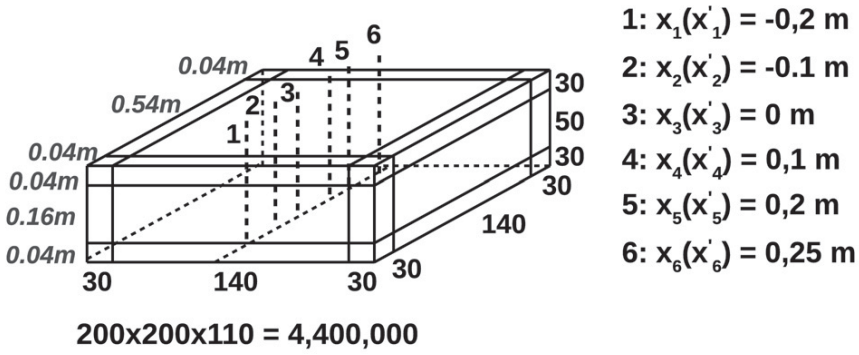

Figure 7.30.: Location of the estimation positions between the heated walls along the $z(z')$-axis at $y(y') = 0\,\mathrm{m}$.

Thermophysical properties - temperature and density

Note that the values of the properties components of the rotation mode $\mathrm{rot}_{\mathrm{on}}$ are related this time to the coordinate system in S'_R. Because the components of the estimated fluid properties were related to the coordinate system of S_I in the simulation software, the components had to be transformed component-by-component related to system S'_R according to equation (7.4.6) on page 216 in section 7.4.2, because the coordinate system in S'_R is rotated about the angle α relative to the coordinate system S_I.

As before in case *RayCon* in chapter 6, the temperature profiles of the non-rotation mode $\mathrm{rot}_{\mathrm{off}}$ reveal asymmetrical profiles, as it was expected, because the observed flow is also a NOB convection. In the non-rotation mode $\mathrm{rot}_{\mathrm{off}}$ all profiles lie very close to each other in the bulk region, except in the case of $\Delta T = 15\,\mathrm{K}$.

Each profile in the rotation mode $\mathrm{rot}_{\mathrm{on}}$ shows also an asymmetry which is this time even more distinctive. In comparison to the non-rotation mode $\mathrm{rot}_{\mathrm{off}}$, the bulk temperature is not constant, but shows a linear distribution along the container middle. The temperature distribution in the cell centre differs from the mean temperature T_{mean} and lies at some positions over the reached values of the non-rotation mode $\mathrm{rot}_{\mathrm{off}}$.

All profiles of the rotation mode $\mathrm{rot}_{\mathrm{on}}$ reveal differences along the container middle between the particular estimated positions. This aspect becomes more significant with higher temperature differences ΔT. It is noteworthy, that the profiles at $x(x') = -0.2\,\mathrm{m}$ (black line) reveal the smallest values in all cases of the rotation mode $\mathrm{rot}_{\mathrm{on}}$. This aspect could possibly be caused by the influence of the side wall at this position.

The profiles of the non-rotation mode $\mathrm{rot}_{\mathrm{off}}$ reveal steeper gradients at the heated walls and hence smaller boundary layers as in case of the rotation mode $\mathrm{rot}_{\mathrm{on}}$ for all chosen temperature differences. From $\Delta T = 15\,\mathrm{K}$ on, the gradients become steeper in the rotation

mode rot_{on} and the boundary layers decrease, but still not as steep as in the non-rotation mode. The density profiles are mirror-inverted to the temperature distributions, as it was expected due to the relation between both properties.

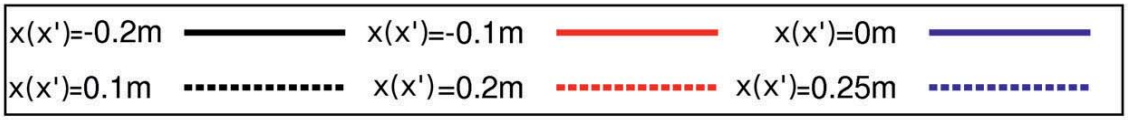

Figure 7.31.: Legend of the fluid properties profiles in figures 7.32 - 7.37.

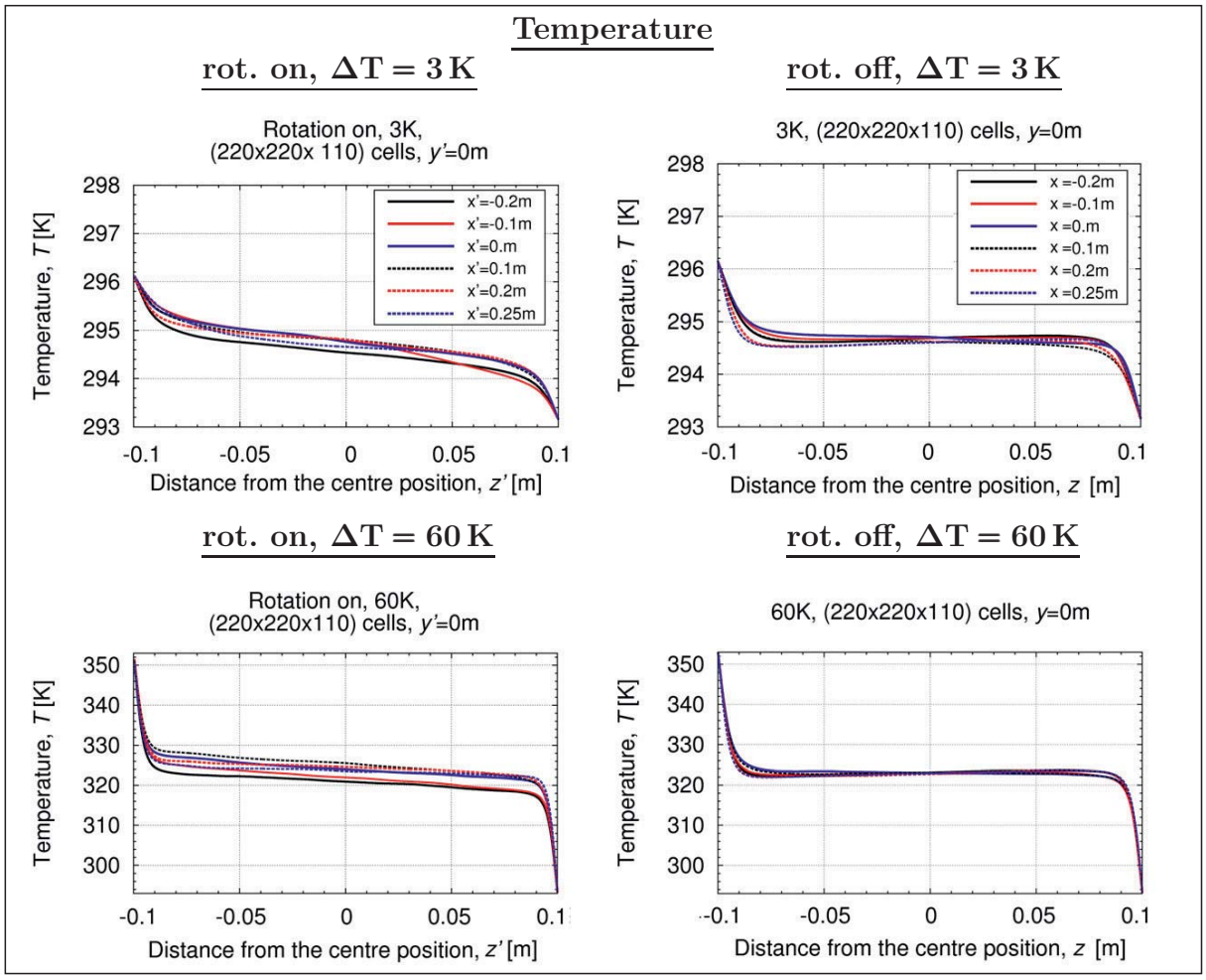

Figure 7.32.: Time-averaged temperature profiles. **Left:** Rotation mode rot_{on}. **Right:** Non-rotation mode rot_{off}. **Top row:** $\Delta T = 3\text{K}$. **Bottom row:** $\Delta T = 60\text{K}$. Estimated at $y(y') = 0\,\text{m}$ (centre position) along the vertical axis $z(z')$ at different positions: - (black solid line) $x(x') = -0.2\,\text{m}$, - (red solid line) $x(x') = -0.1\,\text{m}$, - (blue solid line) $x(x') = 0\,\text{m}$, -- (black dashed line) $x(x') = 0.1\,\text{m}$, -- (red dashed line) $x(x') = +0.2\,\text{m}$, -- (blue dashed line) $x(x') = 0.25\,\text{m}$.

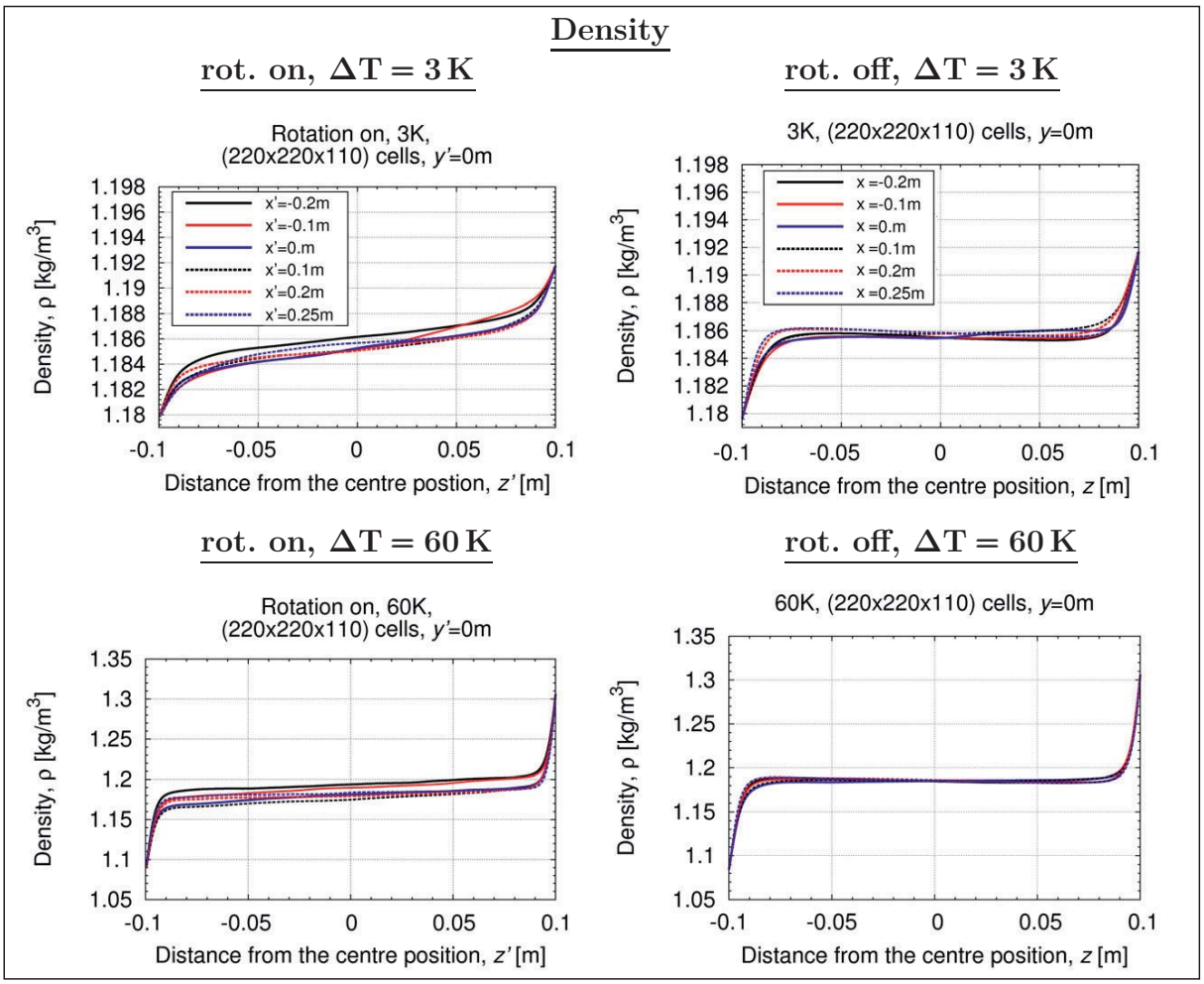

Figure 7.33.: Time-averaged density profiles. **Left:** Rotation mode $\mathrm{rot}_{\mathrm{on}}$. **Right:** Non-rotation mode $\mathrm{rot}_{\mathrm{off}}$. **Top row:** $\Delta T = 3\mathrm{K}$. **Bottom row:** $\Delta T = 60\mathrm{K}$. Estimated at $y(y') = 0\,\mathrm{m}$ (centre position) along the vertical axis $z(z')$ at different positions: - (black solid line) $x(x') = -0.2\,\mathrm{m}$, - (red solid line) $x(x') = -0.1\,\mathrm{m}$, - (blue solid line) $x(x') = 0\,\mathrm{m}$, - - (black dashed line) $x(x') = 0.1\,\mathrm{m}$, - - (red dashed line) $x(x') = +0.2\,\mathrm{m}$, - - (blue dashed line) $x(x') = 0.25\,\mathrm{m}$.

Velocity profiles

The velocity distributions are exhibit in figures 7.34 - 7.36 on pages 248 - 250. For the locations of the estimated positions see figure 7.30 on page 245 and the legend in the top of each following figure 7.34 - 7.36. Again, a small asymmetry can be seen in all profiles and both modes. Note that the values of the profiles in the rotation mode $\mathrm{rot}_{\mathrm{on}}$ are related to the coordinate system of S'_R. The components are transformed component-by-component to system S'_R according to equation (7.4.6) on page 216 in section 7.4.2. Only the results of case $\Delta T = 3\,\mathrm{K}$ and case $\Delta T = 60\,\mathrm{K}$ are presented at this point. The results of the other cases can be found in the appendix A, section A.2.2.2, figures A.9 - A.11 on pages 288 - 290. In the non-rotation mode $\mathrm{rot}_{\mathrm{off}}$, the vertical component u_z reflects well the convection cell structure from figure 7.19 on page 232. The highers values are reached for all depths positions at the centre position $z = 0\,\mathrm{m}$. For all cases the positions $x = 0\,\mathrm{m}$ (blue solid

line), $x = -0.1\,\mathrm{m}$ (red solid line) and $x = 0.1\,\mathrm{m}$ (black dashed line) reveal the highest values.

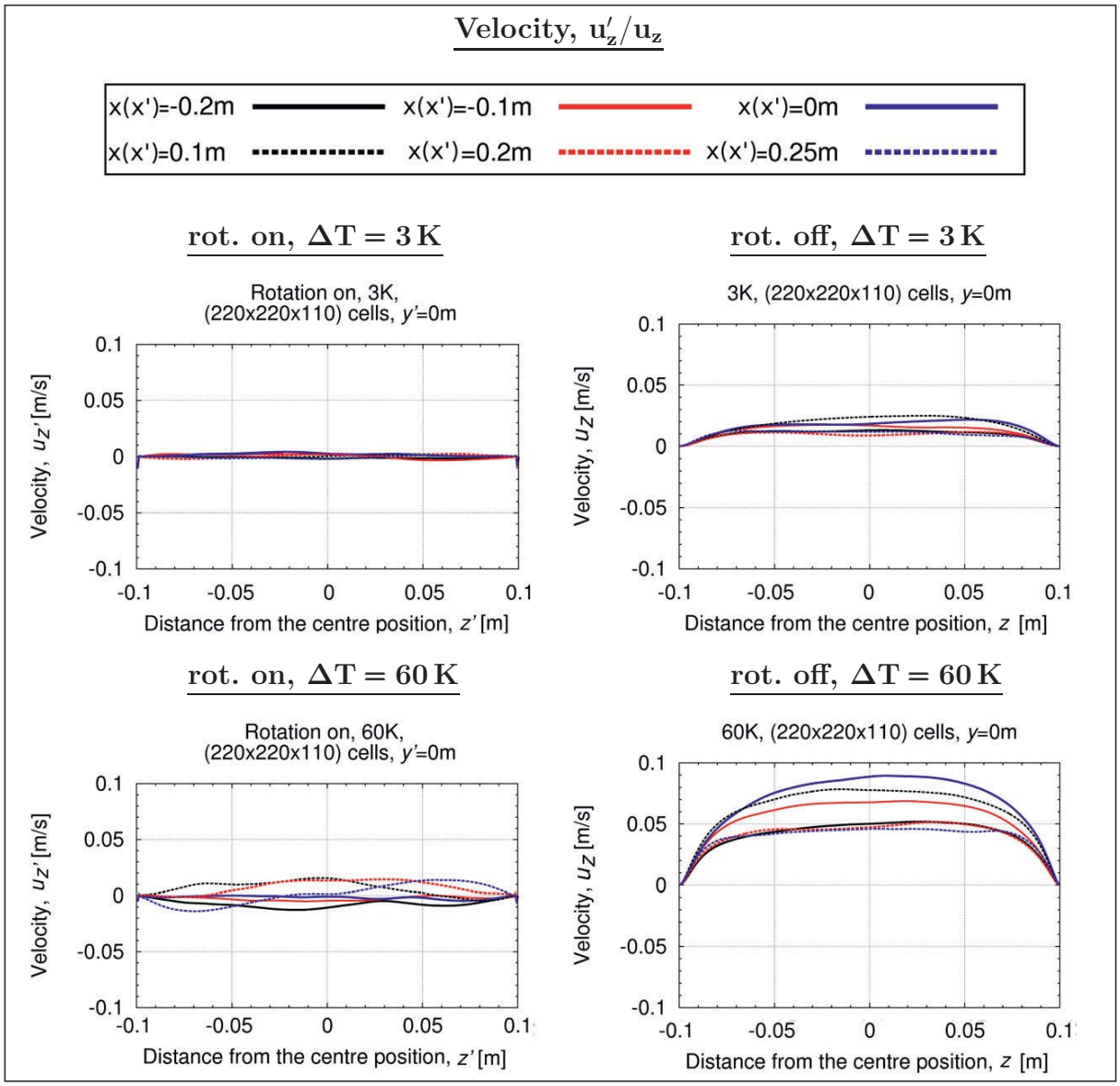

Figure 7.34.: Time-averaged profiles of the vertical velocity component u'_z/u_z. **Left:** Rotation mode $\mathrm{rot_{on}}$. **Right:** Non-rotation mode $\mathrm{rot_{off}}$. **Top row:** $\Delta T = 3\mathrm{K}$. **Bottom row:** $\Delta T = 60\mathrm{K}$. Estimated at $y(y') = 0\,\mathrm{m}$ (centre position) along the vertical z'-axis at different positions: - (black solid line) $x(x') = -0.2\,\mathrm{m}$, - (red solid line) $x(x') = -0.1\,\mathrm{m}$, - (blue solid line) $x(x') = 0\,\mathrm{m}$, - - (black dashed line) $x(x') = 0.1\,\mathrm{m}$, - - (red dashed line) $x(x') = +0.2\,\mathrm{m}$, - - (blue dashed line) $x(x') = 0.25\,\mathrm{m}$.

The only exception is the case of $\Delta T = 15\,\mathrm{K}$, there the highest values are reached for position $x = -0.1\,\mathrm{m}$ (red dashed line) and $x = 0.1\,\mathrm{m}$ (black solid line) due to the changed convection cell structure. The values of u_z are smaller at the outer x-positions, near to the side walls (see figure 7.34). The mentioned displacement of fluid particles which is caused by the Coriolis acceleration can clearly be seen in the vertical velocity u'_z profile in all cases.

Along the vertical z'-axis an up and down movement of air layers can be detected for each position in all profiles. Ascending hot air layers are displaced by descending cold layers. The movements can clearly be seen for higher ΔT. Due to the high velocity values of u'_z near the heated walls, also the profile of the Coriolis acceleration component $a_{Cy'}$ is high at these positions (see figure 7.37 on page 252). Hence, the flow particles are strongly displaced at these positions.

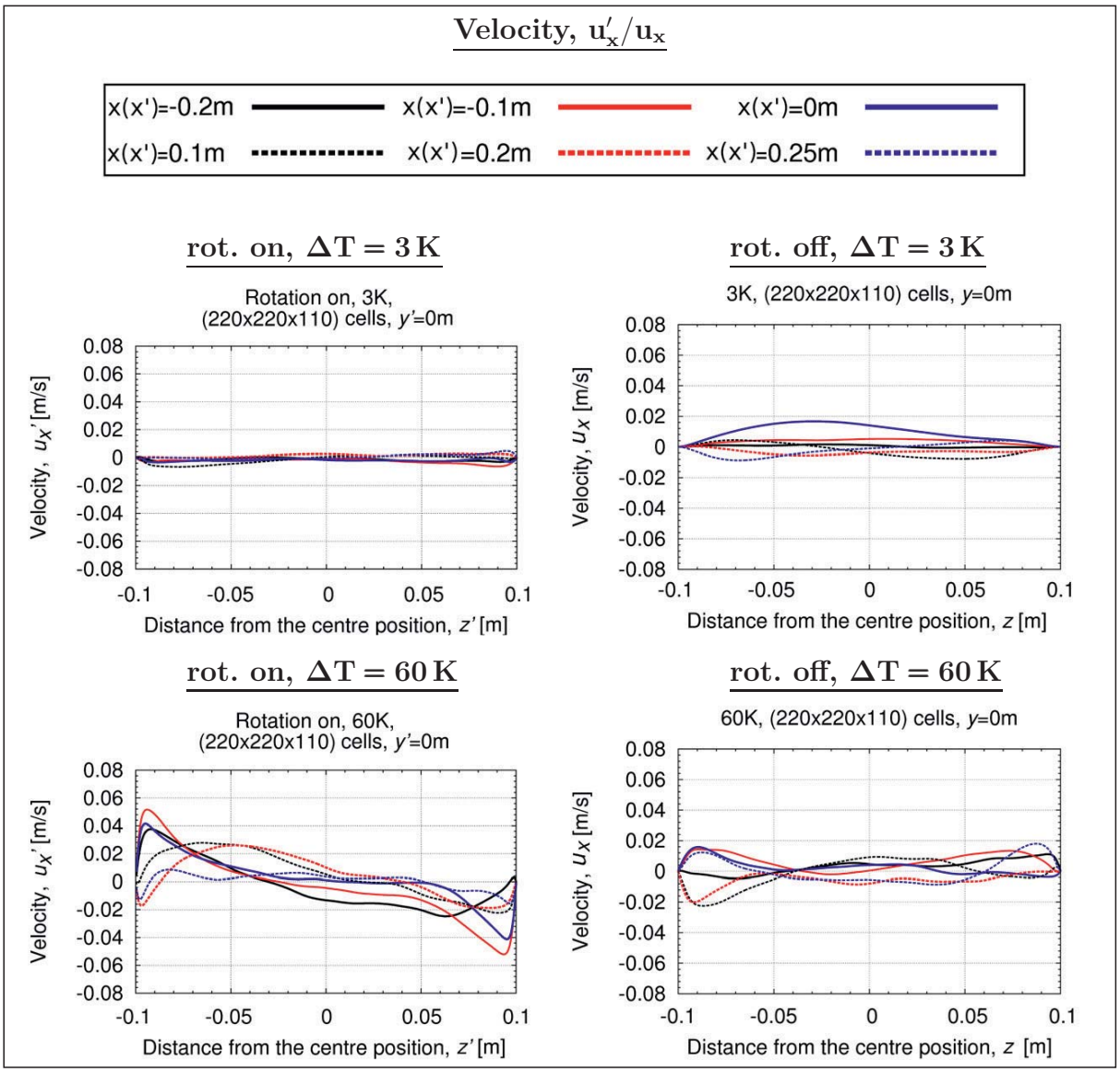

Figure 7.35.: Time-averaged profiles of the velocity component u'_x/u_x. **Left:** Rotation mode rot_{on}. **Right:** Non-rotation mode rot_{off}. **Top row:** ΔT = 3K. **Bottom row:** ΔT = 60K. Estimated at $y(y') = 0\,\text{m}$ (centre position) along the vertical z'-axis at different positions: **-** (black solid line) $x(x') = -0.2\,\text{m}$, **-** (red solid line) $x(x') = -0.1\,\text{m}$, **-** (blue solid line) $x(x') = 0\,\text{m}$, **- -** (black dashed line) $x(x') = 0.1\,\text{m}$, **- -** (red dashed line) $x(x') = +0.2\,\text{m}$, **- -** (blue dashed line) $x(x') = 0.25\,\text{m}$.

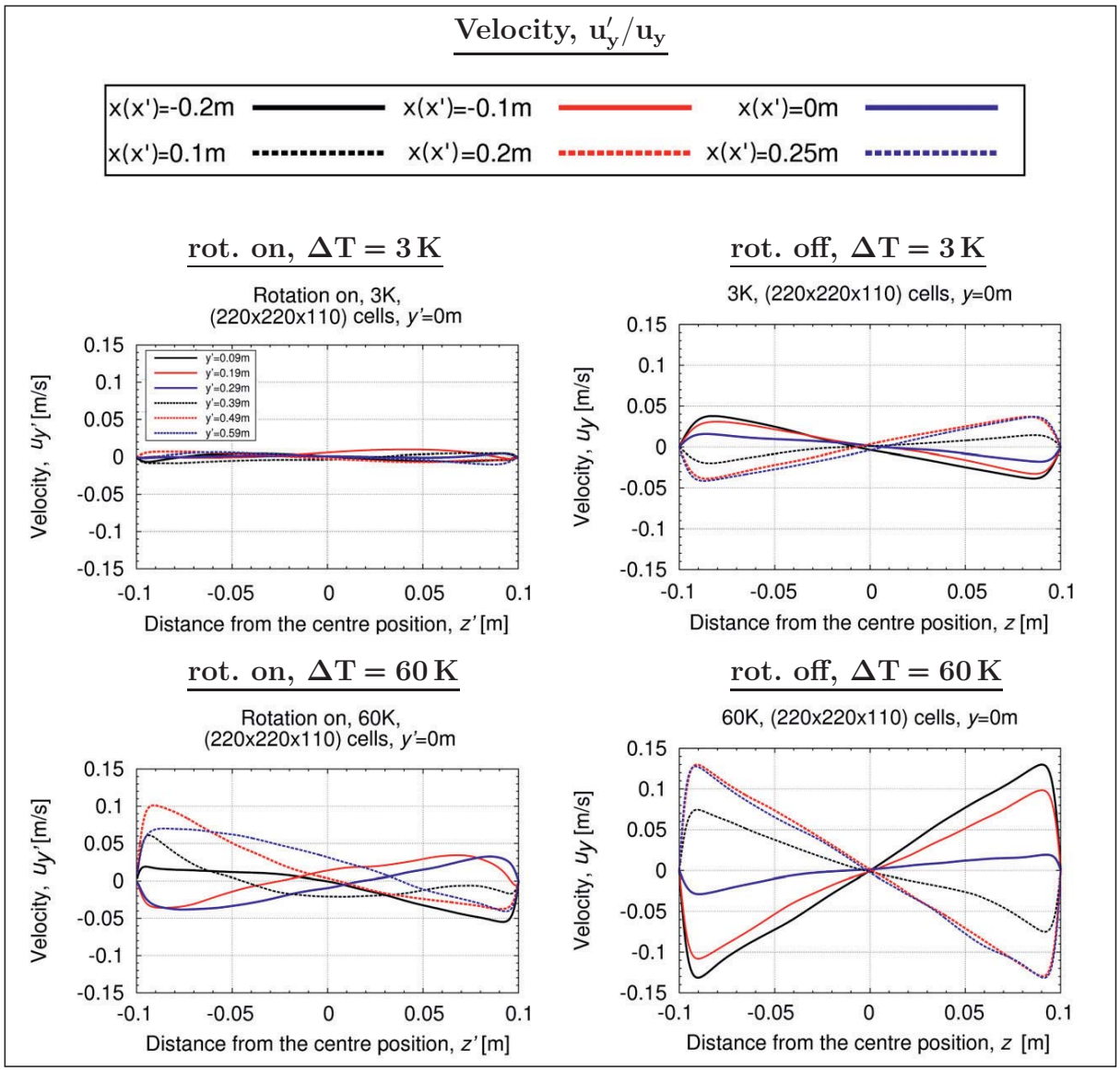

Figure 7.36.: Time-averaged profiles of the velocity component u'_y/u_y. **Left:** Rotation mode $\mathrm{rot_{on}}$. **Right:** Non-rotation mode $\mathrm{rot_{off}}$. **Top row:** $\Delta T = 3\mathrm{K}$. **Bottom row:** $\Delta T = 60\mathrm{K}$. Estimated at $y(y') = 0\,\mathrm{m}$ (centre position) along the vertical z'-axis at different positions: - (black solid line) $x(x') = -0.2\,\mathrm{m}$, - (red solid line) $x(x') = -0.1\,\mathrm{m}$, - (blue solid line) $x(x') = 0\,\mathrm{m}$, - - (black dashed line) $x(x') = 0.1\,\mathrm{m}$, - - (red dashed line) $x(x') = +0.2\,\mathrm{m}$, - - (blue dashed line) $x(x') = 0.25\,\mathrm{m}$.

The results of the horizontal velocity component u_x conform at all positions with the location of the four convection cells along the container midplane (s. figure 7.21 on page 233). Due to the arrangement of the four cells, only small values of the horizontal velocity component u_x are reached at the midplane $y = 0\,\mathrm{m}$ compared to both other velocity components. The obtained results at all x-positions lie close to each other for smaller temperature differences. The results show higher values close to the heated walls and close to the centre position for each ΔT-case. With higher ΔT, the reached peak values rise and the particular results differ more from each other (see also appendix A, section A.2.2.2, figures A.9 - A.11 on pages 288 - 290).

The results of the horizontal velocity component u_x and $\Delta T = 15\,\mathrm{K}$ differs from the other results due to the different arrangement of the convection cells. u'_x reflects the profiles of u'_y in all ΔT cases at all positions with lower peak values, as it was expected due to the symmetric layout of the container and the symmetric arrangement of convection cells. Thus, a similar displacement of the fluid can be detected in direction of the x'-axis (see figure 7.23 - 7.26 from page 236 on). High values are reached near the heated walls which increase with higher temperature differences. In the profiles of the second horizontal velocity component u_y one can clearly see the circulation direction of the four convection cells. High values are reached near the heated walls. Directly in the centre position this velocity component is zero. The profiles show positive or negative values depending on the circulation direction of the particular convection cell. The only exception is again case $\Delta T = 15\,\mathrm{K}$.

Likewise to the profiles of the other horizontal velocity component u'_x, the u'_y component reveals a similar structure in its profiles, but with slightly higher values. Like in the u'_x-profiles, high values are reached near the heated walls which increase with higher ΔT. But the results of the non-rotation mode $\mathrm{rot}_{\mathrm{off}}$ show higher peak values in each ΔT case. Compared to both other velocity components of both modes, u'_x/u_x and u'_z/u_z, the component u'_y/u_y has the highest values in the rotation mode $\mathrm{rot}_{\mathrm{on}}$, respectively non-rotation mode $\mathrm{rot}_{\mathrm{off}}$.

Coriolis acceleration profiles

Figure 7.37 on page 252 presents the time-averaged results of the Coriolis acceleration components estimated along the vertical z'-axis at the centre position $y' = 0\,\mathrm{m}$ and different depth x'-positions. For the locations of the estimated positions see figure 7.30 on page 245 and the legend in the top left plots in figure 7.37.

Note that the estimated values in the rotation mode $\mathrm{rot}_{\mathrm{on}}$ are related to the coordinate system of S'_R. The values of each component are transformed component-by-component to system S'_R according to equation (7.4.6) on page 216 in section 7.4.2. Only the results of $\Delta T = 3\,\mathrm{K}$ and $\Delta T = 60\,\mathrm{K}$ are presented at this point. The results of the other cases can be found in the appendix A, section A.2.2.2, figures A.12 - A.13 on pages 292 - 293.

According to equation (7.4.26) on page 220, the Coriolis force and also the Coriolis acceleration is dependent on the velocity vector $\boldsymbol{u}'_{S'_R}$ and the angle α which arises relative between the direction of the velocity vector and the direction of the angular velocity vector $\boldsymbol{\omega}$, thus the rotation axis. Due to the relative rotated coordinate system in S'_R, $a_{Cy'}$ and $a_{Cz'}$ show a different relative angle between their movement plane and the rotation axis in S_I.

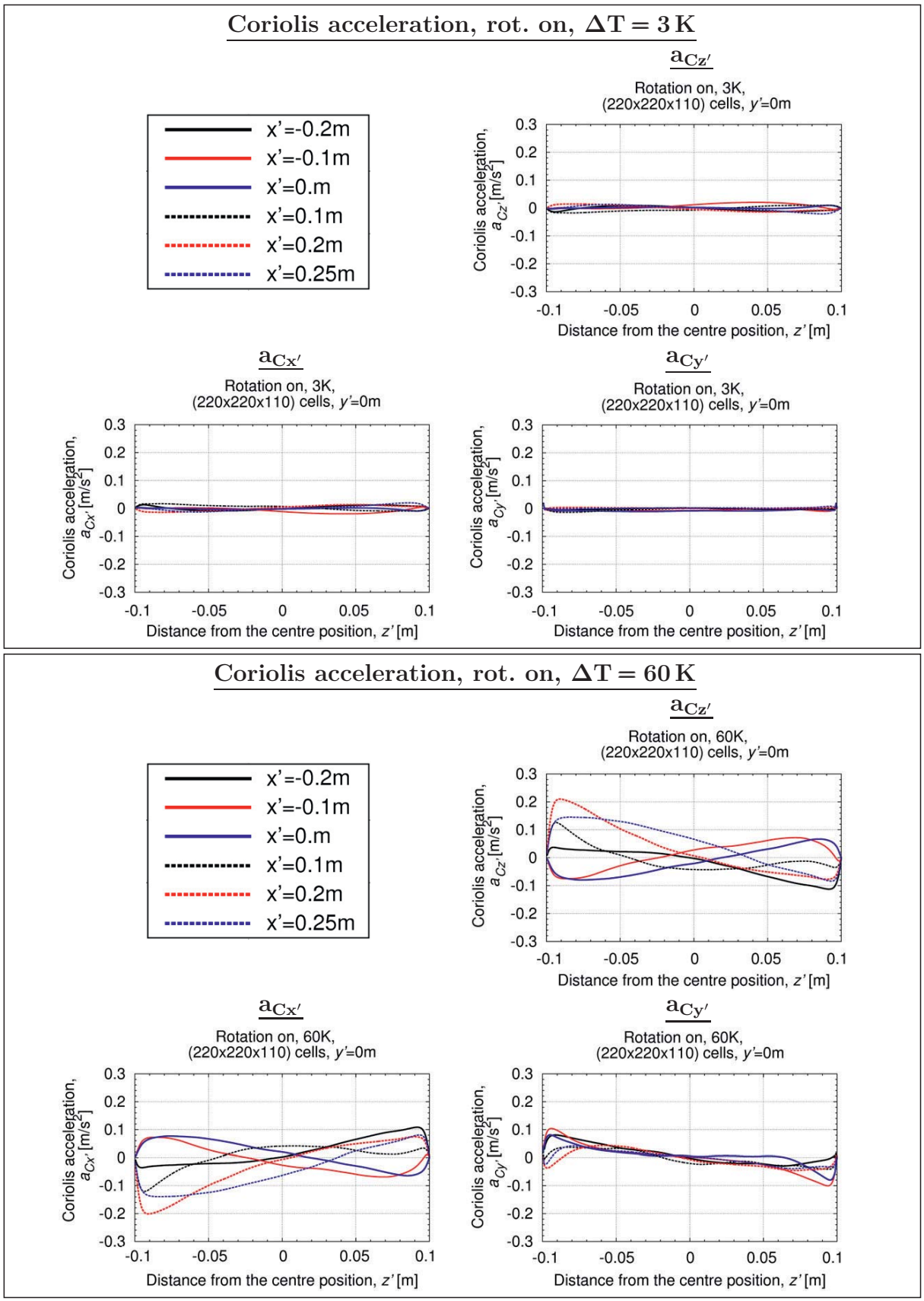

Figure 7.37.: Time-averaged profiles of the Coriolis acceleration components. **Top box:** $\Delta T = 3$K. **Bottom box:** $\Delta T = 60$K. Rotation mode $\mathrm{rot}_{\mathrm{on}}$. **Clockwise direction in each box, starting left top:** Legend, $a_{Cz'}$, $a_{Cx'}$ and $a_{Cy'}$. Estimated at $y' = 0\,\mathrm{m}$ (centre position) along the vertical z'-axis at different positions, see legends in the top left plots.

The profiles of the $a_{Cx'}$-component show higher values than the ones of the $a_{Cy'}$-component at most of the estimated locations, despite higher velocity values of u'_y. The $a_{Cy'}$ component has its peak values near the heated walls which increase with increasing ΔT.

The values of the $a_{Cz'}$-component resemble the ones of the $a_{Cx'}$-component with slightly higher values and a mirrored profile. Both components reveal the same relative angle between their movement plane and the rotation axis of the system (see also equation (7.4.6) on page 216 in section 7.4.2). The highest values can be observed for both components in the case of $\Delta T = 60\,\mathrm{K}$, thus in this case the flow particles are affected by the strongest displacement

7.7. Simulation results versus experimental data

Note that some of the following presented contents of the next sections 7.7.1 and 7.7.2 are also discussed in the study of [Zimmermann14b].

7.7.1. Experimental setup of the light-section and camera installation

To record the flow structures in the experiment with help of a camera, the fluid has to be visualised by tracer particles of magnesium carbonate (MgCO3) (s. section 7.1). The flow is monitored by the video camera in front of the container at position K (s. section 7.1, figure 7.7, page 207). The camera is fixed parallel to the longitudinal side of the container and rotates with it. The moving tracer particles are illuminated at different planes parallel to the camera by a movable light-section which is installed at the right sidewall of the container (s. figure 7.1 page 201 and figure 7.9 on page 208, section 7.1).

Note that it was not possible to obtain quantitative measured data from the experiment. Only visualised data could be obtained at this point of the study due to restricted financial circumstances of the project. Measured values of fluid properties inside the container may be a possible step in future works.

To obtain information of the whole flow profile in the experimental setup, different planes were observed by the camera intending a uniform distribution of the illuminated planes. The 2-dimensional velocity field is investigated at the several illuminated planes in the experiment as well as in the simulation. The velocity field in the simulation is estimated in the same regions as the experiment.

Because the influence of the walls play an important role in the turbulence production, the first plane, which should be observed, was chosen close to the side wall. The locations of the investigated planes are located at the positions: $x_1(x'_1) = 0\,\mathrm{m}$ (centre position),

$x_2(x_2') = -0.1\,\mathrm{m}$, $x_3(x_3') = -0.2\,\mathrm{m}$ and $x_4(x_4') = -0.25\,\mathrm{m}$ (in distance to the centre position $x(x') = 0\,\mathrm{m}$). Due to symmetry effects of the setup only one half of the container in $y(y')$-direction is recorded by the camera, as it is indicated in figure 7.38 (see also figure 7.9 on page 208 in section 7.1).

Unfortunately, an analyse of the videos revealed, that no sharp records were recorded of plane $x_1(x_1') = 0\,\mathrm{m}$ and plane $x_4(x_4') = -0.25\,\mathrm{m}$ during the experimental series. This aspect was caused by a fixed camera focus which could not be changed during one rotation mode period. In one period all planes had to be recorded due to restrictions in the centrifuge. In possible future works, the installation of the camera-light-section-combination has to be modified to solve this problem.

To evaluate the flow structures on the basis of the recorded videos, a Particle Image Velocimetry (PIV) is performed with help of the computing software MATLAB®Version R2011a. For further details to the used PIV algorithm it is referred to [Mori02]. The PIV method calculates the movement of one tracer particle on the basis of an inter-correlation function using its coordinates in two sequentially following pictures. The result is a 2-dimensional velocity vector which describes the movement of the observed tracer particle between both sequentially following pictures. Subsequently, the algorithm estimates the 2-dimensional velocity vectors of all tracer particles between both sequentially following pictures and subsequently in the whole sequence of pictures. The estimated regions in both methods are shown in figure 7.38 with help of a snapshot of the container inside.

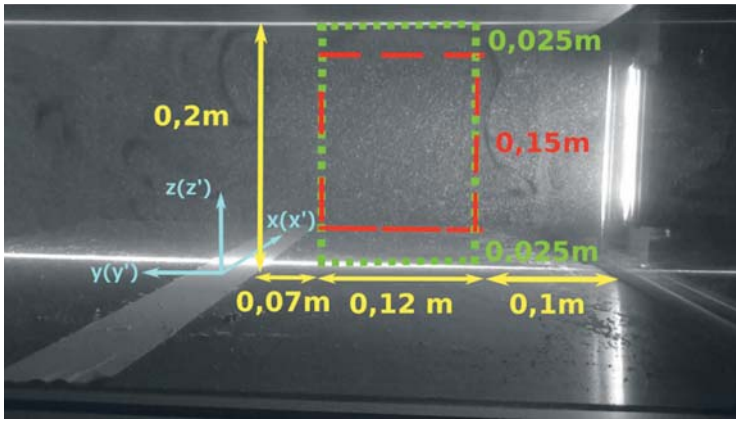

Figure 7.38.: Region of the estimated 2-dimensional velocity field in the experiment (PIV method) and in the simulation (as in [Zimmermann14b]). **Green dashed rectangle:** Estimated region in the simulation results. **Red dashed rectangle:** Estimated region in the experimental results.

Figure 7.38 illustrates the estimated region on basis of plane $x_2(x_2') = -0.1\,\mathrm{m}$. The green dashed rectangle marks the region which was estimated in the simulation results. The red dashed rectangle stands for the region which was estimated in the experimental results (PIV method). The tape, which is glued to the bottom hot wall in the experimental setup,

marks the middle of the container length. Note that the left- and right-side-border of the estimated region in the simulation data coincide with the side-boarders of the estimated region in the PIV method, as it is displayed in figure 7.38. But the top- and bottom-border of the estimated region in the simulation (green dashed rectangle) are higher than the top- and bottom-border of the estimated region in the experiment (red dashed rectangle).

The simulation results show the whole container height of 0.2 m between the top cold and bottom hot wall. Because the degree of image contrast varies strongly at the right side of the container (due to the light-slit-section), only a smaller region could be estimated with help of the PIV method. The estimated region in the simulation has a height of 0.2 m and a width of 0.12 m. In the experimental results the estimated region has a height of 0.15 m and a width of 0.12 m.

7.7.2. Visualisation of velocity structures in the simulation and in the experiment

In this section, the information of the 2-dimensional velocity field obtained at plane $x_2(x_2') = -0.1\,\mathrm{m}$ and $x_3(x_3') = -0.2\,\mathrm{m}$ are presented. The figures 7.39 - 7.42 on pages 256 - 259 display the results of the time-averaged velocity field. The results of the simulation are illustrated by time-averaged 2-dimensional direction vectors. The results of the PIV method show for all cases the same estimated region, as it was displayed in figure 7.38. Only the number of detected particles varies from case to case. Each entry in the 2-dimensional flow field stands for one mean velocity direction vector of one detected particle at the particular location. In some results, the PIV method detected more particles for the same estimated region than in case of others. Thus, one obtains in these cases a more "compact" velocity field distribution. It has to be regarded that only visualised data could be estimated with help of the PIV method. Unfortunately, it was not possible to obtain values of the velocity rate.

Each figure displays the simulation data versus the PIV results from the experimental data. At this point, only the results of $\Delta T = 3,\ 5,\ 28\,\mathrm{K}$ and $\Delta T = 60\,\mathrm{K}$ are displayed to emphasis the obtained conclusions. The results of the cases $\Delta T = 8.5,\ 15\,\mathrm{K}$ are placed in the appendix A.2.3.1 in figures A.14 - A.15 on pages 295 - 296. In each figure, four plots are displayed for each plane. In this way the results of both modes and both estimation types can be compared directly. The red coloured arrows in figures 7.39 - 7.42 (respectively, figures A.14 - A.15 in the appendix A.2.3.1) are added additionally in all results as visualisation additives to clarify the main flow directions. It is not expected, that the results of the simulation show the exact same flow structures as the experiment, because the estimation is only a statistical analysis of a turbulent flow. At each plane, the results show clearly that the simulation and the experiment reveal both similar flow structures.

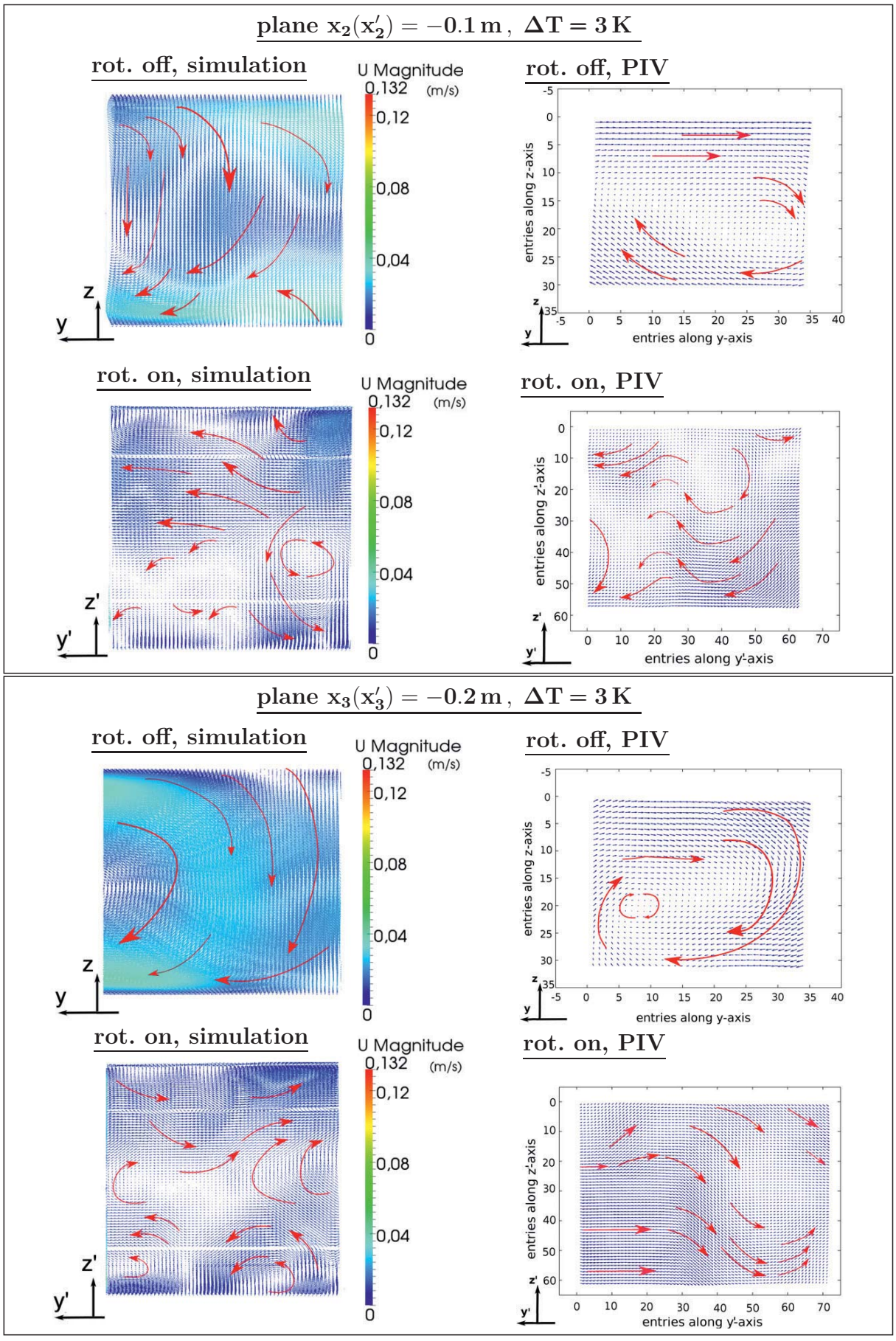

Figure 7.39.: Time-averaged 2-dim. velocity field. Simulation vs. experiment (PIV method). $\Delta T = 3\,\mathrm{K}$. **Top box:** Plane $x_2(x_2') = -0.1\,\mathrm{m}$. **Bottom box:** Plane $x_3(x_3') = -0.2\,\mathrm{m}$ (as in [Zimmermann14a]).

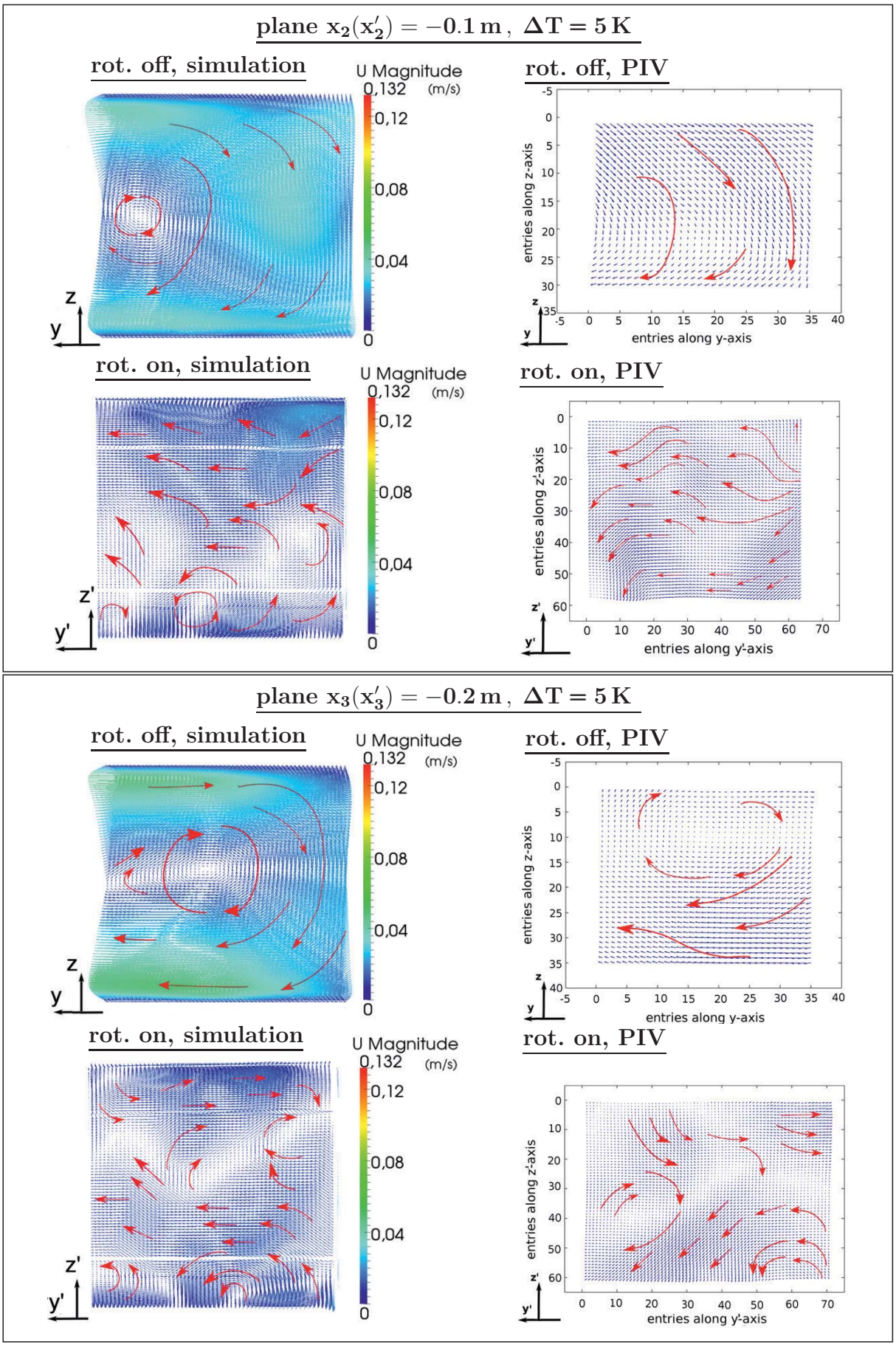

Figure 7.40.: Time-averaged 2-dim. velocity field. Simulation vs. experiment (PIV method). $\Delta T = 5\,\mathrm{K}$. **Top box:** Plane $x_2(x_2') = -0.1\,\mathrm{m}$. **Bottom box:** Plane $x_3(x_3') = -0.2\,\mathrm{m}$.

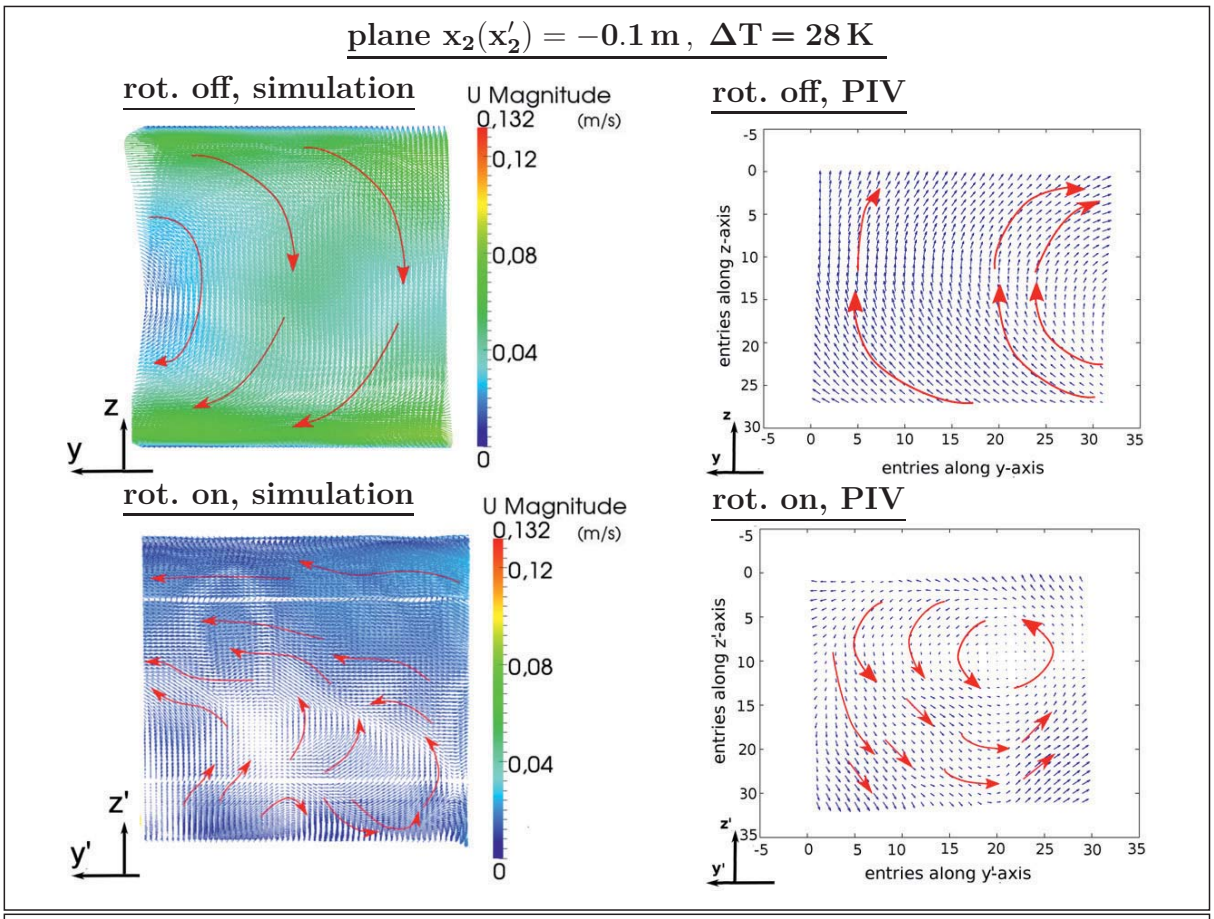

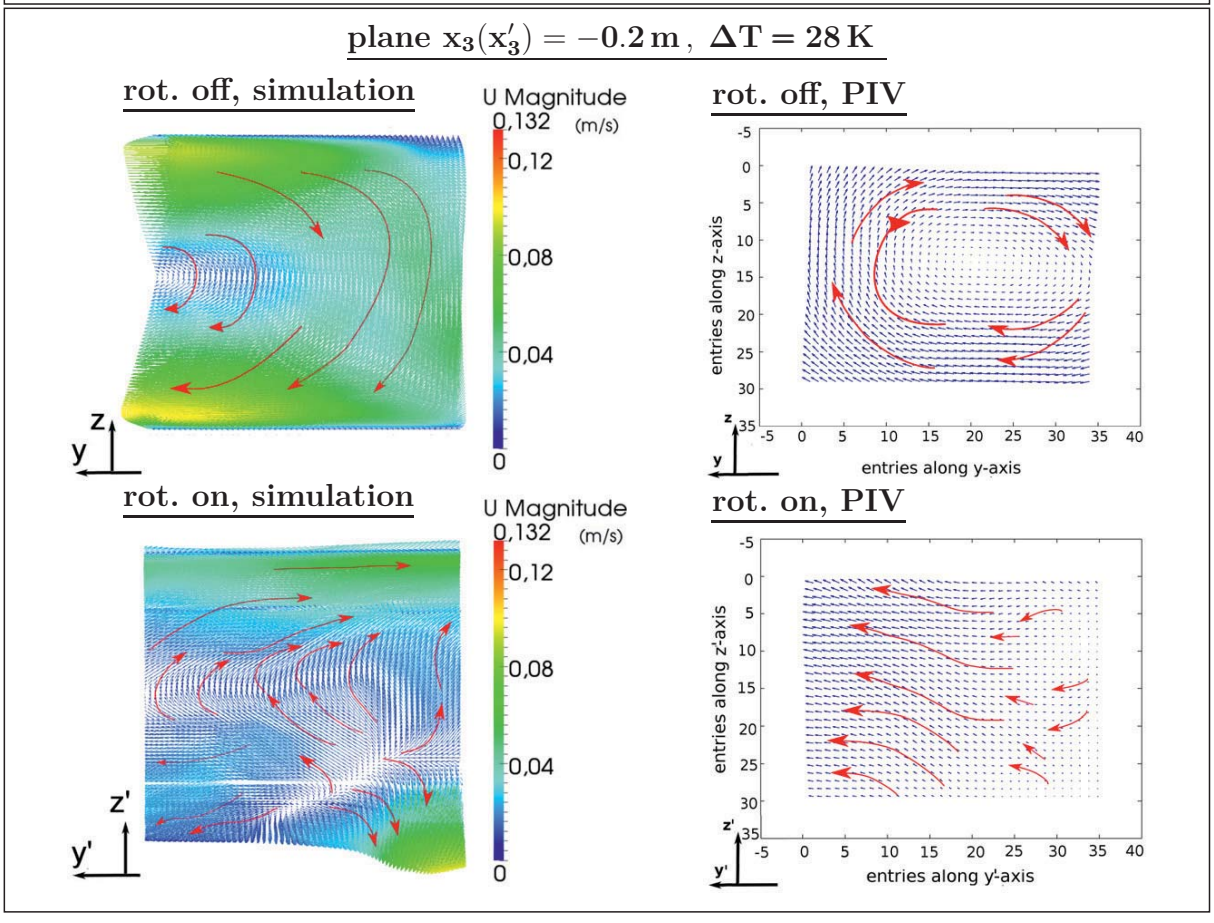

Figure 7.41.: Time-averaged 2-dim. velocity field. Simulation vs. experiment (PIV method). $\Delta T = 28\,\mathrm{K}$. **Top box:** Plane $x_2(x_2') = -0.1\,\mathrm{m}$. **Bottom box:** Plane $x_3(x_3') = -0.2\,\mathrm{m}$.

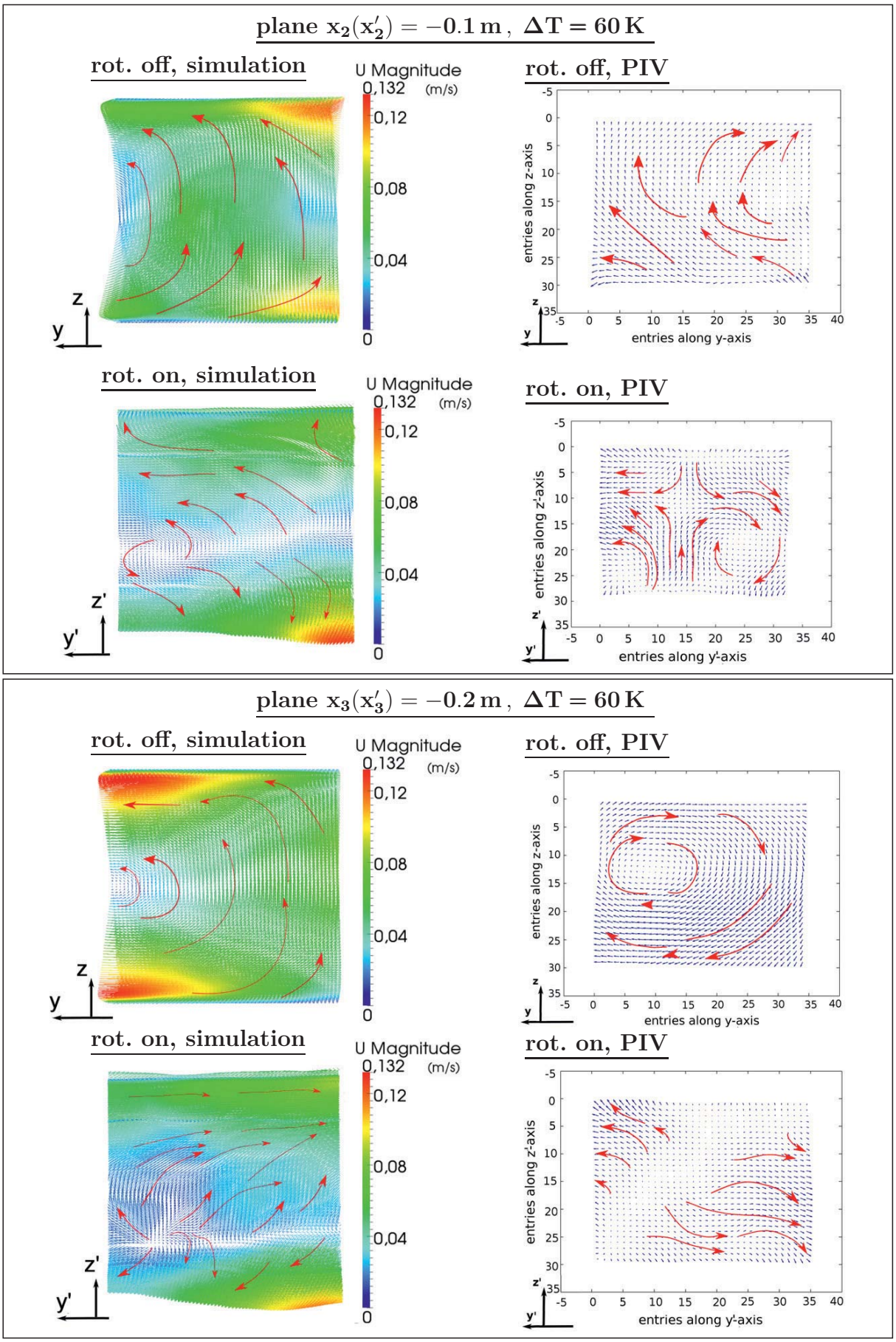

Figure 7.42.: Time-averaged 2-dim. velocity field. Simulation vs. experiment (PIV method). $\Delta T = 60\,\mathrm{K}$. **Top box:** Plane $x_2(x_2') = -0.1\,\mathrm{m}$. **Bottom box:** Plane $x_3(x_3') = -0.2\,\mathrm{m}$ (as in [Zimmermann14a]).

In the non-rotation mode $\mathrm{rot}_{\mathrm{off}}$ large scale structures, which are typical for a RB configuration, can be seen in both results in the same way. In the simulation and both rotation modes, it is visible, that the reached velocities at plane $x_3(x_3') = -0.2\,\mathrm{m}$ are higher than at plane $x_2(x_2') = -0.1\,\mathrm{m}$. This aspect could possibly be caused by the influence of the wall. The velocity magnitude is increasing with higher temperature differences ΔT.

In the non-rotation mode $\mathrm{rot}_{\mathrm{off}}$ large scale structures, which are typical for a RB configuration, can be seen in both results in the same way. In the simulation and both rotation modes, it is visible, that the reached velocities at plane $x_3(x_3') = -0.2\,\mathrm{m}$ are higher than at plane $x_2(x_2') = -0.1\,\mathrm{m}$. This aspect could possibly be caused by the influence of the wall. The velocity magnitude is increasing with higher temperature differences ΔT.

In the non-rotation mode $\mathrm{rot}_{\mathrm{off}}$ higher velocity values can be seen than in the rotation mode $\mathrm{rot}_{\mathrm{on}}$ until up to and including a temperature difference of $\Delta T = 28\,\mathrm{K}$. The flow structures at both planes seem to be similar to each other in the non-rotation, respectively rotation, mode. In the rotation mode $\mathrm{rot}_{\mathrm{on}}$, the increase of turbulent structures, which are caused by the Coriolis force, can clearly be seen in the simulation as in the PIV results for all ΔT-cases in the same way.

For smaller temperature differences $\Delta T = 3\,\mathrm{K}$, $\Delta T = 5\,\mathrm{K}$, (and hence small effective Rayleigh numbers $\mathrm{Ra}_{\mathrm{eff}}$) the turbulence production seems to be lower than in case of a higher ΔT, as $\Delta T = 28\,\mathrm{K}$ and $\Delta T = 60\,\mathrm{K}$. Smaller spatial scales of flow structures and smaller vortexes are the result in both last mentioned cases.

With higher temperature differences ΔT, the turbulent flow structures become smaller, due to the increasing effective Rayleigh number $\mathrm{Ra}_{\mathrm{eff}}$. This relation can be seen in both results in the same way. The turbulent structures seem also to be more irregular as in case of $\Delta T = 3\,\mathrm{K}$ or $\Delta T = 15\,\mathrm{K}$.

It is noteworthy, that the simulation results of $\Delta T = 3\,\mathrm{K}$, $\Delta T = 5\,\mathrm{K}$ display not only the same flow direction as in the PIV results, but show also similar flow structures and vortexes. However, these structures are not exact at the same positions, which was not expected. The results of case $\Delta T = 5\,\mathrm{K}$ at plane $x_2(x_2') = -0.1\,\mathrm{m}$ display in both studies similar velocity structures and flow directions (s. figure 7.40 on page 257).

7.7.3. Vortex regions estimated in the simulation

To analyse the turbulent structures and especially the observed vortex regions further, a criterion has to be found to identify these regions in the simulation.

Hunt et. al characterise these regions in [Hunt1988] by zones where the irrotational strain rate is smaller than the vorticity $\nabla \times \boldsymbol{u}$. This definition is restated in [Hossain12], where

Hossain et. al reformulate the above definition on the basis of a criterion Q which is specified by (in terms of the in this study used LES)

$$Q = \frac{1}{2}\left(\tilde{\Omega}_{ij}\tilde{\Omega}_{ij} - \tilde{S}_{ij}\tilde{S}_{ij}\right) = -\frac{1}{2}\frac{\partial \tilde{u}_i}{\partial x_j}\frac{\partial \tilde{u}_j}{\partial x_i} = \frac{1}{2}\left(\|\tilde{\boldsymbol{\Omega}}\|^2 - \|\tilde{\boldsymbol{S}}\|^2\right) > 0\,. \tag{7.7.1}$$

The unit of Q is

$$[Q] = \frac{1}{\mathrm{s}^2} = \mathrm{Hz}^2. \tag{7.7.2}$$

In equation (7.7.1) $\tilde{S}_{ij}$ is the filtered strain rate tensor

$$\tilde{S}_{ij} = \frac{1}{2}\left(\frac{\partial \tilde{u}_i}{\partial x_j} + \frac{\partial \tilde{u}_j}{\partial x_i}\right) \tag{7.7.3}$$

which is the symmetric part of the velocity gradient $\nabla\tilde{\boldsymbol{u}}$ (s. chapter 3, section 3.3.2). Ω_{ij} is the rotational tensor

$$\tilde{\Omega}_{ij} = \frac{1}{2}\left(\frac{\partial \tilde{u}_i}{\partial x_j} - \frac{\partial \tilde{u}_j}{\partial x_i}\right) \tag{7.7.4}$$

which is the antisymmetric part of the velocity gradient $\nabla\tilde{\boldsymbol{u}}$. The vortex regions can then be identified by zones, where the vorticity is greater than the strain rate tensor. Thus, the second invariant of the velocity gradient $\nabla\tilde{\boldsymbol{u}}$ and therefore criterion Q have to be positive in these zones according to [Hossain12].

The criterion Q is used in the following to detect and visualise the vortex regions in the simulation in the rotation and non-rotation mode. The criterion Q is only a measurement for the outcome of turbulent structures and not for their cause. The generated vortex structures are illustrated in figure 7.43 on page 262 for the cases of $\Delta T = 3\,\mathrm{K}$ and $\Delta T = 60\,\mathrm{K}$. The snapshots in figure 7.43 show the instantaneous iso-surfaces of criterion Q in the last time step of the simulated process at $t = 400\,\mathrm{s}$ for both modes.

The iso-surfaces envelope the regions where Q reaches a particular value. Each snapshot shows the iso-surfaces inside one half of the container. In the appendix A.2.3.2, the results of the other ΔT-cases and different values of criterion Q can be found in the figures A.16 - A.17, from page 297 on. The number of vortex regions is significantly raising with increasing ΔT and increasing effective Rayleigh numbers for both modes.

This aspect was also visible in the case of the 2-dimensional velocity profiles (see figures 7.39 -7.42 on pages 256 - 259). In both modes different frequencies appear. The form of the vortex structures in the rotation mode $\mathrm{rot}_{\mathrm{on}}$ differ from the ones in the non-rotation mode $\mathrm{rot}_{\mathrm{off}}$. They seem to be more compact and mixed up than in case of the non-rotation mode $\mathrm{rot}_{\mathrm{off}}$. They show also a more irregular structure. The structures in the non-rotation mode $\mathrm{rot}_{\mathrm{off}}$ seem to be more smooth. They reveal also larger spatial scales as the ones in the rotation mode $\mathrm{rot}_{\mathrm{on}}$. The vortex structures seemed to be smaller with increasing effective Rayleigh numbers in the rotation mode.

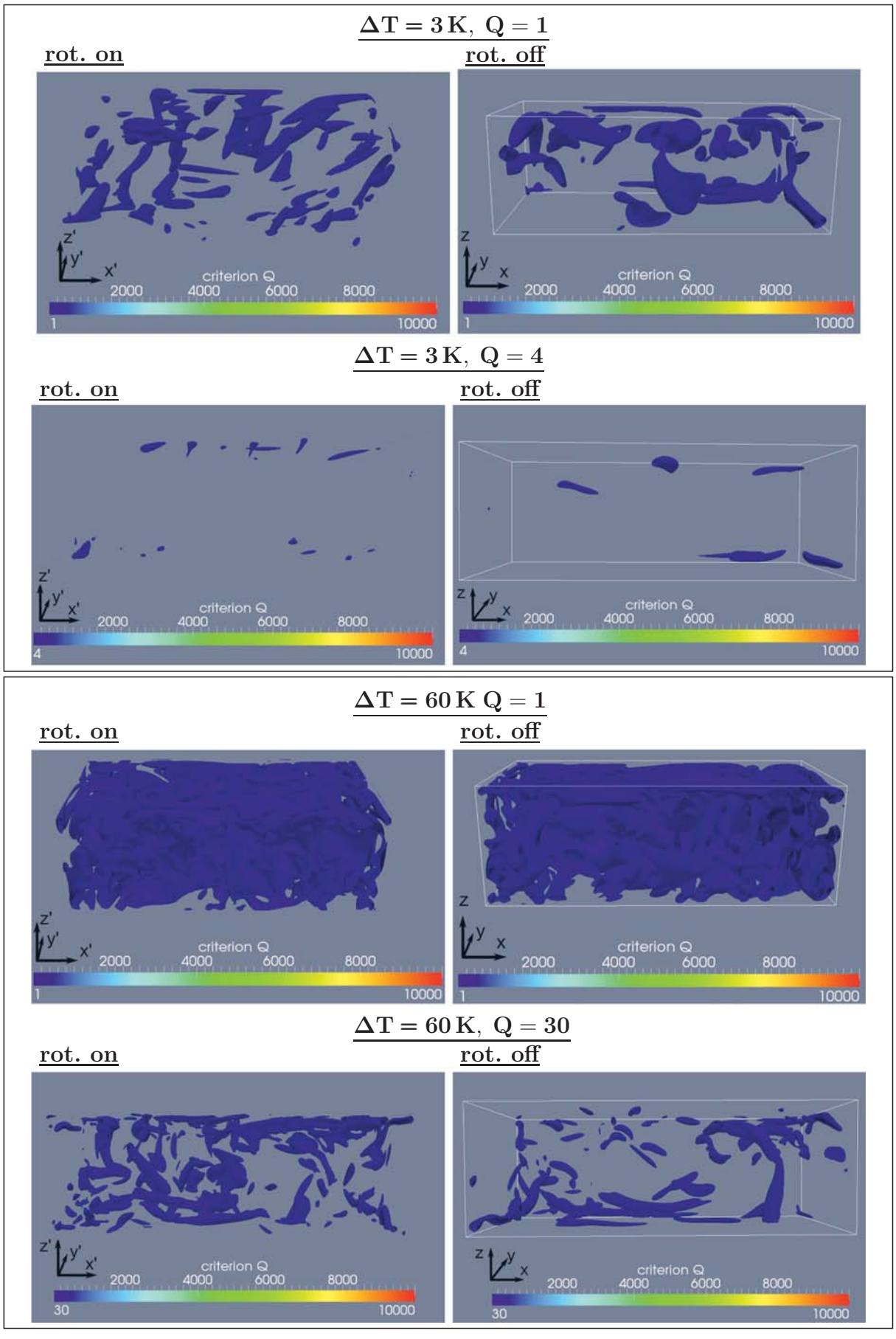

Figure 7.43.: Instantaneous vortex structures in the simulation (iso-surfaces of criterion Q), $t = 400\,\mathrm{s}$, rotation mode $\mathrm{rot_{on}}$ (left), non-rotation mode $\mathrm{rot_{off}}$ (right). $Q = 1$, $Q = 4$ and $Q = 30$. **Top box:** $\Delta T = 3\,\mathrm{K}$. **Bottom box:** $\Delta T = 60\,\mathrm{K}$.

The vortex structures in the rotation mode $\mathrm{rot_{on}}$ reveal a significant drift pointing in direction of the x' axis which is distinctive for smaller effective Rayleigh numbers and can be clearly seen in figure 7.43. This drift is caused by the rotational movement of the test case. The structures are axially aligned to the rotation axis of the centrifuge. With an increasing Rayleigh number this drift is superposed by an increasing turbulence production inside the container.

Relation between criterion Q and the effective Rayleigh-number

The number of vortex regions is rising with an increasing temperature difference ΔT in both modes. Further, higher values of Q are reached for higher ΔT. Table 7.8 lists the positive maximum values of Q which were reached in one half of the container. Additionally, the maximum values of Q are listed which were reached in the whole container setup.

$\boldsymbol{\Delta T}$ [K]	**eff. Ra**	$\boldsymbol{Q_{max}}$ [1/s^2] half of the setup	$\boldsymbol{Q_{max}}$ [1/s^2] whole setup
$\mathrm{rot_{on}}$, 1 K	1.11×10^6	1	1
$\mathrm{rot_{off}}$, 1 K	7.89×10^5	3	3.29
$\mathrm{rot_{on}}$, 3 K	3.29×10^6	17	134.073
$\mathrm{rot_{off}}$, 3 K	2.33×10^6	10	16.980
$\mathrm{rot_{on}}$, 5 K	5.39×10^6	30	135.36
$\mathrm{rot_{off}}$, 5 K	3.83×10^6	30	21.734
$\mathrm{rot_{on}}$, 8.5 K	8.93×10^6	70	134.465
$\mathrm{rot_{off}}$, 8.5 K	6.33×10^6	40	40.223
$\mathrm{rot_{on}}$, 15 K	1.50×10^7	100	133.649
$\mathrm{rot_{off}}$, 15 K	1.06×10^7	48	49.038
$\mathrm{rot_{on}}$, 28 K	2.54×10^7	520	512.654
$\mathrm{rot_{off}}$, 28 K	1.80×10^7	340	354.935
$\mathrm{rot_{on}}$, 60 K	4.32×10^7	580	613.506
$\mathrm{rot_{off}}$, 60 K	3.06×10^7	650	654.5

Table 7.8.: Positive maximum values of criterion Q, estimated in the simulated process at $t = 400\,\mathrm{s}$. Non-rotation mode $\mathrm{rot_{off}}$ and rotation mode $\mathrm{rot_{on}}$. Estimated in one half of the container setup (s. figure 7.43 on page 262 (respectively figures A.16 - A.17 in the appendix A, A.2.3.2, on page 297 - 298)) and in the whole container setup of *CenCon*.

The dependence between the maximum values of Q from table 7.8 and the realised effective Rayleigh numbers is plotted in figure 7.44 for a Prandtl number of $\mathrm{Pr} = 0.71$. The values which were reached in the rotation mode $\mathrm{rot_{on}}$ are plotted by the black dashed line with

pluses. The values which were reached in the non-rotation mode $\mathrm{rot_{off}}$ are plotted by the black solid line with crosses. For smaller effective Rayleigh numbers, higher frequencies appear in the rotation mode $\mathrm{rot_{on}}$ than in the non-rotation mode $\mathrm{rot_{off}}$. This relation is inverted beyond a Rayleigh number of $\mathrm{Ra_{eff}} = 1.5 \times 10^7$. Then, higher frequencies appear in the non-rotation mode $\mathrm{rot_{off}}$.

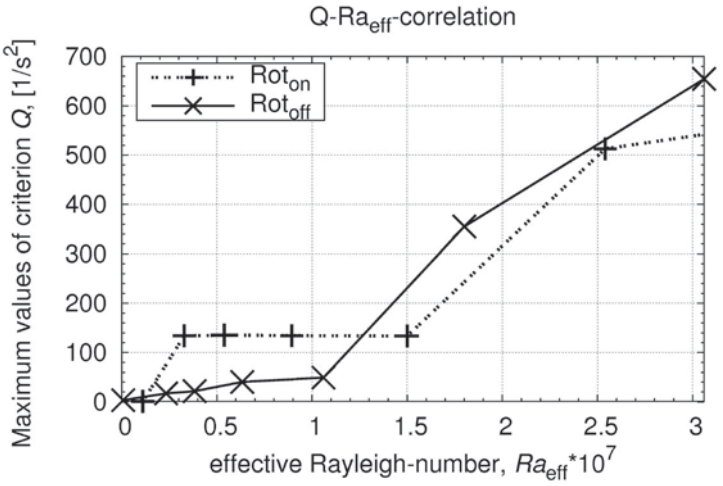

Figure 7.44.: Relation between the positive maximum values of criterion Q (estimated in the whole setup) and the effective Rayleigh number, $t = 400\,\mathrm{s}$. $\mathrm{Pr} = 0.71$. $\cdots+\cdots+$ (black dashed line with pluses): rotation mode $\mathrm{rot_{on}}$, $\times - \times$ (black solid line with crosses): non-rotation mode $\mathrm{rot_{off}}$. Results of the simulation.

7.8. Concluding comments

In this section, a non-Boussinesq, compressible LES was performed for a RB convection inside an air-filled enclosed container where both horizontal walls were heated isothermally. In contrast to the previously presented study of *RayCon*, this setup performed additionally a uniform-rotational movement in a large-scale centrifuge to investigate a possible influence of Coriolis accelerations on the development of flow structures inside the test cell.

Besides a numerical study, also an experimental study was performed. The realised effective Rayleigh numbers lied between $2.33 \times 10^6 \leq \mathrm{Ra} \leq 4.32 \times 10^7$ with a Prandtl number of $\mathrm{Pr} = 0.71$. To investigate the influence of the mentioned Coriolis acceleration on the fluid two different modes were analysed in both studies, a rotation mode and a non-rotation mode. The following aspects were discussed and described in this chapter

1) construction and realisation of an applicable experimental setup,

2) modification and implementation of the governing equations describing the rotating system of *CenCon*,

3) construction and implementation of an equivalent simulation geometry,

4) location of the existing convection cells in the simulation visualised by the mean velocity distribution in the test cell,

5) relation between Nusselt number, temperature gradient, heat flux density and the realised effective Rayleigh numbers for Pr = 0.71, estimated at constant planes parallel to the heated walls, simulation results,

6) estimation of Nusselt number, temperature, density, velocity and Coriolis acceleration profiles between the heated walls, estimated along the vertical axis, simulation results,

7) visualisation of velocity structures in the simulated process and the experiment (PIV method), comparison of both results,

8) investigation of vortex regions in the simulated process.

The coherent structures in the numerical study showed well the influence of the Coriolis acceleration and a resulting displacement of the fluid particles, as it was expected according to theoretical reasoning for the observed angular velocity of this study and the resulting deflection angle between the container axis and the rotation axis of the centrifuge. This displacement and its influence could also be seen significantly in the estimated profiles of the analysed fluid properties.

In the numerical study of [Horn11] slightly increased Nusselt number values were observed in a rotating RB convection cell compared to a non-rotating cell for non-Boussinesq fluids. In the performed simulations of this thesis increased Nusselt number values could not be determined in the rotation mode $\mathrm{rot_{on}}$. The Nusselt number values were smaller and converged with higher effective Rayleigh numbers $\mathrm{Ra_{eff}}$ to the results of the non-rotation mode $\mathrm{rot_{off}}$. Further, the temperature gradients diverged from the gradients of the non-rotation mode $\mathrm{rot_{off}}$. This aspect became more significant with higher effective Rayleigh numbers $\mathrm{Ra_{eff}}$.

The turbulence production was indeed higher in the rotation mode $\mathrm{rot_{on}}$ due to the Coriolis force, but the produced turbulent structures were also smaller and more irregular. Therefore, the heat flux inside the container had not to be necessarily higher than in the non-rotation mode $\mathrm{rot_{off}}$.

From the experimental setup only visualised data of the flow structures inside the container could be gained. Unfortunately, no measured data of any fluid property could be gained inside the container in the experimental study due to restricted financial circumstances of the project. A comparison between simulation and experimental results of the 2-dimensional velocity field revealed similar tendencies of flow structures and vortexes.

Further, both studies showed large scale structures in the non-rotation mode $\mathrm{rot}_{\mathrm{off}}$ as they are typical for a RB configuration. The increase of turbulent structures which were caused by the Coriolis force in the rotation mode $\mathrm{rot}_{\mathrm{on}}$ could be seen in the same way in the simulation as well as in the experiment. With increasing temperature differences ΔT, and hence increasing effective Rayleigh numbers $\mathrm{Ra}_{\mathrm{eff}}$, the turbulent structures seemed to be smaller and the number of appearing vortexes grew in both studies. The identification of vortex regions in the simulation showed an increasing number of vortexes with a rising ΔT, in the non-rotation mode $\mathrm{rot}_{\mathrm{off}}$ as well as in the rotation mode $\mathrm{rot}_{\mathrm{on}}$. Moreover, with higher ΔT, higher values of the identification criterion Q were reached in both modes. Smaller frequencies appeared in the rotation mode than in the non-rotation mode.

The Coriolis acceleration produced structures which were more irregular and mixed up compared to the ones in the non-rotation mode. The turbulent structures in the rotation mode seemed to become smaller with higher effective Rayleigh numbers. The vortex structures were axially aligned to the rotation axis of the centrifuge which could be seen by a drift of these structures to one side of the container, especially in case of smaller effective Rayleigh numbers.

Summarising, the compressible, non-Boussinesq Large-Eddy simulation was applicable to model a RB convection in the presented setup of *CenCon* with and without a rotational movement of the setup. The experimental setup operated correctly in both modes and a fully-turbulent convective flow could be generated inside the container. The obtained simulation results of the 2-dimensional velocity field approximated well the results of the experimental study and conformed to related theoretical assumptions. These assumptions were also confirmed by the investigated fluid properties profiles in the simulation.

8. Summary and conclusions

This thesis dealt with the numerical and in one case also experimental analysis of turbulent natural convection in air inside different configured test case setups. The numerical studies were performed by a compressible, non-Boussinesq Large-Eddy Simulation (LES) considering a Sutherland-model. “Compressible” referred in this case to density changes in the fluid caused by temperature differences and not a definition in terms of the Mach number.

The first part of this thesis outlined the required theory to describe a natural convection and to formulate the resulting system of governing equations. Furthermore, the required computational methods (especially the numerical method of a LES) were presented which were used to solve the before stated governing equations. In the second part of this thesis, which was also the main part, the investigated test cases were presented in detail and the obtained results were discussed. The main focus of all numerical studies lied on the fluid properties profiles estimated between the heated walls. It was important to discuss especially the profiles in the near wall region to understand the structure and dynamic of the whole flow.

The flows were investigated in three different test case configurations which consisted in each case of an enclosed, air-filled, rectangular container. All three test cases were based upon each other. The setups varied in the choice of the two isothermally heated walls and their aspect ratios. The orientation of these walls relative to the effective direction of gravity effected significantly the profile of the main flow field. To reduce a dispensable complexity of the setups, the container properties were chosen simplified in each case. Nevertheless, the setups were still sufficient and commonly used regarding the fundamental investigations of a turbulent natural convection.

Because in the test case of *VerCon* two of the vertical walls were the heated, a quasi-steady state flow was reached in the fluid inside the container. This configuration of a turbulent natural convection represented the basis for both other test cases. After the information of test case *VerCon* were gained and the performed LES was validated, the information and the numerical model were used to study both other test cases.

RayCon based directly on *VerCon* with its by 90° rotated heated walls. *CenCon* and *RayCon* were both build as a Rayleigh-Bénard (RB) problem. In contrast to *RayCon*, a rotational movement was impressed on the setup of *CenCon*, which generated Coriolis

accelerations effecting the fluid inside the container. Regarding the non-rotating state, *CenCon* based directly on *RayCon* regarding its its flow dynamic as well as its fluid properties. Therefore, it was essential to analyse and to understand first the flow dynamic and fluid properties profiles of *RayCon*, before *CenCon* was analysed as the last step of this thesis.

Test case VerCon

In the first test case, *VerCon*, a convection cell in form of a rectangular, air-filled container was investigated numerically. Two of the vertical walls were isothermally heated with a constant temperature difference between both walls. The container had aspect ratios of $\Gamma_x = \frac{L}{H} = 1$, $\Gamma_z = \frac{D}{L} = 2$. The realised Rayleigh number lied at $\mathrm{Ra} = 1.58 \times 10^9$ and the Prandtl number at $\mathrm{Pr} = 0.71$. Lateral walls of the setup were designed with different boundary conditions to analyse possible influences on the flow field.

The numerical results were compared to an analogous experimental setup from [Tian00a] and [Tian00b]. The experimental setup consisted of conducting later walls, while four different related boundary conditions were tested in the numerical study. Additionally to a 3-dimensional simulation, also a 2-dimensional simulation was executed for each boundary condition to obtain possible information on the in [Tian00a] stated two-dimensional main flow field and on grid dependencies.

Taking the different boundary conditions and the non-Boussinesq fluid assumption of the simulation into consideration, all 3-dimensional simulation cases approximated very well the experimental data of [Tian00a]. The results showed similar profile tendencies of the main fluid properties as in [Tian00a], [Tian00b]. Between the 2-dimensional and 3-dimensional simulation cases similar profiles were observed, but especially the velocity and temperature fluctuations profiles revealed significant deviations between both simulation types. Certainly, grid dependencies had an influence here. The deviations could also be connected to the interaction between the chosen numerical methods and the coarse grid resolution.

To analyse these aspects further, another studies have to be performed in possible future works. In comparison to the results of [Tian00a], [Tian00b], the convection cells were dislocated in all simulation results. Moreover, in the *adiabatic bc case* two additional circulation zones could be detected in the top hot and bottom cold corner which showed an inverted circulation direction to the ones in [Tian00a], [Tian00b].

To analyse the 2-dimensional main flow field assumed by [Tian00a], the vertical velocity component was evaluated at different depth positions in the container. The profiles revealed small differences to each other close to the horizontal walls. This aspect indicated a 2-dimensional main flow field as observed by [Tian00a]. The additionally investigated

profile of the transversal velocity component demonstrated indeed low peak values at different heights at the xy-midplane, but showed also a distinctive flow boundary layer near the heated walls. This aspect objected the assumption of a 2-dimensional main flow field and might be seen as an indicator for a 3-dimensional flow profile. To obtain a detailed explanation, this subject should be further investigated in possible future studies.

The chosen LES was qualified to model the flow and its properties in this configuration of a turbulent natural convection. The results of the 3-dimensional simulations approximated very well the experimental data of [Tian00a], [Tian00b], considering the different boundary conditions. On the basis of the, at this point validated, performed LES and the gained information of *VerCon*, test case *RayCon* was analysed next.

Test case RayCon

In the second setup, *RayCon*, a turbulent natural convection in air in an enclosed container was analysed. This time both horizontal walls were isothermally heated. This configuration is also called a RB problem. In comparison to *VerCon*, the heated walls were rotated by 90°. The aspect ratios of the container were in this case $\Gamma_x = \frac{L}{H} = 5$, $\Gamma_y = \frac{H}{D} = 1$. Rayleigh numbers of $\mathrm{Ra} = 6.16 \times 10^7$, $\mathrm{Ra} = 1.92 \times 10^8$ and $\mathrm{Ra} = 4.1 \times 10^8$ were realised with a Prandtl number of $\mathrm{Pr} = 0.71$ which represented the chosen temperature intervals of the working fluid, *air*. For the numerical simulation the same compressible, non-Boussinesq LES was performed which was validated beforehand in the study of *VerCon*.

To observe possible influences of the mesh resolution on the numerical results, two different grid resolutions were chosen which influenced the results mainly in close distance to the heated walls. The time- and in most cases also area-averaged profiles of fluid properties revealed an asymmetry which is typical for a non-Boussinesq convection (NOB) in this configuration. Asymmetrical profiles were also reported by [Ahlers06] for a NOB convection in water an by [Wu1991] for a NOB in cryogenic helium as well as by [Zhang1997] for a NOB convection in glycerol. The asymmetries were caused by non-Boussinesq effects of density changes which were caused by temperature differences inside the fluid. These asymmetries were also detected in the global heat flux structure and its dependent fluid properties profiles.

Major grid dependencies arose which were caused by different quasi-stable states in the container. These states were visible on the basis of the temperature profiles estimated at two mirrored positions near the container middle. This aspect was confirmed on the basis of the convection cell arrangement. The different coherent structures revealed opposite circulation directions. Thus, the reproducibility of the results was destroyed by these structures existing at the mirror-imaged positions.

The non-dimensional temperature profile estimated in the thermal boundary layer at the xy-midplane approximated the analytical function of [Hölling06]. The simulation results matched well with the Nusselt- and Rayleigh-number-correlation of [Grossmann00]. The deviations between the dynamic viscosity profiles of both chosen grid resolutions were caused by grid dependencies.

In comparison to an analogous experimental setup in [Ebert08], the results in the simulation differed significantly from the measured experimental data. The deviations between the anti-symmetrical profiles in the experiment and the asymmetrical profiles in the simulation were caused by non-Boussinesq-effects in the simulation. [Horn11] determined in a DNS of a non-Boussinesq convection an asymmetrical temperature profile compared to an anti-symmetrical profile in a DNS of a Boussinesq convection. The investigated fluid in this study was water. Furthermore, *Horn et al.* observed an increased bulk temperature as well as different boundary layer thicknesses in the non-Boussinesq convection compared to the Boussinesq convection. These aspects could also be seen in the simulations compared to the experimental study of [Ebert08].

Higher temperature gradients and consequently higher Nusselt numbers were observed in the experiment compared to the simulation. These deviations might possibly be caused by a higher heat flux in the experiment. A further determination of this aspect on the basis of other fluid properties was not possible regarding the limited presented results in [Ebert08]. But, the experimental results differed also significantly from the analytical theory of [Grossmann00] as well as of [Hölling06], which were both well approximated by the numerical study of this thesis. This aspect confirmed also the possibility of a higher heat flux in the experiment of [Ebert08].

The chosen LES was qualified also in this case to model the configuration of a RB problem. The obtained results approximated very well the theoretical assumptions and measured data in [Grossmann00] as well as in [Hölling06]. The in [Ahlers06] and in [Horn11] stated asymmetrical profiles of fluid properties could be confirmed by the simulation data. The comparison between the results of the coarse and fine grid resolution showed that a well-resolved mesh is essential to obtain good results, especially in the near wall region when no wall-function is used in the numerical model.

Test case CenCon

In the study of the third test case, *CenCon*, not only a turbulent RB problem in air was analysed, but also a turbulent RB problem which was additionally affected by a Coriolis force. Besides a numerical study, also an experimental study was performed for this configuration. The setup of *CenCon* consisted of an air-filled enclosed container. This time both horizontal walls were isothermally heated. Thus, the test case was similar to the layout of *RayCon*.

In comparison to *RayCon*, the experimental setup was additionally influenced by Coriolis accelerations which were generated by a rotational movement of the test case under hyper-gravity in a large-scale centrifuge. These additional accelerations affected the vertical convective flow which was generated between the heated, horizontal walls. To model the accelerations in the simulation, a modified system of governing equations compared to the governing equations used for *RayCon* was considered.

While *CenCon* was rotating with a constant angular velocity, possible influences on the flow structures, the turbulence production and the fluid properties were observed in both studies. The conditions in the experiment were comparable to the conditions in the atmosphere in the beginning of a twister or hurricane, disregarding the different dimensions between the experiment and atmosphere. The aspect ratios of the test case setup were in both studies $\Gamma_x = \frac{D}{H} = 2.9$ and $\Gamma_y = \frac{L}{D} = 1$. The realised Rayleigh numbers lied between $2.33 \times 10^6 \leq \mathrm{Ra} \leq 4.32 \times 10^7$ with a Prandtl number of $\mathrm{Pr} = 0.71$.

A comparison of the time-averaged 2-dimensional velocity field between simulation and experiment revealed similar tendencies of flow structures and vortexes in the rotation mode as well as in the non-rotation mode in both studies. Large-scale structures, as they are typical for a RB problem, were visible in the non-rotation mode in both studies in the same way.

The Coriolis force increased significantly the development of turbulent structures. Smaller scales of flow structures and vortexes appeared in the rotation mode in both studies. With increasing effective Rayleigh numbers, these turbulent structures became smaller and seemed to be more irregular than in case of smaller effective Rayleigh numbers. The number of vortex regions (investigated only in the simulation) rose also with higher effective Rayleigh numbers in both modes. Moreover, higher frequencies were reached with increasing effective Rayleigh numbers in both modes. Altogether, smaller frequencies appeared in the rotation mode than in the non-rotation mode.

The rotational movement of the setup produced mixed flow structures inside the container which were drifted in direction of the rotation axis of the centrifuge. The influence of the Coriolis acceleration and the resulting displacement of the flow could clearly be seen in the numerical study in the profiles of the fluid properties and in the axially aligned (to the rotation axis) arrangement of the coherent structures. Slightly increased Nusselt number values as in a similar numerical study of [Horn11] could not be determined in the rotation mode in the simulation.

The Nusselt number values were smaller and converged with higher effective Rayleigh numbers to the results of the non-rotation mode. The temperature gradients diverged significantly from the gradients of the non-rotation mode with higher effective Rayleigh numbers. Due to the rotational movement, the turbulence production was higher inside

the setup. But the generated turbulent structures were also smaller and more irregular as in the non-rotation mode. Therefore, the heat flux inside the container had not necessarily to be higher in the rotation mode than in the non-rotation mode.

The performed compressible, non-Boussinesq LES was qualified to model a RB problem in the presented configuration of *CenCon* with and without a rotational movement. The experimental test case operated correctly in both modes and a fully turbulent natural convection was generated in the container. The obtained results of the time-averaged 2-dimensional velocity profile in the simulation approximated well the obtained results of the experiment. The profiles of the fluid properties, estimated only in the simulations, conformed in both modes well to related theoretical assumptions. The results of the non-rotation mode were similar to the results of *RayCon*, as it was expected due to the similar RB problem configuration of both cases.

The Coriolis acceleration had a significantly influence on the turbulent structures inside the fluid. Besides a displacement of the flow and a distortion of the convection cells, the rotational movement caused also an increase of the turbulence production inside the fluid. A stabilising effect of the Coriolis force could not have been observed directly. The Coriolis force was a source of smaller scale structures, which seemed to be mixed up compared to the non-rotating mode, as well as of vortexes in case of the observed angular velocity of this study and the deflection angle between the container and the rotation axis of the centrifuge. With increasing effective Rayleigh numbers the flow structures became smaller and seemed to be more irregular. Further the number of vortex regions rose and smaller frequencies appeared.

Conclusion and Outlook

It was shown that all performed numerical studies of a compressible, non-Boussinesq LES in this thesis were very qualified to model a turbulent natural convection in each investigated configuration. Asymmetrical fluid properties profiles were revealed in each test case which were caused by non-Boussinesq effects in the fluid. The estimated fluid properties profiles approximated well comparable analytical, experimental as well as numerical data from different studies.

The Coriolis acceleration in test case *CenCon* had, as expected, a significantly influence on the turbulent structures inside the fluid. But a stabilising effect of the Coriolis force could not have been observed. It was rather a source of irregular and highly mixed flow structures as well as vortexes.

It is noteworthy, that the reproducibility and comparability of the statistical analysed results in case of the temperature profiles of test case *RayCon* were questioned. Although the obtained results were time-averaged over an sufficient large time-interval, major grid

dependencies as well as different quasi stable-states were revealed in the test case. Consequently, deviations appeared between the temperature profiles estimated at mirrored-imaged positions near the container centre, although similar profiles were expected due to symmetry aspects of the test case. These different quasi stable-states of the coherent structures destroyed the reproducibility of the temperature profiles.

Regarding the results of this thesis, it could be said, that the choice of a compressible dynamic Smagorinsky model as turbulence model or the performance of different numerical schemes would be worth an investigation in future studies. Future work could also consider different approaches of the subgrid scale thermal diffusivity model. Regarding the centrifuge-setup and *CenCon*, hydrodynamic stability aspects of the flow, as for example the influence of disturbing particles (e. g. smaller clumps) placed in the container, would be an interesting topic. Besides the performance of local temperature measurements and a micro LDA, a modification of the setup aspect ratios or a varying angular velocity during the rotational movement would be further important topics.

A. Appendix

A.1. Mathematical formulations

A.1.1. Cartesian tensors

The following definitions are based on the information in ([Spurk07], appendix, A.2). In this thesis we deal with Cartesian tensors which consists of components and basis vectors. The depending tensor space is defined by the number of linear independent *basis vectors*, which span the coordinate system of the tensor space. In case of $\mathbb{R}^3$, these basis vectors are the constant unit vectors $\boldsymbol{e}_i$, $i = 1, 2, 3$ which span the Cartesian coordinate system with the axes x_i, $i = 1, 2, 3$. A tensor can be written only in its components, if the position of the coordinate system is known. A *zero order* tensor is called a *scalar*. A *first order* tensor is, for example, the position vector

$$\boldsymbol{x} = x_j \boldsymbol{e}_j = \sum_{j=1}^{3} x_j \boldsymbol{e}_j \,. \tag{A.1.1}$$

A *second order* tensor can be expressed by the not commutative *dyadic product*

$$\boldsymbol{T} = \boldsymbol{ab} = \sum_{j=1}^{3} \sum_{i=1}^{3} a_j b_i \boldsymbol{e}_j \boldsymbol{e}_i = a_j b_i \boldsymbol{e}_j \boldsymbol{e}_i \tag{A.1.2}$$

or

$$\boldsymbol{T} = t_{ji} \boldsymbol{e}_j \boldsymbol{e}_i \,. \tag{A.1.3}$$

Two basis vectors $\boldsymbol{e}_j, \boldsymbol{e}_i \in \mathbb{R}^3$ belong to each component of a second order tensor.

A.1.2. Einstein notation

In this thesis the *Einstein notation* is used for quantities in index notation. The following definitions are based on the information in ([Spurk07], appendix, A.1). In a term, in which repeated indices appear, this notation implies a summation over all possible values of these indices. For a vector $\boldsymbol{x} \in \mathbb{R}^3$ or the i-th component of a tensor t_i it is

$$\boldsymbol{x} = x_i \boldsymbol{e}_i = \sum_{i=1}^{3} x_i \boldsymbol{e}_i \,, \tag{A.1.4}$$

$$t_i = \tau_{ji} n_j = \sum_{j=1}^{3} \tau_{ji} n_j \,. \tag{A.1.5}$$

The index, over which is summed, is called *summation* index. The double appearing indices are the *dummy* indices, because they vanish after the summation is done. Each index must appear only once.

A.1.3. Matrix properties

The following definitions are based on the information in [Fischer10], chapter 2 and in [Dahmen06], chapter 3. A $(m \times n)$-matrix $A \in \mathbb{R}^{m,n}$

$$A = \begin{pmatrix} a_{11} & a_{12} & \cdots & a_{1n} \\ a_{21} & a_{22} & \cdots & a_{2n} \\ \vdots & \vdots & \ddots & \vdots \\ a_{m1} & a_{m2} & \cdots & a_{mn} \end{pmatrix} \tag{A.1.6}$$

is said to be *symmetric*, if the matrix equals its transposed matrix, $A^T = A$. If a matrix A has the same number of columns as of rows, it is said to be *square*. A square $(n \times n)$-matrix A, $A \in \mathbb{R}^{n,n}$, is said to be *diagonal*, if only the diagonal elements are not equal zero, $a_{ij} = 0$ if $i \neq j$ and $a_{ij} \neq 0$, if $i = j$. A square $(n \times n)$-matrix A, $A \in \mathbb{R}^{n,n}$, is called *upper triangular*, if $a_{ij} = 0$ for $j < i = 1...n$

$$A = \begin{pmatrix} a_{11} & a_{12} & \cdots & a_{1n} \\ 0 & a_{22} & \cdots & a_{2n} \\ \vdots & \vdots & \ddots & \vdots \\ 0 & 0 & \cdots & a_{nn} \end{pmatrix} . \tag{A.1.7}$$

A square $(n \times n)$-matrix A, $A \in \mathbb{R}^{n,n}$, is called *lower triangular*, if $a_{ij} = 0$ for $j > i = 1...n$.

A symmetric, square $(n \times n)$-matrix, $A \in \mathbb{R}^{n,n}$, is said to be *positive definite*, if for all vectors $\boldsymbol{x} \in \mathbb{R}^n$ with $\boldsymbol{x} \neq 0$, it is $\boldsymbol{x}^T A \boldsymbol{x} > 0$.

A symmetric square $(n \times n)$-matrix A, $A \in \mathbb{R}^{n,n}$, is said to be *diagonal dominant*, if it is for the diagonal elements $a_{ii} \geq \sum_j |a_{ij}|$ for $i, j = 1...n$.

Let the elements of p secondary diagonals of a symmetric matrix A, $A \in \mathbb{R}^{n,n}$ be not equal zero, besides the diagonal elements a_{ii}, so has the matrix A a *band structure* of width p.

Let be $m, l \in \mathbb{N}$ with $m, l \geq 0$, so has the symmetric matrix A, $A \in \mathbb{R}^{n,n}$ a band width of $p = m + l - 1$, if it is $a_{ij} = 0$ for $j + m < i$ or $i + l < j$

$$\begin{pmatrix} a_{1,1} & \dots & a_{1,m} & 0 & \dots & \dots & \dots & 0 \\ \vdots & \ddots & & \ddots & \ddots & & & \vdots \\ a_{l,1} & & \ddots & & \ddots & \ddots & & \vdots \\ 0 & \ddots & & \ddots & & \ddots & \ddots & \vdots \\ \vdots & \ddots & \ddots & & \ddots & & \ddots & 0 \\ \vdots & & \ddots & \ddots & & \ddots & & a_{n-m+1,n} \\ \vdots & & & \ddots & \ddots & & \ddots & \vdots \\ 0 & \dots & \dots & \dots & 0 & a_{n,n-l+1} & \dots & a_{nn} \end{pmatrix}. \tag{A.1.8}$$

For a funded description of these subjects and further details it is referred to [Fischer10], chapter 2 and to [Dahmen06], chapter 3.

A.1.4. Angular velocity

The rotational movement of a mass particle can be formulated with help of the angular velocity $\boldsymbol{\omega}$. The angular velocity $\boldsymbol{\omega}$ can be described in 2-dimensional cylindrical coordinates on the basis of figure A.1.

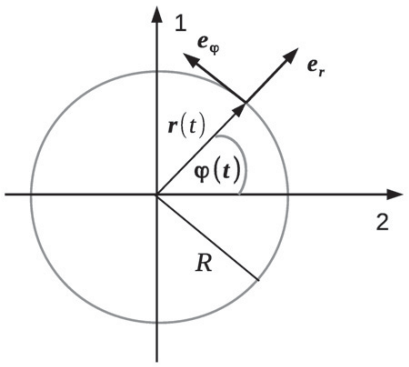

Figure A.1.: Rotation of a mass particle (as seen in [Nolting13]).

The following information are described analogously to [Nolting13], chapter 2, 2.1. It is

$$\begin{aligned} \boldsymbol{r}(t) &= R\boldsymbol{e}_r\,, & \boldsymbol{v}(t) &= R\dot{\boldsymbol{\varphi}}\boldsymbol{e}_\varphi\,, \\ \boldsymbol{a}(t) &= a_r\boldsymbol{e}_r + a_\varphi\boldsymbol{e}_\varphi\,, & a_r &= -R\dot{\boldsymbol{\varphi}}^2, & a_\varphi &= R\ddot{\boldsymbol{\varphi}} \end{aligned} \tag{A.1.9}$$

with the angular velocity $\boldsymbol{\omega}$

$$\boldsymbol{\omega} = \dot{\boldsymbol{\varphi}}\,, \tag{A.1.10}$$

where $\dot{\boldsymbol{\varphi}}(t)$ denotes the change in time of the angle φ. It is further

$$\begin{aligned} v &= R\omega && \text{absolute value of velocity,} \\ a_r &= -R\omega^2 && \text{absolute value centripetal acceleration,} \\ a_\varphi &= R\dot{\omega} && \text{absolute value tangential acceleration.} \end{aligned} \tag{A.1.11}$$

Translated to a 3-dimensional coordinate system, where the angular velocity is allocated to an axial vector which points in direction of a third axis, the rotation axis, it is

$$\boldsymbol{v}(t) = \boldsymbol{\omega} \times \boldsymbol{r}(t) = \omega R \boldsymbol{e}_\varphi. \tag{A.1.12}$$

A.2. Case studies - *CenCon*, a Rayleigh-Bénard problem affected by the Coriolis force

A.2.1. Supplementary notes

Complementary to chapter 3, section 3.5, 3.5.2, the heat transmission in the setup of *CenCon* is discussed in the following. The following estimations are done exemplary on the basis of the maximal temperature values in the non-rotation mode rot_{off} only. Therefore, the following statements are only approximations for test case *CenCon*.

In the experiment, a maximal temperature of $T_{\text{hot}} = 353.15\,\text{K}$ can be realised at the heating wall. The temperature at the cooling wall is always regulated constantly at a value of $T_{\text{cold}} = 293.15\,\text{K}$. The temperature difference between both heating walls is in this case $\Delta T = 60\,\text{K}$. In the beginning of the heating process, the temperature inside the container is taken to be at $T_{\text{air,in}} = 293.15\,\text{K}$ which is equivalent to the temperature at the cold wall.

The surface area of the hot wall is given by $A_P = L \cdot D = 0.58\,\text{m} \cdot 0.58\,\text{m} = 0.3364\,\text{m}^2$. To calculate the maximal convective heat flux from the hot wall to the first air layer above the hot wall, the thermal heat transfer coefficient $\tilde{\alpha}$ has to be known, according to equation (3.5.12) from chapter 3, section 3.5.2 on page 79. According to [VDI06] (page Fa 4), the coefficient can be estimated by the Nusselt number over

$$\text{Nu} = \frac{\tilde{\alpha} l}{\lambda}\,. \tag{A.2.1}$$

The Nusselt number concerning a natural convection as in case of *CenCon* can be approximated by the following expression (see [VDI06], page Fa 4)

$$\text{Nu} = 0.15\,[\text{Ra} \cdot f(\text{Pr})]^{1/3}\,, \tag{A.2.2}$$

where $f(\mathrm{Pr})$ is a function of the Prandtl number. The Rayleigh number is defined with help of the Grashof number by

$$\mathrm{Gr} = \frac{gl^3 \Delta T \beta}{\nu^2} = \mathrm{Ra}/\mathrm{Pr}. \tag{A.2.3}$$

The temperature difference between the hot wall and the first air layer above the hot wall is $\Delta T = T_{\mathrm{hot}} - T_{\mathrm{air,in}} = 353.15\,\mathrm{K} - 293.15\,\mathrm{K} = 60\,\mathrm{K}$. Regarding a mean temperature between the hot wall and the first air layer above the hot wall with $T_{\mathrm{mean,air}} = 323.15\,\mathrm{K}$, one can give an estimation of the Nusselt number and heat transfer coefficient by the following properties

$$\beta = \frac{1}{T_{\mathrm{air}}} = \frac{1}{293.15}\,\frac{1}{\mathrm{K}}, \quad \lambda(323.15) = 0.0281\,\frac{\mathrm{W}}{\mathrm{Km}}\,, \tag{A.2.4}$$

$$\nu(323.15) = 1.822 \cdot 10^{-5}\,\frac{\mathrm{m}^2}{\mathrm{s}}\,, \quad l = \frac{L \cdot D}{2(L+D)} = 0.145\,\mathrm{m}. \tag{A.2.5}$$

The characteristic length l is corresponding to the surface area of the hot wall. The particular properties can be found in [VDI06] (section Dbb). The resulting Grashof and Rayleigh number are then

$$\mathrm{Gr} = 1.84 \times 10^7 \quad \Rightarrow \quad \mathrm{Ra} = 1.31 \times 10^7. \tag{A.2.6}$$

For $\mathrm{Pr} = 0.71$, function $f(\mathrm{Pr})$ in equation (A.2.2) is given by $f(\mathrm{Pr}) = 0.401$, according to [VDI06] (page Fa 4). Hence, one obtains the following Nusselt number and heat transfer coefficient $\tilde{\alpha}$

$$\mathrm{Nu} = 26.07 \quad \Rightarrow \quad \tilde{\alpha} = 5.05\,\mathrm{W}/(\mathrm{Km}^2)\,. \tag{A.2.7}$$

According to equation (3.5.17) (s. chapter 3, section 3.5, 3.5.2, page 80), the maximum convective heat flux $\dot{Q}_{\mathrm{hot}}$ from the hot wall into the container becomes

$$\dot{Q}_{\mathrm{hot}} = A_P \tilde{\alpha} (T_{\mathrm{hot}} - T_{\mathrm{air}}) = 101.93\,\mathrm{W}. \tag{A.2.8}$$

The heat flux density $\dot{q}$ is then

$$\dot{q} = \dot{Q}/A_P = 303\,\mathrm{W}/\mathrm{m}^2. \tag{A.2.9}$$

Note, that this is the heat flux for the maximal chose-able temperature $T_{\mathrm{hot}} = 353.15\,\mathrm{K}$ at the hot wall. For smaller temperatures or other considered temperatures inside the container, the heat flux has to be adapted.

Because the side walls of the experimental setup are not adiabatic, a possible heat loss through these walls has to be considered. The PMMA side walls have all a thickness of

$\delta = 0.01\,\mathrm{m}$, a temperature dependent mean thermal conductivity of $\lambda_\mathrm{w} = 0.19\,\mathrm{W/(Km)}$ and a coefficient of heat transmission of $k = 4.4\,\mathrm{W/(Km^2)}$. The temperature inside the container directly at the side wall is assumed to be on average at $T_{\mathrm{IF,\,fluid}} = 323.15\,\mathrm{K}$, regarding a settlement of the system and case $T_\mathrm{hot} = 353.15\,\mathrm{K}$. Outside the container, the temperature is assumed to be at $T_\mathrm{outs} = 293.15\,\mathrm{K}$. The area of one side wall is $A_S = L \cdot H = 0.58\,\mathrm{m} \cdot 0.2\,\mathrm{m} = 0.116\,\mathrm{m^2}$. According to equation (3.5.18) (s. chapter 3, section 3.5, 3.5.2 on page 80), the heat flux trough one side wall can be calculated as

$$\begin{aligned} \dot{Q}_\mathrm{sideW} &= kA_S(T_1 - T_2) = kA_S(T_{\mathrm{IF,\,fluid}} - T_\mathrm{outs}) \\ &= 4.4\,\mathrm{W/(Km^2)} \cdot (0.58\,\mathrm{m} \cdot 0.2\,\mathrm{m}) \cdot 30\mathrm{K} = 15.31\,\mathrm{W}. \end{aligned} \tag{A.2.10}$$

Then the maximal possible heat flux density is

$$\dot{q}_\mathrm{sideW} = \dot{Q}_\mathrm{sideW}/A_S = 131.98\,\mathrm{W/m^2}. \tag{A.2.11}$$

For all side walls together it is $\dot{Q}_\mathrm{allsideW} = 61.24\,\mathrm{W}$. But this value is only a possible maximum value valid in case of $T_\mathrm{hot} = 353.15\,\mathrm{K}$ and $T_\mathrm{outs} = 293.15\,\mathrm{K}$ with a on average temperature inside the container of $T_{\mathrm{IF,\,fluid}} = 323.15\,\mathrm{K}$. Therefore, a high power rating of the heating wall is chosen. For the case of of the smallest temperature difference and $T_\mathrm{hot} = 296.15\,\mathrm{K}$, a possible heat flux trough one side wall is calculated as

$$\begin{aligned} \dot{Q}_\mathrm{sideW} &= kA_S(T_1 - T_2) = kA_S(T_{\mathrm{IF,\,fluid}} - T_\mathrm{outs}) \\ &= 4.4\,\mathrm{W/(Km^2)} \cdot (0.58\,\mathrm{m} \cdot 0.2\,\mathrm{m}) \cdot 1.5\mathrm{K} = 0.77\,\mathrm{W} \end{aligned} \tag{A.2.12}$$

and

$$\dot{q}_\mathrm{sideW} = \dot{Q}_\mathrm{sideW}/A_S = 6.6\,\mathrm{W/m^2}. \tag{A.2.13}$$

For all side walls it is $\dot{Q}_\mathrm{allsideW} = 3.08\,\mathrm{W}$. The above stated properties of the PMMA side walls can be found in the technical data sheet [Evonik].

A.2.2. Simulation results of *CenCon*

A.2.2.1. Convection cell structures in the test case visualised by the mean velocity distribution, rotation mode

Complementary to chapter 7, section 7.6.1.2, the following figures A.2 - A.5 on pages 281 - 283 display the convection cell arrangement in the simulation for $\Delta T = 5\,\mathrm{K}$, $\Delta T = 8.5\,\mathrm{K}$, $\Delta T = 15\,\mathrm{K}$, $\Delta T = 28\,\mathrm{K}$ and the rotation mode $\mathrm{rot_{on}}$. The convection cells reveal a changed structure compared to the non-rotation mode. The in chapter 7, section 7.6, 7.6.1.2 mentioned displacement caused by the Coriolis force, generated this time several convection cells which are mixed which each other. The convection cells are located next to each

other in the $x'y'$-plane along the container's depth. This can be seen in all of the results. This displacement is also indicated in figure A.2 by the up and down movements and in figure A.5 on page 283 by the wave-like structures. The snapshots in figure A.4 on page 282 show additionally the instantaneous structures of the velocity magnitude for a top view of all cases.

Vortex structures can be seen in the case of $\Delta T = 5\,\mathrm{K}$, $\Delta T = 15\,\mathrm{K}$ and $\Delta T = 28\,\mathrm{K}$. in the left bottom corner (marked by the red coloured circle). For higher temperature differences, as $\Delta T = 15\,\mathrm{K}$ and $\Delta T = 28\,\mathrm{K}$, the visible convection cell structures reveal larger spatial scales in case of lower effective Rayleigh numbers.

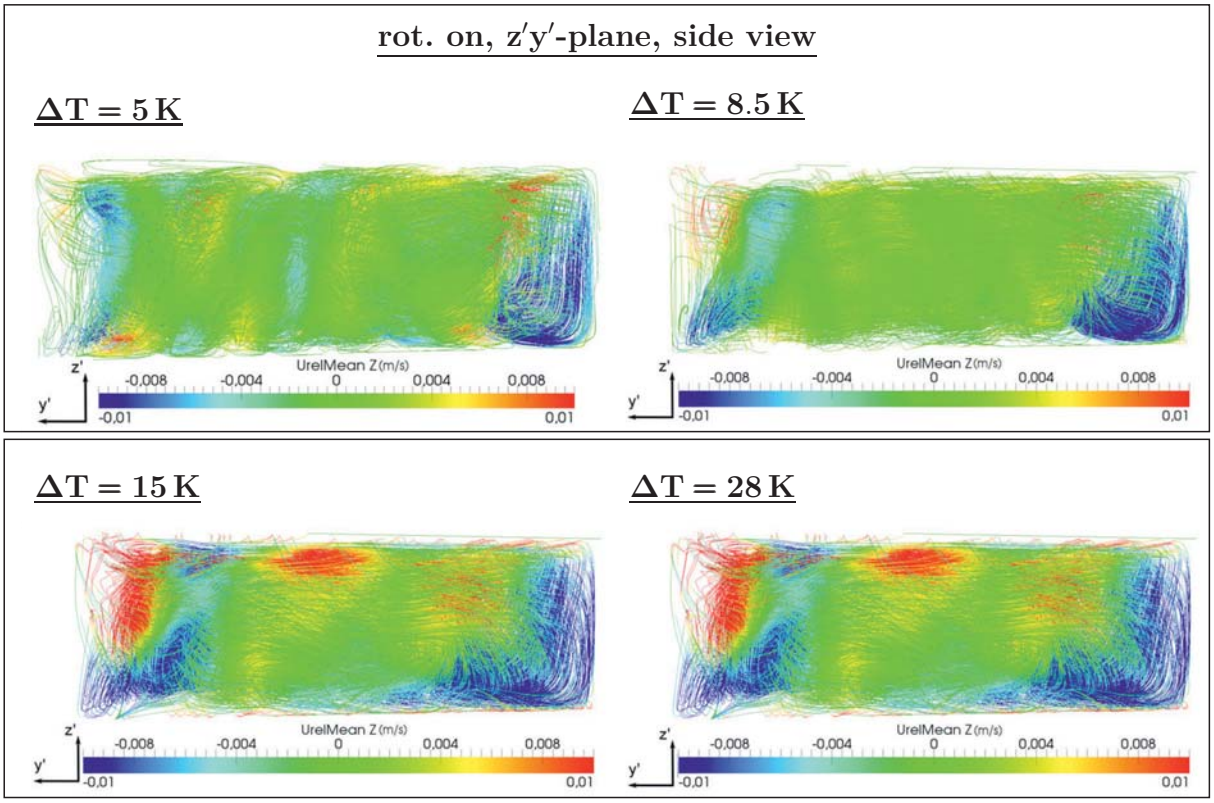

Figure A.2.: Instantaneous snapshots of the mean vertical velocity structures in the $z'y'$-plane, **rotation mode rot$_{\mathbf{on}}$**, side view, $t = 400\,\mathrm{s}$. **Clockwise direction, starting left top:** $\Delta T = 5\mathrm{K}$, $\Delta T = 8.5\mathrm{K}$, $\Delta T = 15\mathrm{K}$, $\Delta T = 28\mathrm{K}$.

In figure A.3 on page 282 an additional side view of the $z'x'$-plane is shown. The snapshots reveal large structures in all cases. The cells reveal in all cases the same orientation. Especially in case of the smaller temperature differences of $\Delta T = 5\,\mathrm{K}$ and $\Delta T = 8.5\,\mathrm{K}$ (and hence smaller effective Rayleigh numbers), the visible structures seem to be more turbulent and mixed up than in cases with a higher temperature difference.

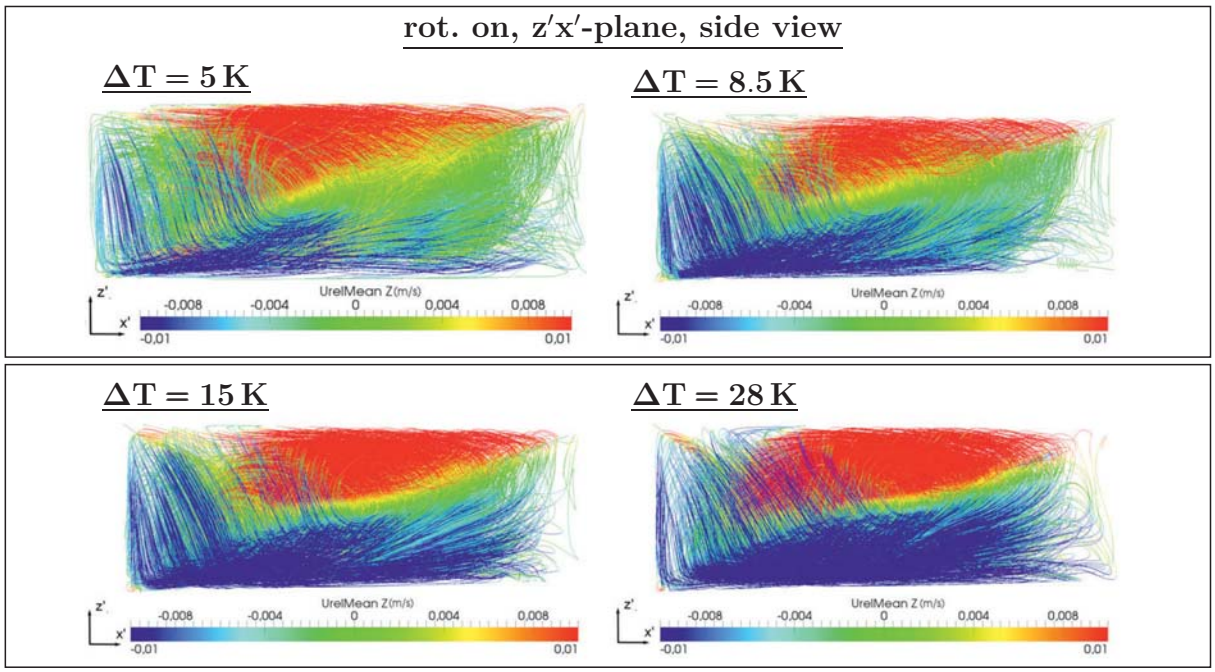

Figure A.3.: Instantaneous snapshots of the mean vertical velocity structures in the $z'x'$-plane, **rotation mode rot$_{\mathbf{on}}$**, side view, $t = 400\,\mathrm{s}$. **Clockwise direction, starting left top:** $\Delta T = 5\mathrm{K}$, $\Delta T = 8.5\mathrm{K}$, $\Delta T = 15\mathrm{K}$, $\Delta T = 28\mathrm{K}$.

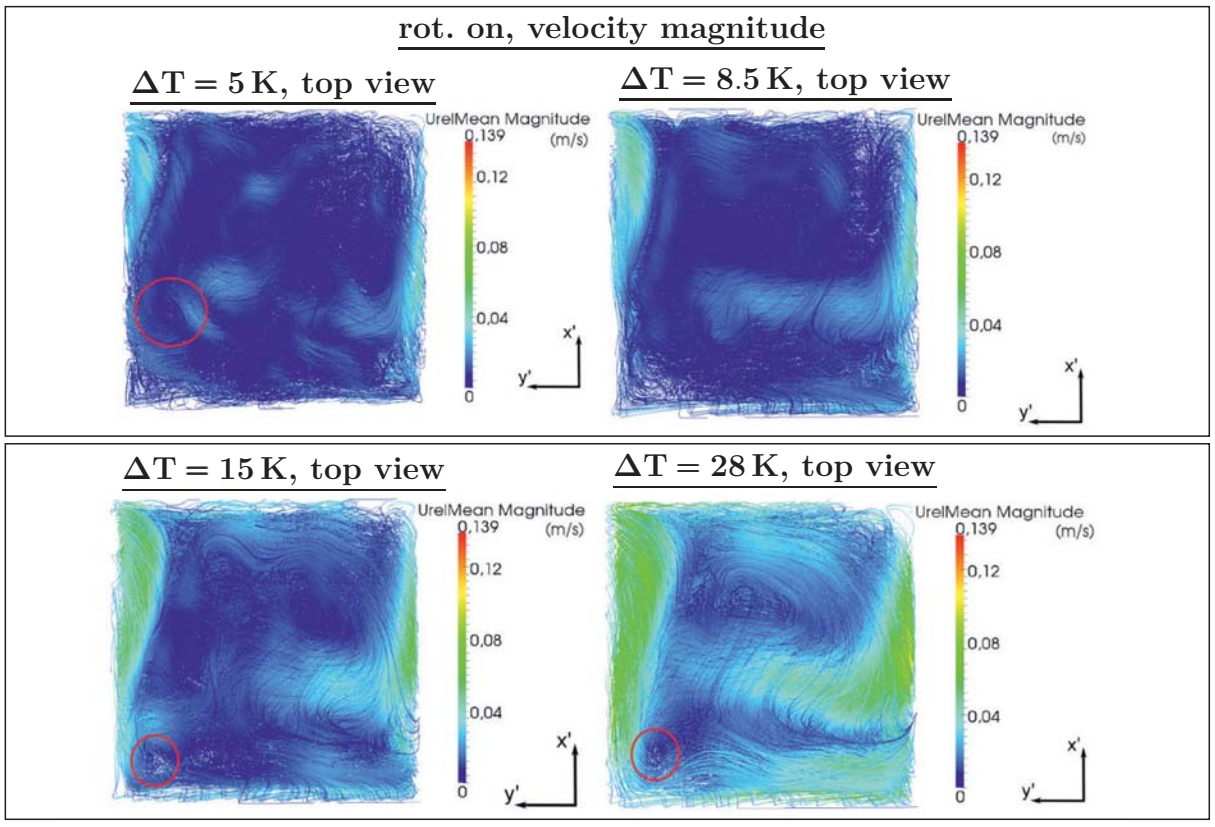

Figure A.4.: Instantaneous mean velocity magnitude structures in the container, **rotation mode rot$_{\mathbf{on}}$**, top view, $t = 400\,\mathrm{s}$. **Clockwise direction, starting left top:** $\Delta T = 5\mathrm{K}$, $\Delta T = 8.5\mathrm{K}$, $\Delta T = 15\mathrm{K}$, $\Delta T = 28\mathrm{K}$.

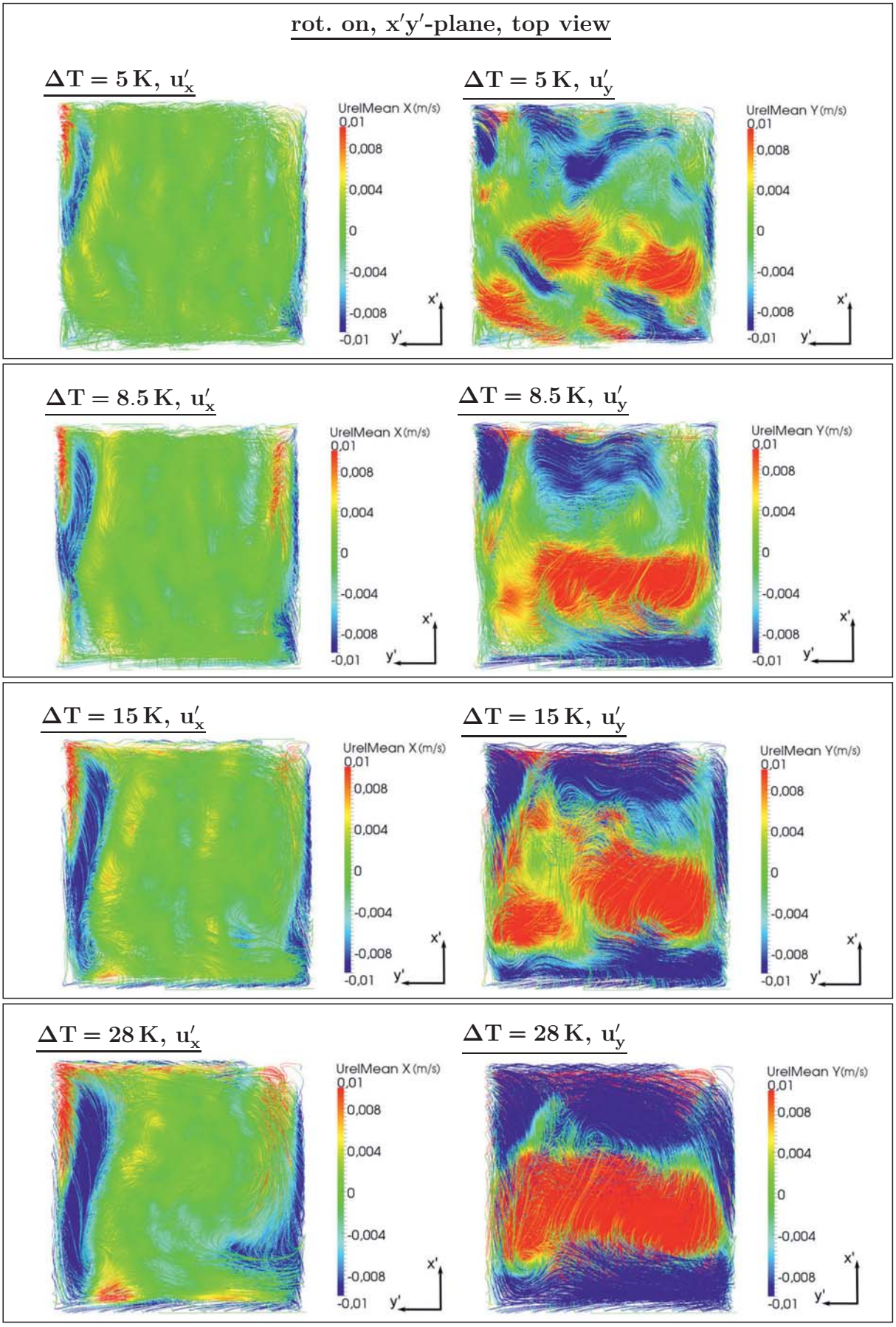

Figure A.5.: Instantaneous snapshots of the mean horizontal velocity structures in the $x'y'$-plane, **rotation mode rot$_{\mathbf{on}}$**, top view, $t = 400\,\mathrm{s}$. **Left:** u'_x. **Right:** u'_y. **Top to bottom:** $\Delta T = 5\mathrm{K}$, $\Delta T = 8.5\mathrm{K}$, $\Delta T = 15\mathrm{K}$ and $\Delta T = 28\mathrm{K}$.

A.2.2.2. Fluid properties between the heated walls - temperature, density, velocity and Coriolis acceleration, estimated along the vertical $z(z')$-axis and different depth positions

Figures A.6 - A.13 show complementary to chapter 7, section 7.6, 7.6.2, the time-averaged profiles of temperature T, velocity $\boldsymbol{u}$, density ρ and Coriolis acceleration components between the heated walls estimated along the $z(z')$-axis at $y(y') = 0\,\mathrm{m}$ at different depth $x(x')$-positions. The results are estimated in both modes in the simulation. They are time-averaged over an interval of $t = 200\,\mathrm{s} - 400\,\mathrm{s}$ in the simulated process. Note that the origin of both coordinate systems lies in the container centre.

The estimated positions are $x(x') = -0.2\,\mathrm{m}$ (black solid line), $x(x') = -0.1\,\mathrm{m}$ (red solid line), $x(x') = 0\,\mathrm{m}$ (blue solid line), $x(x') = 0.1\,\mathrm{m}$ (black dashed line), $x(x') = 0.2\,\mathrm{m}$ (red dashed line), and $x(x') = 0.25\,\mathrm{m}$ (blue dashed line). For an overview of the estimation positions see also figure 7.30 on page 245 in chapter 7, section 7.6.2.3. For a detailed view of the legend see figure 7.31 on page 246 in chapter 7, section 7.6.2.3. The following figures present the results for the temperature differences of $\Delta T = 5\,\mathrm{K}$, $\Delta T = 8.5\,\mathrm{K}$, $\Delta T = 15\,\mathrm{K}$ and $\Delta T = 28\,\mathrm{K}$. Note that the estimated values in the rotation mode $\mathrm{rot}_{\mathrm{on}}$ are related to the coordinate system of S'_R. The values of each component are transformed component-by-component to system S'_R according to equation (7.4.6) on page 216 in section 7.4.2.

Thermophysical properties - temperature and density

Figures A.6 - A.7 on pages 285 - 286 show the time-averaged profiles of temperature T and density ρ. As mentioned before in chapter 7, section 7.6.2, the temperature profiles of the non-rotation mode $\mathrm{rot}_{\mathrm{off}}$ reveal asymmetrical profiles, as it was expected, due to NOB effects (s. chapter 6, section 6.3.2 from page 162 on).

In the non-rotation mode $\mathrm{rot}_{\mathrm{off}}$ all profiles lie very close to each other in the bulk region, except in the case of $\Delta T = 15\,\mathrm{K}$. Each profile in the rotation mode $\mathrm{rot}_{\mathrm{on}}$ shows also an asymmetry which is this time even more distinctive. In comparison to the non-rotation mode $\mathrm{rot}_{\mathrm{off}}$, the bulk temperature is not constant, but shows a linear distribution along the container middle. The temperature distribution in the cell centre differs from the mean temperature T_{mean} and lies at some positions over the reached values of the non-rotation mode $\mathrm{rot}_{\mathrm{off}}$. All profiles of the rotation mode $\mathrm{rot}_{\mathrm{on}}$ reveal differences along the container middle between the particular estimated positions. This aspect becomes more significant with higher temperature differences ΔT.

It is noteworthy, that the profiles at $x(x') = -0.2\,\mathrm{m}$ (black line) reveal the smallest values in all cases of the rotation mode $\mathrm{rot}_{\mathrm{on}}$. This aspect could possibly be caused by the influence of the side wall at this position.

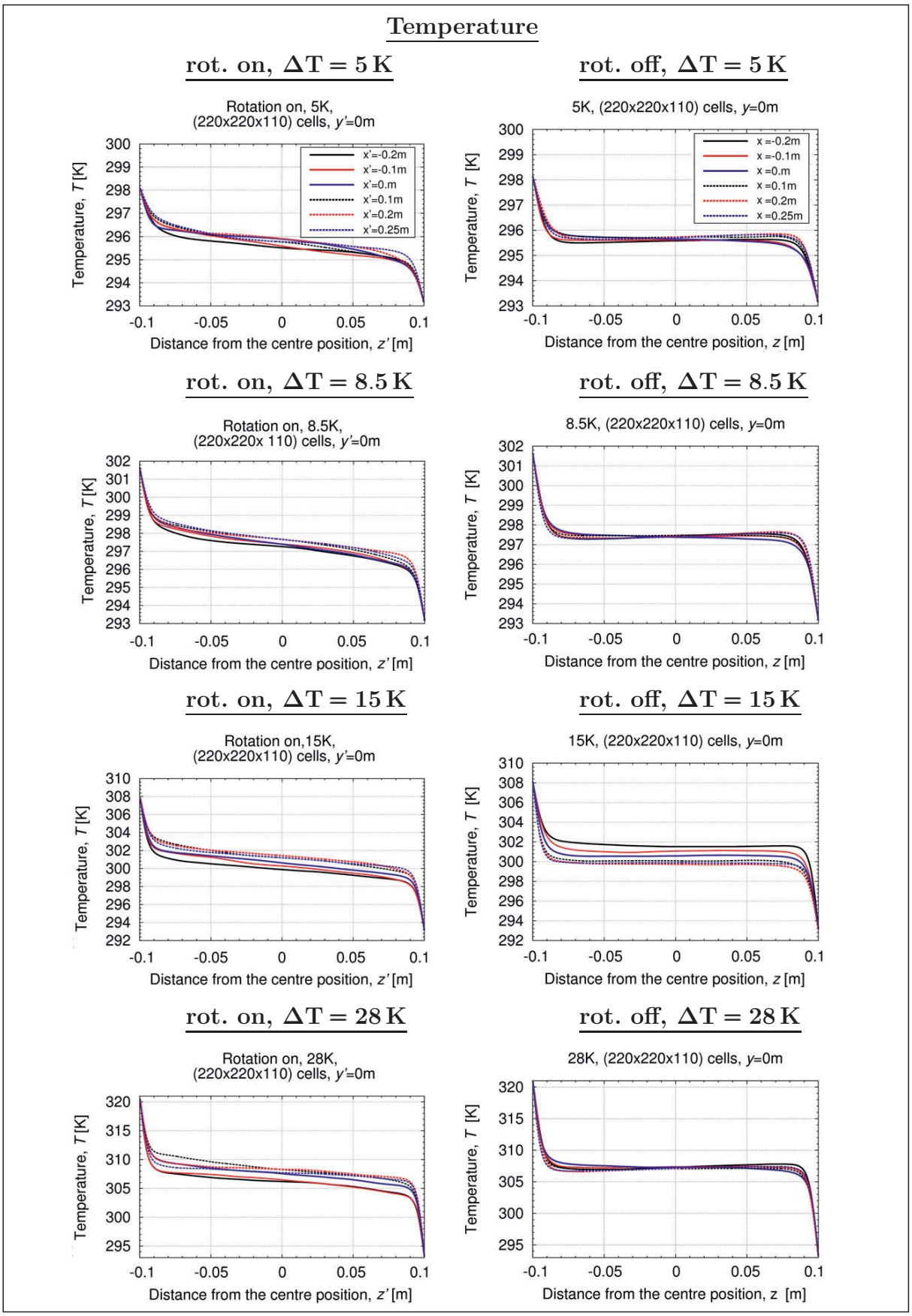

Figure A.6.: Time-averaged temperature profiles. **Left:** Rotation mode $\mathrm{rot}_{\mathrm{on}}$. **Right:** Non-rotation mode $\mathrm{rot}_{\mathrm{off}}$. **Top to bottom:** $\Delta T = 5\mathrm{K}$, $\Delta T = 8.5\mathrm{K}$, $\Delta T = 15\mathrm{K}$, $\Delta T = 28\mathrm{K}$. Estimated at $y(y') = 0\,\mathrm{m}$ (centre position) along the vertical axis $z(z')$ at different positions (see figure 7.31 on page 246 and the legend in the both top plots).

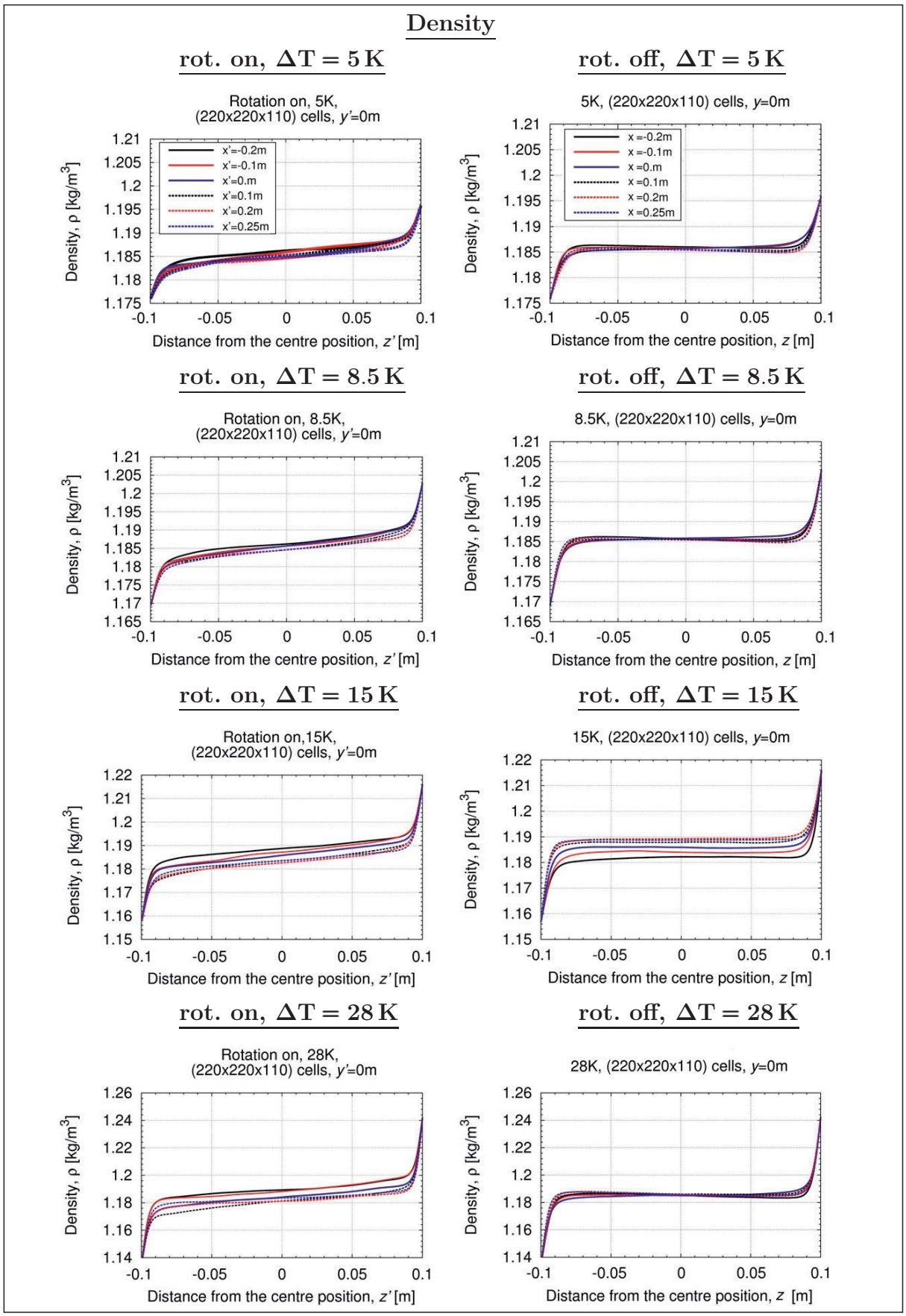

Figure A.7.: Time-averaged density profiles. **Left:** Rotation mode $\mathrm{rot}_{\mathrm{on}}$. **Right:** Non-rotation mode $\mathrm{rot}_{\mathrm{off}}$. **Top to bottom:** $\Delta T = 5\mathrm{K}$, $\Delta T = 8.5\mathrm{K}$, $\Delta T = 15\mathrm{K}$, $\Delta T = 28\mathrm{K}$. Estimated at $y(y') = 0\,\mathrm{m}$ (centre position) along the vertical axis $z(z')$ at different positions (see figure 7.31 on page 246 and the legend in the both top plots).

The profiles of the non-rotation mode $\mathrm{rot}_{\mathrm{off}}$ reveal steeper gradients at the heated walls and hence smaller boundary layers as in case of the rotation mode $\mathrm{rot}_{\mathrm{on}}$ for all chosen temperature differences.

From $\Delta T = 15\,\mathrm{K}$ on, the gradients become steeper in the rotation mode $\mathrm{rot}_{\mathrm{on}}$ and the boundary layers decrease, but still not as steep as in the non-rotation mode. The density profiles are mirror-inverted to the temperature distributions, as it was expected due to the relation between both properties.

Velocity profiles

Figures A.9 - A.11 on pages 288 - 290 show the time-averaged velocity profiles at the mid-plane at $y(y') = 0\,\mathrm{m}$ along the vertical $z(z')$-axis between both temperatured walls at different $x(x')$-locations. Due to a better presentation, the legend of the plots is presented separately in the below figure A.8. For an overview of the estimation positions see also figure 7.30 on page 245 in chapter 7, section 7.6.2.3.

The profiles show positive or negative values depending on the circulation direction of the particular convection cell. The only exception is again case $\Delta T = 15\,\mathrm{K}$. Likewise to the profiles of the other horizontal velocity component u'_x, the u'_y component reveals a similar structure in its profiles, but with slightly higher values. Compared to both other velocity components of both modes, u'_x/u_x and u'_z/u_z, the component u'_y/u_y has the highest values in the rotation mode $\mathrm{rot}_{\mathrm{on}}$, respectively non-rotation mode $\mathrm{rot}_{\mathrm{off}}$.

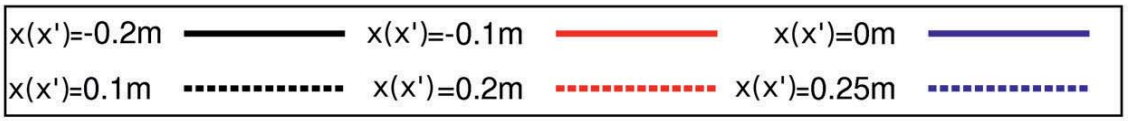

Figure A.8.: Legend of the fluid properties profiles in figures A.9 - A.11.

In the non-rotation mode $\mathrm{rot}_{\mathrm{off}}$, the vertical component u_z reflects well the convection cell structure from figure 7.19 on page 232. The highers values are reached for all depths positions at the centre position $z = 0\,\mathrm{m}$. For all cases the positions $x = 0\,\mathrm{m}$ (blue solid line), $x = -0.1\,\mathrm{m}$ (red solid line) and $x = 0.1\,\mathrm{m}$ (black dashed line) reveal the highest values. In case $\Delta T = 15\,\mathrm{K}$, the highest values are reached for $x = 0.2\,\mathrm{m}$ (red dashed line) and $x = -0.2\,\mathrm{m}$ (black solid line) due to the changed convection cell structure.

The mentioned displacement of fluid particles which is caused by the Coriolis acceleration can clearly be seen in the vertical velocity u'_z profile in all cases. Along the vertical z'-axis an up and down movement of air layers can be detected for each position in all profiles. Ascending hot air layers are displaced by descending cold layers.

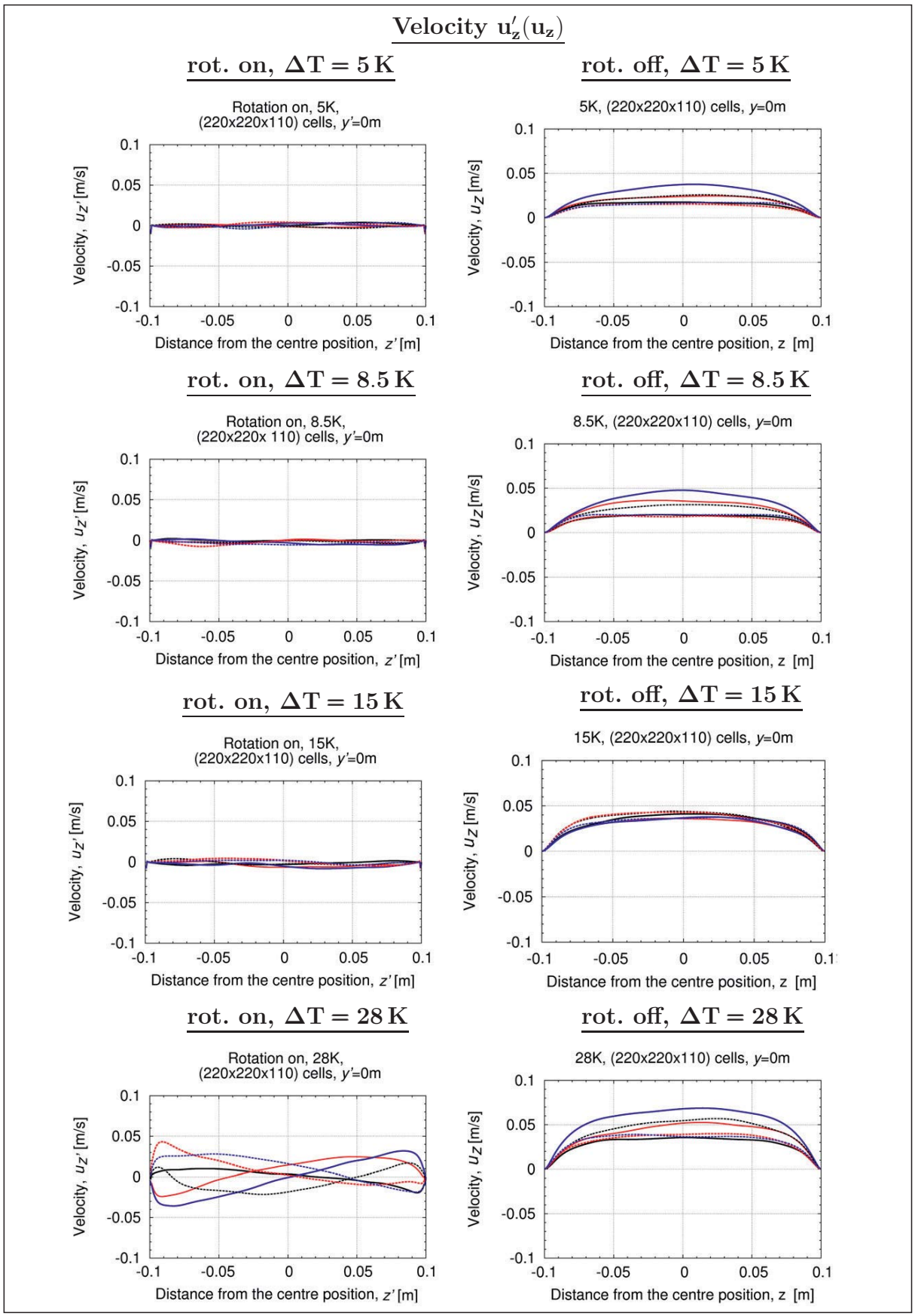

Figure A.9.: Time-averaged velocity profiles $u'_z(u_z)$. **Left:** Rotation mode $\mathrm{rot_{on}}$. **Right:** Non-rotation mode $\mathrm{rot_{off}}$. **Top to bottom:** ΔT = 5K, ΔT = 8.5K, ΔT = 15K, ΔT = 28K. Estimated at $y(y') = 0\,\mathrm{m}$ (centre position) along the vertical axis $z(z')$ at different positions (see figure A.8 on page 287).

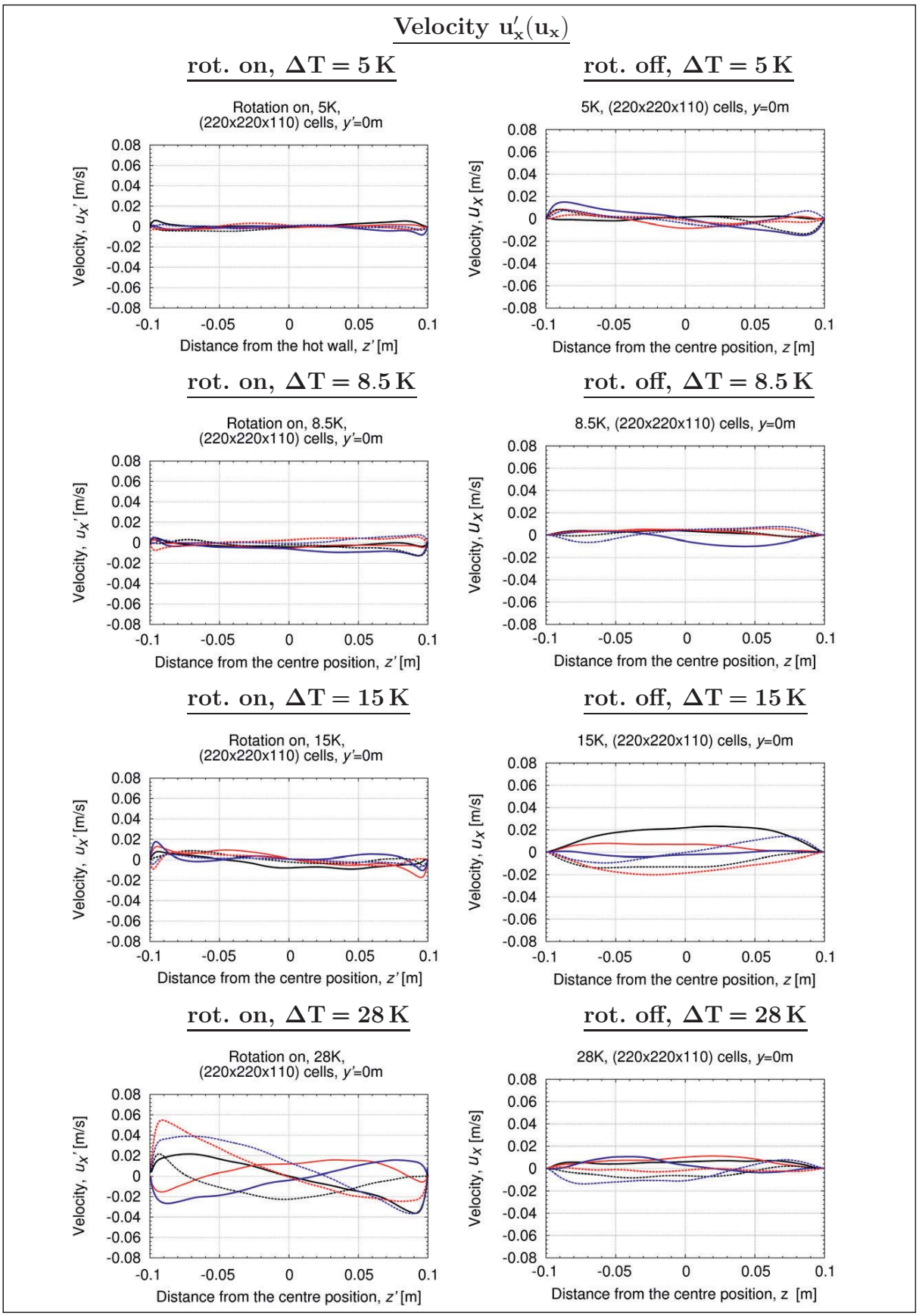

Figure A.10.: Time-averaged velocity profiles $u'_x(u_x)$. **Left:** Rotation mode $\mathrm{rot_{on}}$. **Right:** Non-rotation mode $\mathrm{rot_{off}}$. **Top to bottom:** $\Delta T = 5$K, $\Delta T = 8.5$K, $\Delta T = 15$K, $\Delta T = 28$K. Estimated at $y(y') = 0\,\mathrm{m}$ (centre position) along the vertical axis $z(z')$ at different positions (see figure A.8 on page 287).

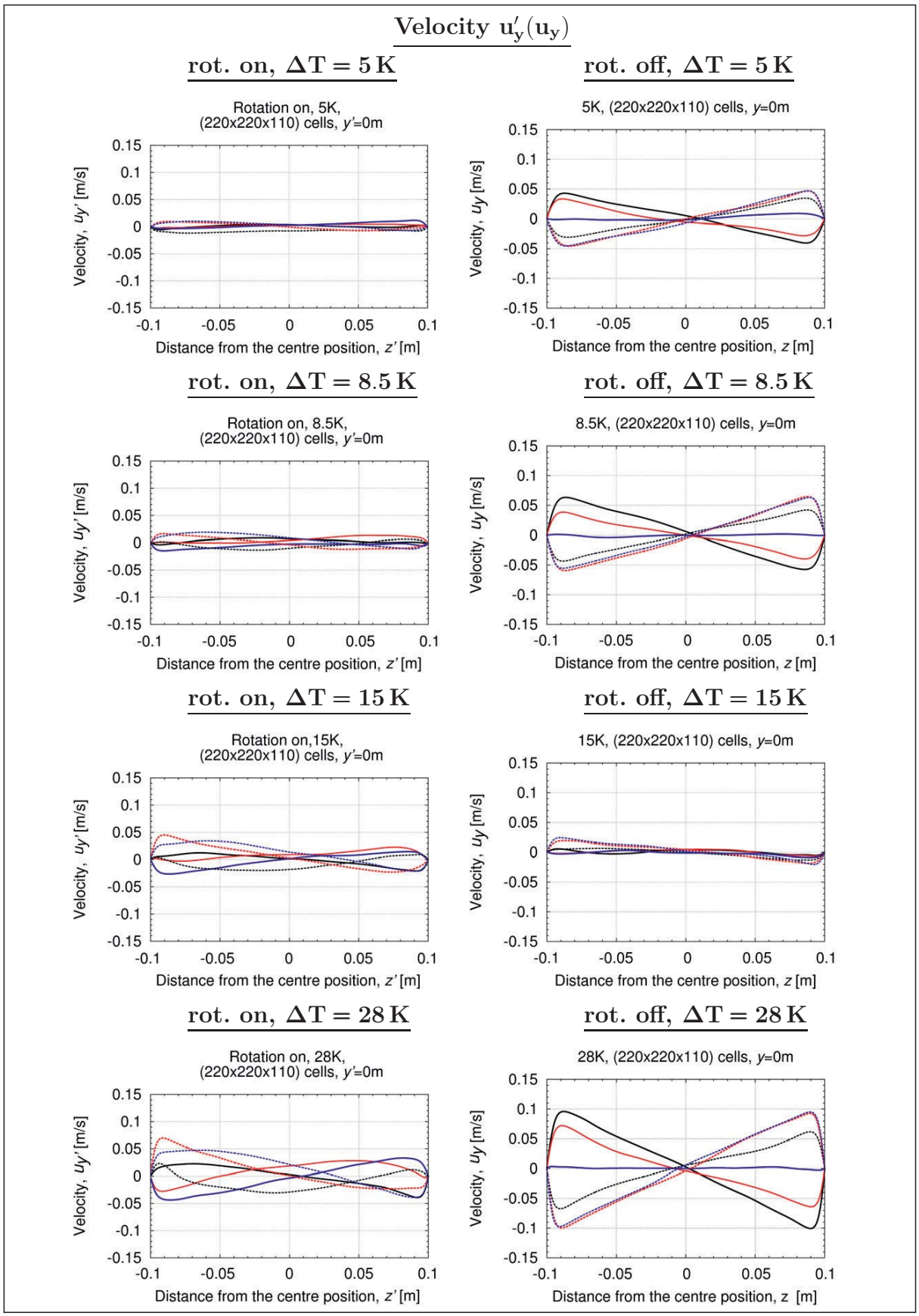

Figure A.11.: Time-averaged velocity profiles $u'_y(u_y)$. **Left:** Rotation mode $\mathrm{rot_{on}}$. **Right:** Non-rotation mode $\mathrm{rot_{off}}$. **Top to bottom:** $\Delta T = 5\mathrm{K}$, $\Delta T = 8.5\mathrm{K}$, $\Delta T = 15\mathrm{K}$, $\Delta T = 28\mathrm{K}$. Estimated at $y(y') = 0\,\mathrm{m}$ (centre position) along the vertical axis $z(z')$ at different positions (see figure A.8 on page 287).

Due to the arrangement of the four cells, only small values of the horizontal velocity component u_x are reached at the midplane $y = 0\,\mathrm{m}$ compared to both other velocity components. The obtained results at all x-positions lie close to each other for smaller temperature differences. The results show higher values close to the heated walls and close to the centre position for each ΔT-case. With higher ΔT, the reached peak values rise and the particular results differ more from each other. The results of the horizontal velocity component u_x and $\Delta T = 15\,\mathrm{K}$ differs from the other results due to the different arrangement of the convection cells.

u'_x reflects the profiles of u'_y in all ΔT cases at all positions with lower peak values, as it was expected due to the symmetric layout of the container and the symmetric arrangement of convection cells. High values are reached near the heated walls which increase with higher temperature differences. In the profiles of the second horizontal velocity component u_y one can clearly see the circulation direction of the four convection cells. High values are reached near the heated walls. Directly in the centre position this velocity component is zero.

Coriolis acceleration profiles

Figures A.12 - A.13 on pages 292 - 293 display the time-averaged profiles of the Coriolis acceleration components estimated between both temperatured walls at the midplane at $y(y') = 0\,\mathrm{m}$ along the vertical $z(z')$-axis and different $x(x')$-locations. For an overview of the estimation positions see also figure 7.30 on page 245 in chapter 7, section 7.6.2.3. For a detailed view of the legend see the top left plots in figures A.12 - A.13 or the legend in figure A.8 on page 287.

According to equation (7.4.26) on page 220, the Coriolis force and also the Coriolis acceleration is dependent on the velocity vector $\boldsymbol{u}'_{S'_R}$ and the angle α which arises relative between the direction of the velocity vector and the direction of the angular velocity vector $\boldsymbol{\omega}$, thus the rotation axis. Due to the relative rotated coordinate system in S'_R, $a_{Cy'}$ and $a_{Cz'}$ show a different relative angle between their movement plane and the rotation axis in S_I. The profiles of the $a_{Cx'}$-component show higher values than the ones of the $a_{Cy'}$-component at most of the estimated locations, despite higher velocity values of u'_y. The $a_{Cy'}$ component has its peak values near the heated walls which increase with increasing ΔT.

The values of the $a_{Cz'}$-component resemble the ones of the $a_{Cx'}$-component with slightly higher values and a mirrored profile. Both components reveal the same relative angle between their movement plane and the rotation axis of the system (see also equation (7.4.6) on page 216 in section 7.4.2). The highest values can be observed for both components in the case of $\Delta T = 60\,\mathrm{K}$, thus in this case the flow particles are affected by the strongest displacement.

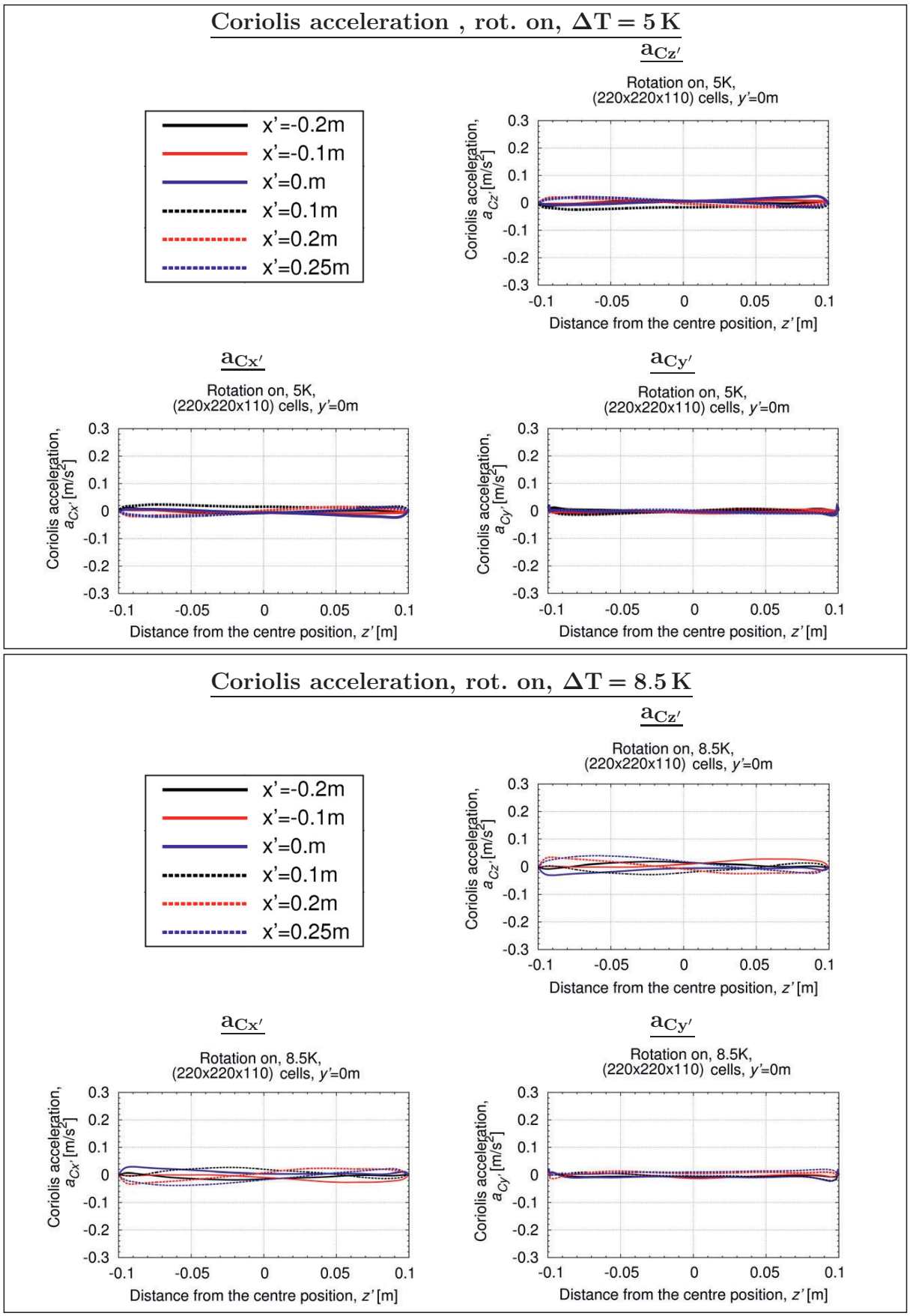

Figure A.12.: Time-averaged profiles of the Coriolis acceleration components. **Top box**: $\Delta T = 5$K. **Bottom box:** $\Delta T = 8.5$K. **Clockwise direction in each box, starting left top:** Legend, $a_{Cz'}$, $a_{Cx'}$ and $a_{Cy'}$. Estimated at $y(y') = 0\,\mathrm{m}$ (centre position) along the vertical axis $z(z')$ at different positions (see the legends in the top left plots).

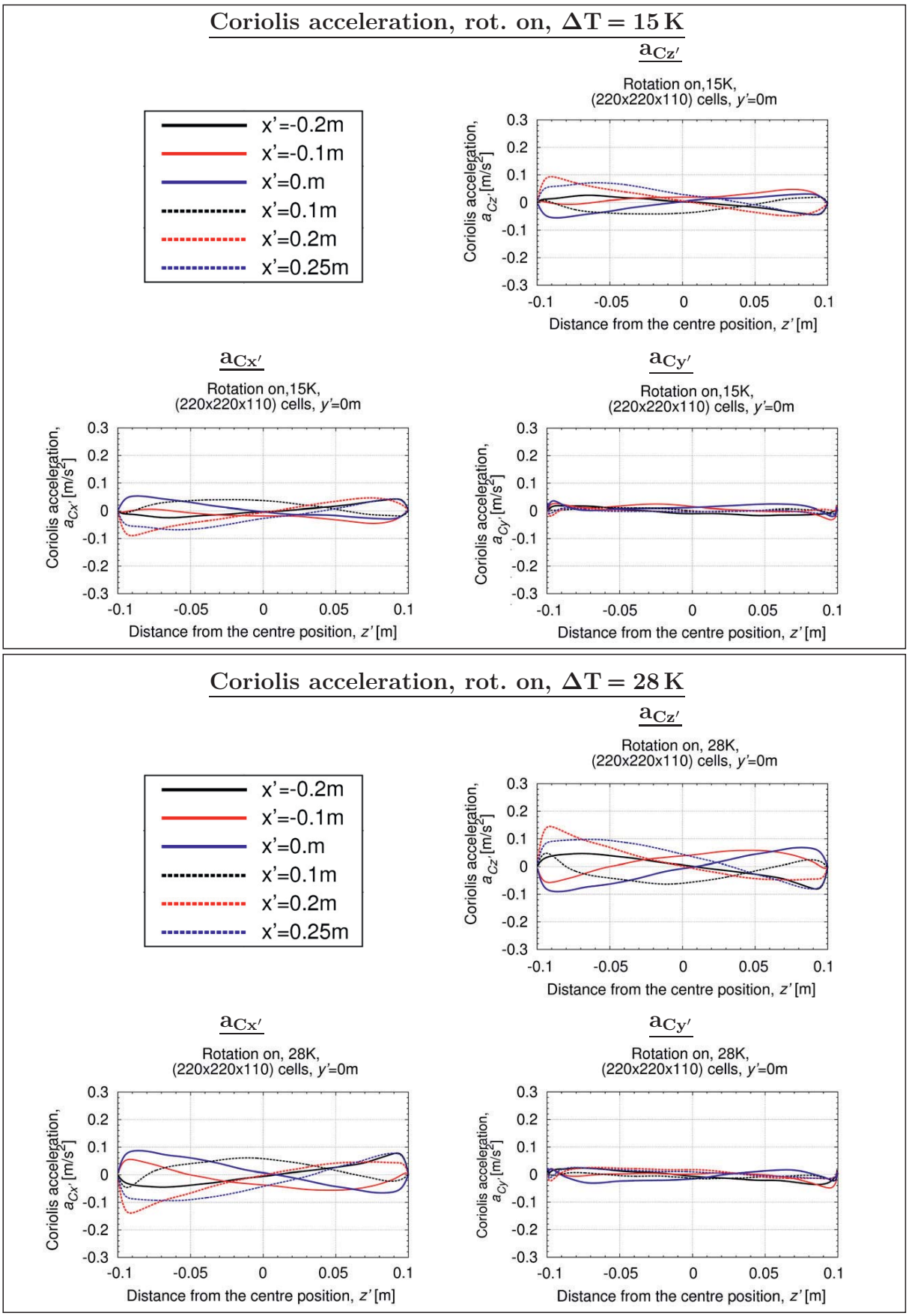

Figure A.13.: Time-averaged profiles of the Coriolis acceleration components. **Top box**: $\Delta T = 15$K. **Bottom box:** $\Delta T = 28$K. **Clockwise direction in each box, starting left top:** Legend, $a_{Cz'}$, $a_{Cx'}$ and $a_{Cy'}$. Estimated at $y(y') = 0\,\mathrm{m}$ (centre position) along the vertical axis $z(z')$ at different positions (see the legends in the top left plots).

A.2.3. Simulation results versus experimental data

A.2.3.1. Visualisation of velocity structures in the simulation and in the experiment

Analogously to chapter 7.1, section 7.7.2, the figures A.14 - A.15 on pages 295 - 296 illustrate the time-averaged 2-dimensional velocity field estimated in the simulation as well as in the experiment (PIV method). For an overview of the estimated region see figure 7.38 on page 254 in chapter 7.1, section 7.7.2. It is not expected, that the results of the simulation reveal exact the same flow structures as the results of the experiment, due to the statistical analysis of the turbulent flow. But the results of both cases show similar tendencies of flow structures. In the non-rotation mode $\mathrm{rot}_{\mathrm{off}}$, large-scale structures as they are typical for a Rayleigh-Bénard configuration can be seen in both studies. It is noteworthy, that the simulation results of $\Delta T = 8.5\,\mathrm{K}$ at plane $x_2 = -0.2\,\mathrm{m}$ display the same main flow directions as in the PIV results. However, the flow structures are not exact at the same positions in both results, which was not expected. As in chapter 7.1 mentioned, the presented results confirm that the turbulence production seems to be higher in case of increasing temperature differences. Smaller spatial scales of flow structures and smaller vortex regions are the result. This relation can be seen in both studies in the same way.

A.2.3.2. Vortex regions estimated in the simulation

The following figures A.16 - A.17 on pages 297 - 298 display complementary to chapter 7, section 7.7.3, the vortex regions in the simulation in the rotation mode $\mathrm{rot}_{\mathrm{on}}$ and the non-rotation mode $\mathrm{rot}_{\mathrm{off}}$ visualised by the criterion Q for $\Delta T = 5\,\mathrm{K}$, $\Delta T = 8.5\,\mathrm{K}$, $\Delta T = 15\,\mathrm{K}$, $\Delta T = 28\,\mathrm{K}$. For the definition of criterion Q and detailed information see chapter 7, section 7.7.3. The criterion Q is only a measurement for the outcome of turbulent structures and not for their cause. Each snapshot in figures A.16 - A.17 show the instantaneous iso-surfaces of criterion Q in the last time step of the simulated process at $t = 400\,\mathrm{s}$ for both modes. The iso-surfaces envelope the regions where Q reaches a particular value. Each snapshot shows the iso-surfaces inside one half of the container. For the exact values of criterion Q it is referred to table 7.8 in chapter 7, section 7.7.3 on page 263. The number of vortex regions is significantly raising with increasing ΔT and an increasing effective Rayleigh number. In both modes appear different frequencies. The vortex structures in the rotation mode $\mathrm{rot}_{\mathrm{on}}$ reveal a significant drift pointing in direction of the x' axis which is distinctive for smaller effective Rayleigh numbers. This drift is caused by the rotational movement of the test case. The form of the vortex structures in the rotation mode $\mathrm{rot}_{\mathrm{on}}$ seem to be more compact and mixed than in case of the non-rotation mode $\mathrm{rot}_{\mathrm{off}}$. The vortexex show a more irregular structure and seemed to become smaller with increasing effective Rayleigh numbers. The structures in the non-rotation mode $\mathrm{rot}_{\mathrm{off}}$ seem to be more smooth and show larger spatial scales.

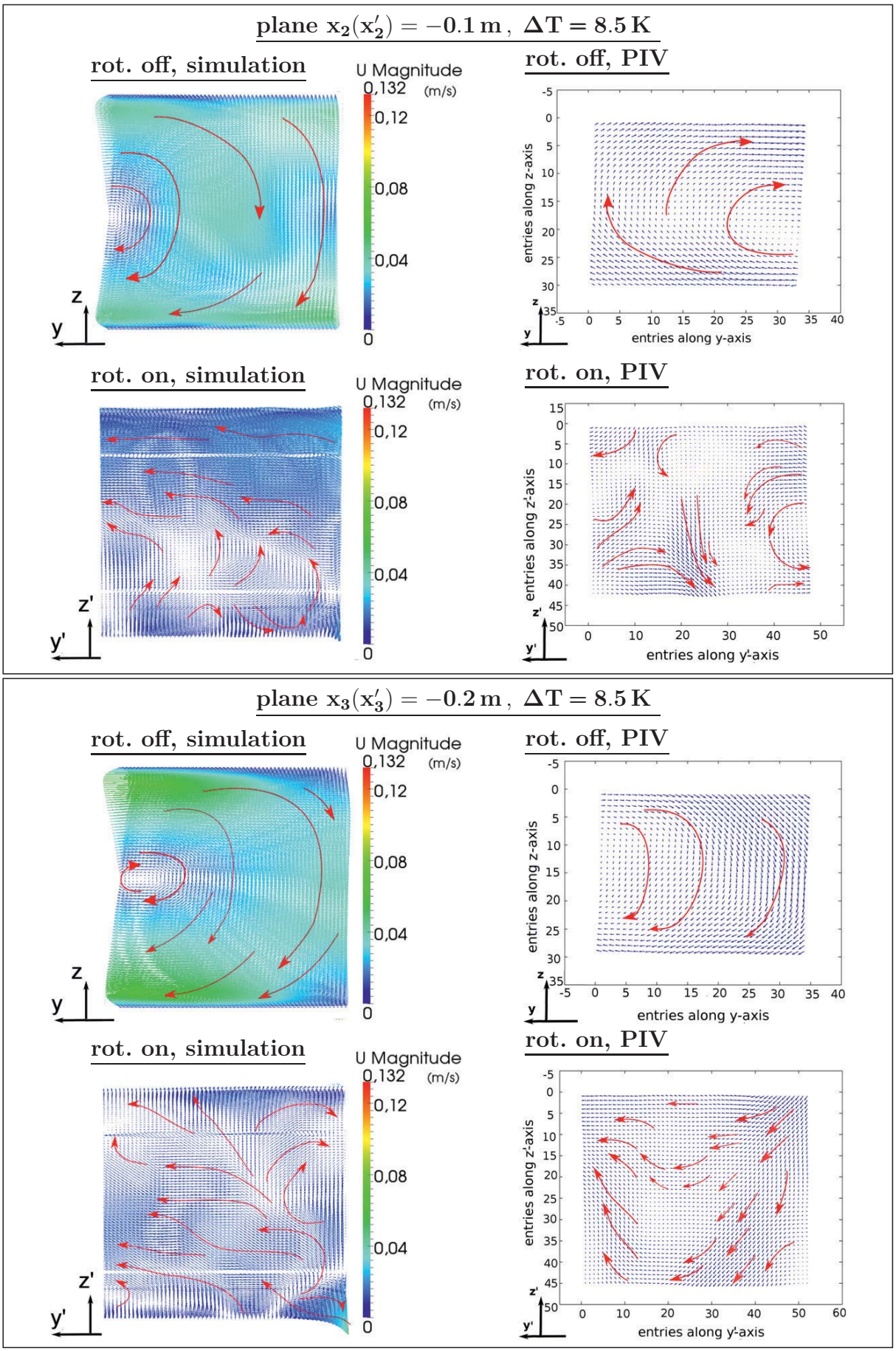

Figure A.14.: Time-averaged 2-dim. velocity field. Simulation vs. experiment (PIV method). $\Delta T = 8.5\,\mathrm{K}$. **Top box:** Plane $x_2(x_2') = -0.1\,\mathrm{m}$. **Bottom box:** Plane $x_3(x_3') = -0.2\,\mathrm{m}$.

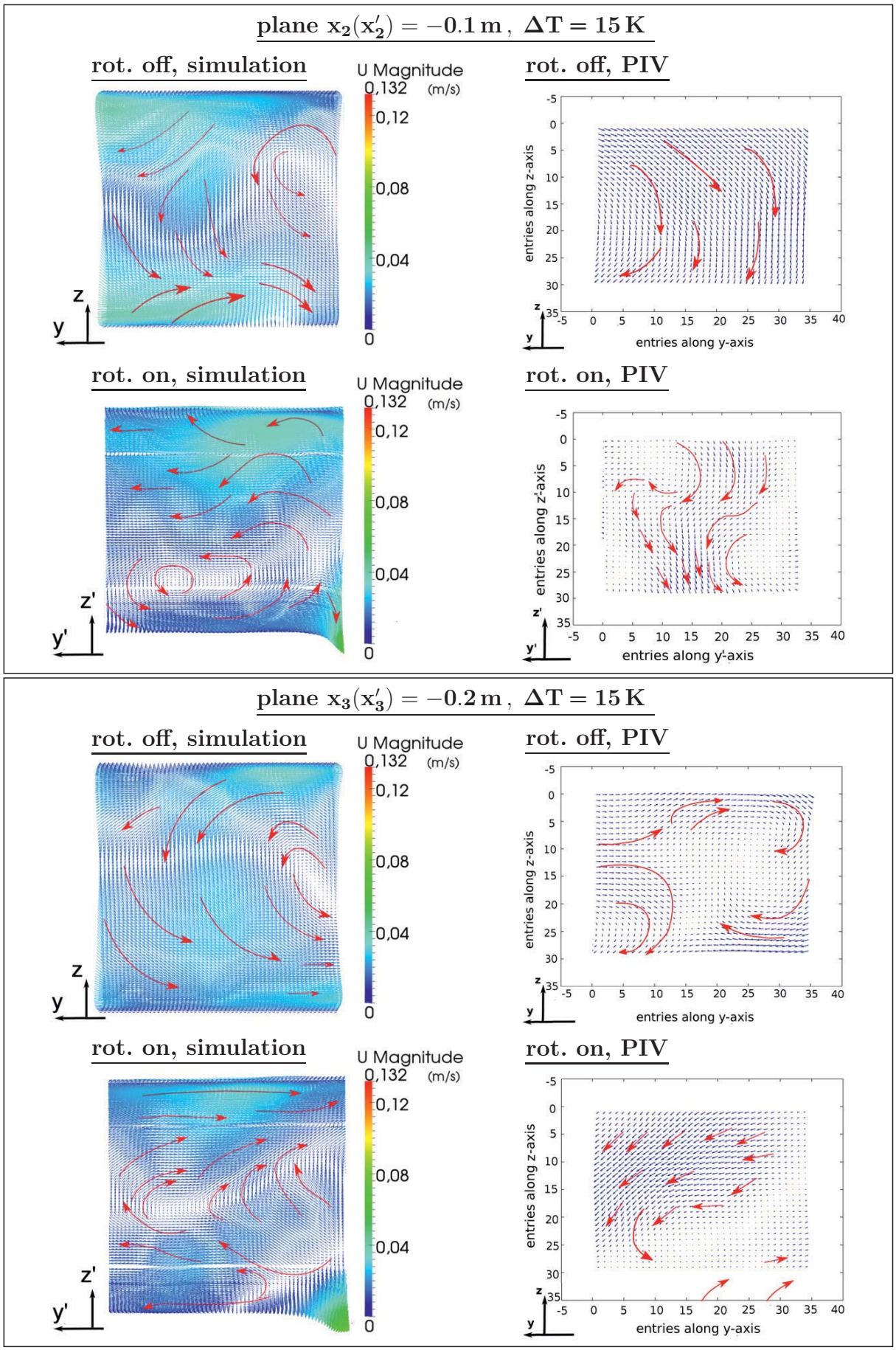

Figure A.15.: Time-averaged 2-dim. velocity field. Simulation vs. experiment (PIV method). $\Delta T = 15\,\mathrm{K}$. **Top box:** Plane $x_2(x_2') = -0.1\,\mathrm{m}$. **Bottom box:** Plane $x_3(x_3') = -0.2\,\mathrm{m}$.

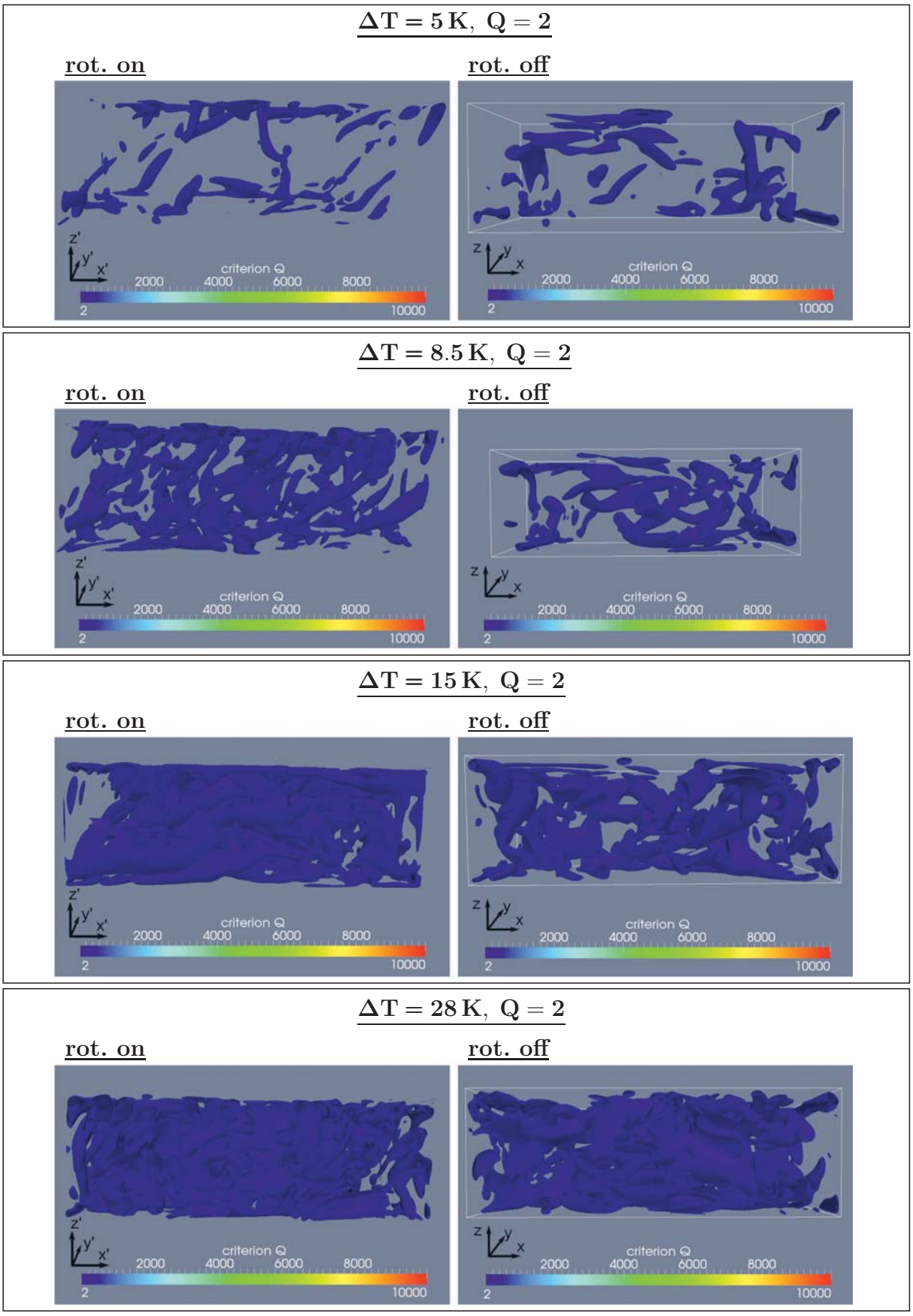

Figure A.16.: Instantaneous vortex structures in the simulation (iso-surfaces of criterion Q), $t = 400\,\mathrm{s}$, $Q = 2$. **Top to bottom:** $\Delta T = 5\mathrm{K}$, $\Delta T = 8.5\mathrm{K}$, $\Delta T = 15\mathrm{K}$, $\Delta T = 28\mathrm{K}$. **Left:** Rotation mode $\mathrm{rot}_{\mathrm{on}}$. **Right:** Non-rotation mode $\mathrm{rot}_{\mathrm{off}}$.

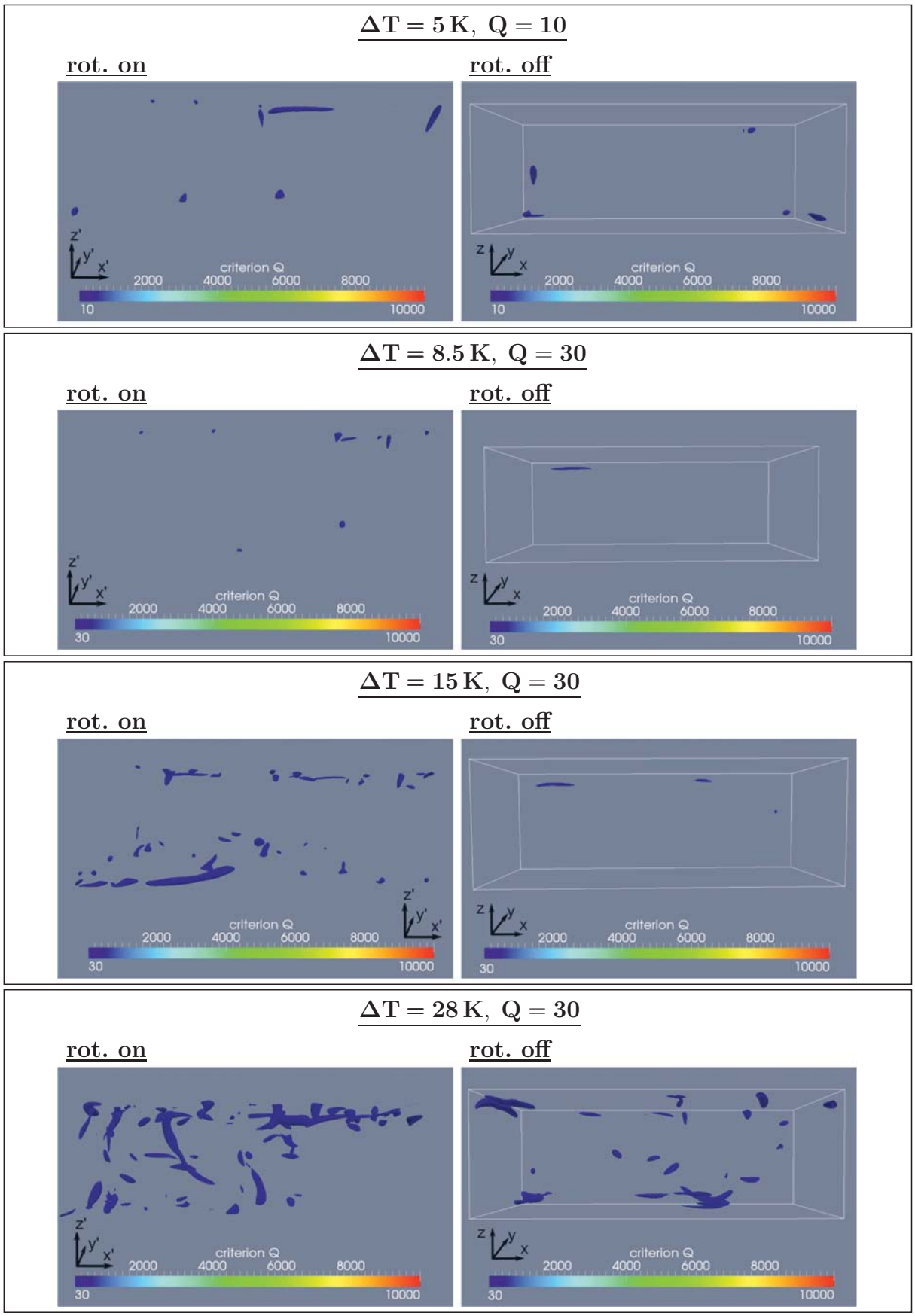

Figure A.17.: Instantaneous vortex structures in the simulation (iso-surfaces of criterion Q), $t = 400\,\mathrm{s}$, $Q = 10$ and $Q = 30$. **Top to bottom:** $\Delta T = 5\mathrm{K}$, $\Delta T = 8.5\mathrm{K}$, $\Delta T = 15\mathrm{K}$, $\Delta T = 28\mathrm{K}$. **Left:** Rotation mode $\mathrm{rot}_{\mathrm{on}}$. **Right:** Non-rotation mode $\mathrm{rot}_{\mathrm{off}}$.

List of Figures

List of Tables

Bibliography

[Ahlers06] Ahlers, G., Brown, E., Araujo, F. F., Funfschilling, D., Grossmann S. and Lohse, D.: *Non-Oberbeck-Boussinesq effects in strongly turbulent Rayleigh-Bénard convection*, Journal of Fluid Mechanics, **569**, pp. 409 - 445, 2006.

[Alonso1967] Alonso, M. and Finn, E. J.: *Fundamental University Physics: Mechanics*, Addison-Wesley Publishing Company, 1th edition, Massachusetts, USA, 1967.

[Amann08] Amann, H. and Escher, J.: *Analysis III*, Birkhäuser Verlag, 2th edition, Basel, Boston, Berlin, 2008.

[Baehr08] Baehr, H. D. and Stephan, K.: *Wärme- und Stoffübertragung*, Springer Verlag, 6th edition, Berlin, Heidelberg, New York, 2008.

[Beghein93a] Beghein, C., Penot, F., Mergui, S. and Allard, F.: *Numerical and experimental evaluation of turbulent models for natural convection simulation in a thermally driven square cavity*, in: Proc. of the ASME Conf., **93-WA/ HT-46**, pp. 1 - 12, 1993.

[Beghein93b] Beghein, C., Allard, F. and Draoui, A.: *Numerical modelling of turbulent convection in a thermally-driven square cavity*, R. A. W. M. Henkes, C. J. Hoogendoorn (Eds.), Turbulent Natural Convection in Enclosures - A Computational and Experimental Benchmark Study, Editions Européennes Thermique et Industrie, Paris, France, pp. 31 - 42, 1993.

[Bénard1900] Bénard, M. H.: *Les tourbillons cellulaires dans une nappe liquide*, Rev. Gén. Sciences Pure Appl., **11**, pp. 1261 - 1271 and pp. 1309 - 1328, 1900.

[Betts00] Betts, P. L., Bokhari I. H.: *Experiments on turbulent natural convection in an enclosed tall cavity*, Int. Journal of Heat and Fluid Flow, **21**, pp. 675 - 683, 2000.

[Bircumshaw1929] Bircumshaw, L. I. and Stott, V. H.: *Viscosity of gases*, Int. critical tables, 5, 1 - 6, McGraw-Hill Book Co., New York, USA, 1929.

[Boussinesq1903] Boussinesq, J.: *Theorie Analytique de la Chaleur,* ***2***, Gauthier-Villars, Paris, France, 1903.

[Bressloff01] Bressloff, N. W.: *A parallel pressure implicit splitting of operators algorithm applied to flows at all speeds*, Int. Journal for numerical methods in fluids, **36**, pp. 497 - 518, 2001.

[Brown08a] Brown, E. and Ahlers, G.: *Rotations and cessations of the large-scale circulation in turbulent Rayleigh-Bénard convection*, Journal of Fluid Mechanics, **568**, pp. 351 - 386, 2008.

[Brown08b] Brown, E. and Ahlers, G.: *Effect of the Earth's Coriolis force on the large-scale circulation of turbulent Rayleigh-Bénard convection*, Physics of Fluids, **18**, pp. 125108-1 - 125108-15, 2008.

[Cebeci1968] Cebeci, T. and Smith, A. M. O.: *Investigation of heat transfer and of suction for tripping boundary layers*, J. Aircraft, **5**, pp. 450 - 454, 1968.

[Churchill1983] Churchill, S. W.: *Free convection around immersed bodies*, in: Heat Exchanger Design Handbook, Hemisphere Publ. Corp., Washington, D.C., 1983.

[Concus1978] Concus, P., Golub, G. H. and O'Leary, D. P.: *Numerical solution of nonlinear elliptic partial differential equations by a generalised conjugate gradient method*, Computing, **19**, pp. 321 - 339, 1978.

[Coriolis1835] Coriolis, G.-G. de: *Mémoire sur les équations du mouvement relatif des systèmes de corps*, Journal de l'École polytechnique, **15**, cahier 24, pp. 142 - 154, 1835.

[Courant1928] Courant, R., Friedrichs, K. and Lewy, H.: *Über die partiellen Differenzengleichungen der mathematischen Physik*, Mathematische Annalen, **100**, pp. 32 - 74, 1928.

[Dafa'Alla1996] Dafa'Alla, A. A. and Betts, P. L.: *Experimental study of turbulent natural convection in a tall air cavity*, Experimental Heat Transfer, **9**, pp. 165 - 194, 1996.

[Dahmen06] Dahmen, W. and Reusken, A.: *Numerik für Ingenieure und Naturwissenschaftler*, Springer Verlag, 1th edition, Berlin, Heidelberg, New York, 2006.

[Deardorff1973] Deardorff, J. W.: *The use of subgrid transport equations in a three - dimensional model of atmospheric turbulence*, Journal of Fluid Engineering, **95**, pp. 429 - 438 , 1973.

[Demirdžić1993] Demirdžić, I., Lilek, Ž. and Perić, M.: *A collocated finite volume method for predicting flows at all speeds*, Int. J. for Numerical Methods in Fluids, **16**, pp. 1029 - 1050, 1993.

[Ebert08] Ebert, A., Resagk, C. and Thess, A.: *Experimental study of temperature distribution and local heat flux for turbulent Rayleigh-Bénard convection of air in a long rectangular enclosure*, Int. Journal of Heat and Mass Transfer, **51**, pp. 4238 - 4248, 2008.

[Erlebacher1992] Erlebacher, G., Hussaini, M. Y., Speziale, C. G. and Zang, T. A.: *Toward the Large-Eddy Simulation of compressible turbulent flows*, Journal of Fluid Mechanics, **238**, pp. 155 - 185, 1992.

[Evonik] Evonik Industries: Technical data sheets of PMMA walls, found on: URL: http://www.plexiglas.de/product/plexiglas/de/produkte/technische-daten/pages/default.aspx (up to date 05.08.2015).

[Faddejew1964] Faddejew, D. K. and Faddejewja, W. N.: *Numerische Methoden der linearen Algebra*, Oldenbourg R. Verlag GmbH, 1th edition, München, Germany, 1964.

[Favre1983] Favre, A.: *Turbulence: space-time statistical properties and behavior in supersonic flows*, Physics of Fluids, **26**, pp. 2851 - 2863, 1983.

[Ferziger02] Ferziger, J. H. and Perić, M.: *Computational Methods for Fluid Dynamics*, Springer Verlag, 3th revised edition, Berlin, Heidelberg, New York, 2002.

[Fischer10] Fischer, G.: *Lineare Algebra*, Vieweg+Teubner Verlag, 17th edition, Wiesbaden, Germany 2010.

[Fletcher1976] Fletscher, R.: *Conjugate gradient methods for indefinite systems*, Lecture notes in mathematics, **506**, pp. 73 - 89, 1976.

[Fröhlich06] Fröhlich, J.: *Large-Eddy Simulation turbulenter Strömungen*, B.G. Teubner Verlag, 1th edition, Wiesbaden, 2006.

[Funfschilling04] Funfschilling, D. and Ahlers, G.: *Plume motion and large scale circulation in a cylindrical Rayleigh-Bénard cell*, Phys. Review Lett., **92**, pp. 194502-1 - 194502-4, 2004.

[Fureby1996] Fureby, C.: *On subgrid scale modeling in Large-Eddy Simulations of compressible fluid flow*, Physics of Fluids, **8**, pp. 1301 - 1311, 1996.

[George1979] George, W. K. Jr. and Capp, S. P.: *A theory for natural convection turbulent boundary layers next to heated vertical surfaces*, Int. Journal of Heat and Mass Transfer, **22**, pp. 813 - 826, 1979.

[Germano1986] Germano, M.: *A proposal for a redefinition of the turbulent stresses in the filtered Navier - Stokes equations*, Physics of Fluids, **29**, pp. 2323 - 2324, 1986.

[Germano1991] Germano, M., Piomelli, U., Moin, P. and Cabot, W. H.: *A dynamic subgrid-scale eddy viscosity model*, Physics of Fluids A, **3**, pp. 1760 - 1765, 1991.

[Gersten1992] Gersten, K., Herwig, H.: *Strömungsmechanik. Grundlagen der Impuls-, Wärme- und Stoffübertragung aus asymptotischer Sicht*, Vieweg-Verlag, 1th edition, Braunschweig/Wiesbaden, 1992.

[Getling1998] Getling, A. V.: *Rayleigh-Bénard convection: Structures and dynamics*, World Scientific Publishing Co., 1th edition, Singapore, 1998.

[Gifford1991] Gifford, W. A.: *Natural convection in a square cavity without the Boussinesq-approximation*, 49th Annual Technical Conference-ANTEC '91, pp. 2448 - 2454, 1991.

[Groll10] Groll, R.: *Computational fluid dynamics*, Lecture notes, Bremen University, Bremen, Germany, 2010.

[Groll10a] Groll, R.: *Modelling turbulent flows*, Lecture notes, Bremen University, Bremen, Germany, 2010.

[Groll10b] Groll, R.: *Thermofluid dynamics*, Lecture notes, Bremen University, Bremen, Germany, 2010.

[Grossmann00] Grossmann, S. and Lohse, D.: *Scaling in thermal convection: a unifying theory*, Journal of Fluid Mechanics, **407**, pp. 27 - 56, 2000.

[Grossmann01] Grossmann, S. and Lohse, D.: *Thermal convection for large Prandtl numbers*, Phys. Rev. Lett., **86**, pp. 3316 - 3319, 2001.

[Herwig1984] Herwig, H.: *Näherungsweise Berücksichtigung des Einflusses variabler Stoffwerte bei der Berechnung ebener laminarer Grenzschichtströmungen um zylindrische Körper*, Forsch. Ing.-Wes., **50**, pp. 160 - 166, 1984.

[Herwig1985] Herwig, H., Wickern, G. and Gersten, K.: *Der Einfluss variabler Stoffwerte auf natürliche laminare Konvektionsströmungen*, Wärme und Stoffübertragung, **19**, pp. 19 - 30, 1985.

[Heuser09] Heuser, H.: *Lehrbuch der Analysis. Teil 1*, Vieweg+Teubner Verlag, 17th edition, Berlin, Heidelberg, New York, 2009.

[Hölling05] Hölling, M. and Herwig, H.: *Asymptotic analysis of the near-wall region of turbulent natural convection flows*, Journal of Fluid Mechanics, **541**, pp. 383 - 397, 2005.

[Hölling06] Hölling, M. and Herwig, H.: *Asymptotic analysis of heat transfer in turbulent Rayleigh-Bénard convection*, Int. Journal of Heat and Mass Transfer, **49**, pp. 1129 - 1136, 2006.

[Horn11] Horn, S., Shishkina, O. and Wagner, C.: *The influence of non-Oberbeck-Boussinesq effects on rotating turbulent Rayleigh-Bénard convection*, Journal of Physics: Conference Series, **318**, section 8, pp. 1 - 5, 2011.

[Hossain12] Hossain, Md. S., Chakravarty, R., Bergstrom, D. J., Samani, M., Chen, X.-B. and Summer, D.: *Vortex structures in three-dimensional turbulent lid-driven cavity flow*, in: Proceedings of the Seventh International Symposium On Turbulence, Heat and Mass Transfer, Palermo, Italy, 24-27 September, 2012, Hanjalić, K., Nagano, Y., Borello, D. and Jarkirlić, S. (Eds.), ICHMT, Begell House Inc., West Redding, USA, pp. 183 - 186, 2012.

[Hunt1988] Hunt, J. C. R., Wary, A. A. and Moin, P.: *Eddies stream and convergence zones in turbulent flows*, Center for Turbulent Research, Proceedings of Summer Programme 1988, pp. 193 - 208, 1988.

[Issa1986] Issa, R. I.: *Solution of the implicitly discretised fluid flow equations by operator-splitting*, Journal of Computational Physics, **62**, pp. 40 - 65, 1986.

[Kenjereš1999] Kenjereš, S. and Hanjalić, K.: *Transient analysis of Rayleigh-Bénard convection with a RANS model*, Int. Journal Heat Fluid Flow, **20**, pp. 329 - 340, 1999.

[King1989] King, K. J.: *Turbulent natural convection in rectangular air cavities*, PhD thesis, Queen Mary and Westfield College, University of London, London, UK, 1989.

[Kosmol1993] Kosmol, P.: *Methoden zur numerischen Behandlung nichtlinearer Gleichungen und Optimierungsaufgaben*, Teubner Verlag, 2nd edition, Stuttgart, Germany, 1993.

[Kosović02] Kosović, B., Pullin, D. I. and Samtaney, R.: *Subgrid-scale modeling for large-eddy simulations of compressible turbulence*, Physics of Fluids, **14**, pp. 1511 - 1522, 2002.

[Kuchling1999] Kuchling, H.: *Taschenbuch der Physik*, Fachbuchverlag Leipzig, 16th edition, Leipzig, Germany, 1999.

[Lankhorst1991] Lankhorst, A. M.: *Laminar and turbulent natural convection in cavities - numerical modelling and experimental validation*, PhD thesis, Technology University of Delft, Delft, The Netherlands, 1991.

[Laurien09] Laurien, E. and Oertel, H.: *Numersiche Strömungsmechanik*, Vieweg+Teubner Verlag, 3th edition, Wiesbaden, Germany, 2009.

[Leonard1974] Leonard, A.: *Energy cascade in Large Eddy Simulations of turbulent fluid flow*, Adv. Geophysics., **18A**, pp. 237 - 248, 1974.

[Lesieur1996] Lesieur, M. and Métais, O.: *New trends in Large-Eddy Simulations of turbulence*, Annu. Rev. Fluid Mech., **28**, pp. 45 - 82, 1996.

[Lilly1992] Lilly, D. K.: *A proposed modification of the Germano sugridscale closure method*, Physics of Fluids A, **4**, pp. 633 - 635, 1992.

[Liu13] Liu, G. R. and Quek, S. S.: *The finite element method - a practical course*, Butterworth-Heinemann, 1th edition, Oxford, UK, 2013.

[Marek12] Marek, R. and Nitsche, K.: *Praxis der Wärmeübertragung: Grundlagen - Anwendungen - Übungsaufgaben*, Carl Hanser Verlag GmbH & Co, 3th edition, München, Germany, 2012.

[Maystrenko07] Maystrenko, A., Resagk, C. and Thess, A.: *Structure of the thermal boundary layer for turbulent Rayleigh-Bénard convection of air in a long rectangular enclosure*, Physical Review E, **75**, pp. 066303-1 - 066303-11, 2007.

[Mergui1993] Mergui, S., Penot, F. and Tuhault, J. L.: *Experimental natural convection in an air-filled square cavity at* $Ra = 1.7 \times 10^9$, R. A. W. M. Henkes, C. J. Hoogendoorn (Eds.), Turbulent Natural Convection in Enclosures - A Computational and Experimental Benchmark Study, in: Proceedings of the Eurotherm Seminar no 22, March 25-27, 1993,

Delft, the Netherlands, Editions Européennes Thermique et Industrie, Paris, France, pp. 97 - 108, 1993.

[Montgomery1947] Montgomery, R. B.: *Viscosity and thermal conductivity of air and diffusivity of water vapor in air,* Journal of Meteorology, **4**, pp. 193 - 196, 1947.

[Mori02] Mori, N. and Chang, K. - A.: *Introduction to MPIV - PIV toolbox in MATLAB® - version 0.965*, 2002, can be found on: URL: http://www.oceanwave.jp/softwares/mpiv/index.php?FrontPage (up to date 05.08.2015).

[Navier1823] Navier, M.: *Mémoire sur les lois du mouvement des fluides*, Mem. Acad. R. Sci. Paris, **6**, pp. 389 - 440, 1823.

[Noll1993] Noll, B.: *Numerische Strömungsmeachanik*, Springer Verlag, 1th edition, Berlin, Heidelberg, New York, 1993.

[Nolting13] Nolting, W.: *Grundkurs Theoretische Physik 1, Klassische Mechanik*, Springer Spektrum Verlag, 10th edition, Berlin, Heidelberg, New York, 2013.

[Oberbeck1879] Oberbeck, A.: *Über die Wärmeleitung der Flüssigkeiten bei Berücksichtigung der Strömungen infolge von Temperaturdifferenzen*, Annalen der Physik, **243**, pp. 271 - 292, 1879.

[Oertel06] Oertel, H., Böhle, M. and Dohrmann, U.: *Strömungsmechanik,* Vieweg Verlag, 4th edition, Wiesbaden, Germany, 2006.

[Okong'O 00] Okong'O, N., Knight, D. D. and Zhou, G.: *Large-Eddy Simulations using an unstructured grid compressible Navier-Stokes algorithm,* Int. Journal of Computational Fluid Dynamics, **13**, issue 4, pp. 303 - 326, 2000.

[OpenFOAMa] Information on the open-source simulation software tool *OpenFOAM®* can be found on: URL: http://www.openfoam.org/ (up to date 05.08.2015).

[OpenFOAMb] Wiki of the open-source simulation software tool *OpenFOAM®* can be found on: URL: https://openfoamwiki.net/index.php/See_the_MRF_development (up to date 05.07.2015).

[Pantakar1980] Pantakar, S. V.: *Numerical heat transfer and fluid flow*, McGraw-Hill Book Company, 1th edition, Washington, New York, London, 1980.

[Poel13] Poel, E. P., van der, Stevens, R. J. A. M. and Lohse, D.: *Comparision between two- and three dimensional Rayleigh-Bénard convection*, Journal of Fluid Mechanics, **736**, pp. 177 - 194, 2013.

[Pohlhausen1921] Pohlhausen, K.: *Zur näherungsweisen Integration der Differentialgleichung der laminaren Grenzschicht*, ZAMM - Zeitschrift für angewandte Mathematik und Mechanik, **1**, pp. 252 - 268, 1921.

[Pope00] Pope, S. B.: *Turbulent flows*, Cambridge University Press, 1th edition, Cambridge, UK, 2000.

[Rayleigh1916] Rayleigh, Lord : *On convection currents in a horizontal layer of fluid, when the higher temperature is on the under side*, Phil. Mag. Series 6, **32**, pp. 529 - 546, 1916.

[Reeuwijk08a] Reeuwijk, M. van, Jonker, H. J. J. and Hanjalić, K.: *Wind and boundary layers in Rayleigh-Bénard convection. I. Analysis and modeling*, Phys. Rev. E 77, pp. 036311-1 - 036311-15, 2008.

[Reeuwijk08b] Reeuwijk, M. van, Jonker, H. J. J. and Hanjalić, K.: *Wind and boundary layers in Rayleigh-Bénard convection. II. Boundary layer character and scaling*, Phys. Rev. E 77, pp. 036312-1 - 036312-10, 2008.

[Richard11] Richard, H. A. and Sander, M.: *Technische Mechanik. Dynamik: Grundlagen - effektiv und anwendungsnah*, Vieweg+Teubner Verlag, 2th edition, Wiesbaden, Germany, 2011.

[Schlichting06] Schlichting, H. and Gersten, K.: *Boundary Layer Theory*, McGraw-Hill, 10th edition, New York, USA, 2006.

[Schlünder1970] Schlünder, E. U.: *Über eine zusammenfassende Darstellung der Grundgesetze des konvektiven Wärmeübergangs*, Verfahrenstechnik 4., pp. 11 - 16, 1970.

[Seiter1995] Seiter, C.: *Numerische Simulation turbulenter Auftriebsströmungen in horizontalen Kanälen*, Dissertation, Institut für Reaktorsicherheit, Forschungszentrum Karlsruhe Gmbh, Karlsruhe, Germany, 1995, can be found on:
URL: http://bibliothek.fzk.de/zb/berichte/FZKA5505.pdf
(up to date 05.08.2015).

[Sergent03] Sergent, A., Joubert, P. and Le Quéré, P.: *Development of a local subgrid diffusivity model for Large-Eddy simulation of buoyancy driven flows: Application to a square differentally heated cavity*, Numerical Heat Transfer, Part A: Applications, **44**, pp. 789 - 810, 2003.

[Shishkina06] Shishkina, O. and Wagner, C.: *Analysis of thermal dissipation rates in turbulent Rayleigh-Bénard convection*, Journal of Fluid Mechanics, **546**, pp. 51 - 60, 2006.

[Shishkina08] Shishkina, O. and Wagner, C.: *Analysis of sheet-like thermal plumes in turbulent Rayleigh-Bénard convection*, Journal of Fluid Mechanics, **599**, pp. 383 - 404, 2008.

[Shishkina09] Shishkina, O. and Thess, A: *Mean temperature profiles in turbulent Rayleigh-Bénard convection of water*, Journal of Fluid Mechanics, **633**, pp. 449 - 460, 2009.

[Silano10] Silano, G., Sreenivasan, K. R. and Verzicco, R.: *Numerical simulations of Rayleigh-Bénard convection for Prandtl numbers between* 10^{-1} *and* 10^4 *and Rayleigh numbers between* 10^5 *and* 10^9, Journal of Fluid Mechanics, **662**, pp. 409 - 446, 2010.

[Smagorinsky1963] Smagorinsky, J.: *General circulation experiments with the primitive equations*, Monthly weather review, **91**, no. 3, pp. 99 - 164, 1963.

[Spurk07] Spurk, J. H. and Aksel, N.: *Strömungslehre*, Springer Verlag, 7th edition, Berlin, Heidelberg, New York, 2007.

[Stevens13] Stevens, R. J. A. M., Poel, E. P. van der, Grossmann, S. and Lohse, D.: *The unifying theory of scaling in thermal convection: the updated prefactors*, Journal of Fluid Mechanics, **730**, pp. 295 - 308, 2013.

[Stokes1845] Stokes, Sir G. G.: *On the theories of the internal friction of fluids in motion*, Trans. Cambridge Phil. SOC., **8**, pp. 287 - 305, 1845.

[Sutherland1893] Sutherland, W.: *The viscosity of gases and molecular force*, Philosophical Magazine Series 5, **36**, pp. 507 - 531, 1893.

[Tian00a] Tian, Y. S. and Karayiannis, T. G.: *Low turbulence natural convection in an air filled square cavity, Part I: the thermal and fluid flow fields*, Int. Journal of Heat and Mass Transfer, **43**, pp. 849 - 866, 2000.

[Tian00b] Tian, Y. S. and Karayiannis, T. G.: *Low turbulence natural convection in an air filled square cavity, Part II: the turbulence quantities*, Int. Journal of Heat and Mass Transfer, **43**, pp. 867 - 884, 2000.

[VDI06] VDI-Gesellschaft Verfahrenstechnik und Chemieingenieurwesen: *VDI-Wärmeatlas: Berechnungsblätter für den Wärmeübergang*, VDI-Verlag GmbH, 10th edition, Düsseldorf, Germany, 2006.

[Velarde1980] Velarde, M. G. and Normand, C.: *Convection*, Scientific American, **243**, pp. 92 - 108, 1980.

[Versteegh1998] Versteegh, T. A. M. and Nieuwstadt, F. T. M.: *A direct numerical simulation of natural convection between two infinite vertical differentially heated walls scaling laws and wall functions*, Int. Journal of Heat and Mass Transfer, **42**, pp. 3673 - 3693, 1998.

[Weiss11] Weiss, S. and Ahlers, G.: *Turbulent Rayleigh-Bénard convection in a cylindrical container with aspect ratio* $\Gamma = 0.5$ *and Prandtl number* $Pr = 4.38$, Journal of Fluid Mechanics, **676**, pp. 5 - 40, 2011.

[White1991] White, F. M.: *Viscous Fluid Flow*, Mcgraw-Hill Inc., 2th edition, New York, USA, 1991.

[Wu1991] Wu, X. Z. and Libchaber, A.: *Non-Boussinesq effects in free thermal convection*, Physical Review A, **43**, pp. 2833 - 2839, 1991.

[ZARM] Center of applied space technology and microgravity (ZARM), URL: http://www.zarm.uni-bremen.de/
(up to date 05.08.2015).

[Zhang1997] Zhang, J., Childress, S. and Libchaber, A.: *Non-Boussinesq effect: Thermal convection with broken symmetry*, Physics of Fluids, **9**, pp. 1034 - 1042, 1997.

[Ziai1983] Ziai, S.: *Turbulent natural convection in a large rectangular air cavity*, PhD thesis, Queen Mary and Westfield College, University of London, London, UK, 1983.

[Zimmermann12] Zimmermann, C. and Groll, R.: *Modelling turbulent heat transfer of a Rayleigh-Bénard Problem with compressible Large-Eddy Simulation*, in: Proceedings of the Seventh International Symposium On Turbulence, Heat and Mass Transfer, Palermo, Italy, 24-27 September, 2012, Hanjalić, K., Nagano, Y., Borello, D. and Jarkirlić, S. (Eds.), ICHMT, Begell House Inc., West Redding, USA, pp. 615 - 622, 2012.

[Zimmermann14a] Zimmermann, C. and Groll, R.: *Modelling turbulent heat transfer in a natural convection flow*, Journal of Applied Mathematics and Physics, **2**, pp. 662 - 670, 2014.

[Zimmermann14b] Zimmermann, C. and Groll, R.: *Experimental and numerical investigation of a Rayleigh-Bénard convection affected by Coriolis force*, Journal of Flow Control, Measurement & Visualization, **2**, pp. 165 - 172, 2014.

[Zimmermann15] Zimmermann, C. and Groll, R.: *Computational investigation of thermal boundary layers in a turbulent Rayleigh - Bénard problem*, Int. J. Heat Fluid Flow, **54**, pp. 276 - 291, 2015.